P. Thambidurai
T. N. Singh *Editors*

Landslides: Detection, Prediction and Monitoring

Technological Developments

Springer

Landslides: Detection, Prediction and Monitoring

P. Thambidurai · T. N. Singh
Editors

Landslides: Detection, Prediction and Monitoring

Technological Developments

Springer

Editors
P. Thambidurai
Department of Coastal Disaster Management, School of Physical Chemical and Applied Sciences
Pondicherry University
Port Blair, India

T. N. Singh
Indian Institute of Technology Patna
Bihta, Bihar, India

ISBN 978-3-031-23858-1 ISBN 978-3-031-23859-8 (eBook)
https://doi.org/10.1007/978-3-031-23859-8

This Springer imprint is published by the registered company Springer Nature Switzerland AG
The registered company address is: Gewerbestrasse 11, 6330 Cham, Switzerland

Dedicated to
Dr. Kalavathi Thambidurai
IIT Bombay

Preface

In the past few decades, the world witnessed several episodes of severe landslides. Accordingly, the studies of landslides have significantly increased in scope. We all know that landslides represent a significant threat to human life, properties, infrastructure, and natural environments, mostly in the mountainous regions. Extensive and in-depth research projects have been launched mainly on developing different technologies for detecting, predicting, and monitoring landslides. Many advanced technological tools have evolved the opportunities to apply innovative techniques to the different stages of landslide investigations. Indeed, there are challenges in bringing an effective system of landslide mitigation to various levels of development. New technology adaptation must be used to support the investigations on slope failure and related matters, particularly in detection, monitoring, and predictions. Knowledge dissemination will hopefully prove helpful in mitigating the landslide hazards, once these have occurred. Also, knowledge could be gathered from different professionals both at the grassroots levels and at the levels of imparting the higher-level technology to scientists, operators, governmental bodies, and institutions. The seed for this edited volume was sown during our research interaction with a friend at Michigan University, USA. So, we have brought out this book entitled "*Landslides: Detection, Prediction and Monitoring—Technological Developments*," a scientific volume drawn from different fields of technology in the landslide research arena. This volume is an exceptionally collective enterprise, and it owes its existence the cumulative knowledge of all its contributors.

On the one hand, it is impossible to examine the real hazards for the effective risk mitigation of landslide issues. On the other, sound technologies must be employed the right way to address, evaluate, and understand the output, which provides pathways to finding solutions benefitting society. Also, experts, based on the scientific process,

should closely cooperate with policymakers for possible adaptation. We strongly feel that this volume might be helpful to those, who want to dedicate their research time to Landslide Science and Engineering for purposes of finding and executing solutions.

Andamans, India — P. Thambidurai
Patna, India — T. N. Singh

Acknowledgments

The editors are thankful to all the authors for contributing their chapters to this book, and for their unfailing commitment and cooperation.

We sincerely thank Ms. Margaret Deignan, Senior Publishing Editor, Geography and Sustainability Research, Springer-Nature, for accepting our proposal. The editors also acknowledge the entire publishing team.

We express our heartfelt thanks to Prof. Anil Kumar Dikshit, Environmental Science & Engineering Department, Indian Institute of Technology Bombay, for his remarkable and untiring support and encouragement since the very beginning of this project.

Introduction

Technological development has been tremendously supportive of the study of landslide sciences. Different technologies are applied to understand the Earth's processes and phenomena to reduce landslide disasters and help improve its mitigation, management, preparedness, etc. Indeed, investigation and instrumentation play a fundamental role in understanding landslide mechanics. Their ability and effectiveness in scientific study and engineering applications have prevented and controlled landslide events. The landslide features frequently differ according to the geo-environmental settings and characteristics of the terrain. Also, the measurement parameters, analysis methodology, classification, and monitoring parameters are quietly changing with time. Computational participation in all the science and engineering domains is an unavoidable tool. An adequate infrastructure of physical models to characterize the material of geotechnical properties is more important concerning understanding the main triggering factors similar to rainfall and earthquake events. Numerical modelling is used to address slope failure and its magnitude with handling extensive datasets. Also, data integration in relation to data observation is a tough task in computational modeling, which is very important and getting more attention nowadays. Geospatial technology is unparalleled in acquiring knowledge of the Earth's processes through different advanced remote sensing, like the application of multi-sensor satellite data and airborne and ground-based techniques utilized for the landslide sciences. Optical and microwave imaging systems and laser scanning are used for more accurate rainfall measurements and terrain movements. Remote sensing techniques cover almost all kinds of ground investigations in landslide research to make inventory and database mapping, hazard assessment, monitoring, and prediction of landslides. The early warning system is engineering wonders in the technological development, which ishelping to understand the regional scale and to assess the probability of landslide occurrence over a priori-defined warning zone.

Monitoring and evolution of an unstable slope is a complex process; however, recent technologies can provide important information to achieve vast knowledge and better understanding. A real-time monitoring system is an active process for detecting, monitoring, and predicting landslide events.

The integration of the observed landslide displacements, soil properties, and rainfall measurement into predictive models is the common approach toward the prediction of landslides. Here, the technological developments offer new chances to record more information from the field. While on one side, remote sensing plays a growing role in landslide monitoring, the ground-based (geodetic, extensometer, global navigation satellite system techniques) and subsurface-based methods (geotechnical and hydrogeological sensors in boreholes, ground-penetrating radar, microseismic sensors) are, on the other hand, still fundamental to give locally precise in-situ observations. An important trend can be noticed in the development of smart sensor networks, distributed sensor networks (such as MEMS—micro-electro-mechanical systems), and general low-cost solutions. These are of paramount relevance for the implementation in developing countries, which face the budgetary limitations. In landslide risk assessment, the technology contributes indirectly, by providing information about predisposing factors (geomorphology, topography, geology, land cover, and hydrogeology), triggering factors (mainly rainfall and earthquakes), and for model validation. Here, remote sensing techniques have become more and more important in the general context of spatial geo-information, especially for the assessment at the regional level. Accordingly, the support of technology in strategic risk reduction is at both non-structural and structural measures. In the former, it contributes to the preparation of land use plans and to early-warning systems, which can be considered as risk mitigation tool. Also, the development of decision support systems is important to this field. In the latter, the technology is strictly related to the design and construction of physical protection barriers. Due to their peculiarity, the structural measures are out of the scope of this book. The last subdomain where up-to-date technology has allowed an important step forward, especially with satellite remotely sensed data, is landslide mapping for inventory and database creation and update.

There are 20 chapters in this book, which are as follows:

- Chapter 1 (Modern Methods of Rock Mass Characterisation and Rockfall Monitoring: A Review) reviews various modern methods to characterise rock masses and to monitor rock falls and rock slope stability.
- Chapter 2 (Rock Mass Characterization and Rockfall Monitoring: Traditional Approaches) presents traditional methods can be used within the monitoring demanding sites such as mountainous areas, deep gorges with steep slopes, or even active landslide sites. and bring high-quality monitoring results, sometimes with higher precision than modern state-of-art methods. Traditional methods have also been compared against newly introduced, modern state-of-art methods discussed in Chapter 1.
- Chapter 3 (Criteria of the Prehistoric Rock Avalanches Identification and Discrimination) describes the basic criteria allowing well-grounded identification of the prehistoric rock avalanches and distinguishing their deposits from moraines and debris flow fans. They are exemplified by case studies from Central Asia and the Himalayas.

- Chapter 4 (Stability Assessment of Markundi Hills Using Q-slope, SMR and Simulation Tools) presents various methods to assess and curtain the instability of the sandstone cut slope of the Markundi Hills in the district of Sonbhadra, Uttar Pradesh, India.
- Chapter 5 (Geotechnical Investigation of Landslide in Ooty, India) investigates the geotechnical approach for five locations at Gandhi Nagar, a spot in Ooty city in the Nilgiris district of Tamil Nadu is one of the critical sites for frequent landslides. Several limit equilibrium methods such as the Ordinary Swedish Method of Slices, Morgenstern-Price, Janbu, Bishop, and Spencer were utilized for stability analysis.
- Chapter 6 (Geomechanical and Kinematic Stability Analysis of Unstable Slopes (Near 9th km Stone) on Palani—Kodaikkanal Ghat Section in Tamil Nadu) presents a study in the affected area of Kodaikanal, a famous hill town in Tamil Nadu, indicates ten unstable slopes, of which seven numbers are rock slides and three numbers are soil slides. The most commonly adopted remedial measure for steep cut slopes, i.e., altering the slope geometry to a stable angle for soil slopes, has been recommended.
- Chapter 7 (Geological and Geotechnical Studies of Nungkao Landslide Along Imphal-Jiribam National Highway, NH-37, Manipur, India) examines current geotechnical state the rock mass and the locations of potential failures in the Imphal Jiribum national highway of (NH-37) in Manipur. Based on study, specific preventive measures are suggested to improve slope stability accordingly.
- Chapter 8 (Stability Assessment of Lateritic Soil Slope Along NH-66, Ratnagiri Maharashtra, India) aims to generate an understanding of the vulnerability status of the soil slope and remediate it for long-term stability for National Highway 66, linking Mumbai to Goa, which has been affected by persistent slope stability problems across the Ratnagiri district. A two-stage stabilization process has been proposed.
- Chapter 9 (Rockfall Hazard: A Comprehensive Review of Current Mitigation Practices) discusses the kinematics of a rockfall, which forms the framework for the selection of mitigation strategies. Various mitigation strategies used to arrest or divert the falling rock and reduce the economic damage and loss of lives in mountainous regions has been discussed in details.
- Chapter 10 (Debris Flow Hazard in India: Current Status, Research Trends, and Emerging Challenges) attempts to present a detailed description of the composition, classification, causes, and characteristics of debris flow. The major triggering factors responsible for occurrences of debris flows in India and the status of debris flow research in India has also been discussed. According to this study, debris flow constitutes the main reason for a destructive disaster costing the loss of many lives and a lot of properties every year. Debris flow hazard-vulnerability-risk assessment for its effective management is the need of this hour in the Indian context.
- Chapter 11 (Forewarning System for Rainfall-Induced Landslide—A Laboratory Prototype Model) discusses rainfall-induced slope failure mechanism prototype and validation via laboratory experiment. The study showed that the forewarning

system model is effective and could be adapted as a warning system for landslides in mountainous regions.

- Chapter 12 (Study and Instrumental Monitoring of Landslides at the "Russkie Gorki" Site in the Mzymta River Valley, Sochi Region, Russia) presents the case study on the landslide site called "Russkie Gorki" situated in the valley of the Mzymta left tributary in Russia. Here, the Instrumental monitoring systems such as inclinometers, extensometers, piezometers, and pressure sensors were installed. The instrumental monitoring technique has been found to be effective for the detection of real-time landslide scenario at this site.
- Chapter 13 (Application of Scoops3D and GIS for Assessing Landslide Hazard in Trung Chai Commune, Sapa, Vietnam) presents the results of a landslide hazard assessment due to rainfall using a physically-based Scoops3D model in the Trung Chai commune, Sapa district in Vietnam. Such assessment allowed the development of solutions to enhance the prediction quality of future studies.
- Chapter 14 (Landslide Susceptibility Assessment Using Frequency Ratio Model in Turung Mamring, South District of Sikkim, India) focuses on preparing a landslide susceptibility zonation (LSZ) map for Sikkim state situated in north eastern India, using geospatial technology and statistical analyses. The final LSZ map has been found useful for landslide hazard prevention, proper infrastructure planning, and geo-environmental development.
- Chapter 15 (Mapping of Annual Ground Displacement Using Remote Sensing Methods for Critical Slopes Along the Bhagirathi River in Uttarakhand, India) presents a study in Uttarakhand, India, where two slopes at prime locations, namely Zero Bridge and Chainage 1.60 km from the Zero Bridge, have been studied for the magnitude of displacements using synthetic aperture radar (SAR) microwave data and LISS IV optical data over a selected time period.
- Chapter 16 (Landslides Inventory of Active Ramgarh Thrust Zone Through Image Processing and GIS Techniques in Sikkim, India) demonstrates the application of remote sensing techniques in help identifying the landslide occurrence and potential area in the active thrust zone in Ramgarh region of Sikkim.
- Chapter 17 (Landslide Susceptibility Zonation Mapping Using Frequency Ratio, Information Value Model, and Logistic Regression Model: A Case Study of Kohima District in Nagaland, India) discusses a study, where frequency ratio (FR), Information Value Model (IVM), and Logistic Regression (LR) model are used to develop a landslide susceptibility map of Kohima District, Nagaland, using GIS spatial analysis techniques. A total of 356-landslide locations were identified.
- Chapter 18 (Unmanned Aerial Vehicles Technology for Slope Hazard Assessment, Monitoring, and Post Failure Management) elaborates on the advantages of using UAV to acquire data and a thorough assessment, based on resolution (temporal and spatial), operation cost, type of data acquired, deployment of operation, and limitations, has been presented.
- Chapter 19 (Landslide Hazard Assessment Using Machine Learning and GIS) presents the research work aimed to predict landslide hazard zones in Ramban area of Jammu & Kashmir, India using spatial analysis by applying multi-criteria analysis methods and machine learning-based computation technologies.

- Chapter 20 (Social and Economic Impacts of Kotropi Landslide on National Highways of Himalayas—A Case Study) reveals the social and economic impacts of the 2017 Kotropi slope failure in Himanchal Pradesh, India.

We hope the book shall be of immense use to teachers, students, researchers, scientists, engineers, and decision makers. Enjoy the book…Any feedback or suggestion is welcome.

P. Thambidurai

Contents

Editors and Contributors

About the Editors

Dr. P. Thambidurai is an Assistant Professor in the Department of Coastal Disaster Management at Pondicherry University—Port Blair Campus, Andaman and Nicobar Islands, India. He received his Ph.D. in Hydrogeology from the Department of Earth Sciences, Indian Institute of Technology Bombay, India and *Gian Maria Zuppi* scholarship for high-achieving in research in the international student category, awarded by the University of Venice during his doctoral degree. He completed his graduate and post-graduate degrees from Periyar University, Salem, India. He joined Amrita Vishwa Vidyapeetham, Kerala as a *Research Associate* after finishing his Ph.D. in 2015 and then, served there as an *Assistant Professor* till 2018. He has intensive field and consultancy experiences in Geo Technical Mining Solution, Dharmapuri, Tamil Nadu, India.

He has vast field experience in hydrogeology, where he contributed to building the national level policy called *Revitalization of Rivers in India Draft Recommendation—The Fundamentals* to improve the groundwater and surface water resources. This River policy has been adopted by Government of India—Ministry of Environment, Forest & Climate Change and Jal Sakthi to Rejuvenate 13 major rivers in India. He is intensively involving on landslide simulation research. He has published about 20 scientific articles in international journals, conference proceedings, and book chapters.

Dr. T. N. Singh is presently the Director of Indian Institute of Technology Patna, India. Prior to IIT Patna, Prof. Singh was Vice- Chancellor of Mahatma Gandhi Kashi Vidhyapith, Varanasi.

He has published more than 360 journals papers and 160 conference proceeding. He has also published more than dozen edited books. He has received several national awards also. Prof. Singh guided more than 45 Ph.D. students in various field like slope stability, blasting tunnelling, rock-fall protection, climatic change, etc.

Contributors

R. Aravinth Institute of Environment Education and Research, Bharathi Vidyapeeth University, Katraj-Dhanakwadi, Pune, Maharashtra, India

Manoj K. Arora BML Munjal University, Gurgaon, India

I. V. Averin "Enginernaya Geologiya" Ltd., Moscow, Russia

Iftikhar Hussain Beigh Department of Civil Engineering, National Institute of Technology, Srinagar, India

Ramesh Murlidhar Bhatawdekar Department of Mining Engineering, Indian Institute of Technology Kharagpur, Kharagpur, West Bengal, India;
Geotropik—Centre of Tropical Geoengineering, Department of Civil Engineering, Universiti Teknologi Malaysia, Johor Bahru, Johor, Malaysia

Riya Bhowmik Indian Institute of Technology, Jammu, Jammu and Kashmir, India

Prakash Biswakarma University School of Environment Management, Guru Gobind Singh Indraprastha University, New Delhi, India

Jan Blahůt Department of Engineering Geology, Institute of Rock Structure and Mechanics, Czech Academy of Sciences, V Holešovičkách 94/41, Prague, Czech Republic

R. Chandra Devi Department of Civil Engineering, Sri Krishna College of Engineering and Technology, Coimbatore, India

Rajesh Kumar Dash Geo-Hazard Risk Reduction Group, CSIR-Central Building Research Institute, Roorkee, Uttarakhand, India

P. Dinesh Department of Civil Engineering, National Institute of Technology Silchar, Silchar, India

I. K. Fomenko Ordzhonikidze Russian State Geological Prospecting University (MGRI), Moscow, Russia

Snehasish Ghosh Earthquake Research Cell & Department of Civil Engineering, College of Engineering and Technology, Faculty of Engineering and Technology, SRM Institute of Science and Technology, Kattankulathur, Kanchipuram, Chennai, India

G. Gowrisankar Divecha Centre for Climate Change, Indian Institute of Science, Bangalore, India;
Department of Geology, Anna University, Chennai, India

Neha Gupta Department of Earthquake Science and Engineering, Indian Institute of Technology Roorkee, Roorkee, India

Amit Jaiswal Department of Mining Engineering, Indian Institute of Technology BHU, Varanasi, India

Varun Joshi University School of Environment Management, Guru Gobind Singh Indraprastha University, New Delhi, India

Ashutosh Kainthola Geo-Engineering and ML Laboratory, Department of Geology, Institute of Science, Banaras Hindu University, Varanasi, India

Debi Prasanna Kanungo Geo-Hazard Risk Reduction Group, CSIR-Central Building Research Institute, Roorkee, Uttarakhand, India;
Academy of Scientific and Innovative Research (AcSIR), Ghaziabad, India

M. Kaviyarasu Department of Civil Engineering, Sri Krishna College of Engineering and Technology, Coimbatore, India

Rohan Kumar Department of Chemical and Petroleum Engineering, Lovely Professional University, Jalandhar, India

Keshar Kr. Luitel Department of Mines and Geology, Government of Sikkim, Sikkim, India

Shreya Maheshwari Indian Institute of Technology, Jammu, Jammu and Kashmir, India

Edy Tonnizam Mohamad Geotropik—Centre of Tropical Geoengineering, Department of Civil Engineering, Universiti Teknologi Malaysia, Johor, Malaysia

Kh. Mohon Singh Department of Geology, Imphal College, Imphal, Manipur, India

Kien Trung Nguyen Institute of Geological Sciences, Vietnam Academy of Science and Technology, Hanoi, Vietnam

Anurag Niyogi Department of Applied Geology, Indian Institute of Technology (Indian School of Mines), Dhanbad, Jharkhand, India

M. Okendro Department of Geology, Imphal College, Imphal, Manipur, India

Sanjit Kumar Pal Department of Applied Geophysics, Indian Institute of Technology (ISM), Dhanbad, India

Vishnu Himanshu Ratnam Pandey Geo-Engineering & Computing Laboratory, Department of Geology, Banaras Hindu University, Varanasi, India

Ha Ngoc Thi Pham Hanoi University of Mining and Geology, Hanoi, Vietnam

A. A. Ponomarev "EngZashita" Ltd., Sochi, Russia

C. Prakasam Department of Geography, School of Earth Sciences, Assam University Diphu Campus, Diphu, Karbi Anglong, Assam, India

S. Prasanna Venkatesh Department of Applied Geology, School of Earth and Atmospheric Science, University of Madras, Chennai, India

Ondřej Racek Department of Engineering Geology, Institute of Rock Structure and Mechanics, Czech Academy of Sciences, V Holešovičkách 94/41, Prague, Czech Republic;
Department of Physical Geography and Geoecology, Faculty of Science, Charles University, Albertov 6, Prague, Czech Republic

Tabish Rahman Department of Applied Geology, Indian Institute of Technology (Indian School of Mines), Dhanbad, Jharkhand, India

N. Rajeshwara Rao Department of Applied Geology, School of Earth and Atmospheric Science, University of Madras, Chennai, India

I.A. Rodkina Lomonosov Moscow State University, Moscow, Russia

Manojit Samanta Geotechnical Engineering Group, CSIR-Central Building Research Institute, Roorkee, Uttarakhand, India;
Academy of Scientific and Innovative Research (AcSIR), Ghaziabad, India

E. N. Samarin Lomonosov Moscow State University, Moscow, Russia

S. E. Saranaathan School of Civil Engineering, SASTRA Deemed University, Thanjavur, India

Kripamoy Sarkar Department of Applied Geology, Indian Institute of Technology (Indian School of Mines), Dhanbad, Jharkhand, India

Swati Sharma Amity Institute of Remote Sensing and GIS, Amity University, Noida, India

HarAmrit Singh Department of Civil Engineering, Punjab Engineering College, Chandigarh, India

Jayraj Singh Department of Civil Engineering, Indian Institute of Technology Delhi, New Delhi, India

P. K. Singh Department of Earth and Planetary Sciences, University of Allahabad, Prayagraj, India

Prasoon Kumar Singh Department of Environmental Science and Engineering and CWRM, Indian Institute of Technology (ISM), Dhanbad, India

T. N. Singh Department of Civil and Environmental Engineering, Indian Institute of Technology, Patna, Bihar, India

O. N. Sirotkina Lomonosov Moscow State University, Moscow, Russia

R. Sivakumar Earthquake Research Cell & Department of Civil Engineering, College of Engineering and Technology, Faculty of Engineering and Technology, SRM Institute of Science and Technology, Kattankulathur, Kanchipuram, Chennai, India

Alexander Strom Geodynamics Research Centre LLC, Moscow, Russia

P. Thambidurai Department of Coastal Disaster Management, School of Physical, Chemical and Applied Sciences, Pondicherry University-Port Blair Campus, Port Blair, Andaman and Nicobar Islands, India

Binh Van Duong Hanoi University of Mining and Geology, Hanoi, Vietnam; Ordzhonikidze Russian State Geological Prospecting University (MGRI), Moscow, Russia

Ramesh Veerappan Centre for Geoinformatics, Jamsetji Tata School of Disaster Studies, Tata Institute of Social Sciences (TISS), Mumbai, India

A. K. Verma Department of Mining Engineering, Indian Institute of Technology BHU, Varanasi, India

Dang Hong Vu Vietnam Institute of Geosciences and Mineral Resources, Hanoi, Vietnam

Manish Yadav Department of Applied Geophysics, Indian Institute of Technology (ISM), Dhanbad, India

O. V. Zerkal Lomonosov Moscow State University, Moscow, Russia

Chapter 1
Modern Methods of Rock Mass Characterisation and Rockfall Monitoring: A Review

Jan Blahůt and Ondřej Racek

Abstract Modern methods to characterise rock masses and monitor rockfalls and rock slope stability are evolving incredibly fast during the last decade. The rapid increase in new techniques, miniaturization, affordability, computational power, or remote sensing data availability allows deployment in more areas in higher amounts with higher frequency and accuracy of acquisition. The current rapid development of monitoring methods is also induced by engineering challenges when new infrastructures are being constructed in more complicated geological conditions, like mountainous areas or deep gorges with steep slopes. This chapter brings an overview of modern methods used for rock mass characterisation and rockfall monitoring and shows the basic needs for complex monitoring systems and data processing. Finally, it describes the main groups of monitoring methods based on cluster analysis and principal trends in research papers related to modern methods in rock mass characterisation and rockfall monitoring.

Keyword Rock mass characterisation · Rockfall · Monitoring

1.1 Introduction

Current state-of-art rockfall and rock stability research is struggling mainly with a lack of data about rock slope slow destabilization processes, which are complicated to gain, mainly because of terrain setting in rockfall source areas (Fey and Wichmann 2017) or difficulties in recognition of unstable rock slope parts (Teza et al. 2012). New methods to characterise unstable rock slopes and monitor rockfalls emerged to bridge this gap, taking advantage of fast technological development. This is accelerated by the rapid increase in miniaturization, afford-ability, computational power, or

J. Blahůt (✉) · O. Racek
Department of Engineering Geology, Institute of Rock Structure and Mechanics, Czech Academy of Sciences, V Holešovičkách 94/41, 182 09 Prague, Czech Republic
e-mail: blahut@irsm.cas.cz

O. Racek
Department of Physical Geography and Geoecology, Faculty of Science, Charles University, Albertov 6, 128 00 Prague, Czech Republic

P. Thambidurai and T. N. Singh (eds.), *Landslides: Detection, Prediction and Monitoring*,
https://doi.org/10.1007/978-3-031-23859-8_1

remote sensing data availability. It is also accelerated by engineering challenges when new infrastructures are being constructed in more complicated geological conditions, like mountain areas (Chuang and Shiu 2018) or deep gorges with steep slopes (Singh et al. 2013; Kalogirou and Iliaskos 2019). Additionally, the growth of urban areas brings urban development to geologically and morphologically challenging sites (Youssef et al. 2015). Recent technological developments in sensors, data transmission, storage, and processing bring new rock slope stability monitoring opportunities. Sensors are compact and durable (Engel and Schweimler 2016), but for meaningful data, it is critical to design the monitoring system according to its purpose and placement (Burland and Chapman 2012). This is especially important when monitoring is applied for early warning applications like road protection (Loew et al. 2017), railroads (Manikandan et al. 2017; Yan et al. 2019), in urban areas (Abellan et al. 2011), to preserve cultural heritage (Frodella et al. 2016) or within the mining industry (Carla et al. 2017). This chapter presents a review of modern rockfall monitoring and rock slope observation methods. They can be divided into modern geodetical (Gili et al. 2000; Wagner 2016), geophysical (Leopold et al. 2013; Dussauge-Peisser et al. 2003), geotechnical (Hong et al. 2016; Schenato 2017) or remote sensing (Antonello et al. 2004; Gundersen et al. 2018) methods. Afterwards, the basic needs for complex monitoring systems are presented, and some examples of complex monitoring systems are shown. Additionally, main groups of monitoring methods based on cluster analysis are presented together with principal trends in research papers related to modern methods in rock mass characterisation and rockfall monitoring for an overview of traditional monitoring techniques reported by Racek and Blahůt (2023, Chapter 2).

1.2 Modern Methods

Modern, state-of-art methods have been widely applied in the last 20 years. They use complex sensors and need complicated data collection and/or processing software. Modern monitoring methods quickly evolve with general technological progress and provide more precise data with greater temporal and spatial resolution. The following classification is based on traditional techniques, but in some cases, one method can belong to two categories (e.g., TLS to geodetic as well as remote sensing methods). An overview of modern monitoring methods is presented in Fig. 1.1.

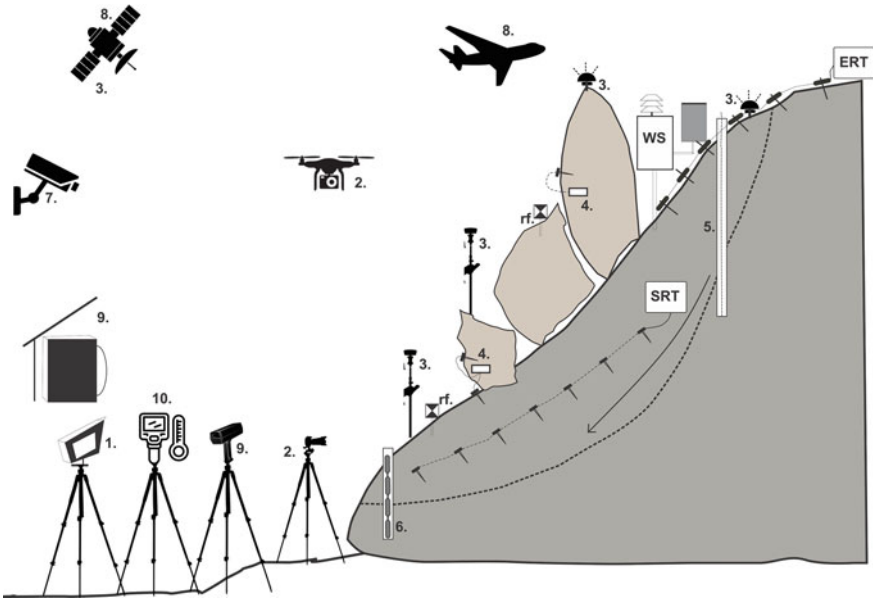

Fig. 1.1 Overview of modern rock mass monitoring methods. **1** TLS, **2** Digital photogrammetry, UAV, **3** GNSS monitoring, **4** Micro seismic monitoring, **5** Optical fiber methods, **6** Compound borehole probe, **7** Camera monitoring, **8** Aerial monitoring, **9** GB InSAR, **10** Thermal camera. SRT: Seismic tomography, ERT: Electrical resistivity tomography, WS: weather station, rf.: reflector

1.2.1 Geodetic Methods

Modern geodetic methods can obtain a large quantity of data quickly. They use sophisticated, time-demanding data processing techniques.

1.2.1.1 Terrestrial Laser Scanning

Terrestrial laser scanning (TLS) is nowadays one of the most popular methods of rockfall and rock slope investigation (Jaboyedoff et al. 2012). TLS provides Spatio-temporal information about the whole rock face or unstable rock slope element from a distance. For this reason, there is no need to visit dangerous or inaccessible areas personally (Gigli et al. 2014). Resulting point clouds can be used for rock slope structural analyses (Riquelme et al. 2017; Monsalve et al. 2019), estimation of unstable blocks dimensions (Gigli et al. 2014; Riquelme et al. 2015), or surface roughness estimation (Mills and Fotopoulos 2013; Zhang et al. 2017). Unlike classical methods, such as geological compass measurement, TLS scan observes structural element trace, from which average spatial orientation is later calculated (Santana et al. 2012). TLS allows rockfall event identification with the following volume estimation (Abellan et al. 2009; Oppikofer 2009; Santana et al. 2012). Compared with

traditional rockfall volume estimation methods, TLS is faster and collects data with a greater spatial resolution (Gigli et al. 2014). The typical precision of TLS in rock fall monitoring is ±5 cm, decreasing with monitored rock face distance (Zang et al. 2019; Westoby et al. 2018). Another application of TLS is continuous rock fall monitoring with repeated scans. This needs a permanently placed automatic TLS station (van Veen and Lato 2017) or frequent campaigns. From consecutive scans, changes of ±1 cm both in the source areas and the accumulation zones can be identified (Abellan et al. 2009). Continuous TLS monitoring is used within active sites such as cliffs (Medjkane et al. 2018), mountainous areas with permafrost retreat (Kenner et al. 2014), volcanically active areas (Jones et al. 2015), river banks (Longoni et al. 2016) or large complex rock slope movements (Abellan et al. 2011). A continuous scanner survey makes it possible to recognise individual stages of a rock fall event if these stages last longer than one scanning survey (Kromer et al. 2017; Williams et al. 2019). TLS is relatively simple to manipulate and offers fast data collection and the possibility to measure spatial changes over large portions of a rock face. In ideal conditions, TLS can record millimetric spatial changes within rock faces using advanced point cloud data processing techniques (Abellan et al. 2009). The main disadvantages of TLS are a high initial investment in a scanner and a large amount of point cloud data resulting from laser scanning surveys leading to time-consuming data processing (Weinmann et al. 2011). Nowadays, Unmanned Aerial Vehicles (UAVs) can carry small laser scanners (Torresan et al. 2018). This approach overcomes the disadvantages of ground-based scanners, like the shadowing effect (Mah et al. 2016) or the impossibility of placing TLS at an optimal distance from the rock face (Tan and Cheng 2020). However, generated point clouds from UAV-held scanners are even more complicated to process, spatially align or combine (Zhou et al. 2020).

1.2.1.2 Digital Photogrammetry

Digital photogrammetry is widely used in geological, geomorphological research, and earth sciences (Gomez and Purdie 2016; Micheletti et al. 2015; Mancini and Salvin 2019). The possibility of digital image processing makes photogrammetry a powerful tool. Photogrammetry campaigns are usually carried out by the Structure from Motion (SfM) method (Westoby et al. 2012; Anderson et al. 2019) using a ground-based camera (Loucks et al. 2018), high-performance UAV systems (Sarro et al. 2018; Vanneschi et al. 2019), or full-size aircraft (Ferrero et al. 2011). UAVs are capable of carrying photogrammetric campaigns significantly closer to the rock face in more complicated terrain (Barlow et al. 2017), which leads to more detailed photographs in complex morphological settings, such as alpine relief or deep gorges (Vanneschi et al. 2019). Photogrammetry is used to generate point clouds and along with laser scanning, it is used to get structural data such as discontinuity systems and their orientation, spacing and persistence (Erharter et al. 2018; Fazio et al. 2019), partial blocks dimensions, even if rock slope surface unreachable in person (Blistan et al. 2016). Digital photogrammetry, especially in combination with UAV, allows

filling point cloud blank areas that are, in the case of TLS, shadowed by the shape of rock slope or resulting from scanner positioning (Sasak et al. 2019). The precision of point clouds resulting from TLS and digital photogrammetry is comparable (Balek and Blahůt 2017). Photogrammetry can be used for near-continuous monitoring of a highly active rockfall site (Gilham et al. 2019). A fixed array of digital cameras can be used as an alternative to permanently fixed TLS or GB SAR units (Kromer et al. 2019). In the case of complex morphology, where a single device is not able to deal with the shading effect, an array of digital cameras will be a more precise and cheaper alternative to a single fixed TLS. One high-resolution photogrammetric campaign is conducted in minutes (Kromer et al. 2019). Fine temporal scale means that pre-failure movements and dynamics of the rock fall event can be captured with all partial stages. The ability of photogrammetry to record surface colour helps in case of rock fall scar detection, changes in surface moisture, vegetation growth estimation, or snow/ice accumulation. The cost-effectiveness of this approach decreases with the number of high-quality cameras. Generated digital rock slope models can be afterwards used for hazard zonation (Krsak et al. 2016; Polat and Murat 2018), and rockfall numerical modelling (Zabota et al. 2019). The spatial accuracy of 3D models created by photogrammetry is ~1 cm for simple flat, rectangular shapes. In the case of complicated non-rectangular features, accuracy significantly decreases (Tannant 2015; Rossini et al. 2018). To get precisely spatially oriented models or point clouds, tie points with known coordinates should be used when the point cloud is aligned (James et al. 2017).

1.2.1.3 GNSS Monitoring

Global Navigation Satellite Systems GNSS (GPS, Galileo, GLONASS) are extensively used for mass wasting monitoring, mainly in the case of relatively rapid moving landslides or rockslides (Gili et al. 2000; Crosta and Agliardi 2002; Kristensen and Blikra 2013). The device is placed within a moving rock mass, and temporal position changes are recorded. For slower spatial changes, differential GPS (dGPS) uses two receivers (base station and rover). The base station is set up in a fixed location and is considered motionless. The second receiver (rover) is mobile and can be relocated to an unstable feature. For dGPS monitoring, two methods are usually used:

The real-time kinematics (RTK) method is where both receivers communicate and compare their positions continuously in real time (Lambiel and Delaloye 2004). This approach does not require clear visibility between the two receivers. In the case of fast movements or complicated terrain set-up, moving the reference receiver is unnecessary. On the other hand, this method needs a wide topographic horizon to receive good-quality signals from satellites. Fully grown trees or complicated terrain can disrupt signals (Bastos and Hasegawa 2013). The precision of RTK measurements is less than 1 cm in the case of the horizontal component and less than 2–3 cm in the case of the vertical component. Fast-static (FS) method with two static stations. This method is relatively robust in the case of satellite signal loss. However, it takes about 20 min to measure a single point with the FS method. Also, this method

requires advanced data processing approaches after field measurement, which is time demanding, and a detailed description of using GPS within mass wasting monitoring by Gili et al. (2000).

1.2.2 Geophysical Methods

Geophysical methods for mass wasting investigation are complexly reviewed by Jongmans and Garambois (2007) and Pazzi et al. (2019). Most geoscience studies use geophysical methods to investigate or monitor landslides, not rockslides formed by compact rock mass (Pazzi et al. 2019). The application of geophysical methods within steep rock slopes is complicated. Geophysical methods are used for rock mass stability estimations (Pappalardo et al. 2016) or for rock fall temporal monitoring (Dietze et al. 2017). More often, they are used for rock mass internal properties characterization. In this, they can partly replace expensive borehole drilling. Geophysical data processing and interpretation are relatively complicated and demand an experienced user (Schrott and Sass 2008). To help with complicated data interpretation, geophysical surveys can be combined with laboratory testing of rock samples, which allows for validation and interpret the measurements (Solberg et al. 2012).

1.2.2.1 Electrical Resistivity Tomography

Electrical resistivity tomography (ERT) is extensively used in cases of landslide (s.s), and monitoring was recorded by Perrone et al. (2014) for further review. This, nowadays relatively affordable method, is suitable for monitoring underground water flows inside the landslide body (Palis et al. 2017), for 3D landslide spatial characterization (Chambers et al. 2011), or slip surface depth determination (Kristyanto et al. 2017). Application of ERT in the rock mass is problematic, mainly because of the lack of sufficient conductivity for measurement electrodes in the compact rock mass. Moreover, resistivity contrast inside solid, homogeneous rock mass is relatively small (Krautblatter et al. 2010; Portal et al. 2019). ERT often monitors temporal permafrost dynamics and follows rock slope destabilization (Krautblatter et al. 2010; Magnin et al. 2015) and in-depth freeze–thaw cycle identification (Sass 2005; Onaca et al. 2013). ERT is used to identify weathered, fractured, or differently weakened zones in the depth of a rock slope (Chigira et al. 2002; Leopold et al. 2013; Thambidurai and Ramesh 2017; Thambidurai et al. 2022). This kind of stability estimation using ERT can be performed for rock slopes where it is possible to establish profiles (Udphuay et al. 2011; Rosas Carbajal et al. 2016). When rock mass is affected by wide aperture discontinuities or tectonic faults, ERT can be used to detect these below the surface (Majzoub et al. 2017). By monitoring campaigns, ERT is capable of describing temporal changes in the hydrogeological regime of a rock mass (Heincke et al. 2010), causing temporal resistivity changes. ERT is widely used for underground cavities or cave systems detection (Pánek et al. 2010; Park

et al. 2014). Results of ERT are usually presented in the form of 2D transects or 3D models, which present the resistivity/conductivity of a rock mass. ERT uses different electrode combinations that are used for different lithologies or structural settings (Perrone et al. 2014). Using ERT directly on the rock slope surface is challenging, especially within near-vertical rock slopes. However, it can be performed when safety measures are followed (Uhlemann et al. 2018). The spatial resolution of ERT output depends on the distance between electrodes. In geological applications, high resolution is considered to be approximately 0.5–1 m horizontally and 0.25 m vertically (Greggio et al. 2018).

1.2.2.2 Seismic Tomography

As well as ERT, seismic tomography (ST) surveys mainly monitor landslides. The typical use of this method is the slip surface depth estimation (Whiteley et al. 2019). But in some cases, ST is used for internal rock slope properties estimation (Heincke et al. 2006, 2010; Colombero et al. 2016). The seismic signal is generated by a hammer or more complex vibration-inducing devices. Seismic tomography is used to determine the depth of weathering weakened zone (Olona et al. 2010), discontinuities detection, or approximate lithological characterization (Deparis et al. 2011; Babacan et al. 2014). ST can identify tectonic faults (Improta and Bruno 2007). Discontinuity systems can be partially described using seismic tomography; however, this method is not as spatially precise in identifying single small discontinuities (Heincke et al. 2010; Deparis et al. 2011). ST can identify weakened zones, thus determining future rock fall or rock slide dimensions (Dussauge-Peisser et al. 2002; Crosta et al. 2014). For in-depth rock mass characterization cross-hole seismic tomography (CHST) (Bregman et al. 1989) is used. CHST array uses geophones and seismic signal generators combined with surface seismic tomography inside boreholes. CHST provides better spatial resolution in deeper parts of the rock mass (Mari et al. 2019). Results of ST surveys are presented in the form of 2D transect profiles or 3D models showing the speed of seismic waves velocity in the mass. The measuring process in the field is time-consuming and increases with profile length. Data processing and interpretation demand experienced researchers. ST brings better results than ERT in identifying different rock mass weathering grades (Olona et al. 2010). Spatial resolution increases with the number and spacing of used geophones. Using close placed geophones, spatial resolution increases to ± 1 m in the case of surface profiling and higher in the case of vertical seismic profiling and the CHST method (Mari et al. 2019), a detailed research detail of the seismic tomography method used within geosciences by Gu et al. (2002) or the paper of Jongmans and Garambois (2007).

1.2.2.3 Ambient Vibration Monitoring

The ambient vibration (AV) monitoring technique is traditionally used in civil engineering to monitor structures such as bridges or buildings (Wenzer and Pichler 2009).

From this application, the technique was adapted to monitor various rock slopes (Amitrano et al. 2005, 2010; Bottelin et al. 2013; Kleinbrod et al. 2017). AV monitoring system is composed of geophones connected to a datalogger, which processes and stores seismic signals (Valentin et al. 2016). Ambient vibration monitoring allows continuous monitoring, and it is durable, cheap, and easy to install and maintain (Bottelin et al. 2013). Monitoring of an unstable rock slope is done with an array of two geophones. The first is placed within the stable part of the rock slope, and the second is on the monitored unstable element. This setup allows the comparison of two vibration patterns and permits observing changes caused by destabilization (Valentin et al. 2016). Ambient vibration pattern depends on the rock mass's internal properties and structure (Moore et al. 2018). The pattern consists of reversible and irreversible frequency changes. Reversible changes are caused mainly by thermally induced dilatation. Irreversible changes are explained by internal changes linked with crack opening, suffusion process, or rock bridge collapses (Bottelin et al. 2014). Identification of the irreversible changes in vibration patterns is crucial to detect ongoing rock slope destabilization (Burjanek et al. 2018), as the pattern of unstable feature frequencies of ambient resonation significantly drops before a collapse (Lévy et al. 2010). Multiple geophones setup allows for determining the spatial orientation of opening discontinuity from the received polarized signal (Panzera et al. 2014). The main advantage of the AV technique is cost-effectiveness, simplicity of installation, and low maintenance requirements (Wenzer and Pichler 2009). AV patterns also can indicate structural changes or fracture evolution in a short time in great rock mass depths (Kleinbrod et al. 2019). The limitation of this method is data management, where a large amount of data must be processed. This can be overcome by using large dataloggers or cloud services (Burjanek et al. 2018), and a further review of AV monitoring can be referred to in Kleinbrod et al. (2019).

1.2.2.4 Microseismic Monitoring

Before regular use of this method for mass movement monitoring, large rockfalls/rockslides were randomly captured by regular seismic stations (Fuchs et al. 2018). Microseismic monitoring was introduced within the mining industry to prevent roof collapses (Obert and Duvall 1942). Later, technological development and cheap maintenance requirements were adapted for rock slope monitoring (Arosio et al. 2009). Monitoring of in-situ microseismicity is focused on recording and evaluating local seismic emissions caused by rockfalls. These low-magnitude seismic emissions can also be generated by discontinuity propagation inside the mass (Tripolitsiotis et al. 2015; Mourot 2016). Crack propagation in rock slope depth is a crucial element of rock slope destabilization (Hall et al. 2006). Conventional methods can monitor crack propagation or widening on rock slope surfaces, but discontinuity behaviour inside rock mass remains unknown (Arosio et al. 2009). Microseismic monitoring can record this crack propagation or rock bridge collapse. Microseismic monitoring is used for continuous monitoring, which provides data about in-depth discontinuity propagation (Colombero et al. 2016; Taruselli et al.

2018). Microseismic monitoring can reveal precursory events, which are a foretaste of larger failure (Arosio et al. 2017). With multiple geophones setups, spatial detection of events is possible by triangulation (Chambers et al. 2010; Zhang et al. 2019). Identified unstable parts of rock slopes can be later instrumented with a direct geotechnical monitoring/warning system (Salvoni and Dight 2016; Arosio et al. 2017). Site-specific microseismic monitoring typically contains at least one geophone, amplifying and filtering units, and datalogger (Hardy 2003; Arosio et al. 2009; Amitrano et al. 2010). Two approaches of microseismic monitoring are used:

1. "General monitoring" uses one geophone to monitor local seismic activity without the possibility of event spatial localization (Amitrano et al. 2010). By "general monitoring," it is possible to describe rockfall frequency or seismicity caused by the widening of discontinuities. This setup is cheap to install and maintain.
2. "Location monitoring," where several triaxial geophones are used to determine the three-dimensional hypocentre of microseismic emissions (Hardy 2003). This approach is more expensive; however, spatial localization of seismic events helps understand specific rock slope behaviour and allows for determining the most susceptible areas.

The ability of this method to detect even the smallest rockfall events means that it is frequently used in combination with other, less sensitive methods in complex monitoring systems (Coccia et al. 2016; Arosio et al. 2017). Rockfalls, or rockslides can be detected by their specific seismic signature (Dietze et al. 2017; Le Roy et al. 2019). By further data processing of the seismic signature, rockfall properties, such as volume, duration, or the number of stages, can be determined (Hibert et al. 2017). Crucial is the recognition of rockfall seismic signature from other disturbances, like traffic, animals, or weather-related signals (Amitrano et al. 2007). Thanks to relatively large data demand, microseismic monitoring systems need a stable power supply (Amitrano et al. 2010), which can be challenging in the case of remote areas. Due to continuous data flow, data should be transmitted to a cloud to diminish complicated in situ data storage. The spatial resolution of the seismic event location reaches ±0.5 m (Weber et al. 2017). Microseismic monitoring also ensures great temporal resolution when sub-second lasting events can be captured.

1.2.2.5 Borehole Temperature Monitoring

Rock slope destabilization processes (ice wedging, rock wedging, permafrost thaw, rock mass dilatation) are driven by temperature cycles (Gunzburger et al. 2005; do Amaral Vargas et al. 2013; Collins and Stock 2016). To identify temperature cycles, it is necessary to use sensors placed in a borehole within the rock mass (Schneider and Hauck 2012; Hugentobler et al. 2020). It is important to properly seal the head of the borehole and the space between multiple sensors to avoid air circulation inside the borehole (Jin et al. 2007; Racek et al. 2021). Nowadays, temperature transducers can be replaced by optical fiber-based monitoring methods (Siska et al. 2016).

1.2.3 Geotechnical Methods

Traditional geotechnical rock slope monitoring methods directly measure spatial changes on rock slope surface or in-depth (Racek and Blahůt 2022, in this volume for further details). Modern geotechnical methods allow measuring rock mass strain/stress field changes together with temperature over large distances.

1.2.3.1 Optical Fiber Methods

This is a rapidly evolving geotechnical technique nowadays (Hong et al. 2016). Optical fibers are used for stress/strain field and temperature change monitoring (Siska et al. 2016). Optical fiber monitoring is cheap and suitable for a hostile environment; further information is available in research articles by Hong et al. (2016), Schenato (2017), and Zheng et al. (2020). Two optical fiber-based monitoring approaches are used. The first approach is based on Bragg wavelength shift (Schroeder et al. 2001). Wavelength shift in light pulses is caused by strain applied on optical fiber which is fixed on a rock face or inside a rock mass/borehole (Gage et al. 2014). Within optical Fiber Bragg Gratings (FBG) are placed. When the FBG is illuminated with a broadband light pulse, each FBG reflects a specific wavelength while other wavelengths remain undisturbed (Moore et al. 2010). The return times of specific reflected wavelengths from each FBG are measured, and by that, it is possible to compute distance changes between FBGs (Zhao et al. 2016). FBG system is usually used to monitor movements at known slip surfaces or discontinuities where the movement was confirmed by traditional methods (Wang et al. 2015). The limitation of the FBG approach is that a relatively small number of FBGs can be deployed within one fiber. This means that multiple FBG cables must be deployed in a complex monitoring system. Moreover, commercially available FBG interrogators can handle only a small number of FBGs (Tang and Cheng 2018). This limitation leads to the cost ineffectiveness of this method for monitoring complex mass movements (Motil et al. 2016). In the case of a simple one-directional movement, the FBG method can provide sub-millimetric accuracy. That makes it suitable for slow rockslides or tilting movement monitoring. When FBG fiber is installed properly, detection of micrometric deformations is also possible (Glisic and Inaudi 2008). The second approach is called Brillouin optical time-domain reflectometry (BOTDR) (Kurashima et al. 1993). This approach uses one optical fiber stimulated by laser pulses (Linker and Klar 2017). The principal of BOTDR implements Brillouin scattering, a physical process representing the interaction between light and optical medium (Méndez and Diatzikis 2006). Light pulse, which is sent through optical fiber, travels in the original direction, and a small portion of the light pulse is scattered. Three types of scattering affect pulse transmission in the optical fiber: (a) Rayleigh scattering caused by the change of refractive index; (b) Raman scattering induced by an optical phonon; (c) Brillouin scattering, which is caused by an acoustic phonon. In Brillouin scattering, scattered light reaches a peak over its spectrum at a specific wavelength. This is called

Brillouin Frequency Shift (BFS), which is caused by longitudinal strain applied on optical fiber and temperature (Méndez and Diatzikis 2006). Spatially, the deformation is determined by the time interval between launching a light pulse and receiving scattered light (Ohno et al. 2001). These advantages make the BOTDR method suitable for temperature and strain monitoring over long distances (+10 km) with just one optical fiber (Zhang and Wu 2008). BOTDR-based strain monitoring works reach a very high precision ±0.01 mm (Nan and Gao 2011). BOTDR and FBG techniques are also suitable for underground water pore pressure monitoring (Schenato 2017; Xue et al. 2018) or groundwater level variation with a precision ~0.5 cm (Schenato 2017). Both methods are limited to relatively small movements as larger movements can easily break the fiber. For measuring pressure changes inside a rock mass, distribute pressure sensing (DPS) cable is used. One or more optical fibers are deployed in a zig-zag pattern inside an elastic band. When pressure is applied to the cable, strain is induced on fibers in a specific part of the cable (Schenato et al. 2020). The precision of DPS is 1 με with a spatial resolution of 2 cm.

1.2.3.2 Compound Borehole Probe

Recently, a combined sensor using inclinometer, piezometric, thermal, and accelerometric measurement has been developed, allowing precise measurement in 3D (Foglino et al. 2018). Such a device can describe borehole deformation, thus rock slide deformation in all its length. The precision of the in-situ compound borehole probes is two to four times higher than a commonly used inclinometric probe (Lovisolo and Della Giusta 2005), and they are widely applied in an early warning for large rockslides, such as Åknes rockslide in Norway (Blikra 2012) or Mont de la Saxe in Italy (Crosta et al. 2012).

1.2.4 Remote Sensing Methods

The advantage of remote sensing methods lies in the application within inaccessible, dangerous, or spatially extensive sites. Remote sensing methods are usually used in combination with other methods in complex monitoring systems.

1.2.4.1 Continual Camera Monitoring

This method is used in complex monitoring systems or early warning systems for natural or artificial rock slopes (Scheikl et al. 2000; Nishii and Matsuoka 2010; Kellerer-Pirklbauer and Rieckh 2016). The system uses one or several digital cameras, which are used for time-lapse photography sensing, or continuous video recording. By temporal comparison of photo or video frames, small changes in

rock slope geometry are detectable (McHugh and Girard 2002). Detection of differences between analogue photographs was traditionally done manually (Belknap and Gilmore 1987). Digital images, however, can be easily processed by specialized software (Kenner et al. 2018). To increase spatial precision, reflectors can be placed within rock faces, but the installation of such a reflector can be complicated or even dangerous (McHugh and Girard 2002). Photography analyses without reflectors or tie points were first introduced to detect roof deformation in underground mines (Kukutsch et al. 2010; Ghabraie et al. 2015). Image processing software allows the detection of small rock slope spatial changes on time-lapse photos (Royan et al. 2015). Photos/frames are compared pixel by pixel to determine possible changes in shape or colour. The highest precision is achieved with a fixed camera; however, photos from different angles can be used with new data processing techniques (Le Moigne et al. 2011). Real-time data processing is possible thanks to increased computational capacity, which is necessary for early warning systems (Fantini et al. 2017; Manikandan et al. 2017). Continuous video recording is ideal for early warning systems or for highly active rockfall site monitoring (Hürlimann et al. 2012; Loew et al. 2017). Video camera-based warning systems are used in open-pit mines where initial phases of mine slope collapse can be detected and trigger an alarm. The system is typically composed of a digital video camera and data processing control unit, which compares pixels of subsequent video frames and detects rock slope destabilization. The resolution of the digital video camera is usually reasonably low, which simplifies and accelerates continuous data processing (McHugh and Girard 2002). Video is stored only when movement accelerates and triggers an alarm (Hugh 2006). The warning system can be carried by a single or multiple-camera setup. Multiple camera systems data can also be used for photogrammetric-based digital model construction (McHugh and Girard 2002; Hugh 2006). When the camera is fixed in the right spot, properties of rockfall events such as range, velocity, volume, or height of bounces can be determined from the footage (Giani et al. 2004; Volkwein et al. 2018), and the 3D trajectory of rockfall can be estimated (Azzoni et al. 1995). This approach is used to describe parameters of artificially triggered rockfalls with known parameters. Data from such experiments are later used for numerical model construction and validation to improve the accuracy of numerical models (Li and Lan 2015; Matas et al. 2020).

The advantage of camera monitoring is its cost-effectiveness. Monitoring systems can provide continuous data, and minimal storage space is needed in the case of a warning system. A disadvantage is that a single camera is not able to provide three-dimensional data. Long-lasting slow deformations which continuously destabilize rock slopes cannot be detected with short-term monitoring deployment. High-resolution cameras can record and process movements with ±1–10 cm precision. Low spatial resolution is balanced by high temporal resolution up to sub-millisecond.

1.2.4.2 Aerial Monitoring

Due to technological development and the commercial availability of UAVs, aerial monitoring is continuously rising (Colomina and Molina 2014; Gomez and Purdie 2016). In the field of geosciences, aerial monitoring is used to describe the Spatio-temporal behaviour of complex, extensive, rapidly evolving systems, like landslides (Fiorucci et al. 2011; Strozzi et al. 2013), fluvial systems (Szabó et al. 2020), glaciers (Veettil and Kamp 2017) over the large area (Gillan et al. 2016; Slimane et al. 2018). Outputs of aerial monitoring are digital elevation models (DEM), 3D point clouds, and hyperspectral or RGB high-resolution images. Advanced aerial systems can collect multiple outputs within one flight. Precise DEM can be constructed using airborne laser scanning or photogrammetry (Korsgaard et al. 2016; Fernandez et al. 2020). Characterization of a single slope is complicated, except when a UAV is used. Aerial data are inaccurate in the case of near-vertical surfaces because full-size aircraft are not able to get close to the rock face to get high-resolution data. That means only large slope deformation such as rockslides or rock tower toppling can be monitored using full-size aircraft (Young et al. 2010; Lato et al. 2015). A High-resolution regional-scale survey can be carried out using airborne laser scanning (ALS) (Sailer et al. 2012; Fanos et al. 2016). ALS is applied within large or inaccessible areas, where the use of conventional terrestrial methods would be extremely time-demanding, or the range of TLS is inadequate (Haas et al. 2012; Lazar et al. 2018). ALS produces point clouds, from which it is possible to define the structural properties of a given rock slope (Jaboyedoff et al. 2012; Assali et al. 2014) or temporal surface changes (Zangerl et al. 2010; Henderson and Saintot 2011). ALS data provide volumetric changes within the rockfall accumulation zone or speed of rock slope back wearing (Vehling et al. 2017; Wziatek et al. 2019). ALS-produced DEMs are used for regional rockfall susceptibility or hazard assessment (Losasso et al. 2017; Fanos et al. 2018).

For similar applications, high-resolution orthorectified photos can be used, which help with temporal change detection in both rockfall accumulation and source zones (Koukouvelas et al. 2015; Bauer and Proske 2017). With orthophotos, it is possible to map and quantify damages caused by rockfalls or other mass- wasting events (Ferlisi et al. 2012; Moos et al. 2018), monitor large rockslides' temporal evolution (De Vita et al. 2013), block size distribution within rockfall accumulation area (Ruiz Carulla et al. 2015). Properties of past rockfalls can be determined from visible rockfall traces (Manousakis et al. 2016). For regional susceptibility studies, inventorying of unstable elements using orthophotos is possible (Hermanns et al. 2011, 2013; Oppikofer et al. 2015). Full-size aircrafts are used for hyperspectral imaging-based geological mapping over large regions (McHugh and Girard 2002). In rock slope stability assessment, multispectral imaging is used to identify weakened zones such as discontinuities, weathered zones, or parts of mass formed with different rock types (Riaza et al. 2001; Sun et al. 2017; Park and Kim 2019). Sensors can be used for petrological mapping over large areas or within a single rock face (Kurz et al. 2012). The spatial resolution of airborne monitoring with low flight altitude can reach ± 1 cm.

High-altitude aircraft or satellite images work usually with ±1 m spatial resolution. Temporal resolution usually ranges from hours (UAVs) to weeks/months (satellites).

1.2.4.3 Radar Interferometry

Monitoring with interferometric radar can be carried out terrestrially (GB SAR/GB InSAR) (Rouyet et al. 2017) or satellite/aircraft-based (SAR/InSAR) (Lauknes et al. 2020). For rock slope monitoring, it is necessary to sense near-vertical surfaces, and this limitation means that mainly GB InSAR is applied within this field (Eriksen et al. 2017). The final results of GB InSAR monitoring are 2D interferometric maps that represent the surface distance from the interferometric radar. When these images are temporally compared, it is possible to quantify Spatio-temporal rock slope behaviour. GB InSAR allows measuring the distance with a precision up to 0.1 mm (Bardi et al. 2016). This method is suitable for measuring small, bare-eye invisible displacements at great distances with such precision. These small movements destabilize rock faces and foreshadow rockfall events (Crosta et al. 2017; Frodella et al. 2017). Continuous monitoring with GB InSAR makes it possible to obtain information about movement velocity, locate possible rockfall source areas, and quantify changes within the accumulation zone. GB InSAR provides continuous data without the need for daylight (Antonello et al. 2004). Humidity (rain, fog) affects signal quality, so these atmospheric errors must be filtered using signal processing methods (Wang et al. 2020). Only movements in that specific area can be registered if a rock slope unstable element is known in advance. For high spatial precision, the atmospheric effects should be compensated constantly according to locally placed weather stations (Luzi et al. 2004). A less complicated atmospheric compensation technique is multiple scan averaging (Pipia et al. 2008; Wang et al. 2020), or the use of averaging sliding window method for each image. The main disadvantage of GB InSAR is the price of the device and complicated installation, including a stable base with rails and securing against vandalism.

For monitoring large unstable areas with a lower temporal resolution, satellite/aircraft radar interferometry is used (Strozzi et al. 2010). The precision of satellite SAR increases with the duration of monitoring. In the long term (years), subcentimeter precision is achievable. To increase precision, permanently placed corner reflectors are used. With these, measurement of spatial changes of ±1 mm is achievable (Bovenga et al. 2017). Temporal resolution is determined by the frequency of satellite flight over the monitored feature. Maximal achievable temporal resolution is approximately two days when the whole pallet of available satellites is used (Eppler et al. 2015).

1.2.4.4 Remote Vibration Measurement

Installation of ambient vibration sensors within unstable rock slopes can be dangerous in some cases, time-demanding, or the feature itself is inaccessible. Monitoring

multiple unstable blocks along a transport corridor would be expensive and time-consuming when multiple transducers and a complex monitoring system are used (Uehan et al. 2012). Rockfall events can also damage geophones installed within extremely unstable rock slope parts (Wei and Liu 2020). Doppler radar distant vibration monitoring can be used in such cases (Ma et al. 2015). Monitoring Doppler radar array can be placed temporarily or can be portable to monitor multiple unstable blocks in campaigns. If three Doppler monitoring stations are deployed, it is possible to calculate an unstable block's 3D spatial displacement and vibration pattern. That makes it possible to calculate the direction of destabilization, and eventually predict the time and mechanism of collapse (Uehan et al. 2012).

1.2.4.5 Thermal Camera Monitoring

Thermal cycles and spatial distribution of temperature within rock face lead to thermally-induced stress/strain changes within the whole rock mass into considerable depths (Gunzburger et al. 2005; Eppes et al. 2016). To describe Spatio-temporal distribution of temperatures within rock faces, the easiest way is the use of thermal camera campaigns (Teza et al. 2012). Through thermal image time-series analyses, it is possible to calculate the temporal temperature pattern for each pixel (Fiorucci et al. 2018; Guerin et al. 2019). Continuous thermal imaging makes it possible to derive diurnal or seasonal cycles together with heating and cooling trends (Pappalardo et al. 2016) and visualize discontinuities' influence on heath transitions and temperature distribution within a rock slope (Seo et al. 2017). Rock bridge detection is possible from temporal rock face temperature data, which facilitates rock slope stability estimation (Guerin et al. 2019). Rock bridges are detectable as temperature anomalies (small colder areas surrounded by a warmer rock face during the heating phase) within the rock face (Pappalardo et al. 2016; Guerin et al. 2019)., To detect rock bridges, it is necessary to exclude other temperature anomalies caused by rock mass colour or rock slab aspect (Ghosh et al. 2014). Thermal imaging of rock slopes is used to detect weathered or otherwise weakened areas within rock faces (Mineo and Pappalardo 2016). Non-homogeneities in rock material or weakened rock mass cause differences in thermal conductivity, which leads to temperature anomalies in visible heating/cooling phases (Loche et al. 2021). The thermal behaviour of rock mass is also influenced by the rock type, intrusions, moisture, fluidal percolation, or shallow surface fractured zone (Pappalardo and Mineo 2019). In structural monitoring of larger rock slopes, thermal imaging allows larger discontinuities mapping; during the cooling phase, discontinuities cool differently than intact rock mass (Barla et al. 2016). Simple thermal scanning campaigns can detect discontinuities filled with warmer air during the cold season (Baroň et al. 2014). By processing thermal images by specialized software, it is possible to get information about rock mass internal structure (Frodella et al. 2017; Guerin et al. 2019). The main advantage of the thermal camera is its ability to quantify the Spatio-temporal distribution of temperature within rock face, with cost-effectivity and spatial resolution, in comparison with multiple temperature transducers. Thermal cameras have become relatively affordable, and

even low-resolution thermal cameras can bring high-quality data (Sobrino et al. 2016). Nowadays, smaller devices can be attached to a common smartphone. The spatial resolution of IR thermal camera sensors can be up to 1,024 × 768 pixels. The precision of measured temperatures differs for each device. An absolute error can be relatively high, up to ±5 °C; however, relative error within one image is, in most cases, low, up to 0.025 °C (He et al. 2010).

1.2.5 Dating Methods

Traditional dating methods usually evaluate age from macroscopic properties of trees (dendrochronological methods), surfaces (degree of weathering), or surface-growing lichen species (lichenometry). Modern methods require complicated laboratory analyses of field-collected samples when state-of-art chemical and physical analyses are performed.

1.2.5.1 Cosmogenic Radionuclides Dating

Cosmogenic radionuclides dating is a method extensively used in geosciences (Granger et al. 2013; von Blanckenburg and Willenbring 2014). Dating using different cosmogenic radionuclides is widely applied in the case of deglaciation dating (Ivy-Ochs and Jason 2014; Stroeven et al. 2016), fault surface dating (Pierce et al. 2017; Robertson et al. 2019), sedimentation processes dating (Cesta and Ward 2016; McEwen et al. 2020), or to erosion rate estimation (Marrero et al. 2018; Zhao et al. 2019). The dating of rockfall events using this method is complicated. Accumulated rockfall material is exposed to cosmogenic nuclides even when it is still attached to the rock face (Ivy-Ochs and Kober 2008). Therefore, exposure dating can be performed for exactly identified rockfall scars (Gallach et al. 2018) or for the dating of exposed slip surfaces (Böhme et al. 2015; Blahůt et al. 2020). The second application of cosmogenic radionuclide dating is the burial time estimation for rock slide-covered surfaces (Balco et al. 2013; Martin et al. 2014). Cosmogenic radionuclides dating can be also used for velocity estimation in the case of slow, long-lasting rockslides (Sanhueza Pino et al. 2011; Sturzenegger et al. 2015). Dating of exposure is used for toppled blocks (Benedetti and van der Woerd 2014) and for dating collapsed precariously balanced rocks in paleoseismological research. Dating helps to estimate the time of exposure of the bedrock, which corresponds with a historical seismic event that destabilized precariously balanced rock (Balco et al. 2013). In comparison with traditional methods, cosmogenic radionuclides dating provides lower temporal precision but can reach further into the past (tens of thousands of years). Spatial resolution is dependent on the scale of the study, generally, meters to kilometres, and an extensive review of cosmogenic dating was reported by Ivy-Ochs and Kober (2008).

1.2.5.2 Luminescence Dating

For dating mass movements within a compact rock, optical luminescence can be used as a widely established method in dating quaternary processes (Sohbati et al. 2012). Two approaches are used: (1) thermoluminescence; (2) optical luminescence (Preusser et al. 2009). Luminescence is used mainly for surface burial age estimation. Eventually, it can be applied for exposure time estimation (Polikreti et al. 2003; Sohbati et al. 2012). This method is limited to rocks containing quartz or feldspar in geological applications. Optical luminescence dating of exposure time is based on the principle of residual luminescence profiles in different rock mass depths. The longer the exposure time is, the deeper inside the rock mass is the luminescence signal rewritten (Sohbati et al. 2012). Combining the dating of concealed surface or underlying surface burial age makes it possible to date rockfall events within a whole range of environments. That is useful in the case of localities when tree rings or lichenometry cannot be used or these methods are out of the expected range (Chapot et al. 2012). When a rockfall scar is easily distinguishable, luminescence dating is a suitable method for rockfall age dating. Compared with cosmogenic radionuclides dating, it is a less time-consuming method with similar temporal precision. Optical luminescence is not biased with a shielding effect compared to cosmogenic radionuclides. Optical luminescence dating has the potential to date the exposure period before the burial event occurred, which can provide complex long-term temporal rock slope evolution data (Chapot et al. 2012). A thorough review of luminescence dating was provided by Fuchs and Lang (2009), Madsen and Murray (2009), and Bateman (2019).

1.3 Data Storage and Processing

The use of the monitoring method determines data storage, processing, and presentation of the results (Table 1.1). Data storage is not a big issue when monitoring campaigns, even when modern methods with large data outputs are used. Data are stored within the user device and processed later in the office (McCaffrey et al. 2005; Jordan and Napier 2016). Field data are recorded in notebooks and processed in the office when classical methods are used. When monitoring frequency is high or continuous monitoring is deployed, it is important to prevent data loss or damage with safe cloud data storage or durable and reliable dataloggers (Ohbayashi et al. 2008). Recently, the use of the Internet of Things (IoT) allows cheaper and more reliable data transmission possibilities than GPRS or other systems. Data processing becomes more complicated when deployed by a continuous or multi-sensor monitoring system. When the amount of data rises, it is more convenient, time-effective, and safe to use automated data processing and storage (Rozsypal 2001). Automated data management methods allow using a finer temporal resolution that demands higher computing capacity and storage space. Photogrammetric SfM surveys or TLS scans can easily exceed volumes of 10 GB (Xiong et al. 2017; Monsalve et al.

Table 1.1 A list of methods and their data acquisition/collection principles, data storage purpose, data processing approaches and results in presentation is listed (traditional methods overview details, Racek and Blahůt 2022, in this volume)

Methods	Data reading/collection	Data storage	Data processing	Results presentation
Mapping	Personal/subjective	Notebook/HDD	Expert estimate	Map/hazard zonation
Geotechnical classification	Manual/objective	Notebook/HDD	Expert estimate	Stability index/table
Catch-net monitoring	Personal/objective	Notebook/HDD	V-f estimate	Table/graph
Classic geodetical	Manual/objective	HDD/Web cloud	Position change estimate	Table/graph/map
Dendrochronology	Manual/objective	Wood samples	Age estimate	Table/graph/map
Lichenometry	Manual/objective	Notebook/HDD	Age estimate	Table/graph
Degree of weathering	Manual/objective	Notebook/HDD	Exposure age estimate	Table/graph
Geotechnical	Manual/automatic	HDD/Web cloud	Position/strain change estimate	Table/graph
Modern geodetical	Manual/automatic	HDD/Web cloud	Position/geometry change estimate	Table/graph/3D model
Geophysical	Manual/automatic	HDD/Web cloud	Physical properties estimate	Table/graph/2D profile/3D model
Remote sensing	Manual/automatic	HDD/Web cloud	Position/geometry/temperature change estimate	Table/graph/3D models/photos/video

2019), and processing such large files can be time-consuming. Monitoring results are usually presented using temporal graphs, maps, tables, photographs, 2D/3D transects or models. Measured variable time series can be statistically explored to find trends, seasonality, oscillations, or measurement errors (Uzielli 2008). Measured trends help to predict future rock slope behaviour (Zvelebil and Moser 2001; Crosta and Agliardi 2002). Such a prediction requires a clear understanding of the destabilization process and the influence of driving external factors (Sattele et al. 2016).

1.4 Complex Monitoring Systems

Rock slope destabilization heading to rockfall event is a complex process. Description of triggering or preparatory mechanisms with a single monitored variable is insufficient to describe the whole destabilisation process (Rosser et al. 2007). Early-warning monitoring can track a single critical variable, such as crack opening, ambient vibrations, or rock face spatial changes. When properly chosen, only one variable can

provide data about temporal rock slope destabilization (Staehli et al. 2015). Monitoring to understand the rockfall processes in their complexity must be composed of a wide range of sensors monitoring different variables. Such a system should be placed within active rockfall sites where continual information about the dynamic and activity is required and can be acquired (Jaboyedoff et al. 2011; Janeras et al. 2017). The first step in the final goal of understanding the rock slope destabilization process is to compare the rock slope dynamic with in-situ measured meteorological variables (D'Amato et al. 2016; Di Matteo et al. 2017). The combination of used methods is variable and determined by local conditions. Scheikl et al. (2000) used geotechnical (wire extensometer, crack gauge, tiltmeter, optical fiber), geodetical (direction of deformation), geophysical (surface and borehole geophones), and remote sensing (TLS, video camera, Doppler radar) methods for a large rockfall monitoring. Arosio et al. (2009) deployed remote sensing and geodetical techniques in combination with microseismic methods for roadcut monitoring. Di Matteo et al. (2017) used GB InSAR, crack gauges, video cameras, and meteorological monitoring for complex, highly active rockslide monitoring. Loew et al. (2017) presented monitoring of large rockslides using manual and automatic crack meters with a total station. Fantini et al. (2017) introduced a multi-sensor monitoring/warning system consisting of weather stations, a rock mass temperature sensor, six strain gauges, 10 extensometers, and an optical camera. The goal of this setup was to develop a warning system for railway corridors. Janeras et al. (2017) used a monitoring system consisting of total station, crack meters, TLS scanning, and GB InSAR continuous monitoring. Racek et al. (2021) used a combination of crack gauges, meteorological data, and thermal monitoring to decipher rockfall triggering factors and long-term rock mass development at various sites and geomorphological conditions.

Maintenance requirements and the price of sensors can be time and financially demanding. Additionally, using different sensors brings complications in data storage and processing. Usually, more data processing systems are deployed within one multisensor monitoring system. Additional costs are related to experienced technicians, and data analysts as one person cannot usually operate many sophisticated systems. Complex and expensive monitoring systems are deployed within known unstable rock slopes that pose a threat to critical infrastructure or urban areas. Examples of such monitoring can be Åknes rockslide in Norway (Jaboyedoff et al. 2011), Randa and Preonzo rockslides in Switzerland (Loew et al. 2012, 2017), or Monsterrat rock in Spain (Janeras et al. 2017). There, the expenses for the construction and operation of the system are justified by lowering the risk of fatal failure.

1.5 Concluding Remarks

This paper brings an overview of modern methods used for rock slope characterization, rock slope stability assessment, rockfall monitoring, and early warning. Monitoring methods are presented in five groups according to their primary purpose and principle (i.e., geodetical, geotechnical, geophysical, remote sensing, and dating

methods). In the last twenty years, a constant increase in the number of published papers can be seen with the "rockfall/landslide monitoring" topic reaching exponential growth (Blahůt et al. 2021). The share of different modern monitoring methods (based on the topic "rock mass/rockfall monitoring") from the Web of Science Core Collection (WoS) is shown in Fig. 1.2. A relatively stable share of different methods has changed since 2015 when the rapid growth of UAV applications and a decrease in GNSS methods can be observed. Or, more generally, an increase in remote sensing techniques compared to geodetical and geophysical ones is clearly visible in the share of different traditional techniques mentioned in a detailed way by Racek and Blahůt (2022, in this volume). A grouping was performed using cluster analysis to

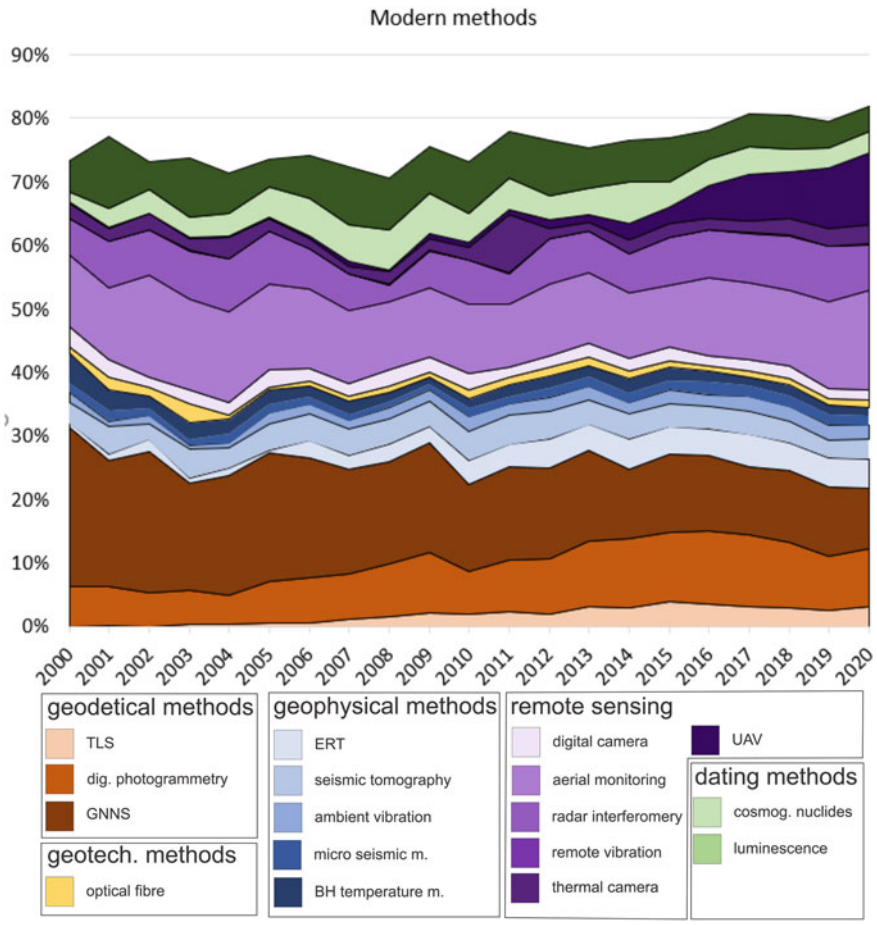

Fig. 1.2 Modern methods and their percentual share within papers published on the WoS with the topic "rock mass/rock slope/ rock fall monitoring"

have a deeper idea about the methods used in rock mass characterisation and rockfall monitoring.

Traditional and modern rock slope monitoring methods can be grouped according to various properties (i.e., primary and secondary purpose, principal of measurement, sensor placement, spatial and temporal resolution, precision and spatial extent. The results of such cluster analysis are shown in Fig. 1.3.

It is evident that the first cluster shows mostly single-measurement methods used for rock slope/mass characterisation, while the second cluster displays mapping and geotechnical classifications. The third cluster summarizes dating techniques. The fourth and largest cluster shows precise geodetical and geotechnical widely-used methods, while the fifth cluster depicts modern geophysical methods. The sixth and second-largest cluster represents the remote sensing methods. The presented methods are rarely used independently and are usually combined in complex systems to get data about rock slope dynamics and their influencing factors. Systems are designed site-specifically to get the best possible results. Their design depends on the monitoring purpose, financial resources, and required data outcomes. The use of a particular method depends on the type and velocity of movement, accessibility of the monitored feature, and purpose of the designed system. When these conditions are abided, good quality and meaningful data are obtained. Due to a lack of understanding of rock fall triggering and preparatory mechanisms, the design of the monitoring system requires an experienced researcher. Additionally, well-trained operators (technicians and data analysts) are needed for specialised and complicated monitoring systems and techniques. The ultimate goal of monitoring design is to deploy as few sensors as it is possible to ensure robustness but still be able to describe the complex rock slope

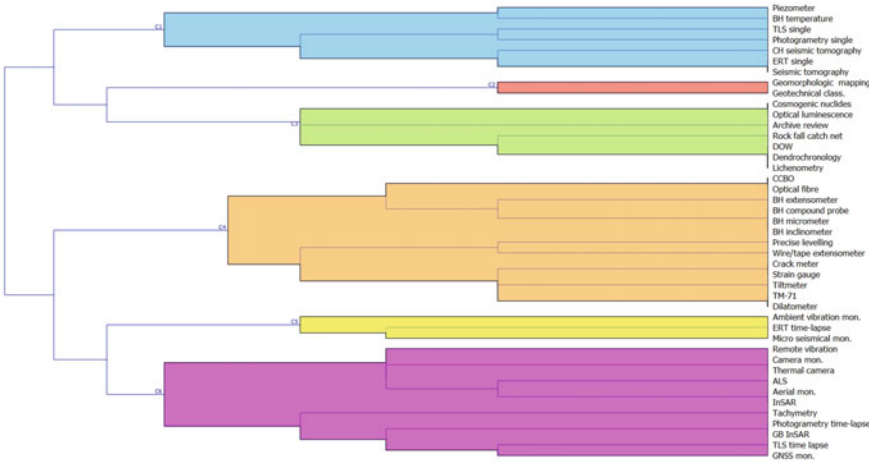

Fig. 1.3 Traditional and modern monitoring methods grouped into clusters based on their main application potential

behaviour. Also, there are emerging new initiatives such as LandAware (www.landaware.org), where experts (i.e., scientists, managers, stakeholders) in landslide monitoring exchange their experience and innovations related to landslide monitoring and early warning.

Acknowledgements We would like to thank Charles University and the Czech Academy of Sciences for their financial support. This research was performed in the framework of the long-term conceptual development research organisation RVO: 67985891, TAČR project no. SS02030023 "Rock environment and resources" within the programme "Environment for life", internal financing from Charles University Progress Q44 and SVV (SVV260438) and the Charles University Grant Agency (GAUK 359421).

References

Abellan A, Jaboyedoff M, Oppikofer T, Vilaplana JM (2009) Detection of millimetric deformation using a terrestrial laser scanner: experiment and application to a rockfall event. Nat Hazards Earth Syst Sci 9:365–372. https://doi.org/10.5194/nhess-9-365-2009

Abellan A, Vilaplana JM, Calvet J, Garcia-Selles D, Asensio E (2011) Rockfall monitoring by terrestrial laser scanning – case study of the basaltic rock face at Castellfollit de la Roca (Catalonia, Spain). Nat Hazards Earth Syst Sci 11:829–841. https://doi.org/10.5194/nhess-11-829-2011

Amitrano D, Grasso JR, Senfaute G (2005) Seismic precursory patterns before a cliff collapse and critical point phenomena. Geophys Res Lett 32:L08314. https://doi.org/10.1029/2004GL022270

Amitrano D, Gaffet S, Malet J-P, Maquaire O (2007) Understanding mudslides through microseismic monitoring: the Super-Sauze (South-East French Alps) case study. Bull Soc Geol Fr 178:149–157. https://doi.org/10.2113/gssgfbull.178.2.149

Amitrano D, Arattano M, Chiarle M, Mortara G, Occhiena C, Pirulli M, Scavia C (2010) Microseismic activity analysis for the study of the rupture mechanisms in unstable rock masses. Nat Hazards Earth Syst Sci 10:831–841. https://doi.org/10.5194/nhess-10-831-2010

Anderson K, Westoby MJ, James MR (2019) Low-budget topographic surveying comes of age: structure from motion photogrammetry in geography and the geosciences. Prog Phys Geo Earth Environ 43:163–173. https://doi.org/10.1177/0309133319837454

Antonello G, Casagli N, Farina P, Leva D, Nico G, Sieber AJ, Tarchi D (2004) Ground-based SAR interferometry for monitoring mass movements. Landslides 1:21–28. https://doi.org/10.1007/s10346-003-0009-6

Arosio D, Longoni L, Papini M, Scaioni M, Zanzi L, Alba M (2009) Towards rockfall forecasting through observing deformations and listening to microseismic emissions. Nat Hazards Earth Syst Sci 9:1119–1131. https://doi.org/10.5194/nhess-9-1119-2009

Arosio D, Corsini A, Giusti R, Zanzi L (2017) Seismic noise measurements on unstable rock blocks: the case of Bismantova rock cliff. In: Mikoš M, Arbanas Ž, Yin Y, Sassa K (eds) Advancing culture of living with landslides. WLF 2017. Springer, Cham, pp 325–332. https://doi.org/10.1007/978-3-319-53487-9_37

Assali P, Grussenmeyer P, Villemin T, Pollet N, Viguier F (2014) Surveying and modeling of rock discontinuities by terrestrial laser scanning and photogrammetry: semi-automatic approaches for linear outcrop inspection. J Struct Geol 66:102–114. https://doi.org/10.1016/j.jsg.2014.05.014

Azzoni A, Labarbera G, Zaninetti A (1995) Analysis and prediction of rockfalls using a mathematical model. Int J Rock Mech Min Sci & Geomech Abstr 32:709–724. https://doi.org/10.1016/0148-9062(95)00018-C

Babacan AE, Gelisli K, Ersoy H (2014) Seismic tomography and surface wave analysis-based methodologies on evaluation of geotechnical properties of volcanic rocks: a case study. J Earth Sci 25:348–356. https://doi.org/10.1007/s12583-014-0417-7

Balco G, Soreghan GS, Sweet DE, Marra KR, Bierman PR (2013) Cosmogenic-nuclide burial ages for Pleistocene sedimentary fill in Unaweep Canyon, Colorado, USA. Quat Geochronol 18:149–157. https://doi.org/10.1016/j.quageo.2013.02.002

Balek J, Blahůt J (2017) A critical evaluation of the use of an inexpensive camera mounted on a recreational unmanned aerial vehicle as a tool for landslide research. Landslides 14:1217–1224. https://doi.org/10.1007/s10346-016-0782-7

Bardi F, Raspini F, Ciampalini A, Kristensen L, Rouyet L, Lauknes TR, Frauenfelder R, Casagli N (2016) Space-borne and ground-based InSAR data integration: the Åknes test site. Remote Sens 8:237. https://doi.org/10.3390/rs8030237

Barla G, Antolini F, Gigli G (2016) 3D Laser scanner and thermography for tunnel discontinuity mapping. Geomech Tunn 9:29–36

Barlow J, Gilham J, Cofra II (2017) Kinematic analysis of sea cliff stability using UAV photogrammetry. Int J Remote Sens 38:2464–2479. https://doi.org/10.1080/01431161.2016.1275061

Baroň I, Bečkovský D, Míča L (2014) Application of infrared thermography for mapping open fractures in deep-seated rockslides and unstable cliffs. Landslides 11:15–27. https://doi.org/10.1007/s10346-012-0367-z

Bastos AS, Hasegawa H (2013) Behaviour of GPS signal interruption probability under tree canopies in different forest conditions. Eur J Remote Sens 46:613–622. https://doi.org/10.5721/EuJRS20134636

Bateman MD (2019) Handbook of luminescence dating. Whittles Publishing, Dunbeith, Scotland

Bauer C, Proske H (2017) Rockfall runout modelling for hazard zonation considering macro-topographic dispersion. Z Geomorphol 61:225–241. https://doi.org/10.1127/zfg/2017/0461

Belknap EP, Gilmore JB (1987) Use of time-lapse movie photography in landslide monitoring. Transp Res Rec 1119:39–46

Benedetti L, van der Woerd J (2014) Cosmogenic nuclide dating of earthquakes, faults, and toppled blocks. Elements 10:357–361. https://doi.org/10.2113/gselements.10.5.357

Blahůt J, Mitrovic-Woodell I, Baroň I, René M, Rowberry M, Blard P-H, Hartvich F, Balek J, Meletlidis S (2020) Volcanic edifice slip events recorded on the fault plane of the San Andrés Landslide, El Hierro Canary Islands. Tectonophysics 776:228317. https://doi.org/10.1016/j.tecto.2019.228317

Blahůt J, Jaboyedoff M, Thiebbes B (2021) "Novel approaches in landslide monitoring and data analysis" special issue: trends and challenges. Appl Sci 11(21):10453. https://doi.org/10.3390/app112110453

Blikra LH (2012) The Åknes rockslide, Norway. In: Clague JJ, Stead D (eds) Landslides: types, mechanisms and modelling. Cambridge University Press, pp 323–335. https://doi.org/10.1017/CBO9780511740367.027

Blistan P, Kovanic L, Zeliznakova V, Palkova J (2016) Using UAV photogrammetry to document rock outcrops. Acta Montan Slovaca 21:154–161

Böhme M, Oppikofer T, Longva O, Jaboyedoff M, Hermanns RL, Derron MH (2015) Analyses of past and present rock slope instabilities in a fjord valley: implications for hazard estimations. Geomorphology 248:464–474. https://doi.org/10.1016/j.geomorph.2015.06.045

Bottelin P, Jongmans D, Baillet L, Lebourg T, Hantz D, Levy C, Le Roux O, Cadet H, Lorier L, Rouiller JD, Turpin J, Darras L (2013) Spectral analysis of prone-to-fall rock compartments using ambient vibrations. J Environ Eng Geophys 18:205–217. https://doi.org/10.2113/JEEG18.4.205

Bottelin P, Jongmans D, Daudon D, Mathy A, Helmstetter A, Bonilla-Sierra V, Cadet H, Richefeu V, Lorier L, Baillet L, Villard P, Donze F (2014) Seismic and mechanical studies of the artificially triggered rockfall at Mount Néron (French Alps, December 2011). Nat Hazards Earth Syst Sci 14:3175–3193. https://doi.org/10.5194/nhess-14-3175-2014

Bovenga F, Pasquariello G, Pellicani R, Refice A, Spilotro G (2017) Landslide monitoring for risk mitigation by using corner reflector and satellite SAR interferometry: the large landslide of Carlantino (Italy). CATENA 151:49–62. https://doi.org/10.1016/j.catena.2016.12.006

Bregman ND, Bailey RC, Chapman CH (1989) Crosshole seismic tomography. Geophysics 54:200–215. https://doi.org/10.1190/1.1442644

Burjanek J, Gischig V, Moore JR, Fah D (2018) Ambient vibration characterization and monitoring of a rock slope close to collapse. Geophys J Int 212:297–310. https://doi.org/10.1093/gji/ggx424

Burland JB, Chapman T (2012) ICE manual of geotechnical engineering. ICE, London

Carla T, Farina P, Intrieri E, Botsialas K, Casagli N (2017) On the monitoring and early-warning of brittle slope failures in hard rock masses: examples from an open-pit mine. Eng Geol 228:71–81. https://doi.org/10.1016/j.enggeo.2017.08.007

Cesta J, Ward DJ (2016) Timing and nature of alluvial fan development along the Chajnantor Plateau, Northern Chile. Geomorphology 273:412–427. https://doi.org/10.1016/j.geomorph.2016.09.003

Chambers K, Kendall MJ, Brandsberg-Dahl S, Rueda J (2010) Testing the ability of surface arrays to monitor microseismic activity. Geophys Prospect 58:821–830. https://doi.org/10.1111/j.1365-2478.2010.00893.x

Chambers JE, Wilkinson PB, Kuras O, Ford JR, Gunn DA, Meldrum PI, Pennington CVL, Weller AL, Hobbs PRN, Ogilvy RD (2011) Three-dimensional geophysical anatomy of an active landslide in Lias Group mudrocks, Cleveland Basin, UK. Geomorphology 125:472–484. https://doi.org/10.1016/j.geomorph.2010.09.017

Chapot MS, Sohbati R, Murray AS, Pederson JL, Rittenour TM (2012) Constraining the age of rock art by dating a rockfall event using sediment and rock-surface luminescence dating techniques. Quat Geochronol 13:18–25. https://doi.org/10.1016/j.quageo.2012.08.005

Chigira M, Nakamoto M, Nakata E (2002) Weathering mechanisms and their effects on the landsliding of ignimbrite subject to vapor-phase crystallization in the Shirakawa pyroclastic flow, northern Japan. Eng Geol 66:111–125. https://doi.org/10.1016/S0013-7952(02)00035-2

Chuang YC, Shiu YS (2018) Relationship between landslides and mountain development—Integrating geospatial statistics and a new long-term database. Sci Total Environ 622–623:1265–1276. https://doi.org/10.1016/j.scitotenv.2017.12.03

Coccia S, Kinscher J, Valle A (2016) Microseismic and meteorological monitoring of Séchili-enne (French Alps) rock slope destabilisation. In: 3. International symposium rock slope stability (Rss2016), Nov 2016, Lyon, France, pp 31–32

Collins B, Stock GM (2016) Rockfall triggering by cyclic thermal stressing of exfoliation fractures. Nat Geosci 9:395–400. https://doi.org/10.1038/ngeo2686

Colombero C, Comina C, Umili G, Vinciguerra S (2016) Multiscale geophysical characterization of an unstable rock mass. Tectonophysics 675:275–289. https://doi.org/10.1016/j.tecto.2016.02.045

Colomina I, Molina P (2014) Unmanned aerial systems for photogrammetry and remote sens.: a review. ISPRS J Photogramm Remote Sens 92:79–97. https://doi.org/10.1016/j.isprsjprs.2014.02.013

Crosta GB, Agliardi F (2002) How to obtain alert velocity thresholds for large rockslides. Phys Chem Earth 27:1557–1565. https://doi.org/10.1016/S1474-7065(02)00177-8

Crosta GB, Cancelli P, Tamburini A, Alberto W, Broccolato M, Castellanza R, Frattini P, Agliardi F, Rivolta C, Leva D (2012) Chasing a complete understanding of a rapid moving rock slide: the La Saxe landslide. Geophys Res Abstracts 14:EGU2012–11813

Crosta GB, Di Prisco C, Frattini P, Frigerio G, Castellanza R (2014) Chasing a complete understanding of the triggering mechanisms of a large rapidly evolving rockslide. Landslides 11:747–764. https://doi.org/10.1007/s10346-013-0433-1

Crosta GB, Agliardi F, Rivolt C, Alberti S, Dei Cas L (2017) Long-term evolution and early warning strategies for complex rockslides by real-time monitoring. Landslides 14:1615–1632. https://doi.org/10.1007/s10346-017-0817-8

D'Amato J, Hantz D, Guerin A, Jaboyedoff M, Baillet L, Mariscal AM (2016) Influence of meteorological factors on rockfall occurrence in a middle mountain limestone cliff. Nat Hazards Earth Syst Sci 16:719–735. https://doi.org/10.5194/nhess-16-719-2016

De Vita P, Carratu MT, La Barbera G, Santoro S (2013) Kinematics and geological constraints of the slow-moving Pisciotta rock slide (southern Italy). Geomorphology 201:415–429. https://doi.org/10.1016/j.geomorph.2013.07.015

Deparis J, Jongmans D, Garambois S, Lévy C, Baillet LL (2011) Geophysical detection and structural characterization of discontinuities in rock slopes. Rockfall engineering. Wiley, ISTE, pp 1–38

Di Matteo L, Romeo S, Kieffer DS (2017) Rock fall analysis in an Alpine area by using a reliable integrated monitoring system: results from the Ingelsberg slope (Salzburg Land, Austria). Bull Eng Geol Environ 76:413–420. https://doi.org/10.1007/s10064-016-0980-5

Dietze M, Mohadjer S, Turowski JM, Ehlers TA, Hovius N (2017) Seismic monitoring of small alpine rockfalls – validity, precision and limitations. Earth Surf Dyn 5:653–668. https://doi.org/10.5194/esurf-5-653-2017

do Amaral Vargas E, Velloso RQ, Chávez LE, Gusmao L (2013) On the effect of thermally induced stresses in failures of some rock slopes in Rio de Janeiro, Brazil. Rock Mech Rock Eng 46:123–134. https://doi.org/10.1007/s00603-012-0247-9

Dussauge-Peisser C, Wathelet M, Jongmans D, Havenith H Couturier B, Teerlynck H (2002) Seismic tomography and ground penetrating radar applied on rock slope instability analysis. Application on a limestone cliff in the Chartreuse Massif, France. In: EGU general assembly conference abstracts (vol 27)

Dussauge Peisser C, Wathelet M, Jongmans, D, Hantz, D, Couturier, B, Sintes, M (2003) Investigation of a fractured limestone cliff (Chartreuse Massif, France) using seismic tomography and ground-penetrating radar. Near Surf Geophys 1:161–170. https://doi.org/10.3997/1873-0604.2003007

Engel P, Schweimler B (2016) Design and implementation of a modern automatic deformation monitoring system. J Appl Geod 10:79–85. https://doi.org/10.1515/jag-2015-0024

Eppes M, Magi B, Hallet B, Delmelle E, Mackenzie-Helnwein P, Warren K, Swami S (2016) Deciphering the role of solar-induced thermal stresses in rock weathering. Geol Soc America Bull 128:1315–1338. https://doi.org/10.1130/B31422.1

Eppler J, Kubanski M, Sharma J, Busler J (2015) High temporal resolution permafrost monitoring using a multiple stack InSAR technique. Int Arch Photogrammetry Remote Sens Spatial Inf Sci 40:1171–1176

Erharter DS, Kieffer DS, Prager C (2018) UAV-based discontinuity analyses and rock fall source mapping in Alpine Terrain (Pletzachkogel/Tyrol/Austria). In: IAEG/AEG annual meeting proceedings, San Francisco, California vol 1. Springer Cham, San Francisco, California

Eriksen H, Lauknes TR, Larsen Y, Corner GD, Bergh SG, Dehls J, Kierulf HP (2017) Visualizing and interpreting surface displacement patterns on unstable slopes using multi-geometry satellite SAR interferometry (2D InSAR). Remote Sens Environ 191:297–312. https://doi.org/10.1016/j.rse.2016.12.024

Fanos A, Pradhan B, Aziz AA, Jebur MN, Park HJ (2016) Assessment of multi-scenario rockfall hazard based on mechanical parameters using high-resolution airborne laser scanning data and GIS in a tropical area. Environ Earth Sci 75:1129. https://doi.org/10.1007/s12665-016-5936-3

Fanos A, Pradhan B, Mansor S, Yusoff ZM, Abdullah AFB (2018) A hybrid model using machine learning methods and GIS for potential rockfall source identification from airborne laser scanning data. Landslides 15:1833–1850. https://doi.org/10.1007/s10346-018-0990-4

Fantini A, Fiorucci M, Martino S (2017) Rock falls impacting railway tracks: detection analysis through an artificial intelligence camera prototype. Wireless Commun Mobile Comput 386928:1–11. https://doi.org/10.1155/2017/9386928

Fazio NL, Perrotti M, Andriani GF, Mancini F, Rossi P, Castagnetti C, Lollino P (2019) A new methodological approach to assess the stability of discontinuous rocky cliffs using in-situ surveys supported by UAV-based techniques and 3-D finite element model: a case study. Eng Geol 260:105205. https://doi.org/10.1016/j.enggeo.2019.105205

Ferlisi S, Cascini L, Corominas J, Matano F (2012) Rockfall risk assessment to persons travelling in vehicles along a road: the case study of the Amalfi coastal road (southern Italy). Nat Hazard 62:691–721. https://doi.org/10.1007/s11069-012-0102-z

Fernandez T, Luis Perez-Garcia J, Miguel Gomez-Lopez J, Cardenal J, Calero J, Sanchez-Gomez M, Delgado J, Tovar-Pescador J (2020) Multitemporal analysis of gully erosion in olive groves by means of digital elevation models obtained with aerial photogrammetric and LiDAR data. ISPRS Int J Geo-Inf 9:260. https://doi.org/10.3390/ijgi9040260

Ferrero AM, Migliazza M, Roncella R, Segalini A (2011) Rock cliffs hazard analysis based on remote geostructural surveys: the Campione del Garda case study (Lake Garda, Northern Italy). Geomorphology 125:457–471. https://doi.org/10.1016/j.geomorph.2010.10.009

Fey C, Wichmann V (2017) Long-range terrestrial laser scanning for geomorphological change detection in alpine terrain – handling uncertainties. Earth Surf Proc Landforms 42:789–802. https://doi.org/10.1002/esp.4022

Fiorucci F, Cardinali M, Carla R, Rossi M, Mondini AC, Santurri L, Ardizzone F, Guzzetti F (2011) Seasonal landslide mapping and estimation of landslide mobilization rates using aerial and satellite images. Geomorphology 129:59–70. https://doi.org/10.1016/j.geomorph.2011.01.013

Fiorucci M, Marmoni GM, Martino S, Mazzanti P (2018) Thermal response of jointed rock masses inferred from infrared thermographic surveying (Acuto test-site, Italy). Sensors 18(7):2221. https://doi.org/10.3390/s18072221

Foglino S, Foglino L, Foglino V, Lovisolo M (2018) DMS® 3D PLUS: a new automatic in-place instrument for geotechnical multiparametric monitoring. 10th international symposium on field measurements in geomechanics FMGM 2018. Rio de Janeiro, p 6

Frodella W, Ciampalini A, Gigli G, Lombardi L, Raspini F, Nocentini M, Scardigli C, Casagli N (2016) Synergic use of satellite and ground based remote sens. methods for monitoring the San Leo rock cliff (Northern Italy). Geomorphology 264:80–94. https://doi.org/10.1016/j.geomorph.2016.04.008

Frodella W, Gigli G, Morelli S, Lombardi L, Casagli N (2017) Landslide mapping and characterization through infrared thermography (IRT): suggestions for a methodological approach from some case studies. Remote Sens 9:1281. https://doi.org/10.3390/rs9121281

Fuchs M, Lang A (2009) Luminescence dating of hillslope deposits—a review. Geomorphology 109:17–26. https://doi.org/10.1016/j.geomorph.2008.08.025

Fuchs F, Lenhardt W, Bokelmann G, Tardif P (2018) Seismic detection of rockslides at regional scale: examples from the Eastern Alps and feasibility of kurtosis-based event location. Earth Surf Dyn 6:955–970. https://doi.org/10.5194/esurf-6-955-2018

Gage JA, Wang HF, Fratta D, Turner AL (2014) In situ measurements of rock mass deformability using fiber Bragg grating strain gauges. Int J Rock Mech Min Sci 1997(71):350–361. https://doi.org/10.1016/j.ijrmms.2014.07.021

Gallach X, Ravanel L, Egli M, Brandova D, Schaepman M, Christl M, Gruber S, Deline P, Carcaillet J, Pallandre F (2018) Timing of rockfalls in the Mont Blanc massif (Western Alps): evidence from surface exposure dating with cosmogenic 10Be. Landslides 15:1991–2000. https://doi.org/10.1007/s10346-018-0999-8

Ghabraie B, Smith G, Holden L (2015) Application of 3D laser scanner, optical transducers and digital image processing techniques in physical modelling of mining-related strata movement. Int J Rock Mech Min Sci 1997(80):219–230. https://doi.org/10.1016/j.ijrmms.2015.09.025

Ghosh A, Sharma AK, Nayak B, Sagar SP (2014) Infrared thermography: an approach for iron ore gradation. Miner Eng 62:85–90. https://doi.org/10.1016/j.mineng.2013.12.002

Giani GP, Giacomini A, Migliazza M, Segalini A (2004) Experimental and theoretical studies to improve rock fall analysis and protection work design. Rock Mech Rock Eng 37:369–389. https://doi.org/10.1007/s00603-004-0027-2

Gigli G, Morelli S, Fornera S, Casagli N (2014) Terrestrial laser scanner and geomechanical surveys for the rapid evaluation of rock fall susceptibility scenarios. Landslides 11:1–14. https://doi.org/10.1007/s10346-012-0374-0

Gilham J, Barlow J, Moore R (2019) Detection and analysis of mass wasting events in chalk sea cliffs using UAV photogrammetry. Eng Geol 250:101–112. https://doi.org/10.1016/j.enggeo.2019.01.013

Gili J, Corominas J, Rius J (2000) using global positioning system techniques in landslide monitoring. Eng Geol 55:167–192. https://doi.org/10.1016/S0013-7952(99)00127-1

Gillan J, Karl JW, Barger NN, Elaksher A, Duniway MC (2016) Spatially explicit rangeland erosion monitoring using high-resolution digital aerial imagery. Rangeland Ecol Manage 69:95–107. https://doi.org/10.1016/j.rama.2015.10.012

Glisic B, Inaudi D (2008) Fibre optic methods for structural health monitoring. Wiley

Gomez C, Purdie H (2016) UAV-based photogrammetry and geocomputing for hazards and disaster risk monitoring–a review. Geoenviron Disasters 3. https://doi.org/10.1186/s40677-016-0060-y

Granger D, Lifton NA, Willenbring JK (2013) A cosmic trip: 25 years of cosmogenic nuclides in geology. Geol Soc Am Bull 125:1379–1402. https://doi.org/10.1130/B30774.1

Greggio N, Giambastiani BMS, Balugani E, Amaini C, Antonellini M (2018) High-resolution electrical resistivity tomography (ERT) to characterize the spatial extension of freshwater lenses in a salinized coastal aquifer. Water 10:1067. https://doi.org/10.3390/w10081067

Gu C, Zaitian M, Jianhua G, Jingzhong C (2002) A review on the growth of seismic tomography. Progress in exploration geophysics 3

Guerin A, Jaboyedoff M, Collins BD, Derron MH, Stock GM, Matasci B, Boesiger M, Lefeuvre C, Podladchikov YY (2019) Detection of rock bridges by infrared thermal imaging and modeling. Sci Rep 9:13138–13138. https://doi.org/10.1038/s41598-019-49336-1

Gundersen R, Norland R, Denby CR (2018) Ground-based differential interferometric radar monitoring of unstable mountain blocks in a coastal environment. Remote Sens 10:914. https://doi.org/10.3390/rs10060914

Gunzburger Y, Merrien-Soukatchoff V, Guglielm Y (2005) Influence of daily surface temperature fluctuations on rock slope stability: case study of the Rochers de Valabres slope (France). Int J Rock Mech Min Sci 1997(42):331–349. https://doi.org/10.1016/j.ijrmms.2004.11.003

Haas F, Heckmann T, Wichmann V, Becht M (2012) Runout analysis of a large rockfall in the Dolomites/Italian Alps using LIDAR derived particle sizes and shapes. Earth Surf Processes Landforms 37:1444–1455. https://doi.org/10.1002/esp.3295

Hall S, De Sanctis F, Viggian G (2006) Monitoring fracture propagation in a soft rock (Neapolitan Tuff) using acoustic emissions and digital images. Pure Appl Geophys 163:2171–2204. https://doi.org/10.1007/s00024-006-0117-z

Hardy HR (2003) Acoustic emission/microseismic activity: volume 1: principles, techniques and geotechnical applications. Taylor and Francis

He MC, Gong WL, Zhai HM, Zhang HP (2010) Physical modeling of deep ground excavation in geologically horizontal strata based on infrared thermography. Tunn Undergr Space Technol 25:366–376. https://doi.org/10.1016/j.tust.2010.01.012

Heincke B, Maure H, Green AG, Willenberg H, Spillmann T, Burlini L (2006) Characterizing an unstable mountain slope using shallow 2D and 3D seismic tomography. Geophysics 71:B241–B256. https://doi.org/10.1190/1.2338823

Heincke B, Guenther T, Dalsegg E, Ronning JS, Ganerod GV, Elvebakk H (2010) Combined three-dimensional electric and seismic tomography study on the Åknes rockslide in western Norway. J Appl Geophys 70:292–306. https://doi.org/10.1016/j.jappgeo.2009.12.004

Henderson IH, Saintot A (2011) Regional spatial variations in rockslide distribution from structural geology ranking: an example from Storfjorden, Western Norway. Geol Soc, London Special Publications 351:79–95

Hermanns RL, Fischer L, Oppikofer T, Bøhme M, Dehls JF (2011) Mapping of unstable and potentially unstable slopes in Sogne og Fjordane. NGU Rapport 2011.055, p 198

Hermanns RL, Blikra LH, Anda E, Saintot A, Dahle H, Oppikofer T, Fischer L, Bunkholt H, Böhme M, Dehls JF, Lauknes TR, Redfield T, Osmundsen PT, Eiken T (2013) Systematic mapping of large unstable rock slopes in Norway. In: Landslide science and practice. Springer, Berlin Heidelberg. https://doi.org/10.1007/978-3-642-31325-7_3

Hibert C, Malet JP, Bourrier F, Provost F, Berger F, Bornemann P, Mermin E (2017) Single-block rockfall dynamics inferred from seismic signal analysis. Earth Surf Dyn 5:283–292. https://doi.org/10.5194/esurf-5-283-2017

Hong CY, Zhang YF, Zhang MX, Gordon LLM, Liu LQ (2016) Application of FBG sensors for geotechnical health monitoring, a review of sensor design, implementation methods and packaging techniques. Sens Actuators A Phys 244:184–197. https://doi.org/10.1016/j.sna.2016.04.033

Hugentobler M, Loew S, Aaron J, Roques C, Oestreicher N (2020) Borehole monitoring of thermo-hydro-mechanical rock slope processes adjacent to an actively retreating glacier. Geomorphology 362:107190. https://doi.org/10.1016/j.geomorph.2020.107190

Hugh EL (2006) Video motion detection for real-time hazard warnings in surface mines. The National Institute for Occupational Safety and Health (NIOSH)

Hürlimann M, Abanco C, Moya J (2012) Rockfalls detached from a lateral moraine during spring season. 2010 and 2011 events observed at the Rebaixader debris-flow monitoring site (Central Pyrenees, Spain). Landslides 9:385–393. https://doi.org/10.1007/s10346-011-0314-4

Improta L, Bruno PP (2007) Combining seismic reflection with multifold wide-aperture profiling: an effective strategy for high-resolution shallow imaging of active faults. Geophys Res Lett 34. https://doi.org/10.1029/2007GL031893

Ivy-Ochs S, Jason P (2014) Dating disappearing ice with cosmogenic nuclides. Elements 10:351–356. https://doi.org/10.2113/gselements.10.5.351

Ivy-Ochs S, Kober F (2008) Surface exposure dating with cosmogenic nuclides. E&G Quaternary Sci J 57:179–209. https://doi.org/10.3285/eg.57.1-2.7

Jaboyedoff M, Oppikofer T, Derron MH, Blikra LH, Böhme M, Saintot A (2011) Complex landslide behaviour and structural control: a three-dimensional conceptual model of Åknes rockslide, Norway. Geol Soc Spec Publ 351. https://doi.org/10.1144/SP351.8

Jaboyedoff M, Oppikofer T, Abellan A, Derro MH, Loye A, Metzge R, Pedrazzini A (2012) Use of LIDAR in landslide investigations: a review. Nat Hazard 61:5–28. https://doi.org/10.1007/s11069-010-9634-2

James M, Robson S, Smith MW (2017) 3-D uncertainty-based topographic change detection with structure-from-motion photogrammetry: precision maps for ground control and directly georeferenced surveys. Earth Surf Processes Landforms 42:1769–1788. https://doi.org/10.1002/esp.4125

Janeras M, Jara JA, Royan MJ, Vilaplana JM, Aguasca A, Fabregas X, Gili JA, Buxo P (2017) Multi-technique approach to rockfall monitoring in the Montserrat massif (Catalonia, NE Spain). Eng Geol 219:4–20. https://doi.org/10.1016/j.enggeo.2016.12.010

Jin H, Yu Q, Lii L, Guo D, He R, Yu S, Sun GLY (2007) Degradation of permafrost in the Xing'anling Mountains, northeastern China. Permafr Periglac Processes 18:245–258. https://doi.org/10.1002/ppp.589

Jones L, Kyle PR, Oppenheimer C, Frechette JD, Oka MH (2015) Terrestrial laser scanning observations of geomorphic changes and varying lava lake levels at Erebus volcano, Antarctica. J Volcanol Geotherm Res 295:43–54. https://doi.org/10.1016/j.jvolgeores.2015.02.011

Jongmans D, Garambois S (2007) Geophysical investigation of landslides: a review. Bull Soc Geol Fr 178:101–112. https://doi.org/10.2113/gssgfbull.178.2.101

Jordan CJ, Napier B (2016) Developing digital fieldwork technologies at the British Geological Survey. Geol Soc Spec Publ 436:219–229. https://doi.org/10.1144/SP436.6

Kalogirou K, Iliaskos E (2019) Monitoring of tempi valley critical rock masses: establishment of special monitoring network and procedures in Aegean Motorway S.A. concession project. 4 th joint international symposium on deformation monitoring (JISDM), 15–17 May 2019, Athens, Greece

Kellerer-Pirklbauer A, Rieckh M (2016) Monitoring nourishment processes in the rooting zone of an active rock glacier in an alpine environment. Z Geomorphol Suppl 60:99–121. https://doi.org/10.1127/zfg_suppl/2016/00245

Kenner R, Buehler Y, Delaloye R, Ginzler C, Phillips M (2014) Monitoring of high alpine mass movements combining laser scanning with digital airborne photogrammetry. Geomorphology 206:492–504. https://doi.org/10.1016/j.geomorph.2013.10.020

Kenner R, Phillips M, Limpach P, Beutel J, Hiller M (2018) Monitoring mass movements using georeferenced time-lapse photography: Ritigraben rock glacier, western Swiss Alps. Cold Reg Sci Technol 145:127–134. https://doi.org/10.1016/j.coldregions.2017.10.018

Kleinbrod U, Burjanek J, Hugentobler M, Amann F, Fah D (2017) A comparative study on seismic response of two unstable rock slopes within same tectonic setting but different activity level. Geophys J Int 211:1428–1448. https://doi.org/10.1093/gji/ggx376

Kleinbrod U, Burjanek J, Fah D (2019) Ambient vibration classification of unstable rock slopes: a systematic approach. Eng Geol 249:198–217. https://doi.org/10.1016/j.enggeo.2018.12.012

Korsgaard N, Nuth C, Khan SA, Kjeldsen KK, Bjork AA, Schomacker A, Kjaer KH (2016) Digital elevation model and orthophotographs of Greenland based on aerial photographs from 1978–1987. Sci Data 3:160032–160032. https://doi.org/10.1038/sdata.2016.32

Koukouvelas I, Litoseliti A, Nikolakopoulos K, Zygour V (2015) Earthquake triggered rock falls and their role in the development of a rock slope: the case of Skolis Mountain, Greece. Eng Geol 191:71–85. https://doi.org/10.1016/j.enggeo.2015.03.011

Krautblatter M, Verleysdonk S, Flores-Orozco A, Kemna A (2010) Temperature-calibrated imaging of seasonal changes in permafrost rock walls by quantitative electrical resistivity tomography (Zugspitze, German/Austrian Alps). J Geophys Res 115. https://doi.org/10.1029/2008JF001209

Kristensen L, Blikra LH (2013) Monitoring displacement on the Mannen rockslide in Western Norway. In: Landslide science and practice. Springer, Berlin, Heidelberg, pp 251–256. https://doi.org/10.1007/978-3-642-31445-2_32

Kristyanto THW, Indra TL, Syahputra R, Tempessy AS (2017) Determination of the landslide slip surface using electrical resistivity tomography (ERT) technique. In: Workshop on world landslide forum. Springer, Cham, pp 53–60. https://doi.org/10.1007/978-3-319-53498-5_7

Kromer R, Abellan A, Hutchinson DJ, Lato M, Chanut MA, Dubois L, Jaboyedoff M (2017) Automated terrestrial laser scanning with near-real-time change detection – monitoring of the Séchilienne landslide. Earth Surf Dyn 5:293–310. https://doi.org/10.5194/esurf-5-293-2017

Kromer R, Walton G, Gray B, Lato M (2019) Development and optimization of an automated fixed-location time lapse photogrammetric rock slope monitoring system. Remote Sens 11:1890. https://doi.org/10.3390/rs11161890

Krsak B, Blistan P, Paulikova A, Puskarova P, Kovanic L, Palkova J, Zeliznakova V (2016) Use of low-cost UAV photogrammetry to analyze the accuracy of a digital elevation model in a case study. Measurement 91:276–287. https://doi.org/10.1016/j.measurement.2016.05.028

Kukutsch R, Zurek P, Stolarik M (2010) Monitoring and documentation of flaking-off phenomena in the historical Jeronym mine. Acta Geodyn Geomater 7:343–348

Kurashima T, Horiguchi T, Izumita H, Furukava S, Koyamada Y (1993) Brillouin optical-fibre time-domain reflectometry. IEICE Trans Commun E76B:382–390

Kurz T, Dewit J, Buckley SJ, Thurmond JB, Hunt DW, Swennen R (2012) Hyperspectral image analysis of different carbonate lithologies (limestone, karst and hydrothermal dolomites): the Pozalagua Quarry case study (Cantabria, North-west Spain). Sedimentology 59:623–645. https://doi.org/10.1111/j.1365-3091.2011.01269.x

Lambiel C, Delaloye R (2004) Contribution of real-time kinematic GPS in the study of creeping mountain permafrost: examples from the Western Swiss Alps. Permafr Periglac Processes 15:229–241. https://doi.org/10.1002/ppp.496

Lato M, Hutchinson DJ, Gauthier D, Edwards T, Ondercin M (2015) Comparison of airborne laser scanning, terrestrial laser scanning, and terrestrial photogrammetry for mapping differential slope change in mountainous terrain. Can Geotech J 52:129–140. https://doi.org/10.1139/cgj-2014-0051

Lauknes TR, Grahn J, Royet L, Larsen Y, Böhme M, Dehls JF, Kristiansen L (2020) Mapping and characterization of unstable slopes with Sentinel-1 multi-geometry InSAR (activity line 2: public sector applications), Final report. NORCE Norwegian Research Centre, p 43

Lazar A, Beguž T, Vulič M (2018) Monitoring of the Belca rockfall. Acta Geotech Slov 15:2–15. https://doi.org/10.18690/actageotechslov.15.2.2-15.2018

Le Moigne J, Netanyahu NS, Eastman RD (2011) Image registration for remote sensing. Cambridge University Press

Le Roy G, Helmstetter A, Amitrano D, Guyoton F, Le Roux-Mallouf R, Tardif P (2019) Seismic analysis of the detachment and impact phases of a rockfall and application for estimating rockfall volume and free-fall height. J Geophys Res Earth Surf 124:2602–2622. https://doi.org/10.1029/2019JF004999

Leopold M, Voelkel J, Huber J, Dethier D (2013) Subsurface architecture of the Boulder Creek Critical Zone Observatory from electrical resistivity tomography. Earth Surf Processes Landforms 38:1417–1431. https://doi.org/10.1002/esp.3420

Lévy C, Baillet L, Jongmans D, Mourot P, Hantz D (2010) Dynamic response of the Chamousset rock column (Western Alps, France). J Geophys Res Earth Surf 115(F4). https://doi.org/10.1029/2009JF001606

Li L, Lan H (2015) Probabilistic modeling of rockfall trajectories: a review. Bull Eng Geol Environ 74:1163–1176. https://doi.org/10.1007/s10064-015-0718-9

Linker R, Klar A (2017) Detection of sinkhole formation by strain profile measurements using BOTDR: simulation study. J Geophys Res Earth Surf 143. https://doi.org/10.1061/(ASCE)EM.1943-7889.0000963

Loche M, Scaringi G, Blahůt J, Melis MT, Funedda A, Da Pelo S, Erbì I, Deiana G, Meloni MA, Cocco F (2021) An infrared thermography approach to evaluate the strength of a rock cliff. Remote Sens 13(7):1265. https://doi.org/10.3390/rs13071265

Loew S, Gischig V, Willenberg H, Alpiger A, Moore JR (2012) 24 Randa: kinematics and driving mechanisms of a large complex rockslide. Landslides: types, mechanisms and modeling, pp 297–309

Loew S, Gschwind S, Gischig V, Keller-Signer A, Valenti G (2017) Monitoring and early warning of the 2012 Preonzo catastrophic rockslope failure. Landslides 14:141–154. https://doi.org/10.1007/s10346-016-0701-y

Longoni L, Papini M, Brambilla D, Barazzetti L, Roncoroni F, Scaioni M, Ivanov VI (2016) Monitoring riverbank erosion in mountain catchments using terrestrial laser scanning. Remote Sens 8:241. https://doi.org/10.3390/rs8030241

Losasso L, Jaboyedoff M, Sdao F (2017) Potential rock fall source areas identification and rock fall propagation in the province of Potenza territory using an empirically distributed approach. Landslides 14:1593–1602. https://doi.org/10.1007/s10346-017-0807-x

Loucks EA, Neely A, DiBiase RA (2018) Using ground-based structure-from-motion photogrammetry to quantify heterogeneity in bedrock hillslope morphology. In: AGU Fall meeting abstracts

Lovisolo M, Della Giusta A (2005) Precision of D.M.S. columns from real time in-place measurements and improvement in micro-movements analysis with early warning function. WIT Transactions on Modelling and Simulation 41:177–186

Luzi G, Pieraccini M, Mecatti D, Noferini L, Guidi G, Moia F, Atzeni C (2004) Ground-based radar interferometry for landslides monitoring: atmospheric and instrumental decorrelation sources on experimental data. IEEE Trans Geosci Remote Sens 42:2454–2466. https://doi.org/10.1109/TGRS.2004.836792

Ma GC, Sawada K, Yashima A, Saito H (2015) Experimental study of the applicability of the remotely positioned laser doppler vibrometer to rock-block stability assessment. Rock Mech Rock Eng 48:787–802. https://doi.org/10.1007/s00603-014-0577-x

Madsen AT, Murray AS (2009) Optically stimulated luminescence dating of young sediments: a review. Geomorphology 109:3–16. https://doi.org/10.1016/j.geomorph.2008.08.020

Magnin F, Krautblatter M, Deline P, Ravanel L, Malet E, Bevington A (2015) Determination of warm, sensitive permafrost areas in near-vertical rockwalls and evaluation of distributed models by electrical resistivity tomography. J Geophys Res Earth Surf 120:745–762. https://doi.org/10.1002/2014JF003351

Mah J, McKinnon SD, Samson C, Thibodeau D (2016) Wire mesh filtering in 3D image data of rock faces. Tunnelling Underground Space Technol 52:111–118. https://doi.org/10.1016/j.tust.2015.11.005

Majzoub A, Stafford KW, Brown WA, Ehrhar JT (2017) Characterization and delineation of gypsum karst geohazards using 2D electrical resistivity tomography in Culberson County, Texas, USA. J Environ Eng Geophys 22:411–420. https://doi.org/10.2113/JEEG22.4.411

Mancini F, Salvin R (2019) Applications of photogrammetry for environmental research. ISPRS Int J Geoinf 8:542. https://doi.org/10.3390/ijgi8120542

Manikandan R, Balasubramanian M, Palanivel S (2017) Early warning system-vision based obstacle detection on railway track. Int J Pure App Math 117:1–10

Manousakis J, Zekkos D, Saroglou F, Clark M (2016) Comparison of UAV-enabled photogrammetry-based 3D point clouds and interpolated DSMs of sloping terrain for rockfall hazard analysis. Int Arch Photogramm Remote Sens Spatial Inf Sci XLII:71–77. https://doi.org/10.5194/isprs-archives-XLII-2-W2-71-2016

Mari JL, Mendes M, Chauris H, Yven B, Hayet M (2019) Seismic imaging: a practical approach. EDP Sciences

Marrero S, Hein AS, Naylor M, Attal M, Shanks R, Winter K, Woodward J, Dunning S, Westoby M, Sugden D (2018) Controls on subaerial erosion rates in Antarctica. Earth Planet Sci Lett 501:56–66. https://doi.org/10.1016/j.epsl.2018.08.018

Martin S, Campedel P, Ivy-Ochs S, Vigano A, Alfimov V, Vockenhuber C, Andreotti E, Carugati G, Pasqual D, Rigo M (2014) Lavini di Marco (Trentino, Italy): 36Cl exposure dating of a polyphase rock avalanche. Quat Geochronol 19:106–116. https://doi.org/10.1016/j.quageo.2013.08.003

Matas G, Lantada N, Corominas J, Gili J, Ruiz-Carulla R, Prades A (2020) Simulation of full-scale rockfall tests with a fragmentation model. Geosciences 10(5):168. https://doi.org/10.3390/geosciences10050168

McCaffrey KJW, Jones RR, Holdsworth RE, Wilson RW, Clegg P, Imber J, Hollman N, Trinks I (2005) Unlocking the spatial dimension: digital technologies and the future of geoscience fieldwork. J Geol Soc 162:927–938. https://doi.org/10.1144/0016-764905-017

McEwen LJ, Matthews JA, Owen G (2020) Development of a holocene glacier-fed composite alluvial fan based on surface exposure-age dating techniques: the Illåe fan, Jotunheimen, Norway. Geomorphology 363:1–15. https://doi.org/10.1016/j.geomorph.2020.107200

McHugh EL, Girard JM (2002) Evaluating techniques for monitoring rock falls and slope stability

Medjkane M, Maquaire O, Costa S, Roulland T, Letortu P, Fauchard C, Antoine R, Davidson R (2018) High-resolution monitoring of complex coastal morphology changes: cross-efficiency of SfM and TLS-based survey (Vaches-Noires cliffs, Normandy, France). Landslides 15:1097–1108. https://doi.org/10.1007/s10346-017-0942-4

Méndez A, Diatzikis E (2006) Fiber optic distributed pressure sensor based on Brillouin scattering. In: Optical fiber sensors. Optical Society of America

Micheletti N, Chandler JH, Lane SN (2015) Investigating the geomorphological potential of freely available and accessible structure-from-motion photogrammetry using a smartphone. Earth Surf Processes Landforms 40:473–486. https://doi.org/10.1002/esp.3648

Mills G, Fotopoulos G (2013) On the estimation of geological surface roughness from terrestrial laser scanner point clouds. Geosphere 9:1410–1416. https://doi.org/10.1130/GES00918.1

Mineo S, Pappalardo G (2016) the use of infrared thermography for porosity assessment of intact rock. Rock Mech Rock Eng 49:3027–3039. https://doi.org/10.1007/s00603-016-0992-2

Monsalve J, Baggett J, Bishop R, Ripepi N (2019) Application of laser scanning for rock mass characterization and discrete fracture network generation in an underground limestone mine. Int J Min Sci Technol 29:131–137. https://doi.org/10.1016/j.ijmst.2018.11.009

Moore JR, Gischig V, Button E, Loew S (2010) Rockslide deformation monitoring with fiber optic strain sensors. Nat Hazards Earth Syst Sci 10:191–201. https://doi.org/10.5194/nhess-10-191-2010

Moore J, Geimer PR, Finnegan R, Thorne MS (2018) Use of seismic resonance measurements to determine the elastic modulus of freestanding rock masses. Rock Mech Rock Eng 51:3937–3944. https://doi.org/10.1007/s00603-018-1554-6

Moos C, Fehlmann M, Trappmann D, Stoffel M, Dorren L (2018) Integrating the mitigating effect of forests into quantitative rockfall risk analysis – Two case studies in Switzerland. Int J Disaster Risk Reduct 32:55–74. https://doi.org/10.1016/j.ijdrr.2017.09.036

Motil A, Bergman A, Tur M (2016) State of the art of Brillouin fiber-optic distributed sensing. Opt Laser Technol 78:81–103. https://doi.org/10.1016/j.optlastec.2015.09.013

Mourot P (2016) A real-time seismic and displacement monitoring system for rock instability assessment—case studies in the French Alps. Proceedings of the first Asia Pacific slope stability in mining conference. Australian Centre for Geomechanics, pp 629–637

Nan S, Gao Q (2011) Application of distributed optical fiber sensor technology based on BOTDR in similar model test of backfill mining. In: Proceedings of 2nd international conference on mining engineering and metallurgical technology. Macau China, pp 34–39

Nishii R, Matsuoka N (2010) Monitoring rapid head scarp movement in an alpine rockslide. Eng Geol 115:49–57. https://doi.org/10.1016/j.enggeo.2010.06.014

Obert L, Duvall WI (1942) Use of subaudible noises for the pre-diction of rock burst. Part II: report of Investigations 3654. US Bureau of Mines

Ohbayashi R, Nakajima Y, Nishikado H, Takayama S (2008) Monitoring system for landslide disaster by wireless sensing node network. In: 2008 Sice Annual Conference. IEEE, pp 1704–1710

Ohno H, Naruse H, Kihara M, Shimada A (2001) Industrial applications of the BOTDR optical fiber strain sensor. Opt Fiber Technol 7:45–64. https://doi.org/10.1006/ofte.2000.0344

Olona J, Pulga JA, Fernandez-Viejo G, Lopez-Fernande C, Gonzalez-Cortina JM (2010) Weathering variations in a granitic massif and related geotechnical properties through seismic and electrical resistivity methods. Near Surf Geophys 8:585–599. https://doi.org/10.3997/1873-0604.2010043

Onaca A, Urdea P, Ardelean A, Serban R (2013) Assessment of internal structure of repiglacial landforms from southern Carpathians (Romania) using DC resistivity tomography. Carpathian J Earth Environ Sci 8:113–122

Oppikofer T (2009) Detection, analysis and monitoring of slope movements by high-resolution digital elevation models. PhD Thesis, University of Lausanne. Switzerland

Oppikofer T, Nordahl B, Bunkholt H, Nicolaisen M, Jarna A, Iversen S, Hermanns RL, Böhme M, Molina FXY (2015) Database and online map service on unstable rock slopes in Norway—From data perpetuation to public information. Geomorphology 249:69–81. https://doi.org/10.1016/j.geomorph.2015.08.005

Palis E, Lebourg T, Vidal M, Levy C, Tric E, Hernandez M (2017) Multiyear time-lapse ERT to study short- and long-term landslide hydrological dynamics. Landslides 14:1333–1343. https://doi.org/10.1007/s10346-016-0791-6

Pánek T, Margielewski W, Taborik P, Urban J, Hradecky J, Szura C (2010) Gravitationally induced caves and other discontinuities detected by 2D electrical resistivity tomography: case studies from the Polish Flysch Carpathians. Geomorphology 123:165–180. https://doi.org/10.1016/j.geomorph.2010.07.008

Panzera F, Pischiutta M, Lombardo G, Monaco C, Rovell A (2014) Wavefield polarization in fault zones of the western flank of Mt. Etna: observations and fracture orientation modelling. Pure Appl Geophys 171:3083–3097. https://doi.org/10.1007/s00024-014-0831-x

Pappalardo G, Mineo S (2019) Study of jointed and weathered rock slopes through the innovative approach of InfraRed thermography. In: Landslides: theory, practice and modelling. Springer, Cham, pp 85–103. https://doi.org/10.1007/978-3-319-77377-3_5

Pappalardo G, Imposa S, Mineo S, Grassi S (2016) Evaluation of the stability of a rock cliff by means of geophysical and geomechanical surveys in a cultural heritage site (south-eastern Sicily). Ital J Geosci 135:308–323. https://doi.org/10.3301/IJG.2015.31

Park J, Kim K (2019) Quantification of rock mass weathering using spectral imaging. J S Afr Inst Min Metall 119:1039–1046. https://doi.org/10.17159/2411-9717/708/2019

Park MK, Kim S, Son M, Kim JH, Abraham AA (2014) Application of electrical resistivity tomography (ERT) technique to detect underground cavities in a karst area of South Korea. Environ Earth Sci 71:2797–2806. https://doi.org/10.1007/s12665-013-2658-7

Pazzi V, Morelli S, Fanti R (2019) A review of the advantages and limitations of geophysical investigations in landslide studies. Int J Geophys 2983087:1–27. https://doi.org/10.1155/2019/2983087

Perrone A, Lapenna V, Piscitelli S (2014) Electrical resistivity tomography technique for landslide investigation: a review. Earth Sci Rev 135:65–82. https://doi.org/10.1016/j.earscirev.2014.04.002

Pierce IKD, Wesnousky SG, Owen LA (2017) Terrestrial cosmogenic surface exposure dating of moraines at Lake Tahoe in the Sierra Nevada of California and slip rate estimate for the West Tahoe Fault. Geomorphology 298:63–71. https://doi.org/10.1016/j.geomorph.2017.09.030

Pipia L, Fabregas X, Aguasca A, Lopez-Martinez C (2008) atmospheric artifact compensation in ground-based DInSAR applications. IEEE Geosci Remote Sens Lett 5:88–92. https://doi.org/10.1109/LGRS.2007.908364

Polat N, Murat U (2018) An experimental analysis of digital elevation models generated with Lidar Data and UAV photogrammetry. J Indian Soc Remote Sens 46:1135–1142. https://doi.org/10.1007/s12524-018-0760-8

Polikreti K, Michael CT, Maniatis Y (2003) Thermoluminescence characteristics of marble and dating of freshly excavated marble objects. Radiat Meas 37:87–94. https://doi.org/10.1016/S1350-4487(02)00088-4

Portal A, Fargier Y, Labazuy P, Lenat JF, Boivin P, Miallier D (2019) 3D electrical imaging of the inner structure of a complex lava dome, Puy de Dôme volcano (French Massif Central, France). J Volcanol Geotherm Res 373:97–107. https://doi.org/10.1016/j.jvolgeores.2019.01.019

Preusser F, Degering D, Fuchs M, Hilgers A, Kadereit A, Klasen N, Krbetsech M, Spencer JQG, Spencer D (2009) Luminescence dating: basics, methods and applications. E&G Quat Sci J 57:95–149

Racek O, Blahůt J (2023) Rock mass characterisation and rock fall monitoring: traditional approaches. In: Landslides: detection, monitoring & prediction—technological developments. Springer Nature, Switzerland

Racek O, Blahůt J, Hartvich F (2021) Observation of the rock slope thermal regime, coupled with crackmeter stability monitoring: initial results from three different sites in Czechia (Central Europe). Geosci Inst Methods Data Sys 10:203–218. https://doi.org/10.5194/gi-10-203-2021

Riaza A, Strob P, Beisl U, Hausold A (2001) Spectral mapping of rock weathering degrees on granite using hyperspectral DAIS 7915 Spectrometer Data. Int J Appl Earth Obs Geoinf 3:345–354

Riquelme A, Abellan A, Tomas R (2015) Discontinuity spacing analysis in rock masses using 3D point clouds. Eng Geol 195:185–195. https://doi.org/10.1016/j.enggeo.2015.06.009

Riquelme A, Cano M, Tomas R, Abellan A (2017) Identification of rock slope discontinuity sets from laser scanner and photogrammetric point clouds: a comparative analysis. Proc Eng 191:838–845. https://doi.org/10.1016/j.proeng.2017.05.251

Robertson J, Meschis M, Roberts GP, Ganas A, Gheorghiu DM (2019) Temporally constant quaternary uplift rates and their relationship with extensional upperâplate faults in South Crete (Greece), constrained with 36Cl cosmogenic exposure dating. Tectonics 38:1189–1222. https://doi.org/10.1029/2018TC005410

Rosas Carbajal M, Komorowsk JC, Nicollin F, Giber D (2016) Volcano electrical tomography unveils edifice collapse hazard linked to hydrothermal system structure and dynamics. Sci Rep 6:29899–29899. https://doi.org/10.1038/srep29899

Rosser N, Lim M, Petley D, Dunning S, Allison R (2007) Patterns of precursory rockfall prior to slope failure. J Geophys Res 112. https://doi.org/10.1029/2006JF000642

Rossini M, Di Mauro B, Garzonio R, Baccolo G, Cavallin G, Mattavelli M, De Amicis M, Colombo R (2018) Rapid melting dynamics of an alpine glacier with repeated UAV photogrammetry. Geomorphology 304:159–172. https://doi.org/10.1016/j.geomorph.2017.12.039

Rouyet L, Kristensen L, Derron MH, Michoud C, Blikra LH, Jaboyedoff M, Lauknes TR (2017) Evidence of rock slope breathing using ground-based InSAR. Geomorphology 289:152–169. https://doi.org/10.1016/j.geomorph.2016.07.005

Royan M, Abellan A, Manuel Vilaplana J (2015) Progressive failure leading to the 3 December 2013 rockfall at Puigcercós scarp (Catalonia, Spain). Landslides 12:585–595. https://doi.org/10.1007/s10346-015-0573-6

Rozsypal A (2001) Control monitoring and risks in geotechnics. Jaga, Bratislava

Ruiz Carulla R, Corominas J, Mavrouli O (2015) A methodology to obtain the block size distribution of fragmental rockfall deposits. Landslides 12:815–825. https://doi.org/10.1007/s10346-015-0600-7

Sailer R, Bollmann E, Hoinkes S, Rieg L, Spross M, Stoetter J (2012) Quantification of geomorphodynamics in glaciated and recently deglaciated terrain based on airborne laser scanning data. Geogr Ann Ser A Phys Geogr 94A:17–32. https://doi.org/10.1111/j.1468-0459.2012.00456.x

Salvoni M, Dight PM (2016) Rock damage assessment in a large unstable slope from microseismic monitoring – MMG Century mine (Queensland, Australia) case study. Eng Geol 210:45–56. https://doi.org/10.1016/j.enggeo.2016.06.002

Sanhueza Pino K, Korup O, Hetzel R, Munack H, Weidinger JT, Dunning S, Ormukov C, Kubik PW (2011) Glacial advances constrained by10Be exposure dating of bedrock landslides, Kyrgyz Tien Shan. Quat Res 76:295–304. https://doi.org/10.1016/j.yqres.2011.06.013

Santana D, Corominas J, Mavrouli O, Garcia-Selles D (2012) Magnitude–frequency relation for rockfall scars using a Terrestrial Laser Scanner. Eng Geol 145:50–64. https://doi.org/10.1016/j.enggeo.2012.07.001

Sarro R, Riquelme A, Carlos Garcia-Davalillo J, Maria Mateos R, Tomas R, Luis Pasto J, Cano M, Herrera G (2018) Rockfall simulation based on UAV photogrammetry data obtained during an emergency declaration: application at a cultural heritage site. Remote Sens 10:1923. https://doi.org/10.3390/rs10121923

Sasak J, Gallay M, Kanuk J, Hofierka J, Minar J (2019) Combined use of terrestrial laser scanning and UAV photogrammetry in mapping Alpine terrain. Remote Sens 11:2154. https://doi.org/10.3390/rs11182154

Sass O (2005) Temporal variability of rockfall in the Bavarian Alps, Germany. Arctic, Antarctic, and Alpine Res 37:564–573. https://doi.org/10.1657/1523-0430(2005)037 [0564:TVORIT]2.0.CO;2

Sattele M, Krautblatter M, Brundl M, Straub D (2016) Forecasting rock slope failure: how reliable and effective are warning systems? Landslides 13:737–750. https://doi.org/10.1007/s10346-015-0605-2

Scheikl M, Angerer H, Dölzlmüller J, Poisel R, Poscher G (2000) Multidisciplinary monitoring demonstrated in the case study of the Eiblschrofen rock fall. Felsbau 18

Schenato L (2017) A review of distributed fibre optic sensors for geo-hydrological applications. Appl Sci 7:896. https://doi.org/10.3390/app7090896

Schenato L, Galtarossa A, Pasuto A, Palmieri L (2020) Distributed optical fiber pressure sensors. Opti Fiber Technol 58:102239. https://doi.org/10.1016/j.yofte.2020.102239

Schneider S, Hauck C (2012) Influence of surface and subsurface heterogeneity on observed borehole temperatures at a mountain permafrost site in the Upper Engadine, Swiss Alps. Cryosphere 6:517–531. https://doi.org/10.5194/tc-6-517-2012

Schroeder K, Ecke W, Mueller R, Willsch R, Andreev A (2001) A fibre Bragg grating refractometer. Meas Sci Technol 12(7):757. https://doi.org/10.1088/0957-0233/12/7/301

Schrott L, Sass O (2008) Application of field geophysics in geomorphology: advances and limitations exemplified by case studies. Geomorphology 93:55–73. https://doi.org/10.1016/j.geomorph.2006.12.024

Seo H, Choi H, Park J, Lee IM (2017) Crack detection in pillars using infrared thermographic imaging. Geotech Test J 40:20150245. https://doi.org/10.1520/GTJ20150245

Singh PK, Wasnik AB, Kainthola A, Sazid M, Singh TN (2013) The stability of road cut cliff face along SH-121: a case study. Nat Hazard 68:497–507. https://doi.org/10.1007/s11069-013-0627-9

Siska P, Latal J, Bujok P, Vanderka A, Klempa M, Koudelka P, Vasinek V, Pospisil P (2016) Optical fiber based distributed temperature systems deployment for measurement of boreholes temperature profiles in the rock massif. Opt Quantum Electron 48:108. https://doi.org/10.1007/s11082-016-0379-3

Slimane AB, Raclot D, Rebai H, Le Bissonnais Y, Planchon O, Bouksila F (2018) Combining field monitoring and aerial imagery to evaluate the role of gully erosion in a Mediterranean catchment (Tunisia). Catena 170:73–83. https://doi.org/10.1016/j.catena.2018.05.044

Sobrino J, Del Frate F, Drusch M, Jimenez-Munoz JC, Manunta P, Regan A (2016) Review of thermal infrared applications and requirements for future high-resolution sensors. IEEE Trans Geosci Remote Sen 54:2963–2972. https://doi.org/10.1109/TGRS.2015.2509179

Sohbati R, Murray AS, Chapot MS, Jain M, Pederson J (2012) Optically stimulated luminescence (OSL) as a chronometer for surface exposure dating. J Geophys Res 117. https://doi.org/10.1029/2012JB009383

Solberg IL, Hansen L, Ronning JS, Haugen ED, Dalsegg E, Tonnesen JF (2012) Combined geophysical and geotechnical approach to ground investigations and hazard zonation of a quick clay area, mid Norway. Bull Eng Geol Environ 71:119–133. https://doi.org/10.1007/s10064-011-0363-x

Staehli M, Saettele M, Huggel C, McArdell BW, Lehmann P, Van Herwijnen A, Berne A, Schleiss M, Ferrari A, Kos A, Or D, Springman SM (2015) Monitoring and prediction in early warning systems for rapid mass movements. Nat Hazard Earth Syst Sci 15:905–917. https://doi.org/10.5194/nhess-15-905-2015

Stroeven A, Hattestrand C, Kleman J, Heyman J, Fabel D, Fredin O, Goodfellow BW, Harbor JM, Jansen JD, Olsen L, Caffee MW, Fink D, Lundqvist J, Rosqvist GC, Stromberg B, Jansson KN (2016) Deglaciation of Fennoscandia. Quat Sci Rev 147:91–121. https://doi.org/10.1016/j.quascirev.2015.09.016

Strozzi T, Delaloye R, Kaab A, Ambrosi C, Perruchoud E, Wegmueller U (2010) Combined observations of rock mass movements using satellite SAR interferometry, differential GPS, airborne digital photogrammetry, and airborne photography interpretation. J Geophys Res 115. https://doi.org/10.1029/2009JF001311

Strozzi T, Ambrosi C, Raetzo H (2013) Interpretation of aerial photographs and satellite SAR interferometry for the inventory of landslides. Remote Sens 5:2554–2570. https://doi.org/10.3390/rs5052554

Sturzenegger M, Stead D, Gosse J, Ward B, Froese C (2015) Reconstruction of the history of the Palliser Rockslide based on 36Cl terrestrial cosmogenic nuclide dating and debris volume estimations. Landslides 12:1097–1106. https://doi.org/10.1007/s10346-014-0527-4

Sun L, Khan SD, Sarmiento S, Lakshmikantha MR (2017) Ground-based hyperspectral imaging and terrestrial laser scanning for fracture characterization in the Mississippian Boone Formation. Int J Appl Earth Obs Geoinf 63:222–233. https://doi.org/10.1016/j.jag.2017.08.008

Szabó Z, Tóth CA, Holb I, Szabó S (2020) Aerial laser scanning data as a source of terrain modeling in a fluvial environment: biasing factors of terrain height accuracy. Sensors 20:2063. https://doi.org/10.3390/s20072063

Tan K, Cheng X (2020) Distance effect correction on TLS intensity data using naturally homogeneous targets. IEEE Geosci Remote Sens Lett 17:499–503. https://doi.org/10.1109/LGRS.2019.2922226

Tang B, Cheng H (2018) Application of distributed optical fiber sensing technology in surrounding rock deformation control of TBM-excavated coal mine roadway. J Sens 2018:1–10. https://doi.org/10.1155/2018/8010746

Tannant DD (2015) Review of photogrammetry-based techniques for characterization and hazard assessment of rock faces. Int J Geores Environ-IJGE 1:76–87. https://doi.org/10.15273/ijge.2015.02.009

Taruselli M, Arosio D, Longoni L, Papin M, Corsini A, Zanzi L (2018) Rock stability as detected by seismic noise recordings-Three case studies. In: 24th European Meeting Of Environmental And Engineering Geophysics. European Association of Geoscientists & Engineers, pp 1–5

Teza G, Marcato G, Castelli E, Galgaro A (2012) IRTROCK: a MATLAB toolbox for contactless recognition of surface and shallow weakness of a rock cliff by infrared thermography. Comput Geosci 45:109–118. https://doi.org/10.1016/j.cageo.2011.10.022

Thambidurai P, Ramesh MV (2017) Slope stability investigation of Chandmari in Sikkim, Northeastern India. In: Mikos M, Tiwari B, Yin Y, Sassa K (eds) Advancing culture of living with landslides. WLF 2017. Springer, Cham. https://doi.org/10.1007/978-3-319-53498-5_42

Thambidurai P, Omman T, Keshar Kr Luitel (2022) Landslide investigation using electrical resistivity and geotechnical approach in Mangan Town, Sikkim, Northeastern India. In: Landslides: detection, monitoring & prediction – technological developments. Springer Nature, Switzerland

Torresan C, Berton A, Carotenuto F, Chiavetta U, Miglietta F, Zaldei A, Gioli B (2018) Development and performance assessment of a low-cost UAV Laser Scanner System (LasUAV). Remote Sens 10:1094. https://doi.org/10.3390/rs10071094

Tripolitsiotis A, Daskalakis A, Mertikas S, Hristopulos D, Agioutantis Z, Partsinevelos P (2015) Detection of small-scale rockfall incidents using their seismic signature. Third International Conference on Remote Sens and Geoinformation of the Environment 9535, pp 1–9

Udphuay S, Guenther T, Everett ME, Warden RR, Briaud JL (2011) Three-dimensional resistivity tomography in extreme coastal terrain amidst dense cultural signals: application to cliff stability assessment at the historic D-Day site. Geophys J Int 185:201–220. https://doi.org/10.1111/j.1365-246X.2010.04915.x

Uehan F, Saito H, Ma G (2012) Fundamental study on the remote vibration measuring system for evaluating rock slope stability. In: 15th World Conference on Earthquake Engineering, Lisbon

Uhlemann S, Chambers J, Falck WE, Tirado AA, Fernandez GJL, Espin de Gea A (2018) Applying electrical resistivity Tomography in ornamental stone mining: challenges and solutions. Minerals 8:491. https://doi.org/10.3390/min8110491

Uzielli M (2008) Statistical analysis of geotechnical data. In: Geotechnical and geophysical site characterization. CRC Press, pp 173–193

Valentin J, Capron A, Jongmans D, Baille L, Larose E, Bottelin P (2016) Dynamic response of prone-to-fall rock compartments to ambient vibrations: application for rock-fall hazard assessment. Landslides And Engineered Slopes: experience. Theory And Practice, Napoli, pp 1965–1970

Vanneschi C, Di Camillo M, Aiello E, Bonciani F, Salvini R (2019) SfM-MVS photogrammetry for rockfall analysis and hazard assessment along the ancient roman via Flaminia Road at the Furlo Gorge (Italy). ISPRS Int J Geo-Inf 8:325. https://doi.org/10.3390/ijgi8080325

van Veen M, Lato M (2017) The role of survey design in developing rock fall frequency-magnitude relationships using terrestrial laser scanning: a case study from the CN railway at White Canyon, BC. 3rd North American symposium on Landslides

Veettil BK, Kamp U (2017) Remote sensing of glaciers in the tropical Andes: a review. Int J Remote Sens 38(23):7101–7137. https://doi.org/10.1080/01431161.2017.1371868

Vehling L, Baewert H, Glira P, Moser M, Rohn J, Morche D (2017) Quantification of sediment transport by rockfall and rockslide processes on a proglacial rock slope (Kaunertal, Austria). Geomorphology 287:46–57. https://doi.org/10.1016/j.geomorph.2016.10.032

Volkwein A, Bruegger L, Gerber W, Krummenacher B, Kummer P, Lardon J, Sutter T (2018) Repetitive rockfall trajectory testing. Geosciences 8:88. https://doi.org/10.3390/geosciences8030088

von Blanckenburg F, Willenbring JK (2014) Cosmogenic nuclides: dates and rates of earth-surface change. Elements 10:341–346. https://doi.org/10.2113/gselements.10.5.341

Wagner A (2016) A new approach for geo-monitoring using modern total stations and RGB+ D images. Measurement 82:64–74. https://doi.org/10.1016/j.measurement.2015.12.025

Wang YL, Shi B, Zhang TL, Zhu HH, Jie Q, Sun Q (2015) Introduction to an FBG-based inclinometer and its application to landslide monitoring. J Civ Struct Health Monit 5:645–653. https://doi.org/10.1007/s13349-015-0129-4

Wang P, Xing C, Pan X (2020) Reservoir dam surface deformation monitoring by differential GB-InSAR based on image subsets. Sensors 20:396. https://doi.org/10.3390/s20020396

Weber S, Beute J, Faillettaz J, Hasler A, Krautblatter M, Vieli A (2017) Quantifying irreversible movement in steep, fractured bedrock permafrost on Matterhorn (CH). Cryosphere 11:567–583. https://doi.org/10.5194/tc-11-567-2017

Wei SC, Liu KF (2020) Automatic debris flow detection using geophones. Landslides 17:349–359. https://doi.org/10.1007/s10346-019-01258-9

Weinmann M, Hinz S, Jutzi B (2011) Fast and automatic image-based registration of TLS data. ISPRS J Photogramm Remote Sens 66:S62–S70. https://doi.org/10.1016/j.isprsjprs.2011.09.010

Wenzer H, Pichler D (2009) Ambient vibration monitoring. In: Encyclopedia of structural health monitoring. Wiley

Westoby MJ, Brasington J, Glasser NF, Hambrey MJ, Reynolds JM (2012) 'Structure-from-Motion' photogrammetry: a low-cost, effective tool for geoscience applications. Geomorphology 179:300–314. https://doi.org/10.1016/j.geomorph.2012.08.021

Westoby MJ, Lim M, Hogg M, Pound MJ, Dunlop L, Woodward J (2018) Cost-effective erosion monitoring of coastal cliffs. Coast Eng 138:152–164. https://doi.org/10.1016/j.coastaleng.2018.04.008

Whiteley JS, Chambers JE, Uhlemann S, Wilkinson PB, Kendall JM (2019) Geophysical monitoring of moisture-induced landslides: a review. Rev Geophys 57:106–145. https://doi.org/10.1029/2018RG000603

Williams J, Rosser NJ, Hardy RJ, Brain MJ (2019) The importance of monitoring interval for rockfall magnitude-frequency estimation. J Geophys Res Earth Surf 124:2841–2853. https://doi.org/10.1029/2019JF005225

Wziatek D, Terefenko P, Kurylczyk A (2019) Multi-temporal Cliff Erosion analysis using airborne laser scanning surveys. Remote Sens 11:2666. https://doi.org/10.3390/rs11222666

Xiong L, Wang G, Wessel P (2017) Anti-aliasing filters for deriving high-accuracy DEMs from TLS data: a case study from Freeport, Texas. Comput Geosci 100:125–134. https://doi.org/10.1016/j.cageo.2016.11.006

Xue Z, Shi JQ, Yamauchi Y, Durucanm S (2018) Fiber optic sensing for geomechanical monitoring: (1)-Distributed strain measurements of two sandstones under hydrostatic confining and pore pressure conditions. Appl Sci 8:2103. https://doi.org/10.3390/app8112103

Yan Y, Li T, Liu J, Wang W, Su Q (2019) Monitoring and early warning method for a rockfall along railways based on vibration signal characteristics. Sci Rep 9:6606–6606. https://doi.org/10.1038/s41598-019-43146-1

Young A, Olsen MJ, Driscoll N, Flick RE, Gutierrez R, Guza RT, Johnstone E, Kuester F (2010) Comparison of airborne and terrestrial Lidar estimates of Seacliff Erosion in Southern California. Photogramm Eng Remote Sens 76:421–427. https://doi.org/10.14358/PERS.76.4.421

Youssef A, Pradhan B, Al-Kathery M, Bathrellos GD, Skilodimou HD (2015) Assessment of rockfall hazard at Al-Noor Mountain, Makkah city (Saudi Arabia) using spatio-temporal Remote Sensing data and field investigation. J Afr Earth Sci 1994(101):309–321. https://doi.org/10.1016/j.jafrearsci.2014.09.021

Zabota B, Repem B, Kobal M (2019) Influence of digital elevation model resolution on rockfall modelling. Geomorphology 328:183–195. https://doi.org/10.1016/j.geomorph.2018.12.029

Zang Y, Yang BLJ, Guan H (2019) An accurate TLS and UAV image point clouds registration method for deformation detection of chaotic hillside areas. Remote Sens 11:647. https://doi.org/10.3390/rs11060647

Zangerl C, Eberhardt E, Perzlmaier S (2010) Kinematic behaviour and velocity characteristics of a complex deep-seated crystalline rockslide system in relation to its interaction with a dam reservoir. Eng Geol 112:53–67. https://doi.org/10.1016/j.enggeo.2010.01.001

Zhang H, Wu Z (2008) Performance evaluation of BOTDR-based distributed fiber optic sensors for crack monitoring. Struct Health Monit 7:143–156. https://doi.org/10.1177/1475921708089745

Zhang G, Karakus M, Tang H, Ge Y, Jiang Q (2017) Estimation of joint roughness coefficient from three-dimensional discontinuity surface. Rock Mech Rock Eng 50:2535–2546. https://doi.org/10.1007/s00603-017-1264-5

Zhang C, Qiao W, Che X, Lu J, Men B (2019) Automated microseismic event location by amplitude stacking and semblance. Geophysics 84:KS191–KS210. https://doi.org/10.1190/GEO2018-0409.1

Zhao T, Liu W, Xu Z, Liu T, Xu S, Cui L, Shi C (2019) Cosmogenic nuclides (10Be and 26Al) erosion rate constraints in the Badain Jaran Desert, Northwest China: implications for surface erosion mechanisms and landform evolution. Geosci J 23:59–68. https://doi.org/10.1007/s12303-018-0010-7

Zhao Y, Zhang N, Si G (2016) A fiber Bragg grating-based monitoring system for roof safety control in underground coal mining. Sensors 16:1759. https://doi.org/10.3390/s16101759

Zheng Y, Zhu ZW, Xiao W, Deng QX (2020) Review of fiber optic sensors in geotechnical health monitoring. Opt Fiber Technol 54:102127. https://doi.org/10.1016/j.yofte.2019.102127

Zhou W, Chen F, Guo H, Hu M, Li Q, Tang P, Zhen W, Liu J, 'an Luo R (2020) UAV Laser scanning technology: a potential cost-effective tool for micro-topography detection over wooded areas for archaeological prospection. Int J Digital Earth 13(11):1279–1301. https://doi.org/10.1080/17538947.2019.1711209

Zvelebil J, Moser M (2001) Monitoring based time-prediction of rock falls: three case-histories. Phys Chem Earth Part B 26:159–167. https://doi.org/10.1016/S1464-1909(00)00234-3

Chapter 2
Rock Mass Characterization and Rockfall Monitoring: Traditional Approaches

Ondřej Racek and Jan Blahůt

Abstract Rock mass characterization and rockfall/rock slope stability monitoring methods are one of the fastest evolving research areas in the field of geosciences. Traditionally, simple mapping, geodetical or geotechnical methods are used. The ongoing rapid development of monitoring methods is conditioned by engineering challenges when new infrastructure is nowadays being constructed in complicated geological conditions. These are represented by mountainous areas, deep gorges with steep slopes, or even active landslide sites. Traditional methods can be used within these monitoring demanding sites and bring high-quality monitoring results, sometimes with higher precision than modern state-of-art methods. This chapter reviews traditional rock slope stability monitoring methods and discusses their advantages, applicability, and strong/weak sides. Traditional methods are compared against newly introduced, modern state-of-art methods.

Keywords Rock slope · Monitoring methods · Rockfall · Stability

2.1 Introduction

Rock mass characterization, together with rock slope stability monitoring methods, belongs to the fastest evolving research fields within geosciences (Fig. 2.1). Due to the expansion of civil engineering to geologically complicated sites, monitoring + of unstable rock slopes has become an irreplaceable part of engineering projects.

Since the first half of the twentieth century or even longer, traditional methods have been used. Despite the age, these are still not fully replaceable by modern methods. Even though they do not provide fast data collection or spatial resolution, traditional methods can still achieve high precision results. Often monitoring is carried out

O. Racek (✉) · J. Blahůt
Department of Engineering Geology, Institute of Rock Structure and Mechanics, Czech Academy of Sciences, V Holešovičkách 94/41, 182 09 Prague, Czech Republic
e-mail: racek@irsm.cas.cz

O. Racek
Faculty of Science, Department of Physical Geography and Geoecology, Charles University, Albertov 6, 128 00 Prague, Czech Republic

P. Thambidurai and T. N. Singh (eds.), *Landslides: Detection, Prediction and Monitoring*,
https://doi.org/10.1007/978-3-031-23859-8_2

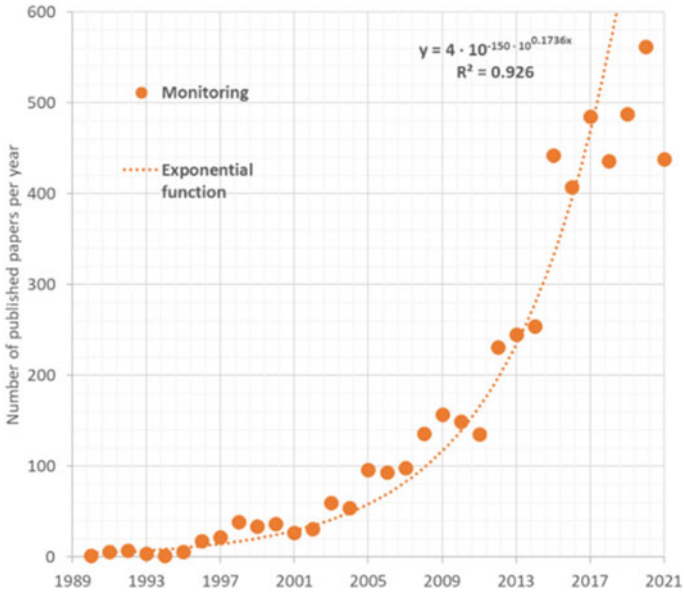

Fig. 2.1 Slope stability monitoring domain data—published in research papers (WOS database) (Blahůt et al. 2021)

using traditional methods that are cheaper to establish and run. In comparison with modern methods (Blahůt and Racek 2023, Chapter 1) traditional methods usually demand experienced users to process and evaluate results. This paper summarizes traditional methods used for rock mass characterization and rock slope monitoring and provides a brief overview of monitored rock slope/rock mass properties. Though rockfall is a well-known process, mechanisms of rockfall triggering, or previous destabilizing processes are usually not fully described (Dorren 2003). The rockfall is a rapid process generally lasting a few seconds to minutes. Rockfall events result from long-lasting external factors (Gunzburger et al. 2005) in combination with internal site-specific properties of the rock slope (D'Amato et al. 2016). It is necessary to understand and quantify both the properties of the rock slope and the influence of exogenous processes on its stability (Fischer et al. 2012) to improve the knowledge about rock slope temporal dynamic and rockfall triggering/preparatory factors. For that, in-situ monitoring of rock slope activity is necessary (Fantini et al. 2016). Monitoring systems are used to observe natural rockfall events, rock slope temporal development (Fantini et al. 2016; Lazar et al. 2018), or for early warning infrastructure.

Traditional methods are limited by lower temporal resolution. Rock mass stability is traditionally estimated using empirical or heuristic methods based on subjective experience and knowledge of the researcher combined with empirical data (Abramson et al. 2001). This approach is applicable in well-mapped areas or known active rockfall sites. These expert methods often do not provide quantitative data;

however, in the case of risk estimation expert point of view remains irreplaceable. The ability to predict future rock slope behavior is strongly dependent on the researcher's subjective experience (Krishnan and Sommer 1994). For effective monitoring design and placement, it is crucial to cooperate with an experienced specialist/researcher to ensure solid and meaningful results (Masoumi et al. 2017). Monitoring design must reflect the main mechanisms of rock slope destabilization, the magnitude of the processes, power supply effectiveness, and data processing effectivity, together with a balanced budget (Bond et al. 2013). Each monitoring method is suitable for measuring different variables in different spatial and temporal resolutions. A monitoring system design aims to choose appropriate methods to get meaningful and easily interpretable data (Farrokh and Intrieri 2011).

Monitoring systems can use a single method (Boyd et al. 1973) or complex systems (Blahůt and Racek 2023, Chapter 1) use multiple monitoring methods (Janeras et al. 2017; Racek et al. 2021). Traditional methods are usually based on geotechnical in situ measurements. Properties of rock slopes are traditionally described by simple geological/geomorphological methods (Olona et al. 2010) or geotechnical indices (Ding et al. 2000).

2.2 Rock Properties and Monitored Variables

For rock slope temporal stability estimation, it is important to characterize the rock slope's initial stability and internal properties. For the rock slope, dynamic monitoring is important to track external (meteorological, seismic) factors (Gaffet et al. 2010). General stability estimation is, in most cases, done by an expert qualitative, and afterward, the appropriate quantitatively monitoring methods are selected and deployed.

2.2.1 Rock Slope/Rock Mass Properties

For rock slope characterization, long-term stable descriptive variables are used. These include rock mass mechanical properties such as Young's modulus, elasticity modulus, hardness, roughness, or thermal properties (Rocha and Cording 1981). Variables are laboratory-obtained using representative rock samples or estimated in the field using geophysical methods (Blahůt and Racek 2023, Chapter 1; Klose et al. 2007). These variables determine rock mass's physical and mechanical behavior, thus rock slope stability. Rock slope stability is further affected by its structure, mainly by the discontinuities within rock mass (Einstein et al. 1983). These are crucial in rockfall development because determining unstable blocks overall weakens the rock mass (Macciotta and Derek 2015). Discontinuities are characterized by orientation (dip/dip direction), spacing, persistence, roughness, wall strength, aperture, filling, seepage, number of sets, block size, and discontinuities surface roughness or filling

(Kulatilake and Wu 1984; Barton 1974). These data are obtained in the field by direct observation or using a geological compass (dip/dip direction), a feeler gauge (aperture), roughness broom (roughness), or Schmidt hammer (hardness). Temporal stability estimation is important to know rockfall frequency, volume, and source area for rock slope. These data bring the possibility to approximately predict future rockfall dynamics of rock slope. Rockfall catch net is generally used for the direct rock slope observation to gain overall rock slope activity data (Krautblatter and Moser 2009).

2.2.2 External Variables/Factors Monitoring

Rock slope temporal stability is affected by exogenous meteorological factors. Dilatation of rock mass and partial blocks, together with freeze–thaw cycles, is determined by temperature cycles (Weber et al. 2017). Rockfall events can also be triggered by severe rainfall (Maria et al. 2012) or high-velocity wind gusts (Sass 2005). These can be quantified using weather stations. Measured rock slope dynamics should be compared with the closest available meteorological data. It is possible through such a data to find correlations between rock slope dynamics and meteorological influences (Royan et al. 2015; Pratt et al. 2019). Rockfalls are often triggered by earthquake events (Marzorati et al. 2002). Therefore, seismic activity monitoring is desirable to distinguish seismically triggered events (Wieczorek and Snyder 2009).

2.3 Overview of Rock Slope Description and Monitoring Methods

Rockfall is a complex and fast process driven by multiple factors and variables. This makes monitoring using traditional methods (Fig. 2.2) challenging. Unlike landslide monitoring, rockfall except for slow large rockslides is a rapid movement (lasting seconds) (Stoffel and Hitz 2008; Lambert and Nicot 2013). Rock slope destabilization and consequent rockfalls are induced by the interaction of predisposing elements with external variables (Gunzburger et al. 2005; D'Amato et al. 2016). Rockfall can also be triggered artificially by human activities (Bauer et al. 2005). Conditions that destabilize rock slope affect the rock slope in the long term up to tens of thousands of years (Gunzburger et al. 2005). Changes of these or their thresholds overcoming can be recorded with traditional or modern (Blahůt and Racek 2023, Chapter 1) monitoring methods.

The purpose of the monitoring system determines the use of the specific method. Methods should be chosen according to the duration of monitoring, accessibility of the monitoring site, the safety of workers, financial resources, desirable results, and Spatio-temporal scale of the survey (Hartmeyer et al. 2012). Traditional (T) and

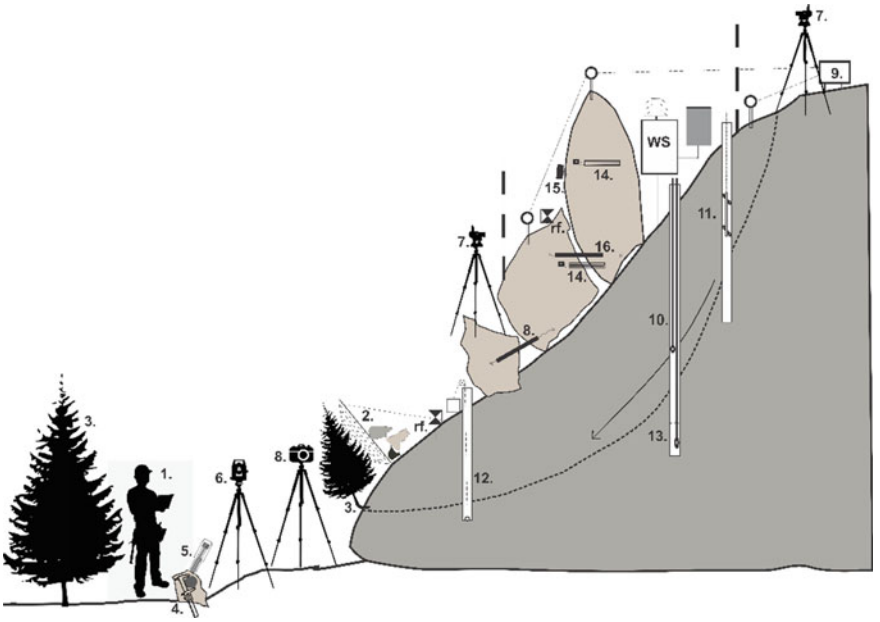

Fig. 2.2 Overview of traditional monitoring methods. **1** Expert methods, **2** Catch net, **3** Tree ring, **4** Lichenometry, **5** DOW, **6** Tacheometry, **7** Precise levelling, **8** Photogrammetry, **9** Wire extensometer, **10** BH extensometer, **11** BH inclinometer, **12** BH wire extensometer, **13** Piezometer, **14** Strain gauge, **15** Tilt meter, **16** Crack monitoring. WS: weather station, rf: reflector

modern (M) methods of rock slope stability estimation and dynamic monitoring can be classified according to their purpose as follows:

2.3.1 Estimation of Rock Slope Properties Methods

Methods are chosen based on simple expert rock slope observations or empirically defined stability indices. The expert stability estimations are nearly impossible due to their inherent subjectivity, but the results of geotechnical classifications (stability indices) can be compared between sites. Methods are used for rock slope internal properties estimation, initial stability estimation, or unstable rock slope elements identification.

- Mapping (T)
- Geotechnical classification (T)
- Electrical resistivity tomography (M)
- Seismic tomography (M)

2.3.2 Rockfall Events Dating Methods

Methods that analyses medium-scale Spatio-temporal patterns of rockfall activity or specific unstable rock slope past temporal activity.

- Dendrochronology (T)
- Lichenometry (T)
- Rockfall catch net (T)
- Degree of weathering (T)
- Archive review (T)
- Cosmogenic nuclides (M)
- Luminescence (M)

2.3.3 Spatio-Temporal Monitoring Methods for Rock Slope Activity

Methods used for direct (d) or indirect (i) measuring Spatio-temporal rock slope evolution. These methods allow the quantification of rock slope activity.

- Tachymetry (Ti)
- Precise leveling (Ti)
- Analogue (Ti)/digital (Mi) photogrammetry
- Crack monitoring (Td)
- Extenso/dilatometer (Td)
- Tiltmeter (Td)
- Strain gauges (Td)
- Piezometer (Td)
- Laser scanner terrestrial/aerial (Mi)
- GNNS (Mi)
- Ambient vibration, microseismic monitoring (Md)
- Optical fiber (Md)
- Camera monitoring (Mi)
- Aerial monitoring (Mi)
- Radar interferometry terrestrial/aerial (Mi)
- Remote vibration (Mi)
- Thermal camera (Mi)

2.3.4 External Variables/Factors Monitoring Methods

Monitoring of external variables/factors which contribute to rock slope temporal destabilization. It is not necessary to place sensors directly within rock slopes with

these methods. But, the closer the data are gained, the more represent influence on the rock slope stability.

- Weather station monitoring
- Temperature monitoring
- Seismic station

2.4 Measuring Quality of Results

To evaluate the monitoring results is necessary to quantify the performance of the used sensors. This subchapter is dedicated to the description of measurement errors and uncertainties. All sensors used for monitoring bring uncertainty to monitoring outcomes (Fassò et al. 2005). Uncertainty leads to static measurement errors (Fig. 2.3). Static errors can be divided according to Menditto et al. (2007) as follows:

- **Random errors** are inconsistent and do not appear in the same magnitude or direction except by change. Random errors should be normally distributed (Viswanathan 2005).
- **Systematic errors** are caused by measuring device (system) imperfection or incorrect use. Systematic errors acquire the same value during the whole monitoring campaign and are relatively easy to remove from results. The specific type of systematic error is **Human factor error** caused by improper use of a measuring device. Human factor errors are challenging to prevent or manage (Rozsypal 2001) and can cause inaccuracies in the results. Sowers (1993) documented that human factors caused 88% of failures in geotechnical engineering problems.
- **Total error** is composed of random and systematic errors. It expresses the overall inaccuracy of measurement.

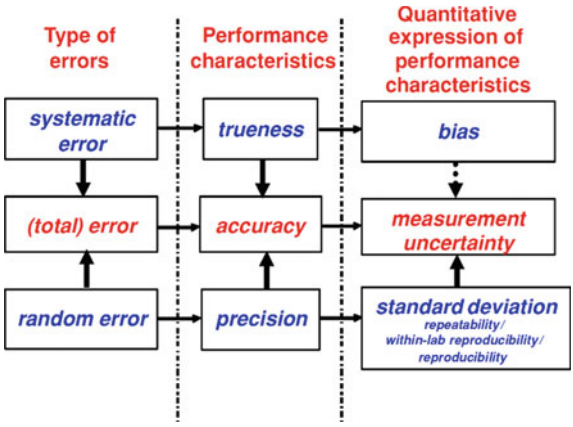

Fig. 2.3 Relationships between type of error, qualitative performance characteristics, and their quantitative expression after (Menditto et al. 2007)

2.4.1 Performance Characteristics

- Knowing the sensors' performance characteristics (Fig. 2.3) is necessary to evaluate monitoring results. Errors in measuring devices can be described by performance characteristics that are obtained by testing devices in the laboratory and should be provided by the manufacturer. The performance of sensors is expressed by static (S) and dynamic (D) performance characteristics (Menditto et al. 2007; Dunnicliff 1993). Static characteristics do not vary over time. Dynamic characteristics are used in the case of high-frequency monitoring (sub-seconds).
- **Accuracy (S)** is the algebraic difference between the indicated value of the sensor (measurement) and the true value of the known measured reference value. The accuracy represents the total error of measurements, quantitatively represented by **measurement uncertainty**.
- **Precision (S)** is an instrument's ability to measure a similar value under similar circumstances repeatedly. Precision represents random errors quantitatively represented by **standard deviation**.
- **Trueness (S)** is the difference between indicated, and true values averaged from large series of tests. The Trueness represents a systematic error, which is quantitatively expressed like **bias**.
- **Sensitivity (S)** is the smallest change in input that invokes changes in the measured value.
- **Repeatability (S)** is precision determined under the same measuring conditions.
- **Reproducibility (S)** is precision determined with different operators with different measuring devices on similar specimens.
- **Resolution (S)** is the specific increment in input value that will cause a change in output from the instrument.
- **Percentage of static error (S)** is the percentage difference between the true value and the value measured by the instrument.
- **Speed of response (D)** is the response time on change in the measured input variable.
- **Lag (D)** is the delay in the response of the measuring instrument to the change in measured quantity.
- **Dynamic error (D)** is the difference between the true and measured values that vary in time.
- **Fidelity (D)** is the degree to which an instrument measures input quantity without any dynamic error.

Some errors and uncertainties can be partly reduced by using multiple sensors, different monitoring methods, or data processing (Peng et al. 2014). Every monitoring results contain uncertainties that must be considered within the resulting conclusions.

2.5 Traditional Methods of Rock Slope Monitoring

Traditional rock slope stability monitoring methods comprise fieldwork and raw data from the rock slope. Only a few traditional geodetical methods can measure rock face spatial changes remotely. This advantage is yet redeemed by extensive time-consuming fieldwork with slow data collection. Often these methods are dependent on the researcher's experience and knowledge of local conditions (Van Westen et al. 1999). Despite mentioned limitations, these methods can provide high precision results even for slow movements. The smallest spatial changes can be detected only by long-term monitoring, where the low temporal resolution of traditional methods is not an issue.

2.5.1 Expert Methods

The use of expert methods demands an experienced researcher. Experts determine rock slope stability and temporal evolution by one visit or repeated visits to the known active area. The results of these methods are qualitative rock slope descriptions or empirically defined stability indices. By their very nature, these methods are subjective yet can produce valuable outcomes. Every thoroughly designed monitoring is based on expert site observation and evaluation of possible future dynamic scenarios.

2.5.1.1 Geomorphologic Mapping (Analyses)

Mapping is usually the first step in rockfall studies or hazard estimations on chosen localities. Mapping itself can be performed on medium to large scales (Copons and Manuel Vilaplana 2008). Demek and Embleton (1978) were documented an overview of mapping methods, and geomorphological mapping (Degraaff et al. 1987) provides rockfall events volume, accumulation area, and sometimes source area spatial data (Wieczorek et al. 1992). A long-term monitoring requires repeated visits to the study area (Luckman 2008), and this method is effective in highly active localities only. The fieldwork can describe the Spatio-temporal pattern of rock slope evolution through the repeated visit to the known locality. Expert mapping of active rock faces determines the exact location of further instrumentation for meaningful data outcomes.

2.5.1.2 Geotechnical Classifications

Geotechnical classifications are used to describe rock mass properties and their initial stability. Widely used methods are RQD (Deere et al. 1967), Q-Slope (Barton and Bar 2015), SMR (Romana 1993), RMR (Bienieawski 1973), or GSI index (Hoek

et al. 1995). Inputs are structural elements of rock slope, properties of the rock mass, and the local hydrogeological regime. The rock slope geotechnical classifications (Q-Slope, SMR, RMR) are based on classical underground rock mass classification methods. Outcomes from the geotechnical classifications are empirically defined stability indexes which describe rock slope stability. The index values are linked to construction works recommendations. Further information about geotechnical classifications provides Yang et al. (2022) or Aksoy (2008).

2.5.1.3 Rockfall Collector

Method is used for rockfall intensity or volume estimation (Krautblatter et al. 2012). It is utilised as mechanical barriers, nets, or walls to get data about rockfall temporal activity at the known active sites (Fahey and Lefebure 1988). Nets and collectors can be well equipped with warning sensors or continual camera monitoring. Usually, recorded rockfall activity or volume is correlated with meteorological data. Through this analysis, typical precipitation thresholds can be calculated, and the triggering of larger rockfalls can be determined. This type of monitoring demands repeated researcher visits or remote surveillance to estimate the changes within material accumulation. This method was documented well by Sass (2005).

2.5.2 Dating Methods

The dating of rockfall events is complicated without continuous monitoring or an extensive database (Guzzetti et al. 1999). Data about past rockfall of temporal patterns can be used for rockfall hazard assessment or zonation and eventual protection. Historical data about rockfall activity should be known before the start of construction works near the rock slope.

2.5.2.1 Dendrochronological/Tree Ring Methods

The method is based on detecting impact scars on trees caused by flying or bouncing boulders towards the down. Past rockfall events are dated from disturbed wood samples or tree rings from drilled cores extracted in the field (Dorren et al. 2007). Resulted Spatio-temporal rockfall distribution is implemented in hazard estimations (Stoffel and Bollschweiler 2008). Tree ring analyses potentially work with monthly temporal resolution (Ortloff et al. 1995). Dendrochronology can theoretically reach hundreds of years into the past when old trees are present near the examined slope. Stoffel (2006) reported a review of this method used for rockfall dating.

2.5.2.2 Lichenometric Analyses

This method is based on the principle of measuring the diameter of particular lichen species on rockfall accumulations (André 1986). The temporal precision of lichenometry dating ranges from one-year precision for young events up to a hundred years for more than a thousand years old events (Bull 1996). A reliable calibration curve is needed to apply this method (Hartvich et al. 2017). A complex review of lichenometry was reported by Joshi et al. (2012).

2.5.2.3 Degree of Weathering Dating (DOW)

The method considers that younger accumulation or recently exposed rockfall scar was less affected by the weathering process; these surfaces should be harder. The DOW is determined in the field using Schmidt hammer surface hardness testing. DOW can be used for absolute dating of accumulation age (Nesje et al. 1994) or, more often, for relative age estimation in the case of complex rockfall sites (Klapyta 2013). The DOW can also be approximately determined from the color of the surface or the absence/presence of secondary biocrust in the case of young events (Dorren et al. 2007). A review of weathering-based dating methods was elaborated by McCarroll (1985).

2.5.2.4 Archive Review

A review of archive sources, such as newspapers or maintenance diaries (roads, railway, ropeway), can provide temporal rockfall information (Hungr et al. 1999). Trough the research of archive sources, it is possible to get information about mass wasting events, such as landslides or voluminous rockfalls, from mass media. Events that affected settlements or infrastructure are mentioned through archive sources. Some extensive works (Raška et al. 2015; Guzzetti et al. 1999) used newspaper articles to enrich landslide inventories.

2.5.3 Geodetical Methods

Geodetical methods are used to measure both relative and absolute spatial changes in rock slope geometry (Gunzburger et al. 2005). The geodetical monitoring systems are mostly in use for landslide monitoring (Saleh and Al-Bayari 2007), glaciers monitoring (Azam et al. 2018), or monitoring of unstable open-pit mines slopes (Osasan and Afeni 2010), together with civil engineering applications (Erol et al. 2004). The possibility of remote data colection makes geodetical methods appropriate for unstable danger rock slopes monitoring.

2.5.3.1 Tachymetry

This is also called tacheometry and telemetry and it is more than a century-old method used for inaccessible or dangerous rock block displacement monitoring (Cuffe 1907). Traditionally, a simple angle measuring theodolites with reflecting prisms is used. Nowadays, this method is being replaced with reflector-less total stations with a precision of approx. 1 cm per 1 km distance (Fengrui 2011). By such a method, even the spatial orientation of surfaces can be measured (Feng et al. 2001); when reflective prisms are placed within unstable features, precision rises to 1.5 mm per 1 km. The advantages of using total stations are easy transportation, simple data processing, long-range, and possible automatization of a permanently placed device (Lambrou and Pantazis 2006). In the case of multiple points are measured with the total station, a simple generalized digital model of rock slope can be created (Isioye and Jobin 2012). The permanent placement of the automatized total station can be considered a modern monitoring method. This application demands the use of reflective prisms. Total stations measuring campaigns are used within complex monitoring systems (Janeras et al. 2017; Corsini et al. 2013), and also Scherer and Lerma (2009) recorded an in-depth information of tachymetry.

2.5.3.2 Precise Leveling

A precise yet straightforward all-around geodetical method is used for landslides monitoring (Savvaidis 2003). In the case of steep rock slope monitoring use of leveling is limited (Stiros et al. 2004) This method is used for slow tilting rock blocks or rock mass subsidence monitoring (Motagh et al. 2007; Košťák et al. 2006). Also, the Spatio-temporal evolution of large, slow rock slides can be determined using precise leveling campaigns (Zangerl et al. 2010) with the precision of up to tenths of millimeters. With a long enough time series, this method leveling can recognize even small movements with low magnitude.

2.5.3.3 Analogue Photogrammetry

This is another traditional method in landslide monitoring. It was used for rock slopes or deep mine monitoring (Chandler and Moore 1989). This tool was used in long-range mode (landforms) and microscale close-range mapping with precision up to millimeters (Welch and Dikkers 1978). The method was also used for slope stability monitoring, where it provides Spatio-temporal information about rock slope surface dynamics in combination with tachymetry. The traditional approach uses fixed reflectors (tie points) positioned within the rock face. The spatial position of reflectors is monitored using time-lapse photos (McVey et al. 1974). The field precision of such a setup was +0.05 m. Due to complicated analog photos processing, it was a marginally used method. Nowadays, digital photogrammetry is used all around geosciences (Walstra et al. 2007).

2.5.4 Geotechnical Methods

Geotechnical sensors are placed within the rock face or inside the rock mass in boreholes. Direct placement brings less complicated and straighter forward, intuitive data interpretation (Dunnicliff 1993). The geotechnical methods are frequently used in the rock slope monitoring. The placement principles and measured quantities remain unchanged, yet the sensors now often work with modern technologies.

2.5.4.1 Crack Monitoring

Monitoring of the crack displacements is a frequently-used method. It describes rock face or unstable rock slope element Spatio-temporal behavior (Bakun-Mazor et al. 2013; Janeras et al. 2017; Collins and Stock 2016). Generally, crack displacement monitoring can be used for rockfall event prediction (Zvelebil and Moser 2001; Arosio et al. 2009). The use of sensor type is determined by the Spatio-temporal scale of the monitored feature. Simple attachable crack meters (vernier calipers) are used for measuring of fast movements or for low-frequency measuring campaigns (Boyd et al. 1973; Zvelebil et al. 2002). For first verification of the ongoing crack dynamic, glass plates are glued over the crack ("tell tale") (Price 2010). In geoengineering, mining or civil engineering used, "tell tales" are made from two overlapping plastic plates, glued or screwed over the monitored crack with an aim and cross (or moiré) pattern with submillimeter resolution (Akbari 2013; Johnson 2005). Displacement transducers (Ellis 1975) or vibrating string crack meters (Wirth and Mario 1968) are used for continuous crack monitoring. These devices can provide continuous data about crack dynamics (Ding et al. 2000; Peters and van der Vliet 2009). Data loggers should be equipped with a thermometer to distinguish thermal dilatation (Thorarinsson 2015). Continuous crack monitoring is one of the key parts of rockfall early warning systems setting on an alarm when movement accelerates (Rozsypal 2001). The precision of the mechanical (vernier) crack meter can reach 0.05 mm (Boyd et al. 1973). Modern position transducer sensitivity can be less than 0.05 mm (Fantini et al. 2016), and a typical precision reaches 0.01 mm (Klimeš et al. 2012) with 0.5% accuracy. Dilatometers are used to measure the displacements between partial blocks of rock slopes (Vařilová and Zvelebil 2005; Zvelebil et al. 2002). Dilatometers can be installed permanently, or portable dilatometers can be applied when only measuring bolts are placed within rock face (Hartvich and Mentlík 2010; Vilímek et al. 2007).

2.5.4.2 3D Moiré Crack Gauges

A long-term monitoring of very slow movements, an optical-mechanic TM-71 gauge (Klimeš et al. 2012) is world widely used. This device can measure relative displacements and rotations between rock blocks in 3D. The sensor is fully analog and does

not require an electricity source to work. TM-71 applicable monitoring of slow movements, such as rockslides, toppling, or tectonic movements, with a precision better than 0.007 mm (Stemberk et al. 2010). In the case of rotation, precision is better than 0.00016 rad (Košťák et al. 2011). The device can be fully automated when long-term monitoring is needed. Then data can be subtracted remotely.

2.5.4.3 Tape/Wire Extensometer

It is convenient to use an invar method to measure movements over greater distances in the complicated topography (Duffield and Burford 1973) by tape/wire extensometer (Lazar et al. 2018; Baroň and Supper 2013). The main advantage of this method is that the extensometer profile does not have to be straight or level. It is one of the perfect methods for large complex rockslides velocity and development monitoring or unstable block monitoring (Greif et al. 2006; Crosta and Aligardi 2002). This monitoring provides continuous data with a permanent extensometer (Lazar et al. 2018). Eventually, only the anchors are permanent, and measurement is done in campaigns (Glawe et al. 1993). The highest sub-millimetric precision is limited to approx. 60 m profile length (Osasan and Afeni 2010).When a profile is longer, outcomes can be biased by invar thermal expansion. When rockslide velocity is higher than wire thermal expansion bias, the profile can be longer (Janeras et al. 2017; Zangerl et al. 2010). Long profiles can be measured underground where the temperature is stable (Bhalla et al. 2005). The precision of wire extensometer monitoring is about 0.01 mm when accuracy decreases with profile length (Osasan and Afeni 2010).

2.5.4.4 Borehole Extensometer

A borehole extensometer is used to measure slow rock mass sliding movements, like a creep (Gunatilake et al. 2002) or deep-seated slope deformations (Salvini et al. 2015). The root of the extensometer is placed in a deep stable part of the rock slope, and the borehole head is moving together with the surface. Multiple extensometers rooted in different depths to detect possible slip surface in different depths (Huang et al. 2009) must be deployed. The precision of a borehole extensometer is approximately 0.1 mm (analogue) or 0.01 mm (digital/MEMS) (Angeli et al. 2000). This method is traditionally used in civil engineering or geological application within compact rocks or soils. Burland et al. (1972) provides an overview of this method.

2.5.4.5 Borehole Micrometer

A borehole micrometer is used to measure slow, predominantly vertical movements. Special borehole casings allow fixing micrometer probes in each length of the device to identify vertical movements like subsidence or heaving in the whole depth profile

of the borehole (Li et al. 2012). The precision of this device is about 0.002 mm. The device can also measure changes in borehole casing inclination.

2.5.4.6 Borehole Wire Extensometer

Wire borehole extensometers can monitor deep-seated rockslide velocity (Crosta et al. 2014). The wire is anchored in the stable bottom of the borehole. The head of the borehole with a reading device is moving along with sliding mass and applies tension on the wire, which transfers rockslide movement on to logger. The stable temperature inside the borehole does not affect the results by wire thermal expansion (Riley 1984). Boreholes can be drilled horizontally or inclined (Crosta et al. 2014), and the precision of the extensometer can exceed 0.001 mm (Mentes 2012).

2.5.4.7 Tiltmeter

The method is applied on rock slopes (Sugawara et al. 2003; Blikra and Christiansen 2014), unstable blocks (Lambert and Nicot 2013; Janeras et al. 2017), or civil engineering monitoring (Kiremidjian et al. 1997). Monitoring can be continuous (Blikra and Christiansen 2014), or the monitored feature is instrumented with a standardized base for tiltmeter campaigns. The Tiltmeter surveys in rock slide profiles allow for decomposing partial movements within complex rockslides (Strouth et al. 2006). It provides precise data up to $\pm 0.005°$ (Woschitz and Macheiner 2007).

2.5.4.8 Borehole Inclinometer

A inclinometer allows for determining the velocity of the rockslide at different depths, and it is used for slow rock slide monitoring. Thus the slip surface/s depth (Crosta et al. 2014; Zangerl et al. 2010) can be determined. The inclinometer borehole casing is vulnerable, making this method suitable only for measuring small inclination changes (slow movements). Fast slope movement leads to deformation of the casing that does not allow passage of the inclinometer probe (Deschamps et al. 1998; O'Connor and Dowding 1999). This limitation can be partially overpassed by using a modern, flexible inclinometer probe (Zhang et al. 2018). The precision of the portable inclinometer is circa 1 mm/50 m of the borehole. A combined inclinometer/micrometer is used. This device measures horizontal and vertical spatial changes through the borehole profile (Frodl and Naterop 2007; Wittke 2014). The precision of this device is 0.002 to 0.003 mm in case of vertical changes and 0.0001 mm in case of lateral displacement (Frodl and Naterop 2007) and decreases with borehole depth. If continual monitoring is needed, it is possible to equip the borehole with a permanent inclinometer that provides continuous data about inclination and length change (Bell and Maud 1996).

2.5.4.9 Piezometric Measurements

Monitoring groundwater pressure in landslide-prone zone areas with piezometers is an effective tool used in large, relatively slow rock slides. The first approach is underground water level monitoring is used because the rise of underground water levels often causes reactivation or acceleration of a rockslide (Crosta et al. 2014; Cloutier et al. 2015). The second approach is to measure changes in pore pressure using closed piezometers (Strauhal et al. 2016; Blikra et al. 2019).

2.5.4.10 Strain Gauges

Tensiometers (strain gauges) are used for small rock mass strain changes measurement. Measurement is based on the principle of resistivity changes within a semiconductor grid (Ivor and Moxon 1965; Kanagawa et al. 1986). The Tensiometers are installed on the rock face (Fiorucci et al. 2020) or inside boreholes, perpendicular to the presumed stress directions (Lo et al. 1995). From the known changes in resistivity (strain) and Young's modulus, it is possible to compute changes in the stress field. A conical head borehole device (CCBO) is used to determining 3D tensor of the stress field inside the rock mass (Sugawara and Obara 1999), and Ljunggren et al. (2003) have been reviewed for strain measurement in rock mass.

2.6 Concluding Remarks

This paper enumerates the methods used for rock slope characterization, rock slope stability assessment, and rockfall monitoring. The first part of this chapter presents a short overview of rock mass properties monitored variables and rock slope stability influencing factors. After that, basic principles of functional monitoring system design are outlined. The key part of this chapter describes traditional methods for rock slope monitoring (Figs. 2.2 and 2.4). Nowadays, these methods are often replaced by their modern alternatives and are used less frequently (Fig. 2.4). Firstly, simple qualitative methods like geotechnical classifications or rockfall collector monitoring are mentioned. These methods describe rock mass characteristics, slope stability indexes, or short-term Spatio-temporal rockfall activity distribution. In contrast, the dating methods provide complex Spatio-temporal rockfall data even in the past. The enumeration and description of geodetical and geotechnical rock slope monitoring methods conclude the key part of this chapter.

All rock slope monitoring methods, traditional and modern (Blahůt and Racek 2023, Chapter 1) were primarily classified into four groups as follows:

- General properties of rock slope estimation
- Rockfall event dating
- Spatio-temporal rock slope activity

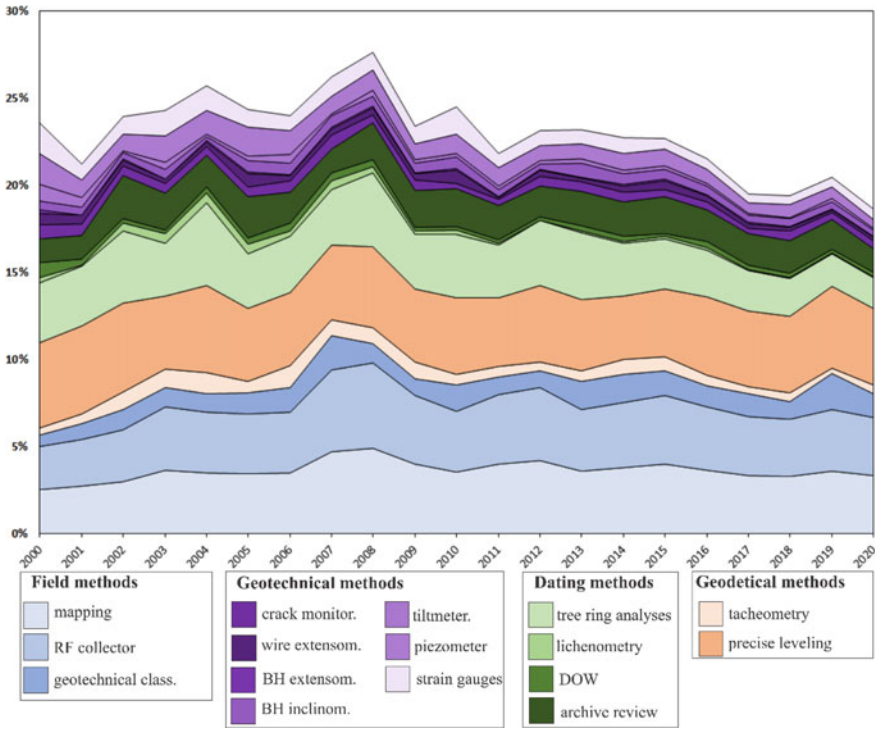

Fig. 2.4 Traditional methods of rock slope monitoring. Percentage share of each method within published scientific papers mentioning method in the topic

- External variables/factors monitoring

The four groups listed above reflect the purpose of the methods and which variables are obtained using the listed methods. Then the traditional methods are fully described. Intelligibility these are, according to their principles, divided into four groups:

1. Expert methods should be the first step in rock slope monitoring. Complex mapping and initial stability estimation decide on future monitoring design. Quality monitoring cannot be designed without a good understanding of ongoing rock slope processes and destabilization regimes. It means expert methods will not be replaced in the future because these are still irreplaceable. The only disadvantage is low temporal resolution, as they are time-consuming and lack quantitative results.
2. Traditional geodetical methods measure Spatio-temporal rock slope surface changes. Thus these methods are selective, and the spatial change is monitored precisely with several representative points of interest. The use of traditional geodetical methods demands repeated visits to the site by the researcher.

This limitation lowers the temporal resolution of results. Some of the geodetical methods allow remote monitoring of highly active sites.

3. Dating methods include archive review, tree-ring analyses, lichenometry, and DOW are other traditional methods. These traditionally used methods provide dating possibilities up to several thousand years in the past. Their advantages over modern dating methods are the simplicity of data processing, cost-effectiveness, and ease of processing. The reach of these methods is limited, yet, their precision can overcome new, state-of-the-art dating methods.
4. Geotechnical methods measure surficial or sub-surfaced spatial changes, stress field dynamics, or underground water level changes. Traditional geotechnical approaches are still irreplaceable in rock slope monitoring. These are the key part of direct monitoring systems. These methods produce high-precision spatial data with reasonable temporal resolution. More precise sensors are still developed, but operation and sensor placement principles remain unchanged. Geotechnical methods remain unsurpassed by modern methods in terms of precision.

The fact that the methods are used traditionally does not mean that these provide low-quality data. On the contrary, traditional methods often provide results even with higher precision than modern methods (Table 2.1). There are crucial expert field methods used for monitoring design for more than a hundred years. Nowadays, traditionally used principles are transferred from analog-based sensors to new electronically-driven, state-of-the-art devices. This means traditional methods will stay in the field even in the future. Moreover, their results will be supported by newly designed, modern sensors. Table 2.1 provides an overview of all rock slope monitoring methods listed in this chapter and Blahůt and Racek (2023) in Chapter 1. It is obvious that traditionally used methods often overcome modern state-of-art methods.

Traditional methods from all groups are rarely used independently and are combined in complex systems (Racek et al. 2021) to get data about rock slope dynamics and their influencing factors. Complex monitoring systems are designed site-specifically to get the best possible results in the case of Spatio-temporal precision and capturing of mass wasting complexity. The design depends on the monitoring purpose, financial resources, and required data outcomes. The use of a particular method depends on the type and velocity of monitored movement, accessibility of the site of interest, and the overall purpose of the designed system. When these conditions are abided, good quality and meaningful data are obtained and further processed. Due to a lack of understanding of rockfall triggering and preparatory mechanisms, the design of the monitoring system requires an experienced researcher. The goal of monitoring design is to deploy as few sensors as possible but still be able to describe complex rock slope behavior. In the future, we can expect the rapid development of new sensors. This development is caused by new engineering challenges caused by infrastructure expansion to new, geologically complicated areas.

Table 2.1 Overview of rock slope monitoring methods and their properties (Traditional and modern methods)

Method	Primary purp.	Secondary purp.	Primary class.	Secondary class.	Measures
Field mapping	Stability estimation	Hazard estimation	General properties	Expert method	Rock slope stability
Geotechnical classification	Stability estimation	Hazard estimation	General properties	Expert method	Rock slope stability
Rockfall collector	RF properties, frequency	Hazard estimation	Event dating	Dating	Rockfall volume, frequency
Archive review	RF properties, frequency	Hazard estimation	Event dating	Dating	Rockfall temporal pattern
Tachymetry	Movement monitoring	Spatial change	Spatio-temporal activity	Geodetical	Spatial position
Precise levelling	Movement monitoring	Stability estimation	Spatio-temporal activity	Geodetical	Spatial position
TLS single	State of rock slope	Spatial change	Spatio-temporal activity	Geodetical	Rock slope geometry
TLS time lapse	Movement monitoring	Stability estimation	Spatio-temporal activity	Geodetical	Spatial position
ALS	State of rock slope	Spatial change	Spatio-temporal activity	Remote sensing	Rock slope geometry
Photogrametry single	State of rock slope	Spatial change	Spatio-temporal activity	Remote sensing	Spatial position
Photog.time-lapse	Movement monitoring	Stability estimation	Spatio-temporal activity	Remote sensing	Spatial position
GNSS monitoring	Movement monitoring	Stability estimation	Spatio-temporal activity	Geodetical	Spatial position
Dendrochronology	Rockfall properties, frequency	Hazard estimation	Event dating	Dating	Rockfall properties, frequency
Lichenometry	Rockfall properties, frequency	Hazard estimation	Event dating	Dating	Rockfall properties, frequency
Degree of weathering	Rockfall properties, frequency	Hazard estimation	Event dating	Dating	Rockfall properties, frequency
Cosmogenic nuclides	Rockfall properties, frequency	Hazard estimation	Event dating	Dating	Rockfall properties, frequency

(continued)

Table 2.1 (continued)

Optical luminescence	Rockfall properties, frequency	Hazard estimation	Event dating	Dating	Rockfall properties, frequency
Crack meter	Movement monitoring	Stability estimation	Spatio-temporal activity	Geotechnical	Spatial position
TM-71	Movement monitoring	Stability estimation	Spatio-temporal activity	Geotechnical	Spatial position
Wire extensometer	Movement monitoring	Stability estimation	Spatio-temporal activity	Geotechnical	Spatial position
BH extensometer	Movement monitoring	Stability estimation	Spatio-temporal activity	Geotechnical	Borehole spatial change
BH micrometer	Movement monitoring	Stability estimation	Spatio-temporal activity	Geotechnical	Borehole spatial change
BH inclinometer	Movement monitoring	Stability estimation	Spatio-temporal activity	Geotechnical	Borehole inclination
BH compound probe	Movement monitoring	Stability estimation	Spatio-temporal activity	Geotechnical	Borehole spatial change
Dilatometer	Movement monitoring	Stability estimation	Spatio-temporal activity	Geotechnical	Spatial position
Tiltmeter	Movement monitoring	Stability estimation	Spatio-temporal activity	Geotechnical	Tilt changes
Piezometer	Pore pressure monitoring	Hydrogeological monitoring	General properties	Geotechnical	Pore pressure, ground water
Strain gauge	Stress field monitoring	Stability estimation	Spatio-temporal activity	Geotechnical	Strain
CCBO	Stress field monitoring	Stability estimation	Spatio-temporal activity	Geotechnical	Strain
Optical fibre	Movement monitoring	Strain monitoring	Spatio-temporal activity	Geotechnical	Strain temperature
ERT single	Rock slope physical properties	Stability estimation	General properties	Geophysical	Rock slope resistivity
ERT time-lapse	Rock slope physical properties	Stability estimation	Spatio-temporal activity	Geophysical	Rock slope resistivity
Seismic tomography	Rock slope physical properties	Stability estimation	General properties	Geophysical	Seismic waves velocity
Ambient vibration	Rock slope physical properties	Stability estimation	General properties	Geophysical	Vibration pattern of rock slope

(continued)

Table 2.1 (continued)

Micro seismical	Rock fall properties, frequency	Stability estimation	Spatio-temporal activity	Geophysical	In situ seismicity
Borehole temperature	Temporal temperature changes	Additional information	General properties	Geophysical	Temperature
Camera monitoring	Movement monitoring	Stability estimation	Spatio-temporal activity	Remote sensing	Rockfall properties, frequency
Aerial monitoring	State of rock slope	Stability estimation	Spatio-temporal activity	Remote sensing	Rock slope state, evolution
GB InSAR	Movement monitoring	Stability estimation	Spatio-temporal activity	Remote sensing	Spatial position
InSAR	Movement monitoring	Stability estimation	Spatio-temporal activity	Remote sensing	Spatial position
Thermal camera	Spatial temperature	Rock slope properties	Spatio-temporal activity	Remote sensing	Temperature of rock face
Remote vibration	Rock slope properties	Stability estimation	Spatio-temporal activity	Remote sensing	Vibration of rock slope
Method	**Measured variables**	**Precision**	**Spatial scale**	**Temporal resolution**	**Mass wasting**
Field mapping	Objective stability	Meters–region	1–1000 m	Days–years	Landslide
Geotechnical class	Stability index	Meters–rock slope	1–1000 m	Days–years	Rockslide
Rockfall collector	Δ volume, time	cm^3	1–100 m	Hours–years	Rockfall
Archive review	Time	Years–hours	Slope–region/state	Hours–years	Landslide
Tachymetry	3D Δx, Δy, Δz	0.1–2 mm	0.01–100 m	Minutes–years	Landslide
Precise levelling	1D Δz	0.1–1 mm	0.001–1 m	Minutes–years	Landslide
TLS single	3D Δx, Δy, Δz	2–10 mm	0.001–10 m	Minutes–hours	Rockfall
TLS time lapse	3D Δx, Δy, Δz	2–10 mm	0.001–10 m	Minutes–years	Rockfall
ALS	3D Δx, Δy, Δz	<1 m	0.01–1000 m	Days–years	Landslide

(continued)

Table 2.1 (continued)

Photogrametry single	3D Δx, Δy, Δz	1–30 mm	0.01–100 m	Seconds–hours	Rockfall
Photog.time-lapse	3D Δx, Δy, Δz	1–30 mm	0.01–100 m	Seconds–years	Rockfall
GNSS mon	3D Δx, Δy, Δz	5–10 mm	0.01–100 m	Hours–years	Landslide
Dendrochronology	Time, 3D Δx, Δy, Δz	<1 year	0.01–1000 m	<years	Landslide
Lichenometry	Time, 3D Δx, Δy, Δz	>1 year	0.01–1000 m	years	Rockfall
Degree of weathering	Time, 3D Δx, Δy, Δz	>10 years	0.1–1000 m	>years	Rockfall
Cosmogenic nuclides	Time, 3DΔx, Δy, Δz	>10 years	0.1–1000 m	>years	Rockfall
Optical luminescence	Time, 3D Δx, Δy, Δz	>10 years	0.1–1000 m	>years	Rockslide
Crack meter	1D Δx	0.001 mm	0.01–1 m	Seconds–years	Rockfall
TM-71	3D Δx, Δy, Δz	0.01–0.03 mm	0.01–0.1 m	Minutes–years	Toppling
Wire extensometer	1D Δx	0.3 mm	0.1–10 m	Seconds–years	Landslide
Borehole extensometer	1D Δx	0.1 mm	0.01–1 m	Seconds–years	Landslide
Borehole micrometer	1D Δx; 2D Δα, Δβ	0.003 mm; 0.001°	0.001–1 m	Days–years	Landslide
Borehole inclinometer	2D Δα, Δβ	0.01°	0.01–5 m	Days–years	Landslide
Borehole compound probe	2D Δα, Δβ, Δx	0.3 mm; 0.003°	0.01–10 m	Seconds–years	Landslide
Dilatometer	1D Δx	0.001 mm	0.01–1 m	Seconds–years	Rockfall
Tiltmeter	1D Δα	0.004°	0.1–100 m	Seconds–years	Toppling
Piezometer	1D Δp	0.01 kPa; 1 mm	0.1–100 m	Seconds–years	Landslide
Strain gauge	1D Δσ1 Pa	5 μm	0.000005–0.001 m	Seconds–months	Rockfall
CCBO	3D Δx, Δy, Δz	5 μm	0.000005–0.001 m	Seconds–years	Rockfall

(continued)

Table 2.1 (continued)

Optical fibre	1D $\Delta\sigma 1$, ΔT	< 10 cm; < 1 °C	0.1–100 m	Seconds–years	Landslide
ERT single	2(3)D Ω	0.5 Ω	0.1–100 m	Days–years	Landslide
ERT time-lapse	2(3)D $\Delta\Omega$	0.5 Ω	0.1–100 m	Hours–years	Landslide
Seismic tomography	m/s	0.0002 m/s	0.1–100 m	Hours–years	Landslide
Ambient vibration	Hz	0.0001 Hz	0.001–1 m	Hours–years	Rockfall
Micro seismical	Hz	0.0001 Hz	0.001–1 m	Seconds–years	Rockfall
Borehole temperature	T	<0.05 °C	1–1000 m	Seconds–years	Rockslide
Camera monitoring	Pixel value	Variable	0.01–1000 m	Seconds–years	Rockfall
Aerial monitoring	Pixel value	Variable	0.1–1000 m	Days–years	Landslide
GB InSAR	3D Δx, Δy, Δz	<1 mm	0.01–100 m	Seconds–years	Rockfall
InSAR	3D Δx, Δy, Δz	1 mm–10 cm	0.1–100 m	Days–years	Landslide
Thermal camera	3D ΔT	Variable	0.1–10 m	Seconds–years	Rockfall
Remote vibration	Hz	0.0001 Hz	0.001–1 m	Seconds–years	Rockfall

Acknowledgements We would like to thank Charles University and the Czech Academy of Sciences for their financial support. We would also like to thank the reviewers and the editor for their beneficial remarks that lead to the improvement of this paper. This research was performed in the framework of the long-term conceptual development research organization RVO: 67985891, TAČR project no. SS02030023 "Rock environment and resources" within the program "Environment for life", internal financing from Charles University Progress Q44 and SVV (SVV260438) and the Charles University Grant Agency (GAUK 359421).

References

Abramson LW, Lee TS, Sharma S, Boyce GM (2001) Slope stability and stabilization methods. Wiley, New York

Akbari R (2013) Crack survey in unreinforced concrete or masonry abutments in short- and medium-span bridges. J Perform Constr Facil 27:203–208. https://doi.org/10.1061/(ASCE)CF.1943-5509.0000298

Aksoy CO (2008) Review of rock mass rating classification: historical developments, applications, and restrictions. J Min Sci 44:51–63. https://doi.org/10.1007/s10913-008-0005-2

André MF (1986) Dating slope deposits and estimating rates of rock wall retreat in northwest Spitsbergen by lichenometry. Geogr Ann Ser B 68(1–2):65–75

Angeli M-G, Pasuto A, Silvano S (2000) A critical review of landslide monitoring experiences. Eng Geol 55:133–147. https://doi.org/10.1016/S0013-7952(99)00122-2

Arosio D, Longoni L, Papini M, Scaioni M, Zanzi L, Alba M (2009) Towards rockfall forecasting through observing deformations and listening to microseismic emissions. Nat Hazards Earth Syst Sci 9:1119–1131. https://doi.org/10.5194/nhess-9-1119-2009

Azam M, Wagnon P, Berthier E, Vincent C, Fujita K, Kargel JS (2018) Review of the status and mass changes of Himalayan-Karakoram glaciers. J Glaciol 64:61–74. https://doi.org/10.1017/jog.2017.86

Bakun-Mazor D, Hatzor YH, Glaser SD, Santamarina JC (2013) Thermally vs. seismically induced block displacements in Masada rock slopes. Int J Rock Mech Min Sci 61:196–211. https://doi.org/10.1016/j.ijrmms.2013.03.005

Baroň I, Supper R (2013) Application and reliability of techniques for landslide site investigation, monitoring and early warning; outcomes from a questionnaire study. Nat Hazards Earth Syst Sci 13:3157–3168. https://doi.org/10.5194/nhess-13-3157-2013

Barton N (1974) A review of the shear strength of filled discontinuities in rock. Norwegian Geotechnical Institute Publication, Olso, p 105

Barton N, Bar N (2015) Introducing the Q-slope method and its intended use within civil and mining engineering projects. In SRM regional symposium-EUROCK 2015. International Society for Rock Mechanics and Rock Engineering.

Bauer A, Paar G, Kaltenböck A (2005) Mass movement monitoring using terrestrial laser scanner for rock fall management. Geo-Information For Disaster Management. Springer, Berlin, pp 393–406

Bell FG, Maud RR (1996) Landslides associated with the Pietermaritzburg Formation in the greater Durban area, South Africa: some case histories. Environ Eng Geosci 2(4):557–573

Bhalla S, Yang YW, Zhao J, Soh CK (2005) Structural health monitoring of underground facilities: technological issues and challenges. Tunnell Undergr Space Tech 20(5):487–500

Bienieawski ZT (1973) Engineering classification of jointed rock masses. Civ Eng S Afr 15:353

Blahůt J, Jaboyedoff M, Thiebes B (2021) Novel approaches in landslide monitoring and data analysis special issue: trends and challenges. Appl Sci 11:10453. https://doi.org/10.3390/app112110453

Blikra LH, Christiansen HH (2014) A field-based model of permafrost-controlled rockslide deformation in northern Norway. Geomorphology 208:34–49. https://doi.org/10.1016/j.geomorph.2013.11.014

Blikra LH, Lovisolo M, Pless G, Kristensen L (2019) Subsurface instrumentation for evaluating water-pressure changes and deformation at the Åknes rockslide, western Norway. Geophys Res Abs 21.

Bond AJ, Schuppener B, Scarpelli G, Orr TLL (2013) Eurocode 7: Geotechnical design worked examples. European Union, Luxembourg

Boyd JM, Hinds DV, Moy D, Rogers C (1973) Two simple devices for monitoring movements in rock slopes. Q J Eng Geol Hydrogeol 6:295–302

Bull W (1996) Dating San Andreas fault earthquakes with lichenometry. Geology 24:111–114. https://doi.org/10.1130/0091-7613(1996)0240111:DSAFEW2.3.CO;2

Burland JB, Moore JFA, Smith PDK (1972) A simple and precise borehole extensometer. Geotechnique 22(1):174–177

Chandler JH, Moore R (1989) Analytical photogrammetry: a method for monitoring slope instability. Q J Eng Geol Hydrogeol 22:97–110. https://doi.org/10.1144/GSL.QJEG.1989.022.02.02

Cloutier C, Locat J, Charbonneau F, Couture R (2015) Understanding the kinematic behavior of the active Gascons rockslide from in-situ and satellite monitoring data. Eng Geol 195:1–15. https://doi.org/10.1016/j.enggeo.2015.05.017

Collins B, Stock GM (2016) Rockfall triggering by cyclic thermal stressing of exfoliation fractures. Nat Geosci 9:395–400. https://doi.org/10.1038/ngeo2686

Copons R, Vilaplana JM (2008) Rockfall susceptibility zoning at a large scale: from geomorphological inventory to preliminary land use planning. Eng Geol 102:142–151 https://doi.org/10.1016/j.enggeo.2008.03.020

Corsini A, Castagnetti C, Bertacchini E, Rivola R, Ronchett F, Capra A (2013) Integrating airborne and multi-temporal long-range terrestrial laser scanning with total station measurements for mapping and monitoring a compound slow moving rock slide. Earth Surf Process Land 38(11):1330–1338

Crosta GB, Agliardi F (2002) How to obtain alert velocity thresholds for large rockslides. Phys Chem Earth 27:1557–1565. https://doi.org/10.1016/S1474-7065(02)00177-8

Crosta GB, Di Prisco C, Frattini P, Frigerio G, Castellanza R (2014) Chasing a complete understanding of the triggering mechanisms of a large rapidly evolving rockslide. Landslides 11:747–764. https://doi.org/10.1007/s10346-013-0433-1

Cuffe OFLW (1907) Survey of inaccessible places by tacheometry. Min Proc Inst Civ Eng 107:315–323

D'Amato J, Hantz D, Guerin A, Jaboyedoff M, Baillet L, Mariscal AM (2016) Influence of meteorological factors on rockfall occurrence in a middle mountain limestone cliff. Nat Hazards Earth Syst Sci 16:719–735. https://doi.org/10.5194/nhess-16-719-2016

Deere DU, Hendron AJ, Patton FD, Cording EJ (1967) Design of surface and near-surface construction in rock: failure and breakage of rock. In: Proceedings of 8th US symposium of rock mechanics, New York, pp 237–302

Degraaff LWS, Dejong MGG, Rupke J, Verhofstand J (1987) A geomorphological mapping system at scale 1: 10,000 for mountainous areas. Z Geomorphol 31:229–242

Demek J, Embleton C (1978) Guide to medium-scale geomorphological mapping, 1st edn. Schweizerbarts, Stuttgart

Deschamps R, Hynes C, Wigh R (1998) Extending the period of data retrieval for vertical inclinometers. J Geotech Geoenviron Eng 124:454–456. https://doi.org/10.1061/(ASCE)1090-0241(1998)124:5(454)

Ding X, Ren DY, Montgomery B, Swindells C (2000) Automatic monitoring of slope deformations using geotechnical instruments. J Surv Eng 126:57–68. https://doi.org/10.1061/(ASCE)0733-9453(2000)126:2(57)

Dorren LKA (2003) A review of rockfall mechanics and modelling approaches. Prog Phys Geogr Earth Environ 27:69–87. https://doi.org/10.1191/0309133303pp359ra
Dorren D, Jonsson M, Krautblatter M, Mölk M, Stoffel M, Wehrli A, Berger F (2007) State of the art in rockfall–forest interactions. Schweiz Z Fur Forstwes 158:128–141
Duffield WA, Burford RO (1973) An accurate invar-wire extensometer. J Res US Geol Surv 1:569–577
Dunnicliff J (1993) Geotechnical instrumentation for monitoring field performance. John Wiley & Sons
Einstein HH, Veneziano D, Baecher GB, O'Reilly KJ (1983) The effect of discontinuity persistence on rock slope stability. Int J Rock Mech Min Sci Geomech Abstr 20:227–236. https://doi.org/10.1016/0148-9062(83)90003-7
Ellis JF (1975) Linear displacement transducer utilizing an oscillator whose average period varies as a linear function of the displacement. U.S. Patent No 3,891,918, 1975
Erol S, Erol B, Ayan T (2004) A general review of the deformation monitoring techniques and a case study: analysing deformations using GPS/levelling. In: XXth ISPRS congress, vol 7, no 5, p 12
Fahey BD, Lefebure TH (1988) The freeze-thaw weathering regime at a section of the Niagara escarpment on the Bruce Peninsula, Southern Ontario, Canada. Earth Surf Process Landf 13:293–304. https://doi.org/10.1002/esp.3290130403
Fantini A, Fiorucci M, Martino S, Marino L, Napoli G, Prestininzi A, Salvetti O, Sarandrea P, Stedile L (2016) Multi-sensor system designed for monitoring rock falls: the experimental test-site of Acuto (Italy). Rend Online Soc Geol Ital 41:147–150. https://doi.org/10.3301/ROL.2016.115
Farrokh N, Intrieri E (2011) Early warning systems for landslides: challenges and new monitoring technologies. 5th Canadian conference on geotechnique and natural hazards. Kelowna.
Fassò A, Nicolis O, Bruzzi D, Pezzeti G (2005) Modelling and reducing uncertainty of field monitoring data in geomechanics by computerized statistical methods. In: Proceedings of 11th IACMAG conference, Torino, pp 595–602
Feng Q, Sjögren P, Stephansson O, Jing L (2001) Measuring fracture orientation at exposed rock faces by using a non-reflector total station. Eng Geol 59(1–2):133–146
Fengrui Z (2011) The discussion of reflectorless measurement accuracy. Bull Surv Map 11.
Fiorucci M, Martino S, Bozzano F, Prestininzi A (2020) Comparison of approaches for data analysis of multi-parametric monitoring systems: insights from the Acuto test-site (Central Italy). Appl Sci 10(21):7658
Fischer L, Purves RS, Huggel C, Noetzli J, Haeberli W (2012) On the influence of topographic, geological and cryospheric factors on rock avalanches and rockfalls in high-mountain areas. Nat Hazards Earth Syst Sci 12:241
Frodl H, Naterop D (2007) Trivec and sliding micrometer: fully digital instruments for geotechnical displacement and deformation measurement. In: 7th FMGM 2007: field measurements in geomechanics. Boston, p 1–12
Gaffet S, Guglielmi Y, Cappa F, Pambrun C, Monfret T, Amitrano D (2010) Use of the simultaneous seismic, GPS and meteorological monitoring for the characterization of a large unstable mountain slope in the southern French Alps. Geophys J Int 182:1395–1410. https://doi.org/10.1111/j.1365-246X.2010.04683.x
Glawe U, Zika P, Zvelebil J, Moser M, Rybář J (1993) Time prediction of a rock fall in the Carnic Alps. Q J Eng Geol Hydrogeol 26:185–192. https://doi.org/10.1144/GSL.QJEGH.1993.026.003.04
Greif V, Sassa K, Fukuoka H (2006) Failure mechanism in an extremely slow rock slide at Bitchu-Matsuyama castle site (Japan). Landslides 3:22–38. https://doi.org/10.1007/s10346-005-0013-0
Gunatilake J, Yushiro I, Takanari Y (2002) Relationship of the faulting to the creep movement of Iwakura landslide in Saga, Japan. Landslides 39:212–223
Gunzburger Y, Merrien-Soukatchoff V, Guglielm Y (2005) Influence of daily surface temperature fluctuations on rock slope stability: case study of the Rochers de Valabres slope (France). Int J Rock Mech Min Sci 1997(42):331–349. https://doi.org/10.1016/j.ijrmms.2004.11.003

Guzzetti F, Carrara A, Cardinali M, Reichenbach P (1999) Landslide hazard evaluation: a review of current techniques and their application in a multi-scale study, Central Italy. Geomorphology 31:181–216. https://doi.org/10.1016/S0169-555X(99)00078-1

Hartmeyer I, Keuschnig M, Schrott L (2012) A scale-oriented approach for the long-term monitoring of ground thermal conditions in permafrost-affected rock faces, Kitzsteinhorn, Hohe Tauern Range, Austria. Austrian J Earth Sci 105(2)

Hartvich F, Mentlík P (2010) Slope development reconstruction at two sites in the Bohemian Forest Mountains. Earth Surf Process Landf 35:373–389. https://doi.org/10.1002/esp.1932

Hartvich F, Blahut J, Stemberk J (2017) Rock avalanche and rock glacier: a compound landform study from Hornsund, Svalbard. Geomorphology 276:244–256

Hoek E, Kaiser PK, Bawden WF (1995) Support of underground excavations in hard rock. AA Balkema, Rotterdam

Huang Q-X, Jialin W, Jian-hui D (2009) Lope deformation character analysis based on monitoring results of multiple multi-point borehole extensometer. Chin J Rock Mechan Eng 28:2667–2673

Hungr O, Yau HW, Tse CM, Cheng LF, Cheng LF (1999) Natural slope hazard and risk assessment framework In: Urban ground engineering. Thomas Telford Publishing, London, pp 332–353

Isioye AO, Jobin P (2012) An assessment of digital elevation models (DEMs) from different spatial data sources. Asian J Eng Sci Technol 2

Ivor H, Moxon S (1965) The measurement of in situ rock stress using the photoelastic biaxial gauge with the core-relief technique. Int J Rock Mech Min Sci Geomech Abstr 2:405–419

Janeras M, Jara JA, Royan MJ, Vilaplana JM, Aguasca A, Fabregas X, Gili JA, Buxo P (2017) Multi-technique approach to rockfall monitoring in the Montserrat massif (Catalonia, NE Spain). Eng Geol 219:4–20. https://doi.org/10.1016/j.enggeo.2016.12.010

Johnson R (2005) Significance of cracks in low-rise buildings: what you need to know. Proc Inst Civ Eng Civ Eng 158:30–35

Joshi S, Upreti DK, Das P, Nayaka S (2012) Lichenometry: a technique to date natural hazards. Earth Sci India 4(2):1–16

Kanagawa T, Hibino S, Ishida T, Hayash M, Kitahara Y (1986) In situ stress measurements in the Japanese islands: over-coring results from a multi-element gauge used at 23 sites. Int J Rock Mech Min Sci Geomech Abstr 23:29–39

Kiremidjian AS, Straser EG, Meng T, Law K, Soon H (1997) Structural damage monitoring for civil structures. In: International workshop-structural health monitoring. SHM, pp 371–382

Klapyta P (2013) Application of Schmidt hammer relative age dating to Late Pleistocene moraines and rock glaciers in the Western Tatra mountains, Slovakia. CATENA 111:104–121. https://doi.org/10.1016/j.catena.2013.07.004

Klimeš J, Rowberry M, Blahůt J, Briestenský M, Hartvich F, Košťák B, Rybář J, Stemberk J, Štěpančíková P (2012) The monitoring of slow-moving landslides and assessment of stabilisation measures using an optical–mechanical crack gauge. Landslides 9(3):407–415. https://doi.org/10.1007/s10346-011-0306-4

Klose CD, Loew S, Giese R, Borm G (2007) Spatial predictions of geological rock mass properties based on in-situ interpretations of multi-dimensional seismic data. Eng Geol 93:99–116. https://doi.org/10.1016/j.enggeo.2007.06.001

Košťák B, Chan B, Rybář J (2006) Deformation trends in the Jezeří Castle Massif, Krušné Hory Mts. Acta Geodyn Et Geomater 3:39–49

Košťák B, Mrlina J, Stemberk J, Chán B (2011) Tectonic movements monitored in the Bohemian Massif. J Geodyn 52(1):34–44. https://doi.org/10.1016/j.jog.2010.11.007

Krautblatter M, Moser M (2009) A nonlinear model coupling rockfall and rainfall intensity based newline on a four year measurement in a high Alpine rock wall (Reintal, German Alps). Nat Hazards Earth Syst Sci 9:1425–1432. https://doi.org/10.5194/nhess-9-1425-2009

Krautblatter M, Moser M, Schrott L, Wolf J, Morche D (2012) Significance of rockfall magnitude and carbonate dissolution for rock slope erosion and geomorphic work on Alpine limestone cliffs (Reintal, German Alps). Geomorphology (Amst) 167:21–34. https://doi.org/10.1016/j.geomorph.2012.04.007

Krishnan R, Sommer HJ (1994) Estimation of rock face stability. Proc SPIE Int Soc Opt Eng 2347, 93–104

Kulatilake, PHSW, Wu, TH (1984) Estimation of mean trace length of discontinuities. Rock Mech Rock Eng 17:215–232. https://doi.org/10.1007/BF01032335

Lambert S, Nicot F (eds) (2013) Rockfall engineering. John Wiley & Sons, New York

Lambrou E, Pantazis G (2006) A new geodetic methodology for the accurate documentation and monitoring of inaccessible surfaces. In: Proceedings of 12th FIG symposium on deformation measurement and analysis/3rd IAG symposium on geodesy for geotechnical and structural engineering. Baden, pp 22–24

Lazar A, Beguž T, Vulič M (2018) Monitoring of the Belca rockfall. Acta Geotech Slovenica 15:2–15 https://doi.org/10.18690/actageotechslov.15.2.2-15.2018

Li SJ, Feng XT, Hudson JA (2012) ISRM suggested method for measuring rock mass displacement using a sliding micrometer. In The ISRM suggested methods for rock characterization, testing and monitoring: 2007–2014. Springer, Cham, pp 169–177

Ljunggren C, Chang Y, Janson T, Christiansson R (2003) An overview of rock stress measurement methods. Int J Rock Mech Min Sci 40(7–8):975–989

Lo TC, Chan PC, Tang Z (1995) Design and characterization of a micro strain gauge. In 1995 IEEE TENCON. IEEE region 10 international conference on microelectronics and VLSI. Asia-Pacific microelectronics 2000. Proceedings. pp 36–39

Luckman BH (2008) Forty years of rockfall accumulation at the mount Wilcox site, Jasper National Park, Alberta, Canada. Geogr Pol 79

Macciotta R, Derek MC (2015) Remote structural mapping and discrete fracture networks to calculate rockfall volumes at Tornado Mountain, British Columbia. In: 49th US rock mechanics/geomechanics symposium, American Rock Mechanics Association, San Francisco

Maria MR, Garcia-Moreno I, Azanon JM (2012) Freeze–thaw cycles and rainfall as triggering factors of mass movements in a warm Mediterranean region: the case of the Tramuntana Range (Mallorca, Spain). Landslides 9:417–432. https://doi.org/10.1007/s10346-011-0290-8

Marzorati S, Luzi L, De Amicis M (2002) Rock falls induced by earthquakes: a statistical approach. Soil Dyn Earthquake Eng 1984(22):565–577. https://doi.org/10.1016/S0267-7261(02)00036-2

Masoumi I, Ahangari K, Noorzad A (2017) Reliable monitoring of embankment dams with optimal selection of geotechnical instruments. Struct Monit Maint 4:85–105. https://doi.org/10.12989/smm.2017.4.1.085

McCarroll D (1985) Weathering-based dating techniques: a critical review. Swansea Geogr 22:27–45

McVey JR, Lewis SR, Guidice SR (1974) Deformation monitoring of underground openings: by photographic techniques. U.S. Bureau of Mines, Washington

Menditto A, Patriarca M, Magnusson B (2007) Understanding the meaning of accuracy, trueness and precision. Accred Qual Assur 12:45–47. https://doi.org/10.1007/s00769-006-0191-z

Mentes G (2012) A new borehole wire extensometer with high accuracy and stability for observation of local geodynamic processes. Rev Sci Instrum 83:015109–015109. https://doi.org/10.1063/1.3676652

Motagh M, Djamour Y, Walter TR, Wetzel HU, Zschau J (2007) Land subsidence in Mashhad Valley, northeast Iran: results from InSAR, levelling and GPS. Geophys J Int 168:518–526. https://doi.org/10.1111/j.1365-246X.2006.03246.x

Nesje A, Blikra LH, Anda E (1994) Dating rockfall-avalanche deposits from degree of rock-surface weathering by Schmidt-hammer tests: a study from Norangsdalen. Nor Geol Tidsskr 74:108–113

O'Connor KM, Dowding CH (1999) Geomeasurements by pulsing TDR cables and probes. CRC Press

Olona J, Pulga JA, Fernandez-Viejo G, Lopez-Fernande C, Gonzalez-Cortina JM (2010) Weathering variations in a granitic massif and related geotechnical properties through seismic and electrical resistivity methods. Near Surf Geophys 8:585–599. https://doi.org/10.3997/1873-0604.2010043

Ortloff W, Goldammer JG, Schweingruber FH, Swetnam TW (1995) Jahrringanalytische Untersuchungen zur Feuergeschichte eines Bestandes von Pinus ponderosa Dougl. ex Laws. in den Santa Rita Mountains, Arizona, USA. Forstarchiv 66:206–214

Osasan K, Afen TB (2010) Review of surface mine slope monitoring techniques. J Min Sci 46:177–186. https://doi.org/10.1007/s10913-010-0023-8

Peng M, Li XY, Li DQ, Jiang SH, Zhang LM (2014) Slope safety evaluation by integrating multi-source monitoring information. Struct Saf 49:65–74. https://doi.org/10.1016/j.strusafe.2013.08.007

Peters E, Van Der Vliet P (2009) Sensor network geo-beads TM serves real time and online geotechnical monitoring of large areas. In: Proceedings of the international conference on landslide processes: from geomorphologic mapping to dynamic modelling. CERG Éditions, Strasbourg

Pratt C, Macciotta R, Hendry M (2019) Quantitative relationship between weather seasonality and rock fall occurrences north of Hope, BC, Canada. Bull Eng Geol Environ 78:3239–3251. https://doi.org/10.1007/s10064-018-1358-7

Price DG (2010) Engineering geology: principles and practice, 1st edn. Springer, Heidelberg

Racek O, Blahůt J, Hartvich F (2021) Observation of the rock slope thermal regime, coupled with crackmeter stability monitoring: initial results from three different sites in Czechia (Central Europe). Geosci Inst Methods Data Sys 10:203–218. https://doi.org/10.5194/gi-10-203-2021

Raška P, Klimes J, Dubisar J (2015) Using local archive sources to reconstruct historical landslide occurrence in selected urban regions of the Czech Republic: examples from regions with different historical development. Land Degrad Devel 26(2):142–157

Riley FS (1984) Developments in borehole extensometry. In: Proceedings of the third international symposium on land subsidence. Venice, Italy

Rocha M, Cording EJ (1981) Basic geotechnical description of rock masses. Int J Rock Mech Min Sci Geomech Abstr 18:85–110

Romana MR (1993) A geomechanical classification for slopes: slope mass rating. In: Rock testing and site characterization, Pergamon, pp 575–600

Royan M, Abellan A, Manuel J, Vilaplana (2015) Progressive failure leading to the 3 December 2013 rockfall at Puigcercós scarp (Catalonia, Spain). Landslides 12:585–595. https://doi.org/10.1007/s10346-015-0573-6

Rozsypal A (2001) Control monitoring and risks in geotechnics. Jaga, Bratislava

Saleh B, Al-Bayari O (2007) Geodetic monitoring of a landslide using conventional surveys and GPS techniques. Surv Rev 39:252–260. https://doi.org/10.1179/175227007X197165

Salvini R, Vanneschi C, Riccucci S, Francioni M, Gullì D (2015) Application of an integrated geotechnical and topographic monitoring system in the Lorano marble quarry (Apuan Alps, Italy). Geomorphology 241:209–223

Sass O (2005) Temporal variability of rockfall in the Bavarian Alps, Germany. Arct Antarct Alp Res 37:564–573. https://doi.org/10.1657/1523-0430(2005)037

Savvaidis PD (2003) Existing landslide monitoring systems and techniques. In From stars to earth and culture, Greece, pp 242–258

Scherer M, Lerma JL (2009) From the conventional total station to the prospective image assisted photogrammetric scanning total station: comprehensive review. J Surv Eng 135(4):173–178

Sowers GF (1993) Human factors in civil and geotechnical engineering failures. Int J Geotech Eng 119:238–256

Stemberk J, Košťák B, Cacon S (2010) A tectonic pressure pulse and increased geodynamic activity recorded from the long-term monitoring of faults in Europe. Tectonophysics 487:1–12. https://doi.org/10.1016/j.tecto.2010.03.001

Stiros S, Vichaz C, Skourtis C (2004) Landslide monitoring based on geodetically derived distance changes. J Surv Eng 130:156–162. https://doi.org/10.1061/(ASCE)0733-9453(2004)130:4(156)

Stoffel M (2006) A review of studies dealing with tree rings and rockfall activity: the role of dendrogeomorphology in natural hazard research. Nat Haz 39(1):51–70

Stoffel M, Bollschweile M (2008) Tree-ring analysis in natural hazards research: an overview. Nat Hazards Earth Syst Sci 8:187–202. https://doi.org/10.5194/nhess-8-187-2008

Stoffel M, Hitz OM (2008) Rockfall and snow avalanche impacts leave different anatomical signatures in tree rings of juvenile Larix decidua. Tree Physiol 28:1713–1720. https://doi.org/10.1093/treephys/28.11.1713

Strauhal T, Loew S, Holzmann M, Zangerl C (2016) Detailed hydrogeological analysis of a deep-seated rockslide at the Gepatsch reservoir (Klasgarten, Austria). Hydrogeol J 24:349–371. https://doi.org/10.1007/s10040-015-1341-3

Strouth A, Burk RL, Eberhardt E (2006) The afternoon creek rockslide near Newhalem, Washington. Landslides 3(2):175–179

Sugawara K, Obara Y (1999) Draft ISRM suggested method for in situ stress measurement using the compact conical-ended borehole overcoring (CCBO) technique. Int J Rock Mech Min Sci Geomech Abstr 36:309–322

Sugawara K, Fukahori D, Faramarzi L, Nakamura N (2003) High-resolution tilt monitoring for slope stability assessment in limestone quarry. In: Environmental rock engineering: proceedings of the first Kyoto international symposium on underground environment. Kyoto

Thorarinsson A (2015) Geotechnical data handling from A to Z. FMGM 2015: proceedings of the ninth symposium on field measurements in geomechanics. Australian Centre for Geomechanics

Van Westen CJ, Seijmonsbergen AC, Mantovani F (1999) Comparing landslide hazard maps. Nat Hazard 20:137–158. https://doi.org/10.1023/A:1008036810401

Vařilová Z, Zvelebil J (2005) Sandstone relief geohazards and their mitigation: rockfall risk management in the Bohemian Switzerland National Park. Ferrantia 44(44):51–55

Vilímek V, Zvelebil J, Klimeš J, Patzelt Z, Astete F, Kachlik V, Hartvich F (2007) Geomorphological research of large-scale slope instability at Machu Picchu, Peru. Geomorphology 89:241–257. https://doi.org/10.1016/j.geomorph.2006.12.004

Viswanathan M (2005) Measurement error and research design. Sage Publications, Thousand Oaks

Walstra J, Chandler JH, Dixon N, Dijkstra TA (2007) Aerial photography and digital photogrammetry for landslide monitoring. Geol Soc Spec Publ 283(1):53–63

Weber S, Beute J, Faillettaz J, Hasler A, Krautblatter M, Vieli A (2017) Quantifying irreversible movement in steep, fractured bedrock permafrost on Matterhorn (CH). Cryosphere 11:567–583. https://doi.org/10.5194/tc-11-567-2017

Welch R, Dikkers K (1978) Educational and research aspects of non-metric, close range analogue photogrammetry. Photogram Rec 9(52):537–547

Wieczorek GF, Snyder JB (2009) Monitoring slope movements. In: Geological monitoring, Geological Society of America, Boulder, pp 245–271

Wieczorek GF, Snyder JB, Alger CS, Isaacson KA (1992) Rock falls in Yosemite Valley, California. US Geological Survey Open-File Report 92

Wirth J, Mario G (1968) Vibrating string for measuring purposes. U.S. Patent No. 3,411,347. 19 Nov 1968

Wittke W (2014) Stabilization of a rock mass slide. Rock Mechanics Based on an Anisotropic Jointed Rock Model (AJRM), pp 803–818

Woschitz H, Macheiner K (2007) Static and kinematic testing of tiltmeters: facilities and results. Vermessung Geoinf 2:134–142

Yang B, Mitelman A, Elmo D, Stead D (2022) Why the future of rock mass classification systems requires revisiting their empirical past. Quat J Eng Geol Hydrogeol 55(1):qjegh2021-039 https://doi.org/10.1144/qjegh2021-039

Zangerl C, Eberhardt E, Perzlmaier S (2010) Kinematic behavior and velocity characteristics of a complex deep-seated crystalline rockslide system in relation to its interaction with a dam reservoir. Eng Geol 112:53–67. https://doi.org/10.1016/j.enggeo.2010.01.001

Zhang Y, Tang H, Li C, Lu G, Cai Y, Zhang J, Tan F (2018) Design and testing of a flexible inclinometer probe for model tests of landslide deep displacement measurement. Sensors 18:224. https://doi.org/10.3390/s18010224

Zvelebil J, Moser M (2001) Monitoring based time-prediction of rock falls: three case-histories. Phys Chem Earth Hydrol Oceans Atmos 26:159–167. https://doi.org/10.1016/S1464-1909(00)00234-3

Zvelebil J, Cílek V, Stemberk J (2002) Partial results of monitoring of stability deterioration on Pravčice rock arch, NW Bohemia. In: Understanding and managing stone decay. SWAPNET 2001 Karolinum, Praha, pp 243–261

Chapter 3
Criteria of the Prehistoric Rock Avalanches Identification and Discrimination

Alexander Strom

Abstract Rock avalanches (dry granular flows) are one of the most disastrous types of landslides. They could be distinguished from other types of slope processes based on the specific combination of morphological and sedimentological characteristics. Such combination allows their recognition both on the space images and in the field and distinguishing them from the deposits left by glaciers, rock glaciers, and extreme debris flows that can occur in the presence of the "intermediate" agent of water or ice. Morphological identification of rock avalanches becomes more problematic for older features significantly reworked by erosion. Their correct identification and differentiation is critically important for both landslide and seismic hazard assessment since rock avalanches, unlike other phenomena listed above, often occur being triggered by large earthquakes. The proposed chapter describes the basic criteria allowing well–grounded identification of the prehistoric rock avalanches and distinguishing their deposits from moraines and debris flow fans. They are exemplified by case studies from Central Asia and the Himalayas.

Keywords Rock Avalanche · Morphology · Grain size composition · Central Asia · Himalaya

3.1 Introduction

Rock avalanches, defined as "extremely rapid, massive, the flow-like motion of fragmented rock from a large rock slide or rockfall" (Hungr et al. 2014) are the most disastrous type of landslides in mountainous regions due to their extreme runout and the possibility of rivers' damming. The extreme destructiveness of such events makes the correct assessment of associated hazards and risks to be one of the most important tasks of landslide studies in high mountains. Such review requires, in particular, good knowledge of similar phenomena that had occurred in the study region in the past. Considering that rock avalanches occur rather rarely, "in the past" means

A. Strom (✉)
Geodynamics Research Centre LLC, Moscow 125008, Russia
e-mail: strom.alexandr@yandex.ru

P. Thambidurai and T. N. Singh (eds.), *Landslides: Detection, Prediction and Monitoring*,
https://doi.org/10.1007/978-3-031-23859-8_3

the historical period and the entire Holocene and even Late Pleistocene. The rock avalanche inventories compiled for such an extended period provide, besides input data for susceptibility analysis, statistical data allowing a better understanding of the regularities of these hazardous natural phenomena. Quite often, well-grounded identification of such objects can be made just by visual interpretation of space images, especially allowing 3D visualization (either stereoscopic or combined with more or less detailed digital elevation models). Their characteristic features are: (1) the concave headscarp on the slope, (2) debris accumulation at its base, and sometimes, (3) evidence of the existing, infilled, or breached dammed lake. Examples of such easily identifiable rock avalanche dams are shown in Fig. 3.1, which demonstrates the rock avalanches in Fergana Range (Tien Shan), about 25 Mm^3 in volume for the northern one that dammed a small valley. It has distinct headscarp below elevation mark 2,080 m a.s.l., partially eroded dam more than 150 m high, and completely silted dammed lake upstream. Debris of the southern rock avalanche, about 40 Mm^3 in volume, moved up to elevation mark 1,430 nm a.s.l. Also, Fig. 3.2 demonstrates the Panjai-Mard rock avalanche, about 100 Mm^3 in volume at in Afghan Badakhshan. Headscarp is marked by red arrows, rock avalanche front by yellow arrows. The rock avalanche dammed a small river valley, and this dammed lake was silted completely, while a small water body in the dammed creek mouth still exists.

However, such univocal interpretation may not be so obvious in many other cases. In the next sections, several complicated cases, mainly from the Central Asian region and the Indian Himalayas, will be discussed briefly. In addition, much more of the Central Asian examples could be found in Strom and Abdrakhmatov (2018).

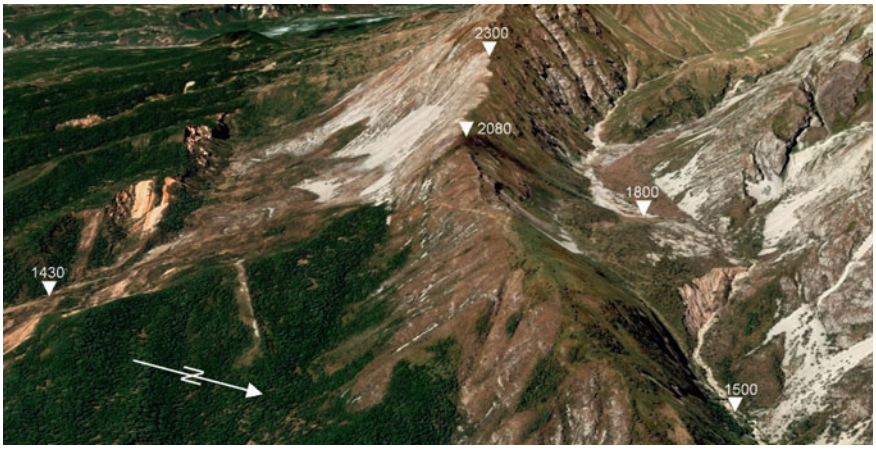

Fig. 3.1 Two rock avalanches from both sides of the watershed in the Fergana Range, Tien Shan (41.394° N, 73.03° E)

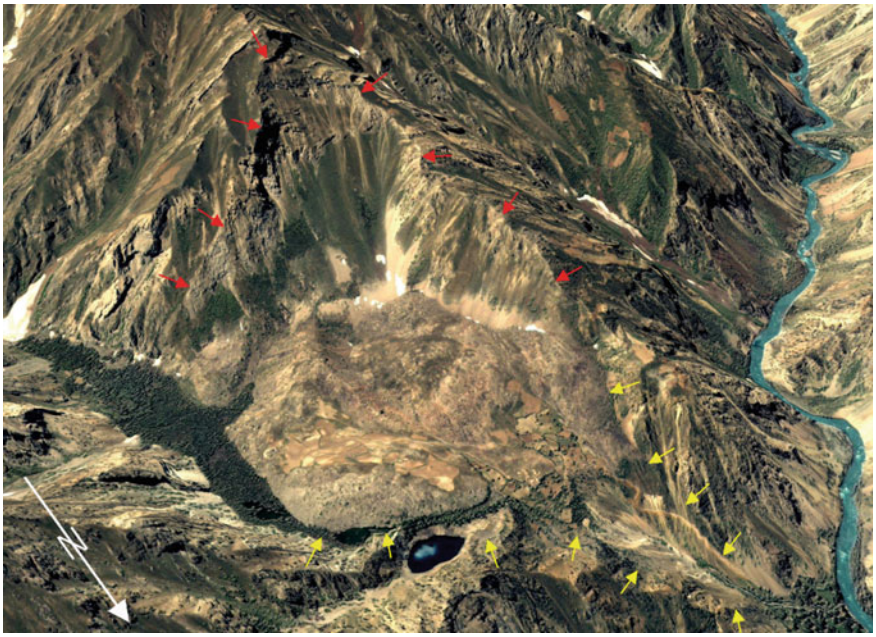

Fig. 3.2 Rock avalanche in the Panjai Mard valley, Afghan Badakhshan (37.87° N, 71.16° E)

3.2 Questionable Case Studies That Required Special Analysis

Rockslides and rock avalanches misinterpretation and their mixing with deposits left by such processes as glaciation, formation of rock glaciers, and extreme debris flows that can occur in the presence of the "intermediate" agent—water or ice, might be caused by several reasons. Among them are the significant reworking of the rockslide landforms by erosion, the large distance between the source zone and deposition zone, and a large amount of moraine material in rock avalanche deposits. Correct identification of the nature of such debris accumulations and discrimination of the prehistoric rock slope failures from landforms created by glaciers or powerful debris flows is important for both landslide and seismic hazard assessment in mountainous regions since rock avalanches, unlike moraines, rock glaciers, and debris flow fans are often, though not always, triggered by large earthquakes. Thus, such prehistoric features can be considered as evidence of strong past seismic events. Considering the contemporary climate changes and glaciers' retreat, modern glaciation cannot produce large-scale damming of the major rivers. On the contrary, rock avalanches can originate regardless of climatic conditions, and nothing prevents their occurrence in the near future if conditions would be favorable.

3.2.1 *Identification of the Real Nature of The Strongly Eroded Debris Accumulations*

Many early Holocene and Late Pleistocene rock avalanches underwent very strong erosion that affected both their source zones and the deposits, reshaping them in such a way that one could hardly identify these landforms as rockslide-related features. Such reworking can be demonstrated by example of the Displaced Peneplain rock avalanche in the Kokomeren River valley in Central Tien Shan (41.9° N, 74.25° E), about 400 Mm^3 in volume (Strom and Abdrakhmatov 2018). It had collapsed from the slope more than 500 m high. Rock avalanche body is composed of fragmented Precambrian dark-red gneiss with schist and some amount of igneous mafic rocks. The rock avalanche had dammed the pre-Kokomeren River valley, and the stream had to erode a new bypass valley through its left bank rock massif composed of light-red granite. Due to significant reworking, this giant feature could hardly be identified visually, both in the field (Fig. 3.3) and on space images (Fig. 3.4).

Most of its headscarp (Fig. 3.5) looks like a high talus slope, while its section visible at the left part of this figure is the huge block that had subsided for several hundred meters but did not fail completely. Each part of this giant feature does not allow a sound conclusion on its origin, but their complex analysis combined with the study of the deposits' lithology and grain-size composition allows its univocal interpretation as the prehistoric rock avalanche. A closer look at the deposits composing the hilly area marked in Fig. 3.4 by the dashed white line shows that rock avalanche body is composed of fragmented rocks outcropping at the source slope that do not exist on the slopes west from the deep gulley passing at the foot of the above-mentioned talus slope. Thus, the latter is the only source zone for this material. Besides, evidence of the inverse grading were found that is characteristic of rock avalanche deposits (Heim 1932; Erismann 1979; Hewitt 1988, 1999, 2006; Strom 1994, 2006, 2021; Davies and McSaveney 1999; Wassmer et al. 2002; Abdrakhmatov

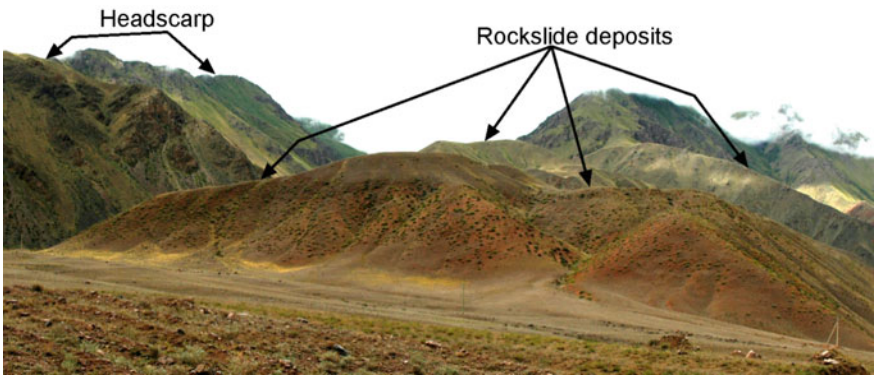

Fig. 3.3 General view of the Displaced Peneplain rock avalanche (light-red slope in the foreground at the right part of the panorama—bedrock granite)

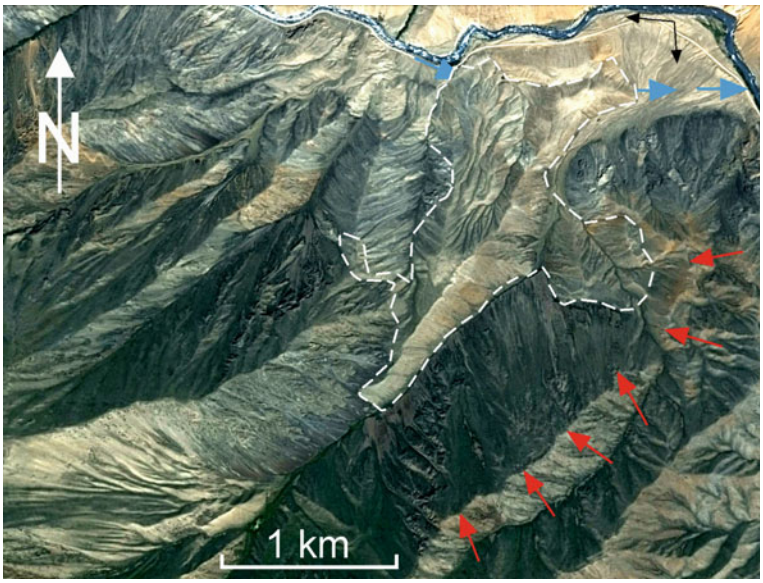

Fig. 3.4 Space image of the Displaced Peneplain rock avalanche. The headscarp is marked by red arrows; the remaining part of the deposits is outlined by white dashed line; the assumed oroginal position of the pre-rockslide Kokomeren River is shown by blue arrows; the panorama shown in Fig. 3.3 was made from the point marked by small black arrows (after Strom and Abdrakhmatov 2018, Reprinted with permission of Elsevier)

Fig. 3.5 Headscarp of the Displaced Peneplain rock avalanche

and Strom 2006; McSaveney and Davies 2006; Dufresne et al. 2009, 2016; Dufresne and Dunning 2017). Such a combination of the lithology of crushed debris that clearly show from where it could originate, and a very specific grain-size composition proves the rock avalanche origin of the deposits in question.

Fig. 3.6 Rounded boulders (stream alluvium) resting at the "entrance" of the abandoned river valley blocked by the Displaced Peneplain rock avalanche deposits. They are visible behind students at the right part of the photograph

Besides sedimentological evidence, the additional piece of the puzzle that proves the rock avalanche origin of this feature is the existance of the abandoned Kokomeren River valley on the present-day right bank of the stream (Figs. 3.4 and 3.6). This old channel is filled with large well-rounded granite boulders that could be transported by the powerful stream only since no granite outcrops exist on the right bank of the Kokomeren River close to this site. It should be pointed out also that the good roundness of the boulders shows that the river transported them for a long distance. All these indicate that river had passed originally south of its present-day course and had to erode a new gorge when this original way had been blocked.

This example demonstrates that even strongly reworked and reshaped rock avalanches could be identified univocally through the combined analysis of sedimentological and morphological data and careful study of the evolution of the local drainage network.

3.2.2 Distant Position of Rock Avalanche Deposits from Its Source Zone

The extreme mobility of rock avalanches can play a dirty trick on the ability to identify and interpret such features correctly. It complicates establishing natural links between deposits and their assumed source zones, which can be exemplified by the ca. 5 km long Aigyrkul rock avalanche in Southern Tien Shan (38.91° N, 67.93° E). It was identified first as an accumulation of fragmented rock debris covering about 2.3 km of the valley bottom with an area of one square kilometer. It was unclear, however, from where this material could be transported to its present position since no distinct headscarp exist on the surrounding slopes. However, a careful check of the space images revealed the horseshoe-like headscarp at the local watershed, almost 1 km above the valley bottom and about 3 km away from the closest part of the deposits

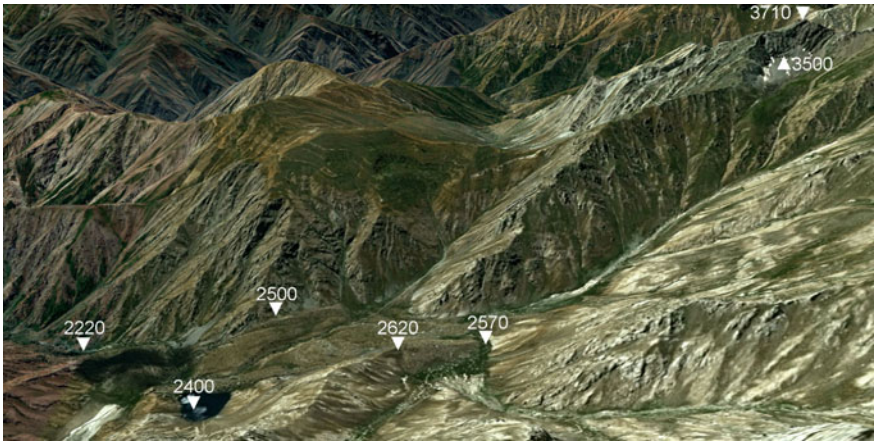

Fig. 3.7 The Aigyrkul rock avalanche in the Tupolangdaria River basin. The source zone is at the top right of the image between elevation marks 3,710 and 3,500 m a.s.l. Rock avalanche deposits stretch from 2,570 to 2,220 m a.s.l. (after Strom and Abdrakhmatov 2018. Reprinted with permission of Elsevier)

(Fig. 3.7). No visible evidence of the clastic material could be found on the way from the headscarp to the rock avalanche body that had split into two parts after collision with a rocky spur at 2,620 m a.s.l. The smaller one turned left and blocked the tributary valley, while the main part flowed ahead up to 2,220 m a.s.l., spreading over the valley bottom and damming a gulley where the small Aigyrkul Lake still exists.

In such cases, it might not be so easy to prove the relationship between the bouldery deposits at the valley bottom and the potential distant source zone. Nevertheless, a thorough analysis of the landforms at the surrounding slopes provides data allowing univocal interpretation of the entire assemblage of the suspicious landforms and deposits.

A similar analysis was performed to specify the origin of the extremely mobile rock avalanches at the northern and eastern boundaries of the Pamir mountains. The Yimake (Yuan et al. 2013; Fig. 3.8), the Komansu (Strom 2014; Robinson et al. 2015; Reznichenko et al. 2017), and the Lenin (Reznichenko et al. 2017) rock avalanches located here had more than 20 km and up to 34 km long runouts.

In all these cases, source zones are located at very high altitudes within the presently glaciated area or very close to it. Glaciation creates negative circus-like landforms similar to most large rockslides' source zones. If niche glaciers form them, their similarity becomes even stronger. Nevertheless, complex analysis allows sound interpretation of all these features as long-runout rock avalanches rather than moraines or landforms of a fluvial origin (Strom and Abdrakhmatov 2018). A correct interpretation of such features is especially important for hazard assessment in the depressions, bounding high mountain ranges. Hazard produced by the gigantic rock avalanches exceeds hazards associated with other mass-waiting phenomena. Glaciers

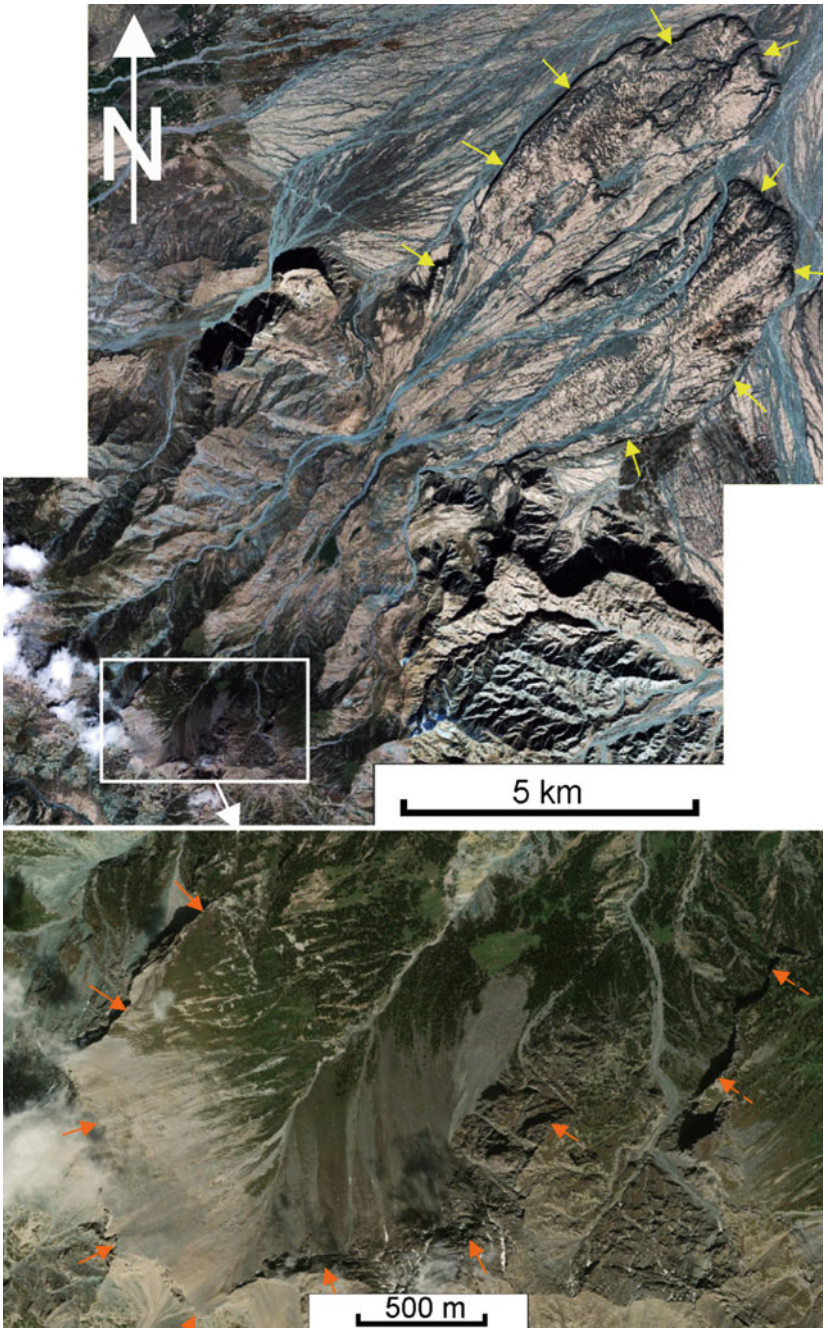

Fig. 3.8 The Yimake rock avalanche at the northeastern foot of the Chinese Pamir (39.2° N, 76.15° E). Yellow arrows show the limits of its' leave-shape body 9 × 5.3 km in size and 15–20 m thick; orange arrows mark the deep headscarp shown in the inset. Dashed orange arrows outline assumed the right part of the source zone

and rock glaciers move not so fast and do not protrude so far towards the plains; most debris flows, excluding those produced by breach of large dams and lahars from major volcanos, lost their destructive power, while spreading over the range foot.

In contrast, rapidly moving dry granular flows millions of cubic meters in volume can destroy almost any affected structure. Besides, rock avalanches produce powerful air blasts reported by eyewitnesses of some catastrophic events, such as the 1949 Khait rock avalanche in Tajikistan (Semionov and Semionova 1958) and some landslides triggered by 2008 Wenchuan earthquake (R. Huang, personal communication 2018). Such effect increases the affected area.

3.2.3 Moraine Material in Rock Avalanche Deposits

The factor that complicates correct discrimination of rock avalanches and glacial deposits at most is the presence of a large amount of glacial material in debris accumulations resting at the slopes' feet. Some researchers consider the presence of sub-rounded boulders in the gravelly-sandy-silty matrix that form part of the deposits as the direct evidence of their glacial origin (Ischuk 2013). However, in high mountains that underwent intensive glaciation in the past, glacial till is widely distributed at the valley's bottoms and on their slopes. That is why large-scale rock slope failures can entrain a large amount of such material that originated as glacial deposits but has been transported to its present position by a purely gravitational process. It can be exemplified by the giant prehistoric Kudara-Pasor rock avalanche of about 1 km^3 in volume (Fig. 3.9) in the Kudara River valley in Central Pamir (38.39° N, 72.58° E), 13 km north of the famous 1911 Usoy rockslide.

The position of the very distinct lithological units forming rock avalanche deposits clearly indicates that it debris motion was across the river valley, rather than along it. This rock slope failure had affected the shoulder of the right-bank valley slope, including the portion of an old glacial trough filled with moraine material that rests now at the proximal part of the dam body (4 in Fig. 3.9). On the way, this rock mass scraped fluvial and, probably, the youngest glacial deposits from the valley bottom and bulldozed them towards the opposite valley slope (1 in Fig. 3.9).

Another very didactic case study is the Imom rock avalanche, about 15 Mm^3 in volume in the Gunt River valley (37.692° N, 72.327° E) in Central Pamir (Fig. 3.10). Its 1,350 m long and up to 600 m wide body rests on the low river terrace. It affected large Late Holocene alluvial fan formed by the debris flows. Such relationships show that rockslide that caved from the 700 m high slope composed of crystalline rocks is quite young. Crushed debris of such rocks forms the inner part of the rock avalanche body with a hummocky microrelief. In contrast, this body's frontal, 50–100 m wide outer belt is composed of rounded and semi-rounded boulders with sandy matrix—typical moraine (Fig. 3.10).

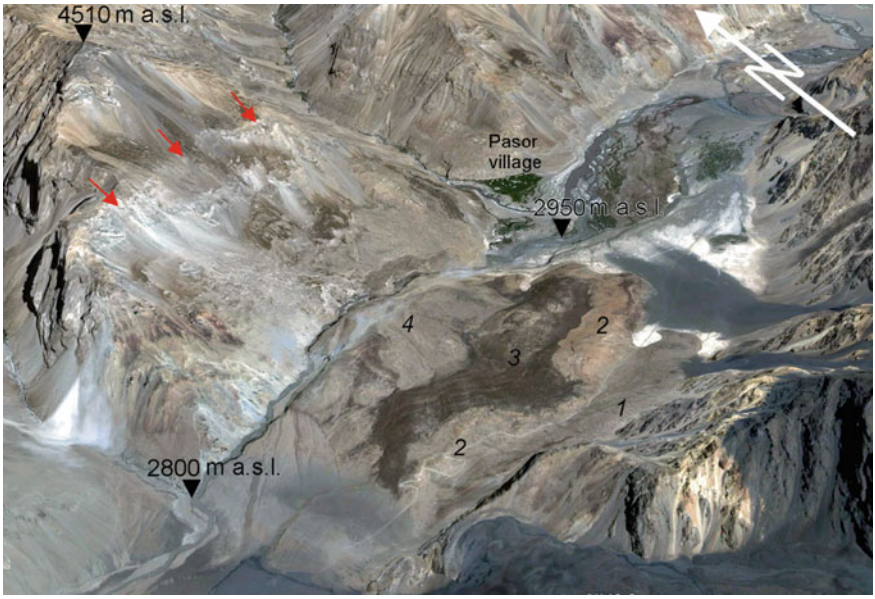

Fig. 3.9 Oblique view of the Kudara-Pasor rock avalanche. 1–4—different lithological units clearly identifiable in the rock avalanche body; red arrows—headscarp crown

3.3 Natural Dams Sourced in the Tributary Valleys

Working in the field, researchers often find huge debris accumulations that block main river valleys being sourced, partially or completely, somewhere in the upper reaches of the tributary valley. Such a feature can be seen, for example, in the Uttarakhand, in the Bhagirathi River valley on the way from Uttarkashi to Gangotri at 30.931° N, 78.681° E (Fig. 3.11). A huge body about 250 m thick came out from the Kanodia-Ghad valley and partially blocked the Bhagirathi River valley. It is composed of intensively fragmented rock debris with distinct varicolored zones corresponding to different lithological units that were transported for a long distance but not mixed, which is typical of rock avalanche deposits. Thorough check of space images confirmed that this body is the distal part of the 5.7 km long rock avalanche that collapsed from the 1,300 m high northern slope of the Kanodia-Ghad valley composed of gneiss, and then turned left and moved more than 3,000 m down the valley (Fig. 3.12). Finally, it blocked the Bhagirathi with a dam that was several dozen meters high.

One more interesting Himalayan case study is in the Himachal Pradesh State, in the Beas River basin, at 32.03° N, 77.127°, opposite the Dhakpo Shedrupling Monastery (N. Singh, personal communication). Here right bank of the Beas River is formed by the fan-shaped body up to 150 m high, stretching for 1.5 km along the river (Fig. 3.13).

Fig. 3.10 Oblique view of the Imom rock avalanche. The inner part of its body is composed of crushed crystalline rocks, while the outer part is by the bulldozed moraine material

It can be just an abnormally large alluvial fan composed of multiple debris flow deposits. However, another possibility cannot be excluded too. Close view of the space images available at Google Earth shows that the tributary valley where this fan-shape body has been sourced is filled by a rockslide (rock avalanche) that caved from the left-bank slope of the valley more than 1 km high and left a distinct headscarp with smooth steep sliding surface. Its downstream face has been eroded significantly, but it can be hypothesized that some part of rock avalanche debris could be ejected through the gulley mouth and accumulate in the Beas River valley forming the fan-shaped body.

Reliability of such mechanism can be seen clearly in the Chinese Tien Shan, in the Muzart River valley at 41.95° N, 80.87° E. The valley here had been blocked at a distance of almost 2 km by the similar, though much larger fan-shape debris accumulation up to 150 m thick and ~250 Mm^3 in volume (Fig. 3.14). First, about 400 Mm^3 of the Proterozoic metasediments and igneous rocks collapsed and formed a dam in the tributary valley. Most likely the secondary rock avalanche was ejected from the downstream side of this dam during the two-stage process (Strom 1996, 2006). It had passed 4.3 km and blocked the Muzart River valley. Moreover, the distal part of this dam was raised on the opposite valley slope for ca. 100 m above the blockage crest. Such runup is typical of rapidly moving dry rock avalanches but not

Fig. 3.11 View on the distal part of the Kanodia-Ghad rock avalanche

of water-rich debris flows. Their viscosity is much less and, thus, debris flow would spread up and downstream the main valley. Morphological similarity of this didactic feature to the case study from the Beas River valley allows the assumption that the same process could create the latter landform. Of course, the site shown in Fig. 3.13 requires a more detailed field study to conclude the real nature of the suspicious landforms.

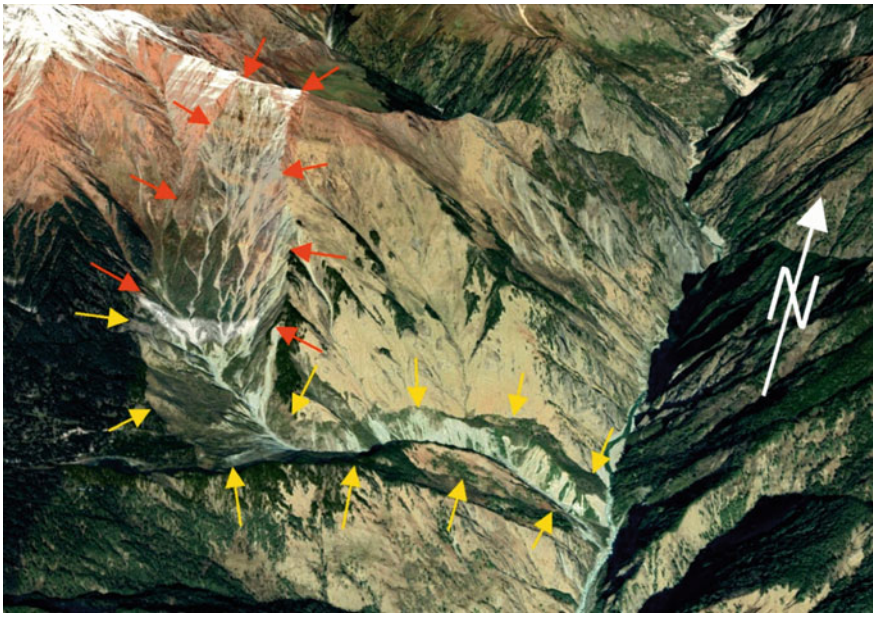

Fig. 3.12 Oblique view of the Kanodia-Ghad rock avalanche site. Red arrows—headscarp: by yellow arrows mark the travel path of rock avalanche

3.4 Conclusions

This chapter has attempted to demonstrate briefly the possibility of rock avalanches' identification and well-grounded discrimination from debris accumulations formed by other mass wasting processes even in controversial cases from Central Asia and the Himalayas. Such justification should be based on the complex analysis of the overall and detailed morphology of the suspicious landforms combined with a thorough analysis of the deposit's grain-size composition and of their internal structure. Rock avalanches are characterized by the absence of mixing of various lithologies that collapse from the slope and by the distinct inverse grading with intensively fragmented body facies and coarse bouldery carapace. It is very important for researchers working in this field to learn about similar features worldwide. It will help to compare the study objects identified in a particular region with possible analogues worldwide, which can be very helpful.

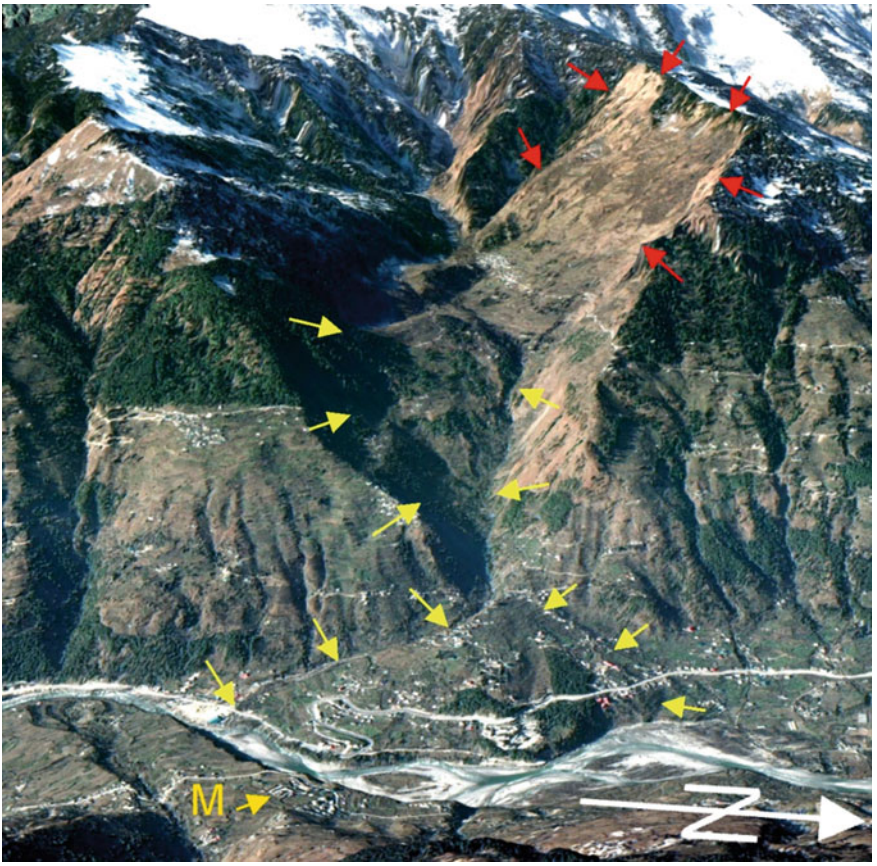

Fig. 3.13 Oblique view of rock avalanche in the right tributary of the Beas River. Headscarp is marked by red arrows, boundaries of the assumed rock avalanche deposits—by yellow arrows; M—the Dhakpo Shedrupling Monastery

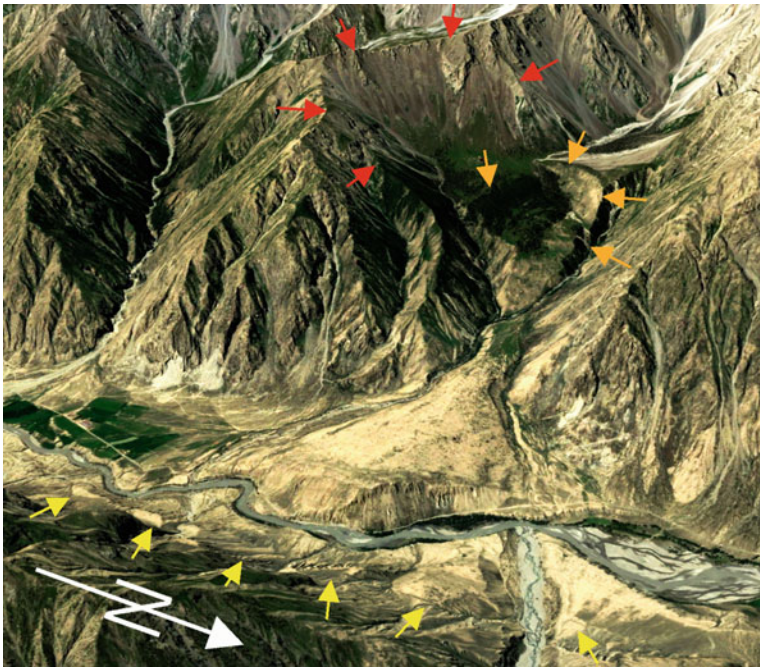

Fig. 3.14 Oblique view of the secondary rock avalanche in the Muzart River valley. Red arrows mark the headscarp crown, orange arrows—the secondary scar (headscarp of the secondary rock avalanche that had blocked the Muzart River), and yellow arrows—rock avalanche front on the left side of the Muzart River valley

Declaration Author has no conflict of interest of any type.

References

Abdrakhmatov K, Strom A (2006) Dissected rockslide and rock avalanche deposits; Tien Shan Kyrgyzstan. In: Evans SG, Scarascia Mugnozza G, Strom A, Hermanns RL (eds) Landslides from massive rock slope failure. NATO science se-ries: IV: Earth and environmental sciences, vol 49. Springer, New York, pp 551–572

Davies TR, McSaveney MJ (1999) Runout of dry granular avalanches. Can Geotech J 36:313–320

Dufresne A, Davies TR, McSaveney MJ (2009) Influence of runout-path material on emplacement of the Round Top rock avalanche, New Zealand. Earth Surf. Proc. Landf. 35:190–201

Dufresne A, Bösmeier A, Prager C (2016) Sedimentology of rock avalanche deposits—case study and review. Earth-Sci Rev 163:234–259

Dufresne A, Dunning SA (2017) Process dependence of grain size distributions in rock avalanche deposits. Landslides 14:1555–1563

Erismann TH (1979) Mechanisms of Large Landslides. Rock Mech. 12:15–46

Heim A (1932) Bergsturz und Menschenleben. Fretz and Wasmuth, Zürich

Hewitt K (1988) Catastrophic landslide deposits in the Karakoram Himalaya. Science 242:64–67

Hewitt K (1999) Quaternary moraines vs catastrophic rock avalanches in the Karakoram Himalaya, Northern Pakistan. Quat Res 51:220–237

Hewitt K (2006) Rock avalanches with complex run out and emplacement, Karakoram Himalaya, Inner Asia. In: Evans SG, Scarascia Mugnozza G, Strom A, Hermanns RL (eds) Landslides from massive rock slope failure. NATO science se-ries: IV: Earth and environmental sciences, vol 49. Springer, pp 521–550

Hungr O, Leroueil S, Picarelli L (2014) Varnes classification of landslide types, an update. Landslides 11:167–194

Ischuk NR (2013) The origin of the mountain river dams in Tajikistan. In: Margottini C, Canuti P, Sassa K (eds) Landslide science and practice risk assessment, volume 6 management and mitigation. Springer, Heidelberg, pp 13–17

McSaveney MJ, Davies TRH (2006) Rapid rock-mass flow with dynamic fragmentation: inferences from the morphology and internal structure of rockslides and rock avalanches. In: Evans SG, Scarascia Mugnozza G, Strom A, Hermanns RL (eds) Landslides from massive rock slope failure. NATO science series: IV: earth and environmental sciences, vol 49. Springer, Heidelberg, pp 285–304

Reznichenko NV, Andrews GR, Geater RE, Strom A (2017) Origin of large hummock deposits "chukuryi" in Alai Valley, Northern Pamir: geomorphological and sedimentological investigation. Geomorphology 285:347–362

Robinson TR, Davies TRH, Reznichenko N, De Pascale GP (2015) The extremely long runout Komansu rock avalanche in the Trans Alay range Pamir Mountains. Southern Kyrgyzstan. Landslides 12:523–535

Semionov PG, Semionova VA (1958) Catalogue of earthquakes felt on the territory of Tajikistan during the periods of 1865–1940 and 1941–1952. Proc Inst Seismol Acad Sci Tajik SSR 86(3) (in Russian)

Strom AL (1994) Mechanism of stratification and abnormal crushing of rockslide deposits. In: Proc. 7th international IAEG congress 3. Balkema, Rotterdam, pp 1287–1295

Strom AL (1996) Some morphological types of long-runout rockslides: effect of the relief on their mechanism and on the rockslide deposits distribution. In: Senneset K (ed) Landslides. Proc. of the seventh international symposium on landslides, Trondheim, Norway, Rotterdam, Balkema, pp 1977–1982

Strom AL (2006) Morphology and internal structure of rockslides and rock avalanches: grounds and constraints for their modelling. In: Evans SG, Scarascia Mugnozza G, Strom A, Hermanns RL (eds) Landslides from massive rock slope failure. NATO science series: IV: earth and environmental sciences, vol 49. Springer, Heidelberg, pp 305–328

Strom A (2014) Catastrophic slope processes in glaciated zones of mountainous regions. In: Shan W, Guo Y, Wang F, Marui H, Strom A (eds) Landslides in cold regions in the context of climate change, environmental science and engineering. Springer International Publishing, Switzerland, pp 3–10. https://doi.org/10.1007/978-3-319-00867-7_1

Strom A (2021) Rock avalanches: basic characteristics and classification criteria. In: Vilimek V, Wang F, Strom A, Sassa K, Bobrowsky P, Takara K (eds) Understanding and reducing landslide disaster risk, vol 5, pp 3–23

Strom A, Abdrakhmatov K (2018) Rockslides and rock avalanches of Central Asia: distribution, morphology, and internal structure. Elsevier. ISBN: 978–0–12–803204–6

Wassmer P, Schneider J-L, Pollet N (2002). Internal structure of huge mass movements: a key for a better understanding of long runout. The multi-slab theoretical model. In: Proc int symp landslide risk mitigation and protection of cultural and natural heritage. Kyoto University, Kyoto, pp 97–107

Yuan Z, Chen J, Owen LA, Hedrick KA, Caffee MW, Li W (2013) Nature and timing of large landslides within an active orogen, eastern Pamir, China. Geomophology 182:49–65

Chapter 4
Stability Assessment of Markundi Hills Using Q-slope, SMR and Simulation Tools

Ashutosh Kainthola, Vishnu Himanshu Ratnam Pandey, P. K. Singh, and T. N. Singh

Abstract Stable roads in hilly regions are not only a boon for the economy but also contribute to betterment of human lives and infrastructure. However, safe and cost-effective excavation design for road construction is a challenge. Lithology, slope geometry, rock mass-discontinuity, hydrogeology, excavation methods, etc., possess an intense influence on stability of excavated hill slopes. There are numerous methods to assess and curtail the instability, from conventional chart-based methods to cutting-edge numerical simulation techniques. Yet, all the techniques have their advantages and disadvantages. Thus, in order to conduct a holistic instability assessment, it becomes essential to use different assessment techniques in conjunction. In the present study, sandstone cut slopes of Markundi hills in the district of Sonbhadra, Uttar Pradesh (UP), India, have been examined to ascertain the instability attributes. The cut slopes were initially investigated through kinematic analysis in DIPS software and then geomechanical classification techniques, viz., Q-slope and Continuous-SMR. This assessment enabled us to designate the modes of structurally controlled failures and their extent. Afterward, the RocFall program was employed to verify and corroborate the results of the rockfall dynamic in the study area. The slopes in the Markundi region were found stable on a large scale; however, small-scale localized failures due to intersecting discontinuities were a pressing issue, discovered in the study and validated in the field. The study emphasizes the risks associated with the detached blocks lying on the road, while passing through the region. Also, slight flattening (1°–3°) of the slopes at all these studied sections may reduce the risk to a great extent.

Keywords Slope failure · Kinematic analysis · Q-slope · CSMR · Markundi ills

A. Kainthola · V. H. R. Pandey (✉)
Geo-Engineering & Computing Laboratory, Department of Geology, Banaras Hindu University, Varanasi 221005, India
e-mail: pandey.vhr@bhu.ac.in

P. K. Singh
Department of Earth and Planetary Sciences, University of Allahabad, Prayagraj 211002, India

T. N. Singh
Department of Civil and Environmental Engineering, Indian Institute of Technology, Patna 801106, Bihar, India

P. Thambidurai and T. N. Singh (eds.), *Landslides: Detection, Prediction and Monitoring*,
https://doi.org/10.1007/978-3-031-23859-8_4

4.1 Introduction

The ancient human civilizations settled mainly along river plains; however, alarming population growth forced them to shift towards hilly terrains in search of better habitable space (Petley et al. 2005; Deng et al. 2018). Mountains constitute an important segment of several countries, and numerous people make their living in these perilous landforms. Until the last century, there were no sophisticated means of commutable infrastructure in the mountainous regions. Hence, the hilly people remained unconnected with the rest of the world. With scientific advancement in the construction sector and government initiatives to bring these regions into the mainstream of the nation's growth, major civil and engineering projects were launched (Singh et al. 2010, 2013, 2017; Ray et al. 2020). Still, the challenges are quite big in implementing these construction works as the engineers and policymakers have to consider rugged topography, tectonic disturbances, seismic activities, disturbed geological setup, and frequent landslide and rainfall phenomena in the mountainous regions (Glade et al. 2000; Singh et al. 2018; Kundu et al. 2022).

The slope instability is the leading concern in fostering safe and economic highway projects in hilly regions. Therefore, a thorough comprehension of slope mass geotechnical and geological attributes is mandatory in planning these megaprojects (Dikshit et al. 2020). The inherent discontinuities present in the rock mass has good control over slope stability, and it can be comprehended through kinematic analysis (Yoon et al. 2002). Moreover, the availability of meteorological data pertaining to these construction areas can boost the safety concern of the slope's failures to a great extent by addressing the issue of pore water pressure (Glade 2003; Glade et al. 2006). Certain instances of glacial melting had been reported as a causal factor of these unfortunate events, owing to the flow of melted water in cracks, fractures, and pore spaces present in the slope mass (Kos et al. 2016). Based on their proximity to tectonic plate boundaries, one needs to check the pseudo-static and dynamic earthquake forces operating in the study area (Zhou et al. 2015). The chief causes of instability differ from one place to another; however, these aforementioned factors always need careful consideration. The gentler cut slopes are generally stable but are uneconomical, and working area constraints are also significant (Tiwari et al. 2020).

On the contrary, steeper slopes can be unstable (Mahanta et al. 2016), although cost-effective. The cut slopes, which possess overall stability, show localized failures, especially rockfalls (Castelli et al. 2021; Singh et al. 2016). Rockfalls signify the swift downward movement of a broken block of rock through rolling, bouncing, and falling (Castelli et al. 2009; Scavia et al. 2020; Wei et al. 2022). Therefore, a thorough investigation is necessary to ascertain the rock mass behaviour, as a function of slope geometry, rock mass strength, and hydrological and stress regime of the area (Ansari et al. 2021). The representative geometric and strength properties are further employed to discern the factor of safety of the slope, which is the ratio of resisting to driving forces acting on the failure surface (Kainthola et al. 2013).

Many new and existing road projects are being developed by the Indian government (Financial Express 2022). Better transportation will facilitate the timely transfer

of goods and services from one part of the nation to another and boost the country's economy. Road widening and construction in hilly regions pose a peculiar stability and safety challenge (Kainthola et al. 2021). Slope collapses, regardless of scale, are hazardous to the moving traffic and economy (Infante et al. 2019). Around 15% of the Indian territory is vulnerable to landslides (NDMA 2022). Often, the highway excavation is unscientific, with minimal consideration for the geotechnical, engineering, and geological attributes of the slope forming material. The analysis is further aggravated for rock masses which are discontinuous, in-homogeneous, anisotropic and non-elastic (Hudson and Harrison 2000). The analysis of rock slopes generally entails either the assessment of structural instability-limit equilibrium-numerical simulation (Prakash et al. 2015). However, all the stability analysis techniques are underpinned by certain assumptions. It is thus recommended to use different approaches for the investigation.

In the present research, a combination of Q-slope, Continuous Slope mass rating (CSMR), and rockfall simulation approaches have been used to discern the stability of Markundi hills (Sonbhadra, UP) in Northern India. The hills are intersected by a state highway, continuing the regions to different parts of India. Based on the primary field investigation, three locations were chosen for the present study.

4.2 Study Area

The study area is a part of the Son-Valley region, the eastern extension of the Vindhyan Supergroup. Vindhyan Supergroup is the ramification of sedimentary processes operated in the Proterozoic Eon without any major evidence of metamorphism or tectonic activity (Kumar et al. 2002). The earlier workers classified the Vindhyan sequence into two groups, namely, the Upper Vindhyan (Bhander—Rewa—Kaimur Groups) and the Lower Vindhyan (Semri Group) (Auden 1933). The sickle-shaped intracratonic basin is an approximately 4.3 km thick sequence of sandstone-limestone-shale, exposed to over the area of 105 km^2, the rest being masked by Deccan traps and Gangetic Plains (Krishnan and Swaminath 1959; Tripathy and Singh 2015). The system of Son-Narmada Fault encloses the sequence, the Monghyr-Saharsa Ridge, Great Boundary Fault in the south, east, and west, respectively, whereas in the north-side Bundelkhand Massif along with Indo-Gangetic Plain is its border (NDR 2022). The basin is assigned the status of largest as well as thickest sedimentary sequence across the planet.

The area of interest, Markundi, is located at an elevation of 318 m above sea level in the Sonbhadra district of Uttar Pradesh (India). It is 370 km (in the south-east) from the state capital Lucknow and 94 km (in the south) from the holy city of Varanasi. The village houses nearly 7,303 people who speak Hindi, and their literacy rate is 47.5% (Census of India 2011). The steep cliff-forming Markundi hill has been traversed by state highway-5 (SH-5). The SH-5 is quite busy and often poses difficulty in conducting slope investigations. The dominant rock type in the area are Dhandrual quartzite and Scarp sandstone, which belong to the Kaimur Group

of the Upper Vindhyan Supergroup (Mishra and Sen 2012; Quasim et al. 2019) as presented in Fig. 4.1, with the google earth image pointing the research sites, along the State Highway-5. The Dhandrual sandstone formations, found at the top of the Kaimur group, are dirty to pure white, arenaceous, and medium to coarse-grained; they are underlain by Scarp sandstone formations, which are variegated with medium grains (Mishra and Sen 2011). The Marklund-Jamual fault is also present in the lower part of the hill, separating the scarp sandstones from underlying basement rocks (Bhattacharya et al. 2008). The studied sections are composed of Dhandrual sandstones. These sandstone beds are tabular with high lateral continuity. Numerous sedimentary structures can be noticed, namely large-scale cross bedding, ripples marks, flute, load casts, and herringbone structures. The area (Sonbhadra district) receives an annual rainfall of 928.7 mm, most of which comes as monsoonal precipitation, i.e., 840.8 mm (Guhathakurta et al. 2020). A research-based on the annual rainfall and temperature data collection for 20 years demonstrates a trend of yearly rise in temperature and fall in precipitation (Kumar et al. 2020).

4.3 Methodology

Initially, the field investigation was conducted in the Markundi area to acquire structural and geological data, based on which suitable samples were brought to the laboratory to examine their strength parameters. The field and laboratory data facilitated the calculation of Q-slope and CSMR and rockfall simulation. The field investigation aimed to collect the geological-structural-geometrical-geotechnical data of the cut slopes. Recordings were taken of the discontinuity sets, roughness, persistence, continuity, and hydrological signatures. The structural orientations of geological discontinuities were measured by the Brunton compass and classified into different sets based on their direction and amount of dip. The readings of the joint roughness were ascertained by Barton comb, while persistence was taken using a measuring tape. Scanline survey was employed for the enumeration of rock quality designation (RQD) in the field, through the calculation of joint frequency. The representative RQD for the slope locations has been assessed through the Eqs. (4.1) and (4.2) proposed by Priest and Hudson (1976).

$$\mathrm{RQD} = 100e^{-0.1\lambda}(0.1\lambda + 1) \tag{4.1}$$

where λ is the discontinuity frequency. For λ in the range of 6–6 m^{-1}, a reliable estimate of the equation is:

$$\mathrm{RQD} = 110.4 - 3.68\lambda \tag{4.2}$$

Further, the representative samples of the Dhandraul sandstone were tested in the laboratory. Three locations were chosen for the assessment based on visual evidence of vulnerability and failure (Fig. 4.2a and b). The rock mass at each location was

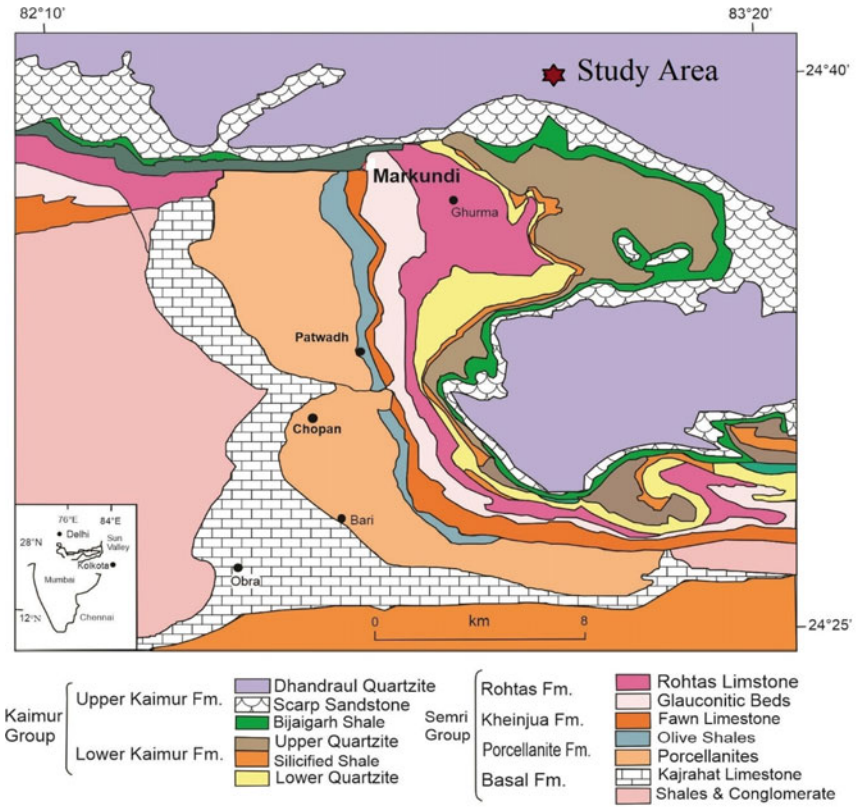

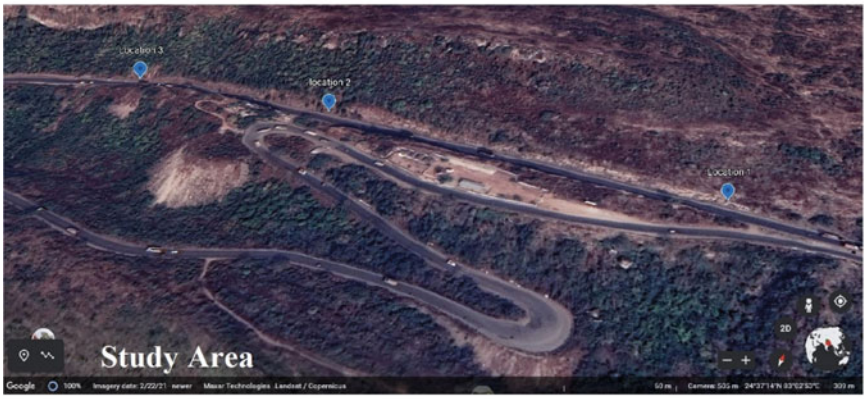

Fig. 4.1 Geological map of the study area (after Mishra and Sen 2012)

traversed by three sets of prominent joints. Failed rock blocks were also noticed along these chosen sections of the slope. Three prominent sets of discontinuities were marked in the field, as given in Table 4.1. The frequency of the joint sets was designated as J_1, J_2, and J_3, and the structural data was used to carry out a kinematic analysis. The DIPS software eases the identification of possible modes of failure (plane-wedge-topple) for each of these locations (Rocscience Inc. 2022). The analysis involves using stereographic projection of discontinuities in an equal area net to identify the blocks that permit movement (Basahel and Mitri 2017). This analysis considers the orientation of the discontinuity planes with respect to the slope face, plunge of intersecting discontinuities, and angle of internal friction along the joint plane. The kinematic examination was conditioned for planar, wedge, and toppling failures. The software needs inputs like structural discontinuities in the rock mass of the cut-slopes at each location combined with slope face orientation and angle of internal friction along these joint planes.

Additionally, the intact rock specimens were tested to discern their point load strength index (PLSI) (Fig. 4.3). Afterward, these index values were transformed

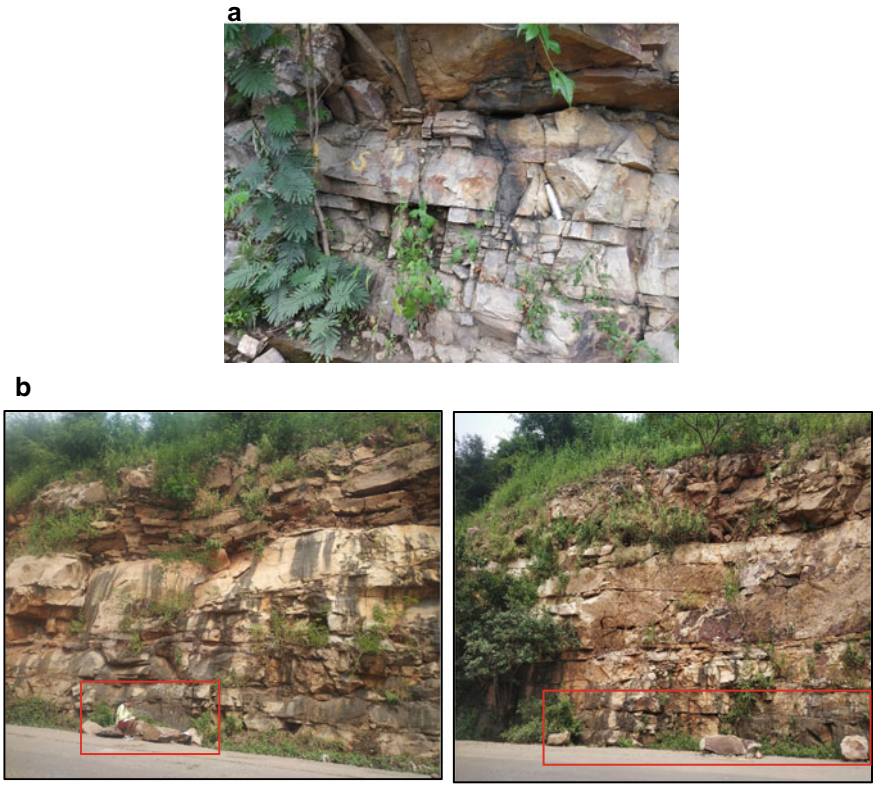

Fig. 4.2 **a** Rock mass condition at location 1, **b** Detached blocks lying on the road at locations 2 and 3 (in the red box)

Table 4.1 Structural orientation of the discontinuities in the rock mass along the studied sections

Locations	J_1		J_2		J_3		Slope	
	Dip Amount	Dip Direction	Dip Amount	Dip Direction	Dip Amount	Dip Direction	Angle	Aspect
1	20°	290	55°	110	60°	250	75°	190
2	05°	235	70°	110	80°	210	80°	180
3	70°	160	22°	030	78°	205	80°	190

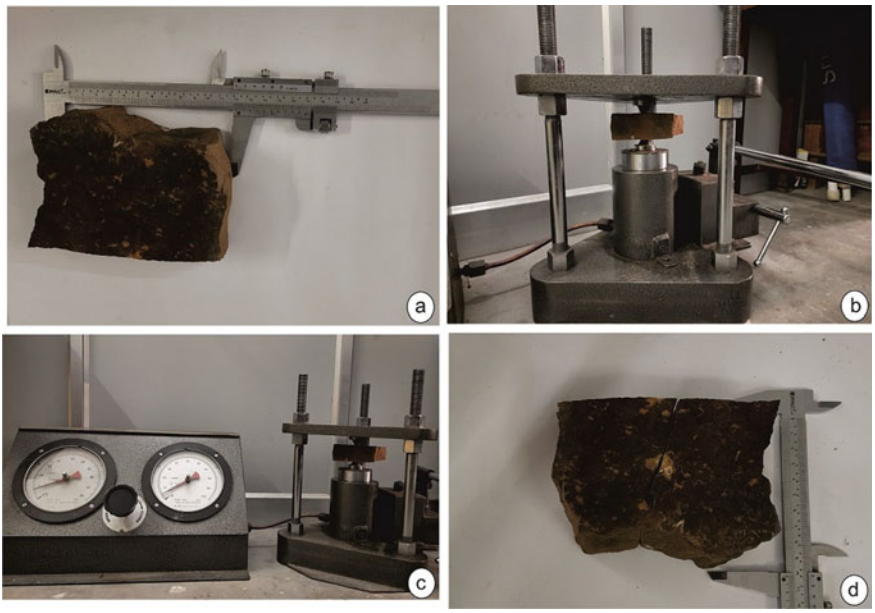

Fig. 4.3 Laboratory examination of rock sample for point load strength index (a) specimen's measurement before testing, (b) experimental setup, (c) experiment's data recording, and (d) broken rock sample after testing

into uniaxial compressive strength (UCS) using Eq. (4.3), mentioned in the literature. Previously, many researchers have recommended mathematical functions to translate PLSI values into uniaxial compressive strength (UCS) of rocks (Singh et al. 2012; Li and Wong 2013). These values were used for the geomechanical classification of the rock mass, basic-rock mass rating (RMRbasic), and further in the estimation of continuous slope mass rating (CSMR) and Q-Slope.

$$\mathrm{UCS} = k * \mathrm{PLSI} \tag{4.3}$$

where k ranges from 20 to 24. However, to comprehend the pragmatic rock mass scenario at the site and prevent the overestimation of UCS, 20 is assigned to k.

Finally, along with strength data, the rock mass of the slopes was classified, using Q-slope, $RMR_{basic,}$ and CSMR. In the evaluation of RMR_{basic} and CSMR, the authors have used open source QuickRMR software package (Kundu et al. 2020). Rock mass rating (RMR_{basic}) is a geomechanical classification scheme to designate the quality of the rock mass based on its UCS, RQD, joint spacing, groundwater condition, and discontinuity orientations (Bieniawski 1989). The first five parameters constitute RMR_{basic}, which is used to classify the rock mass, ignoring the joint orientation regarding the type of excavation/construction (Eq. 4.4).

$$RMR_{basic} = UCS + RQD + DS + DC + GW \tag{4.4}$$

where UCS corresponds to uniaxial compressive strength of the intact rock, RQD is rock quality designation, DS is spacing between the discontinuity, DC denotes the discontinuity condition, and GW stands for groundwater conditions.

The rock mass at the three locations has been ascribed with an RMR_{basic} value which has been further used to classify the slope, considering the corrections factor (adjustment rating). In the present work, continuous slope mass rating (CSMR) has been used to assess the stability of slopes. The CSMR is a modification to the earlier slope mass rating (SMR) scheme (Romana 1985). Measurement for discontinuity spacing, discontinuity condition, and groundwater attributes was made in the field investigation. Later ascertained values were used as input in the QuickRMR to calculate RMR_{basic} and then Continuous-SMR on applying adjustment rating factor owing to discontinuity orientations.

Q-slope is an excellent empirical approach for the quick estimation of safe slope angle for reinforcement free excavated slopes (Barton and Bar 2015). It takes inspiration from the Q-system designed especially for examining the rock-mass conditions in the tunnels and underground excavations in order to design suitable support system (Barton and Grimstad 2014). Similarly, one can devise a suitable mechanical stabilization or reinforcement needed for the slopes being excavated/examined or infer the maximum stable slope angle (without heavy support techniques) using the Q-slope method in the field itself. The basic structure of the Q-system remains the same in Q-slope, with few modifications in the existing parameters and the involvement of the orientation-factor (O-factor) in Eq. (4.5) (Bar and Barton 2017).

$$\text{Q-slope} = \left(\frac{RQD}{J_n}\right) * \left(\frac{J_r}{J_a} * \text{O-factor}\right) * \left(\frac{J_{wice}}{SRF_{slope}}\right) \tag{4.5}$$

where RQD, J_n, J_r, J_a, J_{wice}, SRF_{slope} are Rock Quality Designation, Joint set number, Joint roughness number, Joint alteration number, Geological and environmental condition of the excavated slope, and Strength reduction factors (a, b, and c) respectively. The maximum among the SRF_a, SRF_b, and SRF_c is always the best choice to correctly determine the steepest and most stable slope without any complicated support system. The steepness (β) of the unsupported safe slope can be determined using Eq. (4.6) (Singh et al. 2020) based on the determined Q-slope.

$$\beta = \left[20\log_{10}(\text{Q-slope}) + 65\right]^{\circ} \tag{4.6}$$

Eventually, rockfall analysis was done owing to the field evidence through the RocFall simulation package by Rocscience. The software calculates the energy and bounces height properties for each slope condition to comprehend the various conditions pertaining to rockfalls in the region. This information can be used to design mitigation measure in order to avert any future calamity. The mode of block movement (roll, bounce, fall) is a function of the slope steepness (Fig. 4.4); therefore, special consideration to slope angle should be given in rockfall studies. Apart from that, the shape and size of the rock-blocks plays a key role in deciding the rockfall trajectory. The slope roughness and effect of vegetation are critical factors that need to be assimilated in rockfall simulation programs to model block paths judiciously. As the greater the slope roughness, the higher the chances of divergence from original falling rock pieces. Also, the density of vegetation has a significant control on block movement, as it can either stop or deflect the natural path of the detached block from the source zone. However, in the present research owing to enormous slope steepness (75°–80°), "fall" will be the type of block movement. Therefore, the negligible collision between the slope surface and falling block will occur, and the effect of slope roughness can be neglected here. Additionally, the role of vegetation can also be ignored in the present work, as the hindrance offered by small trees and plants (on the basis ground-condition) can be ignored due to the slope's steepness and higher volume of falling blocks (~2 m^3).

For simulating the rockfall scenario at the three locations, a 2-D slope sections were designed to mimic the real slope geometry (based on determined slope angle and slope height as per field observation). The slope heights of 35 m, 32 m and 25 m were incorporated in the RocFall model, while slope angles were 75°, 80°, and 80° at locations 1, 2, and 3, respectively. The width of road (highway) was kept 7 m in the simulation. Afterwards, the slope material properties were assigned to these sections, and the bedrock lithology was taken for the inclined slopes, whereas asphalt material's property was assigned to the road. The bedrock lithology can be categorized by its characteristic normal restitution coefficient (0.35 ± 0.04), tangential restitution coefficient (0.85 ± 0.04), dynamic friction (0.5 ± 0.04), rolling friction (0.15 ± 0.02), and friction angle (30 ± 2)°. Furthermore, the asphalt (road) material has a normal restitution coefficient of 0.4 ± 0.04 and tangential restitution coefficient of 0.9 ± 0.03. The source (seeder) of the rockfall was the topmost point of the inclined slopes, with an initial horizontal velocity of 0.5 ± 0.1 m/s, while initial vertical and rotational velocity were kept 0 m/s. The rigid masses of 10 blocks were allowed to fall in each simulation, and outcomes were enumerated using the Monte-Carlo probabilistic numerical method. In each case, initially, the blocks fall on the slope-road boundary and bounce across the road.

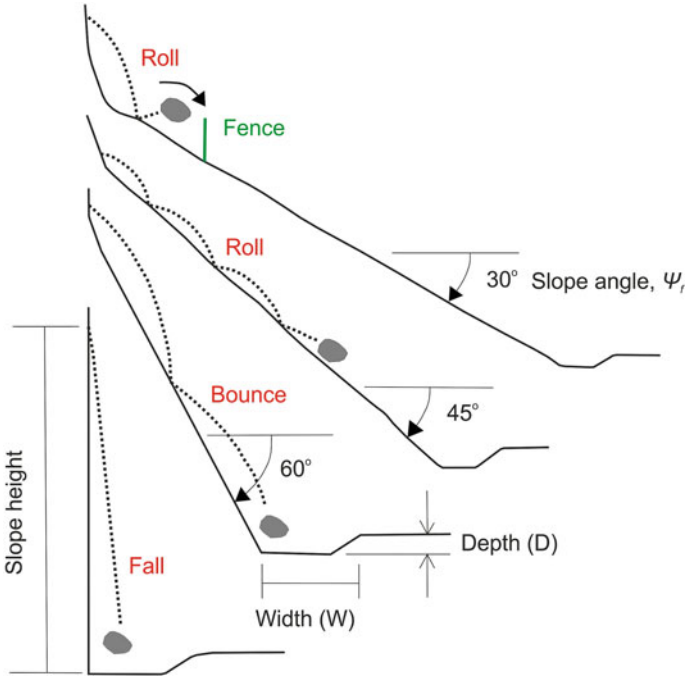

Fig. 4.4 Control of slope angle on the mode of rockfall (modified after Bar et al. 2016)

4.4 Results

The present analysis found that, for location 1, planar failure (with no limits) has a probability of 33.3% (Fig. 4.5a). The adjustment rating for the planar failure has been enumerated to calculate continuous slope mass rating (CSMR) for this site. This mode of sliding can be attributed to joint set 3 (Table 4.1), dipping 60° towards 250°. Additionally, the orientation factor (O-factor) for the analysis of J_r/J_a ratio in case of Q-slope will be ascertained for the planar failure (with no limits) along the same joint-set.

A similar analysis was done for location 2 (Fig. 4.5b), where the probability of wedge failure was affirmed along the intersection of joint sets J_2–J_3 (Table 4.1). One can either adopt planar or toppling failures to examine the adjustment rating. In this location, no such sliding was confirmed in the kinematic analysis. Hence, to decide the adjustment ratings for ascertaining the Continuous-SMR, one can assume the case of planar failure (without limits), as it has a slightly greater possibility than toppling with little change in geometry of either joints or slope.

Hence, the joint dipping at 80° towards 210 is considered for evaluating the adjustment rating of slopes. Moreover, to acquire Q-slope analysis for the site, one will consider the case of wedge failure along the intersection of joint-sets J_2 (70° → 110°) and J_3 (80° → 210°) to evaluate the orientation factor for J_r/J_a ratios.

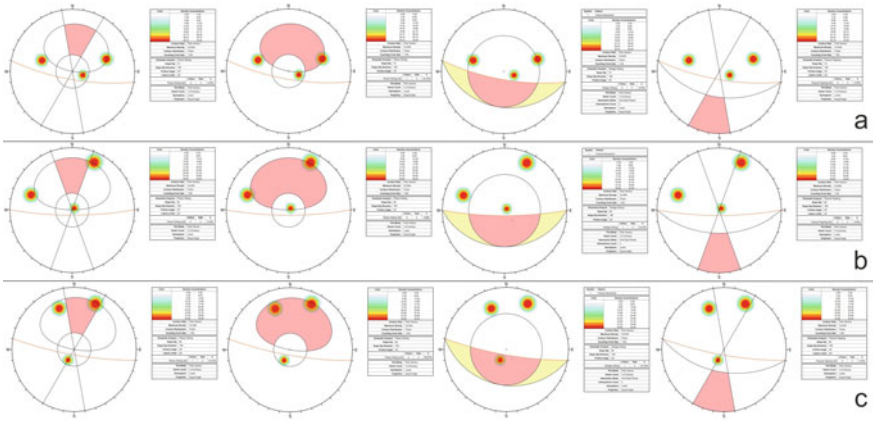

Fig. 4.5 Kinematic analysis at location 1 (a), location 2 (b), and location 3 (c)

Table 4.2 Point Load Strength Index (PLSI) for the samples collected in the study area

S.No.	Rock type	Thickness (mm)	Length (mm)	Width (mm)	Failure load (*N*)	PLSI (MPa)
1	Sandstone	42	59	85	24.5	7.50
2	Sandstone	72	43	80	37	7.81
3	Sandstone	40	80	90	16	4.87
4	Sandstone	55	74	78	27.5	7.34
5	Sandstone	47	78	74	22	7.01
Average PLSI						6.90

The outcomes of kinematic analysis of the slope at location 3 indicate that all the modes of failure are possible except toppling (Fig. 4.5c). The planar sliding, planar sliding (with no limits), and wedge sliding can occur with a probability of 33.3%, 66.6%, and 33.3%, respectively. Adjustment factor of SMR has been established considering the planar failure with the most critical joint set dipping 78° towards 205°. Furthermore, one will encompass wedge failure along the intersection of joint-sets J_1 (70° → 160) and J_3 (78° → 205) to get the orientation factor of J_r/J_a and perform the Q-slope analysis at the location 3. The laboratory examination of collected rock specimens concluded that the PLSI of the Dhandraul sandstone ranged between 4.87 to 7.81 MPa, indicating high strength samples (Table 4.2). Also, the UCS of these rocks had a median value of 138 MPa, on account of Eq. (4.3). The calculated RMR_{basic} values were 65, 62, and 67 for the locations 1, 2, and 3, respectively (Fig. 4.6). Similarly, the obtained values of continuous-SMR were 56, 52, and 32 for locations 1, 2, and 3, respectively, based on all the parameters accounted for in the present work (Table 4.3).

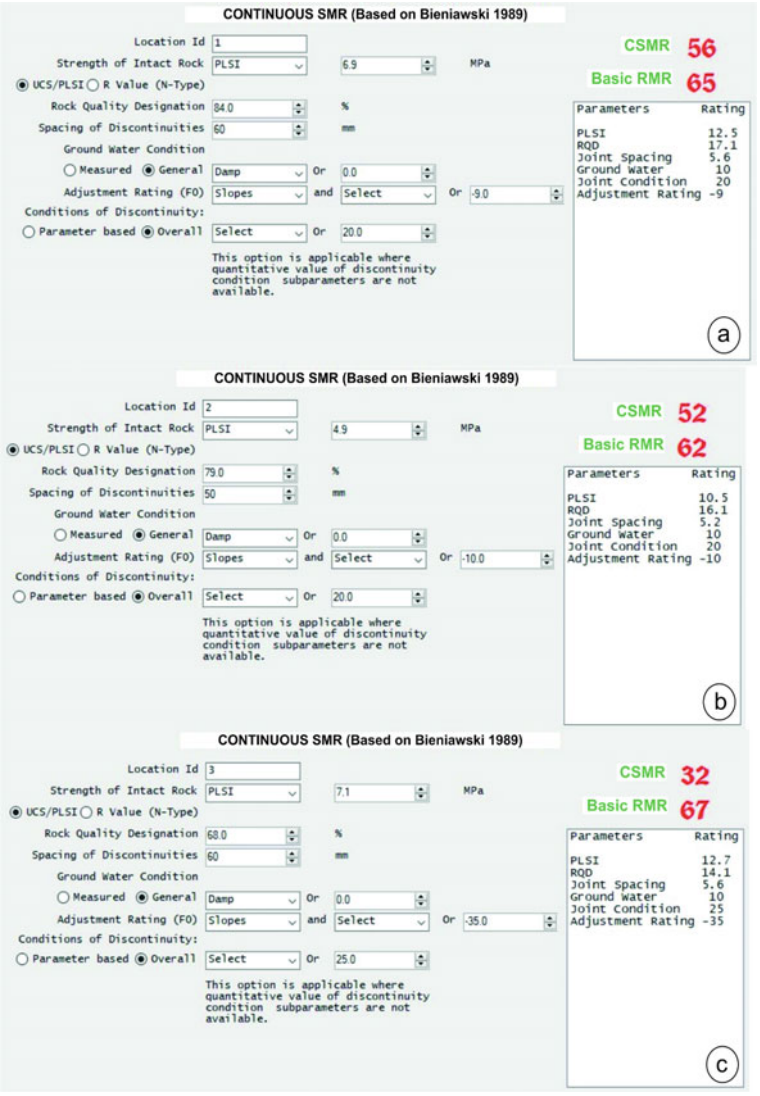

Fig. 4.6 Rock mass rating calculation using QuickRMR software for locations 1, 2, and 3

Apart from the CSMR, the Q-slope approach was incorporated into the study. Hence, a swift and scientific estimation of the maximum safe slope angles, without any heavy engineering accompaniments, can be made in the field. The present work acquired the following values of RQD, J_n, J_r, J_a, O-factor, J_w, and SRFslope through rigorous field investigation, kinematic analysis, and a short of arithmetic (Table 4.4).

For the investigated sections, the calculated values of the Q-slope range were 2.8, 4.21, and 5.44 for sites 1, 2 and 3, respectively. Therefore, the maximum slope angle

Table 4.3 Attributes of RMR_{basic} and CSMR, and their calculated values in the study area

Location	RQD (%)	PLSI (MPa)	Joint spacing (mm)	Joint condition	Ground-water condition	Adjustment rating	RMR_{basic}	CSMR
1	84	6.9	60	Slightly rough surfaces, separation <1 mm, highly weathered walls	Damp	– 9 ($F_1 = 0.15$; $F_2 = 1$; $F_3 = –60$; $F_4 = 0$)	65	56
2	79	4.87	50	Slightly rough surfaces, separation <1 mm, highly weathered walls	Damp	– 10 ($F_1 = 0.4$; $F_2 = 1$; $F_3 = –25$; $F_4 = 0$)	62	52
3	68	7.1	60	slightly rough surfaces, separation <1 mm, slightly weathered walls	Damp	– 35 ($F_1 = 0.7$; $F_2 = 1$; $F_3 = –50$; $F_4 = 0$)	67	32

Table 4.4 The deciding properties of Q-slope in the study area, and its' values (After, Bar and Barton 2017)

Q-slope parameters	Location 1	Location 2	Location 3
Kinematic Analysis	Planar sliding (with no-limits)	Wedge sliding along joint sets J_2 and J_3	Wedge sliding along joint sets J_1 and J_3
RQD	84%	79%	68%
J_n	Three joint sets	Three joint sets	Three joint sets
J_r	Rough or irregular plane	J_{r1}: Rough or irregular, undulating (for J_2) J_{r2}: Smooth, undulating (for J_3)	J_{r1}: Rough or irregular, undulating (for J_1) J_{r2}: Rough or irregular, undulating (for J_3)
J_a	Unaltered joint walls and surface staining only	J_{a1}: Unaltered joint wall and surface staining only (for J_2) J_{a2}: Unaltered joint wall and surface staining only (for J_3)	J_{a1}: Unaltered joint wall and surface staining only (for J_1) J_{a2}: Unaltered joint wall and surface staining only (for J_3)
O-factor	Quite favourable	O-factor (1): Very unfavourable (for J_2) O-factor (2): Very unfavourable (for J_3)	O-factor (1): Very unfavourable (for J_1) O-factor (2): Very unfavourable (for J_3)
J_{wice}	Stable-competent rocks lie in tropical storm	Stable-competent rocks lie in tropical storm	Stable-competent rocks lie in tropical storm
SRF_{Slope}	SRF_a: Slight loosening due to surface location, disturbance due to blasting or excavation SRF_b: $(\sigma_c/\sigma_1)^* = 171.42$ SRF_c: Not applicable	SRF_a: Slight loosening due to surface location, disturbance due to blasting or excavation SRF_b: $(\sigma_c/\sigma_1)^* = 170.43$ SRF_c: Not applicable	SRF_a: Slight loosening due to surface location, disturbance due to blasting or excavation SRF_b: $(\sigma_c/\sigma_1)^* = 246.95$ SRF_c: Not applicable
	Q-slope = 2.8 $\beta = 73.94°$	Q-slope = 4.21 $\beta = 77.40°$	Q-slope = 5.44 $\beta = 79.71°$

σ_c and σ_1 are the UCS and maximum principal stress; β is the maximum slope-angle stable without any heavy mechanical support (with 0.1% probability of failure)

that would be stable without installing any heavy engineering solutions is 73.94°, 77.40°, and 79.71°. Moreover, these estimated slope angles are 1° to 3° less than the actual cut-slope angle at these study sites. Hence, smaller localized failure cases may arise, which is evident in the study area as well. Several sandstone blocks of nearly rectangular to squared shapes were found scattered along the roadside during the field visit, as shown in Figs. 4.2, 4.3, and 4.4. Sudden loosening and fall of these blocks pose a major threat to the vehicles plying on the state highway-5A. On average, the blocks sizes were 1.266 × 1.266 × 1.266 m^3 in dimensions (2 m^3 in volume), with a dry density in the range 2,463 ± 266 kg/m^3 (Tenzer et al. 2011), with an equivalent weight of nearly 5,000 ± 500 kg.

Moreover, the rock blocks covered nearly one-fourth of the road at a few places, posing a considerable threat to the passing vehicles. The state highway is used by heavy vehicles like trucks, buses, and tractors to transport sand, sandstone, limestone, and other crucial goods. Even a tiny rockfall event can cause accidents, and also, a minor distraction while driving along these studied sites can lead to severe damage due to the collision with these existing detached rock blocks. Therefore, a scientific study of rockfall dynamics is necessary in the RocFall program (RocScience Inc. 2022). The detailed rockfall dynamics (like rockfall trajectory, bounce height, total kinetic energy, translational velocity, rotational velocity, and end-points) can be interpreted through Figs. 4.7, and 4.8 for each research area.

The rockfall examination at site 1 indicates a maximum total kinetic energy (TKE) of 1,550 ± 50 kJ, and the mean TKE is 1,200 ± 50 kJ at the slope-road boundary. Moreover, the TKE is reduced as blocks move further across the road, and finally, 70% of blocks come to rest just before crossing the road, while the rest, 30%, were stopped closer to the slope-road boundary. Additionally, the blocks attain an average height of 3 m, while the maximum height can reach 6 m across the road. The mean translational and rotational velocity of the falling blocks may vary in the range of 6–22 m/s and 1–7 rad/s, respectively, across the road. Similarly, at location 2, mean TKE

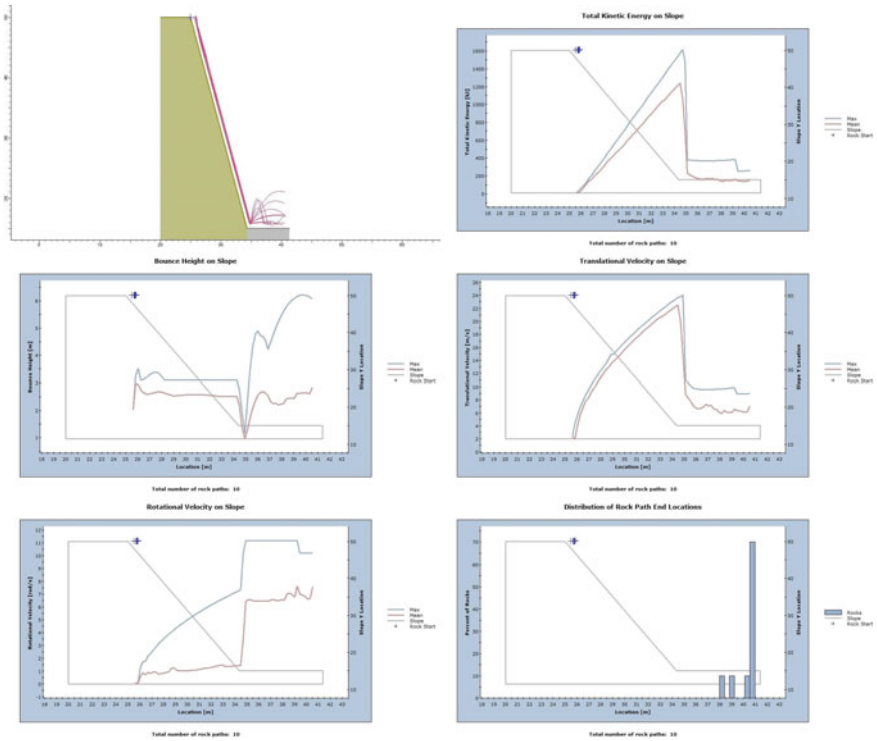

Fig. 4.7 Outcome of rockfall analysis at location 1

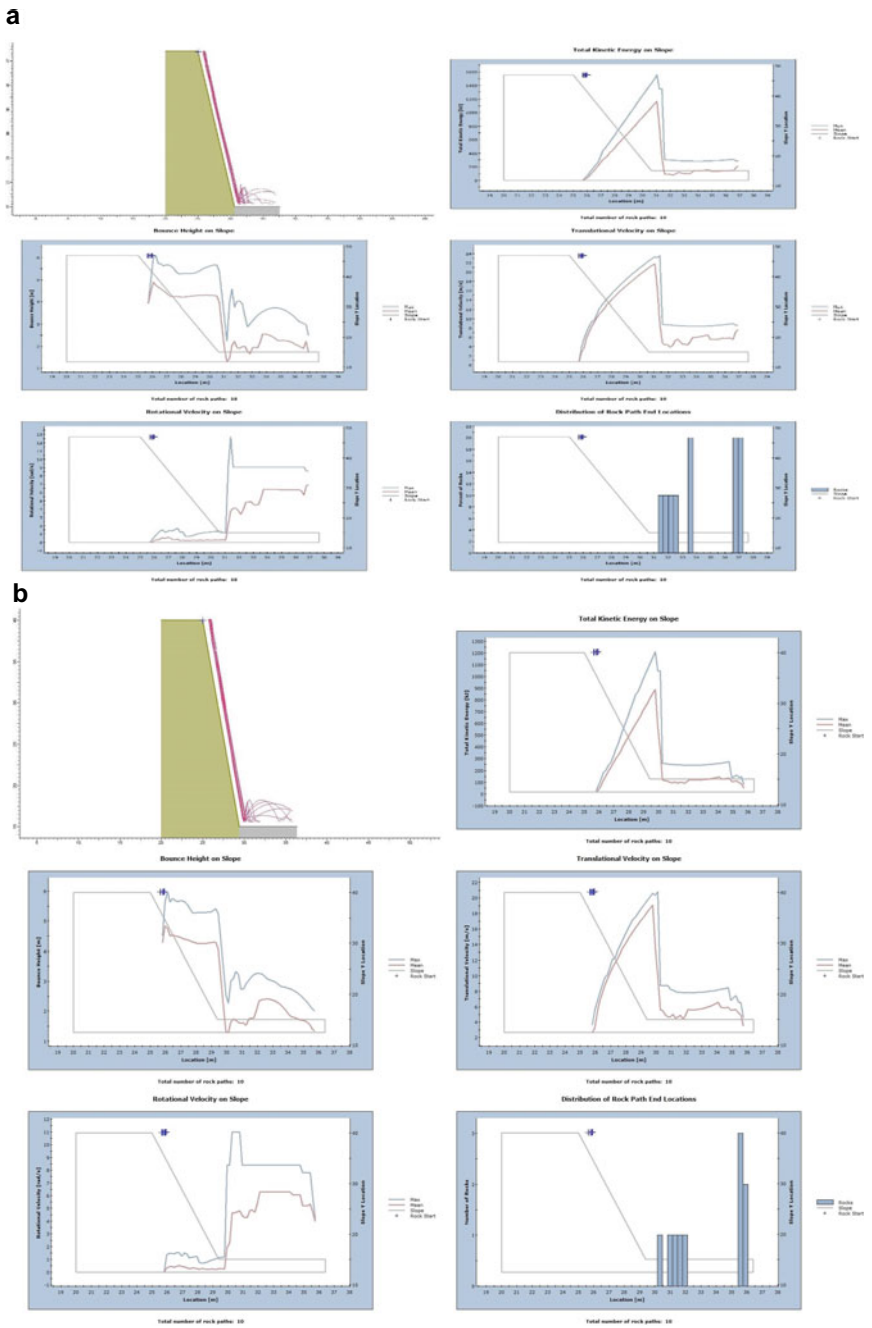

Fig. 4.8 Outcome of rockfall analysis at **(a)** locations 2 and **(b)** location 3

varies in the ranges of 100–1,100 kJ, while the mean bounce height achieved was in the range of 1.5–4 m across the road. The distribution of rock-path end locations reveals that approximately 40% of blocks were stopped within 2 m from the slope's toe, and 40% were stopped before 1 m at the other end of the road. Moreover, the simulated translation and rotational velocity of detached blocks were high and indicated rockfall danger. Furthermore, a detached block from the seeder at site 3 of the study area may bounce as high as 5 m and simultaneously gain a maximum TKE of 1,200 kJ. Approximately 50% of the blocks cross the road, and the rest 50% remained within 2 m from the slope-road boundary. Also, the mean translational velocity varies between 4 and 19 m/s, and mean rotational velocity ranges within 0–6 rad/s across the road.

4.5 Discussion

In this study, three sections have been investigated to assess the overall stability and in particular rockfall instability, in the upper reaches of Markundi hills, along state-highway-5, UP (India). Rock mass along the excavated slopes was blocky with three sets of prominent joints, plus a few random joints. The RQD values for three sections adapting scanline survey in the field were affirmed to be 84, 79 and 68 for the sites 1, 2, and 3, respectively. Due to the contrast in the joint condition, orientation, and hydrological conditions, the corresponding RMR_{basic}, CSMR, Q-slope, and rockfall simulation results vary at these locations. The kinematic analysis also demonstrated the possibility of planar failure in location-1 and wedge failure in locations 2 and 3. A previous study for kinematic and empirical assessment was conducted for two stretches of the hill slopes (Kumar et al. 2019). The ascribed RMR values in the present research work are in a similar range as in work done by Kumar et al (2019), through some RMR and SMR values given by them are lower range. As per Q-slope analysis, the excavated slopes were slightly steeper than the values recommended for reinforcement-free stable slopes. Thus, though the slopes are globally stable, it shows a propensity toward localized failures. Therefore, rockfall analysis was conducted to ascertain the rockfall trajectory, bounce height, total kinetic energy, translational velocity, rotational velocity, and end-points for all the locations. The possibility of rockfall events, irrespective of the failed blocks' size, is a critical factor in deciding the safety of a roadway. These parameters are crucial for designing mitigation measures in the studied section.

A median uniaxial compressive strength value of 138 MPa is incorporated to estimate CSMR and Q-slope based on laboratory testing. For location 1, kinematic analysis confirmed the case of planar failure (with no limits). This failure mode becomes the basis of adjustment rating and O-factor in a further empirical study. The RMR_{basic} and CSMR values determined for the site are 65 and 56, respectively, as the adjustment rating for the continuous slope mass rating is –9. Additionally, the study about Q-slope value 2.8 shows that the maximum slope angle at location-1 is 73.34°, without installing any sophisticated protection works. Also, the rockfall simulation

performed for the site reveals that the average total kinetic energy is ~1,200 kJ at the slope-road boundary. Most of the motion taken by detached blocks is of "fall" type until their first collision with the road surface. The maximum mean bounce height for the blocks are ~ 3 m, whereas the range of mean translational velocities is 6–22 m/s. In the same way, the tools and techniques employed at site-2 led to the understanding of slope safety concerns and ensuing better design. In this line of work, the slope was marked critical to wedge failure, but planar failure may occur with any unfavourable change in slope direction. So, the criteria of O-factor in the case of Q-slope considers the wedge instability condition, whereas the CSMR adopts the concepts of planar mode. The study shows the RMR_{basic} was designated a value of 62 at the second location, and owing to the adjustment rating (−10) the CSMR value was ascribed as 52 in the QuickRMR tool. Furthermore, the Q-slope study indicates that the steepest, safe, and engineering-free slope for location-2 should have an angle of 77.40° (~3° less than the present slope inclination). Additionally, the rockfall simulations at location 2 yielded a bounce height of 1.5–4 m, with a mean translational velocity of 4–21 m/s and a mean rotational velocity of 0–7 rad/m.

In-depth analysis for location-3 demonstrated a possibility of planar failure, planar failure (with no lateral limits), and wedge failure. RMRbasic value of 67 was designated for the slope, and while considering the contributing factors, the CSMR values calculated was 32, rendering it unstable. The safe slope angle for this slope section was 79.71°, quite close to the present slope angle, for the corresponding Q-slope value of 5.44. The rockfall analysis for this site assessed the mean total kinetic energy of the falling blocks to be 160–850 kJ, while the mean bounce height was 0.5–4.5 m. Also, the mean translational velocity of 4–19 m/s and rotational velocity of 0–6 m/s were calculated for this site. It can be seen that CSMR and Q-slope are not directly correlated and thus provide different information. Thus, it is judicious to use different approaches together for slope stability assessment to get a holistic examination.

4.6 Conclusion

Four distinct approaches were used for the analysis of 3 locations at state highway-5, Markundi hills. It is quite clear from the study that the approaches have both their utility and limitations. While kinematic analysis can demonstrate the possible failure mode, CSMR can be used to ascertain overall slope health in conjunction with kinematic analysis. Further, Q-slope is useful for finding the safe slope angle for a given rock mass and rockfall simulation tools are a great aid in calculating the bounce height and kinetic energy, which are used to design rockfall barriers and other protection measures. Analysis indicates that the studied slopes are under threat of rockfall hazards and need immediate installation of protection measures according to rockfall dynamics, as presented in this work. Additionally, the two-dimensional simulation of rockfall indicates that the construction of ditches and trenches near the slope-road boundary can reduce the risk to a greater extent. However, the ditches and trenches should provide the way for draining water. Otherwise, it may increase pore

water pressure, and eventually, slope failure can occur. It is also recommended to achieve the stability, to flatten the slopes at locations 1 and 2 by 2 and 3, respectively.

Acknowledgements Author AK is thankful to the BHU-IOE seed grant fund for the financial support. The authors are also grateful to Rocscience Inc., Canada, for the simulation suite.

References

Ansari T, Kainthola A, Singh KH, Singh TN, Sazid M (2021) Geotechnical and microstructural characteristics of phyllite derived soil; implications for slope stability, lesser Himalaya, Uttarakhand, India. Catena 196:104906

Auden JB (1933) Vindhyan sedimentation in the Son Valley, Mirzapur district. Mem Geol Surv India 62(2):141–250

Bar N, Barton N (2017) The Q-slope method for rock slope engineering. Rock Mech Rock Eng 50:3307–3322. https://doi.org/10.1007/s00603-017-1305-0

Bar N, Nicoll S, Pothitos F (2016) Rock fall trajectory field testing, model simulations and considerations for steep slope design in hard rock. In: Dight PM (ed) APSSIM 2016: proceedings of the first asia pacific slope stability in mining conference. Australian Centre for Geomechanics, Perth, pp 457–466. https://doi.org/10.36487/ACG_rep/1604_29_Bar

Barton N, Bar N (2015) Introducing the Q-slope method and its intended use within civil and mining engineering projects. In: Schubert W, Kluckner A (eds) Future development of rock mechanics; Proceedings of the ISRM regional symposium, Eurock 2015 and 64th geomechanics colloquium, Salzburg, 7–10 Oct 2015, pp 157–162

Barton N, Grimstad E (2014) Forty years with the Q-system in Norway and abroad, vol 4.1–4.25. Fjellsprengningsteknikk, Bergmekanikk, Geoteknikk, NFF, Oslo.

Basahel H, Mitri H (2017) Application of rock mass classification systems to rock slope stability assessment: a case study. J Rock Mech Geotech Eng 9(6):993–1009. https://doi.org/10.1016/j.jrmge.2017.07.007

Bhattacharya D, Joshi GB, Sharma GS, Sen DB (2008) A note on the uranium mineralisation along Jamual-Markundi fault, Sonbhadra and Sidhi districts, Uttar Pradesh and Madhya Pradesh. J Geol Soc India 71(1):125–128

Bieniawski ZT (1989) Engineering rock mass classification: a complete manual for engineers and geologists in mining, civil and petroleum engineering. John Wiley and Sons, New York

Castelli M, Scavia C, Bonnard C, Laloui L (2009) Mechanics and velocity of large landslides. Eng Geol 1(109):1–4

Castelli M, Torsello G, Vallero G (2021) Preliminary modeling of rockfall runout: definition of the input parameters for the QGIS plugin QPROTO. Geosciences 11(2):88

Census of India (2011) https://censusindia.gov.in/pca/cdb_pca_census/Houselisting-housing-UP.html. Accessed 29 Apr 2022

Deng X, Xu D, Zeng M, Qi Y (2018) Landslides and cropland abandonment in China's mountainous areas: spatial distribution, empirical analysis and policy implications. Sustainability 10(11):3909

Dikshit A, Sarkar R, Pradhan B, Segoni S, Alamri AM (2020) Rainfall induced landslide studies in Indian Himalayan region: a critical review. Appl Sci 10(7):2466

Financial Express (2022) https://www.financialexpress.com/events/national-road-infra-conclave-2022, Accessed 7 Feb 2022

Glade T (2003) Landslide occurrence as a response to land use change: a review of evidence from New Zealand. CATENA 51(3–4):297–314

Glade T, Crozier M, Smith P (2000) Applying probability determination to refine landslide-triggering rainfall thresholds using an empirical "Antecedent Daily Rainfall Model." Pure Appl Geophys 157(6):1059–1079

Glade T, Anderson MG, Crozier MJ (eds) (2006) Landslide hazard and risk. Wiley, New York

Guhathakurta P, Sudeep BL, Menon P, Prasad AK, Sable ST, Advani SC (2020) Observed rainfall variability and changes over Uttar Pradesh State. Climate Research and Services, India Meteorological Department, Ministry of Earth Sciences Pune. https://imdpune.gov.in/hydrology/rainfall%20variability%20page/uttar_final.pdf. Accessed on 29 Apr 2022

Hudson JA, Harrison JP (2000) Engineering rock mechanics. An introduction to principles, Elsevier Science Ltd., Oxford

Infante D, Martire D, Calcaterra D, Miele P, Scotto D, Santolo A, Ramondini M (2019) Integrated procedure for monitoring and assessment of linear infrastructures safety (I-Pro MONALISA) affected by slope instability. Appl Sci 9(24):5535. https://doi.org/10.3390/app9245535.

Kainthola A, Verma D, Thareja R, Singh TN (2013) A review on numerical slope stability analysis. Int J Sci Eng Technol Res 2(6):1315–1320

Kainthola A, Sharma V, Pandey VH, Jayal T, Singh M, Srivastav A, Singh PK, Champati PK, Singh TN (2021) Hill slope stability examination along Lower Tons valley, Garhwal Himalayas, India. Geomat Nat Haz Risk 12(1):900–921. https://doi.org/10.1080/19475705.2021.1906758

Kos A, Amann F, Strozzi T, Delaloye R, Von Ruette J, Springman S (2016) Contemporary glacier retreat triggers a rapid landslide response, Great Aletsch Glacier, Switzerland. Geophys Res Lett 43(24):12–466

Krishnan MS, Swaminath J (1959) The Great Vindhyan Basin of northern India. J Geol Soc India 1:10–30

Kumar B, Sharma SD, Sreenivas B, Dayal AM, Rao MN, Dubey N, Chawla BR (2002) Carbon, oxygen and strontium isotope geochemistry of proterozoic carbonate rocks of the Vindhyan Basin, central India. Precambr Res 113(1–2):43–63

Kumar S, Pandey HK, Singh PK, Venkatesha K (2019) Demarcation of probable failure zones based on SMR and kinematic analysis. Geomat Nat Haz Risk 10(1):1793–1804

Kumar S, Mishra AN, Singh AK, Mishra SR, Shahi AK (2020) Studies on the climatic variability analysis of Vindhyan Zone District Sonbhadra of Eastern Uttar Pradesh.

Kundu J, Sarkar K, Singh AK, Singh TN (2020) QuickRMR beta. A rock mass rating calculator based on continuous functions. https://jkundu.com/quickrmr. Accessed 2 Mar 2022

Kundu J, Sarkar K, Verma AK, Singh TN (2022) Novel methods for quantitative analysis of kinematic stability and slope mass rating in jointed rock slopes with the aid of a new computer application. Bull Eng Geol Env 81(1):1–9

Li D, Wong LNY (2013) Point load test on meta-sedimentary rocks and correlation to UCS and BTS. Rock Mech Rock Eng 46:889–896. https://doi.org/10.1007/s00603-012-0299-x

Mahanta B, Singh HO, Singh PK, Kainthola A, Singh TN (2016) Stability analysis of potential failure zones along NH-305, India. Nat Hazards 83(3):1341–1357

Mishra M, Sen S (2011) Geochemical signature for the grain size variation in the siliciclastics of the Kaimur Group, Vindhyan Supergroup from Markundi Ghat, Sonbhadra district, (U.P.), India. Geochem Int 49(3):290–305. https://doi.org/10.1134/S0016702911010071

Mishra M, Sen S (2012) Provenance, tectonic setting and source-area weathering of Mesoproterozoic Kaimur Group, Vindhyan Supergroup, Central India. Geol Acta 10(3):283–293. https://doi.org/10.1007/s11631-010-0021-1

NDMA (2022) https://ndma.gov.in/Natural-Hazards/Landslide. Accessed 01 Mar 2022

NDR (2022) https://www.ndrdgh.gov.in/NDR/?page_id=831&page_id=831. Accessed 29 Apr 2022

Petley DN, Dunning SA, Rosser NJ, Hungr O (2005) The analysis of global landslide risk through the creation of a database of worldwide landslide fatalities. Landslide Risk Manag 52:367–373

Prakash C, Agarwal KK, Sharma VK (2015) Structural control of landslides in Eastern Kumaun Himalaya: case study from Sukhidhang—Ladhiya section. J Geol Soc India 86(5):507–512

Priest SD, Hudson J (1976) Discontinuity spacing in rock. Int J Rock Mech Min Sci Geomech Abstr 13(5):135–148

Quasim MA, Ahmad AH, Sachan HK, Ghosh SK (2019) Recrystallization and provenance history of the upper Kaimur Group siliciclastics, Son Valley, India: coupled petrographic and fluid inclusion proxy. J Geol Soc India 93(2):177–184. https://doi.org/10.1007/s12594-019-1148-2

Ray A, Kumar V, Kumar A, Rai R, Khandelwal M, Singh TN (2020) Stability prediction of Himalayan residual soil slope using artificial neural network. Nat Hazards 103(3):3523–3540

RocScience Inc (2022) A bundle of 2D and 3D geotechnical tools. https://www.rocscience.com/

Romana M (1985) New adjustment ratings for application of Bieniawski classification to slopes. In: Proceedings of the international symposium on the role of rock mechanics. ISRM, Zacatecas, pp 49–53

Scavia C, Barbero M, Castelli M, Marchelli M, Peila D, Torsello G, Vallero G (2020) Evaluating rockfall risk: some critical aspects. Geosciences 10(3):98

Singh TN, Verma AK, Sarkar K (2010) Static and dynamic analysis of a landslide. Geomat Nat Haz Risk 1(4):323–338

Singh TN, Kainthola A, Venkatesh A (2012) Correlation between point load index and uniaxial compressive strength for different rock types. Rock Mech Rock Eng 45(2):259–264

Singh PK, Wasnik AB, Kainthola A, Sazid M, Singh TN (2013) The stability of road cut cliff face along SH-121: a case study. Nat Hazards 68(2):497–507

Singh PK, Kainthola A, Panthee S, Singh TN (2016) Rockfall analysis along transportation corridors in high hill slopes. Environ Earth Sci 75(5):1–1

Singh PK, Singh KK, Singh TN (2017) Slope failure in stratified rocks: a case from NE Himalaya, India. Landslides 14(4):1319–1331

Singh AK, Kundu J, Sarkar K (2018) Stability analysis of a recurring soil slope failure along NH-5, Himachal Himalaya, India. Nat Hazards 90(2):863–885

Singh HO, Ansari TA, Singh TN, Singh KH (2020) Analytical and numerical stability analysis of road cut slopes in Garhwal Himalaya, India. Geotech Geol Eng 38(5):4811–4829

Tenzer R, Sirguey P, Rattenbury M, Nicolson J (2011) A digital rock density map of New Zealand. Comput Geosci 37(8):1181–1191

Tiwari VN, Pandey VHR, Kainthola A, Singh PK, Singh KH, Singh TN (2020) Assessment of Karmi Landslide Zone, Bageshwar, Uttarakhand, India. J Geol Soc India 96(4):385–393. https://doi.org/10.1007/s12594-020-1567-0

Tripathy GR, Singh SK (2015) Re-Os depositional age for black shales from the Kaimur Group, Upper Vindhyan, India. Chem Geol 413:63–72. https://doi.org/10.1016/j.chemgeo.2015.08.011

Wei L, Hu K, Hu X, Wu C, Zhang X (2022) Quantitative multi-hazard risk assessment to buildings in the Jiuzhaigou valley, a world natural heritage site in Western China. Geomat Nat Haz Risk 13(1):193–221. https://doi.org/10.1080/19475705.2021.2004244

Yoon WS, Jeong UJ, Kim JH (2002) Kinematic analysis for sliding failure of multi-faced rock slopes. Eng Geol 67(1–2):51–61

Zhou X, Qian Q, Cheng H, Zhang H (2015) Stability analysis of two-dimensional landslides subjected to seismic loads. Acta Mech Solida Sin 28(3):262–276

Chapter 5
Geotechnical Investigation of Landslide in Ooty, India

R. Chandra Devi, M. Kaviyarasu, G. Gowrisankar, and P. Dinesh

Abstract Landslides are the most typical hazards in the hilly regions; pose threat to human life and infrastructures. The sliding soil mass induces shear stresses along a probable failure surface more than the strength of the soil, causing a landslide. Gandhi Nagar, a spot in Ooty city in the Nilgiris district of Tamil Nadu is one of the critical site for frequent landslides. However, there is a lack of a technical database, even though it has witnessed several landslides in the last five decades. Several investigations have reported landslide hazard zonation and mapping in this district, no study has been attempted to validate the findings with geotechnical investigation data. This chapter investigates the geotechnical approach for five locations at Gandhi Nagar. Extensive fieldwork observations and geotechnical data were utilised to perform numerical modeling. Several limit equilibrium methods viz. the Ordinary Swedish Method of Slices, Morgenstern and Price, Janbu, Bishop, and Spencer were utilized for stability analysis. The results show that the result of Morgenstern and Price method analysis was satisfactory with respect to the slope factor of safty; the factor safety varied 0.455–0.751 without pore-water pressure and 0.281–0.469 with pore-water pressure effect. Based on the detailed investigation, the study location can be recognised as a hazardous landslide zone, and there is a need for immediate slope stabilization measures to prevent any forthcoming landslide risks. Also, it is essential to design and install a real-time landslide monitoring system for the site under the study.

Keywords Landslide · Limit equilibrium method · Slope instability · Geotechnical investigation · Nilgiris

R. Chandra Devi (✉) · M. Kaviyarasu
Department of Civil Engineering, Sri Krishna College of Engineering and Technology, Coimbatore 641008, India
e-mail: chandradevir@skcet.ac.in

G. Gowrisankar
Divecha Centre for Climate Change, Indian Institute of Science, Bangalore 560012, India

Department of Geology, Anna University, Chennai 600025, India

P. Dinesh
Department of Civil Engineering, National Institute of Technology Silchar, Silchar 788010, India

P. Thambidurai and T. N. Singh (eds.), *Landslides: Detection, Prediction and Monitoring*,
https://doi.org/10.1007/978-3-031-23859-8_5

5.1 Introduction

Landslides are the most terrible disasters in hilly landscapes and often cause severe harm to human and property. In India, about 12.6% of the area is vulnerable to landslides, and out of this, 21% area includes the Western Ghats in Tamil Nadu, where the frequency of landslides is significant during monsoon (Chandrasekaran et al. 2019; GSI 2022; MoES 2022). Especially, the Nilgiris in the western ghats of India have a considerable history of landslides (Fig. 5.1). Nilgiris district has a rugged hilly terrain having altitude of 1,000–2,601 m above mean sea level, and its area is around 2,553 km^2. The latitude and longitude extends from 11°12′ N to 11°37′ N and 76°30′ E to 76°55′ E, respectively. Nilgiris receives maximum rainfall from the south-west monsoon (June–August) and north-east monsoon (October–December) every year. Nilgiris district includes the city of Ooty, Wellington, Kotagiri, Gudalur, and Coonoor. The landslides are more often due to heavy rainfall. The past landslide in 1978 was due to the incessant heavy rain, thus initiating many landslides more than area of 250 sq.km. in district, many people died in Ooty during this landslide. Then, in the next year, more than 100 landslides occurred in district, resulting in huge loss of human and infrastructure. As per the government of Tamil Nadu, around 140 landslides occurred in 2019 (Megha and Priyanka 2019; PTI 2019) and the respective pictures are presented in Fig. 5.2. In Nilgiris, many landslides occur largely due to rainfall-induced slope failures (Subbarayan et al. 2020; Yuvaraj and Dolui 2021). As of now, 284 locations in the Nilgiris district have been recognized as most vulnerable spots for landslides.

In the last few decades, several studies had reviewed landslides in Nilgiris district and reported hazard zonation and mapping (Naveen et al. 2011; Ganapathy and Hada 2012; Vaani and Sekar 2012; Muthukumar 2013; Abdul et al. 2014; Saravanan

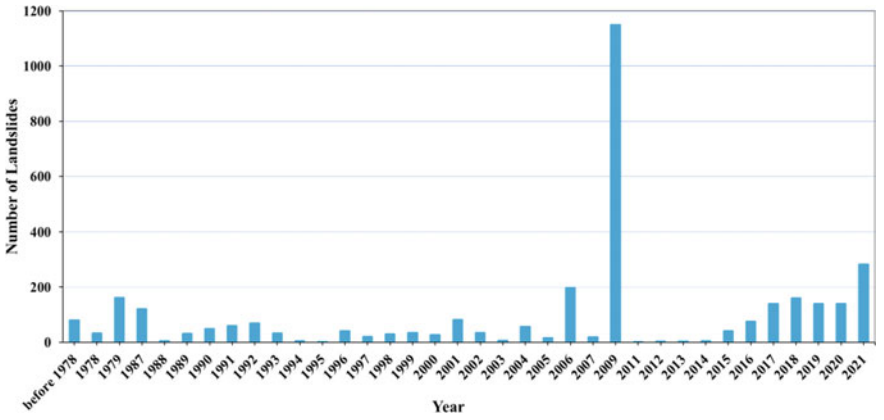

Fig. 5.1 Landslides history in Nilgiris district (*Data Source* Thennavan and Pattukandan 2020; GSI 2022)

Fig. 5.2 Recent landslides in Nilgiris district 2019 (*Source* Megha and Priyanka 2019; Press Trust of India)

et al. 2021; Thennavan and Pattukandan 2020; Yuvaraj and Dolui 2021). In addition, the assessment of infrastructure damages after landslide disasters was reported (Chandrasekaran et al. 2013; Edison et al. 2016). A few studies predicted landslide hazard zone; however, they did not attempt to analyse and validate their findings with geotechnical investigations. Very limited studies assessed the landslide in the prospect of geotechnical failure (Pradeep et al. 2012; Nalina et al. 2014; Senthilkumar et al. 2017; Senthilkumar and Chandrasekarn 2019). Pradeep et al. (2012) considered the field soil properties to analyse the landslide using Bishop's method, in which fundamental forces on soil slices were ignored. Nalina et al. (2014) utilised geotechnical properties of soils of 32 locations in Kallar-Coonoor hill road stretch and analysed backpropagation of artificial neural network model for landslides. Senthilkumar et al. (2017) and Senthilkumar and Chandrasekaran (2019) investigated the rainfall-induced landslide occured in 2009 at Marappalam and Achanakkal with geotechnical investigation data. Using a numerical model, the study confirmed that landslide was induced by rainfall and respective pore-water pressure. Geotechnical investigations are must for all landslide-prone areas in the Nilgiris district. Before proposing any remedial measures or installing any real-time monitoring system, it is essential to undertake detailed geotechnical investigations (Satyam et al. 2021). Hence, this chapter presents the geotechnical investigation of the slope at one of the most vulnerable hotspots at Gandhi Nagar in Ooty district of Nilgiris.

5.2 Materials and Methods

5.2.1 Description of Study Area

About 284 locations in the Nilgiris district are been reported as prone to landslides, and out of these, 49 locations are situated near or along highways. Gandhi Nagar is at Ooty city in the southwest of Tamil Nadu, India. It was chosen based on the information from a previous report and preliminary fieldwork conducted at five locations

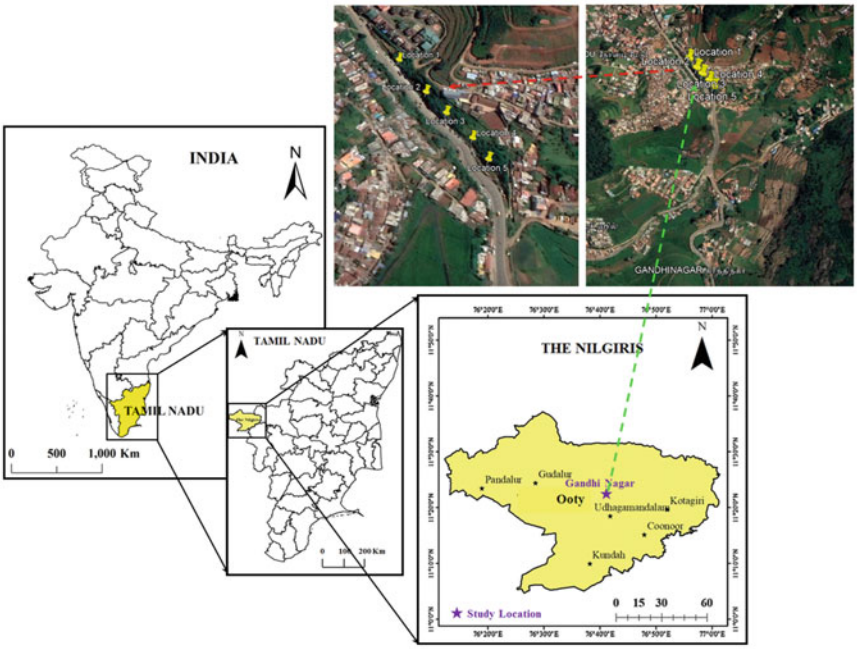

Fig. 5.3 Map of India showing the location of Gandhi Nagar, Ooty

with data collections (Fig. 5.3). Ooty is situated in the area of 11°24′36.72″ N latitude and 76°41′42″ E longitude, having altitude of 2,240 m above sea level. The Ooty has an average rainfall of 1,050 mm annually. The climate of the Nilgiris district is moderate, and the temperature varies between 5.1 and 22.1 °C. The summer starts in March, and the maximum temperature reaches in April. The weather cools down gradually, and the mean daily temperature drops to 5.1 °C in January (NWM 2014).

Nilgiris district is fully comprised of the crystalline Metamorphic rocks of the Archean age. The main rock types include Alluvium, Laterite, Dolerites, Granites, Quartzite, Gneisses, Charnockites, and Schists. The district forms part of the Western Ghats and hence, fully hilly area with steep slopes. Charnockite forms the bulk of the rock units in the district, which constitutes the basement in the high-grade metamorphic terrain (NWM 2014). Most of the peaks are Charnockite. Biotite gneissic rock is found at the lower level of the district. Further, the gneiss occurs as lenses within the Charnockite. The major soil is lateritic, red sandy, colluvial and red loam. There are nine-fold land uses such as woods, barren lands, non-agricultural use land, cultivable waste dumping land, permanent grasslands, forests not considered in the area seeded, current tills, other till lands and net area seeded (CGWB 2008).

5.2.2 *Field Investigation and Laboratory Testing*

The investigated locations have slope of 13 m in height; the soil was sampled from the top and bottom layers of each location. In order to achieve exactness, three samples were collected at each site, preserved, and transported to the laboratory within 12 h. The slope height, width, and slope inclinations were measured in the field and the susceptible direction of the landslide were observed (Fig. 5.4). There is no evidence of the groundwater table cut through the slope in the study location. The field density of the soil was measured using a core sampler of height 15 cm and diameter of 12 cm. The transported thirty soil samples were immediately tested for water content in the laboratory. Further, the samples were dried out in the shade, and then, the specific gravity, Atterberg's limit, permeability, unconfined compressive strength, cohesion, and angle of shearing resistance were determined (Fig. 5.5), and the soil was classified as per the standards (BIS 2007).

Fig. 5.4 Study locations showing the susceptible direction of landslide

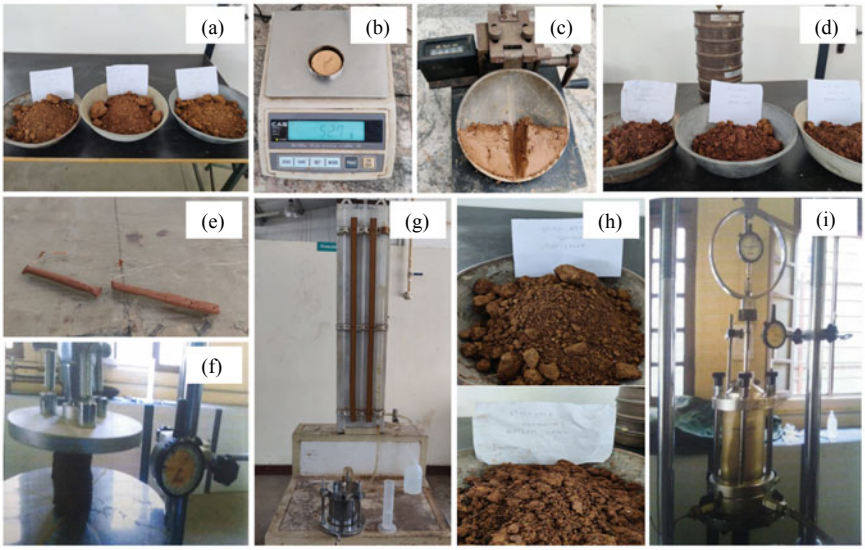

Fig. 5.5 Collected soil samples and laboratory testing **a** Samples collected at location 1; **b** Shrinkage limit; **c** Liquid limit; **d** Samples collected at location 3; **e** Plastic limit; **f** Unconfined compressive strength test; **g** Permeability test; **h** Samples collected at location 4; **i** Triaxial test

5.2.3 Limit Equilibrium Method

The various reasons for occurance of landslides in the hilly region are mainly geological (weathered materials, jointed/fissured materials), morphological (slope angle, fluvial erosion), physical (intense rainfall, surface runoff), and anthropogenic activities (excavation, loading, land use pattern change). The shear stress induces landslide of soil mass, and existing strength of soil demonstrates a significant role in slope stability. Ratio of soil shear strength to the shear stress on a failure plane provides a factor of safety. The main purposes of the stability analysis are locating susceptible areas, studying geotechnical aspects of potential failure, and then recommending suitable remedial measures. The soil is assumed at the verge of failure in limit equilibrium, and the methods are statically indeterminate. The stress–strain relationships along the assumed failure surface are not recognized, which is the main limitation of this limit equilibrium method. Hence, it is essential to make assumptions, and the system becomes statistically determined; it can be easily analysed. The assumptions are as follows:

1. The stress system is two-dimensional, and the stress in the third direction is assumed as zero.
2. Mohr–Coulomb's theory for shear strength is applicable.
3. Plastic failure condition is assumed to be satisfied along the critical surface.

4. Seepage and water table conditions are known, and the pore pressure could be estimated.

In limit equilibrium method of analysis, the resultant of all sliding forces for slope failure is determined (Krishna 2006), and strength of soil found from geotechnical data together determines factor of safety. The concept of converting potential failure soil mass into a number of slices was first presented by Petterson (1916) and followed by Fellenius (1936), who introduced the Ordinary Swedish circle method. Further, Janbu (1954) and Bishop (1955) progressed in method, and mathematical formulations were reported by Morgenstern and Price (1965) and by Spencer (1967). The limit equilibrium method is easy to adopt, so manual calculations can verify those solutions. In all the methods, sliding soil mass is divided into number of slices. The key assumptions and limitations of various methods are presented in Table 5.1.

Table 5.1 Assumptions and factor of safety (FS) in various limit equilibrium methods

Method	Assumption	Factor of safety (FS)
Ordinary	Interslice forces are ignored	$\frac{\sum [c\beta + N \tan\phi]}{\sum W \sin\alpha}$
Bishop	Normal interslice forces are taken into account, but shear forces between soil slices are ignored. This method fulfills moment equilibrium but not force equilibrium	$\frac{1}{\sum W \sin\alpha} \sum \left[\frac{c\beta + W \tan\phi - \frac{c\beta}{FS} \sin\alpha \tan\phi}{m_\alpha} \right]$ $m_a = \frac{\cos\alpha + \sin\alpha \tan\phi}{FS}$ c = cohesion, β = slice base length, N = base normal ($W \cos\alpha$), ϕ = friction angle, W = slice weight, and α = slice base inclination
Janbu	Normal interslice forces are taken into account, but shear forces between soil slices are ignored. This method fulfills horizontal force equilibrium but not moment equilibrium	
Morgenstern and Price	The direction of the resultant forces between soil slices is determined. This method satisfies moment and force equilibrium	
Spencer	The resultant forces between the slices have the same slope throughout the sliding soil mass. The line of push is the degree of freedom	

5.2.4 Numerical Analysis Using GeoStudio

The slope stability analysis is the conventional numerical study in geotechnical engineering. The stability of slopes should be assessed to ensure the safety and resistance against sliding of soil mass. GeoStudio is a geotechnical numerical modelling software in which the field geometry and conditions of the slope can be simulated and analysed using the limit equilibrium method. The GeoStudio can solve all the limit equilibrium methods, and respective factors of safety with critical slip circle can be estimated. However, in order to rely on the numerical modelling data, it has to be initially validated. Hence, a geotechnical numerical model for a trial soil slope was considered. The slope was analysed manually for the Ordinary method and compared with numerical data. Further, the numerical model study using GeoStudio was performed for all five locations, considering the soil slope field geometry, material, and boundary conditions. The numerical models were analyzed using all limit equilibrium methods without pore-water pressure conditions; thus, the respective critical surface and factor of safety were reported. Further, the analysis was performed for the Morgenstern and Price method by including pore-water pressure conditions near the ground surface, as it includes both force and moment equilibrium.

5.3 Results and Discussion

5.3.1 Geotechnical Characteristics of Soil

The geotechnical characteristics of the soils were determined in laboratory, and results are presented in Table 5.2. The minimal water content was observed in the top and bottom layers ranging from 1.5–2.2% and 5.4–6.2% respectively. The density in the top layer was lower (1.12–1.49 g/cc) than in the bottom layer (1.22–1.65 g/cc); hence the voids were observed more in the top layer (0.52–0.91) than in the bottom layer (0.34–0.89). The consistency limits were also observed, and the soil was classified as silt clay of low compressibility as per Indian standards (BIS 2007). The cohesion was found as 5.5–9.2 kPa, and large particles (10–13 mm) were observed in more quantity in the sample. The reduction in cohesion was due to the residual strength of the soil, which already failed due to shear stress. The permeability was observed as $1.53 \times 10^{-3} - 2.14 \times 10^{-3}$ cm/s, valid for fine-grained silts and sands. The geotechnical investigation confirmed that the soil had low shear strength, thus there was a possibility of further shear failure in the soil mass.

Table 5.2 Geotechnical characteristics of soil

Properties	Location 1		Location 2		Location 3		Location 4		Location 5	
	Top layer	Bottom layer	Top layer	Bottom layer	Top layer	Bottom layer	Top layer	Bottom layer	Top layer	Bottom layer
Water content w (%)	1.7	5.8	2.5	6.2	1.8	5.4	2.2	6.3	1.5	5.6
Bulk density ρ (g/cc)	1.17	1.26	1.12	1.22	1.33	1.5	1.49	1.6	1.38	1.65
Dry density ρ_d (g/cc)	1.15	1.19	1.09	1.15	1.31	1.42	1.46	1.51	1.36	1.56
Unit weight γ_t (kN/m^3)	11.48	12.36	10.99	11.97	13.05	14.72	14.62	15.70	13.54	16.19
Specific gravity G	2.15	2.19	2.02	2.08	2.44	2.64	2.78	2.85	2.06	2.09
Void ratio e	0.87	0.84	0.85	0.81	0.87	0.86	0.91	0.89	0.52	0.34
Porosity n (%)	46.49	45.62	45.91	44.77	46.46	46.09	47.56	47.19	34.00	25.24
Liquid limit w_l (%)	17.00	15.45	14.32	12.46	18.45	16.22	19.28	15.24 ara>	18.69	16.64
Plastic limit w_p (%)	12.90	10.62	12.50	9.26	13.16	11.65	16.36	12.33	14.90	12.14
Shrinkage limit w_s (%)	9.82	7.24	8.18	6.44	10.11	8.26	12.81	9.86	10.12	8.48
Permeability k (cm/s) × 10^{-3}	1.74	1.53	1.88	1.65	1.76	1.57	2.14	1.86	1.73	1.57

(continued)

Table 5.2 (continued)

Properties	Location 1		Location 2		Location 3		Location 4		Location 5	
	Top layer	Bottom layer	Top layer	Bottom layer	Top layer	Bottom layer	Top layer	Bottom layer	Top layer	Bottom layer
Undrained compressive strength q_u (kPa)	12.0	16.0	13.0	18.0	11.0	17.0	14.0	17.0	13.2	18.4
Cohesion c (kPa)	6.0	8.0	6.5	9.0	5.5	8.5	7.0	8.5	6.6	9.2
Angle of friction φ (°)	13	7	12	6	11	5	13	6	14	8
Indian standard classification (Based on plasticity chart)	Silt–clay of low compressibility		Silt of low compressibility		Clay of low compressibility		Silt of low compressibility		Silt–clay of low compressibility	

5.3.2 *Numerical Model Analysis*

In order to rely further on the numerical analysis, the geotechnical numerical model was run for a trial soil slope of 6 m height, slope angle 40˚, cohesion 20 kPa, angle of shearing resistance of 12˚, as shown in Fig. 5.6. The slope was analysed manually for the Ordinary method of slices, and the resisting moment and sliding moment were computed as 2,772.21 kNm and 1,501.35 kNm, respectively. The numerical model was analysed using GeoStudio and the resisting moment and sliding moment were reported as 2,770.56 kNm and 1,504.84 kNm, respectively. The factor of safety was found as 1.85 manually and 1.84 using numerical analysis (Table 5.3), thus it validates that the created numerical model and the same could be used for further analysis.

Without pore-water pressure: All the five locations were numerically defined (Fig. 7a) for the existing physical boundary in the field. The slope height, slope width, slope angle, and the in-situ properties of the soil were simulated as per Table 5.2. The numerical model was analysed for the Ordinary (Fig. 7b), Bishop (Fig. 7c), Janbu (Fig. 7d), Morgenstern and Price (Fig. 7e), and Spencer (Fig. 7f) methods. The respective critical slip circle is presented for location 3. In field, there was no observation of water table and porewater influence on the slope; hence it was ignored in the initial analysis. The analysis is called as total stress analysis, in which porewater pressure is taken as zero. The slope height was 13 m and the slope angle 42˚ for all the locations, but the surface profile varied based on slope sliding at a random time, which changed the sliding moment and respective factor of safety. The computed

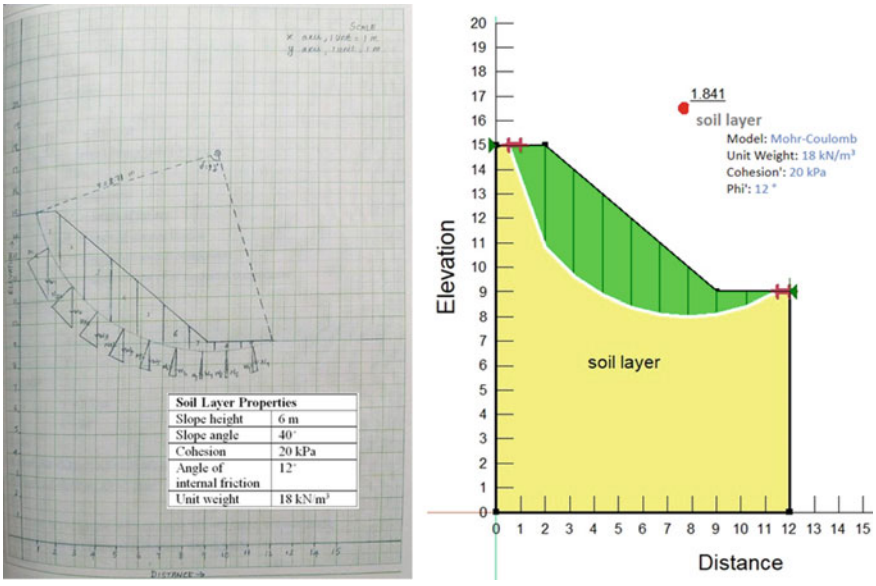

Fig. 5.6 Validation of numerical simulation software

Table 5.3 Comparison of manual and numerical analysis for ordinary Swedish method of slices

Slice numbers	Location of slice		Manual analysis		Numerical analysis	
	X ordinate (m)	Y ordinate (m)	Normal stress (kPa)	Shear stress (kPa)	Normal stress (kPa)	Shear stress (kPa)
1	1.25	12.94	10.38	0.71	4.34	0.92
2	2.58	10.27	37.57	6.22	36.74	7.81
3	3.75	9.28	50.3	12.26	52.38	11.13
4	4.92	8.63	56.63	9.56	58.64	12.46
5	6.08	8.24	54.86	14.41	55.43	11.78
6	7.25	8.05	42.34	7.31	43.84	9.32
7	8.42	8.05	24.66	6.82	25.87	5.49
8	9.63	8.26	11.54	3.48	12.48	2.65
9	10.88	8.71	3.16	0.67	4.29	0.91
$\sum$ stress			294.01	61.44	291.44	62.47
Resisting moment kNm			2,772.21		2,770.56	
Sliding moment kNm			1,501.35		1,504.84	
Factor of safety			1.85		1.84	

resisting moment was 5,260.35 kNm and the sliding moment was 9,019.36 kNm by the Ordinary method. The factor of safety was found as 0.549. Compared to other methods, the Ordinary and Janbu method demonstrated the least factor of safety. Morgenstern and Price and Spencer's method of limit equilibrium analysis considers all the soil slice forces and moment; hence this equilibrium increased the resisting moment, thereby the factor of safety. However, all the safety factors were less than one (Table 5.4) and the field investigation also witnessed the feasibility of sliding at any moment. During field studies, it was found that concrete wall construction could be proposed in order to prevent the sliding; hence the technical data obtained through numerical modelling also validated the field observation. All the five locations were not in a safe zone, even though there was no consideration of porewater pressure.

With porewater pressure: All the five locations were found to be endangered for landslide hazards at any moment though there was no consideration of porewater pressure. Since, the study locations are in heavy rainfall zone, and the development of porewater pressure in the soil slope during the intense rainfall is possible. The best way of describing the porewater pressure condition in the numerical model is with a piezometric line, as shown in Fig. 8a for location 3. For better simulation of rainfall or rise of the water table to ground level, the pore pressure profile was assumed to be near the slope's surface. Now, a further study using Morgenstern and Price method by defining the porewater pressure boundary in the model was conducted for all the locations. The respective critical slip circle is presented for location 3 are presented in Fig. 8b. Similar study was reported by Acharya et al. (2016) for seven slopes in Niihama city at Shikoku Island in western Japan based on GeoStudio. The computed factor of safety less than 1, in the present study, confirms

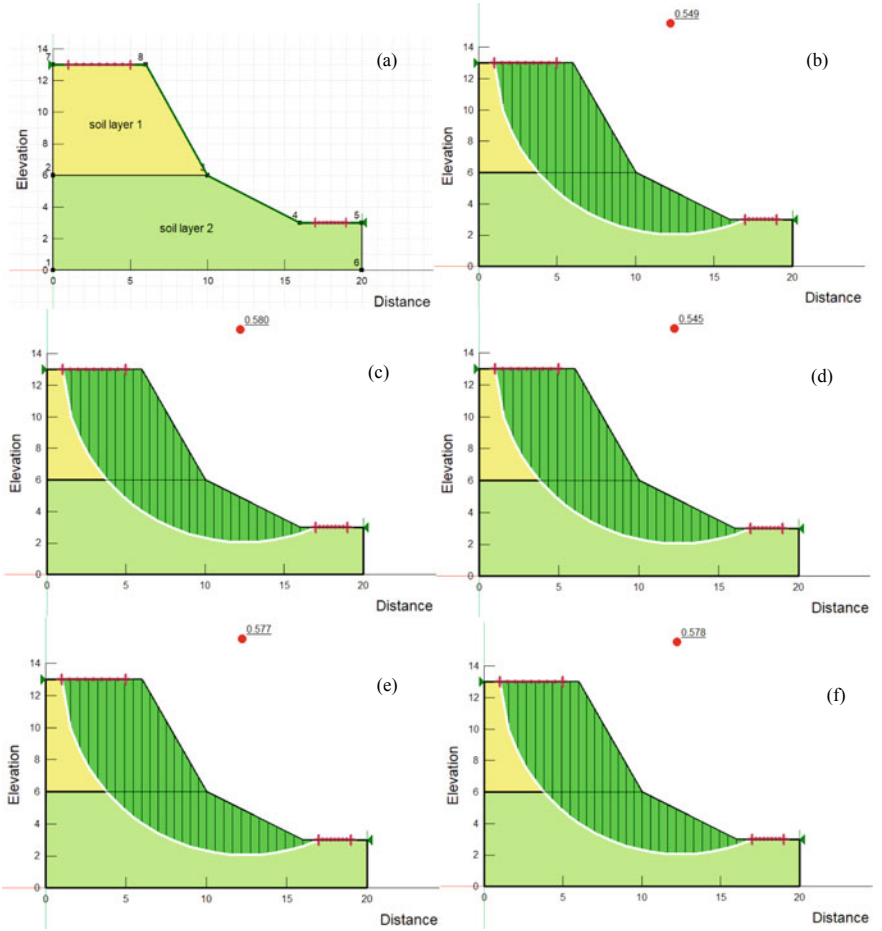

Fig. 5.7 Location 3 **a** Soil layers; **b** Ordinary; **c** Bishop; **d**Janbu; **e** Morgenstern and Price; **f** Spencer methods of analysis

Table 5.4 Factor of safety for all the five slopes using limit equilibrium methods

Method	Location 1	Location 2	Location 3	Location 4	Location 5
Ordinary	0.583	0.594	0.549	0.450	0.697
Bishop	0.609	0.616	0.580	0.455	0.753
Janbu	0.574	0.583	0.545	0.447	0.685
Morgenstern and Price	0.607	0.615	0.577	0.455	0.751
Spencer	0.606	0.614	0.578	0.456	0.751

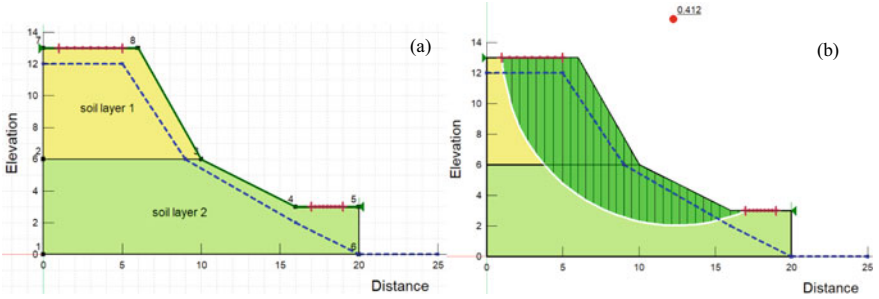

Fig. 5.8 Location 3 **a** Pore-water pressure profile in soil layers; **b** Morgenstern and Price method of analysis

that the landslide might occur anytime. Another study by Thambidurai and Ramesh (2017) investigated the Chandmari landslide in the eastern of Gangtok, Sikkim in north-east India using GeoStudio. They reported reduction in strength of the soil and factor of safety was determined as 1.14, which indicated sudden failure due to any unexpected triggers. Shah et al. (2021) investigated landslide in Malingaon village in Pune district, Maharashtra, India and reported the hill slope investigated was not stable, having factor of safety less than one and demonstrated higher chances of landslide failure.

Pore pressure observed in all the 31 slices of soil mass for the critical slip surface 5 is shown in Fig. 5.9. Numerical analysis considering pore pressure is termed an effective stress analysis, in which the application of pore-water pressure is on failure surface. Variation of pore pressure is based on size of the soil slices. The forces acting in the soil slice 6 and the respective free body diagram is presented in Fig. 5.10. The forces acting in each slice include self-weight, normal, shear stress along critical slip surface and stress from the two sides of the slices. The free diagram shows the degree and path of the forces acting on soil slices. The factor of safety using Morgenstern and Price method is found as 0.281–0.469 (Table 5.5) and it is identified that location 4 was most critical. It may also be inferred that all five locations should be immediately stabilized to prevent any further landslides.

5.3.3 Remedial Measures

The geotechnical investigation and numerical data for the studied locations confirmed the feasibility of a landslide at any moment with intense rainfall. Before failure, during failure, after failure, and reactivation are the four possible stages of landslide activity, as explained by Leroueil et al. (1996). Hence, it is essential to implement remedial measures to prevent further landslide disasters, especially before the monsoon. The major landslide remedial measures are modifications in slope geometry, constructing retaining structures, and installing internal slope reinforcement. As the study sites

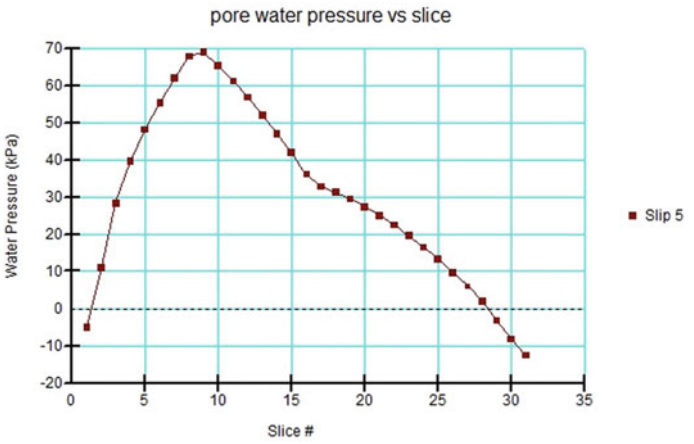

Fig. 5.9 Pore-water pressure for all 31 slices for location 3

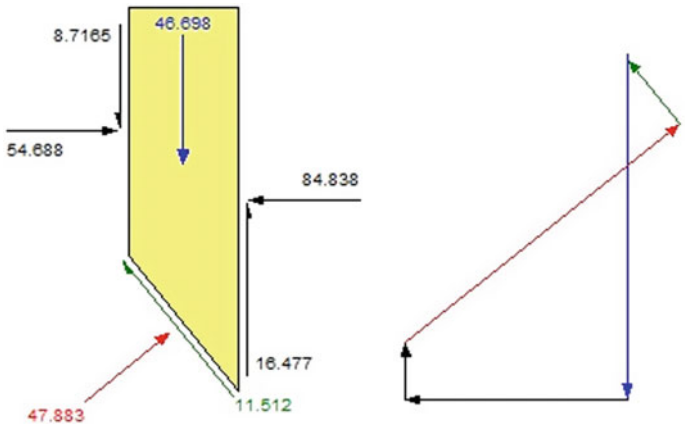

Fig. 5.10 Force polygon and free body diagram for slice number 6 (Location 3)

Table 5.5 Factor of safety of slope with pore-water pressure

Location	Morgenstern and Price
1	0.359
2	0.381
3	0.412
4	0.281
5	0.469

are located near the highways, modifications in slope geometry by adding material to reduce slope angle are not possible. The internal slope reinforcement is also not reliable, as the soil has less residual shear strength, and not possible to hold any additional reinforcement (rock bolts, soil nailing, micro piles, anchors, etc.). However, the construction of cast-in-situ reinforced concrete retaining walls is the best option to retain the sliding soil mass in the study area.

5.4 Conclusions

The geotechnical investigation was performed at five most vulnerable landslide hotspots in Gandhi Nagar, Ooty, Nilgiris district of Tamil Nadu. The investigation confirmed the slope instability and possibility of landslides in the study area at any moment. The limit equilibrium method discretized the soil mass and analyzed the slope stability using several slip surfaces. Out of all limit equilibrium methods, Morgenstern and Price was found suitable. It considered both force and moment equilibrium, and safety factor at the study locations was estimated as 0.455–0.751 without pore-water pressure influence and 0.281–0.469 with pore-water pressure influence, respectively. Based on the geotechnical investigation and numerical model simulation, all study locations were identified as unsafe. Hence, immediate implementation of remedial measures like concrete walls or other alternative measures are needed to prevent future hazards. Also, these locations need to be under continuous monitoring by appropriate real-time landslide monitoring system.

References

Abdul RS, Aruchamy S, Jegankumar R (2014) Geospatial approach on landslide hazard zonation mapping using multicriteria decision analysis: A study on Coonoor and Ooty, part of Kallar Watershed, The Nilgiris, Tamil Nadu. Int Arch Photogramm Remote Sens Spat Inf Sci XL-8:1417–1422 https://doi.org/10.5194/isprsarchives-XL-8-1417-2014

Acharya KP, Bhandary NP, Dahal RK, Yatabe R (2016) Seepage and slope stability modelling of rainfall-induced slope failures in topographic hollows. Geomat Nat Haz Risk 7(2):721–746

Bishop AW (1955) The use of slip circle in the stability analysis of slopes. Geotechnique 5:7–17

Bureau of Indian Standards (BIS): 1498–1970 (Reaffirmed 2007) Indian Standard classification and identification of soils for general engineering purposes. New Delhi

Central Government Water Board (CGWB) (2008) Ministry of Water Resources, Technical report series, District Groundwater Brochure Nilgiris District, Government of India

Chandrasekaran SS, Sayed OR, Ashwin S, Rayansh JM, Prasanth S, Venugopalan RB (2013) Investigation on infrastructural damages by rainfall-induced landslides during November 2009 in Nilgiris, India. J Nat Haz 65:1535–1557

Chandrasekaran SS, Senthilkumar V, Maji VB (2019) Landslides in Nilgiris: causal factors and remedial measures. In: Ilamparuthi K, Robinson R (eds) Geotechnical design and practice. Developments in geotechnical engineering. Springer, Singapore. https://doi.org/10.1007/978-981-13-0505-4_16

Edison T, Ganapathy GP, Chandrasekarn SS, Rajawat AS (2016) Use of GIS in assessing building vulnerability for landslide hazard in the Nilgiris, Western Ghats, India. J Int Soc Prev Miti Nat Haz 82:1031–1050

Fellenius W (1936) Calculation of the stability of earth dams. In: Proceedings of the second congress of large dams. Washington DC, vol 4, pp 445–463

Geological Survey of India (GSI) (2022). https://www.gsi.gov.in/

Ganapathy GP, Hada CL (2012) Landslide hazard mitigation in the Nilgiris District, India—Environmental and societal issues. Int J Env Sci Dev 3(5):497–500

Janbu N (1954) Applications of composite slip surfaces for stability analysis. In: Proceedings of European conference on the stability of earth slopes. Stockholm, Sweden, vol 3, pp 43–49

Krishna PA (2006) Slope stability evaluations by limit equilibrium and finite element methods. Ph.D. thesis, Norwegian University of Science and Technology

Leroueil S, Locat J, Vaunat J, Picarelli L, Lee H, Faure R (1996) Geotechnical characterization of slope movements. In: Senneset K (ed) Landslides. Balkema, Rotterdam

Megha K, Priyanka T (2019). The news minute article on 9 Aug 2019. https://www.thenewsminute.com/article/4-women-killed-rains-tn-s-nilgiris-district-106960.

Ministry of Earth Sciences (MoES) (2022) https://www.moes.gov.in/

Morgenstern NR, Price VE (1965) The analysis of the stability of general slip surfaces. Geotechnique 15:79–93

Muthukumar M (2013) GIS based geosystem response modeling for landslide vulnerability mapping parts of Nilgiris, South India. Dis Adv 6:58–66

Nalina P, Meenambal T, Sathyanarayan SR (2014) Slope stability analysis of Kallar-Coonoor hill road stretch of the Nilgiris. J Com Sci 10:1107–1114

National Water Mission (NWM). (2014). Report in groundwater resources in Nilgiris District, Government of India

Naveen RT, Ram MV, Backiaraj S, Muthusamy S (2011) Landslide hazard zonation using the relative effect method in south eastern part of Nilgiris, Tamil Nadu, India. Int J Eng Sci Tech 3:3260–3266

Petterson KE (1916) Kajraset i Gotenborg des 5te Mars (Collapse of a quay wall at Gothenburg March 5th 1916). Tek. Tidskr. (in Swedish)

Pradeep KV, Lakshumanan C, Viveganandan S (2012) Evaluation of limit equilibrium method for landslide susceptibility analysis (LSA)—A case study on Nilgiris district. Int J Adv Rem Sen GIS 1:234–243

Press Trust of India (PTI) (2019) India TV news. https://www.indiatvnews.com/news/india-nilgiris-district-landslides-tamil-nadu-chief-minister-542135

Saravanan S, Jennifer JJ, Singh L. et al. (2021) Impact of land-use change on soil erosion in the Coonoor Watershed, Nilgiris Mountain Range, Tamil Nadu, India. Arab J Geosci 14:407. https://doi.org/10.1007/s12517-021-06817-w

Satyam N, Oommen T, Cuomo S (2021) Editorial-special issue: landslides: forecasting, assessment and mitigation. Ind Geo J 51:625–626

Senthilkumar V, Chandraskearan S (2019) Failure mechanism of long-runout landslide triggered by heavy rainfall in Achanakkal, Nilgiris, India. J Geo Geoenv Eng 145:9

Senthilkumar V, Chandrasekaran S, Maji V (2017) Geotechnical characterization and analysis of rainfall—induced 2009 landslide at Marappalam area of Nilgiris district, Tamil Nadu state, India. Landslides 14:1803–1814. https://doi.org/10.1007/s10346-017-0839-2

Shah CR, Sathe SS, Bhagawati PB, Mohite SS (2021) A hill slope failure analysis: a case study of Malingoan village, Maharashtra, India. Geol Ecol Landsc 5(1):1–6. https://doi.org/10.1080/24749508.2019.1695714

Spencer E (1967) A method of analysis of the stability of embankments assuming parallel inter-slice forces. Geotechnique 17:11–26

Subbarayan S, Jacinth JJ, Leelambar S, Abijith D (2020) Analysis of sinmap in landslide susceptibility mapping of Coonoor Watershed, Nilgiris, India. Research Square, US

Thambidurai P, Ramesh MV (2017) Slope stability investigation of Chandmari in Sikkim, Northeastern India. In: Mikos M, Tiwari B, Yin Y, Sassa K (eds) Advancing culture of living with landslides. WLF 2017. Springer, Cham. https://doi.org/10.1007/978-3-319-53498-5_42

Thennavan E, Pattukandan GG (2020) Evaluation of landslide hazard and its impacts on hilly environment of the Nilgiris District: a geospatial approach. Geo Dis 7:3. https://doi.org/10.1186/s40677-019-0139-3

Vaani N, Sekar SK (2012) Regional landslide hazard zonation and vulnerability analysis using AHP and GIS: a case study of Nilgiris district, Tamil Nadu, India. J Dis Adv 5:171–176

Yuvaraj RM, Dolui B (2021) Statistical and machine intelligence based model for landslide susceptibility mapping of Nilgiri district in India. Environ Chall 5:100211. https://doi.org/10.1016/j.envc.2021.100211

Chapter 6
Geomechanical and Kinematic Stability Analysis of Unstable Slopes (Near 9th km Stone) on Palani—Kodaikkanal Ghat Section in Tamil Nadu

S. Prasanna Venkatesh, N. Rajeshwara Rao, and S. E. Saranaathan

Abstract The queen of hills, Kodaikanal, is a famous hill town in Tamil Nadu and is located within fragile mountains facing fast urbanisation in recent times. The Kodaikanal—Palani road of 32 km, and within this stretch, a selection of 1.2 km length from 8.8 to 10.0 km takes repeated curves with fairly steep cut slopes. Concentrated rains in the area during 2017 caused heavy damage in this zone, leading to a few major and minor landslides. A study in the affected area indicates ten unstable slopes, of which seven numbers are rock slides and three numbers are soil slides. These unstable slopes are often reactivated, affecting the traffic in the area. Initially, an examination of rock slides was carried out using a modified slope mass rating. The study showed that four slopes are stable conditions (R3 J1–J4, R4 J1, R6 J1–J2, R7 J2–J4; SMR values range 79—96), and four are unstable conditions (R1 J1–J3, R2 J1–J2, R3 J2–J4, R6 J2, SMR values ranges 44–58). Later, the Hoek and Bray method conducted a detailed stability analysis of unstable rock slopes. The planar analysis shows that four numbers of rock slope discontinuities are unstable (R1–J1, R2–J1, R3–J5, R7–J1), and in wedge analysis, six numbers of rock slope joint sets are unstable (R1 J–J3, R3 J1–J4 and J1–J5, R4 J1–J2, R6 J1–J2, R7 J2–J4). Using the circular failure chart method, three potentially unstable soil slopes were studied for their stability analysis between 9.1–10.0 km. The research indicates that all slopes are stable under dry conditions; however, two soil slopes (S1 and S3) become unstable under saturated conditions. Finally, the most commonly adopted remedial measure for steep cut slopes is recommended, i.e., altering the slope geometry to a stable angle for soil slopes.

Keywords Factor of safety · Geo-mechanical analyses · Kinematic and CFC methods · Kodaikkanal

S. Prasanna Venkatesh · N. Rajeshwara Rao
Department of Applied Geology, School of Earth and Atmospheric Science, University of Madras, Chennai 600025, India

S. E. Saranaathan (✉)
School of Civil Engineering, SASTRA Deemed University, Thanjavur 613401, India
e-mail: esaranathan@yahoo.co.in

P. Thambidurai and T. N. Singh (eds.), *Landslides: Detection, Prediction and Monitoring*,
https://doi.org/10.1007/978-3-031-23859-8_6

6.1 Introduction

Slope instability is a common problem in hilly regions, which generally affect the hill roads leading to traffic blockade and loss of life in some cases (Aleotti and Chowdhury 1999). The present article is mainly motivated by the geotechnical appraisal and instability examination of the 9th km stone landslide along with Perumal malai—Palani road, Tamil Nadu. The queen of hills, Kodaikanal, is located within fragile mountains facing fast urbanisation in recent times. This hill town is well connected to Palani, Periyakulam, and Dindigul through all-weather roads. The Kodaikanal—Palani road section has a length of 52 km, of which 32 km is located within hills. Within this stretch, a section of 1.2 km length from 8.8 to 10.0 km takes repeated curves with fairly steep cut slopes. Heavy rains in the area during 2017 caused several damages in this zone, leading to a few major and minor landslides. A geological traverse has been taken along this stretch by carrying out the selected sections slope mass rating (SMR) and detailed stability investigation. The strength of rock-cut slopes is a critical aspect in hilly regions. Romana (1985) developed an analysis scheme called SMR to apply the rock mass rating (RMR) of Bieniawski (1989), mainly to evaluate the rock-cut slope stability. Since it does not include the displacement type, Anbalagan et al. (1992) modified the technique, including the structural geological factors and type of failure. It is a primary and quick hazard calculation method to quickly cover large areas. Similarly, debris instability analysis of hill slopes has been studied earlier by many authors (Anbalagan et al. 2008; Sharma et al. 2013; Singh et al. 2010; Saranaathan and Kannan 2017; Vinay et al. 2018; Kumar et al. 2020). A detailed study of rock slope stability by identifying the pattern of failures like a plane failure and wedge failure was discussed by Hoek and Bray (1981). The circular failure chart method (Hoek and Bray 1981; Kannan et al. 2017) is a simple method for studying soil slope stability using the available standard charts depending on the existing field condition.

6.2 Study Area

Kodaikanal is located in the southern part of the higher Palani range in the Western Ghats (Fig. 6.1). Thousands of people visit daily to enjoy the natural sceneries and its salubrious climate. Kodaikanal—Dindugal road is an important road providing access to the hill station. The study area includes a stretch of 1.2 km length from 8.8 to 10.0 km, which experienced rock and soil slope failures during the heavy rains of 2017. The study area starts from 77° 33′ 39.6″ E—10° 18′ 32.4″ N and ends at 77° 33′ 46.8″ E—10° 18′ 25.2″ N in the ghat section. The study area is covered by Hornblende biotite gneiss. Major fault systems fully control these areas. Nearby two significant faults recognised in this study area are the Theyvankarai Ar displacement from Perumal malai to the confluence of Theyvankarai Ar and Gundar R and another at the Senbaganur—Perumal malai fault. The Senbaganur—Perumal malai section is

formed in the major structural valley in the southwestern part of the Perumal malai. It is extended up to the end of the Palani hills. This is controlled by the NE–SW fault system, parallel to the Eastern Ghat Orogeny (Anbazhagan and Saranathan 2001). It is shown in Fig. 6.2.

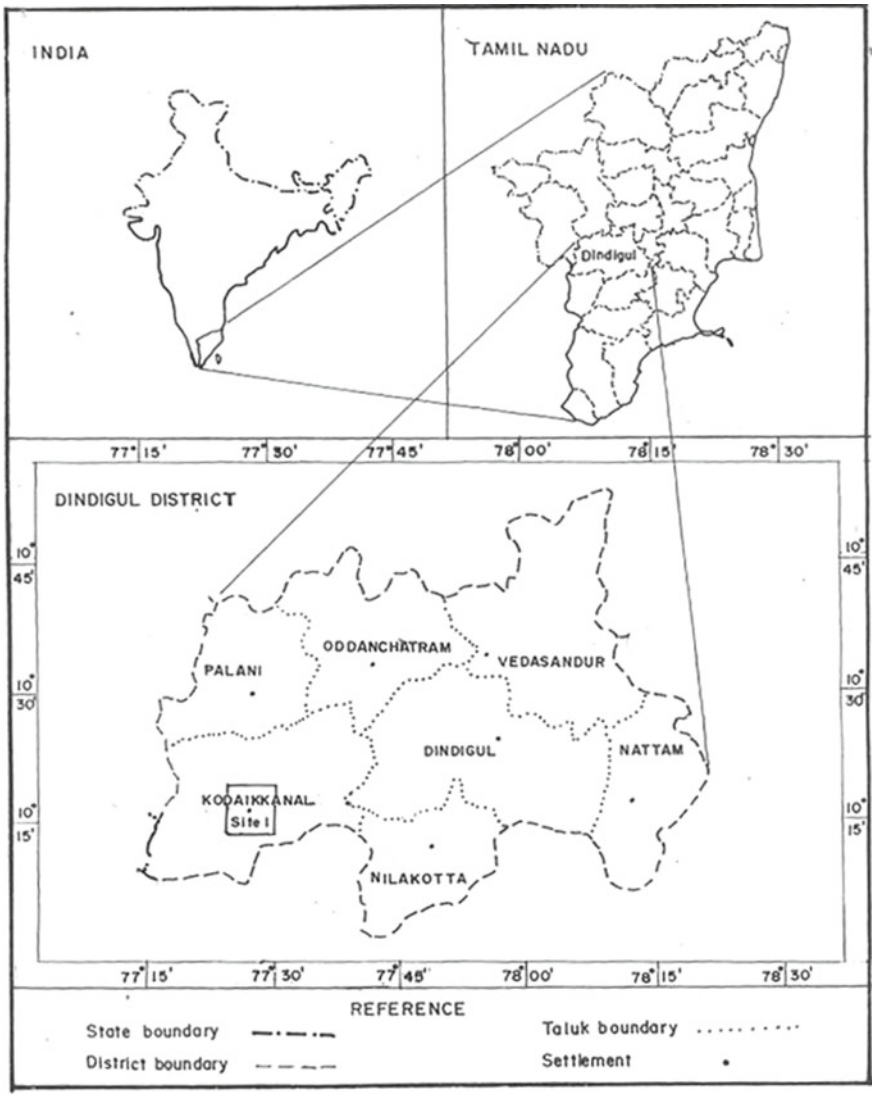

Fig. 6.1 Location of map of the study area

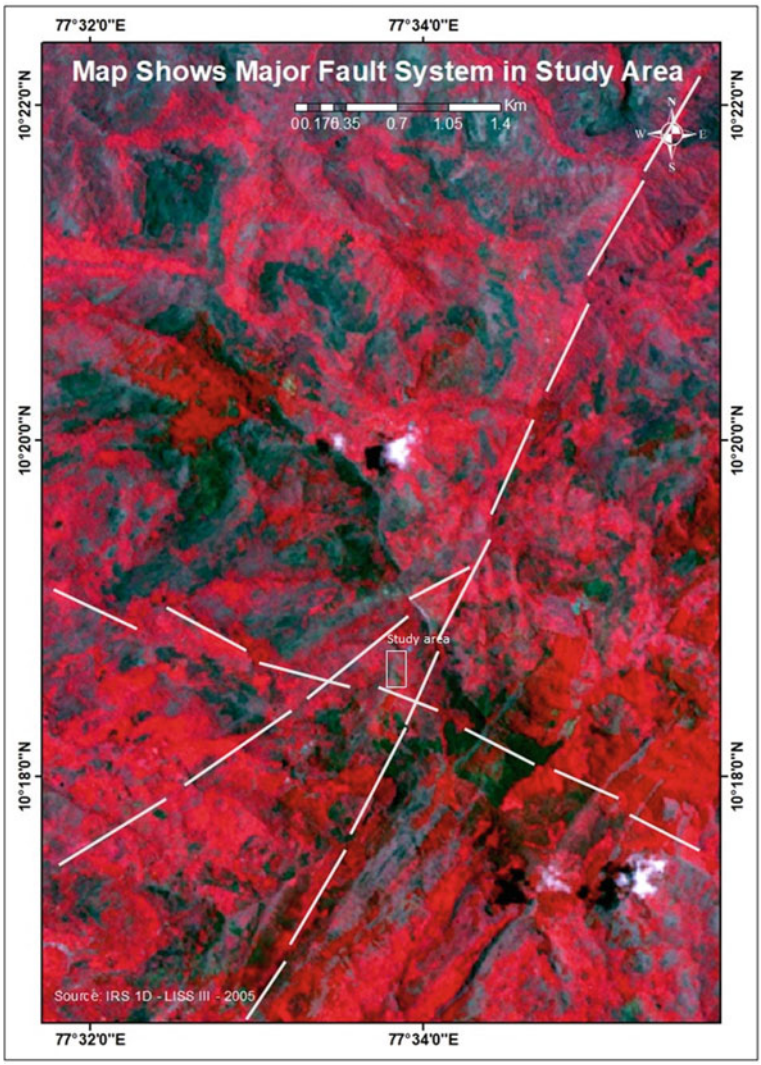

Fig. 6.2 Satellite imagery shows major faults occurrence in the study area

6.3 Methodology

The detailed methodology adopted in this study is presented as a flow chart in Fig. 6.3.

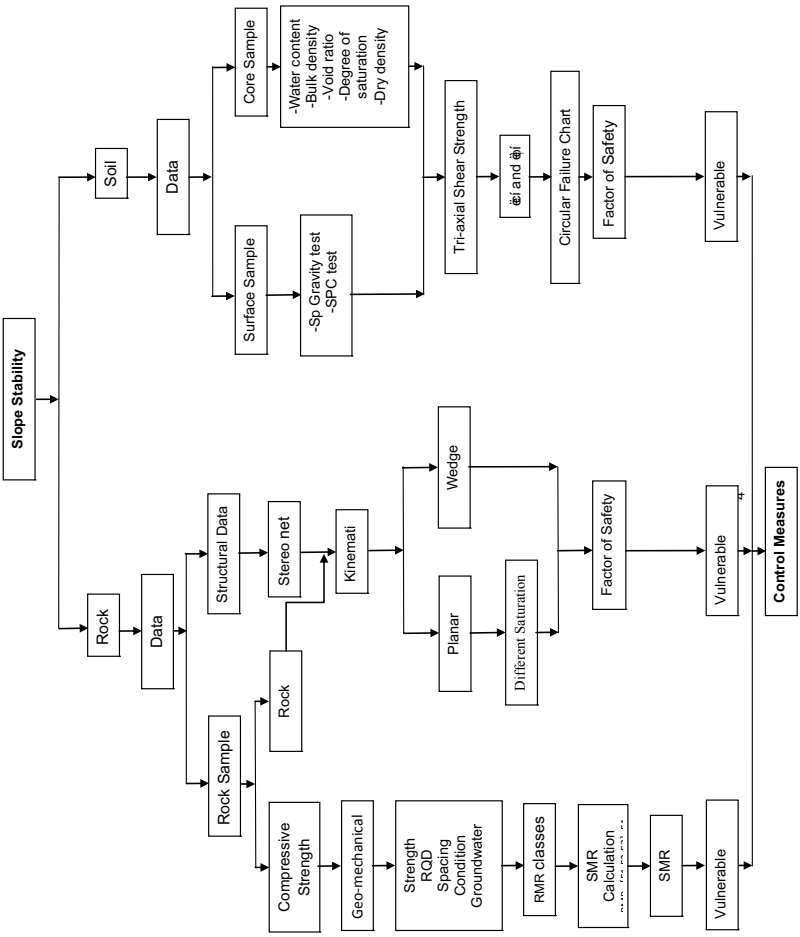

Fig. 6.3 Methodology flow chart

6.3.1 Rock Analysis

6.3.1.1 Rock Mass Rating (RMR)

RMR system, also called Geomechanical analysis, was developed by CSIR-South Africa (Bieniawski 1973). Bieniawski changed methodology in 1974, 1976, 1979, 1984, and 1989. The geometry and mechanical classification concern five important parameters are as follows (Anon IS 13365 Part I 1998).

1. UCS
2. RQD
3. Spacing of joints
4. Condition of joints
5. Groundwater condition.

Based on the above said parameter RMR_{basic} rating is obtaining a maximum value of 100. The maximum rating is classified into five different classes a very good rock (80–100), good rock (60–80), fair rock (40–60), poor rock (20–40), and very poor rock (0–20). The results are presented to conduct a detailed study in fair to deplorable rock conditions.

6.3.1.2 Slope Mass Rating (SMR)

SMR was developed by Romana (1985) and modified by Anbalagan et al. (1992) as an application of Bieniawski's (1989) RMR. Slope instability is assessed by risk parameter, failure mode, and excavation of the slope. SMR is derived from RMR by including correction factors. The SMR is calculated from the below Eq. (6.1)

$$\mathrm{SMR} = \mathrm{RMR}_{\mathrm{basic}} + (\mathrm{F1} \cdot \mathrm{F2} \cdot \mathrm{F3}) + F4 \tag{1}$$

where

F1—associated with discontinuities striking parallel to the slope
F3—regarding the slope inclination compared to the joint inclination angle; and
F2—correlated to the joint inclination for planar failure;
F4—involves the technique of excavation.

The maximum value obtained from SMR is 100. The rock slopes are divided into five stable classes totally unstable (<20), unstable (20–40), partially stable (40–60), stable (60–80), and fully stable (80–100). The study result demonstrated preliminary ideas to do a detailed study in particular planar and wedge discontinuity in the rock section. The density and unit weight of the rock sample was calculated by ISRM (1981) procedure and adapted to ASTM (1994).

6.3.2 Kinematic Analysis

The Kinematic analysis was introduced by Markland (1972), and Goodman (1989) explains kinematics to rock mass movement without indicating the forces that cause them to move. The discontinuities include geological disruptions such as foliation, faults, bedding planes, and sear zones, possibly as catastrophe planes. The kinematic analysis discontinuous surface of joints within the rocks has a relative displacement/movement. The joints and fractures in cut-slopes are measured using the Brenton compass in dip and strike. It calculates stability analysis of the slope on the stereo net used for plotting plane poles and dips vectors (Hoek and Bray 1981; Saranathan et al. 2014). This analysis is also called the graphical illustration of joints and slope data on the equal area/ angle stereo net. The straightforward method brings out an initial indication of probable failure and is delivered as an important structural geology tool. The main importance of this technique is that it represents and analyses three-dimensional orientation data of joint and slope face in two dimensional by removing one dimensional from consideration so lines and points, respectively, can represent that plan and lines. The seven vulnerable cut slopes were selected to perform this analysis. This analysis obtained through stereographic representation for seven sites using manual calculation infers the probability of wedge and planar failure modes as major structural instability on slopes.

Plane failure rarely occurs in rock sections, and all the geometrical circumstances shall cause failure in the actual slope. The wedge is a specific event and may rock specialists indulge the plane failure. The safety factor of these rock slopes in the ghat section is calculated using Hoek and Bray's simplified equation (Eq. 6.2). When the conditions of the inclination and penetration of water in the joint planes are identified, finding the factor of safety is simple

$$\mathrm{F} = (2\mathrm{c}/\gamma\mathrm{H}) \times P + \{\mathrm{Q} \times \cot\psi_{\mathrm{p}} - R(P+S)\}/\mathrm{Q} + R \times S \cot\psi_{\mathrm{p}} \quad (2)$$

The ratios P, Q, R, and S are dimensionless factors.

In planar, failures result from rock sections sliding on a sloping plane, but wedge failure occurs in the sloping summit, where slides happen along the line of intersections of two joint sections. The factor of safety is derived using Hoek and Bray's assumptions.

$$\mathrm{F} = \{3/\gamma\mathrm{H}\,(\mathrm{c_A} \cdot \mathrm{X} + \mathrm{c_B} \cdot \mathrm{Y})\} + \{(\mathrm{A} - (\gamma_{\mathrm{w}}/2\gamma) \cdot \mathrm{X})\} \tan\phi_{\mathrm{A}} + (\mathrm{B} - (\gamma_{\mathrm{w}}/2\gamma) \cdot \mathrm{Y}) \tan\phi_{\mathrm{B}} \quad (3)$$

The ratio X, Y, A, and B are dimensionless factors in Eq. (6.3).

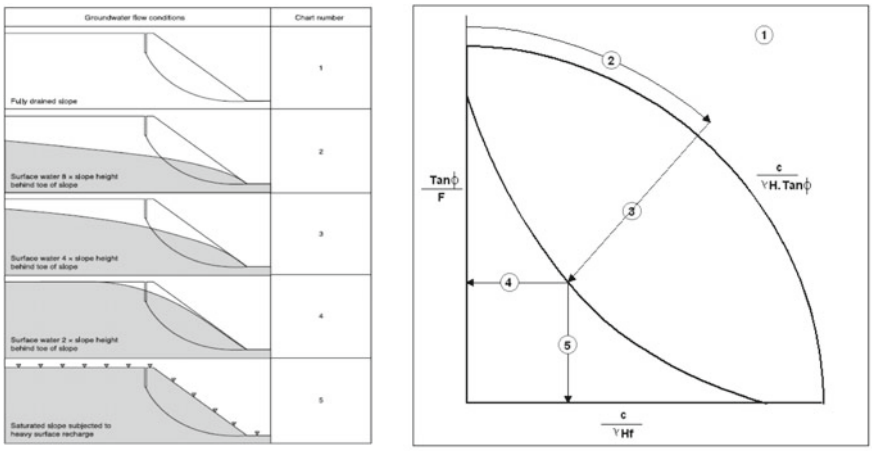

Fig. 6.4 **a** CFC groundwater flow conditions and **b** calculation of factor of safety from CFC (after Hoek and Bray 1981)

6.3.3 Circular Failure Chart (CFC) Method

In the rock slope, geological features play a major role in controlling the disaster. In the case of soil, a clear structural failure outline is absent, and the displacement surface is free to fail along the slope. The CFC was produced using Hewlett—Packard 91,008 calculator (Hoek and Bray 1981), and the charts were numbered 1–5 to correspond with groundwater conditions (Fig. 6.4a). The stages of failure outline are presented to determine the factor of safety of a soil slope using equation and the soil slope's geotechnical parameters. The dimensionless relation can be fixed in the fringe of each chart, and the joint of the radial line with the resultant slope inclination can be calculated. From this intersection, the factor of safety of *X* and *Y* is determined, and the average factor of safety is also determined (Fig. 6.4b). The basic geomechanical properties of rock and soil were determined to conduct the analysis.

6.4 Results and Discussion

6.4.1 Geo-mechanical Analysis

Seven rock slopes and three soil sections were identified and shown in Fig. 6.5. In this study, intact rock strength varies from 53.84 to 11.61 kg/cm^2 in all rock slopes. The rock strength has been calculated and differs from one slope to another, depending mainly on lithology, weathering, and available rock joints. The main purpose of this study is to identify the structural complication of soil and rock slopes. The planar

and wedge failure are the most predominant in intact rock (Chatziangelou et al. 2002; Kumar et al. 2020). Based on slope conditions and field observations, geomechanical parameters have been determined and presented in Table 6.1. Based on the SMR, slopes are grouped into five categories. At different locations, the rock mass values varied from 55 to 78.5, except for only two sections (R4 and R2) with good rock mass classes. Vulnerable rock slopes were assessed based on the obtained RMR and SMR values. Vulnerable sections were categorised into five SMR classes. The analysis shows that out of the seven rock slopes, two sections fall in class I (completely stable), two sections come under class II (stable), and four are in-classes III (partially stable). Table 6.2 presents the final result of SMR, which reveals more than 50% of the sections come under partially stable, and the remaining 50% fall under the stable and completely stable zone.

6.4.2 Kinematic Analysis

6.4.2.1 Plane Analysis

Based on the kinematic analysis, the possible pattern of failures is identified, and the safety factor is calculated (Hoek and Bray 1981; Anbalagan et al. 2007; Ramesh et al. 2017). As per Markland's test, a section has the possibility of plane displacement if it fulfills $\psi s > \psi p > \phi$ (inclination of the slope, failure plane, and angle of friction). After collecting the field data, seven vulnerable cut slopes were investigated in detail. The 5 sections, namely R1–J1; R2–J1; R3–J2, J3; R6–J2; and R7–J1, satisfy the plane failure condition. The details are given in the following, R1 rock section is present in 10° 18′ 33″ N; 77° 33′ 32″ E latitude and longitude, respectively. The safety factor was calculated by Hoek and Bray equation (Eq. 6.3), and the slope condition is $z = z_w$. The factor of safety of the joint is less than one in partially and fully saturation conditions. In the R2 section, three sets of joints are identified, and joint 1 is taken for a factor of safety analysis. The safety factor is less than one (0.9, 0.6, and 0.3) and shows unstable conditions. The location R3 is very near the 9th km stone, and a major slide occurred. The tension cracks are wide-open on the upper slopes. The rock section is steep (65°). Joints J2 and J3 fulfil the criteria, and the safety factor is 0.8 and 0.16, respectively. The J2 is almost close to the natural slope, showing unstable conditions. This is further indicated in the stereo-net study. In the R6 section, J2 satisfies the condition. The inclination of the joint (26°) is very near to the natural slope (27°). As per the calculation, the factor of safety of this slope is 3.6, 1.2, and 0.8. It is shown that the cut slope is unstable in fully saturation conditions. R7 section, five prominent joint sets are present. It is 150 m away from the 9th km stone. The factor of safety is less than one (0.717) as per the calculation. This section is not stable, and the results are presented in Table 6.3.

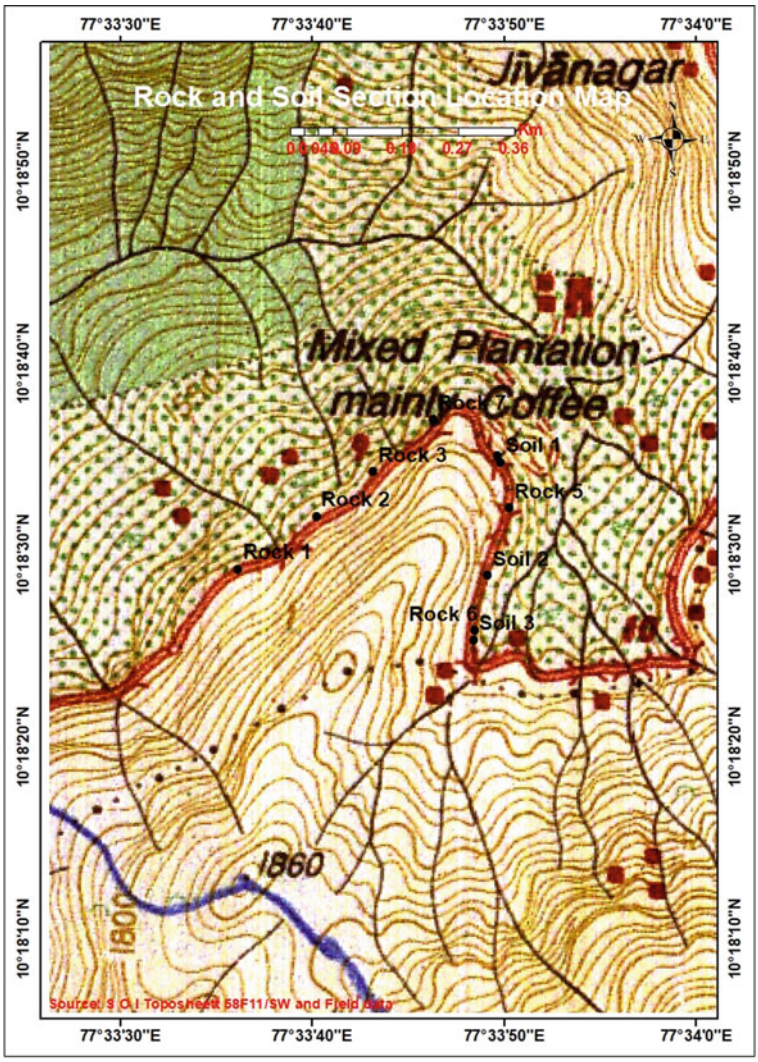

Fig. 6.5 Major and minor Slides in topo sheet No. 58F/11-SW

6.4.2.2 Wedge Analysis

The possible wedge catastrophe is evident where several joint groups and one or two face planes in the rock occur. In the rock sections, typically, there are two free discontinuities present. The lower portion could have a high dip, while the upper outcrop can be a horizontal surface or a low-angle dip. In all the above cases, the wedge failure study can be performed. Of the total of seven vulnerable rock slopes, five slopes fulfilled the condition of wedge failure ($\psi s > \psi i > \phi$). The wedge failure

Table 6.1 RMR rating

Location	Rock type	Joint ID	Ratings					RMR value	Class	Description	C kPa	Phi (°)
			Strength of rock	RQD	Spacing of discontinuity	Condition of discontinuity	Ground water condition					
R1	Gneiss	J1	15	13	10	10	10	58	III	Fair rock	290	34
R2		J1	15	13	10	12	10	60	III	Fair rock	300	35
R3		J3	15	17	15	08	0	55	III	Fair rock	275	32
R4		J1	15	17	15	22	10	79	II	Good	395	44
R5		J2	12	8	10	18	10	58	III	Fair rock	290	34
R6		J2	12	8	15	20	10	55	III	Fair rock	275	32 30′
R7		J1	15	20	20	13.5	10	78.5	II	Good	390	44

Table 6.2 Stability classes based on SMR rating

Slope section No.	RMR	SMR along probable failure planes	Min. SMR	Class	Stability
R1	58	J1 = 21 [P]; J1–J3 = 22 [W]	58	III	Partially stable
R2	60	J1 = 24 [P]; J1–J2 = 24 [W]	44	III	Partially stable
R3	55	J2 = 32 [P]; J2–J4 = 34 [W]	59.2; 58.82	III	Partially stable
R3	55	J3 = 88 [P]	79	II	Stable
R3	55	J1–J4 = 52 [W]	98	I	Completely stable
R4	79	J1 = 64 [P]	96	I	Completely stable
R6	55	J2 = 26 [P]	55.36	III	Partially stable
R6	55	J1–J2 = 26 [W]	66.68	II	Stable
R7	78.5	J1 = 20 [P]; J4–J5 = 10 [W]; J2–J4 = 22 [W]; J1–J5 = 16 [W]	78.5	II	Stable

Table 6.3 Factor of Safety of Planar analysis

Sl. No.	Rock section	Factor of safety in		
		Dry condition	50% saturation	Fully saturation
1	R1/J1	0.4558	0.1068	<1
2	R2/J1	0.9823	0.6378	0.3254
3	R3/J3	1.0023	0.454	<1
4	R3/J5	0.5621	0.367	0.1122
5	R3/J2	5.3262	2.1823	0.8245
6	R6/J2	3.6242	1.1274	0.8125
7	R7/J1	2.6528	0.7171	0.3914

was examined and completed after observed field data associated with the geological joints and it has been plotted through in the stereo-net (Hoek and Bray 1981). The detailed analysis results of the five sections (R1 J1–J3; R3 J1–J2, J1–J4, J2–J4; R4 J1–J2; R6 J1–J2; R7 J1–J5, J2–J4, J4–J5) showed as fallow, in the R1 section, three joints are present and well exposed with gneissic rock, and this cut slope J1 and J3 is a fulfilling condition. The factor of safety value is determined as less than one. R3 section is located in 9th km stone. The wedge analysis stabilises J1–J4; J2–J4 and J1–J5, and J1–J2 discontinuity, and factor of safety is 0.221, 5.304, 0.703, and 4.162, respectively. The plunge of wedges J1–J4 and J1–J5 are high light on the slope, showing that it is unsafe. The R4 section is located in 10° 18′14″ N and 77° 33′ 43″ E. The tension crack and joints are exposed on the upper slope. The J1 and J2 satisfy the wedge analysis. The plunge is N 55°, and dip 64° is visible in the rock section.

Table 6.4 Factor of safety of wedge analysis

Sl. No.	Section No.	Discontinuity	Factor of safety
1	R1	J1–J3	<1
2	R3	J2–J4	5.3509
3	R3	J1–J4	0.2213
4	R3	J1–J5	0.7038
5	R3	J1–J2	4.162
6	R4	J1–J2	0.354
7	R6	J1–J2	0.499
8	R7	J4–J5	1.9217
9	R7	J1–J5	1.9172
10	R7	J2–J4	0.114

The factor of safety is less than one (0.354), and it is obviously unsafe. In the R6 section, three joints are present J2–J1 is taken into wedge analysis. The inclination of the plunge (26°) is very close to the natural slope (27°), and the factor of safety is less than one (0.499). In the R7 section, three prominent wedges are present. In the cut slope, the height is around 12 m. The wedge discontinuity J1–J5; J2–J4; and J4–J5 are calculated. Hoek & Bray's method calculated the factor of safety as 1.917, 0.114, and 1.921. The J2–J4 wedge is unsafe and may fail in moderate rainfall. However, most of the wedge conditions are stable in SMR analysis but unstable in the detailed kinematic wedge investigation performed by Hoek and Bray method. The details are furnished in Tables 6.4.

6.4.3 CFC Analysis

The study area has a rock-dominated terrain with soil and debris materials occupying the surface area in several locations. The soil section (S1, S2, and S3) instability was examined by the CFC method (Hoek and Bray 1981; Kannan et al. 2017). The elevation of the section ranges up to 5 m and can be seen as 50% of the length. Another 50% of the road length may have up to 8 m of height. Three vulnerable soil sections were notified in the present study area. Geotechnical tests were conducted to determine the soil parameters of the collected samples. The laboratory results are presented in Table 6.5, 6.6, 6.7, 6.8, and 6.9. The factor of safety calculated under various groundwater fullness conditions using the CFC technique is given in Table 6.10. The results have shown that slopes S1 and S3 come under unsafe conditions. However, all the soil sections are unsafe for heavy rainfall.

Table 6.5 Pycnometer—Sp. Gravity results

1	Weight of pycnometer (W1) g	0.600
2	Weight of pycnometer + dry soil (W2) g	0.872
3	Weight of pycnometer + soil + water (W3) g	1.514
4	Weight of pycnometer + water (W4) g	1.360
5	Specific gravity	0.1940

Table 6.6 Density of soil results using Core cutter method

1	Weight of core cutter (W1) g	0.966
2	Weight of soil + core cutter (W2) g	2.348
3	Weight of soil (W2–W1) g	1.382
4	Volume of core cutter (V) cm^2	1020.825
5	Field density of soil (W2–W1)/V	1.3538

Table 6.7 Shows dry density of soil

1	Weight of container + wet soil g	0.048
2	Weight of container + dry soil g	0.040
3	Weight of dry soil g	2.22
4	Weight of water g	0.008
5	Water content (w) %	36.363
6	In-situ dry density of the soil g/cm^3	0.03623

Table 6.8 Standard Proctor lab results

Description	Trial 1	Trial 2	Trial 3	Trial 4	Trial 5	Trial	Trial 7	Trial 8
Wt. of mould with compacted soil (W2) g	3.448	3.538	3.598	3.716	3.848	3.914	3.960	3.952
Wt. of compacted soil (W2–W1) g	3.228	3.318	3.378	3.496	3.628	3.649	3.740	3.732
Wet density (Pb) g/cm^3	3.288	3.379	3.441	3.561	3.695	3.763	3.8095	3.8013
Dry density (Pd) g/cm^3	0.088	0.0904	0.0921	0.0953	0.0989	0.1007	0.1019	0.1017
Moisture content %	10	13	16	20	23	26	29	30

6.5 Conclusions

The geo-mechanical and kinematic method was employed for instability and vulnerability analysis. The geo-mechanical is an easy method for preliminary assessment. The kinematic method is a detailed one and finds factors of safety and slope condition. The continuous heavy rainfall over a localised area and its long-term percolation process are the leading causes of degradation of the soil, rock, and slope failure in this study area. Initially, a detailed geological and geotechnical field survey was carried

Table 6.9 Result of Tri-axial shear test

S.No.	Soil section	Cell pressure (kg/cm^2)	Deviator stress (KN)	Normal stress (KN)	Cohesion of soil (kPa)	Angle of shearing resistance (°)
1	S1	1.0	358.5	458.5	224	22
2		1.5	847.5	997.4		
3		2.0	892.3	1092.3		
4	S2	1.0	594.2	642.0	170	19
5		1.5	793.0	943.0		
6		2.0	673.1	873.1		
7	S3	1.0	781.2	881.25	215	24
8		1.5	625.0	775.0		
9		2.0	924.6	1124.6		

Note The tri-axial shear test has been conducted per the technique given in BIS: 2720

out to examine the in-situ slope condition in this area. The RMR analysis concludes that R1, R2, R3, R5, and R6 belong to fair rock (class III), whereas R4 and R7 belong to good rock (class II). The modified SMR values have been found for the planar and wedge for all rock sections. The cut slopes R1, R2, R3, and R6, give values between 44–58 for wedge failure, and the rock slopes fall in class III, i.e. partially stable. In R3, R6, and R7, rock slopes have SMR values of 79, 66, and 78.5 for existing planar failure (R3) and wedge failures (R6 and R7), respectively. Hoek and Bray's planar analysis show that four rock slope discontinuities are unstable (R1–J1, R2–J1, R3–J5, R7–J1), whereas the factor safety is less than 1. Through the wedge analysis, it is found that there are six rock slopes joint sets are unstable (R1 J–J3, R3 J1–J4 and J1–J5, R4 J1–J2, R6 J1–J2, R7 J2–J4) and having a factor of safety less than 1. As per the CFC method, soil slopes 1 and 3 are unstable for 50% and fully saturated conditions compared to other 3 soil slopes. The soil Sect. 2 demonstrates stable conditions; however it may slide during heavy rainfall conditions.

According to slope ingredients and geometry, a set of control procedures has been recommended to recover slope stability. The most commonly adopted remedial measure for steep cut slopes is to alter the slope geometry to a stable angle. The section above the road is regraded to an inclination of 35°. Individual cut sections with a vertical height of about 1.5 m and a bench width of about 2 m could be excavated to resolve the unsafe slope cut. The regraded section will be more established with an improved factor of safety. On the hillside, just adjoining the road, the slope may be supported with the help of a retaining wall. The retaining walls could be constructed and the easiest and cheapest method is drum filled retaining wall. The valley side of the road may be excavated to a proper depth to facilitate the packing of two to three rows of debris-filled tar drums. Dry boulder pitching should be done on the slope above the drums to prevent erosion. It is suitable for slopes less than 45°.

Table 6.10 Factor of safety of soil section

Sl. No.	Soil section	Soil			Chart no	Water saturation (%)	Intercept		Factor of safety
		Density (kN/m^3)	Cohesion (kPa)	Angle of internal friction (°)			**X**	**Y**	
1	S1	1.3538	224	22	1	25	1.342	1.515	1.428
					3	50	0.502	0.499	0.501
					5	100	0.424	0.423	0.424
2	S2	1.3538	170	19	1	25	1.255	1.186	1.221
					3	50	1.162	1.111	1.136
					5	100	1.034	1.044	1.039
3	S3	13,538	215	24	1	25	1.185	1.174	1.179
					3	50	1.046	1013	1.029
					5	100	0.889	0.880	0.885

Acknowledgements Authors are thankful to Dr. R. Anbalagan, Retired Professor, Department of Earth Science, Indian Institute of Technology Roorkee, India, for his valuable comments and corrections. Authors are also grateful to anonymous referees for their critical comments and suggestion.

References

Aleotti P, Chowdhury R (1999) Landslide hazard assessment: summary review and new perspectives. Bull Eng Geol Env 58:21–44. https://doi.org/10.1007/s100640050066.

American Society for Testing Materials (ASTM) (1994) Annual book for ASTM standards-construction: soil and Rocks. ASTM Publication, West Conshohocken, PA.

Anbalagan R, Sharma S, Raghuvanshi TK (1992) Rock mass stability evaluation using modified SMR approach. In: 6th national symposium on rock mechanics, proceedings, vol 1, p 258–268.

Anbalagan R, Singh B, Chakraborty D, Kohli A (2007) A field manual for landslide investigation. Government of India, Delhi.

Anbalagan R, Kohli A, Chakraborty D (2008) Geotechnical evaluation of Harmony landslide on Karnaprayag-Gwaldam Road. Uttarakhand Himalaya. Curr Sci 94(12):1613–1619.

Anbazhagan S, Saranathan E (2001) Structure and its impact on the drainage in part of Ponnaiyar river basin, Tamilnadu using remote sensing techniques. J. Indian Soc. Remote Sens 29(4):187–195.

Anon (2012). Hill road manual. The Indian Roads Congress (IRC), Jamnagar House, New Delhi.

Anon, Bureau of Indian Standard, IS 13365 (Part 1) (1998) Quantitative classification systems of rock mass guidelines—rock mass rating (RMR) for predicting engineering properties. BIS, New Delhi.

Bieniawski ZT (1973) Engineering classification of jointed rock masses. Trans South Af Inst Civil Eng 15(12):335–344.

Bieniawski ZT (1976) Rock mass classification in rock engineering. In: Bieniawski ZT (ed) Exploration for rock engineering, proceedings of the symposium exploration. Rock Engineering, Johannesburg, p 97–10.

Bieniawski ZT (1979) The geomechanics classification in rock engineering applications. In: Proceedings of the 4th international congress rock mechanics, Montreux, Balkema, Rotterdam, vol 2, p 41–48.

Bieniawski ZT (1989) Engineering rock mass classifications. Wiley, Chichester.

Chatziangelou M, Christaras B, Dimopoulos G, Soulios G, Kilias A (2002) Support of unstable wedges along the Platamon railway tunnel under construction, in northern Greece. Eng Geol 65:233–243.

Goodman RE (1989) Introduction to rock mechanics, 2nd edn. Wiley, New York.

Hoek E, Bray JW (1981) Rock slope engineering. Stephen Austin and Sons Limited Publishers, Hertford.

International Society of Rock Mechanics (ISRM) (1981) Rock characterisation, testing and monitoring. In: Brown ET (ed) ISRM suggested methods. Pergamum Press, Oxford.

Kannan M, Saranaathan SE, Anabalagan R (2017) Soil slope stability analysis by circular failure chart method, A case study in Bodi—Bodimettu Ghat section, Theni district, Tamil Nadu. India. Int J Earth Sci Eng 10(6):1163–1167. https://doi.org/10.21276/ijee.2017.10.060

Kumar KPVM, Aravind S, Ramkumarm K, Saranaathanm SE, Prasanna Venkatesh S (2020) Slope stability evaluation by geo-mechanical and kinematic analysis in 403 & 403A km stretch between Vaiyampatti—Ayyalur Railway section, Dindigul, Tamil Nadu. Int J Latest Res Eng Technol 6(8):31–44.

Markland, JT (1972) A useful technique for estimating the stability of rock slopes when the rigid wedge sliding type of failure is expected. Imperial College Rock Mechanics Research Report No. 19.

Ramesh V, Anabazhagan S, Saranaathan SE (2017) Cut slope stability assessment along Ghat Section of Kolli Hills, India. Nat Haz 86(3):1081–1104. https://doi.org/10.1007/s11069-016-2731-0.

Romana, M (1985) New adjustment ratings for application of Bieniawski classification to slopes. In: Proceedings of the international symposium on the role of rock mechanics in excavations for mining and civil works. International society of rock mechanics, Zacatecas, p 49–53.

Saranaathan SE, Kannan M (2017) SMR and kinematic analysis for slope instability along Bodi—Bodimettu Ghat section, Tamil Nadu, India. J Geol Soc India 89:589–599. https://doi.org/10.1007/s12594-017-0648-1.

Saranathan SE, Kanagasabai S, Kannan M, Venkatraman GK (2014) A geotechnical assessment of slope stability condition at Lovedale Club Slide, Lovedale, The Nilgiris, Tamil Nadu. Int J Earth Sci Eng 7(1):251–259.

Sharma RK, Mehta BS, Jamwal CS (2013) Cut slope stability evaluation of NH-21 along Natayan-Gambhrola section, Bilaspur district, Himachal Pradesh, India. Nat Haz 66:249–270. https://doi.org/10.1007/s11069-012-0469-x.

Singh TN, Verma AK, Sarkar K (2010) Static and dynamic analysis of a landslide. Geomat Nat Haz Risk 1(4):323–338.

Vinay, PN, Prasanna Venkatesh S, Saranaathan SE (2018) Geomechanical analysis of recent (2017) rock fall in Tirupati—Tirumal Ghat Section II near 9th Mile stone, Tirupati, A.P. Int J Earth Sci Eng 11(4):281–287. https://doi.org/10.21276/ijee.2018.11.0404.

Chapter 7
Geological and Geotechnical Studies of Nungkao Landslide Along Imphal-Jiribam National Highway, NH-37, Manipur, India

Kh. Mohon Singh and M. Okendro

Abstract Landslide on a mountainous stretch of the National Highway is a serious concern because they hinder traffic. Anthropogenic activities in the large-scale excavation of the natural slope to expand the existing national highway can significantly alter the slope mass sliding properties. The present study examines the rock mass current geotechnical state and the locations of potential failures in the Imphal Jiribum national highway of (NH-37) in Manipur. Rock mass characterizations and uniaxial compression strength tests have been carried out for the entire study area. According to kinematic analysis and field observations, the study result reveals that the Nungkao landslide is unstable. Wedge collapses are dominant. The factor of safety for rock wedge failure mode has indicated stable conditions. Based on the plasticity index chart, soil samples collected from the site have lower moisture content, which indicates that the soil is of an inorganic origin. The negative (−ve) value of the liquidity index (−1.18) and the positive (+ve) value of the consistency index (3.03) infer that the slope materials remain in the solid-state or semi-solid state, which indicates the slope is stable. Safety factor calculation also shows stable soil slope conditions. However, frequent slides still occur in the area. Effective preventive measures are suggested to improve slope stability accordingly.

Keywords Slope mass rating (SMR) · Kinematic analysis · Uniaxial compressive strength (UCS) · Factors of safety · Nungkao—Manipur

7.1 Introduction

Landslide generally occurs in mountainous and hilly areas with thick or thin soil and/ or weathered rocks. It is a common natural hazard in the hilly terrain of Manipur, causing immense threats to life, extensive losses, and environmental problems. Despite advances in science and technology, economic and societal losses due

Kh. Mohon Singh (✉) · M. Okendro
Department of Geology, Imphal College, Imphal 795001, Manipur, India
e-mail: khuraijammohonsingh98@gmail.com

P. Thambidurai and T. N. Singh (eds.), *Landslides: Detection, Prediction and Monitoring*,
https://doi.org/10.1007/978-3-031-23859-8_7

to landslides are still a major concern in the public domain. The study area is an integral part of the mobile belt of the Indo-Myanmar Range. In any weather, the frequent landslides on Highway 37 obstruct the free flow of traffic. People and infrastructure may be put at risk because of the unpredictability of rockfall events' frequency and size (Dorren 2003). Natural slopes become more vulnerable to failures when converted into cut slopes by human intervention for the purpose of transportation work, construction of dams, bridges, tunnels and other civil engineering structures (Vishal et al. 2010; Das et al. 2010). In the wet season, Nungkao road cut slope is particularly fragile and often suffers from rock falls. A number of hanging blocks have been discovered on site slopes as a result of blasting and mechanical excavation. The area is vulnerable to collapse because of the steep slope of the road. Geomechanical classification of the rock mass (Bieniawski 1979) was also used, with the application of a rock mass rating (RMR) system (Bieniawski 1974, 1975, 1976, 1989). RMR is a rating-based classification method in which ratings have been given to different parameters influencing the stability of rock mass, and their algebraic sum defines the quality of rock mass.The methodologies applied are obviously simple but an effective ways to describe the potential behaviour of the rock mass with respect to the probability of occurrence of slope movements. A greater knowledge of the variables that lead to landslides may help reduce the risk of rockslides. Rock mass rating (RMR) is a useful tool in describing rock masses among the several approaches for identifying rock masses. The RMR method is used to examine the strength of the exposed rocks on the slope face, the spacing and direction of discontinuities, and the conditions of groundwater. Generally, a landslide study aims to interpret the safety factor of either or both the soil and rock slopes by applying the most feasible and reliable techniques from the available resources.

7.2 Study Area

The Barak basin is a crucial element of the Indo-Myanmar orogenic belts. The Nungkao Landslide is located at 24º46´29.00˝N and 93º18´45.00˝E on toposheet No. 83 H/5 of the Survey of India. The landslide is located at an elevation of 264 m above sea level, around 138.6 kms from Imphal, the capital city (Fig. 7.1). It is located at Tamenglong district of Manipur along Imphal-Jiribam National Highway 37.

The rock exposure in the present study area belongs to the Surma group of rocks (Fig. 7.2). It occupies most of the western hills of the state, Manipur. Surmas are considered as the molasse deposits, which are well developed in Mizoram and have its extension up to Manipur and Nagaland.

Intercalations of light grey, fine to medium grain; thickly bedded, massive sandstones and dark grey, fine-grained; laminated to thinly bedded shale and siltstone form this group. Sandstone from Surma is composed of quartz, lithic pieces (plagioclase), and K-feldspar. The block size varies widely across slopes, resulting in irregular rock falls. Despite the fact that mechanical excavation has caused the parallel bedding joints to lose their continuity, their persistence has been substantially decreased. The

Fig. 7.1 Slope section of Nungkao Landslide showing variable block size due to uncontrolled blasting

most common method of detaching a wedge is not by sliding it along the junction line but rather by causing it to fall naturally. The other causes of the landslide are structural features and lithological parameters, which are aggravated by anthropological and other factors. An attempt has been made to interpret the nature of the slide/fall in the area.

7.3 Methodology

The methodology designed for this study is to identify potential points of failure in the region. To begin with, a geotechnical examination on soil and rock is carried out. Further, combined data (persistence, spacing, aperture, and infilling) are analysed. Using RMR and failure mode analysis, SMR values shall be obtained for each block. The steps in the process are described in detail in the sections that follow.

7.3.1 Geotechnical Approach

In order to determine the strength of the slope-forming rocks and soils, a study on mechanical strength is essential in landslide investigation. The mechanical strength of rock and soil may be evaluated using a variety of techniques. The characteristics of rock strength in uniaxial compression (C_o), in tension (T), and in shear (τ) are widely used parameters of rock mechanics. Uniaxial compression and Brazilian

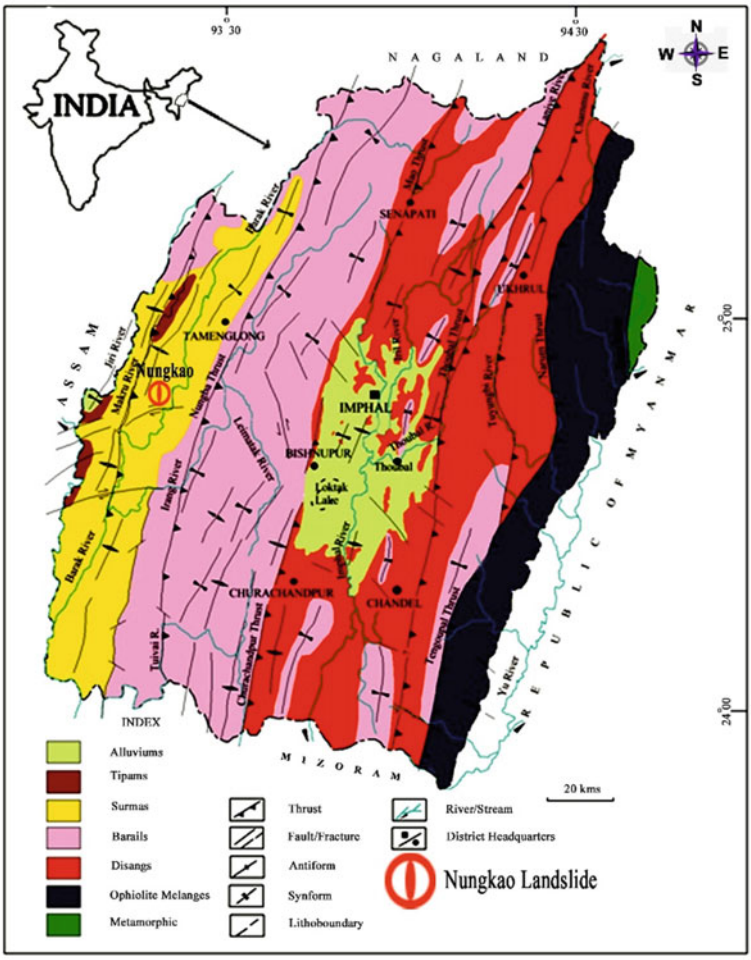

Fig. 7.2 Geological map of Manipur showing Nungkao landslide

tests are used in this investigation to evaluate the unconfined compressive and tensile strengths of rocks from the Surma group in the study region. The "Core Drilling Machine" is used to cut samples perpendicular and parallel to the bedding. Samples of a cylindrical core with a length-to-diameter ratio of 2:1 and 1:1 were obtained for the Compressive and Brazilian tests.

Compressive Strength International Society for Rock Mechanics (ISRM) recommends a standard approach for evaluating the compressive strength of rock with a 42 ± 3 mm diameter cylindrical sample. Four samples, each one parallel to and perpendicular to bedding, have been tested and it is represented by relationship

$$C_0 = C_s(0.8 + 0.2/D) \tag{7.1}$$

Table 7.1 Mean Uniaxial Compressive strength (UCS)

Rock sample nature	Load (P) in kN	Mean diameter (cm)	Radius (cm)	Compressive strength $C_0 = P/A(P/\pi r^2)$ in MPa
Parallel	55.04	3.29	1.65	64.75
Perpendicular	77	3.308	1.655	89.75
Mean	66.02	3.3	1.65	77.25

where, C_0 is the observed compressive strength, D is the diameter of the specimen for which $2 > D > 1/3$ is assumed, C_s is regarded as the standard compressive (uniaxial) strength (at least three tests conducted).

Generally, the uniaxial compressive strength, C_0 is given by

$$C_0 = P/A \tag{7.2}$$

where, P = applied load, A = cross-sectional area of the sample. Uniaxial compressive strength is determined for the Surma sandstones parallel and perpendicular to bedding, and the results are shown in Table 7.1.

Tensile Strength It is also called Brazilian Test. The same compressive machine is used in this test. When the compressive force is applied to the sample, it fails due to tension. So, tensile strength is given by

$$T_b = 2P/\pi DL; \tag{7.3}$$

where P stands for the applied force, D for the sample diameter, and L for the sample length

The International Society for Rock Mechanics (ISRM) recommends a 54-mm diameter, a 200-N-per-second stress rate, and a 200-N-per-second tensile strength (ISRM 1981):

$$T_b = 0.636P/DL; \tag{7.4}$$

where P stands for the applied force, D for the sample diameter, and L for the sample length. Tensile strength determined by the Brazilian test is presented in Table 7.2.

Failure Envelope

Table 7.2 Mean tensile strength

Rock sample nature	Load (P) in kN	Mean diameter (cm)	Mean length (cm)	Tensile strength $T = 2P/\pi DL$(MPa)
Perpendicular	13.96	3.32	3.48	8
Parallel	11.625	3.321	3.4375	6.5
Mean	12.79	3.32	3.43	7.25

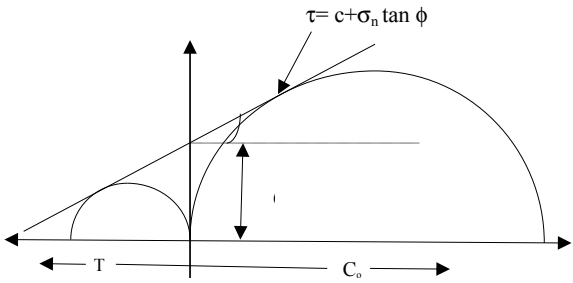

Fig. 7.3 Mohr's failure envelope

Table 7.3 Strength parameters of samples

Rock sample	Cohesion C (MPa)	Internal friction angle, ϕ	Normal stress σ_n (MPa)	Shear strength $\tau = C + \sigma_n \tan\phi$ (MPa)
Perpendicular	12.65	55.75	5.25	23.14
Parallel	9.00	53.87	6.37	17.72
Mean	10.81	54.81	5.81	20.43

Mohr's stress circle, which displays compressive strength values to the right of zero on the circle, can be used to display the results of these tests.

Tensile strength is to the left of zero on the horizontal axis. The diameter of the circles is determined by the uniaxial compressive and tensile strength factors (Fig. 7.3). Figure 7.3 shows a common tangent created between the two circles. When the Y-axis or Shear Stress τ-axis (Y) is intersected with this line, the value of cohesion, C, is calculated. The magnitude of normal stress is given by the point where this tangent intersects the right circle, σ_n (along the x-axis). The failure envelope may be calculated using the formula $\tau = C + \sigma_n \tan\phi$, i.e., its shear strength parameters(Table 7.3).

As a result, an average UCS of 77.25 MPa is used for slope stability study of RMR and SMR rock.

Kinematic Analysis Discontinuities data are collected from the field to analyse various slope failure modes. Rockpack III software is used to establish the mode of slope collapses. The discontinuity data collected from the field is analysed and aggregated in a scientific manner (Fig. 7.4).

The intersecting line of discontinuity planes is found in the shadow zone, with a 60°/092° dip, using Rockpack III. The most common type of landslide collapse is wedge failure. During a wedge failure, the slope face's dip angle is less than the line of discontinuity's plunge angle (Markland test). Researchers Markland (1972), Hocking (1976), Cruden (1978), Goodman (1976), Hoek and Bray (1981), Lucas (1980), Matherson (1988), Yoon et al. (2002) and Saranaathan and Kannan (2017) have used this strategy. The probability of failure and the mode of failure are determined using discontinuity-slope surface connections (Kliche 1999). Technically, the breakdown was caused by a wedge failure (Fig. 7.4).

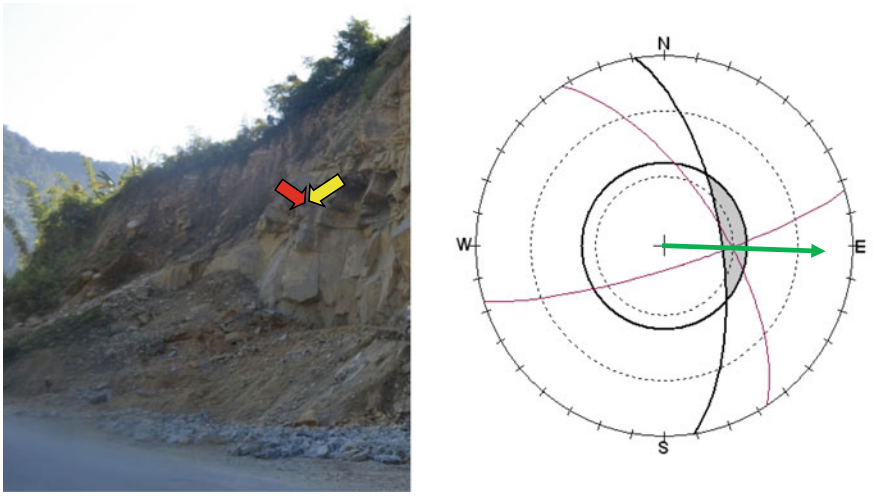

Fig. 7.4 **a** Field photograph and **b** Stereoplot showing probable mode of Wedge failure

7.3.2 Rock Mass Rating (RMR)

The modified RMR (Bieniawski 1979) utilizes the first five parameters, namely rock strength (RQD), spacing of discontinuities (discontinuity conditions), and groundwater conditions, to classify rock masses (and discontinuity orientation). All the ratings are algebraically summarized and can be adjusted with discontinuity orientation as shown in the following equations, and the values so obtained are shown in Tables 7.4, 7.5, and 7.6.

$$\text{RMR} = \text{RMR}_{basic} + \text{adjustment of discontinuity orientation} \tag{7.5}$$

$$\text{RMR}_{basic} = \sum \text{parameters (i + ii + iii + iv + v)} \tag{7.6}$$

Table 7.4 Slope characteristics and Strength Parameters of the Landslide area

Station	Location	Attitude of slope (°)	Type of Rock	Discontinuity attitude (°)	Degree of weathering	Strength
						Qc (MPa)
Nungkao	24º46´29.00˝N 93º18´45.00˝E	65/081	Massive to thickly bedded sandstone	66/057 80/163	Low	77.25

Table 7.5 Orientation of Discontinuities and Slopes

Station	Aj	Bj	As	Bs	Aj–As	Bj + Bs−180	Probable failure
Nungkao	98	81	81	65	17	34	Wedge

Table 7.6 RMR Determination

Station	Strength	RQD	Spacing	jL	jR	jA	jC	Ground water	RMR
Nungkao	7	17	15	2	2	1	4	15	58

jL = joint continuity or length, jR = joint roughness, jA = joint alteration, jC = joint condition factor

The algebraic sum of the parameters is the numerical value of RMR. It is indicated that the RMR value belongs to the fair rock category of class III. Slope mass rating (SMR) is a modified form of Bieniawski's rock mass rating used to evaluate slope stability. To overcome the shortcomings of RMR, Romana (1993) suggested the SMR system, which includes adjustment factors (F_1, F_2, and F_3) in RMR. Finally, Eq. (7.7) can be used to calculate SMR (Romana 1985, 1993; Romana et al. 2003).

$$\mathbf{SMR} = \mathbf{RMR}_b + (\mathbf{F_1} \times \mathbf{F_2} \times \mathbf{F_3}) + \mathbf{F_4} \tag{7.7}$$

Bieniawski rock mass classification RMR index is $\mathbf{F_1}$ is the parallelism between discontinuity dip direction and slope dip; $\mathbf{F_2}$ is the discontinuity dip; $\mathbf{F_3}$ is the slope-discontinuity connection, and $\mathbf{F_4}$ is a correction factor that varies based on the excavation method**.** The value obtained from the addition of adjustment factors is then summed up with RMR_B in order to get the total SMR value (Table 7.7).

Due to the modified SMR study's inability to show the factor of safety (F) instability's full extent, a stability analysis based on Hoek and Bray (1981) wedge failure calculation may be used.

7.3.2.1 Calculation of Factor of Safety (F) for Wedge Failure

In the present study, the calculation of the factor of safety (F) is governed by Hoek and Bray's (1981) method. In the mode of failure, planar, wedge, and toppling are considered. Wedge failure is observed and accordingly makes an attempt to interpret safety factors. For **wedge** failure, the following formula is utilized

$$F = \frac{3}{\gamma H}(C_A.X + C_B.Y) + \left(A - \frac{\gamma_\omega}{2\gamma}.X\right)\mathrm{Tan}\varnothing_A + \left(B - \frac{\gamma_\omega}{2\gamma}.Y\right)\mathrm{Tan}\varnothing_B$$

where, C_A and C_B are the cohesion of the planes A and B.
Φ_A and Φ_B are the angles of friction on joint/weak/discontinuities planes A and B, respectively

Table 7.7 Calculation of SMR and stability classes

Station	RMR	Rating for adjustment factor				SMR	CLASS	Description	Stability	Failure	Support
		F_1	F_2	F_3	F_4						
Nungkao	58	0.7	1.0	−25	0	41	III	Normal	Partially Stable	Some joints or many wedges	Systematic

Table 7.8 Result of soil test for Nungkao

Moisture content	Specific gravity	Plastic limit	Liquid limit	Shrinkage limit	Plasticity index	Liquidity index	Consistency index
12.91	2.6	22.02	26.5	30.22	4.48	−1.18	3.03

Table 7.9 Values of Liquidity Index (I_L) and Consistency Index (I_C) to consistency of soil (Murthy, 2007)

Consistency	Liquidity Index (I_L)	Consistency Index (I_C)
Semi-solid or Solid State	Negative	>1
Very stiff state	0	1
Very soft state	1	0
Liquid State(when disturbed)	>1	Negative

γ is the unit weight of the rock in g/cc, γ_ω is the unit weight of water in g/cc, and H is the total height of the wedge in cm

X, Y, A, and B are dimensionless factors that depend upon the geometry of the wedge

$X = Sin\theta_{24} / Sin\theta_{45}.Cos2_{na}$

$Y = Sin\theta_{13} / Sin\theta_{35}.Cos1_{nb}$

$A = Cos\psi_a - Cos\psi_b.Cos\theta_{na.nb} / Sin\psi_5.Sin2\theta_{na.nb}$

$B = Cos\psi_b - Cos\psi a.Cos\theta_{na.nb} / Sin\psi 5.Sin2\theta_{na.nb}$,

where,ψ_a and ψ_b are the dips of planes A and B, respectively, and ψ_5 is the dip of intersection.

7.3.2.2 Study of Soil Properties

In landslide investigation, it is essential to understand the characteristics of soil morphology. Laboratory analysis of soil samples was done, and the results are presented in Tables 7.8 and 7.9.

The soil samples fall into the inorganic clay group on the plasticity index chart, suggesting a more inorganic soil composition. Consequently, the (−ve) liquidity index (**−1.18**) and the (+ve) consistency index (**3.03**) suggest that the slope-forming materials exist as solid or semi-solid material.

7.3.2.3 Shear Strength

Landslides and foundation failures may occur if the soil does not have the ability to withstand such shear loads (Liu and Evett 1981). Soil gains its shear strength from its internal friction angle and cohesion and can be measured using the Coulomb's equation,

Table 7.10 Normal stress and shear stress parameters of soils of Nungkao Landslide area

Sample No.	σ (kN/m^2)	τ (kN/m^2)
S-1	9.8	3.1
S-2	19.6	4.7
S-3	29.4	6.96

$$t = c + \sigma_n \mathrm{Tan}\phi \tag{7.8}$$

where, c = cohesion, σ_n = Normal stress and ϕ = Internal friction angle.

Three soil samples were taken for direct shear test in the laboratory, and the results are shown in Table 7.10.

The shear strength parameter of the soil is determined as
Cohesion, c = 1 kN/m^2 and
Internal friction angle, $\phi = 20°$.

7.3.2.4 Calculation of Factor of Safety for Soil

Slope angle = 65° Cohesion, c = 1 kN/m^2 = 1, 000 N/m^2
Internal friction angle, $\phi = 20°$ $\tan\phi = \tan 20° = 0.36397$
Slope height, H = 75 m Unit weight, $\gamma = 0.2548$ kN/m^3 = 254.8 N/m^3

Now we get,

$$\frac{c}{\gamma \cdot \mathrm{H} \cdot \mathrm{Tan}\phi} = \frac{1000}{254.8 \times 75 \times 0.36397} = 0.1438$$

Again, from the Chart 2 (after Hoek and Bray 1981), corresponding to this value which intersects slope angle (20°),

$$\frac{\mathrm{Tan}\phi}{F} = 0.28$$

$$\Rightarrow F = \frac{0.36397}{0.28} = 1.3$$

As a result, the slope of Nungkao has a factor of safety of 1.3, which is greater than 1, and so falls under the stable slope criterion.

7.4 Results and Discussion

Prepared core samples which are perpendicular to bedding showed higher compressive strength than those taken parallel to bedding, suggesting the presence of structurally weak planes or surfaces, as well as other irregularities that are almost invisible to the naked eye. The main type of rocks comprises the intercalations of Sandstones and Shales, where the outcrop exhibits near horizontal bedding and many joint sets. Block/wedge failure results from a succession of varying-sized wedges formed by the intersection of joint planes with respect to the slope angle. In Table 7.11 (Slope Stabilization), the Rock Mass Rating value is 58, which is in the fair category of class III (Table 7.12).

After a thorough investigation of the soil it is inferred that the factor of safety for soil has 1.3, suggesting stable condition. The soil cover at slopes is very thin, and therefore, it may not cause any kind of major landslide. A small stream of first-order runs near the area which may bring changes in the hydrostatic condition of the site by increasing its weight after getting saturated with water during the rainy season. In addition, anthropogenic activity such as a faulty road cut design and an incorrect blasting technique might have triggered the slip and fall.

7.4.1 Wedge Failure Safety Factor Calculation

See (Table 7.13).

Two Prominent joint planes are mainly responsible for the failure of this slope which is clearly revealed through kinematic analysis (Fig. 7.4), and consequent analysis interpret the factor of safety following the Hoek and Brown wedge failure technique using stereo plot (Fig. 7.5). From the analysis it shows that the wedge failure analysis through stereo-net, the plunge of the two intersections is 60º and its direction of movement is at N92. The safety factor is greater than 1, indicating stable

Table 7.11 Description of SMR classes (Romana, 1985)

CLASS	III
SMR	41
DESCRIPTION	Fair
STABILITY	Partially stable
FAILURE	Some joints or many Wedges
SUPPORT	Systematic

Table 7.12 Support for SMR Classes (Romana, 1985)

SMR CLASS	Support	Description
III	Systematic	Systematic bolting, dental treatment, bolting, net toe drains

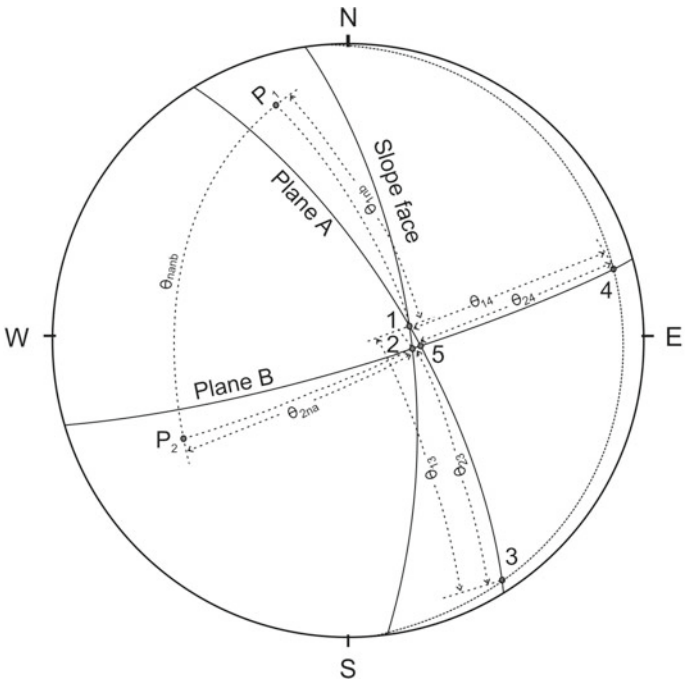

Fig. 7.5 Stereo-plot of data for wedge stability analysis

Table 7.13 Wedge analysis calculation (Hoek and Bray, 1981)

Inputs	Values	Calculation
$\psi_a = 66°$ $\psi_b = 80°$ $\psi_5 = 60°$ $\theta_{na.nb} = 96°$	Cos $\psi_a = 0.407$ Cos $\psi_b = 0.407$ Sin $\psi 5 = 0.866$ Cos $\theta_{na.nb} = -0.105$ Sin $\theta_{na.nb} = 0.995$	$A = \frac{cos\psi a - cos\psi b.cos\theta na.nb}{sin\varphi_5.sin^2\theta na.nb} = 0.524$ $B = \frac{cos\psi b - cos\psi a.cos\theta na.nb}{sin\varphi_5.sin^2\theta na.nb} = 0.522$
$\theta_{24} = 51°$ $\theta_{45} = 48°$ $\theta_{2na} = 79°$ $\theta_{13} = 75°$ $\theta_{35} = 66°$ $\theta_{1nb} = 80°$	Sin $\theta_{24} = 0.777$ Sin $\theta_{48} = 0.743$ Cos $\theta_{2na} = 0.191$ Sin $\theta_{13} = 0.966$ Sin $\theta_{35} = 0914$ Cos $\theta_{1nb} = 0.174$	$X = \frac{Sin\theta_{24}}{Sin\theta_{45}Cos\theta_{2na}} = 5.481$ $Y = \frac{Sin\theta_{13}}{Sin\theta_{35}Cos\theta_{1nb}} = 6.089$
$\Phi_A = 55°$ $\Phi_B = 55°$ $\gamma = 2.65$ g/cc $\gamma_\omega = 1$ g/cc $C_A = 1{,}080$ g/cc $C_B = 1{,}080$ g/cc H = 1,600 cm	Tan $\Phi_A = 1.428$ Tan $\Phi_B = 1.428$ $\gamma = 2.65$ $\gamma_\omega/2\gamma = 0.1885$ $3C_A/\gamma H = 0.763$ $3C_B/\gamma H = 0.763$	$F = 3\frac{C_A}{\gamma H}.X + 3\frac{C_B}{\gamma H}.Y + \left(A - \frac{\gamma_\omega}{2\gamma}.X\right)Tan\varnothing_A +$ $\left(B - \frac{\gamma_\omega}{2\gamma}.Y\right)Tan\bullet\varnothing_B = 7.2105$

condition. Both soil and rock revealed the stable condition of the study area, but the site has been affected by recurrent slides in almost all the rainy season, either as rock fall or as soil slides and sometimes together.

7.4.2 Preventive Measures

Some loose and dangling blocks have been uncovered on the slopes after an incorrect blasting procedure. A steel wire net must be installed to support the weight of the blocks and prevent them from collapsing into the streets. A popular way to stabilise slopes by minimising movement-inducing stresses is to remove any unstable or potentially unstable blocks. Another measure to be adopted in this site is to reduce the slope angle of the road cut. With respect to the slope height, it is necessary to have at least two benches so that the rock falling from a great height cannot directly hit the road, which is highly dangerous during heavy vehicular traffic movement. Benches at a minimum width of 2.5 m and drainage ditches to remove water away from the slope are highly recommended. Thus the site needs to have a proper drainage facility, otherwise, percolation of rain or surface water through the weak planes can cause weakening of the shear strength of rocks, thereby initiating sliding/falling of rock blocks.

7.5 Conclusions

Using RMR and SMR, the current research area offers information on the nature of the rock mass as a whole. The failure of the wedge is confirmed by a kinematic examination of the region. A stereographic analysis utilising Rock pack III software detected the various types of slope failure by methodically processing and tabulating discontinuity data acquired from the field. There is a strong likelihood that the landslide will fall as a wedge if its joints (J1 and J2) are located in the shadow region, where the intersecting lines of discontinuity are 60°/092°. According to the plasticity index chart, soil samples taken from site slopes have lower moisture content, which indicates that the soil is of an inorganic origin. As a result, the slope-forming materials are solid or semi-solid, as indicated by the (−ve) value of the fluidity index (−1.18) and the (+ve) value of the consistency index (3.03). As a result, the rock mass along NH 37's slopes is only partially stable. Both rock and soil analyses indicate a stable condition of the study area; however, still a major threat to vehicular movement in this area due to the frequent slides almost every year.

References

Bieniawski ZT (1973) Engineering classification of jointed rock masses. CivEng South Afr 15:335–344

Bieniawski ZT (1974) Geomechanics classification in rock massesand its application in tunnelling. In: Advances in rock mechanics, Proc of 3rd congress of ISRM, National Academy of Sciences, Washington, D.C., II (A), pp 27–32

Bieniawski ZT (1975) Case studies: prediction of rock mass behaviour by geomechanics classification. In: Proceedings of 2nd Australia–New Zealand conference geomechanics, Brisbane, pp 36–41

Bieniawski ZT (1976) Rock mass classifications in engineering. In: Proceedings of the symposium on exploration rock engineering, Johannesburg, pp 97–106

Bieniawski ZT (1979) The Geomechanics classification in rock engineering applications. In: Proceedings of the 4th congress of the international society of rock mechanics, Montreux, Switzerland, vol 2. AA Balkema, Rotterdam, pp 41–80

Bieniawski ZT (1989) Engineering rock mass classification. Wiley, New York, p 251

Cruden DM (1978) Discussion of Hocking's paper "A method for distinguishing between single and double plane sliding of tetrahedral wedges". Int J Rock Mech Mining Sci Geomech Abstr 15(4):217–217

Das I, Sahoo S, Van Weston C, Stein A, Hack R (2010) Landslide susceptibility assessment using logistic regression and its comparison with a rock mass classification system, along a road section in the northern Himalayas (India). Geomorphology 114:627–637

Dorren L (2003) A review of rockfall mechanics and modelling approaches. Prog Physgeogr 27(1):68–87

Goodman RE (1976) Methods of geological engineering in discontinuous rocks. West Publishing, San Francisco

Hocking G (1976) A method for distinguishing between single and double plane sliding of tetrahedral wedges. Int J Rock Mech Min Sci Geomech Abstr 13(7):225–226

Hoek E, Bray JW (1981) Rock slope engineering, 3rd edn. Institution of Mining and Metallurgy, London, pp 57, 92, 96, 150, 358

ISRM (1981) Rock characterisation testing and monitoring. In: Brown ET (ed) Pergamon Press, Oxford

Kliche CA (1999) Rock slope stability. SME, Littleton, CO

Liu C, Evett JB (1981) Soils and foundations. Prentice Hall, INC., Englewood Cliffs, New Jersey 07632, p 28

Lucas JM (1980) A general stereographic method for determining possible mode of failure of any tetrahedral rock wedge. Int J Rock Mech Min Sci Geomech Abstr 17:57–61

Markland JT (1972) A useful technique for estimating the stability of rock slopes when the rigid wedge sliding type of failure is expected. Imp Coll Rock Mech Res Rep, pp 10, 19

Matherson GD (1988) The collection and use of field discontinuity data in rock slope design. Q J Eng Geol 22:19–30

Murthy VNS (2007) Soil mechanics and foundation engineering, geotechnical engineering series, 1st ed. In: Satish Kumar J (ed) CBS Publisher & Distributor, New Delhi, pp 81–119.

Romana M (1985) A geomechanical classification for slopes: slope mass rating. In: Hudson JA (ed) Comprehensive Rock Eng. Pergamon Press, London, pp 375–601

Romana M (1993) SMR classification. In: Romana M (ed) Proceeding of the 7th ISRM international congress on rock mechanics, Achen, 16–20 September 1991, vol 2. A.A. Balkema, Rotterdam, pp 955-960; 1991. Int J Rock Mech Mining Sci Geomech Abstr 30:A231–A231

Romana M, Seron JB, Montlar E (2003) SMR geomechanics classification: application, experience and validation. In: Merwe JN (ed) Proceedings of the 10th congress of the international society for rock mechanics. ISRM 2003-technology roadmap for rock mechanics. SouthAfrican Institute of Mining and Metallurgy, pp 1–4.

Saranaathan SE, Kannan M (2017) SMR and kinematic analysis for slope instability along bodi-bodimettu ghat section, Tamil Nadu. Geol Soc India 89:589–599

Vishal V, Pradhan SP, Singh TN (2010) Instability assessment of mine slope—a finite element approach. Int J Earth Sci Eng 3(6):11–23

Yoon WS, Jeong U, Choi JW, Kim JH, Kim WY, Kim CS (2002) Slope failure index system based on the behaviour characteristics, SFi–system. J Kor Geotech Soc 18:23–37

Chapter 8
Stability Assessment of Lateritic Soil Slope Along NH-66, Ratnagiri Maharashtra, India

Anurag Niyogi, Kripamoy Sarkar, Tabish Rahman, and T. N. Singh

Abstract The Western Ghats region in Maharashtra is severely affected by landslides and landslip hazards. National Highway 66, linking Mumbai to Goa, has been affected by persistent slope stability problems across the Ratnagiri district. Any such events impart severe damage to the road and its commuters. The variability of geological and geotechnical conditions directly impacts the steadiness of a slope structure. This study aims to generate an understanding of the vulnerability status of the soil slope and remediate it for long-term stability. For this purpose, a lateritic soil slope was chosen for proper appraisal of its present state. Evaluation of slope stability by conventional limit equilibrium methods and more sophisticated finite element method were employed using deterministic and probabilistic approaches to estimate the factor of safety. The result, thus, achieved is quintessential for designing a safe slope. Furthermore, a two-stage stabilization process has been reviewed with sustainable improvement in design for safety has been proposed.

Keywords Slope stability analyses · Deterministic and probabilistic approach · Sustainable remediation · Ratnagiri

8.1 Introduction

Landslide is defined as a natural phenomenon that embodies the mass movement of a slope under the influence of gravity. Mountainous regions, especially the road passing through them, are severely hit by the crumbling slope materials (Budetta 2004; Vanacker et al. 2007; Brenning et al. 2015). Population explosion has impelled increasing human settlements in sensitive hilly areas causing aggravation in landslide hazards (Santi et al. 2011). In India, the Western Ghats and the Himalayas have

A. Niyogi (✉) · K. Sarkar · T. Rahman
Department of Applied Geology, Indian Institute of Technology (Indian School of Mines), Dhanbad 826004, Jharkhand, India
e-mail: tabun111@gmail.com

T. N. Singh
Department of Civil and Environmental Engineering, Indian Institute of Technology, Patna 801106, Bihar, India

P. Thambidurai and T. N. Singh (eds.), *Landslides: Detection, Prediction and Monitoring*,
https://doi.org/10.1007/978-3-031-23859-8_8

seen a significant rise in the landslide-related event due to urbanization (Westen et al. 2012). In the coming years, the intensity of occurrence of landslides will increase many folds (Temme et al. 2020). The adverse effects of landslides on society and the economy demand a proper understanding of the cause and process involved (Highland and Bobrowsky 2008). Landslide-related events have intricately affected the several regions of Western Ghats. There are many reporting from different locations of Maharashtra Western Ghats. Singh et al. (2013) assessed the vulnerability of rock slopes in Amboli that suffers from rockfall events. Kainthola et al. (2015) performed a slope stability investigation on basaltic road cut slopes of Mahabaleshwar. The study reports the failure recurrence of lateritic soil mass. Ahmad et al. (2015) conducted a study on the lateritic soil slope of Mahabaleshwar and suggested that the soil material is weak, making the slope unstable. Sharma et al. (2017) studied the weathered soil slopes along NH-222 in the Malsej ghat region and assessed the slope stability condition using limit equilibrium method and finite element modeling techniques.

Stability prospects are crucial in managing the failure status of a slope. The in-depth analysis is critical for designing safety measures for road cut slopes. Geoengineering parameters form the basis for material interaction for stability assessment. A slope becomes unstable when existing geometry and constituting material do not sustain the shear stress exerted on its mass under the influence of local climatic conditions. It is significantly important to precisely estimate soil's intrinsic properties. There are several natural as well as artificial influencing factors that invariably affect this condition. The rainfall extremities coupled with tectonic and differential weathering have a dominating response towards slope failure. High precipitation invariably has a landslide triggering effect in tropical regions (Rahardjo et al. 1995; Collins and Znidarcic 2004; Melchiorre and Frattini 2012; Bontemps et al. 2020). Seismic activity has been documented as a destabilizing agent of slope, causing major destruction globally (Tibaldi et al. 1995; Li et al. 2021). Many different analytical, numerical, and conventional techniques are actively used to expose some definitive information about the stability condition (Rabie 2014). Out of these, limit equilibrium methods (LEM) is primarily used in usual practices associated with landslide stability investigation (Duncan 1996; Abramson et al. 2002; Kim et al. 2002; Cala and Flisiak 2020). Moreover, there are specific methods that follow certain equilibrium conditions. In general, Bishop simplified method (moment equilibrium) (Bishop 1955), Janbu simplified method (force equilibrium) (Janbu 1956), and Morgenstern-Price method (force-moment equilibrium) (Morgenstern and Price 1965) are common methods of analysis (Fredlund 1981). Fundamentally, they work on the pre-assuming feature of a failure surface and divide the structure of the slope mass over the failure surface into finite slices. It brings an inevitable shortcoming in determining the precise driving forces that destabilize a slope. The measure of stability is achieved by a distinctive value known as the factor of safety (FoS) that answers whether the slope structure is stable or unstable. The value is crucial and can be decided by deterministic and probabilistic approaches. The methodology includes reduction of cohesion (C) and internal frictional angle (ϕ) of the material's intrinsic parameters such that failure occurs. It is determined by the following equation.

$$\text{FoS} = \frac{\text{Shear strength}}{\text{Shear stress at failure}} \tag{8.1}$$

The finite element modeling (FEM) technique has gained significant accreditation in recent practice. Its ability to assess the exact shear strain location and measure the failure movement has a clear advantage over traditional LEM analysis. The FEM approach has improved the perception of geotechnical engineers in understanding the material behaviour in different conditions to develop proper remediation. Here, the safety factor is obtained from the strength reduction factor (SRF) obtained from the shear strength reduction (SSR) technique that provides the probability of failure (Zienkiewicz et al. 1975; Griffiths and Lane 1999; Zheng et al. 2005). It gives an effective solution as the sliding surface develops in a self-executing manner. In the SSR method, the shear strength of the geomaterial is sequentially reduced by a factor of SRF until the model fails or non-convergence occurs (Matsui and San 1992; Ugai and Leshchinsky 1995; Dawson et al. 1999; Griffiths and Lane 1999; Hammah et al. 2007; Singh et al. 2016). The failure is perceived by the displacement seen in the finite element model. SRF is calculated by the following Eq. (8.2).

$$C_n = \frac{\text{C}}{\text{SRF}} \text{and}\, \phi_n = \arctan\left(\frac{\tan\phi}{\text{SRF}}\right) \tag{8.2}$$

where C_n and ϕ_n are reduced shear strength parameters by factor SRF. The finite element model uses physicomechanical properties of soil.

The geomaterials from the Ratnagiri region of Maharashtra is affected by differential weathering. Due to its geographical positioning and geological attributes, slope failures are frequent along the national highway (NH-66) (Niyogi et al. 2016, 2020). The settlements surrounding the highway are prone to landslide-related hazards. The study area falls in the moderate to high landslide intensity zone (BMTPC 2019). The stability concern of slopes is a pretty common mass movement type in this area where rockfall and soil sliding are common. The present study aims to evaluate the post-failure stability condition of a lateritic soil slope and devise a site-specific remedial measure for its stabilization.

8.2 Geology of the Study Area

The location of the slope lies between Ratnagiri taluka and Sangameshwar taluka in the Ratnagiri district of Maharashtra (Fig. 8.1). The highway plays a key role in the socio-economic development of the district. It connects commercial hotspots such as Mumbai and Goa and is known for tourist commuters. The region largely belongs to Deccan Volcanic Province (DVP), with basaltic rocks and their weathered varieties are found (Beane et al. 1986). The slope, predominantly, is made of lateritic soil that has formed due to extreme chemical alteration of basalt rock. The location has a thick

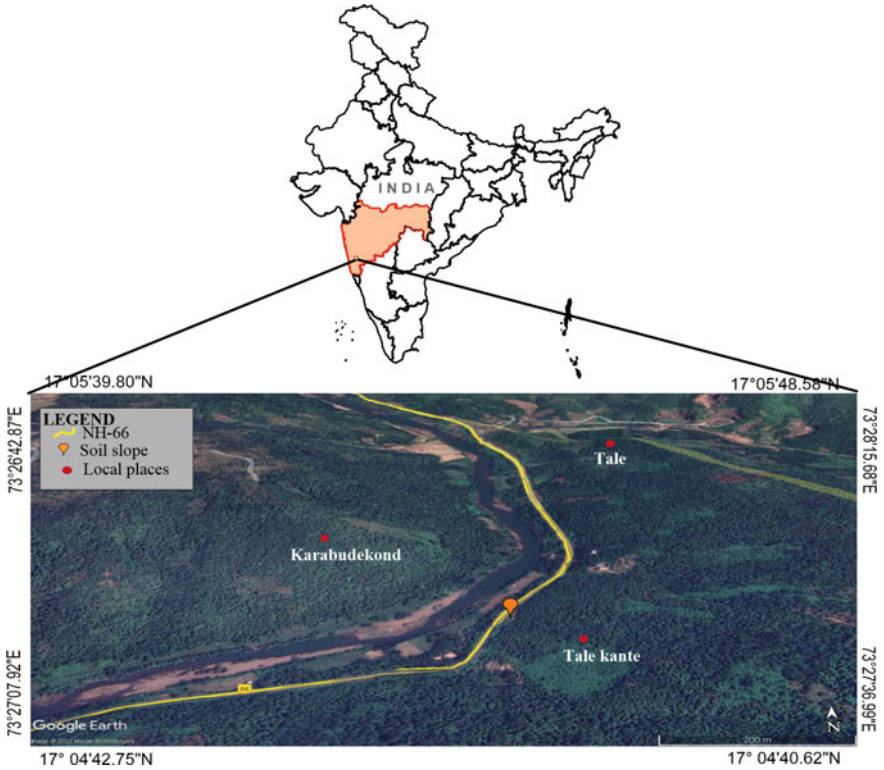

Fig. 8.1 Google imagery of location map of the study area

soil cover of Quaternary formation with surrounding rocks of Upper Cretaceous to Eocene age (Alexander 1981; Sastri 1981). Mainly, the soil is made of silty sand, with minor gravel have been found in the failed slope location.

8.3 Materials and Method

The representative soil samples were collected for testing in the laboratory for accumulation of critical index parameters essential for the determination of stability conditions. Primarily, cohesion and internal frictional angles are essential for ascertaining the shear strength of soil (τ) that follows the Eq. (8.3).

$$\tau = \mathrm{C} + \sigma \mathrm{n} \times \tan\phi \tag{8.3}$$

where σn is normal stress applied on the soil sample.

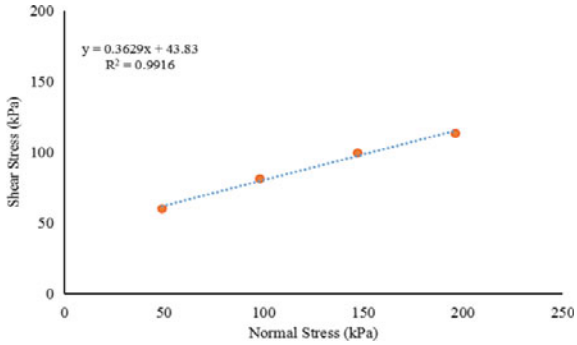

Fig. 8.2 Graphical representation of shear stress behaviour under increasing normal stress for the soil

A set of four soil samples were prepared for the direct shear test. The samples were subjected to following a fixed plane for shearing as per the standard mentioned in ASTM D3080 (2011). A constant strain of 0.2 mm/min at increasing loads of 0.5, 1.0, 1.5, and 2.0 kN/m^2 were considered for the test. At every constant normal stress, a shear stress value is obtained. The sample gets failed after reaching the maximum shear stress it can withstand. A graph is drawn between normal and shear stress to calculate C and ϕ (Fig. 8.2).

Another crucial parameter required for the slope stability analysis is the unit weight of the soil. For this density bottle test has been performed. Oven-dried samples of a batch of three were prepared for two 50 ml density bottles for assessing the specific gravity at room temperature (ASTM D 854 2010). A standard calculation of converting specific gravity into unit weight by multiplying acceleration due to gravity with the density of water has been followed for the concerned samples. A slope for stability estimation has been modeled using the geotechnical inputs discussed in the following section.

8.4 Slope Stability Analysis

The soil slope has been analyzed using LEM and FEM techniques. For this purpose, computer-aided programs viz; *Slide v7.0* and *RS*^{2} *v9.0* were used for LEM and FEM analysis, respectively. Different LE methods assume the failure surface that instantly provides FoS as a stability indicator. Both deterministic FoS (FoS_D) and probabilistic FoS (FoS_P) have been obtained to explicitly discuss the stability situation. The vulnerability condition of the slopes post-failure conditions has been simulated. The (Limit Equilibrium) LE analysis does not include strain relation with the material (Finite Element) FE analysis conducted for the slopes. Similarly probabilistic approach for the aforementioned slope has been used to address the stress-based deformation and displacement magnitudes. The advantage of the inclusion of statistical variability in the material properties helps in achieving the probability of failure (PF). This

Fig. 8.3 Pictorial representation of soil slope **a** Field photograph of the slope and **b** general illustration for slope stability analysis

Table 8.1 Essential input parameters of lateritic soil

Unit weight (kN/m^3)	Cohesion (kPa)	Internal friction angle (°)
25.56	43.83	19.90

in-depth information is sensitive in designing protective arrangements for attaining stabilization.

8.4.1 Stability Analysis of the Soil Slope

The studied slope is precariously situated in close proximity to the road. The field investigation suggests that there has been slope failure recently. The top section was observed to be particularly vulnerable as a major portion shows several trees tilted from its base. The vegetation was sparse on the slope face with small shrubs growth which signifies the creep action of slope movement. These are the viable signature of mass movement. The site is located in Chandivane village in the Ratnagiri taluka. This slope is composed of lateritic soil and has an average height of 14 m. The slope face has been divided into two different slope angles as observed in the field condition. The inclination of the slope face is seen to be approximately 46° to a height of 9 m and a gentler, 40° to the top from the level of the road. It was noticed that the slope is still actively deforming with freshly failed surface visible distinctively (Fig. 8.3). Input parameters associated are unit weight, cohesion, and internal friction angle are listed below (Table 8.1).

8.4.2 Limit Equilibrium Analysis

Limit Equilibrium (LE) analysis has been conducted to address the stability issues. The methodology was chosen using three different equilibrium conditions; Janbu simplified method, Bishop simplified method, and Morgenstern-Price method. Demonstration of stability state is discussed by FoS determination based on both deterministic as well as probabilistic perspectives. Morgenstern-Price method is considered for further stability assessment. The slope is critically stable as FoS_D is found to be in a range between 1.070 and 1.136, whereas FoS_P has similar values of 1.071 to 1.39. It is followed by the surfaces failed after iteration represented by PF% which changes from 1.60 to 11.20 (Table 8.2). The probabilistic LE analysis on the studied slope using the Morgenstern-Price method has been featured in Fig. 8.4.

The critical slip surface was observed to be forming a non-circular shape with a maximum depth of about 6 m from the slope surface. The zone of the sliding surface is divided into 46 slices. Critical stability of the slope may be due to the cohesive force acting positively in accordance with the angle of friction for the analyzed slope dimension. Although the slope is not an unstable one, the present condition does not satisfy safety standards. Hence it should be treated with a proper and sustainable remedial measure for future safety.

Table 8.2 The results of LE analysis of soil slope in field condition

Janbu simplified method			Bishop simplified method			Morgenstern-Price method		
FoS_D	FoS_P	PF%	FoS_D	FoS_P	PF%	FoS_D	FoS_P	PF%
1.070	1.071	11.2	1.130	1.131	2.3	1.136	1.139	1.60

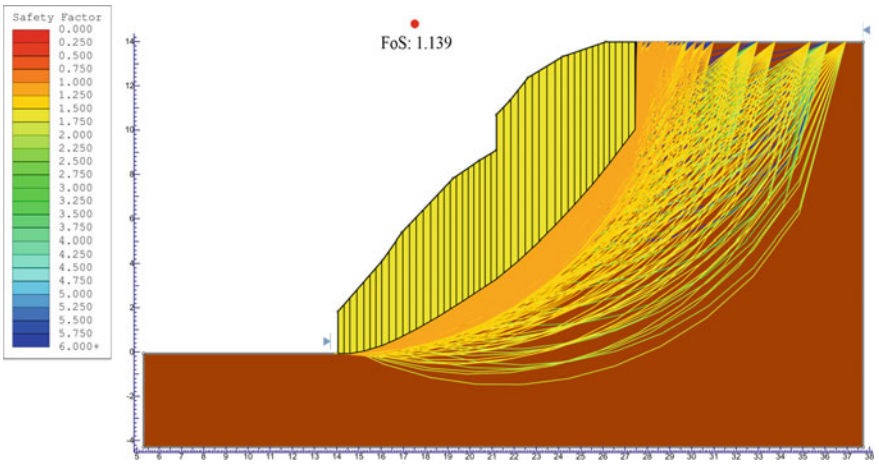

Fig. 8.4 Limit Equilibrium stability analysis of slope using Morgenstern-Price method

8.4.3 Finite Element Analysis

In Finite Element (FE) analysis, a model for simulation has been discretized with the same boundary condition as in LE analysis. Mohr–Coulomb failure criteria have been utilized for the process of two-dimensional plain-strain analysis. The material is considered to be plastic to see the shearing effect under the action of gravity. The initial element loading has been chosen with the combination of field stress and body force. For FE analysis, the elastic properties of the soil are also taken into consideration with mechanical and physical properties. Therefore, elastic properties of soil, such as Young's modulus of 0.50 GPa and Poisson's ratio of 0.32 required for the analysis. The probabilistic mean critical SRF comes out to be 0.97 ± 0.0238, which is considered to be unstable. This is understood by the probability of failure of 88.87%. The analysis shows the maximum shear strain of 0.293, which is concentrated at the toe end of the slope (Fig. 8.5a). The strain occurrence was found to be similar to that in LE analysis. This signifies that shearing will occur with a slip surface in a circular pattern. The slope will deform from the toe end as per the accumulation of stress found there. It can be predicted that the soil mass will flow approximately 2 m from its original boundary and maximum subsidence of 1.32 m from the crown area (Fig. 8.5b). Total displacement will take place at a maximum of 690 mm with velocity vectors indicating directly to the road can cause a rapid flow of slope material over the highway (Fig. 8.5c).

8.4.4 Analysis of Suggestive Preventive Measure

The stability appearance of the studied slope demonstrates the need for an effective remedial measure. The slope lies in close proximity to the highway, which may hamper the movement of traffic. The choice of support system should bear with its economic status and site requirements. As per the type of failure the slope possess, the present situation is prescribed to stop or deviate the movement at its toe end. Two-stage stabilization was seen to satisfy the safety needs according to the standards. For this, a breast wall or a retaining wall is suggested at the first stage, followed by introduction of benching in the second.

8.4.5 Post Mitigation Stability Analysis Using LEM

Initially, the slope was retained using a cantilever wall positioned at the toe of the slope. Since there was not enough space between the slope and the road to establish the retaining wall over the pavement area, it is suggested to engrave inside the soil slope body. The proposed retaining wall has a height of 1.85 m and a base length of 2.243 m. The material of the proposed wall has a unit weight of 29 kN/m^3 with a

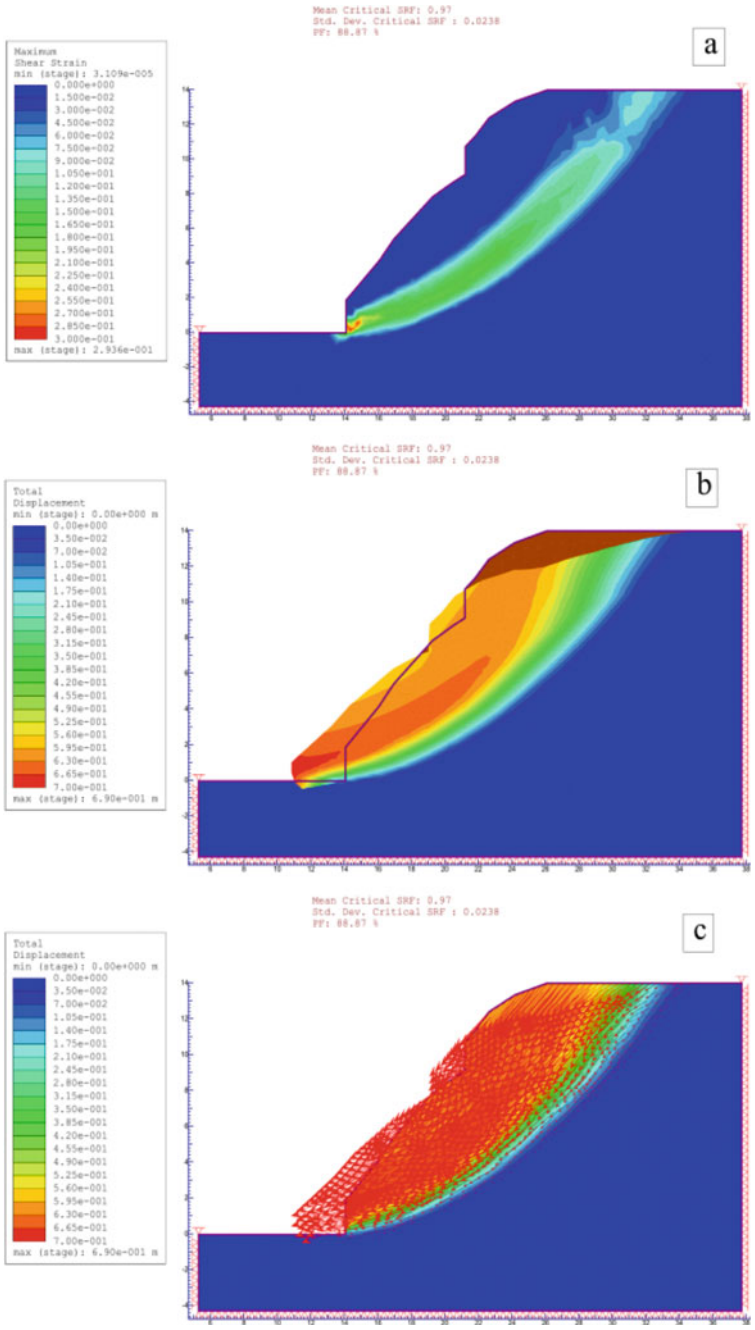

Fig. 8.5 Finite Element analysis of slope depicting (a) Maximum shear strain contour, (b) Deformation contours, (c) Total displacement with velocity vectors

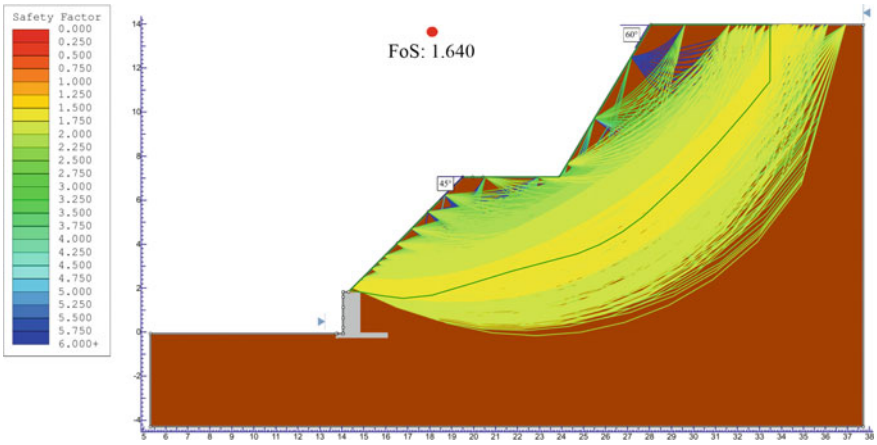

Fig. 8.6 LE analysis with benching and retaining wall using Morgenstern-Price method

tensile strength of 13 MPa. The analysis result shows the FoS to be between 1.228 to 1.371. To enhance the stability situation, benching of the slope face has been done in the second stage. A bench must be constructed at the height of 7 m with a catch bench of 4.369 m.

The top half of the slope face is needed to be trimmed to attain a 60° inclination, whereas the bottom half is required to maintain a 45° inclination. The FoS calculated shows favourable results. The FoS_D after employing the second stage varies from 1.473 to 1.627, whereas FoS_P ranges from 1.475 to 1.640. Figure 8.6 demonstrates the LE stability analysis using the Morgenstern-Price method As far as the failure probability is concerned, there does not appear to be a single failure surface for any of the methods applied.

8.4.6 Post Mitigation Stability Analysis Using FEM

The SSR technique-based FE analysis has been carried out to validate the post stability condition for the proposed preventive prospects already examined via LE methods. The simulated geometry under gravity loading produces a mean critical SRF of 1.4 ± 0.0411 with a failure probability PF of 0.00%. The maximum shear strain of 0.002507 has been seen to be concentrated at the base of the retaining wall (Fig. 8.7a). Make the slope angle gentler by removing the soil layer from the slope's face and dividing it by benching to disperse the stresses at the bottom end of the retaining wall.

The total displacement has been much smaller than 1.34 mm, which can be neglected as no significant impact on stability appears (Fig. 8.7b). It is conclusive to say the slope has been stabilized to a safer condition as no potent stress accumulation is within the slope mass regime.

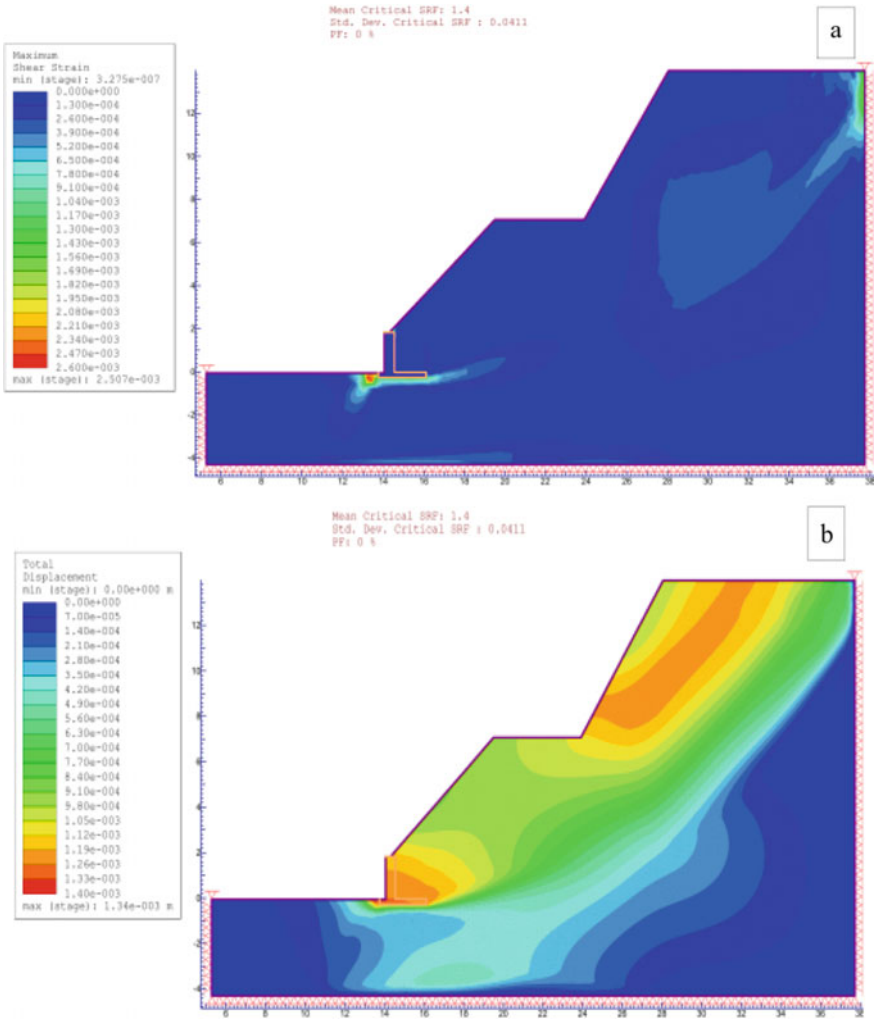

Fig. 8.7 The result of FE analysis of slope with benching and retaining wall depicting (a) Maximum shear strain and (b) Total displacement contours

8.5 Conclusion

The lateritic soil slope investigated in the study area shows a shallow failure. The stability assessment suggests that the slope is critically stable with FoS of 1.139 as per LE analysis by Morgenstern-Price method, but by Janbu simplified method, 11.2% probability of failure is attained. Furthermore, compared to results from FE analysis, the slope appears to be unstable, with a critical SRF of 0.97 and a failure probability of 88.87%. Knowing the location of shear strain concentration, a cantilever retaining

wall has been proposed. Although it significantly improved the factor of safety but still remains in the critical phase of stability. Hence benching technique has been added, resulting in enhanced slope stability with FoS of 1.640 in LE analysis and critical SRF of 1.4 in FE analysis. Additionally, the introduction of remedial measures has further increased the stability of the slope by 43.98% (LEM) and 44.32% (FEM). Therefore, the result is decisive for long-term stabilization as further slope movement is not expected.

Acknowledgements The authors sincerely appreciate the Indian Institute of Technology (Indian School of Mines) Dhanbad for providing financial and laboratory assistance and Rock Science and Rock Engineering (RSRE) lab, the Department of Earth Sciences, Indian Institute of Technology Bombay for providing facilities to conduct experiments.

Declarations The authors declare that there was no conflict of interest regarding this research.

References

Abramson LW, Lee TS, Sharma S, Boyce GM (2002) Slope stability and stabilization methods. Wiley, New York, p 712

Ahmad M, Ansari MK, Singh TN (2015) Instability investigations of basaltic soil slopes along SH-72, Maharashtra, India. Geomat Nat Haz Risk 6(2):115–130

Alexander PO (1981) Age and duration of Deccan volcanism: K-Ar evidence, Deccan volcanism and related basalt provinces in other parts of the world. J Geol Soc India Mem 3:224–258

ASTM, D854-10 (2010) Standard testing methods for specific gravity of soil solids by water pycnometer. ASTM International, West Conshohocken. https://doi.org/10.1520/D0854-10

ASTM, D3080 (2011) Standard test method for direct shear test of soils under consolidated drained conditions. ASTM International, West Conshohocken, PA. https://doi.org/10.1520/D3080_D3080M

Beane JE, Turner CA, Hooper PR, Subbarao KV, Walsh JN (1986) Stratigraphy, composition and form of the Deccan Basalts, Western Ghats, India. Bull Volcanol 48(1):61–83

Bishop AW (1955) The use of the slip circle in the stability analysis of slopes. Geotechnique 5:7–17

BMPTC (2019) Landslide hazard zonation map of India.https://bmtpc.org/topics.aspx?mid=56&Mid1=186

Bontemps N, Lacroix P, Larose E, Jara J, Taipe E (2020) Rain and small earthquakes maintain a slow-moving landslide in a persistent critical state. Nat Commun 11(1):1–10

Brenning A, Schwinn M, Ruiz-Páez AP, Muenchow J (2015) Landslide susceptibility near highways is increased by 1 order of magnitude in the Andes of southern Ecuador. Loja Province. Nat Hazard Earth Sys 15(1):45–57

Budetta P (2004) Assessment of rockfall risk along roads. Nat Hazard Earth Sys 4(1):71–81

Cala M, Flisiak J (2020) Slope stability analysis with FLAC and limit equilibrium methods. In: FLAC and numerical modeling in geomechanics. CRC Press, London, pp. 111–114.

Collins BD, Znidarcic D (2004) Stability analyses of rainfall induced landslides. J Geotech Geoenviron Eng 130(4):362–372

Dawson EM, Roth WH, Dresche RA (1999) Slope stability analysis by strength reduction. Geotechnique 49:835–840

Duncan JM (1996) State of the art: limit equilibrium and finite-element analysis of slopes. J Geotech Eng 122(7):577–596

Fredlund, D. G. (1981). The relationship between limit equilibrium slope stability methods. In: 10th. ICSMFE, vol 3, pp. 409–416.

Griffiths DV, Lane PA (1999) Slope stability analysis by finite elements. Geotechnique 49:387–403
Hammah RE, Yacoub T, Corkum B, Wibowo F, Curran JH (2007) Analysis of blocky rock slopes with finite element shear strength reduction analysis. In: 1st Canada-US Rock Mechanics Symposium, OnePetro
Highland LM, Bobrowsky P (2008) The landslide handbook—a guide to understanding landslides: Reston, Virginia, US. Geol Surv Circ 1325:129
Janbu N (1956) Earth pressure and bearing capacity by generalized procedure of slice. Proc Four Int Conf Soil Mech 2:207–2012
Kainthola A, Singh PK, Singh TN (2015) Stability investigation of road cut slope in basaltic rockmass, Mahabaleshwar, India. Geosci Front 6(6):837–845
Kim J, Salgado R, Lee J (2002) Stability analysis of complex soil slopes using limit analysis. J Geotech Geoenviron Eng 128. https://doi.org/10.1061/(ASCE)10900241(2002)128:7(546)
Li F, Torgoev I, Zaredinov D, Li M, Talipov B, Belousova A, Kunze C, Schneider P (2021) Influence of earthquakes on landslide susceptibility in a seismic prone catchment in central Asia. Appl Sci 11(9):3768
Matsui T, San KC (1992) Finite element slope stability analysis by shear strength reduction technique. Soils Found 32(1):59–70
Melchiorre C, Frattini P (2012) Modelling probability of rainfall-induced shallow landslides in a changing climate, Otta. Central Norway. Climatic Change 113(2):413–436
Morgenstern N, Price V (1965) The analysis of the stability of general slip surfaces. Geotechnique 15:79–93. https://doi.org/10.1680/geot.1965.15.1.79
Niyogi, A, Sarkar, K, Singh, TN (2016) Effect of geomechanical properties on the stability of basaltic road cut slopes at Ratnagiri, Maharashtra. In: INDOROCK: 6th Indian rock conference proceedings, pp 854–862
Niyogi A, Sarkar K, Singh AK, Singh TN (2020) Geo-engineering classification with deterioration assessment of basalt hill cut slopes along NH 66, near Ratnagiri, Maharashtra. India. J Earth Sys Sci 129:115. https://doi.org/10.1007/s12040-020-1378-0
Rabie M (2014) Comparison study between traditional and finite element methods for slopes under heavy rainfall. HBRC J 10(2):160–168
Rahardjo H, Lim TT, Chang MF, Fredlund DG (1995) Shear-strength characteristics of a residual soil. Can Geotech J 32(1):60–77
Santi PM, Hewitt K, VanDine DF, Barillas Cruz E (2011) Debris-flow impact, vulnerability, and response. Nat Hazard 56(1):371–402
Sastri VV (1981) Observations on the age of Deccan Traps and related trap activity in India. Mem Geol Surv India 3:296–299
Sharma LK, Umrao RK, Singh R, Ahmad M, Singh TN (2017) Stability investigation of hill cut soil slopes along National highway 222 at Malshej Ghat, Maharashtra. J Geol Soc India 89(2):165–174
Singh PK, Wasnik AB, Kainthola A, Sazid M, Singh TN (2013) The stability of road cut cliff face along SH-121: a case study. Nat Hazard 68(2):497–507
Singh TN, Singh R, Singh B, Sharma LK, Singh R, Ansari MK (2016) Investigations and stability analyses of Malin village landslide of Pune district, Maharashtra. India. Nat Hazard 81(3):2019–2030
Temme A, Guzzetti F, Samia J, Mirus BB (2020) The future of landslides' past—a framework for assessing consecutive landsliding systems. Landslides 17(7):1519–1528
Tibaldi A, Ferrari L, Pasquarè G (1995) Landslides triggered by earthquakes and their relations with faults and mountain slope geometry: an example from Ecuador. Geomorphology 11(3):215–226
Ugai K, Leshchinsky DOV (1995) Three-dimensional limit equilibrium and finite element analyses: a comparison of results. Soils Found 35(4):1–7
Van Westen CJ, Jaiswal P, Gosh S, Martha TR, Kuriakose SL (2012) Landslide inventory, hazard and risk assessment in India. In: Pradhan B, Buchroithner MF (eds) Terrigenous mass movements. Springer, Berlin, pp 239–282

Vanacker V, Molina A, Govers G, Poesen J, Deckers J (2007) Spatial variation of suspended sediment concentrations in a tropical Andean river system: The Paute River, southern Ecuador. Geomorphology 87(1–2):53–67

Zheng YR, Zhao SY, Kong WX, Deng CJ (2005) Geotechnical engineering limit analysis using finite element method. Rock Soil Mech 26:163–168

Zienkiewicz OC, Humpheson C, Lewis RW (1975) Associated and non-associated visco plasticity and plasticity in soil mechanics. Geotechnique 25:671–689

Chapter 9
Rockfall Hazard: A Comprehensive Review of Current Mitigation Practices

Shreya Maheshwari, Riya Bhowmik, and Manojit Samanta

Abstract This chapter discusses the kinematics of a rockfall which forms the framework for the selection of mitigation strategies. It is followed by a detailed discussion of various mitigation strategies used to arrest or divert the falling rock and reduce the economic damage and loss of lives in mountainous regions. The mitigation strategies of rockfall protection can broadly be categorised into active and passive measures. Mitigation practices using draped meshes, anchors, and grouting are active measures, while practices using embankments, flexible barriers, rock sheds, catch ditches, and forests are categorised under passive measures. The various design approaches typically used for analysing and designing these mitigation measures are also discussed briefly in this chapter. A concise discussion of the limitations of these measures is also provided to aid the practitioners in selecting an adequate mitigation strategy. The primary objective of this chapter is to provide a thorough understanding of the rockfall and current mitigation practices employed in the field for the practitioners involved in hilly infrastructure projects. The comprehensive discussion on the current rockfall mitigation practices could also serve as a potential framework for future improvements in their respective design.

Keyword Rockfall · Kinematics · Mitigation measures · Active measures · Passive measures

S. Maheshwari · R. Bhowmik (✉)
Indian Institute of Technology, Jammu 181221, Jammu and Kashmir, India
e-mail: riya.bhowmik@iitjammu.ac.in

M. Samanta
Academy of Scientific and Innovative Research (AcSIR), Ghaziabad 201002, UP, India

Geotechnical Engineering Group, CSIR–Central Building Research Institute, Roorkee 247667, UK, India

P. Thambidurai and T. N. Singh (eds.), *Landslides: Detection, Prediction and Monitoring*,
https://doi.org/10.1007/978-3-031-23859-8_9

9.1 Introduction

Rockfall is one of the most dangerous landslide types in mountainous regions due to its high mobility and impacting energy. Primarily occurring in areas of heavy precipitation and frequent earthquakes, rockfall is initiated from the rock face due to discontinuities, pore water pressures, and weathering phenomena (Budetta 2004). The complete mechanism of rockfall involves two stages: First, the detachment of rock blocks from the steep slope and, second, the propagation of the rock blocks down the slope (Cruden and Varnes 1996). Thus, rockfall is the rapid downslope movement of one or a few rock blocks of varying size (Vilajosana et al. 2008; Antoniou and Lekkas 2010) through free-falling, bouncing, or rolling/sliding motions (Varnes 1978). Detached rocks from steep slopes can attain high velocity and energy during the downslope movement and can travel large runout distances, resulting in significant fatalities, even though the volume of mobilized rock mass is very low (Fanos et al. 2018; Moos et al. 2018; Li et al. 2019).

Rockfall events pose a hazard through direct impact and the deposition of rock fragments, thus, hindering the traffic flow. This hazard can be mitigated by stabilizing the fragmented materials on the slope or using countermeasures at the toe of the slope, which can protect the infrastructures downhill. However, these protection measures can only be effective when the travel paths of the falling blocks are well-defined and the simultaneous fall of only a few blocks is expected. The size of falling rocks is not too large, and the source area of potential fall materials is large in extent. Effective and efficient countermeasures can mitigate the effect of rockfall impact on vulnerable structures, reduce economic damage, and prevent human fatalities. The present chapter discusses the details of rockfall mitigation and protection strategies. It first presents a brief overview of rockfall kinematics and its study, which forms the primary basis for designing and selecting appropriate mitigation measures. Subsequently, followed by a discussion on active and passive protection measures. The detailed discussion on passive protection measures includes their features and limitations, observations of various experimental and numerical studies conducted on these mitigation measures, and various design approaches typically used for analysing and designing them. The prime aim of this is to present and discuss the current rockfall mitigation practices employed in the field and to provide a potential framework for their selection and design.

9.2 Rockfall Kinematics and Mitigation

According to Corominas (2013), three main techniques are employed to mitigate the rockfall hazard: (a) rockfall risk reduction by the use of stabilization and reinforcement works, (b) restricting and obstructing the rock mass propagation via protective structures with the resulting decrease in its velocity, magnitude, and runout distance,

and (c) protect the exposed elements at risk. For the last two techniques, the parameters of the dynamics of the rocks, such as the velocity, kinetic energy, impact height, and runout distance, must be assessed at the exposed regions. Recent techniques for assessing these parameters use numerical simulations for performing rockfall trajectory analyses. The capacity and efficacy of rockfall protective measures depend on the accurate assessment of these parameters and, thus, form the basis for their selection and design. An adequate protective system is selected depending on the impact energy that the protective structure can absorb without collapse (Vogel et al. 2009). Further design of these sections is done based on the maximum bounce height of the falling rocks and for a typical factor of safety value of 1.5 (Lorentz et al. 2010). Summarily, the selection and design process for rockfall barriers must include: (1) assessing the features of the slope, material, and field conditions via geomorphological and geological survey, (2) evaluating the potentially unstable rock mass volume, (3) evaluating the expected velocity, kinetic energy, and bounce height of blocks through trajectory analysis (Bourrier et al. 2008), (4) designing the barriers as per the assessed velocity and energy, and (5) investigating the dynamic response of the protection structures impacted by rock blocks.

9.3 Rockfall Mitigation Measures

Mitigation strategies are essential where the rockfall hazards exceed tolerable limits and threaten urban areas or roads (Li et al. 2019). For gentle slopes in hilly areas (slopes < 30°), the impact of the rockfall events can be mitigated through natural vegetation cover (Calvino et al. 2001). For steeper slopes, the mitigation measures can be categorised into preventive and protective kinds. The preventive method, also known as active measures, comprises the stabilization methods of precarious rock slopes. The protective methods, or passive measures, uses interceptive structures such as flexible barriers, rock fence, draped mesh, rock sheds, and protection embankments to intercept and/or stop the rockfall in its path in the central or at the end of a slope (Vogel et al. 2009; Dhakal et al. 2011; Bertrand et al. 2012). Figure 9.1 shows the schematic representation of different zones in rockfall and commonly implemented active and passive measures on a slope. The type of mitigation measures required for a slope depends on the catastrophic potential, size, geological and environmental conditions, and the design period of the structures.

9.3.1 Active Measures

The idea of active mitigation measures is to strengthen the stability of dangerous rock, prevent it from falling, and break the chain of rockfall hazards by stopping the rock cells formation process (Chen et al. 2013). Several strengthening techniques are available to hold down the potentially loose rock on a rock-cut slope face. All

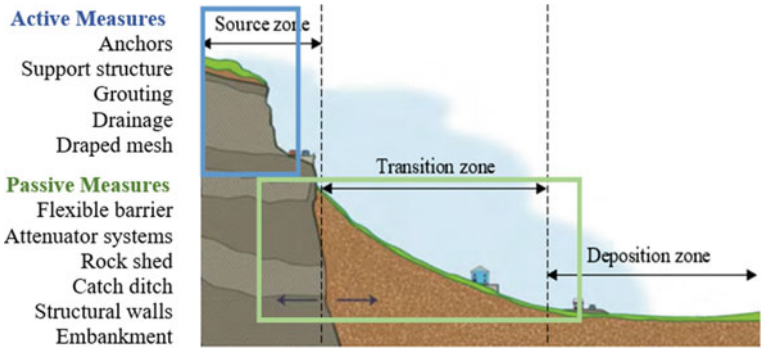

Fig. 9.1 Application of active and passive mitigation measures along a slope profile

of these techniques share the feature of minimising the loosening and relaxation of the rock mass arise from excavation and unloading activities (Hoek 1983). Thus, the active mitigation techniques are utilised to prevent the detachment of unstable rock masses, and to reduce the likelihood of the occurrence of rockfall. Active mitigation techniques include support structures, draped mesh, anchorage, grouting, drainage, and clearing and removal (scaling) of dangerous rock, among others.

9.3.1.1 Support Structures

Support techniques are used to secure the potential fall of rocks and prevent initiating in the first place. These structures, such as arches, pillars, or wall support, create supporting conditions for dangerous rock slopes and prevent them from collapse or failure (Chen et al. 2004, 2006). Under ideal circumstances, support structures are the most significant technique because of their effectiveness and minimal disturbance to the virgin rock mass slope.

9.3.1.2 Draped Mesh

Draped mesh, also known as an anti-breakup safety net, is a preventing system comprising metallic cable nets or wire meshes directly installed on eroded cliffs (Bertolo et al. 2009; Chen et al. 2013). They act primarily by covering the slope, controlling the movement of rock blocks, withstanding the punching force of falling rocks, and preventing the detached rock blocks from freely falling onto the infrastructure downhill. To accomplish these objectives, the mesh needs to be kept as near to the slope as feasible and secured at both the top and bottom of the slope. Additionally, the draped mesh may also be combined with anchors or bolts that are attached to the nets and directly affect the stability of the rock block. This system prevents the rockfall occurrence and controls the rockfall dynamics by directing the falling

fragments of the rock into enclosed mesh regions. When the release area is small, and the anticipated rockfall bounce height or kinetic energy is excessive, this type of rockfall mitigation measure offers an effective alternative to rockfall fences or flexible barriers. It can be used in a variety of situations, including when the degree of fragmentation is high or when localised unstable blocks are highlighted. The draped mesh is primarily subjected to a static force that is resisted by the wire mesh and the anchoring system.

9.3.1.3 Grouting

Rock grouting techniques are mainly used for repairing cracks and fractures in rock slopes. Rock grouting is essentially waterproofing a rock mass where there is a network of flow channels, cracks, and excessive fragmentation. It can strengthen the integrity and shear strength of cracked rock mass. If fissures and cracks are densely covered, pre-grouting is required, but grouting with high pressure is not advisable. Grouts are also used for in-situ reinforcement with rock anchor nails and bolts.

9.3.1.4 Anchors

A quick and efficient technical method for controlling rockfall occurrence is anchoring the unstable slope face (Chen et al. 2013). The three basic categories of anchor techniques are anchor bolt, anchor nail, and anchor rope. Rock anchor bolts are post-tensioned tendons inserted in drilled holes. The rock anchor bolt is divided into two segments, free length and bond length. The bond length is the embedment length inside the rock, where forces are transmitted across the surface area of the grout body and the rock. The free length is the stress-free tendon length that can remain unbounded for re-tensioning and re-grouting at any time, where force adjustment is no longer possible. Due consideration must be given to the durability and corrosion resistance of anchor bolts, nails, and ropes. According to AASHTO, unprotected anchors are utilised for short-term applications of approximately 18 to 36 months. Corrosion protection systems are considered for long-term applications with a life span of 75 to 100 years. The anchoring should be performed with minimal disturbance to the original rock mass. The length and strength of the rock anchor bolts used will depend on the size and density of the unstable rock mass as well as the geotechnical properties of the rock in the stable zone, providing the bond resistance for the anchorage. Generally, the anchor bolts and nails are made of solid thread bar systems, which include a bar, plates, couplers, and nuts. To link unstable rock to stable portions beyond the face, steel thread bars must be able to withstand both tensile and shear loads. An increase in design load or the existence of a weak rock necessarily results in larger diameters or longer lengths of bolts. Also, rock anchors alone cannot secure the weathered or fragmented rocks. However, incorporating a high tensile strength steel mesh facing will likely reduce the quantity of rock anchor

bolts, ropes and nails required and be highly effective for stabilizing weathered or fragmented rocks.

9.3.1.5 Drainage

Drainage is vital for increasing the stability of vulnerable rock slopes, as the pore water pressure is one of the contributing factors to rock slope instability. It generally comprises both surface and subsurface drainage. Constructing drain holes at the bottom of the slope to create a network of water outlets is the conventional technique for lowering pore water pressure. The crucial parameter in constructing drain holes is to place them to intersect the fractures carrying the water. A perforated casing is used to line the drain holes, with the perforations sized to reduce the infiltration of fine particles that are washed from fracture infillings. The disposal of seepage water is another crucial parameter of drain hole construction. If pore water is permitted to infiltrate the toe of the slope, it may cause low-strength materials to deteriorate or create more stability issues downstream of the drains. It might be essential to collect all the seepage water and dispose of it away from the slope. If surface runoff infiltrates exposed cracks, it is beneficial to construct diversion ditches behind the top of the slope and seal the cracks with plastic sheeting or clay. For large slides, it may be impossible to substantially decrease the water pressure in the slope by small drain holes. In such situations, a drainage tunnel can be driven through the base of the slide slope and, subsequently, drill a set of drain holes into the saturated rock.

9.3.2 Passive Measures

Rockfall simulation and risk analysis are effective and convenient for proper land-use planning in hilly areas. However, when the land-use planning does not control the rockfall hazard or damage to the existing infrastructure, selecting appropriate passive mitigation structures, size, and positioning is desirable (Vogel et al. 2009). Passive protective structures act as obstacles to the runout path of the falling rock mass. These structures do not directly interfere with the rockfall occurrence mechanism but control the dynamics of moving rock blocks. Hence, this type of structure is primarily subjected to dynamic/impact loads and includes forests, embankments, structural walls, flexible barriers, and rock sheds. The preference between these structures is primarily governed by the kinetic energy of the rocks and topographical conditions, as shown in Fig. 9.2 (modified after Sun et al. 2016).

9.3.2.1 Forests

The protective nature of mountain forests against rock falls is a natural and cost-effective protection measure. Forests have traditionally been crucial in maintaining

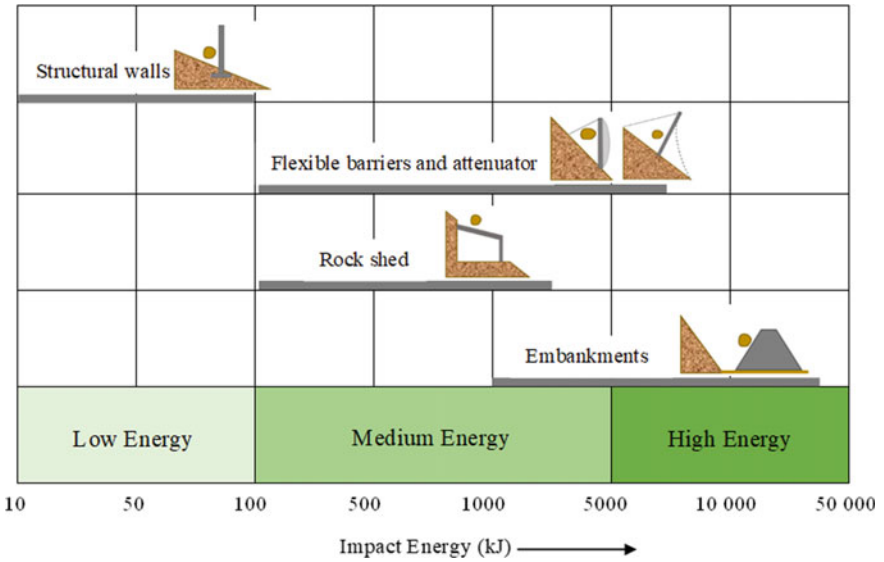

Fig. 9.2 Range of energy capacities for various passive measures

valleys in mountainous areas safe for habitation and travel by reducing the velocity and quantity of falling rock blocks reaching the toe of the slope. However, the region receiving direct protection from the forests is typically small, located below and near the forest. The forests effectively significantly reduce the impacts of rockfall for rocks up to a size of 5 m^3. Three distinct but sometimes overlapping zones can be identified on a slope where rock falls occur: the source zone, the transition zone, and the deposition zone. In the source zone, where blocks are detached, the forest does not perform a significant protective role apart from basic root-holding and water regimentation activities. In certain situations, forests may serve as rockfall-causing factors. The tree roots can get into fractures and increase the effects of frost wedging. Furthermore, roots can produce acidic exudates, which, when mixed with litter, can weather and corrode rocks (in the case of conifers). In addition, when trees sway or are uprooted by severe winds, they can release the pebbles they had been holding. In the transition zone, rocks propagate down the slope through falling, bouncing, rolling, and sliding motions. In this zone, trees work as energy-dissipating components; when the falling rock blocks strike the tree stems, they lose energy (Dorren and Berger 2006; Bertrand et al. 2013). Additionally, the impact against a tree may cause a falling rock to deviate from its travel path or even come to a stop. In the deposition zone, the speed of the rocks either decreases (when the slope diminishes to less than 30°) or comes to a stop (when the slope becomes gentler than 25°). In this terminal zone, the forest may perform a crucial part in reducing rock travel track length by slowing down the rock blocks, similar to the transition zone. The forest can be highly efficient in this zone as the kinetic energy or velocity has already decreased. Thus, even small trees can stop large rocks in the zone of deposition.

9.3.2.2 Flexible Barriers

Among the various types of rockfall protective structures developed since 1951, flexible protective measures show excellent capabilities against rockfall hazards. A cost-energy trade-off study by Yoshida (1999) shows that flexible rockfall barriers are the most attractive substitute for low-to-medium impact energies (<500 kJ) of rockfall events. The flexible protective structures with energy dissipator devices can effectively diminish the damage caused by the rockfall hazard (Peila and Ronco 2009). Rockfall protection fences are extensively employed to protect roadways, rail lines, and structures downstream of a steep slope from falling rock masses of impact energy up to 1,000 kJ and maybe more. A flexible protection barrier has wide protective capacity values varying between 50 and 8,000 kJ (Yang et al. 2019). Flexible protection mainly consists of four components: interception structure, energy dissipators, connecting components, and support cables (Liu et al. 2017), usually made up of metallic elements like nets, cables, and posts (EOTA 2008; Volkwein et al. 2019) as shown in Fig. 9.3. When the flexible barrier is impacted by rockfall, the flexible cable net transforms from a loosed state to a tight state to diffuse the impact force. The complex performance of flexible barriers or fences is characterized by several factors, including huge deflection, dynamic impact, sliding, and contact and/or detachment between components (Yu et al. 2018). Studies reveal that the large deflection of flexible barriers mainly consists of three parts: sliding movements between the components, inelastic deformation, and elastic deformation (Peila et al. 1998; Grassl et al. 2003; Gottardi and Govoni 2010). The plastic deformation of energy dissipation elements is the main cause of energy absorbed due to the inelastic deformation and accounts for 60 to 80% of the entire impact energy on the structure (Grassl et al. 2003). These barriers are usually installed at an inclination to obtain an impact angle of 60° between the barrier and rockfall trajectory (Gerber 2001) or 20° between the barrier and the slope (EOTA 2008).

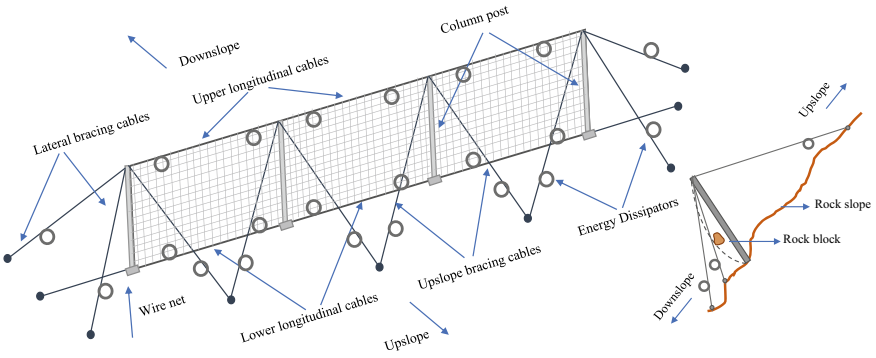

Fig. 9.3 Schematic of rockfall protection flexible barrier

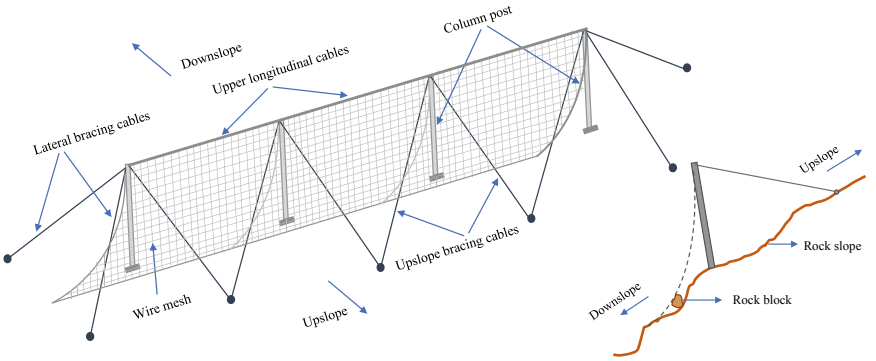

Fig. 9.4 Schematic of rockfall protection attenuator system

9.3.2.3 Attenuator Systems

The studies on rockfall flexible barrier structures have either focused on assessing the performance of flexible barriers (Peila et al. 1998; Gottardi and Govoni 2010; Mentani et al. 2016), or on the performance of the ring nets (Bertolo et al. 2009; Buzzi et al. 2015) and energy dissipators (Castanon-Jano et al. 2017). Over the period, these structures have undergone configuration modifications to improve their capacity and compensate for their limitations. As a result, new flexible rockfall mitigation structures with 5,000 kJ of capacity have been introduced called attenuator or hybrid barrier-drape systems (Badger et al. 2008) in the USA and "pocket-type rock-net" (JRA 2000; Tajima et al. 2009; Dhakal et al. 2011) in Japan. These structures can reduce the damage that occurs due to high-energy rockfall, catch it, and direct it to downslope in a controlled way (Bertrand et al. 2012). A hybrid or attenuator structure is a type of flexible fence system with characteristics of traditional rockfall catchment fences and drape mesh systems used to mitigate rockfall hazards. These are composed of flexible wire nets designed to capture the fallen rocks in the intercept net and to diminish the energy of detached falling blocks. The flexible wire netting is suspended from steel posts with hinged bases (Yang et al. 2019), as shown in Fig. 9.4. Each post is supported with four support cables anchored to the rock face with cable loop anchors and cement grout (Wyllie 2014). Attenuators also include a draping net known as a "tail". Rocks impacting the attenuator system pass under the tail, forcing the blocks to impact the slope surface and losing energy with each impact. Thus, a large structural deformation is not required for energy dissipation, enabling it to be installed on steep slopes next to roads and railways.

9.3.2.4 Rock Sheds

The rock shed, also known as rockfall protection gallery, is a crucial mitigation measure for reducing damage from the regular occurrence of rockfall events on

transportation infrastructure on steep hills. There are primarily two types of rock shed structures: the conventional rock shed (Schellenberg et al. 2012) shown in Fig. 9.5, and the structurally dissipating rock shed (SDR) (Delhomme et al. 2007) shown in Fig. 9.6. The conventional rock shed structures consist of a concrete slab covered with a cushion layer of either sand or gravel (Pichler et al. 2005; Schellenberg et al. 2008; Zhao et al. 2018). The cushion layer acts as an energy dissipator and enables the design of the shed under an equivalent static impact load. However, these cushion layers do have certain drawbacks, including their large weights, difficulties in maintenance, and inadequate buffering capacity. Moreover, it is essential to use a thick cushion layer to meet the actual requirements, which raises the construction cost and results in high dead loads. In place of soil cushion layers at the top of the rock shed, recently developed metal energy dissipators have been successfully installed to improve the impact resistance capacity of rock sheds. These structurally dissipating rock shed (SDR) developed by Mougin et al. (2005) and Delhomme et al. (2007) directly absorbs the impact shock energy through plastic deformation of the RC slab in the center, and buckling of the fuse supports during shocks. Even though SDRs have 1.8 times higher shock absorbing capacity than conventional rock sheds, many times, fuse supports do not buckle without a significant threshold load which causes significant damage to the reinforced concrete slab. The SDRs also enable quick and easy repairs for local impact damage by either replacing and reconstructing the localised damaged concrete or replacing damaged supports. Yong et al. (2019) introduced the graded dissipating inclined steel rock shed (GDISR) (Fig. 9.7), a novel form of rock shed system that is cheap, simple to build, quick to repair, and high efficiency against impact. Compared to conventional and SDR sheds, the GDISR shed slabs are inclined, made of steel, and covered with the energy-dissipating layer (EDL). Additionally, energy-dissipating bumpers (EDB) are used as fuse supports beneath the slab. Overall, compared to other passive rockfall protection structures, rock sheds provide a feasible solution for both medium- and high-energy rockfall impacts (~3,000 kJ) (FEDRO 2008).

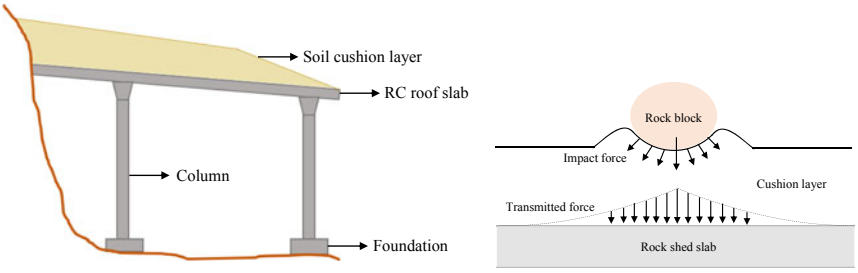

Fig. 9.5 Schematic conventional rock shed for rockfall protection

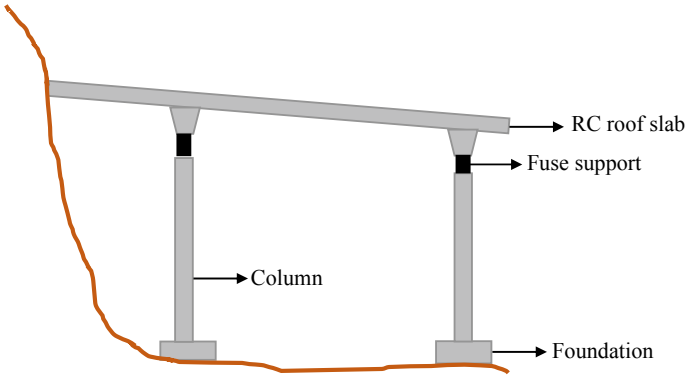

Fig. 9.6 Schematic of structurally dissipating rock shed (SDR)

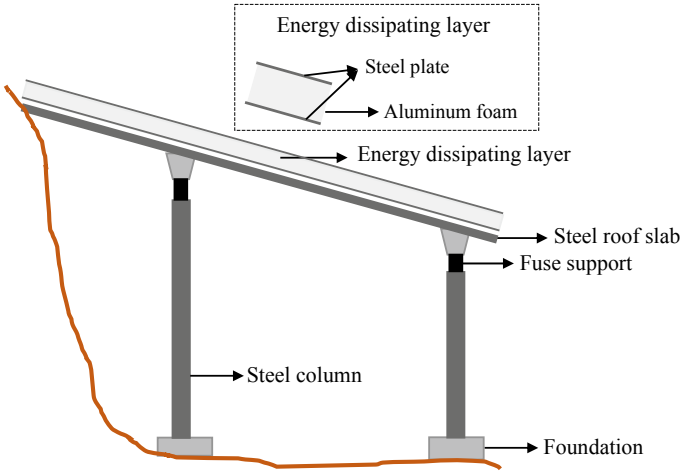

Fig. 9.7 Schematic of graded dissipating inclined steel rock shed (GDISR)

9.3.2.5 Structural Walls

A structural wall is a rigid steep-faced structure made of timber, steel, concrete, and gabion basket. It often has a lower footprint and cross-section area compared to the earthen embankments (Bourrier et al. 2011), as shown in Fig. 9.8. These walls are typically appropriate for lower energy impacts as they are made of stiffer materials (concrete, timber, steel). Instead of dissipating the kinetic energy of falling rocks like flexible nets, structural walls absorb the entire residual kinetic energy and the major portion of the impact. This results in the breaking and destruction of the structures under high-impact loads. Concrete structural walls are adequate for protection when the impact energy is between 60 and 100 kJ (Descoeudres et al. 1999). Concrete walls can also be used along with catchment ditches. If the falling rocks engage

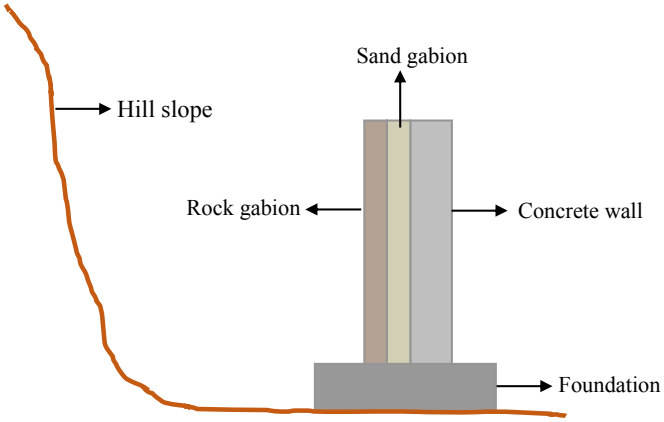

Fig. 9.8 Schematic of rockfall protection structural wall

with the ditch before impacting the wall, the residual energy on the wall is likely to be low; hence, severe damage or collapse of the walls can be prevented. When the rockfall energy surpasses the wall's structural capacity, local and global failures of the walls may happen. Therefore, high-energy rockfall events cannot be stopped by small-sized structural walls. Concrete wall with gabion facia is another common form of installation to provide protection. The primary purpose of a gabion cushion is to prevent localised damage to the protective surface of the structure near the point of contact and to enhance the concrete surface's ability to withstand impacts (Heymann et al. 2011; Lambert et al. 2014; Ng et al. 2016).

9.3.2.6 Embankment

Embankments are extensively used in both mining and civil engineering applications to protect roads and inhabited areas in hilly areas from high-energy rockfall events. These are made up of various components. Three visible sides of the embankment are named upstream side, downstream side, and crest (Calvino et al. 2001), as shown in Fig. 9.9. The major role of the upstream side is to absorb the impact energies of falling rock blocks while maintaining the structural integrity of the embankment, even under multiple impacts. Upstream sides are generally reinforced and are constructed at a slope of 60° or more to ensure stability, and downstream sides comprise a soil abutment of 35° to ensure the stability of the embankment under the rockfall impact. The crest thickness should also be significant, but no exact guidelines are available for this parameter, except that it should be large enough. Various forms of rockfall protection embankments made from compacted soil, reinforced earth, large rock blocks or gabions, etc., have been described (Peila et al. 2007; Kister and Fontana 2015). Originally, ordinary embankments or earthen embankments made of compacted natural soils were designed to obstruct rock impact energies between 1,000 and 5,000 kJ. At

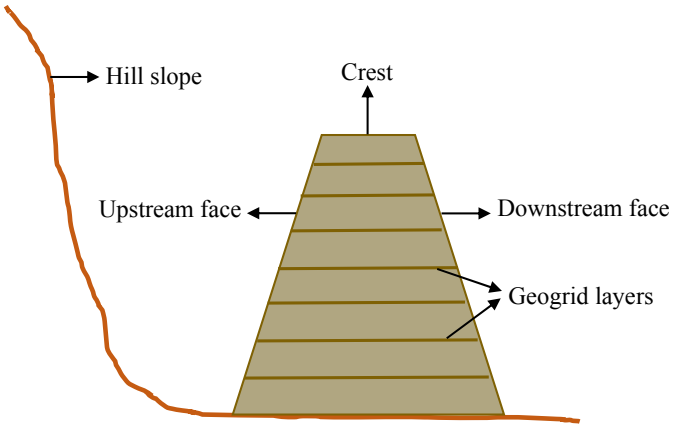

Fig. 9.9 Schematic of rockfall protection reinforced embankment

the end of the 1980s, the concept of ground-reinforced embankments was introduced to resist high energy impacts, even up to 100 MJ (Morino and Grassi 1990). These reinforced embankments for rockfall protection are made from a variety of internal reinforcing elements (such as rip-rap, wood or steel bars, wire mesh, tires filled with compacted soil, and geosynthetic materials) and appropriate facing components (soil, geosynthetics, and rip-rap) designed to resist the high impact energies (Ronco et al. 2009). Over the past two decades, a variety of these embankments have been successfully implemented. The use of reinforcing elements has reduced both their visual impact and footprint (Morino and Grassi 1990; Jaecklin 2006; Brunet et al. 2009; Lorentz et al. 2010). These reinforced embankments have displayed exceptional performance in withstanding external loads owing to their ductile nature due to the closely-spaced reinforcing elements. This ductile nature allows high deformation and compaction in the embankment, thus enabling high absorption of impact energy.

Rockfall protection embankments are preferred over flexible barriers or fences when the energy of impact exceeds 5,000 kJ (Descoeudres et al. 1999). The other benefits are low construction and maintenance expenses and reduced visual impact (Peila et al. 2007; Brunet et al. 2009; Lorentz et al. 2010; Lambert and Bourrier 2013; Lambert and Kister 2018; Kanno et al. 2021). However, these are not suitable for steep slopes and usually require a wide area for construction and easy access for large vehicles. Typically, they have a trapezoidal cross-sectional shape. But in some cases, the concrete wall, prefabricated concrete components, or gabion baskets are used to steep the upstream side (Paronuzzi 1989).

9.3.2.7 Catch Ditches

Catch ditches are a very effective rockfall protection structure with a much less construction cost and a minimal environmental impact (Davis and Shakoor 2005).

These engineered ditches often referred to as rockfall catchment areas are intended to capture and stop falling rock blocks before they impact the vulnerable structure. This technique is often employed along travel paths where the available space and slope geometry permits its construction. When there are constraints on the availability of space, barrier systems may be integrated with catch ditches.

These ditches aim to stop and capture falling rocks by reducing the kinetic energy on the slope profile before reaching transportation routes and inhabited areas (Yepes et al. 2020). The most important aspect of maintaining the efficiency and reliability of the well-designed engineered catch ditch is that it must remain accessible to machinery to remove accumulated rocks regularly. Though rockfall catch ditches exist in various geometrical configurations, the general cross-section of the catch ditch is shown in Fig. 9.10. The currently used design criteria for ditch design assumes the rock-cut slope to be fairly uniform. Natural rock slopes or rock-cut slopes with warping may have undulations that allow initiation of block detachment, causing the blocks to travel far from the toe of the hillslope. The location, shape, depth, and width of the trench are some of the most important parameters to take into account when designing a catch ditch. Therefore, it is important to know the rockfall trajectory, bounce height, impact location, and other relevant dynamic parameters of rocks for designing a rockfall catch ditch. These are the most common and aesthetically pleasing forms of protection since they do not obstruct the view of the surroundings. However, when a wider ditch is constructed on a steep slope, the rock slope cut height may be excessive. Increasing the ditch width could also potentially result in a significant increase in slope height, which would affect its overall stability.

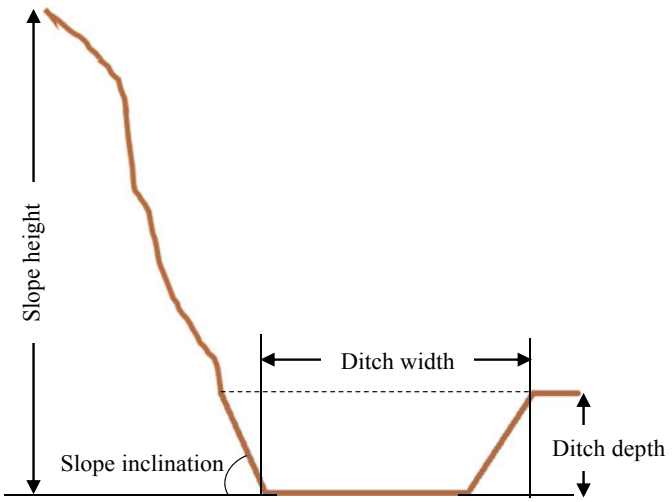

Fig. 9.10 Schematic of rockfall protection catch ditch

9.4 Design Approaches

9.4.1 Analytical Approach

9.4.1.1 Flexible Barrier

Flexible barriers consist of steel wire nets, support cables, posts, and energy-dissipating components and are widely used as natural hazard protection measures. These barriers undergo large deformation to provide energy dissipation. When falling rock strikes the barrier, the impact force is first transmitted to the wire nets and, after that, to the support cables to which energy-dissipating components are installed, resulting in inelastic distortion in these components. The entire process is represented by highly nonlinear mechanical characteristics considering significant sliding, large deformation, contact, detachment, and material yielding. The conversion of work into energy, as shown in Eq. 9.1, is a key part of this process.

$$\frac{1}{2}mv^2 + \mathrm{E}_g = \int_0^{S_{max}} \mathrm{F}(s)ds \tag{9.1}$$

$$\mathrm{E}_{total} = \alpha \mathrm{F}_{max} s_{max} \tag{9.2}$$

where, E_g is the gravitational work after the impact between falling rock and barrier and is dependent on buffer distance; m is the mass of the falling rock; v is the velocity of rock; F is the impact force; s is the deformation; E_{total} is the total energy of the rock; and α is the coefficient obtained from the experiments, ranging from 0.3 to 0.35.

Ye et al. (2010) investigated the rock shape and size influence on the motion modes, velocity, and runout distance and proposed the computation approaches for the impact force based on the impulse theorem. Abad et al. (2013) evaluated the internal force of the supporting cable under the impact force and the vector form of the tangent stiffness matrix. Therefrom, a straightforward method was proposed to analyse the structure of the cable unit, and afterward, a good outcome that more closely matches the actual stress state was obtained by simulating support cables or anchor ropes using a cable unit. Wang et al. (2010) analysed the influence of a single support cable and the net on rockfall and also proposed a computation method for evaluating the resistance capacity of cable nets in rockfall protection. Hambleton et al. (2013) developed the formula for estimating critical velocity and energy by condensing the nets into a two-dimensional model. Liu et al. (2016) proposed a critical preload calculation method based on the energy principle that can be used when the decompression ring is constructed.

9.4.1.2 Rock Shed

The present methods for calculating the rockfall impacting force on reinforced concrete structures are generally developed from the traditional Hertz contact law based on elastic theory. Though, since the rock sheds show signs of plastic deformation, the contact theory has been improved to incorporate this. Thornton (1997) proposed that the normal interaction becomes plastic when the 'limiting contact pressure' reaches the center of the contact region. Vu-Quoc et al. (2000) provided a precise method for the normal force–displacement relation for interacting spherical particles by considering plastic deformation. Since the dynamic response of the rock shed impacted by rock blocks is related to the mechanical features of the rock shed as well as the rockfall characteristic, many researchers combined the Hertz contact theory with rock shed dynamic components to develop the dynamic model for the rock shed. Olsson (2003) developed a Hertz contact theory-based analytical method for delamination initiation and growth under the small mass impact on orthotropic laminated composite plates. Zheng and Binienda (2007) analysed the permanent indentation and central displacement effect on the laminated composite plate under small mass impact loading using the elastoplastic contact theory and also proposed closed-form solutions for the contact force. Wang et al. (2020) established a theoretical computation technique for the rockfall penetration depth and impact force by taking into account the gravel soil strengthening coefficient.

9.4.1.3 Embankments

The embankments are typically designed with simplistic approaches. These include (a) the *Pseudo-Static Approach* which considers a force that is statically equivalent to the dynamic impact force (Jaecklin 2006; Kister and Fontana 2011; Brandl and Adam 2000); (b) *Penetration Criteria-Based Approach* that calculates the rock block penetration into the embankment, and evaluates the minimum embankment thickness by multiplying it with a factor of 2–3 (Brunet et al. 2009); and (c) *Energy Balance Approach* which evaluates the blocking incident translational kinetic energy dissipated in the embankment during the impact. In the *Pseudo-Static Approach,* a safety factor is taken into account for representing the uncertainties related to the theory of a statically equivalent loading. The static stability of the embankment is checked by considering this force combined with the gravity forces. In *Energy Balance Approach,* the friction along shear planes is the first energy dissipation mechanism, assuming that a portion of the embankment deforms like a rigid body (Tissières 1999; Brandl and Adam 2000). Numerous shear planes might be taken into account, particularly along the reinforcement layers (Ronco et al. 2009). The dissipation of energy due to soil compaction is also taken into account (Ronco et al. 2009). The design determines the structural deformation needed to dissipate the kinetic energy of rockfall is compatible with the size of the embankment. For this purpose, the impact force can be used to calculate the upstream deformation due to the block penetration (Ronco et al. 2009). All these approaches typically include finding out the impact force or

the block penetration. For this purpose, various formulas or methods have been used. Kar (1978) and Paronuzzi (1989) developed an expression for evaluating the penetration that can be modified for consideration of reinforcement layers. The expressions provided by Mayne and Jones (1983), Labiouse et al. (1996), or Montani (1998) can be used to estimate the impact force (Jaecklin 2006; Peila et al. 2007; Ronco et al. 2009). The soil parameters taken into account in these expressions were acquired through static testing and mostly related to the elastic response of soils. In addition, the impact force can also be used to determine the block penetration, δ, (Carotti et al. 2004; Peila et al. 2007; Ronco et al. 2009), as shown in Eq. 9.3.

$$\delta = \frac{mv^2}{\mathrm{F}_{max}} \tag{9.3}$$

where F_{max} is the maximum impact force, m is the mass of the rock block, v is the block velocity just before impact, and δ is the block penetration in the embankment. This relation shows that for a given velocity, the higher the penetration, the lower the impact force.

9.4.1.4 Catch Ditch

Based on slope inclination and height, Ritchie (1963) proposed tables and design charts for catch ditches for calculating the minimum width and depth of the ditch and determining the rockfall impact position as a function of the slope steepness and height. Ritchie (1963) also found out the rockfall motion characteristics and suggested a depth up to 2 m and variable width flat-bottomed ditch connected to the road by a constant slope of 1.25H/1V. The given design chart and the FHWA (1989) modification of it represent a significant advancement in the design of roads and rail lines protection. However, Ritchie´s model have some drawbacks: (a) it does not provide cost criteria permitting for the selection of appropriate rock retention capacity for each slope segment; (b) it only provides outcomes for a particular shape ditch (i.e., trapezoidal ditch); and (c) this steep-sloped, deep ditch design makes it challenging for vehicles to return safely to the road and tough to maintain the road margins.

9.4.2 Experimental Approach

Experimental studies help comprehensively analyse the dynamic impact mechanism of falling rocks. Over time, numerous researchers have performed laboratory and field experiments on prototype, small-scale, or real-scale models of the rockfall protection structures to analyse rockfall impacts. These experimental studies have been performed not only to develop an understanding of the rockfall impact but also to calibrate interaction models among the falling rock and protection structures

for parameters such as the impact force, maximum impact energy, impact height, energy dissipation, and maximum structural deformation. But the drawback of these experimental studies is that they only allow the study of a limited number of variations for both the geometries and impact energies due to their complexity.

9.4.2.1 Flexible Barrier

For the testing of flexible barriers, two distinct arrangements are mainly possible depending on how the falling rock is accelerated, namely, vertical drops and inclined guidance of test blocks (Gerber 2001). A summary of experimental testing of flexible barriers to withstand rockfall up to 2008 can be found in Thommen (2008), and the experimental procedures have not greatly changed since then. Tajima et al. (2009) performed real-scale experiments on the flexible barrier with energy-dissipating devices and revealed that energy-dissipating devices could effectively diminish the tension in the net as well as the impact on the steel post and make it stable. Also, the rock vertical drop experiment on the flexible barrier conducted by Gottardi and Govoni (2010) revealed that runout length data of the energy-dissipating devices on the cables help show the distribution of forces between the nets. Besides, Liu et al. (2014, 2016) performed real-scale experiments on flexible barriers subjected to rockfall impact and evaluated the total deformation of the barrier after the impact. The authors also analysed the energy dissipation and destruction mechanism of the ring-type brake energy dissipation devices and the steel column posts. The outcomes show that the steel wire net is a highly significant energy-absorbing element, and optimizing the elements is crucial for future research. Along with this, they observed that initial force in the ring-type brake energy dissipators upsurged with an increase in the thickness of the steel pipe and length of an aluminium skirt, which also improved the flexibility of the barrier systems.

Additionally, researchers also conducted a force and displacement study. Peila et al. (1998) carried out real-scale experiments to analyse the impact energy of rockfall and its influence over the flexible barrier displacement and evaluate the parameters such as the dissipated kinetic energy of rocks and the maximum probable deformation of the barrier. Tajima et al. (2010) conducted rockfall impact experiments on a single module (single span net) made from polyethylene to study the performance of the net and assess its capacity to dissipate energy using the ring-type brake and U-shaped energy dissipators. Bertrand et al. (2012), proposed the 'curtain effect,' which considers the spatial heterogeneity of stiffness and strength as well as the failure rate of the flexible barrier due to rockfall impact. Giacomini et al. (2012) observed that the steel nets in flexible barriers efficiently dissipate the energy of impacts between the falling rock and flexible barrier, resulting in a 60% reduction in the length of the impact area. Thompson et al. (2013) conducted experimental investigations on a single-span net wherein the impact force was imparted on two types of nets with hinged or fixed boundaries. In addition, a prediction of future studies was put forward about the response behavior of various types of nets. Buzzi et al. (2015) performed three small-impact tests to evaluate the effects of stiffness on force transfer in flexible

nets and revealed that the higher the structure conforms to the regulation, the lesser force is transmitted to the net and the column post. Moreover, the 'bullet effect' of rockfall is investigated, and a better grid geometry has been suggested after a few experiments are carried out to examine the effect of rock block size, cable diameter, and net size on the performance of the flexible barrier.

9.4.2.2 Attenuator System

Over the past few decades, the studies are concentrated more on the testing of the attenuator systems. Here, the oblique impact is required; hence, vertical testing is not feasible, as the aim is not to stop the falling rock but to diverge or regulate its fall path or trajectory. Arndt et al. (2009) studied the mechanical behaviors and durability of the net and support cables by performing a real-scale impact test using an attenuator or hybrid flexible protection system. Giacomini et al. (2012) conducted an in-situ impact test of an attenuator system to analyse the rockfall velocity and energy distribution of the system. Some of the reported studies (Glover et al. 2012; Wyllie et al. 2017) investigated the entire process of energy dissipation and diversion of the falling path of rocks by enhancing the interface friction between rock blocks and slope surfaces during the experiments. These studies also analysed the interaction between nets and detached blocks, and the transmission of the impact force, energy dissipation, and net deformation.

9.4.2.3 Embankments

Several reported studies (Burroughs et al. 1993; Tissières 1999; Yoshida 1999; Peila et al. 2007; Lambert et al. 2014) have considered experimental approaches to understand the performance of rockfall protection reinforced embankments under rock block impact. While some studies examined the behavior of granular materials through real-scale impact tests on in-situ soil layers (Pichler et al. 2005), as well as on embankments (Burroughs et al. 1993; Peila et al. 2002). Other studies (Peila et al. 2007; Sung et al. 2008) assessed the deformation behavior of reinforced embankments under the impact. However, only a few relevant design parameters and the safe values of the energy absorption level of the embankment could be assessed. This is due to the high energy values of rock impacts in the field experiment, the limited size and shape of falling rocks, and the limited number of impacts. Small-scale or prototype experiments with kinetic energies <1,000 kJ are also reported for the embankments (Lambert and Kister 2018; Lu et al. 2021). These small-scale experiments are not only cost-saving, but the results are of great qualitative value. The kinetic energy of rocks is mostly >1,000 kJ. While the rockfall protection embankments may withstand multiple impacts of energy low to medium, small-scale experiments usually focus on determining the ultimate capacity of the embankments to withstand the block impact. Some of the reported studies also investigated the post-impact residual features to ensure the effective intercept of the subsequent rockfall (Durville

et al. 2011). Though limited in number, some studies have also been carried out on geosynthetics-reinforced embankments. Burroughs et al. (1993) used rock blocks of varying shapes, masses, and sizes, and rolled them down on an actual slope before hitting the embankments. In such cases, the propagation of the rock blocks is uncertain and could fragment; thus, it is difficult to effectively address a falling rock at a target on an embankment. It is challenging to extrapolate these results for various structural configurations and materials; since the mechanical properties, impacted material thickness, and boundary conditions significantly affect the embankment response (Calvetti 1998; Montani 1998).

9.4.2.4 Rock Shed

Several studies have reported the laboratory and field experiments for the analysis of rock sheds. Pichler et al. (2005) carried out rockfall tests to analyse the relationship in the rock mass, fall height, impact force, impact duration, penetration depth, and the rock shed deformation resistance. Calvetti (2011) performed real-scale experiments to estimate the impacting force of falling rock, its transfer to the soil cushion layer at the interface, and the dynamic response of the rock shed. Calvetti and di Prisco (2012) carried out systematic rockfall experiments on a rock shed, with a reinforced-concrete sphere of diameter 0.9 m and mass 850 kg dropped from heights varying between 5 and 45 m. The force of impact and the deformation of the rock shed are analysed. Zhao et al. (2021) performed a series of experiments to analyse the capacity of two types of composite cushion layers in a rock shed subjected to multiple rock block impacts. The outcomes illustrated that the composite cushion layer made of sand-expandable polyethylene is highly durable and effective against multiple impacts than sand-expandable polystyrene. The studies conducted for the analysis of the dynamic response of the rock shed can be categorised into three phases: elastic compression phase, which occurs just after the block impact; plastic deformation phase, in which the stresses induced by impacting rock on the rock shed surpasses its yield strength; and elastic resilience phase occurs after reaching the maximum compression deformation. While Zheng and Binienda (2007) performed a study based on these three phases, the study considered the constant rock shed elastic modulus in the second phase. It is expected that when plastic deformation increases, the elastic modulus will decrease. The other limitation of this study is that it only analyses the rock shed impact force variation with time, not the impact force variation with the rock shed deformation (Olsson 2003; Zheng and Binienda 2007). Therefore, it is impossible to find the permanent deformation of the rock shed due to rockfall, making it difficult to evaluate the rock shed's safety in the future.

9.4.2.5 Catch Ditch

The Oregon Department of Transportation (ODOT) conducted real-scale experiments between 1992 and 1994, collecting results from three types of catch ditches with

varying inclinations (1H/1V, 4H/1V, and 6H/1V). Rock blocks are dropped from varying heights but along a constant gradient (0.25H/1V) (Pierson et al. 1994). The likelihood of the blocks hitting the road, the frequency of rockfall, and the retention capacity of the catch ditch are estimated. In 2001, the FHWA and the ODOT examined various configurations of the catch ditches. About 11,250 rocks of varying sizes are rolled over four different slopes (0.25H/1V, 0.5H/1V, 0.75H/1V, and 1H/1V) and at various heights. In this case, the efficacy of three different types of triangular catch ditches (1H/0V, 6H/1V, and 4H/1V) is assessed. The outcomes enabled the generation of new design charts (Pierson et al. 2001).

9.4.3 Numerical Approach

Conducting large-scale experiments is very expensive and time-consuming. Therefore, at the design phase, it is necessary to limit their number and use their findings to develop numerical models capable of estimating the behavior of structures at various energy level impacts and to study the influence of block kinematics. Numerous numerical models have been established to consider rock impact dynamics. The widely-used models are either continuum-based models like the finite difference method (FDM) and the finite element method (FEM), or the discrete element method (DEM) based on discontinuous mechanics. The discrete element method (DEM) was first proposed by Cundall and Strack (1979) and has become more widely used. This method uses Newton's equation of motion and generally allows the modeling of large deformation. Discrete element methods (DEM) have been considered by several researchers (Nicot et al. 2007; Plassiard and Donzé 2009; Lorentz et al. 2010; Bourrier et al. 2011) to study the rockfall impact responses of the structures. DEM takes the discrete nature of granular material into account through the clustering of particles that interact with each other at contact points. The macroscopic mechanical nature of the granular particle clustering is influenced by the grading and shape of particles, the porosity of the granular assembly, and the contact characteristics. On the other hand, finite element method (FEM) based techniques involve a re-meshing algorithm and an explicit method to model large distortions and rockfall dynamics (Burroughs et al. 1993; Peila et al. 2007; Sung et al. 2008). Jarrin and Meignan (2010) used the finite difference method (FDM) to model rockfall protection bunds. In order to combine the benefits of the discrete element method in the impact region and of the finite element method in the far field, Breugnot et al. (2016) proposed a composite discrete-continuum method. The effect of the impact position, the shape of block, and the mass to velocity ratio for the same kinetic energy have been examined.

9.4.3.1 Flexible Barrier

The performance of rockfall flexible barriers has been significantly improved using numerical modeling-based studies (Volkwein 2005; Dhakal et al. 2012; Albaba et al.

2017). The nonlinear material behavior, geometrical nonlinearity caused by large deformations, and short-time simulation period have been successfully modeled using explicit finite element analysis strategies such as the Central Differences Method (Bathe 2001). This approach provides a detailed dynamic response to the system. It can also deliver information on the loading and degree of utilisation of any system configuration. The literature has suggested several approaches for simulating steel wire nets in the numerical model, with the most popular being the finite element method (FEM). The FEM has been used to model the impact of falling rocks against a flexible barrier in which the wire nets have been modeled using beam elements, truss elements, shell elements, and special purpose finite elements. For continuum problems, the FEM is well developed for dynamic modeling of nonlinear geometries with complicated contact and mechanical behavior, but for discontinuous problems, computing time becomes a major concern, particularly if the failure of the wire net needs to be taken into account. Therefore, the discrete element method (DEM) is a useful substitute since it is mainly effective for problems requiring dynamic impact and failure. The DEM has special features for analysing the motions and interactions of individual particles (Yu et al. 2018). Bertrand et al. (2008) and Dugelas et al. (2019) suggested a DEM technique for simulating twisted-pair hexagonal nets and a multi-node sliding cable model for the rockfall dynamic analysis. The modeling outcomes are contrasted with the tensile strength experiments performed on the net. Lisjak et al. (2020) use the coupled DEM—FEM to examine the interaction of rock blocks with the slope.

9.4.3.2 Rock Shed

To examine the interaction among the soil cushion and slab of the rock shed, 3D FEM models enable a coupled simulation of the rock shed with all its elements (Khasraghy et al. 2011). The peak impact force can be accurately simulated, though it is challenging to simulate a waveform of the second wave of the impact force. Since the impact resistance nature of the sand cushion layer is mainly discrete, the discrete element method (DEM) can be used to understand this nature. The DEM is considered to numerically analyse the materials (such as sand) cushioning mechanism. The DEM can monitor various deformation patterns, from elastic to plastic deformations, and post-fracture deformations (Matsushima and Chang 2011; Naito et al. 2020).

9.4.3.3 Embankments

Ronco et al. (2009) and Peila et al. (2007) performed finite element method (FEM)-based modeling of rock block impact on geosynthetic reinforced rockfall protection embankment by using explicit FEM code Abaqus. The local deformation of the reinforced embankment to stop a rock block is also modeled, and the total dissipation of kinetic energy by both the plastic deformation and frictional effect is estimated. Cuomo et al. (2020) investigated the performance of geosynthetics-reinforced

embankments through the FEM code Plaxis. Other contributions are provided by Plassiard and Donzé (2009), Wang and Tonon (2011), and Zhao et al. (2017) in simulating the falling rock fragmentation and its impact on the embankment through the DEM approach.

9.4.3.4 Catch Ditch

Pfeiffer and Bowen (1989), Pantelidis (2010), and Nishikawa et al. (2012) employed the numerical approach to develop rockfall propagation expressions and simulate the interaction between the propagating rocks and the ground. Pantelidis (2010) proposed a design chart for catch ditches based on the Ritchie ditch model. The results of this analysis are based on the modeling of the 100 rocks rolling over the slope of hard rock with a catch ditch at the toe of the slope.

9.5 Design Guidelines and Design Considerations

The design guidelines aim to codify/organize a validated general design procedure that is easy to apply while considering the uncertainties in the geotechnical domain and the dynamic propagation models. Presently, limited recommendations or guidelines are available for the design of rockfall protection structures. Since the design methodologies are either fairly new or under development, understanding these structures is constantly developing. The design guidance and recommendations presented here are based on currently accessible methodologies established by researchers and engineers. As the knowledge of the behavior and performance of these structures grow, the design methodologies are being updated. Most of these rockfall protection structures discussed previously are exclusive systems designed and tested at certified testing centers employing standard testing techniques. The designer must select an appropriate methodology for their site, taking into account the structure and associated risks. Thus, employing numerous methods and comparing the outcomes may be beneficial.

9.5.1 Flexible Barriers

Flexible barriers, or fences, are the most well-developed than the other rockfall protection structures, with recently released design guidelines by the Italian Standards Institute (UNI 2012) and the Austrian Standards Institute (ONR 2012). These standards will probably undergo further development when more information concerning the effectiveness of designed flexible barriers becomes available. The following are some of rockfall flexible barriers' most important design considerations.

Design Energy. The designer must first determine whether to design according to service energy level (SEL) or maximum energy level (MEL) load conditions based on ETAG 027 testing standard. Their applications in design are given by Peila and Ronco (2009). In MEL design, the flexible barriers are intended to resist a single impact of design energy. However, it will most likely need to be repaired or replaced after the block impact. This method could be used in instances when the frequency of rockfall incidents is expected to be minimal. While in SEL design, the flexible barriers are intended to resist several impacts of design energy, and it is envisaged that after impact, it will require little to no maintenance. This may be appropriate in regions where frequent rockfall occurrences are expected, or vehicles are easily accessible for repair and maintenance. Manufacturers' energy values are based on their MEL design load. For a flexible barrier with an energy value of 3,000 kJ, the design block would have allowable energy of 3,000 kJ in a MEL design and allowable energy of 1,000 kJ in an SEL design.

Size of Flexible Barrier. ONR (2012) and UNI (2012) suggested a broad approach in which partial safety factors are applied to input and output parameters in rockfall modeling. The partial safety factors are considered for uncertainty in the assumptions in input as well as the fact that ETAG 027 certification of the barrier was carried out under ideal conditions and assumptions (Grimod and Giacchetti 2014). The results of rockfall modeling should be combined with observations obtained during the site assessment when sizing the barrier for both bounce height and energy capacity. The majority of the literature discusses the difficulties of calculating bounce height as well as the limits of rockfall models in this regard. It is critical to evaluate bounce heights in the modeling process through model calibration and sensitivity assessments. If data from recent rockfall events are available, the evaluation of the heights of bounce from the rockfall-prone slope region is also required.

Deflection of flexible barrier. Rockfall protection flexible barriers may significantly deflect when subjected to falling rock impacts. The location of the particular infrastructure to be safeguarded against rockfall must be compared to the potential deflection of the barrier net. According to the Italian standard (UNI 2012), a safety factor of 1.0 to 1.5 should be applied to the maximum deflection of the barrier, based on design approaches (SEL or MEL) and the number of functional modules of flexible barrier or fence (measured during the ETAG 027 testing).

Anchor and Post Foundation Design. The primary component for transferring force to the ground is the anchors, which connect the barrier cables and posts to the ground. Typically, a foundation plate and concrete plinth are used to install the anchors. The manufacturer specifies anchor force based on the forces observed through the ETAG 027 testing of a specific system. In general, a safety factor is applied to the anchor forces, and proof tests should be done to check the functioning of an anchor. Sub-surface surveys may be essential to check the nature of rock and the bedrock depth, as well as the pull-out tests on test anchors, to verify the bond strength of design grout–ground. Whether the foundations or anchors are set in rock, discontinuity alignments should be investigated to see if there's a chance of possible formation of unstable blocks that could shift under anchor loads. Depending on the anchor spacing, group effects also need to be considered. The design safety factors

can be determined from the possible variability of field situations (quality and type of rock, bedrock thickness, etc.) and past knowledge of the site conditions.

Protection against Corrosion. Besides foundation construction and block impacts, the barrier design life will be influenced by the corrosion of its components. The barrier and its components must be treated with corrosion protection at the installation site.

9.5.2 Embankment

In current practice, reinforced rockfall protection embankments are the most widely employed technique of rockfall protection. Lambert and Bourrier (2013) discussed various approaches to embankment design that have been employed in the past. Some of these approaches focus on calculating the block penetration depth in the embankment. Generally, in an embankment, the kinetic impact energy of falling rock is dissipated (Grimod and Giacchetti 2013) via plastic deformation in the form of crater formation (80–85% of the impact energy), friction loss (15–20%), and elastic deformation (1% of the impact energy). The UNI (2012) and ONR (2012) have provided design recommendations for rockfall protection embankment design. The embankment design comprises an evaluation of the embankment geometry based on design rock size, impact height, and energy. These evaluated parameters are considered for calculating the block penetration depth with the help of a series of design charts developed from the physical tests and numerical modeling. The embankment design is either based on the serviceability limit state or the ultimate limit state (Grimod and Giacchetti 2013). The ultimate limit state corresponds to the maximum resistance capacity of the embankment without collapse (deformation >50% of embankment thickness at impact height). The serviceability limit state corresponds to the maximum deformation of the embankment that allows it to be repaired easily (deformation <20% of embankment thickness at impact height). Also, it is typically not more than 30 to 40 cm on the downward side and not more than 50 to 70 cm on the upstream side.

Further, the energy balance approach is adopted for the efficient design and construction of rockfall embankments. This design approach is best described in Ronco et al. (2009) and further updated to encounter the standards of the Technical Guideline provided by Christchurch City Council (CCC) for rockfall protection. The design approach includes two phases: (a) Evaluation of the energy levels of the rockfall and (b) Design of the rockfall protection embankment. The ETAG 27 requirements are considered while calculating the design energy level parameters. The design of the embankment is based on the factored energy values. The factors used comprise MEL (maximum energy level) in the order of 1.3 times the design energy level for low-frequency rockfall events and SEL (service energy level) in the order of 0.3 times the design energy level for multiple rockfall impacts (Ronco et al. 2009). Following are some considerations particular to each site that may

dictate embankment design, including construction sequencing, product limits, and contractor needs, based on experience with rockfall protection embankments.

Embankment Inclination. The hillside face inclination should be as steep as feasible to minimize the chances of blocks rolling up and over the structure. At an inclination of 70°, the probability of rocks passing over the embankment is less as compared to shallower angles because there is less rotational energy (Ronco et al. 2009).

Embankment Fill. To help drainage through the embankment, coarse-grained materials are typically used in the bottom layer of the embankment. The locally available fill material may be used with adequate measures for erosions, stabilization, or soil improvement to reduce the cost of construction.

Embankment Width. The width of the embankment must be adequate for the operation of compaction machinery. According to Lambert and Bourrier (2013), the top crest width should be greater than 1.0 m, and the minimum width of the embankment at the top should be 2 m, although Ronco et al. (2009) suggested embankments with a top crest width of about 0.9 m. Additionally, the embankment width at the block impact position should be greater than two times the penetration depth.

Embankment Height. The embankment height should be sufficient so that the falling block does not overpass. The embankment design must consider a freeboard above the impact height. A normal force is applied at this freeboard height above the impact position and produces shearing resistance against this impact force (Wyllie 2014).

Durability and Reparability. The facing components of the embankment must be durable to endure exposure to the environment. These components should be easy to repair under the SLS conditions; or replaceable under the ULS conditions.

9.5.3 Attenuator System

The primary goal of rockfall attenuator systems is to reduce the intensity of rockfall so that the rocks can pass through the attenuator system, reducing the energy, which is then manageable at a downslope catchment area. Such a catchment area can be a catch ditch, a rockfall barrier, or an additional attenuator in sequence. The major sources of energy losses are achieved through the three interactions, including (a) Net and impacting rock frictional contact; (b) Rock and slope surface frictional contact; and (c) Net and slope surface frictional contact.

The attenuator systems have been used for several decades and subjected to several field testing (Arndt et al. 2009). The Swiss Federal Institute for Forest and Landscape Research (WSL), in collaboration with Geobrugg AG, Switzerland, established the first standard for rockfall attenuator testing. This led to the Swiss standard for rockfall attenuator testing (Gerber 2001), which was later adapted to fulfill a European standard, the ETAG 027 (EOTA 2008). The Geobrugg company carried out the primary experimental program of attenuator system protection against rockfall in 2017. The testing procedure involves an impact of a rock into a rockfall attenuator generated

from a rock in free fall. During the experiment, the accelerometer was mounted in the mid of experimental objects and continuously collected data, including angular velocities and accelerations. Since it is difficult to identify the precise alignment of the block during impact, only general trends rather than exact values are used to compare these data. Numerical approaches are considered for getting a better understanding of the interaction between highly flexible protection structures and impacting rock blocks. To date, although rockfall attenuator systems have been widely applied as a rockfall mitigation solution, their design has been based on much engineering judgment and past experience of a trial-and-error approach. There are no established design guidelines for attenuators as of yet. Up to now, designs have been carried out utilising a theoretical approach based on limited field experiments and observations (Arndt et al. 2009; Glover et al. 2012). The general design recommendations for this kind of rockfall protection structure are given below.

Materials. The attenuator systems are generally designed with the help of ETAG 027 flexible barrier with modifications consisting of the wire net arrangement to make a tail that may be placed across the slope downstream of the system.

Energy capacity. The MEL design approach is used the same as followed for flexible barriers. The dynamic force and energy in the attenuator system are reduced since the system does not retain the rock block.

Drape Net Design. For the design of draped net**,** the material type, weight and durability, and the length of the required net are considered. The slope (slope angle, roughness) over which the net will rest is considered, along with the potential slicing forces resulting due to the bouncing and rotation of the rock. The purpose of the drape is to provide extra frictional contact between the block and the slope surface. If the drape is not appropriately designed, the rock block may be retained underneath the drape (affect future performance), or it may depart with a slight decrease in its energy.

Anchors and Posts. The force acting on an anchor in attenuator systems will generally be less as compared to a flexible barrier or fence. The forces exerted by the weight of the draped net may be taken into account for the post-spacing design.

Corrosion Protection. The design life of the system may be influenced by the frequency of rockfall captured by the system and the environmental situations. Same as considered for rockfall flexible barriers or fences.

9.5.4 Rock Shed

Based on real impact experiments, the first Swiss design guideline for rockfall protection sheds was issued in 1998. The effect of the cushion layer on the force of the impact was the main focus of the test experiments. The guideline applicability is limited to penetration depths that are smaller than half of the depth of the cushion layer. The impact load used in the latest version of the guideline (FEDRO 2008) is a function of the properties of the cushion layer (i.e., thickness, soil modulus, and internal friction angle) and the impacting block (i.e., size, mass, and velocity). A

coefficient C accounts for the structural behavior due to the dynamic load (brittle: C = 1.2, ductile: C = 0.4). Since the design approach uses a quasi-static equivalent force, it does not take into account whether forces are applied as acting on the cushion layer or acting on the slab, or as reactions from the slabs at the supports after the impact. The manual comprising recommendations for various protective measures is the handbook published in Japan (Masuya 2007). Here, the impact force acting on a shed depends on the mass and falling height of the block as well as on an amplification factor for the cushion thickness and Lamé's constants. The important design considerations for rock sheds are given below:

Foundation. The footing would need to be rested on a rock to provide the necessary bearing capacity. Since traffic operations would not provide enough time to construct the foundation on rock, bedrock-drilled rock socketed piers are used to support the foundation (Wyllie 2014). The force on the foundation includes the live load of rock fall impacts, the dead weight of the shed, and the force exerted horizontally on the crash wall.

Crash Wall. The crash wall is a wall that connects the columns holding the slab with a connector. The connector prevents the transfer of moments from the wall into the columns. The crash wall and foundation together would be cast-in-place concrete.

Mountain-side Wall. The mountain-side wall is a continuous wall that serves as both a support for the roof beams and a retainer for the fill. To withstand the weight of retained fill and water pressure that builds up behind the wall, the wall has incorporated tie-backs through the wall and rock anchors embedded in the rock face.

Columns. The columns are pre-cast structures with longitudinal spacing that corresponds to the width of roof beams. A layer of synthetic rubber is embedded in the concrete to give flexibility to the hinge. Pre-stressing cables are incorporated into the crest of all beams to form a rigid connection between the roof beams and the columns.

Roof Slab Beams. The roof slab beams are pre-cast structures. Holes for the post-stressing cables in the columns are included in the outer ends of the beams. The tops of the valley side columns are rigidly connected to the beams. Groups of post-tensioned cables connect the roof slab beams themselves.

Cushion Layer. The layer of loose sand is placed on top of the roof or slab of the rock shed to protect it from falling rocks. The sand is contained on the valley sides and sides of the shed by concrete blocks that are fastened to the outer edge of the slab.

9.6 Summary

Rockfall is a type of dangerous hazard in mountainous regions that is difficult to treat due to its unpredictability, rapidity, and widespread dispersion. The degree of damage caused by rockfall to the roads, rail lines, and infrastructures is highly severe. It is incredibly important to summarize rockfall mitigation strategies systematically. Various types of strategies can be used to mitigate rockfall hazards in mountainous

regions, some of which are employed to prevent the detachment of rocks from the rock-cut slope (active mitigation), while others are designed to protect the infrastructures down the slope by intercepting and stopping the falling rocks during downslope propagation (passive mitigation). To choose the most suitable rockfall mitigation measures in hilly areas, some major active measures to prevent rockfall and passive measures to protect the infrastructures are summarized in this chapter. The implementation of appropriate mitigation measures depends on a detailed investigation of the environmental factors that contribute to the occurrence of the rockfall hazard. According to past studies, passive measures have received more attention compared to active measures owing to the uncertainties associated with rockfall events. Flexible and semi-rigid passive mitigation measures (i.e., fences, attenuators, and embankments) are preferred over rigid, passive mitigation measures (i.e., stiff structural walls). The effectiveness of active measures depends on the precise identification of unstable and dangerous rocks, accurate assessment of failure modes, and thorough study of rock failure mechanisms. The effectiveness of passive measures heavily relies on the accurate assessment of rockfall trajectories, velocities, energies, and bounce heights. Selection of an appropriate mitigation strategy is a crucial and challenging task for various topographical and geological conditions, and this chapter intends to ease this task by presenting a comprehensive review of the mitigation measures.

Funding Information The authors acknowledge the funding received by the Science and Engineering Research Board (SERB), a statutory body of the Department of Science and Technology, Govt. of India, via the sponsored project SRG/2021/002290.

References

Abad SAM, Shooshtari A, Esmaeili V, Riabi AN (2013) Nonlinear analysis of cable structures under general loadings. Finite Elem Anal Des 73. https://doi.org/10.1016/j.finel.2013.05.002

Albaba A, Lambert S, Kneib F, et al (2017) DEM modeling of a flexible barrier impacted by a dry granular flow. Rock Mech Rock Eng 50. https://doi.org/10.1007/s00603-017-1286-z

Antoniou AA, Lekkas E (2010) Rockfall susceptibility map for Athinios port, Santorini Island, Greece. Geomorphology 118:152–166. https://doi.org/10.1016/j.geomorph.2009.12.015

Arndt B, Ortiz T, Turner A (2009) Colorado's full-scale field testing of rockfall attenuator systems. Transp Res E-Circular, E-C141. Transp Res Board, Color

Badger TC, Duffy JD, Sassudelli F, et al (2008) Hybrid barrier systems for rockfall protection. In: Interdisciplinary workshop on rockfall protection. pp 10–12

Bathe KJ (2001) Finite element methoden. Springer-Verlag, Berlin

Bertolo P, Oggeri C, Peila D (2009) Full-scale testing of draped nets for rock fall protection. Can Geotech J 46:306–317. https://doi.org/10.1139/T08-126

Bertrand D, Bourrier F, Olmedo I, et al (2013) Experimental and numerical dynamic analysis of a live tree stem impacted by a Charpy pendulum. Int J Solids Struct 50. https://doi.org/10.1016/j.ijsolstr.2013.01.037

Bertrand D, Nicot F, Gotteland P, Lambert S (2008) Discrete element method (DEM) numerical modeling of double-twisted hexagonal mesh. Can Geotech J 45(8):1104–1117. https://doi.org/10.1139/T08-036

Bertrand D, Trad A, Limam A, Silvani C (2012) Full-scale dynamic analysis of an innovative rockfall fence under impact using the discrete element method: from the local scale to the structure scale. Rock Mech Rock Eng 45. https://doi.org/10.1007/s00603-012-0222-5

Bourrier F, Lambert S, Heymann A, et al (2011) How multi-scale approaches can benefit the design of cellular rockfall protection structures. Can Geotech J 48. https://doi.org/10.1139/T11-072

Bourrier F, Nicot F, Darve F (2008) Physical processes within a 2D granular layer during an impact. Granul Matter 10. https://doi.org/10.1007/s10035-008-0108-0

Brandl H, Adam D (2000) Special applications of geosynthetics in geotechnical engineering. In: 2nd Eurpean conference on geosynthetics, Bologna, Italy

Breugnot A, Lambert S, Villard P, Gotteland P (2016) A discrete/continuous coupled approach for modeling impacts on cellular geostructures. Rock Mech Rock Eng 49:1831–1848. https://doi.org/10.1007/s00603-015-0886-8

Brunet G, Giacchetti G, Bertolo P, Peila D (2009) Protection from high energy rockfall impacts using terramesh embankments: design and experiences. In: 60th Highway geology symposium. pp 107–124

Budetta P (2004) Assessment of rockfall risk along roads. Nat Hazards Earth Syst Sci 4. https://doi.org/10.5194/nhess-4-71-2004

Burroughs DK, Henson HH, Jiang SS (1993) Full scale geotextile rock barrier wall testing, analysis and prediction. In: Proceedings of geosynthetics, pp 959–970

Buzzi O, Leonarduzzi E, Krummenacher B, et al (2015) Performance of high strength rock fall meshes: effect of block size and mesh geometry. Rock Mech Rock Eng 48. https://doi.org/10.1007/s00603-014-0640-7

Calvetti F (1998) Distinct element evaluation of the rock-fall design load for shelters. Riv Ital Di Geotec 3:63–83

Calvetti F (2011) Rockfall shelters covered by granular layers: experiments and design approach. Eur J Environ Civ Eng 15. https://doi.org/10.3166/EJECE.15SI.73-100

Calvetti F, di Prisco C (2012) Rockfall impacts on sheltering tunnels: real-scale experiments. Geotechnique 62. https://doi.org/10.1680/geot.9.P.036

Calvino A, Dumont P, Durville J-L, et al (2001) Parades contre les instabilités rocheuses. In: Guide technique, collection environnement, Les risques naturels, LCPC, Paris, p 143

Carotti A, Prisco C Di, Vecchiotti M, et al (2004) Modeling of geogrid reinforced embankments for rockfall protection. 3rd Euro Geosynth Conf

Castanon-Jano L, Blanco-Fernandez E, Castro-Fresno D, Ballester-Muñoz F (2017) Energy dissipating devices in falling rock protection barriers. Rock Mech Rock Eng 50. https://doi.org/10.1007/s00603-016-1130-x

Chen H, Tang H, Ye S, Zhu H (2006) Perilous rock prevention and control principle. Earthquake Press, Beijing (in Chinese)

Chen HK, Tang HM, Liu GH, et al (2004) Researches on calculation method of support and support-anchorage union to unstable rock. Yantu Gongcheng Xuebao/Chinese J Geotech Eng 26

Chen YC, Li JK, Ran LG (2013) A review of rockfall control measures along highway. Appl Mech Mater 353–354:2385–2391. https://doi.org/10.4028/www.scientific.net/AMM.353-356.2385

Corominas J (2013) Avoidance and protection measures. In: Treatise on Geomorphology

Cruden DM, Varnes DJ (1996) Landslide types and processes. Spec Rep Natl Res Counc Transp Res Board 247

Cundall PA, Strack ODL (1979) A discrete numerical model for granular assemblies. Geotechnique 29. https://doi.org/10.1680/geot.1979.29.1.47

Cuomo S, Moretti S, Frigo L, Aversa S (2020) Deformation mechanisms of deformable geosynthetics-reinforced barriers (DGRB) impacted by debris avalanches. Bull Eng Geol Environ 79:659–672. https://doi.org/10.1007/s10064-019-01589-w

Davis JW, Shakoor A (2005) Evaluation of the effectiveness of catchment ditches along ohio roadways. In: Transportation Research Record

Delhomme F, Mommessin M, Mougin J-P, Perrotin P (2007) Damage mechanisms of a reinforced concrete rock-shed slab impacted by blocks. J Struct Eng 133. https://doi.org/10.1061/(asce)0733-9445(2007)133:10(1426)

Descoeudres F, Montani S, Boll A, et al (1999) Rockfalls. Disaster Resilient Infrastructure. In: Minor HE (ed), Internat Decad Nat Disaster Reduct 37–47

Dhakal S, Bhandary NP, Yatabe R, Kinoshita N (2011) Experimental, numerical and analytical modelling of a newly developed rockfall protective cable-net structure. Nat Hazards Earth Syst Sci 11:3197–3212. https://doi.org/10.5194/nhess-11-3197-2011

Dhakal S, Bhandary NP, Yatabe R, Kinoshita N (2012) Numerical and analytical investigation towards performance enhancement of a newly developed rockfall protective cable-net structure. Nat Hazards Earth Syst Sci 12

Dorren LKA, Berger F (2006) Balancing tradition and technology to sustain rockfall-protection forests in the Alps. For Snow Landsc Res 80

Dugelas L, Coulibaly JB, Bourrier F, et al (2019) Assessment of the predictive capabilities of discrete element models for flexible rockfall barriers. Int J Impact Eng 133. https://doi.org/10.1016/j.ijimpeng.2019.103365

Durville JL, Bonnard C, Potherat P (2011) The Séchilienne (France) landslide: a non-typical progressive failure implying major risks. J Mt Sci 8. https://doi.org/10.1007/s11629-011-2086-7

EOTA (2008) Guidelines for European technical approval of falling protection kits (ETAG 027), Brussels

Fanos AM, Pradhan B, Mansor S et al (2018) A hybrid model using machine learning methods and GIS for potential rockfall source identification from airborne laser scanning data. Landslides 15:1833–1850. https://doi.org/10.1007/s10346-018-0990-4

FEDRO (2008) Directive 12006: actions de chutes de pierres sur les galeries de protection. OFROU, Bern, Switzerland

Gerber W (2001) Guideline for the approval of rockfall protection kits

Giacomini A, Thoeni K, Lambert C et al (2012) Experimental study on rockfall drapery systems for open pit highwalls. Int J Rock Mech Min Sci 56:171–181. https://doi.org/10.1016/j.ijrmms.2012.07.030

Glover J, Denk M, Bourrier F, et al (2012) Measuring the kinetic energy dissipation effects of rock fall attenuating systems with video analysis. In: Proc. Interpraevent congress, pp 151–160

Gottardi G, Govoni L (2010) Full-scale modelling of falling rock protection barriers. Rock Mech Rock Eng 43. https://doi.org/10.1007/s00603-009-0046-0

Grassl H, Volkwein A, Bartelt P (2003) Experimental and numerical modeling of highly flexible rockfall protection barriers. Proc Soil Rock Am 2003, Cambridge, MA

Grimod A, Giacchetti G (2014) Design approach for rockfall barriers tested according to ETAG 027. In: Landslide science for a safer geoenvironment: volume 3: targeted landslides

Grimod A, Giacchetti G (2013) Protection from high energy impacts using reinforced soil embankments: Design and experiences. Landslide Sci Pract Spat Anal Model 3:189–196. https://doi.org/10.1007/978-3-642-31310-3_26

Hambleton JP, Buzzi O, Giacomini A, et al (2013) Perforation of flexible rockfall barriers by normal block impact. In: Rock mechanics and rock engineering

Heymann A, Collombet M, Lambert S, Gotteland P (2011) Use of external testing methods to assess damage on rockfall protection structures. Appl Mech Mater

Hoek E (1983) Strength of jointed rock masses. Geotechnique 33. https://doi.org/10.1680/geot.1983.33.3.187

Jaecklin F (2006) Innovative design for repairing Gondo mudslide by 20 m high geogrid wall. In: 8th International conference on geosynthetics, Ozaka, Japan, pp 1223–1228

Jarrin JP, Meignan L (2010) Geomechanical modelling of rockfall protection bunds submitted to a dynamic impact. In: Proceedings of Journées Nationales de Géotechnique et de Géologie de l'Ingénieur JNGG2010—Grenoble 7–9 juillet 2010

JRA (2000) Japan road association: Japanese rockfall protection handbook (in Japanese)
Kanno H, Moriguchi S, Hayashi S, Terada K (2021) A computational design optimization method for rockfall protection embankments. Eng Geol 284. https://doi.org/10.1016/j.enggeo.2020.105920
Kar AK (1978) Projectile penetration into buried structures. ASCE J Struct Div 104:125–139. https://doi.org/10.1061/jsdeag.0004814
Khasraghy SG, Röthlin C, Vogel T (2011) Evaluation of the load carrying capacity of a rockfall protection gallery. Appl Mech Mater
Kister B, Fontana O (2011) On the evaluation of rockfall parameters and the design of protection embankments–a case study. In: Proceeding of interdisciplinary workshop on rockfall …
Kister B, Fontana O (2015) 2d- and 3d-rock fall simulations as a basis for the design of a protection embankment for a development area. Eng Geol Soc Territory 2: Landslide Processes
Labiouse V, Descoeudres F, Montani S (1996) Experimental study of rock sheds impacted by rock blocks. Struct Eng Int J Int Assoc Bridg Struct Eng 6:171–176. https://doi.org/10.2749/101686696780495536
Lambert S, Bourrier F (2013) Design of rockfall protection embankments: a review. Eng Geol 154
Lambert S, Heymann A, Gotteland P, Nicot F (2014) Real-scale investigation of the kinematic response of a rockfall protection embankment. Nat Hazards Earth Syst Sci 14:1269–1281. https://doi.org/10.5194/nhess-14-1269-2014
Lambert S, Kister B (2018) Efficiency assessment of existing rockfall protection embankments based on an impact strength criterion. Eng Geol 243. https://doi.org/10.1016/j.enggeo.2018.06.008
Li H bo, Li X wen, Li W zhou, et al (2019) Quantitative assessment for the rockfall hazard in a post-earthquake high rock slope using terrestrial laser scanning. Eng Geol 248:1–13. https://doi.org/10.1016/j.enggeo.2018.11.003
Lisjak A, Young-Schultz T, Li B, et al (2020) A novel rockbolt formulation for a GPU-accelerated, finite-discrete element method code and its application to underground excavations. Int J Rock Mech Min Sci 134. https://doi.org/10.1016/j.ijrmms.2020.104410
Liu C, Chen L, Chen C, Deng Y (2016) Full scale test and FEM simulation to ring-type brake energy dissipater in falling rock protection. Yanshilixue Yu Gongcheng Xuebao/Chinese J Rock Mech Eng 35. https://doi.org/10.13722/j.cnki.jrme.2015.0776
Liu C, Wei X, Lu Z, et al (2017) Studies on passive flexible protection to resist landslides caused by the May 12, 2008, Wenchuan earthquake. Struct Des Tall Spec Build 26. https://doi.org/10.1002/tal.1372
Liu CQ, Chen LY, Chen C, Wei T (2014) Experimental study on the passive flexible protection under the rock-fall impact. Chin J Geol Hazard Control 25:37–44
Lorentz J, Plassiard JP, Muquet L (2010) An innovative design process for rockfall embankments: application in the protection of a building at Val d'Isère. In: Proceedings of the 3rd Euro mediterranean symposium on advances in geomaterials and structures—AGS 2010, Djerba, Tunisia, pp 277–282
Lu L, Xiao L, Wang Z, et al (2021) Experimental testing of ground reinforced embankments under low-energy impact of rockfall. Rock Mech Rock Eng. https://doi.org/10.1007/s00603-021-02573-1
Masuya H (2007) Design method of structures under impact action by concept of performance based design, Japan society of civil engineers, committee of structural engineering, subcommittee concerning performance based design of structures against impact action
Matsushima T, Chang CS (2011) Quantitative evaluation of the effect of irregularly shaped particles in sheared granular assemblies. Granul Matter 13. https://doi.org/10.1007/s10035-011-0263-6
Mayne PW, Jones JS (1983) Impact stresses during dynamic compaction. J Geotech Eng 109. https://doi.org/10.1061/(ASCE)0733-9410(1983)109:10(1342)
Mentani A, Giacomini A, Buzzi O, et al (2016) Numerical modelling of a low-energy rockfall barrier: new insight into the bullet effect. Rock Mech Rock Eng 49. https://doi.org/10.1007/s00603-015-0803-1
Montani S (1998) Sollicitation dynamique de la couverture des galleries de protection lors de chutes de blocs

Moos C, Fehlmann M, Trappmann D et al (2018) Integrating the mitigating effect of forests into quantitative rockfall risk analysis—two case studies in Switzerland. Int J Disaster Risk Reduct 32:55–74. https://doi.org/10.1016/j.ijdrr.2017.09.036

Morino A, Grassi P (1990) Design and construction of a reinforced earth embankment for protection against rock falls. Proc 4th Int Congr Geotext Geotext Geomembranes Relat Prod

Mougin JP, Perrotin P, Mommessin M, et al (2005) Rock fall impact on reinforced concrete slab: an experimental approach. Int J Impact Eng 31. https://doi.org/10.1016/j.ijimpeng.2003.11.005

Naito N, Maeda K, Konno H, et al (2020) Rockfall impacts on sand cushions with different soil mechanical characteristics using discrete element method. Soils Found 60. https://doi.org/10.1016/j.sandf.2020.02.008

Ng CWW, Choi CE, Su AY et al (2016) Large-scale successive boulder impacts on a rigid barrier shielded by gabions. Can Geotech J 53:1688–1699. https://doi.org/10.1139/cgj-2016-0073

Nicot F, Gotteland P, Bertrand D, Lambert S (2007) Multiscale approach to geo-composite cellular structures subjected to rock impacts. Int J Numer Anal Methods Geomech 31. https://doi.org/10.1002/nag.604

Nishikawa Y, Masuya H, Moriguti Y (2012) Three dimensional simulation of rock fall motion with consideration of roughness of the slope surface. Trans Japan Soc Comput Eng Sci

Olsson R (2003) Closed form prediction of peak load and delamination onset under small mass impact. Compos Struct 59. https://doi.org/10.1016/S0263-8223(02)00244-1

ONR (2012) ÖNORM 24810: Technical protection against rockfall — Terms and definitions, effects of actions, design, monitoring and maintenance. Austrian standard institute, Vienna (draft 21 August 2012, in German).

Pantelidis L (2010) Rock Catchment Area Design Charts

Paronuzzi P (1989) Probabilistic approach for design optimization of rockfall protective barriers. Q J Eng Geol 22:175–183. https://doi.org/10.1144/gsl.qjeg.1989.022.03.02

Peila D, Oggeri C, Castiglia C (2007) Ground reinforced embankments for rockfall protection: design and evaluation of full scale tests. Landslides 4. https://doi.org/10.1007/s10346-007-0081-4

Peila D, Oggeri C, Castiglia C, et al (2002) Testing and modelling geogrid reinforced soil embankments subject to high energy rock impacts. In: 7th international conference on geosynthetics

Peila D, Pelizza S, Sassudelli F (1998) Evaluation of behaviour of rockfall restraining nets by full scale tests. Rock Mech Rock Eng 31. https://doi.org/10.1007/s006030050006

Peila D, Ronco C (2009) Technical note: design of rockfall net fences and the new ETAG 027 European guideline. Nat Hazards Earth Syst Sci 9. https://doi.org/10.5194/nhess-9-1291-2009

Pfeiffer TJ, Bowen TD (1989) Computer simulation of rockfalls. Bull Assoc Eng Geol 26:135–146

Pichler B, Hellmich C, Mang HA (2005) Impact of rocks onto gravel design and evaluation of experiments. Int J Impact Eng 31:559–578. https://doi.org/10.1016/j.ijimpeng.2004.01.007

Pierson LA, Davis SA, Pfeiffer TJ (1994) The nature of rockfall as the basis for a new catchment area design criteria for 0.25H:1V slopes

Pierson LA, Gullixson CF, Chassie RG (2001) Rockfall catchment area design guide. Final Report SPR-3(032).

Plassiard JP, Donzé FV (2009) Rockfall impact parameters on embankments: a discrete element method analysis. Struct Eng Int J Int Assoc Bridg Struct Eng 19:333–341. https://doi.org/10.2749/101686609788957874

Ritchie AM (1963) Evaluation of rockfall and its control. Highw Res Rec 17, Stab Rock Slopes, Highw Res Board, Natl Res Counc Washington, DC

Ronco C, Oggeri C, Peila D (2009) Design of reinforced ground embankments used for rockfall protection. Nat Hazards Earth Syst Sci 9. https://doi.org/10.5194/nhess-9-1189-2009

Schellenberg K, Ghadimi Khasraghy S, Vogel T (2008) Impact behavior of reinforced concrete slabs subjected to rock fall loading. WIT Trans Built Environ

Schellenberg K, Röthlin C, Ghadimi-Khasraghy S, Vogel T (2012) A review on the design of rock sheds with a cushion layer. In: Landslides and engineered slopes: Protecting society through improved understanding—proceedings of the 11th international and 2nd North American symposium on landslides and engineered slopes, 2012

Sun J, Chu Z, Liu Y, et al (2016) Performance of used tire cushion layer under rockfall impact. Shock Vib 2016. https://doi.org/10.1155/2016/8760592
Sung E, Yashima A, Aminata D, Sugimori K (2008) Numerical assessment of the performance of protecting wall against rockfall, pp 861–868
Tajima T, Maegawa K, Iwasaki M, et al (2009) Evaluation of pocket-type rock net by full scale tests. In: IABSE symposium, Bangkok 2009: sustainable infrastructure—environment friendly, safe and resource efficient
Tajima T, Maegawa K, Iwasaki M, Kawakami K (2010) Evaluation of pocket-type rockfall protection nets using shock absorbers by full scale weight impact tests. Kozo Kogaku Ronbunshu A 56:1088–1100
Thommen R. (2008) NTesting of various types of rockfall flexible wirerope mitigation barrier: an overview of testing to date. In: 59th highway geology symposium, Santa Fe
Thompson AG, Villaescusa E, Player JR, Morton EC (2013) Rock support mesh responses to static and dynamic loadings. In: Rock dynamics and applications—state of the art
Thornton C (1997) Coefficient of restitution for collinear collisions of elastic-perfectly plastic spheres. J Appl Mech Trans ASME 64. https://doi.org/10.1115/1.2787319
Tissières P (1999) Ditches and reinforced ditches against falling rocks. In: Proceedings of the joint Japan-Swiss scientific seminar on impact load by rock fall and design of protection structures, Kanazawa, Japan, pp 65–68
UNI (2012) UNI 11211–4—Opere di difesa dallacaduta massi. Parte 4: Progetto definitivo ed esecutivo (in Italian)
Varnes D (1978) Slope movement types and processes. Spec Rep 176
Vilajosana I, Suriñach E, Abellán A et al (2008) Rockfall induced seismic signals: case study in Montserrat, Catalonia. Nat Hazards Earth Syst Sci 8:805–812. https://doi.org/10.5194/nhess-8-805-2008
Vogel T, Labiouse V, Masuya H (2009) Rockfall protection as an integral task. Struct Eng Int J Int Assoc Bridg Struct Eng 19. https://doi.org/10.2749/101686609788957856
Volkwein A (2005) Numerical simulation of flexible rockfall protection systems. In: Proceedings of the 2005 ASCE international conference on computing in civil engineering
Volkwein A, Gerber W, Klette J, Spescha G (2019) Review of approval of flexible rockfall protection systems according to ETAG 027. Geoscience 9. https://doi.org/10.3390/geosciences9010049
Vu-Quoc L, Zhang X, Laesburg L (2000) A normal force-displacement model for contacting spheres accounting for plastic deformation: force-driven formulation. J Appl Mech Trans ASME 67. https://doi.org/10.1115/1.1305334
Wang M, Shi SQ, Yang YK, Luo X (2010) Mechanical analysis of the resistant capacity of cable nets in the active protection systems. J Logist Eng Univ 26:8–12
Wang Y, Tonon F (2011) Discrete element modeling of rock fragmentation upon impact in rock fall analysis. Rock Mech Rock Eng 44:23–35. https://doi.org/10.1007/s00603-010-0110-9
Wang Y, Xu M, Yang C, et al (2020) Effects of elastoplastic strengthening of gravel soil on rockfall impact force and penetration depth. Int J Impact Eng 136. https://doi.org/10.1016/j.ijimpeng.2019.103411
Wyllie D, Shevlin T, Glover J, Wendeler C (2017) Development of design method for rockfall attenuators. In: 68th highway geology symposium, pp 1–12
Wyllie DC (2014) Rock fall engineering.
Yang J, Duan S, Li Q, Liu C (2019) A review of flexible protection in rockfall protection. Nat Hazards 99. https://doi.org/10.1007/s11069-019-03709-x
Ye S, Chen H, Tang H (2010) The calculation method for the impact force of the rockfall. Zhongguo Tiedao Kexue/China Railw Sci 31
Yepes J, García-González C, Franesqui MA (2020) Rockfall hazard mitigation on infrastructures in volcanic slopes using computer-modelled ditches. Transp Geotech 25:100402. https://doi.org/10.1016/j.trgeo.2020.100402

Yong ACY, Lam C, Lam NTK, et al (2019) Analytical solution for estimating sliding displacement of rigid barriers subjected to boulder impact. J Eng Mech 145. https://doi.org/10.1061/(asce)em.1943-7889.0001576

Yoshida H (1999) Recent experimental studies on rockfall control in Japan. Proc Jt Japan-Swiss Sci Semin Impact Load by Rock Fall Des Prot Struct 69–78

Yu ZX, Qiao YK, Zhao L, et al (2018) A simple analytical method for evaluation of flexible rockfall barrier part 2: application and full-scale test. Adv Steel Constr 14. https://doi.org/10.18057/IJASC.2018.14.2.2

Zhao P, Xie L, Li L, et al (2018) Large-scale rockfall impact experiments on a RC rock-shed with a newly proposed cushion layer composed of sand and EPE. Eng Struct 175. https://doi.org/10.1016/j.engstruct.2018.08.046

Zhao P, Yuan S, Li L, et al (2021) Experimental study on the multi-impact resistance of a composite cushion composed of sand and geofoam. Geotext Geomembranes 49. https://doi.org/10.1016/j.geotexmem.2020.09.004

Zhao T, Crosta GB, Utili S, De Blasio FV (2017) Investigation of rock fragmentation during rockfalls and rock avalanches via 3-D discrete element analyses. J Geophys Res Earth Surf 122. https://doi.org/10.1002/2016JF004060

Zheng D, Binienda WK (2007) Effect of permanent indentation on the delamination threshold for small mass impact on plates. Int J Solids Struct 44. https://doi.org/10.1016/j.ijsolstr.2007.06.005

Chapter 10
Debris Flow Hazard in India: Current Status, Research Trends, and Emerging Challenges

Rajesh Kumar Dash, Manojit Samanta, and Debi Prasanna Kanungo

Abstract Debris flows are very common and frequently occurring geological processes in mountainous regions worldwide. Debris flows are less focused areas of research in India, although they are responsible for blocking the transportation corridors resulting disrupting the traffic, and blocking the rivers by forming potential landslide dams. Many times, debris flow acts as a destructive disaster costing the loss of many lives and a lot of properties every year. Debris flow hazard-vulnerability-risk assessment for its effective management is the need of this hour in the Indian context. This chapter attempts to present a detailed description of the composition, classification, causes, and characteristics of debris flow. The major triggering factors responsible for occurrences of debris flows in India and the status of debris flow research in India has also been discussed. In the last section, the challenges for debris flow research in India have been listed, and also the possible future prospects have been explored. Debris flows as a type of mass movement process needs special attention. The mitigation measures should be executed after a detailed study on the initiation mechanism, flow characteristics, depositional behavior, and overall hazard assessment.

Keywords Debris flow · Triggering factors · Hazards · Modelling · Challenges

R. K. Dash (✉) · D. P. Kanungo
Geo-Hazard Risk Reduction Group, CSIR-Central Building Research Institute, Roorkee 247667, Uttarakhand, India
e-mail: rajesh.geol92@gmail.com

M. Samanta
Geotechnical Engineering Group, CSIR-Central Building Research Institute, Roorkee 247667, Uttarakhand, India

M. Samanta · D. P. Kanungo
Academy of Scientific and Innovative Research (AcSIR), Ghaziabad 201002, India

P. Thambidurai and T. N. Singh (eds.), *Landslides: Detection, Prediction and Monitoring*,
https://doi.org/10.1007/978-3-031-23859-8_10

10.1 Introduction

Debris flows are very common and frequently occurring geological processes in mountainous regions worldwide (Hürlimann et al. 2008). The exact definition of debris flow given by Hungr et al. (2001) can be stated as "a very rapid to the extremely rapid flow of saturated non-plastic debris in a steep channel". In the mountainous region, debris flow represents a serious hazard due to its high mobility as well as impact energy (Kaitna et al. 2007; Iverson et al. 1997). Debris volume and composition govern the mobility and impact energy of the debris flow (Jakob 2005; Iverson 1997). Debris flow comprises three distinct zones: the source zone, the transportation zone, and the deposition zone (Dash et al. 2021). The area from where the debris flow initiates or the mobilization starts is the source zone. The debris flow moves through the transportation zone and gets deposited in the deposition zone as shown in Fig. 10.1.

10.1.1 Composition

Debris flow comprises finer particles (silt and clay) and coarser particles (sand, gravels, and boulders) and moves down the slope along with water due to gravity

Fig. 10.1 Source zone, transportation zone and deposition zone of a typical debris flow **a** pre-event **b** post-event image of Pettimudi debris flow at Idukki district, Kerala State, India (*Source* Google Earth)

(Hutter et al. 1994). Debris can be defined as loose unsorted materials of low plasticity such as that produced by the mass wasting process (colluvium), weathering (residual soil), glacier transport (till or ice contact deposit), explosive volcanism (granular pyroclastic deposits), or unsorted anthropogenic waste such as mine spoil (Hungr et al. 2001). Debris may also contain a significant amount of organic materials, including logs, tree stumps, and organic mulch. The major component of debris flow is water which initiates and maintains the flow process.

10.1.2 Causes of Debris Flow

The morphological characteristics of the slope and the valley, the material characteristics including its grain size distribution and strength parameters play important roles in defining the flow and deposition characteristics. With the preparatory factors, debris flow needs a triggering factor to initiate. The process may start as a debris flow from the beginning, or it may start in the later stage following a landslide or flash flood. Major causes of debris flow include rainfall, cloud burst, snowmelt, glacial lake outburst, and floods. As has also been reported, forest fires and volcanic activities can initiate debris flow to some extent.

10.1.3 Classification of Debris Flow

Stini (1910) seems to be the first to focus on the specific types of landslides that are debris flows in the Austrian monograph "Die Muren". He used terms such as debris-charged floods (Muren), debris-fronted, and surging debris flow (Murgange). The sediment-carrying floods in the mountain torrents were recognized and got attention. Earlier studies on debris flows were mentioned by Stini (1910) and Sharpe (1938). Sharpe coined important terms such as debris flow, debris avalanche, and earth flow. Sharpe (1938) described debris flow as similar to that of Stini (1910) and described it as saturated unsorted debris in a channel. Varnes (1958, 1978) retained and further expanded the framework and published it in the US Transportation Research Board report. Varnes (1978) presented a classification of landslides based on types of materials and types of movement. Types of materials involved in landslides can be classified as rock and soil. Further soils can be classified as debris and earth. Types of movement have been divided as falls, topple, slides, spreads, and flows. A flow is a spatially continuous movement in which the shear surface is short-lived, closely spaced, and usually not preserved (Cruden and Varnes 1996). Hutchinson (1968) recognized debris flows in England and classified them into channelized and hill slope debris flow. Ancey (2001) categorized debris flow under three major families based on the bulk mechanical behaviour: muddy debris flow, granular debris flow, and lahar-like debris flow. Based on the total volume of materials destabilized from the source zone, peak discharge, and area inundated, Jacob (2005)

proposed a tenfold classification according to debris flow size. Based on the material type, water content, presence of excess pore pressure or liquefaction at the source of the landslide, presence of a defined recurrent path (channel) and deposition area (fan), velocity, and peak discharge of the event, Hungr et al. (2001) categorized flow-type landslides into ten types namely non-liquefied sand flow, sand flow slide, clay flow slide, peat flow, earth flow, debris flow, mud flow, debris flood, debris avalanche, and rock avalanche. Based on the topographical and geological characteristics, debris flows can be categorized as hill slope and channelized debris flows. The debris flows moving down the valley slopes as tracks or sheets along their own paths are hillslope debris flows (Cruden and Varnes 1996), whereas channelized debris flows follow a pre-defined channel in mountain valleys (Nettleton et al. 2005). Hillslope debris flows are unconfined in nature and originate due to shallow failures at steep slopes (Hürlimann et al. 2015). Open slope/unchanelized debris flow results due to slope failure, and channelized debris flow follows a pre-existing path due to the mobilization of materials along with or at the base of the channel.

10.1.4 Characteristics of Debris Flow

Debris flows are capable of moving to a greater distance, even over a gentle slope, and can damage infrastructures that come along their path (Cannon and Savage 1988). Mobilization of debris flow starts from static, nearly rigid masses of sediment saturated with water and flows on the channel (Iverson 1997). The debris flow initiates when the poorly sorted soil, rock or debris, and loose and unconsolidated materials get saturated with water and mobilize from hill slopes or channels (Costa 1984). The conditions or factors required for the initiation of debris flow (Calligaris and Zini 2012; Arratano and Marchi 2008) are: (i) availability of materials at the source zone (Davies 1986); (ii) steep slope; (iii) sparse vegetation; and (iv) water. The recurrence interval of debris flow depends upon the availability of loose, unconsolidated materials at the source zone, which is a function of weathering (Costa 1984). Destructive powers of debris flows are because of factors such as the capability of transporting and depositing a huge amount of debris materials, high to extremely high velocity, and steep fronts (Arattano and Marchi 2008). The amount of materials present along the channel and the channel dimension is needed to estimate the debris flow volume (Sarkar et al. 2015). The distance travelled and the area occupied by the debris material in the post-mobilization stage is called debris flow runout. Debris flows run-out distance and areas are not only dependent on the topography and volume of the material but also affected by the debris flow composition and rheology (De Haas et al. 2015).

10.2 Debris Flows in India

According to the report of the National Disaster Management Authority, Ministry of Home Affairs, Government of India (NDMA 2019), about 0.42 million km^2 areas of the landmass (12.6%) are prone to landslides which spread over 65,000 mountainous villages in India. Among the various mass movement processes, debris flows are frequently occurring geological processes in India. Debris flows in India are mainly initiated by rainfall and cloud bursts, and recently debris flows in glacial regions have also been reported. Seismicity-induced debris flow events are not common in India. Areas affected by various mass movement processes in India mainly include three regions: the Indian Himalayan region, Western Ghats, and Eastern Ghats. Landslide-prone Indian Himalayas include three Northwest Himalayan States (Uttarakhand, Himachal Pradesh, and Jammu & Kashmir) and nine Northeast Himalayan States (Sikkim, Arunachal Pradesh, Assam, Nagaland, Manipur, Mizoram, Tripura, Meghalaya, and West Bengal). Debris flows are observed in all landslide-prone regions of India. India has witnessed a number of devastating debris flow events in the past, which include debris flow events in Chamoli District of Uttarakhand (2021), Kerala (2018), Kotropi (Himachal Pradesh) debris flow (2017), Kedarnath (Uttarakhand) disaster-related debris flows (2013), debris flow in Leh Ladakh valley (2010), etc. The major triggering factor for the initiation of debris flow in India is rainfall and cloudbursts. Cloudbursts are observed in high-altitude areas and on the top of the mountain due to the formation of the low-pressure area (Ghosh and Prakash 2010). Extremely high precipitation leads to cloudbursts and flash floods, followed by debris flows (Joshi and Kumar 2006). Most parts of the Himalayas experience cloudburst during the monsoon period. Indian Himalayas and the Western Ghats are the two most crucial locations for various mass movement events such as landslides, debris flows, rockfalls, debris slides, etc. Compared to these two, the Eastern Ghats region is less prone to landslides and debris flows, but few incidences have been reported in the past rainy season. Increasing debris flow events in Indian Himalayas and the Western Ghats are reported in Indian Monsoon, particularly between June and September. It has been observed that in the Indian Himalayan region, the road has been cut across the debris flow channels and when these debris flow channels get activated during monsoon, debris materials disrupt the road network. The debris flow materials reach the river bed level and get deposited on the river course with the possibilities of river damming in two ways: (i) by following the regular pre-defined channel or path along natural drainage feeding the river, and (ii) by clearing the debris deposited at road level and pushing down to the valley side, which subsequently reaches to the river travelling along the natural drainage. The first case arises in the case of channelized debris flow, and the latter is the case of unchanelized or hill slope debris flow. Along the mountainous National Highway corridor, culverts have been provided to make a route for channelized debris flows, and minor tributaries are generally the carriers of debris materials along with channels to the major rivers. Although there are several factors that are responsible for the initiation of debris flows, some of the major causes for debris flow in India can be listed:

- Blocking of the natural channel due to the construction of buildings and other infrastructure
- Lack of maintenance of natural and man-made drainage systems
- Uneven rainfall pattern and cloud burst
- Road cuttings for widening
- Uncontrolled development in hazardous locations
- Sediments present near the channel is added to the main channel.

10.3 Triggering Factors for Debris Flow in India

10.3.1 Debris Flow Due to Rainfall

Rainfall is the major triggering factor for debris flow initiation in India. Due to rainfall, either the slopes get saturated or mobilization starts during the rainfall. Due to the water penetration, pore pressure increases by decreasing the resisting parameters, which may make the saturated slope mobilizing. If the triggering phenomenon is rainfall, the debris flow characteristics might depend on rainfall intensity, overland flow, water content, and degree of saturation of the debris material. The major hydrological factors responsible for the mobilization of debris flow are the availability of adequate water for saturation (fully or partially) and sufficient pore water pressure for the initiation of slope failure (Iverson et al. 1997). Positive pore pressures accompanied by soil saturation result in the initiation and mobilization of debris flow. Positive pore pressure development may occur in two ways: from the direct infiltration of the water on the landslide body or may be from the groundwater inflow (Iverson et al. 1997).

10.3.2 Debris Flow Due to Earthquake

Earthquakes are major devastating natural hazards that claim hundreds of lives and huge property loss in the Indian Himalayas. Some of the major earthquakes in the past include the Assam earthquake (1897), Uttarkashi earthquake (1991), Chamoli earthquake (1999), Sikkim earthquake (2011), etc. These earthquakes triggered many landslides. Most of the Indian Himalayan regions come under zone IV, and V of India's seismic hazard zonation map and are high to very highly susceptible to earthquakes. About 421 landslides were triggered by the 2011 Sikkim earthquake (Ghosh et al. 2012), whereas Martha et al. (2015a) mapped a total number of 1,196 newly triggered landslides using very high-resolution satellite data. The collision of the Indian plate with the Eurasian plate and Intraplate movements within the Indian plate are the two main causes of the earthquake in the Indian Himalayas (Singh and Som 2016). The triggering of landslides due to earthquakes depends upon the distance of the landslide zone/area from the epicenter and the fault rupture, magnitude of the

earthquake, and the maximum shaking intensity (Keefer 1984). Landslides due to earthquakes are of two types such as co-seismic and post-seismic landslides (Parkash 2013). A co-seismic landslide takes place during the earthquake event. Post-seismic landslides generally occur after the earthquake due to the fissures, cracks, and deformations that originally developed due to the earthquake itself. Barnard et al. (2001) conducted mapping of 338 landslides, including 56 earthquake-induced landslides in Garhwal Himalayas after the 1999 Chamoli earthquake. Barnard et al. (2001) found that no debris flow occurred due to the earthquake but reported 33 debris flows mainly due to human activity. Earthquakes are not only responsible for the triggering of fresh landslides but also the reactivation of already existing landslides. In comparison to rainfall-induced debris flows, seismic/earthquake-induced debris flows are less common in Indian Himalayas. When the triggering phenomenon is an earthquake, factors such as the peak ground acceleration (PGA) and the tendency of the soil to liquefy are important.

10.3.3 Debris Flow Due to Landslides

It has been observed in Indian Himalayas that the initiation of debris flow takes place in two ways. In the first case, the materials available along the natural drainage or debris flow channel get saturated by rainfall or cloud bursts and propagate. In the second case, a landslide occurs at the top of the debris flow channel, which acts as a debris flow source zone, and the flow process gets initiated. Iverson et al. (1997) mentioned that mobilization of debris flow from landslide involves three processes: (i) widespread Coulomb failure within a sloping soil, rock, or sediment mass, (ii) partial or complete liquefaction of the mass by high pore-fluid pressure, and (iii) conversion of landslide translational energy to internal vibrational energy.

10.3.4 Debris Flow in the Glacial Region

A massive debris flow occurred on 16 July 2017 near the terminal moraine of the Meru glacier in the Bhagirathi basin of the Garhwal Himalayas (India). A huge amount of loose and unconsolidated debris materials mobilized and blocked the river Bhagirathi by forming a temporary lake (Singh et al. 2018). The major cause of this debris flow was high-intensity rainfall and moraine-dammed Lake Outburst. Due to rapid climate change in the Himalayan region, glaciers are retreating, which leads to debris flow occurrences in glaciated regions (Kumar et al. 2019). Due to the deposition of debris materials in the river valley, there is a shifting of approximately 150 m (Kumar et al. 2019) of the river Bhagirathi from west to east (Singh et al. 2018).

10.4 A Few Recent Debris Flow Events in India

India has witnessed many devastating debris flow events in the recent past. These include the debris flow event in Leh Ladakh (2010), the Kedarnath tragedy (2013), the Kerala flash flood and debris flow (2018), the Kotropi debris flow (2017), etc. Apart from these, numerous debris flows occur in the Indian Himalayan region, which has not been mentioned or studied. In monsoon seasons, these debris flows are the major devastating processes in the Indian Himalayan region and Western Ghats as well.

10.4.1 Kotropi Debris Flow (2017)

The Kotropi debris flow (Fig. 10.2) event occurred on 13 August 2017 in the Kotropi village of Mandi District in the State of Himachal Pradesh along National Highway 154. More than 46 people died because of this debris flow, and ten went missing (Pradhan et al. 2019). This debris flow was so devastating that two State transport buses of Himachal Pradesh were swept away down 800 m from the road, and about 300 m length of the National Highway was completely buried by debris materials (Sharma et al. 2019). The runout length of this debris flow was 1155 m with a width of 190 m and an area of 133,674 m^2 (Saini and Gangwar 2018). Kotropi debris flow was reactivated for the third time with a return period of 20 years in the years 1977, 1997, and 2017 (Pradhan et al. 2019). The main triggering factor for this debris flow was high-intensity rainfall.

10.4.2 Debris Flow Events During Kedarnath Disaster (2013)

The Kedarnath disaster occurred during 16–17 June 2013, when a 600 km long Central segment of Himalayas received extreme rainfall. Due to heavy rainfall, a large number of mass movements took place across the state of Uttarakhand, and the Kedarnath village was destroyed by two large debris flows that took place on 16/17 June 2013 (Allen et al. 2016). Detailed information on the causes and consequences of the 2013 Kedarnath disaster can be found in published literature (Sati and Gahalaut 2013; Das et al. 2015; Martha et al. 2015b; Allen et al. 2016; Chattoraj and Ray 2015; Ray et al. 2016; Rautela 2018). The debris flows completely destroyed the north-western part of the Kedarnath village (Das et al. 2015). Five districts of the Uttarakhand State, namely Rudraprayag, Chamoli, Uttarkashi, Pithoragarh, and Bagheswar, were severely affected (Khanduri 2018) and received very heavy precipitation during this event (Ray et al. 2016). Martha et al. (2015b) identified a total number of 6,013 landslides across the entire Bhagirathi and Alaknanda catchment, out of which a total of 3,472 were triggered due to the June 2013 event. The Kedarnath disaster of 2013 was the worst ever disaster in the history of Uttarakhand State.

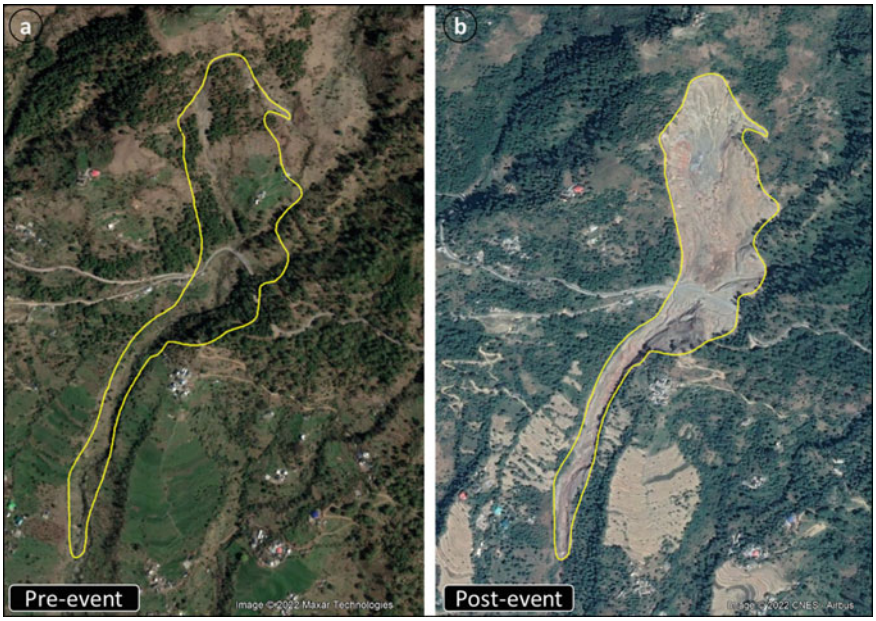

Fig. 10.2 Kotropi debris flow in Himachal Pradesh, Indian Himalayas (*Source* Google Earth)

10.4.3 Debris Flow Events in Kerala (2018)

Due to extremely high rainfall from 1 June to 26 August 2018 in two spells, the State of Kerala witnessed devastating mass movements and flooding (Kanungo et al. 2020). According to the report of the State Government, about 5.4 million people were affected, and 433 persons lost their lives. Due to this event, about 1200 villages in all 14 districts were affected, and 942 buildings were damaged (Hao et al. 2020). Hao et al. (2020) prepared a complete landslide inventory after the 2018 monsoon event in Kerala. A total of 4,728 landslides were identified, out of which debris flows (2,816 in number) were the most common phenomena initiated during this event. The Idukki was the worst affected district of Kerala, having 47.02% of total landslides in Kerala, and debris flows in Idukki District were 679 in number.

10.4.4 Leh Ladakh Debris Flow Event (2010)

Debris flow at Leh valley occurred on 6 August 2010, had a disastrous effect on the valley area. The main triggering factor for this debris flow was a cloud burst (Juyal 2010; Ghosh and Prakash 2010). Due to this disastrous debris flow, 234 lives were lost, more than 800 went missing, and more than 1,000 houses were completely or partially destructed (Gupta et al. 2012). 24 villages of the Leh region were severely

affected, and heavy destruction to the National highways, hospitals, airports, bus terminals, radio stations, mobile towers, and private properties were observed (Ghosh and Prakash 2010).

10.5 Debris Flow Studies in India

In the Indian subcontinent, debris flows generally occur due to rainfall. Cloud burst-induced debris flows occur almost every year in the Indian Himalayan region. In comparison to landslide hazard/susceptibility studies or slope stability assessment studies, very few studies have been conducted specifically on debris flow. Sati (2007) studied the economic and environmental assessment of two debris flow zones in the Garhwal Himalayas. Sujatha and Sridhar (2017) prepared a debris flow susceptibility map of the Palar sub-watershed in the Western Ghats of Tamil Nadu State using an analytical network process (ANP). Chattoraj et al. (2018) carried out 3-dimensional debris flow modelling of the 2014 debris flow event that occurred in Malin Village of Maharashtra State, a part of Western Ghat. The study used a continuum model-based simulation using RAMMS (Rapid mass movement software) for quantification of the debris flow intensity parameters such as the flow height, debris flow velocity, pressure along the path and momentum. Chattoraj et al. (2019) conducted a simulation of four debris flow sites in parts of the Garhwal Himalayas. Kumar et al. (2019) studied the mechanism and evolution of debris flow that occurred in the Gangotri glacier region using pre-and post-event observation, hydro-meteorological data and remote sensing analysis. Negi et al. (2020) carried out debris flow susceptibility assessment of the Ladakh–Nubra region using a GIS-based multi-criteria evaluation method by combining hydrological, topographical and environmental parameters for rainfall-induced debris flow. Chattoraj and Ray (2015) performed debris flow modelling of the 2013 Kedarnath area of Uttarakhand. Sujatha (2020) presented an approach for debris flow susceptibility assessment along the 8 km long Kodaikanal–Palani road corridor (Tamil Nadu State) using an analytical network process (ANP). Runout modelling and calibration of frictional parameters, including geotechnical investigation of Kurichermala debris flow in the Wynad district of Kerala (Western Ghats), was presented by Abraham et al. (2021). Jain et al. (2021) carried out inventory mapping, rainfall data analysis, and debris flow modelling of 6 large debris flows in the Idukki, Malappuram, and Wayanad districts of Kerala (Western Ghat) that occurred during 2018–2020. The debris flow modelling of the 2014 event at Malin (Maharashtra) was performed by Sajwan and Sengupta (2021) using the particle flow code (PFC2D) model. Bera et al. (2021) presented a debris flow susceptibility map of the Kalimpong region in Indian Himalayas by integrating the debris flow initiation and runout areas. Dash et al. (2021) conducted runout modelling, and hazard assessment of active debris flow in the Indian Himalayas (Tangni debris flow) using a continuum theory base model. Dash et al. (2022) generated the debris flow susceptibility zonation map of an approximate 1,200 sq. km area in the Chamoli district of Garhwal Himalaya, India, using statistical models.

Apart from these, several studies on the reporting of debris flow events, mechanism, causes and consequences, and detailed investigation of debris flows have been published by several authors, such as the 2013 Kedarnath disaster and debris flow events (Allen et al. 2016; Ray et al. 2016; Martha et al. 2015b), 2018 Kerala disaster and debris flows (Saini and Gangwar 2018; Vishnu et al. 2018), Kotropi debris flow (Sharma et al. 2019; Martha et al. 2019; Pradhan et al. 2019).

10.6 Scopes and Challenges for Debris Flow Modelling in India

10.6.1 Challenges

Debris flow modelling can be performed using two approaches. In the first approach, back analysis of a well-documented debris flow event is carried out to obtain the flow intensity parameters in which the calibrated values of input parameters can be used to predict the flow intensity parameters of the future potential debris flow. In the second approach, the data that is collected from the field is used and processed suitably for early warning. Both of these approaches are used for the future prediction of debris flow. But for the first approach, well-documented historical data on past debris flow is required, while in the second approach, data from field-based monitoring systems are necessary. The two major challenges for debris flow modelling in India are the lack of historical data on past debris flow events and the absence of field-based monitoring system.

10.6.1.1 Non-availability of Complete Quantitative Historical Data on the Debris Flow Events

Historical data on debris flow events are required for the calibration as well as validation of the numerical or physical models. This needs precise quantitative field data along with the debris flow inventory of those areas to establish the relationship. But lack of data on past events restricts the researchers to go for an alternative approach that can be performed without any past data or limited data. Debris flow susceptibility mapping can be carried out by locating debris flows and integrating them with thematic data layers, which are able to describe the spatial distribution of debris flows. But for debris flow hazard and risk assessment, flow intensity parameters need to be included, and the frequency-magnitude relation plays an important role. Direct measurement of debris flow is quite difficult, and very few researchers have captured it (Berti et al. 1999; Turnbul et al. 2015). Such quantitative data on debris flow are used to calibrate, validate, and predict theoretical and laboratory scale results (McCoy et al. 2010).

10.6.1.2 Absence of Permanent Debris Flow Monitoring System

Direct observation of debris flow is difficult due to (i) remote and inaccessible terrain, (ii) sporadic nature of occurrence (McCoy et al. 2010), and (iii) variation of hydro metrological events such as rainfall. Direct observation of debris flow initiation, propagation, and flow behavior is difficult because of its sudden occurrence & transient character (Sosio et al. 2007), and it takes very less time (Chen and Lee 2007). So, the data collected from field-based monitoring systems are used for calibration and validation and for understanding the debris flow process. But the case is more complex when there is no field-based monitoring system and direct observation of the event. Landslide, early warning system has been installed in very few places on the Indian subcontinent for real-time monitoring of vulnerable slopes, such as at Tangni landslide of Uttarakhand (Chaturvedi et al. 2014), Pakhi landslide of Uttarakhand (Kanungo 2019), Kotropi landslide of Himachal Pradesh (Thakur et al. 2021), Idukki district of Kerala (Ramesh 2009; Ramesh and Vasudevan 2012). But presently, no in-situ debris flow monitoring system is available in India.

10.6.2 Scopes

Debris flow modelling for related hazard and risk assessment, as well as for management and mitigation, is a multi-disciplinary approach. There are a number of aspects of debris flow on which research has been done and also is going on, such as debris flow hazard/susceptibility assessment, rheological modelling, runout modelling, initiation mechanism, depositional mechanism etc. The present paper deals with the scope of the modelling approach of debris flow runout for delineation of inundation areas keeping in view the lack of historical data and permanent monitoring system and by using an indirect method of debris flow modelling with limited data.

10.6.2.1 Development of a Suitable Framework for Debris Flow Modelling with Limited Data and Considering the Present Status of the Debris Flow

Debris flow modelling can be carried out empirically or numerically. Empirical approaches are not suitable in the case of a lack of data. Numerical simulation-based approaches need some field data for validation purposes. So for the Indian scenario, it is essential to formulate a suitable framework, which can be performed with limited data collected from the field in a post-event stage. Indirect methods can be adopted to reconstruct past events. Opinions from local people, as well as the expert working on the same area and familiar with the debris flow, should be considered as key evidence for this. Extensive fieldwork, satellite data, remote sensing-based assessment, and qualitative hazard analysis on the basis of past observation play important roles in such an approach. When there is a complete absence of historical data, laboratory

scale investigation and numerical validation can be a predictive alternative; but the validation of any output with field evidence is considered more accurate.

10.6.2.2 Site-Specific Debris Flow Modelling Through Simulation and Hazard/Risk Assessment with Potential Release Areas

The approaches for runout estimation can be categorized into three major groups such as empirical, analytical, and numerical approaches (Dai et al. 2002). Empirical approaches can be well utilized for the estimation of debris flow runout in a study area with precise and complete historical data on debris flow events. This approach is simple and easy to use. Analytical methods (Sassa 1989; Hutchinson 1986) for estimating debris flow runout are based on lumped mass models, where the entire mass of the debris is considered as a single point (Dai et al. 2002).

Numerical models can be categorized into two broad categories: continuum-based model and discrete element or discontinum model. A numerical model based on continuum mechanics needs a suitable rheological model. The relevant rheological parameters must be found in the field by back analysis or laboratory analysis (Dai et al. 2002; Chen and Lee 2004). The numerical modelling of a debris flow from the Indian Himalayas has been shown in Fig. 10.3. For the assessment of debris flow hazard, two aspects have to be set out: (i) debris flow occurrence and (ii) characteristics of the debris flow (Rickenmann 2005). The probability of debris flow occurrences can be determined from debris flow hazard/susceptibility studies, which will describe the spatial distribution of debris flow in an area. Frequency-magnitude relation is used to determine the probability of debris flow occurrences. This is based on the historical data of past events. In the second stage, the characteristics of a debris flow can be quantified by modelling, which describes the (i) initiation process, (ii) propagation in the channel, including entrainment, and (iii) depositional process.

Hürlimann et al. (2008) evaluated different techniques and approaches that are used to calculate debris flow parameters for hazard assessment by performing the back analysis of well-documented debris flow events. Their specific major findings stated that (i) the empirical model is suitable for a particular study area or condition, where it has been developed or on which it is based; (ii) for hazard mapping, calibration of rheological parameters for past events is the preliminary work; and (iii) numerical modelling is capable of giving the exact values, while analytical methods may be useful for preliminary flow behavior. Pirulli (2010) carried out the forward analysis of a potential debris flow event of 10,000 m^3 of volume by using the rheological outputs obtained from the back analysis of a 2005 debris flow event that took place in the same basin. Forward analysis of the events with the calibrated values for hazard assessment is a useful tool (Pirulli 2010). To adapt the calibration-based approach, the events that are being considered should have similar lithological or material, morphological, and rheological behavior.

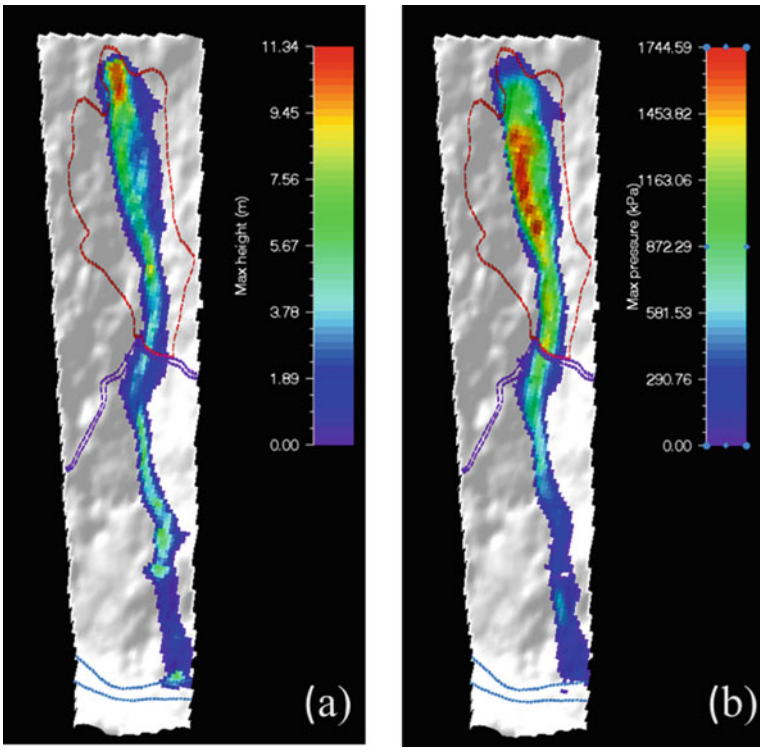

Fig. 10.3 Example of numerical modelling of debris flow runout **a** simulated height **b** simulated pressure

10.6.2.3 Experimental Study on Debris Flow

The entire process of a debris flow can be defined mainly in three stages: failure, propagation, and deposition. The core objectives of debris flow studies focus on understanding the mechanism of each of these stages (Hutter et al. 1994). Debris flows can be studied both in the field as well as in the laboratory. Although the data from the real field are more accurate and precise, it is practically difficult to obtain the data during the debris flow to get quantitative information on the flow intensity parameters such as velocity, flow, deposition height, momentum, and impact energy. Still, there are cases of some direct observations of debris flows in the real field. Due to these difficulties of directly observing natural debris flows and the uncertainties involved in the interpretation of field deposits, the analysis of debris flow has been augmented by experimental studies. So, the common alternatives to this direct observation of debris flow events are reproducing it under controlled conditions at a reduced scale in the laboratory and analyzing it on the basis of accepted theory (Davies 1990).

Experimental studies on debris flows are conducted using a physical scale model established in the laboratory scale. Physical scale modelling of debris flow refers

to the replication of debris flow in the laboratory on a scale-down model, which represents the real field situation and essentially includes all the conditions that exist in the field. There are several ways by which experimental study in the field and in the laboratory can be performed apart from direct observation during the debris flow event (Iverson 2015). One such type includes the installation of sensors in the natural hillslope and watering it artificially to create the rainfall scenario until failure occurs (Ochiai et al. 2004, 2007). Some experimental studies are based on the discharge of debris (mixtures of water and sediment) onto the well-instrumented natural slope or debris flow channel under a controlled environment (Bugnion et al. 2012). Bugnion et al. (2012) conducted a real-scale field experiment to investigate the hillslope debris flow impact pressures by constructing a 41 m long, 8 m wide channel in Cantom Agrgau, Switzerland. The same study can be conducted in the laboratory for the failure mechanism of landslides and for the investigation of the initiation, propagation and deposition mechanism of debris flow.

A debris flow flume model is designed and fabricated in the laboratory of CSIR-Central Building Research Institute, Roorkee, for experimental study on debris flow (Fig. 10.4).

The experimental setup is 6.5 m in length, out of which 1.5 m from the top of the channel section has been utilized as a storage tank to contain the debris flow materials (Fig. 10.4). This storage tank is considered as the source zone of a typical debris flow. The width and height of the flume model are 0.5 m and 1 m, respectively. Lengthwise the whole channel section consists of 3 segments of 1.5 m, 1.5 m, and 2 m in length from top to bottom. These channel sections are interconnected and can

Fig. 10.4 Debris flow experimental facility developed at CSIR-CBRI, Roorkee

Fig. 10.5 Sensors installed on the flow path and the deposition zone **a** laser sensor for measuring flow height **b** pore water pressure sensor **c** the rough surface of the flow path

be tilted to desired angles. The sidewalls of the channel are made up of transparent plexiglass. The base of the channel is made up of an aluminum plate and is rough. The channel section acts as a flow path or transportation zone for the debris flow. The deposition zone for the debris flow material is made horizontal (i.e., flat) with a concrete floor. The storage tank is closed with a provision of an openable gate. Sensors are installed to capture quantitative data on flow intensity parameters. The sensors installed and the base of the flow channel has been shown in Figs. 10.5 and 10.6 shows the runout and deposition of an experimental debris flow conducted at CSIR-CBRI, Roorkee.

10.7 Conclusions

Debris flows are the most destructive geological processes in mountainous terrains. Indian Himalayan region and the Western Ghats, are frequently affected by debris flow processes, which destroy engineering projects and infrastructures as well as huge socio-economic and environmental degradation parallel with loss of lives. For planning and execution of debris flow mitigation measures, debris flow modelling studies should be conducted in order to assess the hazard and risk related to future debris flows in the area under study. The major triggering factor for the initiation and propagation of debris flows in the Indian Himalayan region and in other regions is rainfall. India has witnessed numerous disastrous earthquakes in the past, which have initiated or developed numerous numbers of landslides. But it has not yet been reported in the case of debris flow. In developed countries like Italy, Switzerland, and China, debris flow studies are carried out using past debris flow records and validated with the past documented field parameters. In India, due to the absence of well documented historical data on debris flow events, approaches based on the field observations of recent debris flow events with little past information should be developed. Numerical simulation approaches can be suitable for debris flow modeling and subsequent debris flow hazard and risk assessment in India. One of the major concerns regarding landslide hazard/susceptibility mapping in India is that such a map needs to describe different mass movement processes such as debris flow, rock

Fig. 10.6 Experimental reconstruction of debris flow and depositional morphology depicting the zones of debris flow

fall etc. In debris flow hazard/susceptibility assessment studies, debris flow runout analysis should be incorporated using a suitable approach depending on the data availability and expert knowledge. In case of the absence of historical data, it is difficult to establish the frequency-magnitude relation of debris flow which is used to find out the probability of occurrences of the event with a predicted interval. In such cases, indirect methods can be adopted.

Acknowledgements The authors are grateful to Director, CSIR-Central Building Research Institute, Roorkee, Uttarakhand (India) for granting permission to publish this paper.

References

Abraham MT, Satyam N, Reddy SKP, Pradhan B (2021) Runout modeling and calibration of friction parameters of Kurichermala debris flow, India. Landslides 18:737–754

Allen SK, Rastner P, Arora M, Huggel C, Stoffel M (2016) Lake outburst and debris flow disaster at Kedarnath, June 2013: hydrometeorological triggering and topographic predisposition. Landslides 13(6):1479–1491

Ancey C (2001) Debris flows and related phenomena. In: Geomorphological fluid mechanics. Springer, Berlin, Heidelberg, pp 528–547

Arattano M, Marchi L (2008) Systems and sensors for debris-flow monitoring and warning. Sensors 8(4):2436–2452

Barnard PL, Owen LA, Sharma MC, Finkel RC (2001) Natural and human-induced landsliding in the Garhwal Himalaya of northern India. Geomorphology 40(1–2):21–35

Bera S, Melo R, Guru B (2021) Assessment of exposed elements in a changing built environment by using an integrated model of debris flow initiation and runout (Kalimpong region, Himalaya). Bull Eng Geol Env 80(9):7131–7152

Berti M, Genevois R, Simoni A, Tecca PR (1999) Field observations of a debris flow event in the Dolomites. Geomorphology 29(3–4):265–274

Bugnion L, McArdell BW, Bartelt P, Wendeler C (2012) Measurements of hillslope debris flow impact pressure on obstacles. Landslides 9(2):179–187

Calligaris C, Zini L (2012) Debris flow phenomena: a short overview. In: Earth Sciences. INTECH, Croatia, pp 71–90

Cannon SH, Savage WZ (1988) A mass-change model for the estimation of debris-flow runout. J Geol 96(2):221–227

Chattoraj SL, Ray PC (2015) Simulation and modeling of debris flows using satellite derived data: a case study from Kedarnath Area. Int J Geomat Geosci 6(2):1498

Chattoraj SL, Pardeshi S, Gupta V, Ketholia Y (2018) 3-Dimensional modeling of 2014-malin landslide, Maharashtra using satellite-derived data: a quantitative approach to numerical simulation technique. In: Natural hazards and earth system sciences discussions, pp 1–19

Chattoraj SL, Ray PC, Kannaujiya S (2019) Simulation outputs of major debris flows in Garhwal Himalaya: a geotechnical modeling approach for hazard mitigation. In: Remote sensing of northwest Himalayan ecosystems. Springer, Singapore, pp 37–56

Chaturvedi P, Jaiswal B, Sharma S, Tyagi N (2014). Instrumentation based dynamics study of Tangni landslide near Chamoli, Uttrakhand. Int J Res Adv Technol 2(10)

Chen H, Lee CF (2004) Geohazards of slope mass movement and its prevention in Hong Kong. Eng Geol 76(1–2):3–25

Chen J, Lee CF (2007). Landslide mobility analysis using Madflow. In: Proc. the 2007 international forum on landslide disaster management, vol 2, pp 857–874

Costa JE (1984) Physical geomorphology of debris flows. In: Developments and applications of geomorphology. Springer, Berlin, Heidelberg, pp 268–317
Cruden DM, Varnes DJ (1996) Chapter 3: Landslide types and processes. In: Turner AK, Schuster RL (eds) Landslides investigation and mitigation. Transportation research board, US National Research Council. Special Report 247, Washington, DC, pp 36–75
Dai FC, Lee CF, Ngai YY (2002) Landslide risk assessment and management: an overview. Eng Geol 64(1):65–87
Das S, Kar NS, Bandyopadhyay S (2015) Glacial lake outburst flood at Kedarnath, Indian Himalaya: a study using digital elevation models and satellite images. Nat Hazards 77(2):769–786
Dash RK, Kanungo DP, Malet JP (2021) Runout modelling and hazard assessment of Tangni debris flow in Garhwal Himalayas India. Environ Earth Sci 80(9):1–19
Dash RK, Falae PO, Kanungo DP (2022) Debris flow susceptibility zonation using statistical models in parts of Northwest Indian Himalayas—implementation, validation, and comparative evaluation. Nat Hazards 111(2):2011–2058
Davies TRH (1986) Large debris flows: a macro-viscous phenomenon. Acta Mech 63(1):161–178
Davies TR (1990) Debris-flow surges—experimental simulation. J Hydrol (New Zealand) 29:18–46
De Haas T, Braat L, Leuven JR, Lokhorst IR, Kleinhans MG (2015) Effects of debris flow composition on runout, depositional mechanisms, and deposit morphology in laboratory experiments. J Geophys Res Earth Surf 120(9):1949–1972
Ghosh C, Parkash S (2010) Cloud-burst-induced debris flows on vulnerable establishments at Leh. Indian Landslides 3(2):1–6
Ghosh GK, Ghosh K, De SK, Rawat MS, Joshi V, Ayala IA (2012) An inventory of recent (18th September 2011) earthquake triggered landslides in the Sikkim Himalaya. J Geo-Environ Obs 1:1–94
Gupta P, Khanna A, Majumdar S (2012) Disaster management in flash floods in Leh (Ladakh): a case study. Indian J Community Med 37(3):185–190
Hao L, Rajaneesh A, Van Westen C, Sajinkumar KS, Martha TR, Jaiswal P, McAdoo BG (2020) Constructing a complete landslide inventory dataset for the 2018 monsoon disaster in Kerala, India, for land use change analysis. Earth Syst Sci Data 12(4):2899–2918
Hungr O, Evans SG, Hutchinson IN (2001) A review of the classification of landslides of the flow type. Environ Eng Geosci 7(3):221–238
Hürlimann M, Rickenmann D, Medina V, Bateman A (2008) Evaluation of approaches to calculate debris-flow parameters for hazard assessment. Eng Geol 102(3–4):152–163
Hürlimann M, McArdell BW, Rickli C (2015) Field and laboratory analysis of the runout characteristics of hillslope debris flows in Switzerland. Geomorphology 232:20–32
Hutchinson JN (1968) Mass movement. In: Fairbridge RW (ed) Encyclopedia of geomorphology. Reinhold Publishers, New York, pp 688–695
Hutchinson JN (1986) A sliding–consolidation model for flow slides. Can Geotech J 23(2):115–126
Hutter K, Svendsen B, Rickenmann D (1994) Debris flow modeling: a review. Contin Mech Thermodyn 8(1):1–35
Iverson RM (1997) The physics of debris flows. Rev Geophys 35(3):245–296
Iverson RM (2015) Scaling and design of landslide and debris-flow experiments. Geomorphology 244:9–20
Iverson RM, Reid ME, LaHusen RG (1997) Debris-flow mobilization from landslides. Annu Rev Earth Planet Sci 25(1):85–138
Jain N, Martha TR, Khanna K, Roy P, Kumar KV (2021) Major landslides in Kerala, India, during 2018–2020 period: an analysis using rainfall data and debris flow model. Landslides 18(11):3629–3645
Jakob M (2005) A size classification for debris flows. Eng Geol 79(3–4):151–161
Joshi V, Kumar K (2006) Extreme rainfall events and associated natural hazards in Alaknanda valley Indian Himalayan Region. J Mt Sci 3(3):228–236
Juyal N (2010) Cloud burst-triggered debris flows around Leh. Curr Sci 99(9):1166–1167

Kaitna R, Rickenmann D, Schatzmann M (2007) Experimental study on rheologic behaviour of debris flow material. Acta Geotech 2(2):71–85
Kanungo DP (2019). Ground based real time monitoring system using wireless instrumentation for landslide prediction. In Landslides: theory, practice and modelling. Springer, Cham, pp 105–120
Kanungo DP, Singh R, Dash RK (2020) Field observations and lessons learnt from the 2018 landslide disasters in Idukki District, Kerala India. Curr Sci 119(11):1797–1806
Keefer DK (1984) Landslides caused by earthquakes. Geol Soc Am Bull 95:406–421
Khanduri S (2018) Landslide distribution and damages during 2013 deluge: a case study of Chamoli District Uttarakhand. J Geogr Nat Disast 8(226):2167–2587
Kumar A, Bhambri R, Tiwari SK, Verma A, Gupta AK, Kawishwar P (2019) Evolution of debris flow and moraine failure in the Gangotri Glacier region, Garhwal Himalaya: hydro-geomorphological aspects. Geomorphology 333:152–166
Martha TR, Govindharaj KB, Kumar KV (2015a) Damage and geological assessment of the 18 September 2011 Mw 6.9 earthquake in Sikkim, India using very high resolution satellite data. Geosci Front 6(6):793–805
Martha TR, Roy P, Govindharaj KB, Kumar KV, Diwakar PG, Dadhwal VK (2015b) Landslides triggered by the June 2013 extreme rainfall event in parts of Uttarakhand state India. Landslides 12(1):135–146
Martha TR, Roy P, Khanna K, Mrinalni K, Vinod Kumar K (2019) Landslides mapped using satellite data in the Western Ghats of India after excess rainfall during August 2018. Curr Sci 117(5):804–812
McCoy SW, Kean JW, Coe JA, Staley DM, Wasklewicz TA, Tucker GE (2010) Evolution of a natural debris flow: in situ measurements of flow dynamics, video imagery, and terrestrial laser scanning. Geology 38(8):735–738
NDMA (2019) National landslide risk management strategy. A publication of the National Disaster Management Authority Government of India, New Delhi
Negi HS, Kumar A, Rao NN, Thakur NK, Shekhar MS (2020) Susceptibility assessment of rainfall induced debris flow zones in Ladakh-Nubra region Indian Himalaya. J Earth Syst Sci 129(1):1–20
Nettleton IM, Martin S, Hencher S, Moore R (2005). Debris flow types and mechanisms. In: Scottish road netw landslides study, pp 1–119
Ochiai H et al (2004) A fluidized landslide on a natural slope by artificial rainfall. Landslides 1(3):211–219
Ochiai H, Sammori T, Okada Y (2007) Landslide experiments on artificial and natural slopes. Progress in landslide science. Springer, Berlin, Heidelberg, pp 209–226
Parkash S (2013) Earthquake related landslides in the Indian Himalaya: experiences from the past and implications for the future. Landslide science and practice. Springer, Berlin, Heidelberg, pp 327–334
Pirulli M (2010) On the use of the calibration-based approach for debris-flow forward-analyses. Nat Hazard 10(5):1009–1019
Pradhan SP, Panda SD, Roul AR, Thakur M (2019) Insights into the recent Kotropi landslide of August 2017, India: a geological investigation and slope stability analysis. Landslides 16(8):1529–1537
Ramesh MV (2009) Real-time wireless sensor network for landslide detection. In: 2009 third international conference on sensor technologies and applications. IEEE, pp 405–409
Ramesh MV, Vasudevan N (2012) The deployment of deep-earth sensor probes for landslide detection. Landslides 9(4):457–474
Rautela P (2018) Lessons learnt from June 16/17, 2013 disaster of Uttarakhand, India. In: Science and technology in disaster risk reduction in Asia. Academic Press, pp 273–300
Ray PC, Chattoraj SL, Bisht MPS, Kannaujiya S, Pandey K, Goswami A (2016) Kedarnath disaster 2013: causes and consequences using remote sensing inputs. Nat Hazards 81(1):227–243
Rickenmann D (2005) Runout prediction methods. In: Debris-flow hazards and related phenomena. Springer, Berlin, Heidelberg, pp 305–324

Saini P, Gangwar M (2018) Reactivation of minor scars to major landslides–a satellite-based analysis of Kotropi landslide (13 August 2017) in Himachal Pradesh India. Curr Sci 115(3):395–398
Sajwan A, Sengupta A (2021) Numerical modeling of debris flow during a rainfall induced landslide at Malin in India. In: Geo-extreme, pp 129–138
Sarkar S, Kanungo DP, Sharma S (2015) Landslide hazard assessment in the upper Alaknanda valley of Indian Himalayas. Geomat Nat Hazards Risk 6(4):308–325
Sassa K (1989) Geotechnical model for the motion of landslides (Special lecture). In: Proc. 5th inter. symp. on landslide, vol 1, pp 37–56
Sati VP (2007) Environmental impacts of debris flows-a case study of the two debris-flow zones in the Garhwal Himalaya. In: Chen and Maor (eds) Debris-flow hazards mitigation: mechanics, prediction, and assessment, pp 715–723
Sati SP, Gahalaut VK (2013) The fury of the floods in the north-west Himalayan region: the Kedarnath tragedy. Geomat Nat Hazards Risk 4(3):193–201
Sharma P, Rawat S, Gupta AK (2019) Study and remedy of Kotropi landslide in Himachal Pradesh India. Indian Geotech J 49(6):603–619
Sharpe CFS (1938) Landslides and related phenomena. Columbia University Press, NY, p 1370
Singh H, Som SK (2016) Earthquake triggered landslide–Indian scenario. J Geol Soc India 87(1):105–111
Singh R, Shekhar M, Pandey VK, Kumar R, Sharma RK (2018) Causes and geomorphological effects of large debris flows in the lower valley areas of the Meru and Gangotri glaciers, Bhagirathi basin, Garhwal Himalaya (India). Remote Sens Lett 9(8):809–818
Sosio R, Crosta GB, Frattini P (2007) Field observations, rheological testing and numerical modelling of a debris-flow event. Earth Surf Proc Land 32(2):290–306
Stini J (1910) Die Muren. Verlag der Wagner'shen Universitätsbuchhandlung, Innsbruck (Debris flows, English translation by M. Jakob and N. Skermer, 1997, 1910, EBA Engineering Consultants, Vancouver, Canada, p 106)
Sujatha ER (2020) A spatial model for the assessment of debris flow susceptibility along the Kodaikkanal-Palani traffic corridor. Front Earth Sci 14:326–343
Sujatha ER, Sridhar V (2017) Mapping debris flow susceptibility using analytical network process in Kodaikkanal Hills, Tamil Nadu (India). J Earth Syst Sci 126(8):1–18
Thakur V et al (2021) Early warning of water-triggered landslides. In: Indian geotechnical conference 2019. Springer, Singapore, pp 139–150
Turnbull B, Bowman ET, McElwaine JN (2015) Debris flows: experiments and modelling. C R Phys 16(1):86–96
Varnes DJ (1958) Landslide types and processes. In: Eckel EB (ed) Landslides and engineering practice, special report 28. Highway research board. National Academy of Sciences, Washington, DC, pp 20–47
Varnes DJ (1978) Slope movement types and processes. In: Schuster RL, Krizek RJ (eds) Landslides, analysis and control, special report 176: transportation research board. National Academy of Sciences, Washington, DC, pp 11–33.
Vishnu CL, Sajinkumar KS, Oommen T, Man RA, Thrivikramji KP, Rani VR, Keerthy S (2018) Satellite-based assessment of the August 2018 flood in parts of Kerala, India. Geomat Nat Hazards Risk 10(1):758–767

Chapter 11
Forewarning System for Rainfall-Induced Landslide—A Laboratory Prototype Model

P. Thambidurai

Abstract Intense rainfall in the mountain region is one of the main slope failure factors. Infiltration and subsequent pore pressure increase causes the failure. The rainfall-induced slope failure mechanism is not yet completely understood, either due to lack of engineering application or non-availability of site-specific data. Lots of attempts have been undertaken to investigate the mechanism of landslide occurrence through the real-time monitoring system. In this chapter, the development of the forewarning system, and its validation via laboratory experiment has been discussed. The flume bed was prepared with a mixture of sand-clay soil with a slope angle of 45° and was subjected to rainfall via the rainfall simulation system. Rainfall and moisture were continuously monitored, and pore pressure was found to drastically increase before slope failure occurred. The moisture and pore pressure were built higher in the toe of the slope and gradually decreased towards the crown of the slope. Once the saturation was achieved, the toe of the slope collapsed, and erosion of the soil took place. Antecedent moisture was noticed as a favorable factor with rainfall intensity towards the slope failure. Repeating the experiment many times with different slope angles and changes in rainfall intensity could give more insight into the mechanism. The study showed that the forewarning system model is effective and could be adapted as a warning system for landslides in mountainous regions.

Keywords Landslide flume test · Soil moisture · Pore pressure · Sensor network · Landslide warning system

11.1 Introduction

Landslide is one of the main natural disasters in the mountainous region. The frequency of landslide events is directly causing serious loss of human lives and property (Singh et al. 2016). The landslide is a complex natural process that could

P. Thambidurai (✉)
Department of Coastal Disaster Management, School of Physical, Chemical and Applied Sciences, Pondicherry University—Port Blair Campus, Port Blair 744112, Andaman and Nicobar Islands, India
e-mail: thambiduraip@pondiuni.ac.in

P. Thambidurai and T. N. Singh (eds.), *Landslides: Detection, Prediction and Monitoring*,
https://doi.org/10.1007/978-3-031-23859-8_11

not understand the whole geometry and physical characteristics (Thambidurai and Maneeesha 2017). Intense rainfall is the major factor for triggering the landslide along with other parameters, including geology, slope, etc. Rainfall-induced landslide is one of the frequently occurring events which is a wide distributed complex failure phenomenon, and it causes significant slope failures on various scales (Igwe et al. 2015). Over time, the researchers have arrived to conclusion that massive landslide events are correlated with higher cumulative rainfall (Iverson 2000; Dahal et al. 2006) and is considered one of the significant natural hazards (Segoni et al. 2014). Also, the slope failures occur in marginally stable soil (Anderson and Sitar 1995), and generally, the failures are less than 2 m in depth (Chae et al. 2015). The intense rainfall increases the pore pressure, and decreases the effective stress of soil, which reduces the shear strength of the material, resulting in slope failure (Fang et al. 2012). However, the pore pressure varies by influences of topography, hydraulic properties, weathering, and fracture of soil. Also, the effective pore pressure is directly related to infiltration and percolation to develop a perched water table (Terlien 1998). Always the high-intensity rainfall shall develop dissipation of pore pressure causing larger permeability in the soil, and antecedent moisture also has a minor influence on the occurrence of landslides (Abraham et al. 2021). During the infiltration process, a temporary saturation of soil leads to reduced metric suction, which triggers the mass failure. Also, infiltration modifies the soil structure that weakens the cohesive strength of the soil (Reddi 2003). However, the unsaturated zone above the water table may possibly induce slope failure, but if the groundwater table is in greater depth, the wetting front due to rainfall infiltration contributes to the slope failure (Zhou et al. 2009). A large deformation can occur after the failure of the slope in the toe where the soil experience significant strain. Stability of the slope is weakened in a number of ways due to rainfall. The moisture saturation increases the infiltration and then break the bond between soil particles. Destabilising effect acts fluently on the slope by fluid experts towards downhill because of enough gravity force. It weakens the slope because it decreases the capillary pressure and increases the saturation, increasing the soil mass load due to fractional dragging in the downslope direction (Borja and White 2010). Moisture content and rainfall infiltration together increase sliding force (Liu et al. 2013). In general, slope failure occurs due to increase in value of the following factors such as (1) weight of soil mass, (2) water content in soil, (3) groundwater level, (4) lubrication of slope surface and (5) hydrodynamics pressure. The general mechanism of pore pressure leads to the disintegration of soil particles, and failure mass acts as a fluid-like motion, which has been reported in most of the cases of flow slides (Iverson et al. 1997). A common rain-induced landslide is a shallow depth where the groundwater table is absent and debris flows also at the same level of depth scooped due to steep slope between 30° and 45° in the mountain regions. Majority of cases, in granular soil, the debris flow turns into a flow slide due to the mechanical properties of the soil. Fluid mechanics has an inevitable role in landslide research. The shear resistance drastically decreases due to the sudden increase of pore pressure, and when it dominates, greater than hydrostatic pressure results in debris flow (De Wrachien and Brebbia 2010). Detection of landslides is not an easy task, however, in order to find a good solution it may be fairly possible with

technological development. In the past decades, many pieces of research brought some improvements and development toward understanding the triggers and the movement of landslides worldwide. Although the alert and alarm system has not yet reached upto the mark to prevent the disaster, laboratory simulation models may provide information to understand the way the landslides initiate and evolve.

The landslide by the rainfall-induced event has a disastrous impact on the human community because the flow slide has enormous mass moving with very high speed towards downhill which obviously causes huge damages and casualties. Every year, a rainfall-induced landslide occurs more often and has associated declared many lives lost, also damaging local communities in different parts of the world. The risk reduction measure for rainfall-induced landslides is very difficult to predict the event due to the complexity of the phenomena, which cover different domains of sciences like local perception, topography, geology, and hydrological mechanisms. Early warning-based monitoring system is either not successful or highly expensive with location-specific issues. Many researchers have attempted to develop an efficient-inexpensive way of the warning system. However, there is much need for a proper monitoring system for landslide warning to save lives and also helps to get a better understanding of the mechanism of the landslide process, which can be useful for further enhancement of the system model. The cause of landslides can be reduced by developing a suitable real-time monitoring system. An effective warning system is a better tool, which has ablity to perform site-specific analysis for instability of the slope. However, the warning system needs a test and validation to understand geological material and interaction with rainfall to avoid the uncertainty of forecast information. To attain the validation of the warning system, it must be deployed in the field (landslide-prone zone), which can not only take time but may be less effective. In this chapter, an experimental laboratory setup is proposed, which is basically a physical flume model designed to investigate the landslide initiation with various conditions, mechanisms, and controlling factors with sensors embedded in systems for simulating rainfall-induced landslides.

11.2 Design and Development

A flume test setup was developed step by step, as presented in Fig. 11.1. The physical flume model was designed with a dimension of 4.5 m length, 1 m width, and 1.5 m height in a steel frame with the side walls are made up of tempered acrylic glass. The flume bed was divided into 3.5 m for the trigger and 1 m for the propagation of the slide. The trigger bed was kept at a constant slope angle of 45°, and the rainfall simulation setup was fixed 2 m above this bed. The rainfall simulation system had a water sprinkler system connected to 2,000 litre capacity water tank, which was optimised to ensure the uniformity of rainfall and control surface erosion. The bottom of the flume bed was provided with geotextile to control the friction of soil with a steel plate. The individual sensors were placed in the grid system on the designed flume bed. A total of 12 different sensors were deployed on the flume bed to monitor

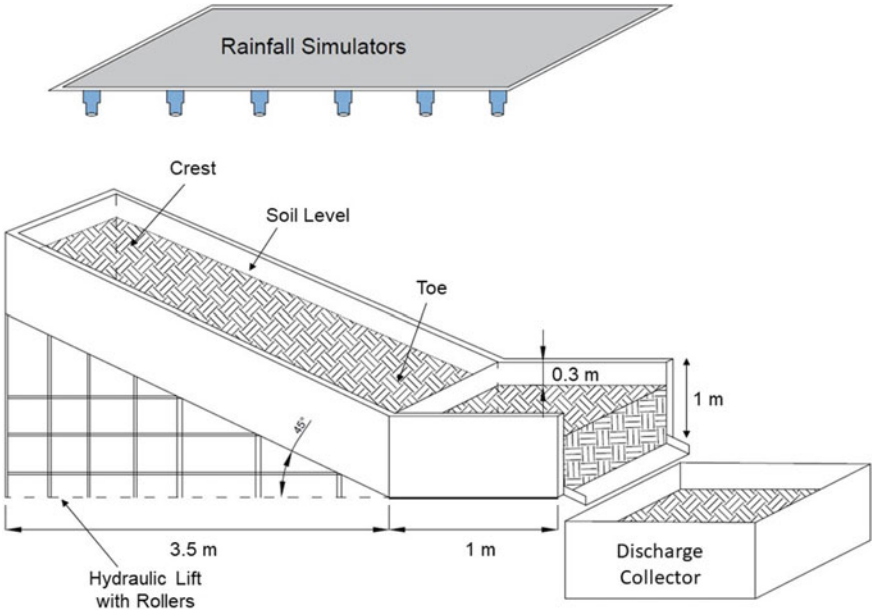

Fig. 11.1 Arrangement of experimental flume system

characteristics and triggering factors of landslide. These sensors included porewater pressure, displacement meter, inclination meter, rainfall tip system, accelerometer, and osmometer. Rain gauges were placed on the top and bottom of the flume bed. Five piezometers were deployed along the slope direction with a depth of 1 m, which covered the porewater pressure changes in the entire process with pre and post-failure behaviour. The entire system was designed to understand the data interpretation and landslide processes in scaled-down conditions. The main purpose of this study was to validate the prototype warning system and its potential detection of landslide events in extreme rainfall conditions.

11.3 Experiments

The validation experiment system was enclosed by flume bed along with a prototype model, which included Sensor Network System (SNS), Data Collection System (DCS), Communication System, Data storage, and Visualisation System. The data collected with data logger and communication system was designed such way to collect data from sensors and then transfer it by Zigbee wireless technology and GSM with serial port server system, which was developed as an alternate data transmit system on the self-organising and self-mesh network for best data collection and transmitted to avoid the data loss or any uncertainties in the system. The data storage server had the capacity to keep huge pockets of data sets and interpretations with

different categories of data sets. The final step in the warning system was visualisation, which showed the sensor position with real-time data streaming in x–y graphical representation, spatial distribution of piezometers, and status of each sensor. The first and foremost step in the flume experiment was choosing a soil mass that interacted with water, generated pore pressure, and subsequently triggered the movement of landslide mass. The sandy-clay was scooped from near the instability slope of the hill. Effect of grain size had an essential role in the displacement and movement of landslide mass. Geotechnical parameters of soil were calculated before filling it into the flume bed, such as density, void ratio, conductivity, clay content, etc., and the proper soil layers were uniformly packed and maintained on the entire flume bed. A serious of experiments were conducted with various ranges of rainfall intensity, antecedent moisture, density and thickness of the soil mass. Each experiment took its own time based on the occurrence of failure with respect to occurrence and failure behaviors. The first top portion of the flume was kept for slope simulation with 3.5 m, followed by the horizontal portion which utilised for self-stabilisation of material and post-failure deposition of the soil mass.

Many sensors were connected to the data acquisition unit for successive data communication from the local control system with an indigenous data logger. The prototype system had sufficient channels to connect more sensor clusters in different field conditions. This technology had more concern for selecting required sensors and their accommodation in real-world conditions without modification of the prototype system. The entire sensor network was connected with a central control system, and then both architectures were powered. Rainfall-induced flume test was conducted with the integrated prototype sensor system, and a total period of time around 6 hours was taken to end the experiment. The experiment included two extreme rainfall intensities to understand and observe the significant failure in the soil mass because the amount of rainfall should trigger the slope failure. The incident rainfall can infiltrate and subsequently saturate the soil mass. The researcher must know to set the necessary amount of rainfall to trigger the slope failure during the test (Wang and Sassa 2003). Based on the earlier experiment, it was assumed that extreme rainfall would trigger slope failure in the present flume experiment. The arrangement was prepared in such a way that controlled water from rainfall simulator only interacts with soil mass. The rainfall rate was regulated at approximately 40 mm/hour. Pore pressure, displacement, soil pressure, borehole pressure, and osmotic pressure were logged and collected in the constant rainfall condition up to the occurrence of slope failure. Data was logged at 5 min intervals for the entire experiment.

11.4 Results and Discussion

The present laboratory experimental study shall be used to better understand the mechanism of rainfall-induced slope failure. Before starting the simulation, moisture and compactness of the soil parameters were measured for reference records. All the sensor connection was thoroughly checked, and the power backup and water source house were investigated. Soil compaction and their density values were checked and

noted at each point of sensor location. The sensor position and numbering system for each point were cross-verified with the compactional program. Data loggers and other transmission gadgets were ensured once again. The experiment was started with a flume slope to simulate the rainfall-induced landslide on a fine morning at 8'o clock. Once the rainfall simulation started and the moisture content steadily increased, the first response from the top of the moisture sensor was soon after rainfall started. The wetting front was progressed towards the base of the slope, and after a short span of time, the moisture sensor at the toe of the slope. After sufficient infiltration, the wetting front reached a peak and was followed by a sudden increase of observed, which increased drastically the saturation of water reached in soil. The moisture was increased stepwise, not in a gradual manner (Fig. 11.2) because of many factors (Gevaert et al. 2014) in soil grain size, slope angle etc. However, high moisture vicinity was observed and measured at the toe of the slope due lateral movement of water. Further, seepage was developed, and that force triggered the instability of the slope. The stability affected due to seepage vector quantity consists of magnitude and direction. The surface and subsurface water flow had more affinity towards the toe of the slope due to gravity after saturation of the pore space of the grains. The soil in the upper part of the slope was not fully getting the saturated condition, because the majority of front wetting occurred along the downslope, not in the opposite direction. The runoff started after the saturation at the toe area, and it resulted in formed gullies followed by erosion. As a consequence of intense rainfall, the formed gullies were extended from toe to towards the upper side of the slope and also the gullies became wider and deeper, giving symptoms of breaking and blocking of the runoff water.

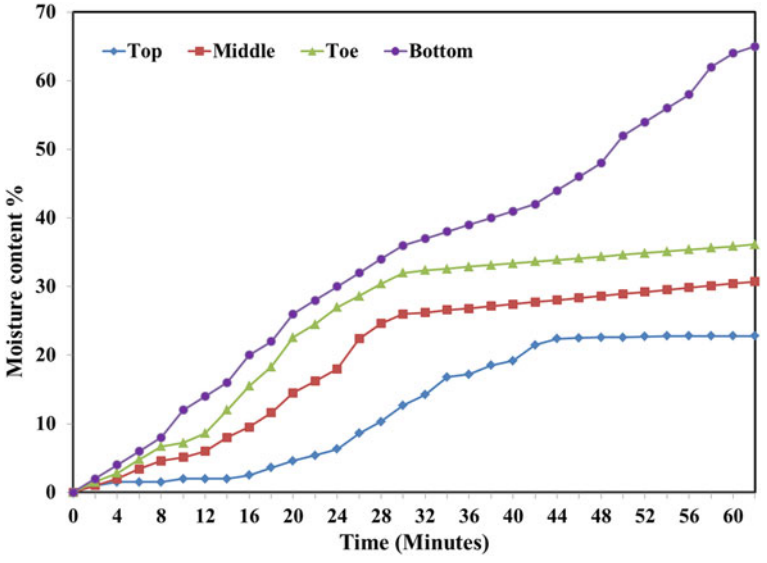

Fig. 11.2 Moisture content variation with time

The study observed that the rainfall intensity was capable of pushing or removing soil from the upper portion of the slope.

The experiment was reached at the peak, and the first slope failure occurred, and it was captured by pressure gauge (pressure) data in the soil mass at 11.10 am (Fig. 11.3). Another failure occurred after 20 minutes, which was observed significantly through the inclinometer data set (Fig. 11.4). The depth of the failure observed in Fig. 11.5. The soil mass movement was noticed half an hour prior to the first failure by sudden changes in the piezometer value of pore pressure and osmometer readings (Fig. 11.6).

The rainfall data showed that the intensity and duration of rainfall had significant influences on the movement of soil from the upper side of the slope to the toe. The mechanism of soil movement dynamics observed that the removed soil, which accumulated at the toe due to gravity, pushed further down because of newly detached soil from the upper portion of the slope. The intensity of the rainfall and its duration had a noticeable effect on the mass movement, however, the effects were initially higher than continuing the same mass removal even after rainfall intensity reduced. It could be losing cohesiveness of soil mass, and it may be a larger amount of fine grain (Mitchell and Soga 2005). The accumulated pore water built pressure within the grains pore spaces, and further percolation and infiltration had developed the groundwater table. The moisture sensors and rainfall data showed that moisture content increased soon after rainfall started, but the piezometer (pore pressure) data value increased after subsurface water saturation. For this mechanism, the porosity

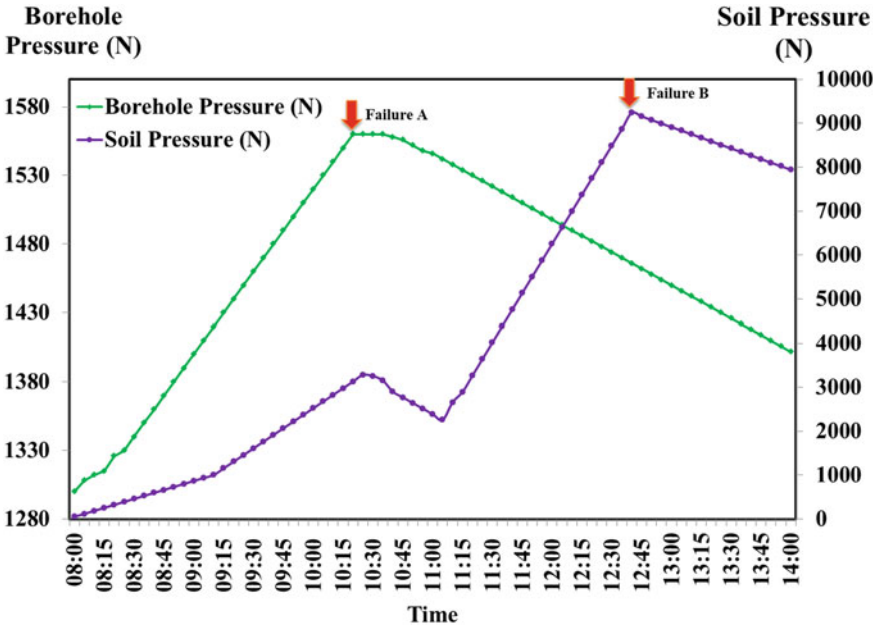

Fig. 11.3 Pressure gauge data with slope failure curves

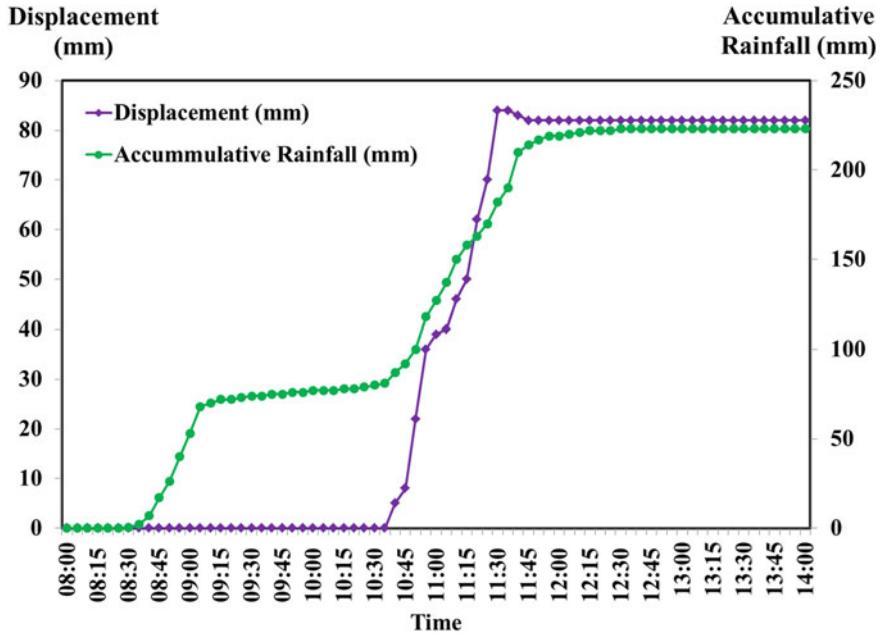

Fig. 11.4 Data plot of rain gauge and the displacement meter

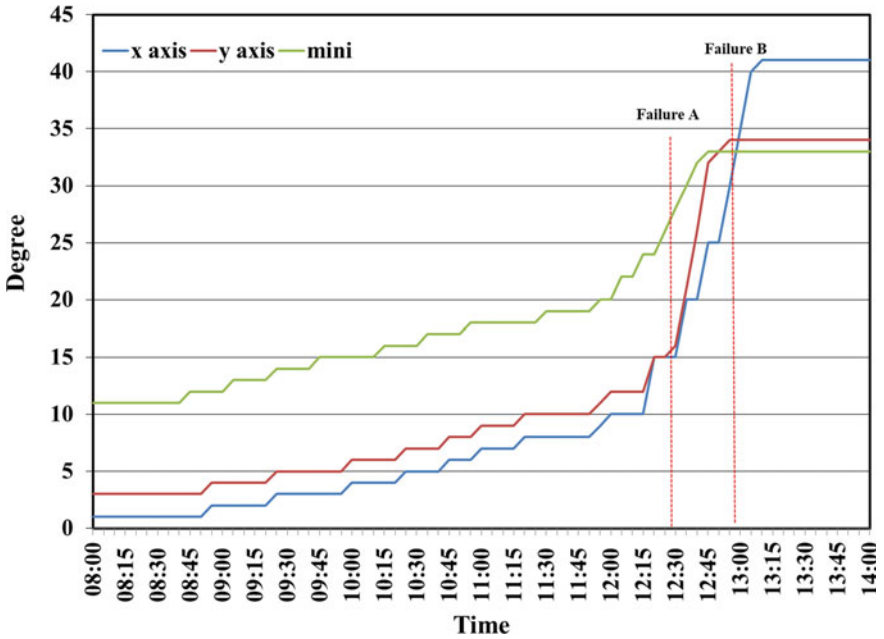

Fig. 11.5 Inclinometer data plot

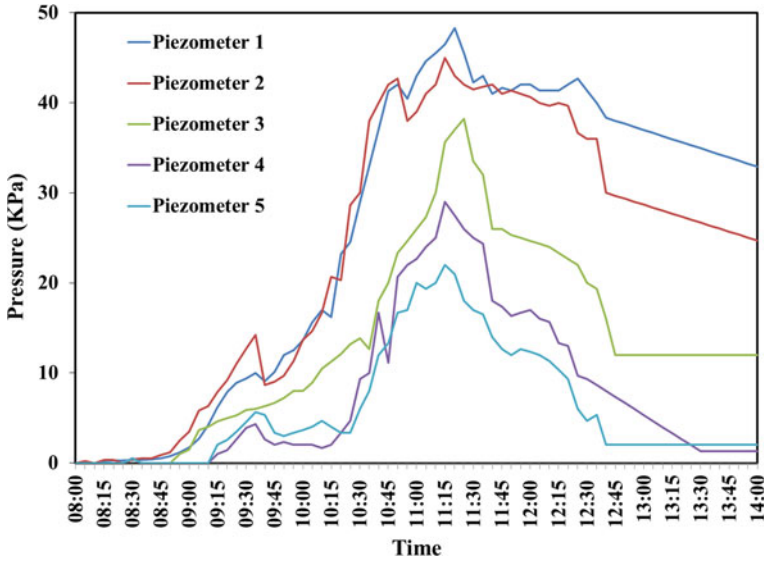

Fig. 11.6 Data plot of piezometers and osmometer

and density of soil acted an important role in controlling the saturation mechanism and water level increased in the subsurface zone soil. The infiltration index contributed to the variation of subsurface water level, which played an important role in the stability of the slope. Generally, rainfall intensity can increase the velocity of infiltration, though it decreases in a certain unit weight of soil (Chae et al. 2015).

The pore pressure value remained constant in the initial stage of the experiment, and it quickly increased, and then after, the values of pore pressure gradually increased until the failure occurred. The pore pressure was very high at the toe points compared to the upper side of the slope. Crack started to occur at the toe area with an indication of water saturation in the soil. Although, if antecedent moisture was present in the base of the slope, then the pore pressure suddenly increased. The pore pressure-building mechanism has to be understood at the specific landslide site, which is necessary to evaluate the feature failure of the slope. However, uncertainty is high, still unable to understand the complete mechanism of landslide failure behaviors. The piezometer values were increased due to high-intensity rainfall. Then after the failure occurred, the values suddenly decreased (Fig. 11.6). The geometry of the slope completely changed after the sudden failure of the soil mass towards the downslope direction. The increased seepage was clearly observed from the top of the slope to the toe direction. Subsequently, the water level increased in the toe, and seepage with pore pressure triggered the further failure. At this juncture, the rainfall intensity continues then sliding motion also continues as a liquefaction process. The sensors placed at the toe area have lost data streaming due to a slide occurring in the toe due to sensors displaced from deployed points. Also, minor cracks occurred simultaneously at the crest of the slope but started at the toe. The cracks at the crest

indicate that failure may occur on the upper side of the slope in the field. A set of experiments conducted before composing the present article, however, made proper the workable model, and receiving reliable data is difficult in small level flume model. However, the designed sensor network and all supporting enclosures performed well and good in the entire laboratory experiment and evaluation of the systems. Despite the success of the research, there are many limitations and barriers in bringing more accuracy and improvement in the designed system.

11.5 Conclusion

The laboratory model experiment was conducted to understand the mechanism of rainfall-induced landslide and evaluation through the flume model of the designed forewarning system. The laboratory experiment is the best practice for understanding landslide phenomena and avoiding the expensive and time-consuming evaluation of the designed system. The study attempts to monitor the moisture and pore pressure changes with respect to intense rainfall on the slope. The antecedent moisture has a great role in building the pore pressure in the soil. The generation of moisture and pore pressure have significant influences on the initiation of slope failure. These parameters are the important controlling factors for soil mass failure. However, rainfall intensity alone influences the slide of the mass in the sense of soil erosion, high infiltration, and high subsurface flow toward the toe of the slope. Also, runoff (surface flow) induced erosion mainly in the toe area, which triggered the instability of the toe of the downslope area. Although the instability continues in the upper direction due to continued rainfall and infiltration. Before the failure occurred in the toe, minor cracks were observed in the crest area due to a slight jerk of soil mass in the toe. The increase in subsurface water level and seepage increased pore pressure significantly in the toe area. Moisture and pore pressure were lower values in the crest area and significantly higher in the toe. Sudden failure of slope due to the sudden jump of pore pressure in the soil mass. Landslide events could be predicted by utilizing moisture and pore pressure sensors in the appropriate points in the toe region with a proper field survey.

References

Abraham MT, Satyam N, Rosi A, Pradhan B, Segoni S (2021) Usage of antecedent soil moisture for improving the performance of rainfall thresholds for landslide early warning, Catena. Elsevier 200:105147

Anderson S, Sitar N (1995) Analysis of rainfall-induced debris flows. J Geotech Eng ASCE 121:544–552

Borja R, White J (2010) Continuum deformation and stability analyses of a steep hillside slope under rainfall infiltration. Acta Geotech Slov 5:1–14

Chae B-G, Lee J-H, Park H-J, Choi J (2015) A method for predicting the factor of safety of an infinite slope based on the depth ratio of the wetting front. Nat Hazards Earth Syst Sci Discuss 3:791–836

Dahal RK, Hasegawa S, Yamanaka M, Nishino K (2006). Rainfall triggered flow-like landslides: understanding from southern hills of Kathmandu, Nepal and northern Shikoku, Japan. In Proceedings of 10th Int. Congr. on IAEG2006. Geol Soc London, vol 819, pp. 1–14

De Wrachien D, Brebbia CA (2010) Monitoring, simulation, prevention and remediation of dense and debris flows III. WIT Press, Southampton, UK

Fang H, Cui P, Pei LZ, Zhou XJ (2012) Model testing on rainfall-induced landslide of loose soil in Wenchuan earthquake region. Nat Hazards Earth Syst Sci 12:527–533

Gevaert AI, Teuling AJ, Uijlenhoet R, DeLong SB, Huxman TE, Pangle LA, Breshears DD, Chorover J, Pelletier JD, Saleska SR, Zeng X, Troch PA (2014) Hillslope scale experiment demonstrates the role of convergence during two-step saturation. Hydrol Earth Syst Sci 18:3681–3692

Igwe O, Effiong BA, Iweanya MR, Andrew OI (2015) Landslide Investigation of Ikwette, Obudu Local Government Area of Cross River State, Nigeria. J Appl Geol Geophy 3(3):01–12

Iverson RM (2000) Landslide triggering by rain infiltration. Water Resour Res 36:1897–1910

Iverson RM, Reid ME, LaHusen RG (1997) Debris-flow mobilization from landslides. Annu Rev Earth Planet Sci 25:85–138

Liu ZZ, Yan ZX, Duan J, Qiu ZH (2013) Infiltration regulation and stability analysis of soil slope under sustained and small intensity rainfall. J Cent South Univ 20:2519–2527

Mitchell JR, Soga K (2005) Fundamentals of soil behavior, 3rd edn. Wiley, Hoboken, New Jersey, p 592

Reddi LN (2003) Seepage in soils, principles and applications. Wiley, USA

Segoni S, Battistini A, Rossi G, Rosi A, Lagomarsino D, Catani F, Moretti S, Casagli N (2014) Technical note: an operational landslide early warning system at regional scale based on space–time variable rainfall thresholds. Nat. Hazards Earth Syst Sci Discuss 2:6599–6622

Singh TN, Singh R, Singh B, Sharma LK, Singh R, Ansari MK (2016) Investigations and stability analyses of Malin village landslide of Pune district, Maharashtra. India Nat Hazards 81(3):2019–2030

Terlien MTJ (1998) The determination of statistical and deterministic hydrological landslide triggering thresholds. Environ Geol 35:124–130

Thambidurai P, Ramesh MV (2017) Slope stability investigation of Chandmari in Sikkim, Northeastern India. In: Mikos M, Tiwari B, Yin Y, Sassa K (eds) Advancing culture of living with landslides. WLF 2017. Springer, Cham. https://doi.org/10.1007/978-3-319-53498-5_42

Wang G, Sassa K (2003) Pore-pressure generation and movement of rainfall-induced landslides: effects of grain size and fine-particle content. Eng Geol 69:109–125

Zhou Z, Wang HG, Fu HL, Liu BC (2009) Influences of rainfall infiltration on stability of accumulation slope by in-situ monitoring test. J Cent South Univ 16:297–302

Chapter 12
Study and Instrumental Monitoring of Landslides at the "Russkie Gorki" Site in the Mzymta River Valley, Sochi Region, Russia

O. V. Zerkal, I. V. Averin, A. A. Ponomarev, E. N. Samarin, I. K. Fomenko, and I.A. Rodkina

Abstract Northern slope of the Aibga Ridge, forming the left-bank slope of the Mzymta River valley, is one of the most landslide-prone areas of the Sochi region. The landslide site "Russkie Gorki" lies in the valley of the Mzymta left tributary and has an elevation range of 700 m and even more. The lower and middle part of the slope is composed of Lower Jurassic terrigenous flysch divided by tectonic fault from Middle Jurassic volcanoclastic sediments developed at the upper part of the slope. The region is seismically prone to high intensity of the anticipated strong motion. Several types of landslides are widespread in the study area. Among them are large-scale rock avalanches that had originated at the upper part of the slopes composed of the porphyry and reach the slope's base; besides, there are variable landslides in the terrigenous flysch. Landslides distribution was studied by compilation of the detailed DEM that helped reconstruct the development of the landslide processes in the study area in Late Quaternary time. Instrumental monitoring systems were installed, including inclinometers, extensometers, piezometers, and pressure sensors at the lower parts of the slope where the most active landslides exist. It allowed to specify the sliding surface depth and reveal the main factors affecting slopes' stability. It was found that the landslide array on the site "Russkie Gorki" has a three-tiered structure. The inclinometric observations for 106 days result showed that the average landslide displacement rates at the "Russkie Gorki" site of landslide rupture ranged from 0.16–0.26 mm/day to 0.55 mm/day in lower and upper, respectively.

O. V. Zerkal (✉) · E. N. Samarin · I.A. Rodkina
Lomonosov Moscow State University, Moscow 119991, Russia
e-mail: igzov@mail.ru

I. V. Averin
"Enginernaya Geologiya" Ltd., Moscow 121351, Russia

A. A. Ponomarev
"EngZashita" Ltd., Sochi 354073, Russia

I. K. Fomenko
Ordzhonikidze Russian State Geological Prospecting University (MGRI), Moscow 117997, Russia

P. Thambidurai and T. N. Singh (eds.), *Landslides: Detection, Prediction and Monitoring*,
https://doi.org/10.1007/978-3-031-23859-8_12

The present study concluded that the instrumental monitoring technique is effective for the detection of real-time landslide scenario at the site.

Keywords Landslide · Landslide-prone areas · Aibga Ridge · Sochi region · Jurassic flysch · Instrumental monitoring

12.1 Introduction

Landslides is one of the natural in the mountainous regions. The high possibility of landslide events is often complicated by anthropogenic activity within the mountainous areas. The negative impact of slope deformations is distributed mainly in the mountain area and experienced ancient large-scale landslides and rock avalanches. Depending on the degree of fragmentation of deposits in the composition of rock avalanches, various facies are distinguished (Zolotarev and Janič 1980; Chigira et al. 2013; Crosta et al. 2007; Dufresne and Dunning 2017; Hewitt et al. 2008; Pedrazzini et al. 2013; Pollet and Schneider 2004; Weidinger et al. 2014). The landslide breccias are usually represented by finely crushed rock with clastic and matrix-clastic material prevalence in the proximal part of the rock avalanche. The finer-grained matrix-supported texture predominates in the distal portion of the rock avalanches as part of the body facies. The displaced, brecciated, and lower strength properties characterize fractured deposits compared to primary rocks. The Mzymta River Valley in Greater Sochi, Russia, is such a mountainous terrain prone to slope failure area. In these territories, the activity of modern landslides is inherited. At the same time, modern secondary landslides here are significantly larger in scale and movement. Anthropogenic activities always provoke landslide deformations. The first historical information about landslides on the territory under consideration dates back to the middle of the XIX century. In the 60–70 years of the XX century, detailed engineering-geological mapping (scale 1:25,000) was carried out here (Ostrovsky et al. 1972). However, large-scale landslides have not been described in the valley of the Mzymta River. The traces of a rock avalanche, well expressed in the relief (on the right side of the valley, downstream), were interpreted as glacial formations. Also, large-scale landslides were not described during the repeated geological mapping carried out from 2000 to 2002 (Lavrishchev et al. 2002). The first information about large-scale landslides and rock avalanches in the region under consideration was obtained during engineering-geological investigations for projects of Olympic construction (Zerkal and Samarin 2008). The results of the investigations conducted at this site allowed us to assess the stress distributions in the rock massif with slopes at this site and confirmed the possibility of the formation of large-scale landslides (Zerkal et al. 2015). A study of secondary shallow landslides was also performed (Kang et al. 2019). Ponomarevet al. (2021) reported the rock avalanches in the upper reaches of the Mzymta river of this region.

The tourism site of "Russkie Gorki" is located within the mountainous part of Greater Sochi, where the Ski-jump complex was built for the Olympic Winter Games

Fig. 12.1 Ski-jump complex "Russkie Gorki"

in Sochi' 2014 (Fig. 12.1). This area is characterized by high landslide activity. The intensity of slope deformations was also affected by construction work, which was accompanied by changes in relief and various man-made impacts. Currently, the Olympic Ski-jump complex is used for sports competitions and tourism. Therefore, information about landslide activity is important for the functioning of the Ski-jump complex. For such sites, violations of the primary occurrence of rocks, their disintegration is typical. This paper presents the results of the study and monitoring of landslide activity at the site "Russkie Gorki".

12.2 Study Area and Its Environment

The Greater Caucasus mountain range is located in the south of the European part of the Russian Federation between the Black and Caspian Seas. This mountain system stretches in the sublatitudinal direction (from northwest to south-east) for 1,500 km and has a width of up to 200 km (Fig. 12.2). The landslide site "Russkie Gorki" is located in the lower part of the northern slope of the Aibga Ridge. Actually, the landslide site "Russkie Gorki" is located on the left bank slope of the local valley of the left tributary of the Mzymta River (Fig. 12.3). The elevations of Aibga Ridge reach 2,200–2,400 m. The elevation marks in the Mzymta River valley on the described site are 480–490 m.

The contracting relief of the territory and the proximity of the Black Sea form a peculiar climate characterized by a large amount of precipitation (up to 4,300 mm per year [according to the Achishkho station]). It should be noted that this is the largest amount of annual precipitation on the territory of the Russian Federation. Up to 60% of this amount falls in the period from November to April. The average annual temperatures in the studied area are positive and amount to about +4 °C. However, in winter, the air temperature can drop to −23 to −29 °C. In the summer

Fig. 12.2 Location of the study area (by Google Earth)

months (July), the air temperature can reach +40 °C. A feature of the effect of climatic factors on the landslide activity of the region is the significant role of snow cover in soil moisture. The average height of the snow cover in winter is 64 cm (according to the Achishkho station), and the maximum values can exceed 470 cm. By the end of the cold period, water reserves in the snow cover may exceed 400 mm in the Mzymta River valley and 1,600 mm on the slope of Aibga Ridge. In the spring period (February–March), there are frequent transitions through 0 °C of air temperature and soil surface. During these periods, surface water flow into the soil mass increases significantly, even in the absence of precipitation. In late spring in the described territory (March–April), soil moisture occurs during the snowmelt during precipitation and due to water from the snow shelter. These periods are characterized by contrasting changes in the groundwater level.

12.3 General Geological and Tectonic Background of the Study Area

Mountain territories in the south of Europe (Caucasus, Alps, Carpathians, etc.) form a front chain mountainous tectonic fold-thrust structure of the Alpine-Himalayan orogenic belt stretching along the southern border of the Eurasian lithospheric plate

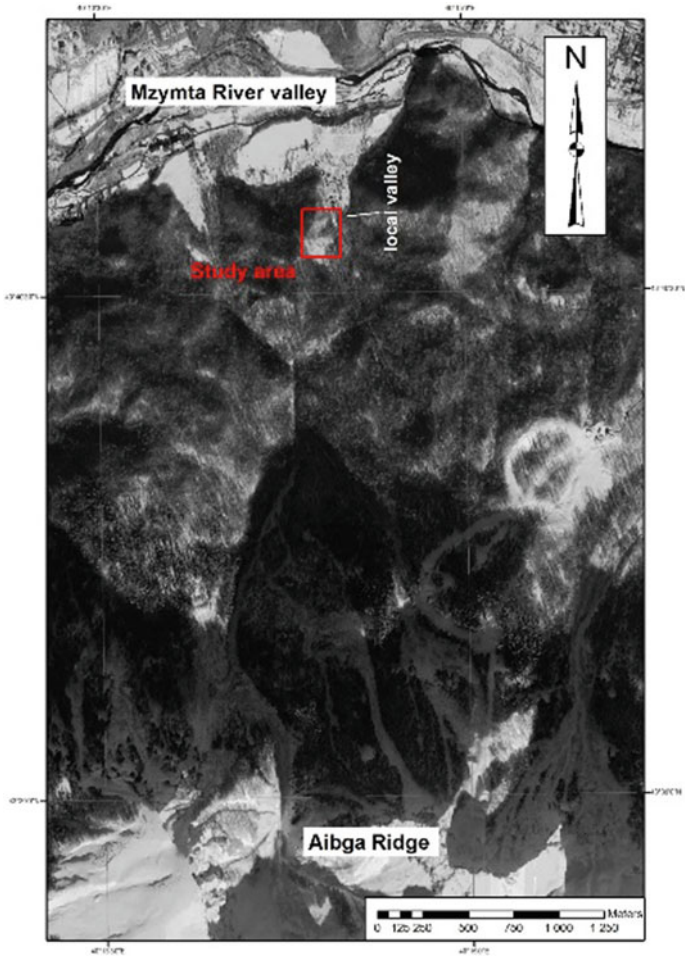

Fig. 12.3 Location of Russkie Gorki landslide sit

(Khain 1998). The active neotectonic displacements contribute to the tectonic fracturing of the rock massifs (Rogozhin et al. 2015). This region is also characterized by high seismic activity. And the magnitude of historical earthquakes reached 8 (Kondorskaya and Shebalin 1982). The Caucasus is also characterized as avery high landslide activity region (Zerkal and Strom 2017).The Caucasus was formed during the Alpine orogenic stage as a result of a collision in the northern part of the area of tectonic interaction of the North-Eurasian and Arabian lithospheric plates. As a result, thrust faults and overthrust are widespread in the region (Lukk and Shevchenko 2019). Still, the active tectonic development of the Caucasus continues. Horizontal displacements of GPS points located within the northern wing of the Greater Caucasus Megaanticlinorium occur in the southern direction at a rate of

3.6–2.4 mm/year (relative to the GPS point Zelenchuk (ZELB) in the central part of the Caucasus). Horizontal displacements of GPS points located south of the Greater Caucasus occur northerly, with a relative velocity of 4.2–4.3 mm/year (Shevchenko et al. 1999).

The Aibga ridge is located in the south-western part of the Caucasus, within the southern limb of the Greater Caucasus Megaanticlinorium. The landslide site "Russkie Gorki" is located on the left (western) bank of the local valley, embedded in the lower part of the northern slope of the Aibga ridge. The macroslope of the Aibga ridge has a total height of about 1.9 km. The slope steepness varied from very shallow (slopes up to 5–7°) terrace-like areas to steep (up to 35–40°) slopes lying between them. The steepness of the Aibga ridge macroslope is 25–30° (on average). The local valley opens on the valley of the Mzymta River, which empties into the Black Sea about 40 km to the west. In the area under consideration, the southern limb of the Greater Caucasus Megaanticlinorium is formed by the structures of the Gagro-Dzhavsky tectonic block, separated from the structures of the axial zone of the mega-anticlinorium by the Main Caucasian thrust fault. The Main Caucasian thrust fault is located 4–5 km north of the landslide site "Russkie Gorki." It has a north-northeast dip with angles of 30–50°. As part of the Gagro-Dzhavsky tectonic block on the northern slope of the Aibga ridge, the Krasnopolyanskaya and Abhazo-Rachinskaya tectonic zones are distinguished. The Krasnopolyanskaya tectonic zone covers the lower part of the northern slope of the Aibga ridge. It is composed of the Lower Jurassic terrigenous (mainly argillite) flysch collected in linear folds. The Abhazo-Rachinskaya tectonic zone is formed by the Middle Jurassic deposits of the terrigenous-volcanogenic (island arc) formation. Volcanogenic-terrigenous flysch (tuff argillites, tuff aleurolite, and tuff sandstones) is located in the lower part of the Middle Jurassic rock mass. The middle and upper parts are formed by deposits of the porphyrite series composed of horizons of porphyrites, tuff argillites, and tuff sandstones. Rocks of the porphyritic series form a sub-latitudinal asymmetric fold with a gentle (from 15–20° to 30–42°) northern limb. The boundary separating the Krasnopolyanskaya tectonic zone from the Abhazo-Rachinskaya tectonic zone is the Krasnopolyansky fault. The fault can be traced in the middle part of the northern slope of the Aibga ridge. It is a right-sided reverse strike-slip fault with a total displacement at the neotectonic stage of 100–130 m.

On the northern slope of the Aibga ridge, many landslides of various types and scales have been detected. Features of the geological structure of the high slope have the occurrence of strong rocks (porphyrites, tuff sandstones—Unit Weight 26.8–27.2 kN/m^3, UCS—75–85 MPa) in the upper part of the slope, which are underlain by moderately weak rocks (argillites, aleurolites—Unit Weight 25.2–25.9 kN/m^3, UCS—29–32 MPa according to intersecting bedding, 18–20 MPa—by bedding). It creates conditions for the formation of rock avalanches. A rock avalanche "Prieskarpnaya" was mapped on the studied areas of the slope (No. 232 according to the "Catalogue of landslides and rockfalls of the northern slope of Aibga ridge" compiled by (Zerkal and Samarin 2008), and the estimated volume is 21.6 million m^3.The main scarp of the rock avalanche "Prieskarpnaya" is located in the area of deposits of the terrigenous-volcanogenic formation in the watershed part of the ridge (at altitudes of

Fig. 12.4 Deposits of the rock avalanche "Priescarpnaya"—landslide mélange, including fragmented rock of Lower Jurassic argillites (black) in a heavily shattered matrix of Middle Jurassic volcanogenic-terrigenous material (in outcrop)

2,080–2,160 m) 3.3 km south of the landslide site "Russkie Gorki." The avalanche has a length of about 4.3 km. The thickness of the avalanche deposits in the central part of the local valley, which is located on the left bank of the landslide site "Russkie Gorki" is 20–24 m (according to drilling). The deposits of the Priescarpnaya rock avalanche are a landslide mélange, including the fragmented rock of lower Jurassic argillites (black) in a largely destroyed matrix of Middle Jurassic volcanogenic-terrigenous material (Fig. 12.4). The lowest level of the displacement of the avalanche "Prieskarpnaya" was the ancient valley of the Mzymta river. The formation of the rock avalanche belongs to the Late Neopleistocene since the alluvium of the II terrace overlies its deposits.

12.4 Engineering-Geological Conditions of the Landslide Site "Russkie Gorki"

The modern conditions of the studied area are the result of a long geological evolution of the territory. On the left, (western) side of the local valley is the landslide site "Russkie Gorki," which has a trough-like shape. The total width of the valley (from watershed to watershed) is 350–400 m. As a result of landslide activity directly on the landslide site "Russkie Gorki," the width of the valley increases to 650–670 m. The width of the relatively flat bottom of the valley is 120–140 m. The height of the left bank of the valley reaches 90–120 m. The formation of the valley seems to have occurred at the beginning of the Late Pleistocene. During this period, the valley was deeper (up to 150–170 m) and had a more V-shaped form. During the formation of the "Priescarpnaya" rock avalanche, the lower part of the valley was filled with landslide material. In the Holocene, a gradual accumulation of debris-flow deposits, composed of clayey course, took place in the valley. The thickness of these deposits is up to 7–8 m. The bedrock deposits in the lower part of the northern slope of the Aibga

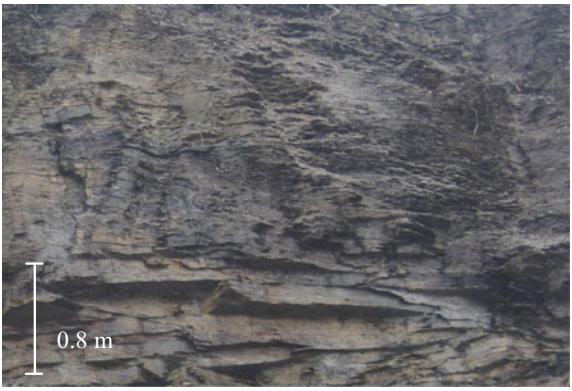

Fig. 12.5 Argillites of the Chvezhipsin formation (J_1čv) in outcrop

ridge in the area of the landslide site "Russkie Gorki" are represented by deposits of the Chvezhipsin formation (J_1čv). The Chvezhipsin deposits are composed of dark gray and black argillites (Fig. 12.5). They are thin-layered and low-strength (UCS—1.8–3.7 MPa). Chvezhipsin argillites are easily soaked in water. When soaking, the Chvezhipsin deposits transform into lean clay (liquid limit is 24–30%, plasticity index is up to 14%). The gross chemical composition of argillites is dominated by SiO_2, the amount of which reaches 53–55%. The content of aluminum oxide (Al_2O_3) averages 10–12%. The amount of iron oxides (Fe_2O_3) does not exceed 3–7% and apparently depends on the degree of weathering. The content of other oxides is of subordinate importance. According to X-ray diffraction analysis, the mineral composition of argillites is dominated by clay minerals (muscovite-type hydromicas, ferruginous chlorite), whose total content reaches 58–65%. The quartz content (in finely dispersed form) is 22–23%. Potassium feldspar (2–4%), plagioclases (4–6%), and organic matter (up to 5–7%) are also present in the composition of argillites. The main geomechanical parameters of the Chvizhepsin argillites and other deposits are presented in Table 12.1. Significant slope steepness (on average 18–19°, locally—up to 40–45°) and low strength characteristics of argillites contributed to the formation of slope deformations in the left (western) bank of the local valley on the landslide site "Russkie Gorki."

12.5 Landslide on the Site "Russkie Gorki"

Currently, the landslide array on the site "Russkie Gorki" (No. 225 according to the "Catalogue of landslides and rockfalls of the northern slope of Aibga ridge" compiled at the Faculty of Geology of Moscow State University [Zerkal and Samarin 2008]) is a multistoried slide compiled by G. Ter-Stepanian (1977) and J. N. Hutchinson (1988). The total volume of the landslide massif is more than 5.6 million m^3. Its total length (in the direction of displacements) reaches 250–270 m, and its width is up to

Table 12.1 Main geomechanical parameters of the geological units

Units	Unit weight, γ (kN/m^3)	Cohesion, C (kPa)	Friction angle, φ (°)	Modulus of deformation, E (MPa)
Argillites (J_1čv)	22.3	99	29	27
Rock avalanche deposits dpIII(J_1čv + J_2pr)	22.2	11	21	27
Argillites in body of rock slide (dp(J_1čv))	21.4	85	27	15
Proluvium (pIII-IV)	22.6	19	19	
zone of landslide rupture	22.7	33	20	

540 m. The general geological structure of the slope at the site "Russkie Gorki" is shown in Fig. 12.6.

The start of landslide displacements refers to the period of active erosion (at the beginning of the Late Pleistocene) during the formation of a local valley. The formation of the multiple rotation block slide (Cruden and Varnes 1996) belongs to this time. The lowest level of the landslide displacement was the thalweg of the ancient V-shaped valley before filling it out with sediments of the rock avalanche "Prieskarpnaya." Currently, the zones of rupture of this ancient landslide have been encountered in wells from 38–40 to 53–54 m depths (Fig. 12.7). After forming the rock avalanche "Prieskarpnaya" in the Late Pleistocene, displacements of the second phase of landslide activity developed on the slope at the site "Russkie Gorki." Slope deformations occurred in the form of a successive rotation block slide (Multilingual 1993). The thickness of the displaced mass during the second phase was less than in the first phase. Currently, the zones of rupture of this second-phase landslide have been encountered in wells at 12–15 m depth.

Shallow rotation and earth slides at various altitude levels occurred due to the construction impacts of the Ski-jump complex. Weathered argillites were involved in the displacements. The depth of the displaced mass of the shallow slides is about 5–6 m. The slope stability assessment performed presented that the slopes on site "Russkie Gorki" are in a limit equilibrium state. With the specified geomechanical parameters (Table 12.1), the safety factor was obtained (1.002) by the Morgenstern and Price (1965) method. Therefore, any possible change in factors affecting slope stability can cause the onset of landslide deformations. This assumption was confirmed by the simulation of the slope stability variation when the groundwater level rises (e.g., due to precipitation). The results of slope stability FEM analysis (Krahn 2007) are shown in Fig. 12.8. The consequence of an increase in the groundwater level may be the destabilization of the entire slope to depths of 35–45 m. The

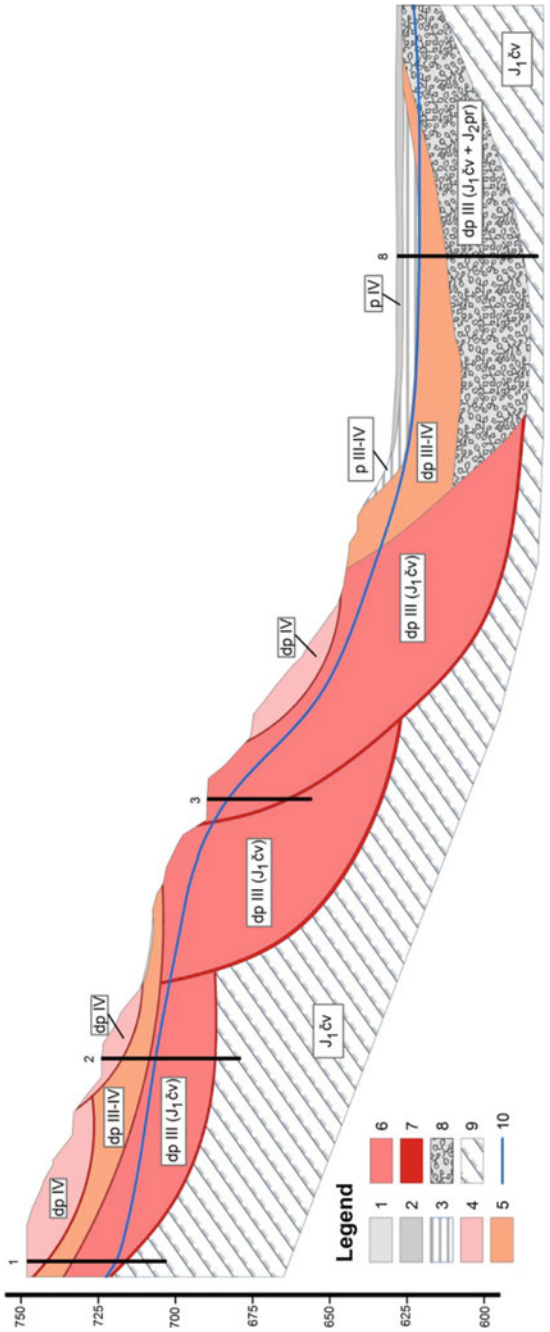

Fig. 12.6 Cross-section through thelandslidesite "RusskieGorki" (*Legend* [1] Man-made deposits [tIV]; Debris flow deposits: [2] Holocene age [pIV]; [3] Late Neopleistocene—Holocene age [pIII-IV]; [4] Landslide deposits: third phase [dpIV]; [5] second phase[dpIII-IV]; [6] first phase[dpIII[J_1čv]]; [7] the zones of rupture; [8] Landslide mélange of rock avalanche "Priescarpnaya" [dpIII[J_1čv + J_2pr]])

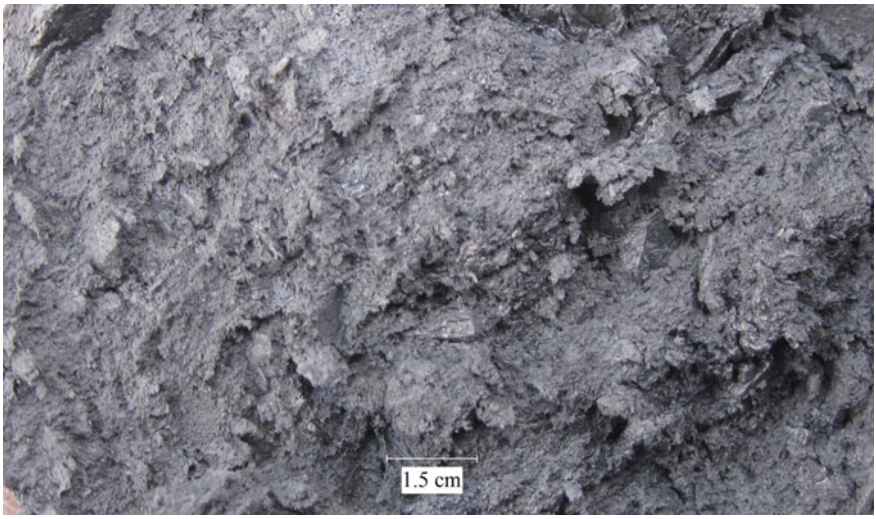

Fig. 12.7 The landslide breccia on the zone of rupture (in the core)

magnitude of landslide displacements (vertical and horizontal) can reach 10 m or more.

12.6 Instrumental Monitoring of Landsides at the "Russkie Gorki" Site

Instrumental monitoring systems network was deployed to monitor the behavior of the slope at the "Russkie Gorki" site, including observations of inclinometric, groundwater levels and of the values of landslide pressure on the foundations of building structures. Meteorological observations were also carried out at the site. Drilled wells were equipped to carry out observations of inclinometric and groundwater levels. The inclinometer (GEOKON model—1,600) is equipped with a sensor designed to measure the deviation from the vertical of the well in two mutually perpendicular directions. The sensor used made it possible to measure the deviation (horizontally) with an accuracy of 0.025 mm/500 mm. Pressure sensors were installed on the foundations of construction from the upper side of the slope. The main objectives of monitoring were verification of ideas about the structure of the landslide massif and verification of the results of the simulation of the slope stability on the site "Russkie Gorki." Instrumental monitoring was carried out in the spring of 2012 (end of February—beginning of June) for 106 days. Meteorological observations have shown that from the end of February to the beginning of April, the daytime air temperature was almost always in the range of −6 °C to +5 °C. At night, until April 02, the air temperature was almost always at levels below 0 °C. The slope

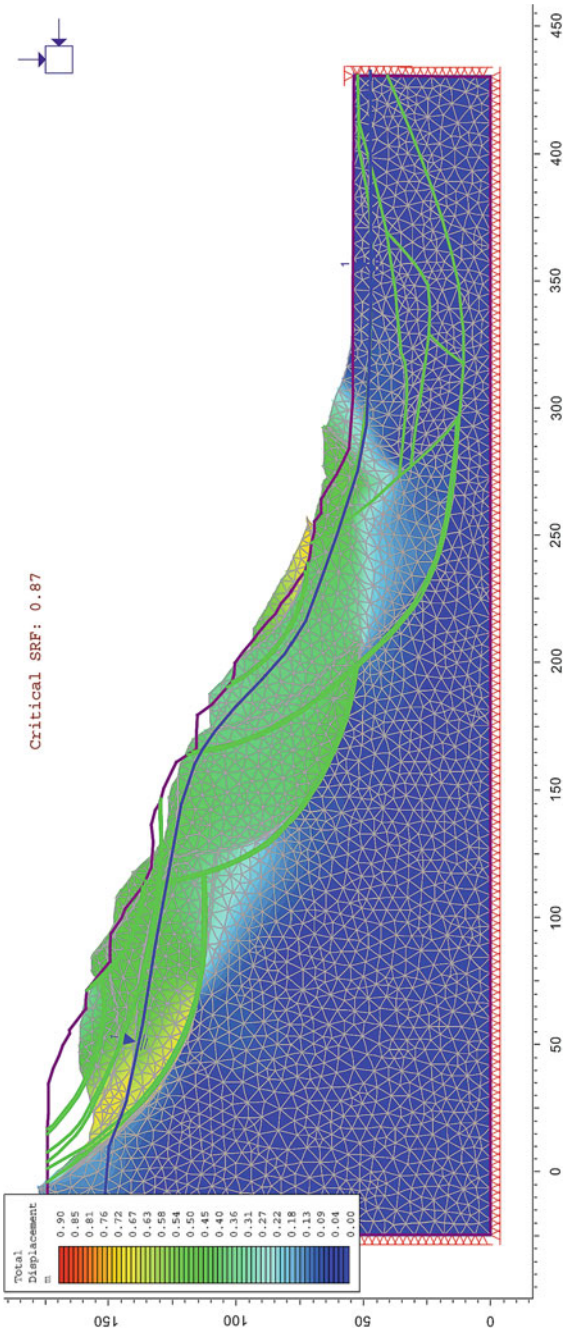

Fig. 12.8 Crack distribution in cross-section through the landslide site "Russkie Gorki"

surface was characterized by a stable snow cover. Its capacity in some areas was more than 1.5 m. Starting from April 03, the air temperature gradually rose to the value of +19 °C. Since that time, a period of active snowmelt began, accompanied by the formation of a large volume of surface water. The air temperature at night at the final stages of observations did not fall below 0 °C.

The inclinometer IH01 was equipped to a depth of 45 m in well No. 1, located near the top of the slope. The difference in the groundwater level during the observation period was 1 m (from 28.5 to 29.5 m). There were no sharp fluctuations in the groundwater level during the observation period. The observed displacements were timed to three the zones of landslide rupture (Fig. 12.9)—with depths in the intervals of 6–7 m (the zone of landslide rupture of the last phase of landslide activity), 15–16 m (the zone of landslide rupture of the second phase of landslide activity), 32–33 m (the zone of landslide rupture of the first phase of landslide activity). Active displacements were recorded from the beginning to April 8 (the 47th day of observations). They, in general, had a smooth, progressive character. Abrupt changes in the rate of deformations were not observed. During this period, the total displacement values were up to 27 mm in the upper zone of landslide rupture and 23 mm in the middle zone of landslide rupture. The total displacement values were about 12 mm for the lower zone of landslide rupture. The average speed of landslide displacements (during the period of movement activity) was 6–7 m (the zone of landslide rupture of the last phase of landslide activity), including per day average with a value of 0.55 mm/day. Likewise, the displacement is about 15–16 m (the zone of landslide rupture of the second phase of landslide activity) with a value per day average of 0.5 mm/day, and also displacement was observed at about 32–33 m (the zone of landslide rupture of the first phase of landslide activity) with an average of 0.26 mm/day.

Deviations of the inclinometer (IH01) were oriented to the southeast, which coincides with the orientation of the slope and can be considered the main direction of displacement of the landslide body. After April 08 (day 47), landslide displacements subsided. The inclinometer IH02 was equipped in well No. 2 to a depth of 45 m, located in the middle part of the slope. The difference in the groundwater level during the observation period was more than 1.5 m (from 17.4 to 19.1 m). The sharpest changes in the groundwater level were observed on March 13–18 (days 21–26). A decrease of ~1 m on March 13 and a sharp rise of 0.9 m) on March 15, and a sharp decline was observed (1.7 m) on March 18. This time was characterized by significant average daily amplitudes of air temperatures (from −6.5 to −6.7 °C). During the daytime, there was an intense melting of snow. The displacements observed by the inclinometer IH02 were timed to three the zone of landslide rupture (Fig. 12.9) with depths in the intervals of 5–6 m (the zone of landslide rupture of the last phase of landslide activity), 15–16 m (the zone of landslide rupture of the second phase of landslide activity), 37–38 m (the zone of landslide rupture of the first phase of landslide activity).The upper zone of landslide rupture is characterized by sharp, abrupt deformations, which were of an impulse nature. Three periods of landslide displacements had an amplitude of about 5 mm (6–7, 41–42, 49–54 days). Deformations in the upper zone of landslide rupture with the greatest amplitude (about 40 mm) occurred from 21 to 26 days of observations. During this period, the rate

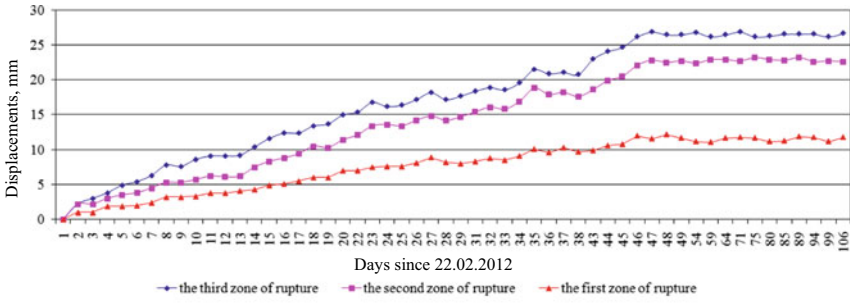

(a)

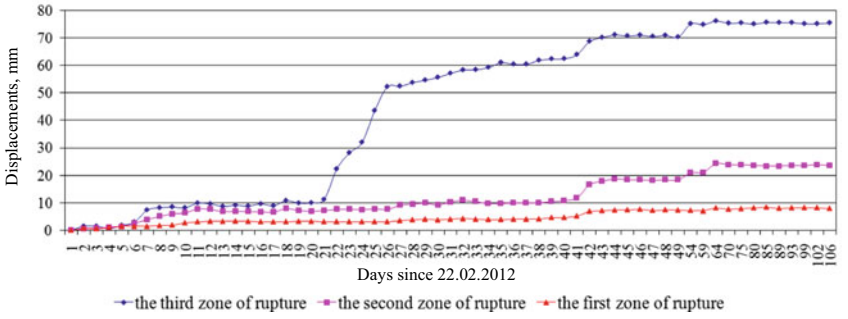

(b)

Fig. 12.9 Inclinometer monitoring history, spanning the period 22.02.2012 to 06.06.2012. **a** Inclinometer IH01 (well No. 1 [Fig. 6]). Interval of the zone of landslide rupture: first –32 to 33 m, second –15 to 16 m, third −6 to 7 m. **b** Inclinometer IH02 (well No. 2 [Fig. 6]). Interval of the zone of landslide rupture: first—about 37–38 m, second −15 to 16 m, third −5 to 6 m

of landslide displacements was 8 mm/day. They occurred against the background of significant fluctuations in average daily air temperatures and sharp changes in the level of groundwater. Deformations in the upper zone of landslide rupture, which occurred from the 21st to the 26th days of observations, were accompanied by an increase in landslide pressure on the foundations of building structures by 24–26 kPa, recorded by pressure sensors. Starting from April 15 (54th day of observations), landslide displacements fade out. The total values of displacements along the upper zone of landslide rupture for the entire observation period amounted to 76 mm.

Recorded by the inclinometer IH02 on the middle and lower, the zones of landslide rupture as a whole had a smooth translational character (Fig. 12.9). There was a trend of increasing pulse, which developed displacements with an amplitude of about 5 mm. Over the entire period, the total displacement values in landslide rupture were recorded up to 24 mm in the middle zone and about 8 mm in the lower zone, respectively. The average speed of landslide displacements (during the period of movement activity) was in the intervals of 15–16 m (the zone of landslide rupture of the second phase of landslide activity)—0.39 mm/day, 37–38 m (the zone of landslide

rupture of the first phase of landslide activity)—0.16 mm/day. Starting from April 25 (64 days of observations) in the middle, the zones of landslide rupture, starting from April 03 (42 days of observations) in the lower the zones of landslide rupture, landslide displacements fade out. Deviations of the inclinometer IH02 were also oriented to the southeast, which coincides with the orientation of the slope and can be considered as the main direction of displacement of the landslide massif.

12.7 Results and Conclusion

The results of instrumental monitoring at the site "Russkie Gorki" study confirmed the ideas about the storied composition of the landslide massif. The zones of landslide rupture, formed at various stages of landslide activity, located at different depths, are associated with modern landslide displacements. The largest values and displacement velocities were recorded for the upper zone of landslide rupture. During the period of inclinometric observations (106 days), the total values of the displacements were noticed as follows; (1) At the instrument IH01 gives 27 mm, and the IH02 showed 76 mm along the upper the zone of landslide rupture (interval 6–7 m). (2) up to 23–24 mm in the middle of the zone of landslide rupture (interval 15–16 m) and about 8–12 mm along the lower zone of landslide rupture (interval 32–33 m for IH01 and 37–38 m for IH02). The average speed of landslide displacements (during the period of movement activity) was recorded in the upper the zone of landslide rupture at about 0.55 mm/day; in the middle of the zone 0.4–0.5 mm/day and finally in the lower zone had about 0.16–0.26 mm/day. The rate of landslide displacements for the upper zone of landslide rupture reached up to 5–8 mm/day during periods of sharp growth of deformation having an impulse nature. The increase in the rate of landslide deformations occurred with significant fluctuations in average daily air temperatures and sharp changes in the groundwater level. The main direction of displacement of the landslide massif (southeast) coincides with the general orientation of the slope. The study results confirmed the outcome of the simulation of the slope stability in this area. It was observed that the mountainside is really in a state of extreme equilibrium. This slope is characterized by alternating "periods of rest" (temporary stability) and "periods of displacements." An engineering structure has been constructed to protect the slope to ensure the functioning of the Ski-jump complex (Fig. 12.10).

The landslide array on the "Russkie Gorki" site has a three phase tiered structure (storied composition). The first phase refers to the beginning of the Late Pleistocene time. Presently, the rupture zones of this ancient landslide have been encountered in wells at depths from 32–33 to 53–54 m. The second phase of landslide activity took place in the Late Neopleistocene. At this time, a rotation block slide was formed. In addition, the zones of rupture of the second-phase landslide were encountered in wells at a depth of 12–16 m. Shallow rotation and earth slide have formed at the present stage of landslide activity. The thickness of the displaced mass of the shallow slides is about 5–7 m. The present study concluded that the instrumental monitoring at the site is safe after effective gabion retaining wall construction.

Fig. 12.10 Gabion retaining wall at site "Russkie Gorki"

References

Chigira M, Hariyama T, Yamasaki S (2013) Development of deep-seated gravitational slope deformation on a shale dip-slope: Observations from high-quality drill cores. Tectonophysics 605:104–113. https://doi.org/10.1016/j.tecto.2013.04.019

Crosta GB, Frattini P, Fusi N (2007) Fragmentation in the Val Pola rock avalanche, Italian Alps. J Geophys Res 112:F01006. https://doi.org/10.1029/2005JF000455

Cruden D, Varnes DJ (1996) Landslide types and processes. In: Turner AK, Schuster RLE (eds) Landslides: investigation and mitigation: transportation research board. Special report 247. National Academy Press, Washington, pp 36–75

Dufresne A, Dunning SA (2017) Process dependence of grain size distributions in rock avalanche deposits. Landslides 14:1555–1563. https://doi.org/10.1007/s10346-017-0806-y

Hewitt K, Clague JJ, Orwin JF (2008) Legacies of catastrophic rock slope failures in mountain landscapes. Earth Sci Rev 87:1–38. https://doi.org/10.1016/j.earscirev.2007.10.002

Hutchinson JN (1988) General report: morphological and geotechnical parameters of landslides in relation to geology and hydrogeology. In: Bonnard C (ed) Proceedings of the 5th international symposium on landslides, vol 1. Balkema, pp 3–35

Kang K, Ponomarev A, Zerkal O, Huang S, Lin Q (2019) Shallow landslide susceptibility mapping in Sochi Ski-Jump area using GIS and numerical modelling. ISPRS Int J Geo Inf 8:148. https://doi.org/10.3390/ijgi8030148

Khain VE (1998) The Pyrenees-Alps-Carpathians-Caucasus: experience of comparative analysis. tectonics and geo-dynamics: general and regional aspects. In: Proceedings of the XXXI Tectonic conference, vol 2. Geos Press, Moscow, pp 241–243 (in Russian)

Kondorskaya NV, Shebalin NV (1982) New catalog of strong earthquakes in the U.S.S.R. from ancient times through 1977. Nauka Press, Moscow

Krahn J (2007) Stability modeling with SLOPE/W. An engineering methodology. GEO-SLOPE International Ltd., Calgary

Lavrishchev VA, Prutsky NI, Semenov VM (2002) State geological map of the Russian Federation scale 1:200 000, 2nd edn. Sheet K-37-V. Explanatory note. VSEGEI Press, Saint-Petersburg

Lukk AA, Shevchenko VI (2019) Seismicity, tectonics, and GPS geodynamics of the caucasus. Phys Earth 4:99–123 (in Russian). https://doi.org/10.31857/S0002-33372019499-123

Morgenstern NR, Price VE (1965) The analysis of the stability of general slip surfaces. Geotechnique 15:79–93

Multilingual Landslide Glossary (1993) The international geotechnical societies. UNESCO working party for world landslide inventory. BiTech Publ., Richmond

Ostrovsky AB, Stroychil MF, Korobkina NS, Chertkov AD (1972) Results of engineering-geological mapping of the 1:25000 scale of the Black Sea coast of the Caucasus. Technical report. Krasnodar. (unpublished report, in Russian)

Pedrazzini A, Jaboyedoff M, Loye A, Derron M-H (2013) From deep seated slope deformation to rock avalanche: Destabilization and transportation models of the Sierre landslide (Switzerland). Tectonophysics 605:149–168. https://doi.org/10.1016/j.tecto.2013.04.016

Pollet N, Schneider J-LM (2004) Dynamic disintegration processes accompanying transport of the Holocene Flims sturzstrom (Swiss Alps). Earth Planet Sci Lett 221:433–448. https://doi.org/10.1016/S0012-821X(04)00071-8

Ponomarev AA, Kang K, Zerkal OV (2021) Rock Avalanches in the upper reaches of the Mzymta River, Russia. In: Vilimek V, Wang F, Strom A, Sassa K, Bobrovsky PT, Takara K (eds) Understanding and reducing landslide disaster risk, vol 5. Catastrophic landslides and frontiers of landslide science. Proceedings of the 5th world landslide forum. Springer, pp 153–158. https://doi.org/10.1007/978-5-030-60319-9_16

Rogozhin EA, Gorbatikov AV, Stepanova MY, Ovsyuchenko AN, Andreeva NV, Kharazova YV (2015) The structural framework and recent geodynamics of the greater Caucasus Megaanticlinorium in the light of new data on its deep structure. Geotectonics 2:36–49 (in Russian). https://doi.org/10.7868/S0016853X15020058

Shevchenko VI, Guseva TV, Lukk AA, Mishin AV, Prilepin MT, Reilinger RE, Hamburger MW, Shempelev AG, Yunga SL (1999) Recent geodynamics of the Caucasus Mountains from GPS and seismological evidence Izvestiya. Phys Solid Earth 9:3–18 (in Russian)

Ter-Stepanian G (1977) Types of compound and complex landslides. Bull Int Assoc Eng Geol 17:72–74

Weidinger JT, Korup O, Munack H, Altenberger U, Dunning SA, Tippelt G, Lottermoser W (2014) Giant rockslides from the inside. Earth Planet Sci Lett 389:62–73. https://doi.org/10.1016/j.epsl.2013.12.017

Zerkal OV, Samarin EN (2008) Assessment of the conditions for the activity of hazardous geological processes at "Rosa Khutor Mountain Ski Complex Construction Project". Technical report. Faculty of Geology of Moscow State University, Moscow (unpublished report, in Russian)

Zerkal OV, Strom AL (2017) Overview of landslides distribution in Russian Federation and variation of their activity due to climatic change. In: Ho K, Lacasse S, Picarelli L (eds) Slope safety preparedness for impact of climatic change. Balkema, pp 253–288

Zerkal OV, Kalinin EV, Panasyan LL (2015) The formation and distribution of stress concentration zones in Heterogeneous Rock Masses with slopes. In: Lollino G, Giordan D, Crosta GB, Corominas J, Azzam R, Wasowski J, Sciarra N (eds) Engineering geology for society and territory. Proceedings of the XII international IAEG congress, vol 2. Landslide processes. Springer, pp 1251–1254. https://doi.org/10.1007/978-3-319-09057-3_219

Zolotarev GS, Janič M (1980) A method of engineering-geological studies of the high rockfall and landslide slopes. Moscow University Press, Moscow (in Russian)

Chapter 13
Application of Scoops3D and GIS for Assessing Landslide Hazard in Trung Chai Commune, Sapa, Vietnam

Binh Van Duong, I. K. Fomenko, Kien Trung Nguyen, Dang Hong Vu, O. N. Sirotkina, and Ha Ngoc Thi Pham

Abstract Landslides are one of the natural disasters that have frequently occurred in the northern region of Vietnam. Located in Laocai province, the Sapa district is known as a landslide hotspot in the mountainous region of Vietnam. The rapid economic development and construction in this area have significantly increased the likelihood of landslides. Therefore, landslide hazard assessment is critical for developing a strategy for reducing landslide risk and long-term territorial planning. This study presents the results of a landslide hazard assessment due to rainfall using a physically-based Scoops3D model in the Trung Chai commune, Sapa district. The initial data for the analysis model in Scoops3D consists of topographic data (DEM, distribution of soil thickness), soil properties, hydrogeological conditions, and earthquake loading. As a result, the factor-of-safety maps (FS maps) have been established, and the study area was divided into four hazard zones: unstable, quasi-stable, moderately stable, and stable. The study results indicate that the unstable zone covers 18.12% of the study area under the influence of rainfall in 16 h, and 61.11% of total landslides were accurately predicted, including the largest landslide in the study area (the Mong Sen landslide). The percentage of landslide ratio for each predicted factor-of-safety class (%LRclass index) of 64.19% demonstrated the acceptable performance of the Scoops3D model in this study. The study results identified the advantages and limits of this model for evaluating landslide hazards

B. Van Duong (✉) · H. N. T. Pham
Hanoi University of Mining and Geology, 100000 Hanoi, Vietnam
e-mail: duongvanbinh@humg.edu.vn

B. Van Duong · B. Van Duong · I. K. Fomenko
Ordzhonikidze Russian State Geological Prospecting University (MGRI), 117997 Moscow, Russia

K. T. Nguyen
Institute of Geological Sciences, Vietnam Academy of Science and Technology, 100000 Hanoi, Vietnam

D. H. Vu
Vietnam Institute of Geosciences and Mineral Resources, 100000 Hanoi, Vietnam

O. N. Sirotkina
Lomonosov Moscow State University, 119991 Moscow, Russia

P. Thambidurai and T. N. Singh (eds.), *Landslides: Detection, Prediction and Monitoring*,
https://doi.org/10.1007/978-3-031-23859-8_13

on a large scale, allowing for the development of solutions to enhance the prediction quality of future studies.

Keywords Landslide · Landslide hazard · Scoops3D · GIS · Limit equilibrium method · Trung Chai · Sapa · Vietnam

13.1 Introduction

Landslide is a natural disaster that occurs because of geodynamic processes, causing the instability of a slope, the displacement of rocks on the slopes, and the destruction of everything in its area of influence (Cruden and Varnes 1996). Landslides may be triggered by different causes, including rainfall, earthquakes, and human activities. Among these causes, rainfall is the most common trigger of landslides (79% of fatal non-seismic landslides from 2004 to 2016) (Froude and Petley 2018). Rainfall-induced landslides have occurred frequently in Vietnam, particularly in the mountainous northern provinces of Hagiang (Hung et al. 2016), Backan (Le and Kawagoe 2018), Hoabinh (Tien Bui et al. 2013), and Laocai (Tien Bui et al. 2017). A study by Nguyen and Dao (2007) indicated eight primary causes of landslides in Northwest Vietnam: the slope of relief; the weathering process of rocks; modern present tectonic movement; hydro-system (surface streams and groundwater); vegetation density; striking and dipping of original rock; physical property and structure of original rock; and human activity. Landslide hazard assessment (LHA) plays a critical role in landslide study and risk management. Over the past three decades, the efficacy of landslide hazard assessments has improved because of the development of GIS-based approaches, such as direct (the landslide inventory method) and indirect (multi-criteria decision-making analysis, probabilistic, deterministic, statistical, and artificial intelligence methods). Deterministic methods based on physical and mechanical processes have been successfully employed in various landslide hazard and susceptibility assessments. These studies have been frequently conducted on a local scale using the B-GeoSVC model (Yang et al. 2019), SLIP and TRIGRS model (Saadatkhah et al. 2015; Marin et al. 2021), Scoops3D model (Zhang and Wang 2019; Rashid et al. 2020), r.slope.stability model (Palacio Cordoba et al. 2020) and on a site-specific scale using PCRaster model (Van Beek and Van Asch 2004), TRIGRS and TiVaSS models (Tran et al. 2017a, b), TRIGRS model (Tran et al. 2017a, b; Fusco et al. 2021). However, deterministic methods have only been employed in a limited number of studies conducted on a regional scale (e.g. Wang et al. 2020). These methods do not require long-term landslide inventory data and are thus more helpful in areas with no landslide inventory data (Luo and Liu, 2018). However, physically-based methods need detailed geotechnical parameters and considerable time and effort for simulations, experiments, and field studies (Yang et al. 2019). Therefore, these methods are only applicable over vast regions with very homogenous geological and geomorphological conditions and simple landslide types.

Because of the difficulties associated with gathering data to build an assessment model, the deterministic method has only been applied to several landslide studies in Vietnam (Loi et al. 2017; Le and Kawagoe 2018; Tran et al. 2021, 2022). In this study, to enhance the efficacy of landslide risk management, a Scoops3D model was developed to assess the landslide hazard caused by rainfall in the Trung Chai commune, Sapa district, Vietnam. Two simulation scenarios were performed to establish Factor of Safety (FS) maps, and the study area was categorised into four hazard zones. Finally, the model's performance was determined by comparing the FS map to the locations of 18 observed landslides.

13.2 Materials and Method

13.2.1 Study Area

In comparison to other northern Vietnamese areas, Sapa, a mountainous district in the northwest of Lao Cai Province, has experienced more landslides and soil erosion (Dang et al. 2018; Tran et al. 2021). Land-use changes associated with the expansion of agricultural and community tourism have accelerated the frequency of natural catastrophes, affecting the sustainability of the Sapa district (Dang et al. 2018). Landslides in Lao Cai, especially in the Sapa district, have garnered significant attention over the past decade because of the high number of fatalities, property loss, and ecological destruction they have caused (Tien Bui et al. 2017). Mountain commune Trung Chai (Fig. 13.1) is located in the northeastern part of the Sapa district, with an area of about 38.4 km^2 and an elevation ranging from 581 to 2176 m. Annual rainfall ranges from 2000 to 3600 mm.

Rainfall is concentrated from June to August, accounting for around 80–85% of total annual rainfall in the study area (Tien Bui et al. 2017). Trung Chai is one of the communes in Sapa that is at the highest risk of landslides. The most well-known landslide in the study area is the Mong Sen event (Fig. 13.2a), which occurred in 1998, 2000, 2002, and 2009. This landslide is located on the 4D national road connecting Laocai city with the Sapa district. The geological composition of the study area is formed of granodiorite, granite, and granite-migmatite rocks of the Posen complex, all of which have reasonably high strength. The weathering process of bedrock led to the formation of a thick cover layer with high permeability, increasing the landslide hazard in the study area. Previous studies have shown that rainfall is the primary cause of landslides in the study area (Tien Bui et al. 2017; Tran et al. 2021). A landslide that occurred in 2020 at Km12 + 600 − Km12 to 900 on provincial road 152 (Fig. 13.2b) was determined to be the result of heavy rainfall and slope excavation.

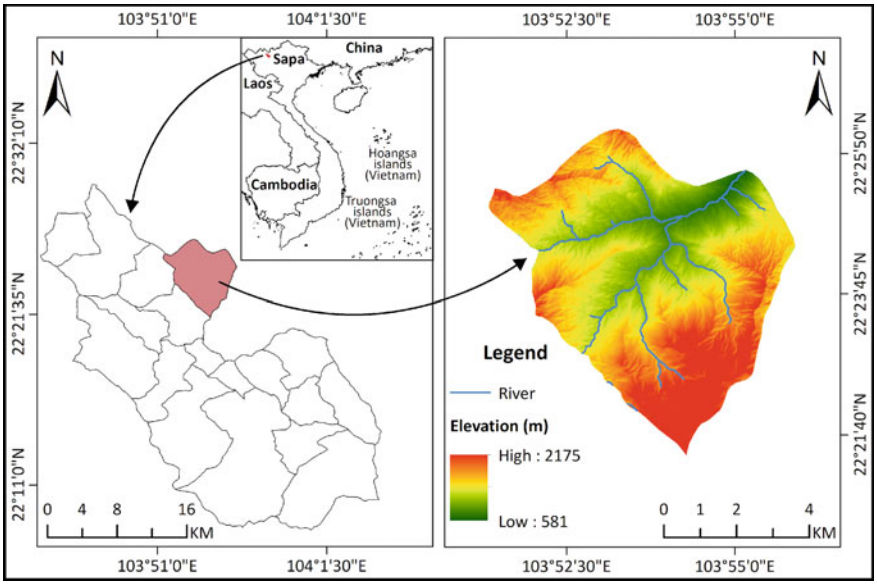

Fig. 13.1 Location of the study area

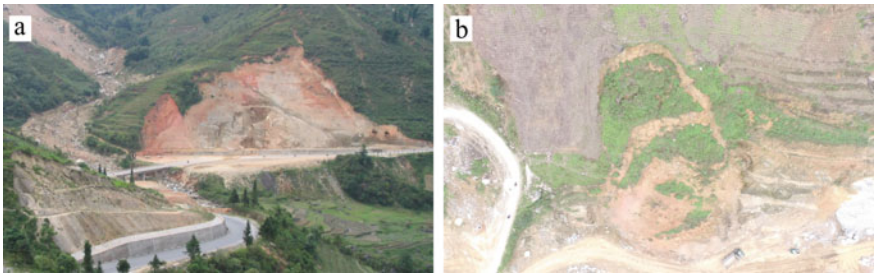

Fig. 13.2 **a** Mong Sen landslide and **b** a landslide on DT152 road

13.2.2 Landslide Hazard Assessment using Scoops3D Model

Scoops3D (Reid et al. 2015) is a computer program developed by the United States Geological Survey (USGS) for assessing landslide stability over a digital terrain expressed by a digital elevation model (DEM). Scoops3D has been effectively used in various landslide stability studies worldwide, including in Vietnam (Zhang and Wang 2019; Rashid et al. 2020; Tran et al. 2021). Using the 3D "method of columns" limit-equilibrium analysis, Scoops3D computes the slope stability with a spherical potential sliding surface (Fig. 13.3).

Scoops3D investigates and evaluates slope stability by determining the FS of millions of potential three-dimensional slope failures at various depths on the DEM

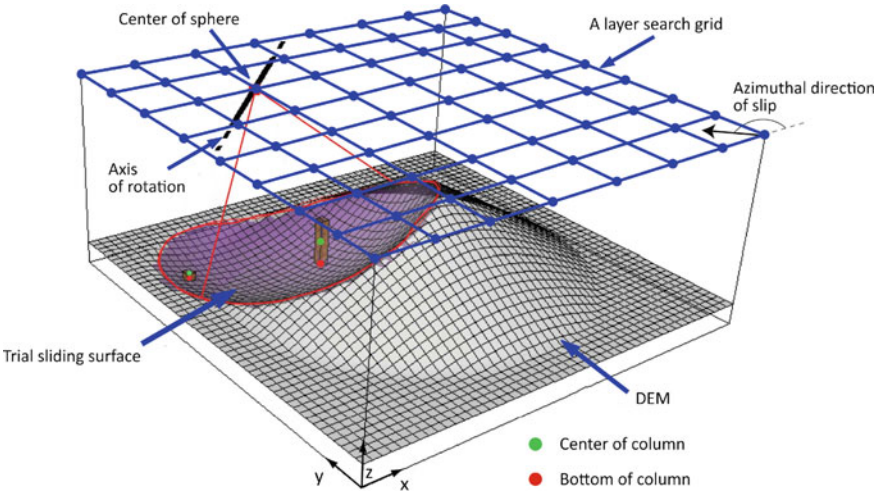

Fig. 13.3 Schematic drawing of Scoops3D model including a DEM with potential trial sliding surface and search grid. Each point on the search grid corresponds to denotes the center of multiple spherical trial surfaces (modified from Reid et al. 2015)

grid (Reid et al. 2000). In Scoops3D, numerous trial surfaces are required in three-dimensional analysis to assess slope stability because of the spatial variations in input data such as local topography, material parameters, and hydrogeological conditions. Compared to other physically based methods, the technique for searching for failure surfaces used by Scoops3D is a significant improvement. For modeling, users may select a suitable range for the 3D grid of sphere centers, which can be any point above the DEM, depending on the time and capability of their computer (Tran et al. 2021).

Generally, in analyzing slope stability by using the limit equilibrium method (LEM), the FS is defined as a ratio of the average shear strength (s), to the shear stress (τ) that controls the limit equilibrium state along a specified trial sliding surface (Tran et al. 2021):

$$FS = \frac{s}{\tau} \tag{13.1}$$

In this equation, the FS is less than one when the shear stress (τ) exceeds the shear strength (s) of material on the examined slope. The shear strength of soil on the trial surface is determined by using the following equation:

$$s = c' + (\sigma_n - u)\tan\varphi' \tag{13.2}$$

where c denotes effective cohesion, φ denotes effective internal friction angle, σ_n denotes normal stress, and u denotes pore-water pressure.

When evaluating the stability of spherical potential sliding surfaces in Scoops3D, Bishop's simplified method (Bishop, 1955) is frequently utilized since it provides more accurate results on the FS. The factor of safety is determined as follows using three-dimensional extensions of Bishop's simplified method:

$$FS_{3D} = \frac{\sum R_{i,j}\left[c_{i,j}A_{h_{i,j}} + \left(W_{i,j} - u_{i,j}A_{h_{i,j}}\right)tan\varphi_{i,j}\right]/m_{\alpha_{i,j}}}{\sum W_{i,j}\left(R_{i,j}sin\alpha_{i,j} + k_{eq}e_{i,j}\right)} \tag{13.3}$$

where:

$R_{i,j}$ denotes the distance from the axis of rotation to the center of the base of a column;

$A_{h_{i,j}}$ denotes the area of the trial surface at the base of each *i, j* column;

$W_{i,j}$ denotes the weight of the column *(i, j)* above the slip surface;

$\alpha_{i,j}$ denotes the apparent dip of the column base in the direction of rotation;

$e_{i,j}$ denotes the horizontal driving force moment arm for a column (equal to the vertical distance from the center of the column to the elevation of the axis of rotation) and

$$m_{\alpha_{i,j}} = cos\varepsilon_{i,j} + (sin\alpha_{i,j}tan\varphi_{i,j})/FS_{3D} \tag{13.4}$$

with $\varepsilon_{i,j}$ denotes the true dip of the trial surface at the column base; and

k_{eq} denotes the horizontal pseudo-acceleration coefficient (Fig. 13.4).

The scheme for assessing landslides using Scoops3D is shown in Fig. 13.5. Generally, Scoops3D, like other physically-based models, needs a variety of input variables related to the spatial distribution and strength parameters of soil layers, soil thickness, pore-water pressure (PWP), earthquake loading, and topographic conditions.

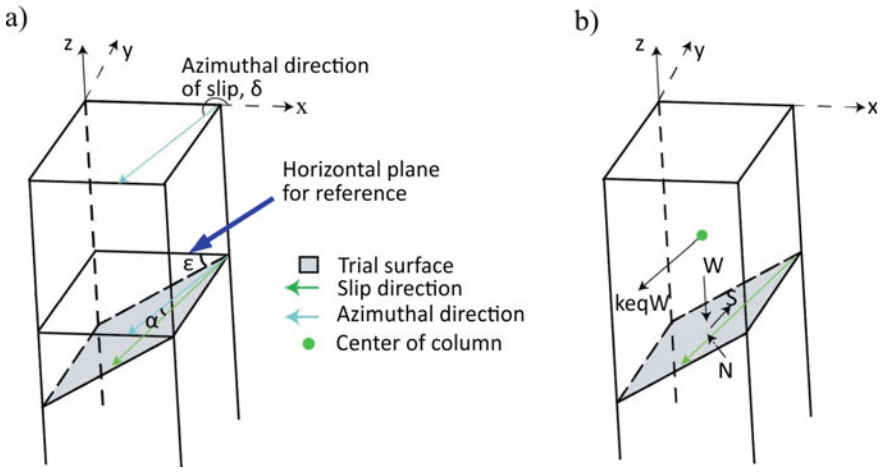

Fig. 13.4 Schematic diagrams illustrating **a** slip direction and **b** forces acting on a 3D column (Reid et al. 2015)

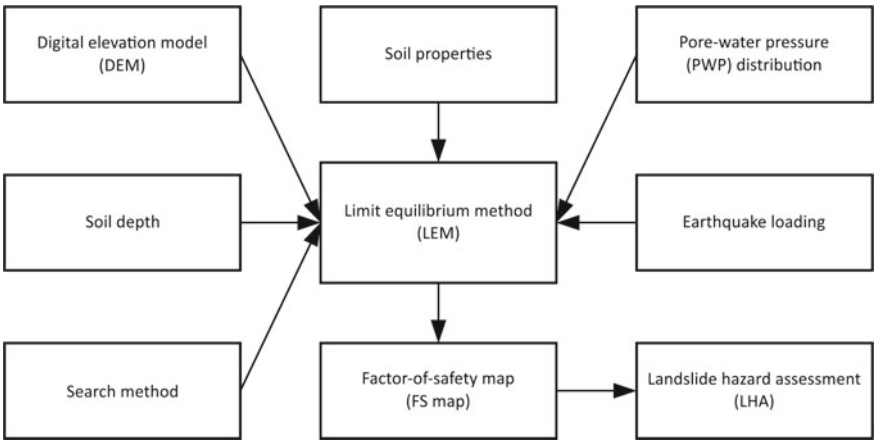

Fig. 13.5 Scheme for assessing landslide hazards using Scoops3D

The quality of the initial data has a significant influence on the prediction performance of the Scoops3D model (Reid et al. 2015).

13.2.3 Data Preparation

The survey results were employed to generate a DEM and determine the distribution of soil depth, PWP, soil properties, and earthquake loading for assessing landslide hazards in the study area. Terrain parameters may be the most critical input data when developing an analysis model for assessing landslide hazards (Tran et al. 2017a, b). Reid et al. (2015) indicated that Scoops3D examines the stability of all parts of a DEM using a systematic slope stability analysis for trial sliding surfaces formed at each node in the search grid. For accounting for all potential sliding surfaces, the vertical extent of the search grid is analyzed in the range of the lowest elevation and the elevation at which the stability map has no change (Tran et al. 2021). A DEM may be produced using various techniques, including Terrestrial Surveying, Aerial Photogrammetry, Light Detection and Ranging (LiDAR), and Interferometric Synthetic Aperture Radar (InSAR). Selecting the appropriate DEM resolution should be based on the purpose of the modeling, the features of the study area, and the availability of relevant data (Tran et al. 2016; Chang et al. 2019). In this study, the 5 m DEM was used for analysing landslide hazards (Fig. 13.6). When conducting a slope-instability study, it is critical to consider the soil thickness on a slope, which relates to the failure depth. Furthermore, soil thickness plays a significant role in the hydrological impact, as shown by the ratio of the saturated depth to the soil thickness (Ho et al. 2012). The prediction of soil thickness is challenging due to its dependency on complex interactions of numerous elements (topography, parent material, climate, biological, chemical, and physical processes) (Tesfa et al. 2009).

Soil thickness may be determined by examining its connection to other variables such as slope (Patton et al. 2018), relative relief (Pradhan and Kim, 2021), slope gradient (Brosens et al. 2020), elevation (Saadatkhah et al. 2015), or a combination of variables (Li et al. 2020). Many authors have developed various models for predicting the spatial distribution of soil thickness (Salciarini et al. 2006; Tesfa et al. 2009; Catani et al. 2010; Park et al. 2013; Tran et al. 2017a, b). However, determining the physico-mechanical properties and soil thickness over a large area is challenging in all simulation cases. The soil layer thickness in this study was determined using the correlation between measured soil thickness in the study area and topographic slope (Salciarini et al. 2006; Tran et al., 2017a, b, 2018). the distribution of soil thickness in the study area is presented Fig. 13.7, which shows values ranging from 2.0 to 20 m.

Pore-water pressure is the most frequently employed hydrological variable in physically-based models for identifying triggering conditions and predicting shallow landslides (Bordoni et al. 2018). Determining the distribution of PWP is critical for assessing slope stability under the influence of rainfall. There are several options for simulating PWP in Scoops3D: the impact of groundwater pressure is not considered; a pore-water pressure ratio (r_u) is used; simulation using a piezometric surface; simulation using a 3D distribution of saturated pore-pressure heads; simulation using

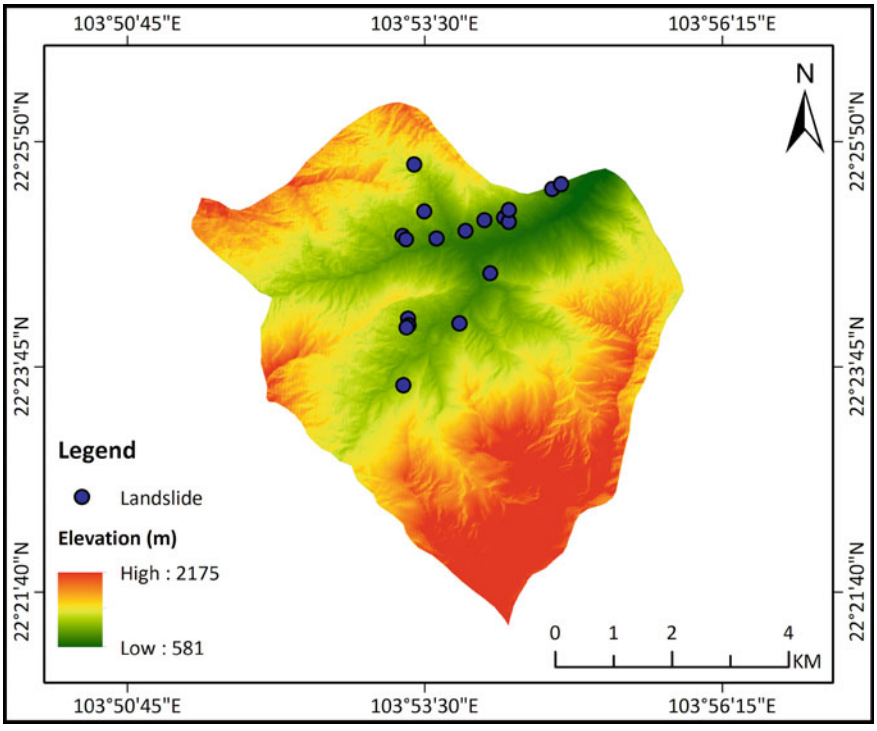

Fig. 13.6 Elevation map of the study area

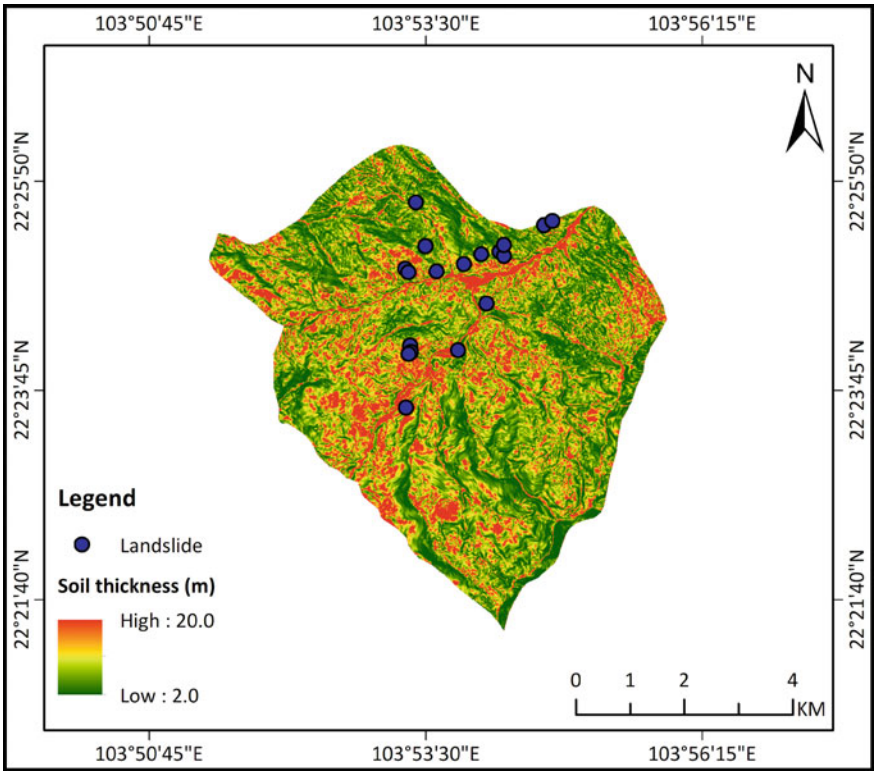

Fig. 13.7 Soil thickness distribution map of the study area

a 3D distribution of variably saturated pore-water heads pressure. Because of the absence of PWP data, the pore-water pressure ratio (r_u) was employed to simulate PWP in this study. The SLIDE model was used to determine the relationship between pore-water pressure ratio and rainwater infiltration in the study area (Liao et al. 2010). The heavy rainfall recorded on May 31, 2020 (Fig. 13.8) represents an "extreme case" for the study area and may be considered as the factor triggering widespread shallow landslides. As a result, the rainfall data, with a cumulative rainfall of 139.1 mm in 16 h and a maximum of 155.9 mm, was used to model landslides' stability.

In Scoops3D, to analyze slope stability, it is necessary to define the properties of all slope materials underlying the DEM. Three methods can be used to determine the distribution of these properties: input uniform, homogeneous properties; input layered material properties; and input 3D spatially varying properties. Because of the data availability, the layered material properties were used to analyze slope stability. Regarding the input data for the Scoops3D model, field studies and laboratory testing have been conducted to determine the shear strength, unit weight, and hydraulic conductivity parameters. The physico-mechanical properties of the soil

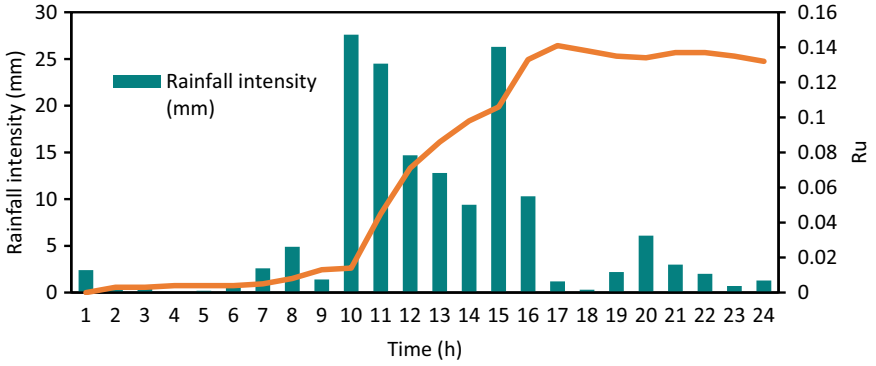

Fig. 13.8 Relationship between rainfall intensity and pore-water pressure ratio

Table 13.1 Soil parameters for landslide hazard assessment

Parameter	Symbol	Unit	Natural state	Saturated state
Unit weight	γ	kN/m^3	18.2	19.3
Friction angle	φ	(°)	16.3	12.2
Cohesion	c	kN/m^2	20.2	15.2

layer, including unit weight (γ), internal friction angle (φ), and cohesion (c), are shown in Table 13.1.

In the mountainous region, an earthquake triggers a landslide due to the mechanism of seismic wave–ground motion. In Scoops3D, the seismic loading is modeled as a uniform horizontal force ($k_{eq}W$), in which k_{eq} is the pseudo-horizontal acceleration coefficient. Previous studies have shown that landslides occurred in Lao Cai province and Sapa district due to rainfall (Tien Bui et al. 2017; Tran et al. 2021; Le et al. 2021). Terzaghi (1950) suggested that a horizontal seismic coefficient of 0.5 is an appropriate value for assessing seismic stability in catastrophic earthquakes. Marcuson and Franklin (1983) proposed that a horizontal seismic coefficient between 1/2 and 1/3 of Peak Horizontal Ground Acceleration (PHGA) might be used. Other reference summarizes values of extensively employed horizontal seismic coefficients in Table 13.2. In addition, no earthquakes have been recorded in the study area when landslides occur. Thus, in this study, we selected $k_{eq} = 0$ when analyzing landslide hazards.

13.2.4 Model Validation

A successful landslide hazard assessment (LHA) model should provide maximum consistency between actual and predicted landslides and reduce the predicted unstable zone to give valuable information for prediction (Park et al. 2013). It is

Table 13.2 Some reference values of k_{eq}

Horizontal pseudo-acceleration coefficient, k_{eq}	Remark	
0.5	Catastrophic earthquakes	Terzaghi (1950)
0.2	Violent, destructive earthquakes	
0.1	Severe earthquakes	
1/2 of PHGA – 1/3 of PHGA	Marcuson and Franklin (1983)	
0.1–0.25	In the United States	Kavazanjian et al. (1997)
0.15–0.25	In Japan	
0.1–0.2	$F_S \geq 1{,}15$ (Seed 1979)	
0.025	Minor Earthquake, $F_S > 1{,}0$	United States Army Corps of Engineers (1970)
0.05	Moderate Earthquake, $F_S > 1{,}0$	
0.1	Major Earthquake, $F_S > 1{,}0$	
0.15	Great Earthquake, $F_S > 1{,}0$	
1/2 of PHGA	$F_S > 1{,}0$ (Hynes-Griffin and Franklin 1984)	

required to compare landslide hazard maps and a landslide inventory map with the appropriate index to evaluate the model performance (Huang and Kao 2006). Various indicators have been proposed for determining the efficacy of landslide hazard assessments. In this study, the $\%LR_{class}$ index proposed by Park et al. (2013) was used to evaluate the performance of the Scoops3D model. Tran et al. (2018) modified the LR_{class} equation developed by Park et al. (2013), resulting in Eq. (13.5). LR_{class} (landslide ratio for each predicted factor-of-safety class) is an intermediate index defined as the ratio of the percentage of landslide locations in each FS class to the area percentage of each FS class. The $\%LR_{class}$ index for FS class i ($\%LR^{i}_{class}$) is the ratio of the LR_{class} value of FS class i to the total value of LR_{class} for all FS classes (Eq. 13.6) (Tran et al. 2018; Marin et al. 2021).

$$LR_{class} = \frac{\%landslidesineachFSclass}{\%areaofeachFSclass} \tag{13.5}$$

$$\%LR^{i}_{class} = \frac{LR^{i}_{class}}{\sum_{i=1}^{n} LR^{i}_{class}} \tag{13.6}$$

13.3 Results

Based on the input data, Scoops3D computes the factor of safety for all DEM cells. It is accepted that predicted zones with FS less than 1.0 are classified as unstable, whereas predicted zones with FS greater than 1.0 are classified as stable. In this study, the Scoops3D model was used to analyze two different scenarios: the stability of slopes in natural state and the stability of slopes under the influence of 16-h rainfall in the study area. As a result, two factor-of-safety maps were established for the study area and classified into hazard zones depicting the distribution of slope conditions based on the change in factor of safety (FS). The FS value has been categorized in these maps using the Mandal and Maiti classification (Mandal and Maiti 2015), which divides the stability state of the slope into four different classes: stable, moderately stable, quasi-stable, and unstable. A detailed description of the classification is represented in Table 13.3.

The analysis results of the distribution of 18 historical landslides indicated that most landslides occurred in zones between 581 and 900 m in elevation (11 landslides) (Fig. 13.9) and with weathering crust thickness ranging from 4 to 12 m (12 landslides) (Fig. 13.10).

The FS map in Fig. 13.11 shows that the study area is not at risk of landslides under natural conditions, such as when there is no rainfall. This result demonstrated that, despite the existence of a weathering crust ranging in thickness from 2 to 20 m, the slopes in the study area are generally stable in the absence of triggering variables like rainfall. According to the statistics, 91.2% of the study area has slopes that exist in a stable condition, with the remaining 8.8% having slopes that exist in a moderately stable condition.

When modeling in the natural conditions, the FS map of the study area was classified into two hazard zones: moderately stable (8.8%) and stable (91.2%). However, under the influence of rainfall, the FS map was classified into four hazard zones: unstable (18.12%), quasi-stable (15.04%), moderately stable (11.92%), and stable zone (54.92%) (Fig. 13.12). The unstable zone demonstrated the effect of rainfall on slope stability in the study area, including the location of 18 historical landslides. Heavy precipitation decreases the shear strength and increases the weight of the soil mass on the slope, increasing the likelihood of landslides occurring.

The model performance evaluation and the landslide location assessment results are presented in Table 13.4 and Fig. 13.13. A relatively good correlation between

Table 13.3 Classification of factor of safety (Mandal and Maiti 2015)

Factor of safety (F_S)	Slope state	Remark
<1.0	Unstable	Stabilizing factors are needed for stability
1.0–1.25	Quasi-stable	Minor destabilizing factor lead to instability
1.25–1.5	Moderately stable	Moderate destabilizing factor lead to instability
>1.5	Stable	Only major destabilizing factors lead to instability

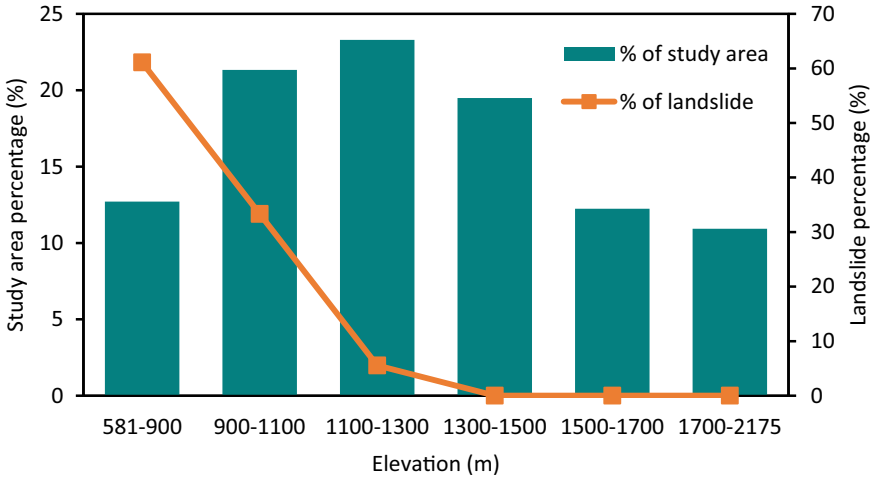

Fig. 13.9 Relationship between the distribution of landslides and elevation

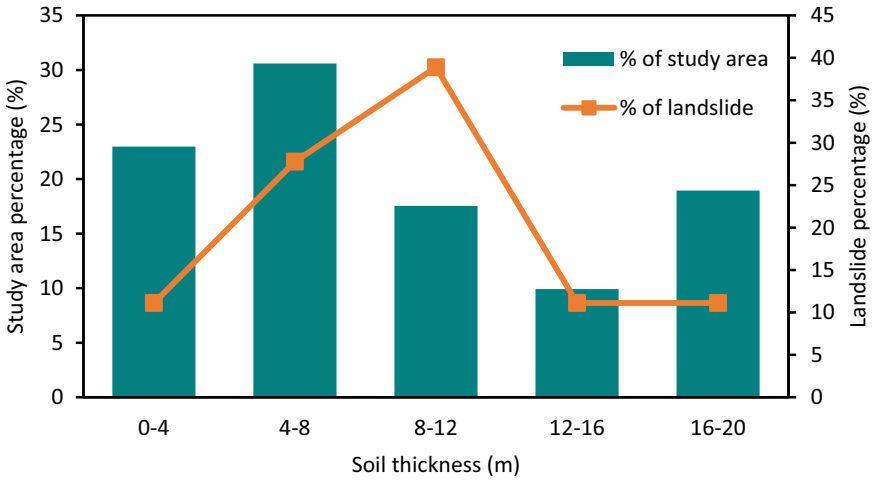

Fig. 13.10 Relationship between the distribution of landslides and soil thickness

the simulated scenario and the observed landslide sites, with an accuracy of around 61% for assessing the landslide location, is illustrated in Fig. 13.13. The results of the $\%LR_{class}$ assessment in Table 13.4 show a significantly acceptable performance of the Scoops3D model in predicting landslides since it accurately predicted the probability of including these landslides by more than 64%.

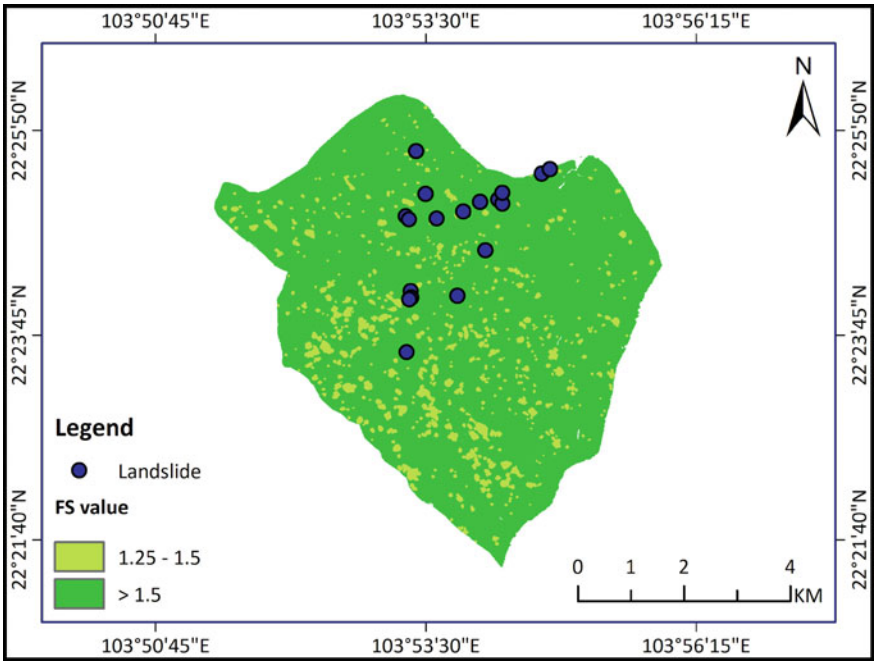

Fig. 13.11 Factor-of-safety map (natural condition)

13.4 Discussion

The preparation of landslide hazard maps is a significant step in landslide risk assessment and management. Even though physically-based models have considerable uncertainty, they have been extensively employed to produce landslide susceptibility and hazard maps (Melchiorre and Frattini 2012; Wang et al. 2019; Park et al. 2022). This uncertainty is caused by the spatial distribution of rock layers with varied thicknesses, the variety of hydrogeological conditions, and the heterogeneity in the physical and mechanical properties of the soil and rock at different locations. The use of physical models provides a better understanding of the process interactions that cause slope instability and may aid in the design of suitable mitigation strategies (Van Beek and Van Asch 2004). For the first time in Vietnam, the Scoops3D physically-based model has been utilized to assess the landslide hazard on a local scale. Due to the rough mountainous terrain of the study area, collecting topographic data, physical and mechanical parameters of soil and rock, and detailed information on the locations of slope failure is challenging. This model has been successfully established using collected data for assessing landslide hazards in the study area with reasonably good results. In physically-based models, including Scoops3D, topographic conditions play a significant role in the spatial and temporal distribution of landslides (Montgomery and Dietrich 1994). Analysis of historical landslides indicated that 61% of

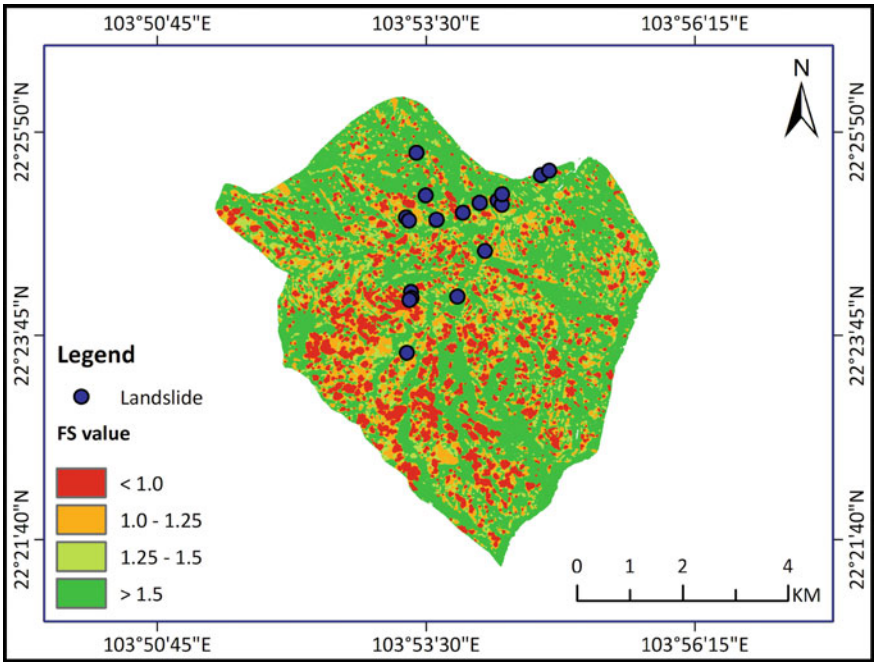

Fig. 13.12 Factor-of-safety map ($t = 16$ h)

Table 13.4 Performance evaluation of Scoops3D model

FS class	% Class area	Number of landslides	% Landslides	LR_{class}	% LR_{class}
<1.0	18.12	11	61.11	3.37	64.19
1.0–1.25	15.04	3	16.67	1.11	21.15
1.25–1.5	11.92	1	5.55	0.47	8.95
>1.5	54.92	3	16.67	0.3	5.71

landslides occurred along roads in an area with an elevation between 581 and 900 m. This area is characterized by high population density, infrastructure construction, and terraced rice fields, thus increasing the likelihood of landslides, particularly during the rainy season (Dang et al. 2018). The combination of water and human activities such as road construction and slope excavation increases the shear stress, reduces the shear strength of slope materials, and plays a significant role in the landslide process (Bozzano et al. 2011; Froude and Petley 2018; Wubalem 2021). As a result, it is possible to conclude that the landslide process in the study area involves a complex interaction of numerous factors, with rainfall acting as a trigger. The study area is located in the Northwest region of Vietnam, where various small and medium earthquakes occur (Nguyen et al. 2011). According to an earthquake catalog published by the Vietnam Institute of Geophysics, 332 earthquakes with local magnitudes ranging

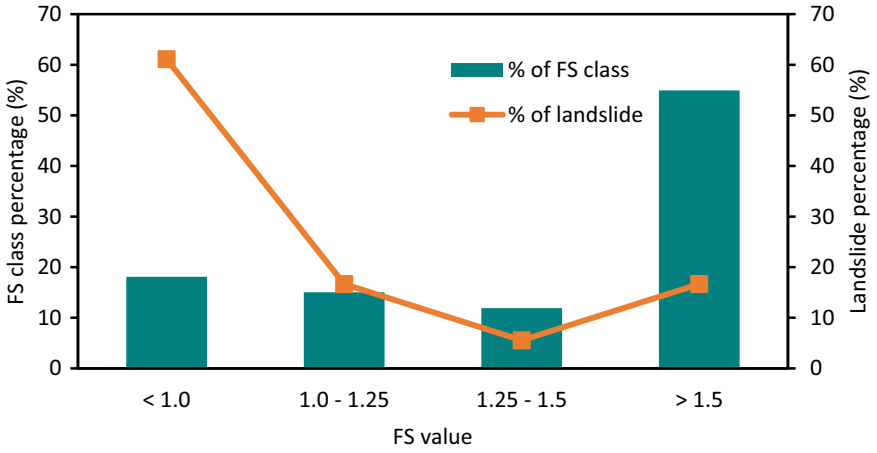

Fig. 13.13 Distribution of landslide locations in each FS class

from 3.0 to 6.8 were recorded in Northwest Vietnam between 1903 and April 2012 (Nguyen 2014). However, neither the Sapa district nor the Trung Chai commune has recorded any earthquake-induced landslides. Consequently, studies for landslide inventory and susceptibility/hazard mapping for the study area and other regions provide promising future research directions.

When data on landslide inventories are insufficient or incomplete, the $\%LR_{class}$ approach is the most recommended (Park et al. 2013; Tran et al. 2018). Along with the AUC value, the $\%LR_{class}$ index has been used in numerous landslide susceptibility/hazard assessment studies to evaluate the efficacy of the Scoops3D prediction model. Tran et al. (2018) determined that $\%LR_{class} = 87.44\%$ for the TRIGRS-Scoops3D coupled model used to assess landslide stability in a 0.4 km^2 area in the southern part of Seoul. Palazzolo et al. (2021) used the Scoops3D model to evaluate the landslide stability of a 2 km^2 river basin in northern Italy with a $\%LR_{class} = 82\%$. A coupled TRIGRS-Scoops3D model has also been utilized to assess landslide stability in the Niangniangba basin, China, with a $\%LR_{class}$ value of 80.16% (He et al. 2021). The comparison of our results ($\%LR_{class} = 64.19\%$) with those mentioned above indicated worse performance. It can be explained that by Tran et al. (2018) and Palazzolo et al. (2021) conducted their studies on a site-specific scale (<10 km^2), thereby reducing the uncertainty of the input data and thus improving model performance. Although He et al. (2021) conducted a study over a larger area (53.81 km^2), the high quality of input data and landslide inventory map and the combination of Scoops3D and TRIGRS models has enhanced prediction efficiency. Because of the lack of high-quality input data and insufficient information on historical landslides in the study area, the effectiveness of the prediction model is decreased. However, the results are considered promising since they provide a reasonable basis for predicting landslide hazards in the study area.

13.5 Conclusion

Enhancing public awareness of landslide hazards and developing effective prediction methods are efforts to manage and mitigate landslide risk in Vietnam's mountainous regions. Based on this idea, a Scoops3D model was used in this study for landslide hazard assessment. For preparing the FS maps, the input data in Scoops3D were selected and analyzed, such as the elevation map, the map of the distribution of soil thickness, rainfall data, soil parameters, and earthquake loading. As a result, the study area was divided into four landslide hazard zones: unstable, quasi-stable, moderately stable, and stable. The results showed that under the effect of heavy rainfall of 139.1 mm within 16 h, the unstable zone increased from 0 (natural conditions) to 18.12% of the study area. The analysis revealed that 61.11% of total landslides were accurately predicted, including the largest landslide of Mong Sen. Most landslides are distributed in areas with an elevation of 581 to 900 m (11 landslides) and a weathering crust thickness of 4–12 m (12 landslides). The performance of the Scoops3D is determined by comparing the FS map to the recorded landslides in the study area using the $\%LR_{class}$ index. Due to the limits and uncertainty of the input data, the Scoops3D model used in this study has worse performance when compared to other landslide stability studies. However, because accurate input data for modeling the initial conditions are not fully available, these outcomes are acceptable for this model. Therefore, the following recommendations may be made to improve the accuracy of the prediction results, including enhancing the quality of input data, establishing a pore-water pressure monitoring system, and combining the Scoops3D model with other prediction models. When the input data quality is improved, the Scoops3D model may be an effective predictor for assessing landslide hazards in the study area. The landslide hazard map can be used for land use management, long-term spatial planning, infrastructure and residential development, disaster management, and early warning in the study area.

Acknowledgements We sincerely thank to the Institute of Geological Sciences—Vietnam Academy of Science and Technology as part of the national science and technology for financial support for this research by project under grant number ĐTĐL.CN-81/21.

Declaration The authors declare that they have no known competing financial interests or personal relationships that could have appeared to influence the work reported in this paper.

References

Bishop AW (1955) The use of the slip circle in the stability analysis of slopes. Géotechnique 5(1):7–17. https://doi.org/10.1680/geot.1955.5.1.7

Bordoni M, Valentino R, Meisina C, Bittelli M, Chersich S (2018) A simplified approach to assess the soil saturation degree and stability of a representative slope affected by shallow landslides in Oltrepò Pavese (Italy). Geosciences 8(12). https://doi.org/10.3390/geosciences8120472

Bozzano F, Cipriani I, Mazzanti P, Prestininzi A (2011) Displacement patterns of a landslide affected by human activities: insights from ground-based InSAR monitoring. Nat Hazards 59(3):1377–1396. https://doi.org/10.1007/s11069-011-9840-6

Brosens L, Campforts B, Robinet J, Vanacker V, Opfergelt S, Ameijeiras-Mariño Y, Minella JP, Govers G (2020) Slope gradient controls soil thickness and chemical weathering in subtropical Brazil: understanding rates and timescales of regional soilscape evolution through a combination of field data and modeling. J Geophys Res Earth Surf 125(6):1–26. https://doi.org/10.1029/2019JF005321

Catani F, Segoni S, Falorni G (2010) An empirical geomorphology-based approach to the spatial prediction of soil thickness at catchment scale. Water Resour Res 46(5). https://doi.org/10.1029/2008WR007450

Chang K-T, Merghadi A, Yunus AP, Pham BT, Dou J (2019). Evaluating scale effects of topographic variables in landslide susceptibility models using GIS-based machine learning techniques. Sci Rep 9(1). https://doi.org/10.1038/s41598-019-48773-2

Cruden D, Varnes DJ (1996) Landslide types and processes. In: Schuster RL, Turner AK (eds) Landslides: investigation and mitigation, vol 247. Transportation Research Board, U.S. National Academy of Sciences, pp 36–75

Dang KB, Burkhard B, Müller F, Dang VB (2018) Modelling and mapping natural hazard regulating ecosystem services in Sapa, Lao Cai province, Vietnam. Paddy Water Environ 16(4):767–781. https://doi.org/10.1007/s10333-018-0667-6

Froude MJ, Petley DN (2018) Global fatal landslide occurrence 2004 to 2016. Nat Hazards Earth Syst Sci 18(8):2161–2181. https://doi.org/10.5194/nhess-18-2161-2018

Fusco F, Mirus BB, Baum RL, Calcaterra D, De Vita P (2021) Incorporating the effects of complex soil layering and thickness local variability into distributed landslide susceptibility assessments. Water 13(5). https://doi.org/10.3390/w13050713

He J, Qiu H, Qu F, Hu S, Yang D, Shen Y, Zhang Y, Sun H, Cao M (2021) Prediction of spatiotemporal stability and rainfall threshold of shallow landslides using the TRIGRS and Scoops3D models. CATENA 197. https://doi.org/10.1016/j.catena.2020.104999

Ho J-Y, Lee KT, Chang T-C, Wang Z-Y, Liao Y-H (2012) Influences of spatial distribution of soil thickness on shallow landslide prediction. Eng Geol 124:38–46. https://doi.org/10.1016/j.enggeo.2011.09.013

Huang JC, Kao SJ (2006) Optimal estimator for assessing landslide model performance. Hydrol Earth Syst Sci 10(6):957–965. https://doi.org/10.5194/hess-10-957-2006

Hung LQ, Van NTH, Duc DM, Ha LTC, Van Son P, Khanh NH, Binh LT (2016) Landslide susceptibility mapping by combining the analytical hierarchy process and weighted linear combination methods: a case study in the upper Lo River catchment (Vietnam). Landslides 13(5):1285–1301. https://doi.org/10.1007/s10346-015-0657-3

Hynes-Griffin ME, Franklin AG (1984) Rationalizing the seismic coefficient method. Miscellaneous paper (U.S. Army Engineer Waterways Experiment Station); GL-84-13. U.S. Army Engineer Waterways Experiment Station, Vicksburg, Mississippi

Kavazanjian E, Matasovic Jr. N, Hadj-Hamou T, Sabatini PJ (1997) Geotechnical Engineering Circular No. 3: Design Guidance. Geotechnical Earthquake Engineering for Highways. Volume I—Design Principles. U.S. Dept. of Transportation, Federal Highway Administration, Office of Engineering: Office of Technology Applications, Washington, DC

Le T, Kawagoe S (2018) Impact of the landslide for a relationship between rainfall condition and land cover in North Vietnam. J Geol Resour Eng 6:239–250. https://doi.org/10.17265/2328-2193/2018.06.002

Le TTT, Tran TV, Hoang VH, Bui VT, Bui TKT, Nguyen HP (2021) Developing a landslide susceptibility map using the analytic hierarchical process in Ta Van and Hau Thao Communes, Sapa, Vietnam. J Disaster Res 16(4):529–538. https://doi.org/10.20965/jdr.2021.p0529

Li X, Luo J, Jin X, He Q, Niu Y (2020) Improving soil thickness estimations based on multiple environmental variables with stacking ensemble methods. Remote Sens 12(21). https://doi.org/10.3390/rs12213609

Liao Z, Hong Y, Wang J, Fukuoka H, Sassa K, Karnawati D, Fathani F (2010) Prototyping an experimental early warning system for rainfall-induced landslides in Indonesia using satellite remote sensing and geospatial datasets. Landslides 7(3):317–324. https://doi.org/10.1007/s10346-010-0219-7

Loi DH, Quang LH, Sassa K, Takara K, Dang K, Thanh NK, Van Tien P (2017) The 28 July 2015 rapid landslide at Ha Long City, Quang Ninh, Vietnam. Landslides 14(3):1207–1215. https://doi.org/10.1007/s10346-017-0814-y

Luo W, Liu C-C (2018) Innovative landslide susceptibility mapping supported by geomorphon and geographical detector methods. Landslides 15(3):465–474. https://doi.org/10.1007/s10346-017-0893-9

Mandal S, Maiti R (2015) semi-quantitative approaches for landslide assessment and prediction. Springer Natural Hazards. Springer, Singapore

Marcuson WF, Franklin AG (1983) Seismic design, analysis, and remedial measures to improve stability of existing earth dams-Corps of Engineers Approach. Seismic design of embankments and caverns. American Society of Civil Engineers, New York, pp 65–78

Marin RJ, Velásquez MF, Sánchez O (2021) Applicability and performance of deterministic and probabilistic physically based landslide modeling in a data-scarce environment of the Colombian Andes. J S Am Earth Sci 108. https://doi.org/10.1016/j.jsames.2021.103175

Melchiorre C, Frattini P (2012) Modelling probability of rainfall-induced shallow landslides in a changing climate, Otta, Central Norway. Climatic Change 113(2):413–436. https://doi.org/10.1007/s10584-011-0325-0

Montgomery D, Dietrich W (1994) A physically based model for the topographic control on shallow landsliding. Water Resour Res 30(4):1153–1171. https://doi.org/10.1029/93WR02979

Nguyen AD (2014) Tectonic deformation and earthquake hazard in Northwestern Vietnam inferred from GPS observations Doctoral Thesis, Nagoya University

Nguyen LM, Lin T-L, Wu Y-M, Huang B-S, Chang C-H, Huang W-G, Le TS, Dinh VT (2011) The first ML scale for North of Vietnam. J Asian Earth Sci 40(1):279–286. https://doi.org/10.1016/j.jseaes.2010.07.005

Nguyen VC, Dao VT (2007) Investigation and research of landslide geohazard in north-western part of Vietnam for the sustainable development of the territory. (eds). Annual Report of FY 2006, The Core University Program between Japan Society for the Promotion of Science (JSPS) and Vietnamese Academy of Science and Technology (VAST), vol. Osaka, Core University Program Office, Ike Laboratory, Div. Of Sustainable Energy and Environmental Engineering, Osaka University, pp 269–280

Palacio Cordoba J, Mergili M, Aristizábal E (2020) Probabilistic landslide susceptibility analysis in tropical mountainous terrain using the physically based r.slope.stability model. Nat Hazards Earth Syst Sci 20(3):815–829. https://doi.org/10.5194/nhess-20-815-2020

Palazzolo N, Peres DJ, Bordoni M, Meisina C, Creaco E, Cancelliere A (2021) Improving spatial landslide prediction with 3D slope stability analysis and genetic algorithm optimization: application to the Oltrepò Pavese. Water 13(6). https://doi.org/10.3390/w13060801

Park DW, Nikhil NV, Lee SR (2013) Landslide and debris flow susceptibility zonation using TRIGRS for the 2011 Seoul landslide event. Nat Hazard 13(11):2833–2849. https://doi.org/10.5194/nhess-13-2833-2013

Park H-J, Kim K-M, Hwang I-T, Lee J-H (2022) Regional landslide hazard assessment using extreme value analysis and a probabilistic physically based approach. Sustainability 14(5). https://doi.org/10.3390/su14052628

Patton NR, Lohse KA, Godsey SE, Crosby BT, Seyfried MS (2018) Predicting soil thickness on soil mantled hillslopes. Nat Commun 9(1). https://doi.org/10.1038/s41467-018-05743-y

Pradhan AMS, Kim Y-T (2021) Development and evaluation of relative relief based soil thickness model: a comparative study in Hilly Terrain, South Korea. KSCE J Civ Eng 25(6):2186–2198. https://doi.org/10.1007/s12205-021-1379-9

Rashid B, Iqbal J, Su L-J (2020) Landslide susceptibility analysis of Karakoram highway using analytical hierarchy process and scoops 3D. J Mt Sci 17(7):1596–1612. https://doi.org/10.1007/s11629-018-5195-8

Reid E, Christian SB, Brien DL, Henderson ST (2015) Scoops3D—Software to analyze 3D slope stability throughout a digital landscape. Techniques and Methods, U.S. Geological Survey, Reston, VA, USA. https://doi.org/10.3133/tm14A1

Reid ME, Christian SB, Brien DL (2000) Gravitational stability of three-dimensional stratovolcano edifices. J Geophys Res Solid Earth 105(B3):6043–6056. https://doi.org/10.1029/1999JB900310

Saadatkhah N, Kassim A, Lee LM (2015) Hulu Kelang, Malaysia regional mapping of rainfall-induced landslides using TRIGRS model. Arab J Geosci 8(5):3183–3194. https://doi.org/10.1007/s12517-014-1410-2

Salciarini D, Godt JW, Savage WZ, Conversini P, Baum RL, Michael JA (2006) Modeling regional initiation of rainfall-induced shallow landslides in the eastern Umbria Region of central Italy. Landslides 3(3):181–194. https://doi.org/10.1007/s10346-006-0037-0

Seed HB (1979) Considerations in the earthquake-resistant design of earth and rockfill dams. Géotechnique 29(3):215–263. https://doi.org/10.1680/geot.1979.29.3.215

Terzaghi K (1950). Mechanism of landslides. In: Paige S (eds) Application of geology to engineering practice, Geological Society of America, pp 83–123. https://doi.org/10.1130/Berkey.1950.83

Tesfa TK, Tarboton DG, Chandler DG, McNamara JP (2009) Modeling soil depth from topographic and land cover attributes. Water Resour Res 45(10):1–16. https://doi.org/10.1029/2008WR007474

Tien Bui D, Pradhan B, Lofman O, Revhaug I, Dick ØB (2013) Regional prediction of landslide hazard using probability analysis of intense rainfall in the Hoa Binh province, Vietnam. Nat Hazards 66(2):707–730. https://doi.org/10.1007/s11069-012-0510-0

Tien Bui D, Tuan TA, Hoang N-D, Thanh NQ, Nguyen DB, Van Liem N, Pradhan B (2017) Spatial prediction of rainfall-induced landslides for the Lao Cai area (Vietnam) using a hybrid intelligent approach of least squares support vector machines inference model and artificial bee colony optimization. Landslides 14(2):447–458. https://doi.org/10.1007/s10346-016-0711-9

Tran TV, Lee G, Kim M (2016) Shallow landslide assessment considering the influence of vegetation cover. J Korean Geoenviron Soc 17(4):17–31. https://doi.org/10.14481/jkges.2016.17.4.17

Tran TV, Lee G, An H, Kim M (2017a) Comparing the performance of TRIGRS and TiVaSS in spatial and temporal prediction of rainfall-induced shallow landslides. Environ Earth Sci 76(8):1–16. https://doi.org/10.1007/s12665-017-6635-4

Tran TV, Lee G, Trinh MT, An H (2017b) Effect of digital elevation model resolution on shallow landslide modeling using TRIGRS. Nat Hazard Rev 18(2):1–12. https://doi.org/10.1061/(ASCE)NH.1527-6996.0000233

Tran TV, Alvioli M, Lee G, An HU (2018) Three-dimensional, time-dependent modeling of rainfall-induced landslides over a digital landscape: a case study. Landslides 15(6):1071–1084. https://doi.org/10.1007/s10346-017-0931-7

Tran TV, Hoang VH, Pham HD, Sato G (2021) Use of Scoops3D and GIS for the assessment of slope stability in three-dimensional: a case study in Sapa, Vietnam. In: Proceedings of the international conference on innovations for sustainable and responsible mining (ISRM 2020). Springer, Cham, pp 210–229. https://doi.org/10.1007/978-3-030-60269-7_11

Tran TV, Alvioli M, Hoang VH (2022) Description of a complex, rainfall-induced landslide within a multi-stage three-dimensional model. Nat Hazards 110(3):1953–1968. https://doi.org/10.1007/s11069-021-05020-0

United States Army Corps of Engineers (1970) Engineering and Design Stability of Earth and Rock-fill Dams. EM 1110-2-1902. Department of the Army, Corps of Engineers, Office of the Chief of Engineers, Washington, DC

Van Beek LPH, Van Asch TWJ (2004) Regional assessment of the effects of land-use change on landslide hazard By means of physically based modelling. Nat Hazards 31(1):289–304. https://doi.org/10.1023/B:NHAZ.0000020267.39691.39

Wang HJ, Xiao T, Li XY, Zhang LL, Zhang LM (2019) A novel physically-based model for updating landslide susceptibility. Eng Geol 251:71–80. https://doi.org/10.1016/j.enggeo.2019.02.004
Wang S, Zhang K, van Beek LPH, Tian X, Bogaard TA (2020) Physically-based landslide prediction over a large region: scaling low-resolution hydrological model results for high-resolution slope stability assessment. Environ Model Softw 124. https://doi.org/10.1016/j.envsoft.2019.104607
Wubalem A (2021) Landslide inventory, susceptibility, hazard and risk mapping. In. Zhang Y, Cheng Q (eds) Landslides, vol. London, IntechOpen. https://doi.org/10.5772/intechopen.100504
Yang Y, Yang J, Xu C, Xu C, Song C (2019) Local-scale landslide susceptibility mapping using the B-GeoSVC model. Landslides 16(7):1301–1312. https://doi.org/10.1007/s10346-019-01174-y
Zhang S, Wang F (2019) Three-dimensional seismic slope stability assessment with the application of Scoops3D and GIS: a case study in Atsuma, Hokkaido. Geoenviron Disasters 6(1):1–14. https://doi.org/10.1186/s40677-019-0125-9

Chapter 14
Landslide Susceptibility Assessment Using Frequency Ratio Model in Turung Mamring, South District of Sikkim, India

P. Thambidurai, Ramesh Veerappan, Iftikhar Hussain Beigh, and Keshar Kr. Luitel

Abstract The Sikkim state is part of the Himalayan hill ranges in north-eastern India, and landslide is one of the most frequent hazards in this region, which affects every year. The present study has been focused on preparing a landslide susceptibility zonation (LSZ) map using geospatial technology and statistical analyses. Eight landslide influencing factors were identified, including slope, aspect, curvature, elevation, lithology, land use and land cover, proximity to drainage, and proximity to lineament. The detailed landslide inventory database was prepared using high-resolution satellite imageries and extensive fieldwork. The independent variables' spatial database was prepared using high-resolution satellite imageries, a digital elevation model, published maps, and field data. The LSZ map was developed using a frequency ratio model by establishing the association between landslide-influencing factors and past landslide regions. Furthermore, the LSZ map was classified into five susceptibility zones: very low, low, medium, high and very high. The success rate of the LSZ map was validated using existing landslide inventory data through Area Under the Curve (AUC) method. The frequency ratio model has shown a fair success rate of 79.45%. The final LSZ map can be used for landslide hazard prevention, proper infrastructure planning, and geo-environmental development.

Keywords Landslide susceptibility zonation · Frequency ratio method · AUC · Sikkim Himalayas · North-Eastern India

P. Thambidurai (✉)
Department of Coastal Disaster Management, School of Physical, Chemical and Applied Sciences, Pondicherry University-Port Blair Campus, Port Blair 744112, Andaman and Nicobar Islands, India
e-mail: thambiduraip@pondiuni.ac.in

R. Veerappan
Centre for Geoinformatics, Jamsetji Tata School of Disaster Studies, Tata Institute of Social Sciences (TISS), Mumbai 400088, India

I. H. Beigh
Department of Civil Engineering, National Institute of Technology, Srinagar 190006, India

K. Kr. Luitel
Department of Mines and Geology, Government of Sikkim, Sikkim 737101, India

P. Thambidurai and T. N. Singh (eds.), *Landslides: Detection, Prediction and Monitoring*,
https://doi.org/10.1007/978-3-031-23859-8_14

14.1 Introduction

Landslides are one of the most prevalent natural tragedies in the mountainous region, with incidents also occurring in residential areas, posing a threat to human life, property loss, and damage to existing road networks and structures in each year (Aleotti and Chowdhury 1999; Nandi and Shakoor 2008). A variety of factors causes slope instability prominently due to natural processes and triggered by intense rainfall, seismic and anthropogenic activities (Gupta et al. 2018). The landslide occurs frequently in many parts of India (Singh et al. 2013, 2016), and the landslide causes hundreds of deaths annually in Sikkim Himalaya (Bhasin et al. 2002) and the past event recorded around 36,000 people died alone at Sikkim in 1968 (Choubey 1992). Landslides in the Himalayas can be difficult to reach, causing significant delays for planners. Nearly every monsoon of Sikkim experience landslide that cause damage to highways, villages, agricultural fields and forests, and human life loss. Several scholars have studied the landslides and investigated the instability and collective movement of hill slopes along hilly highways in Sikkim and North Bengal (Chopra 1977). The previous studies addressed the mechanism of instability of the Lanta Khola landslide (Anbarasu et al. 2010) and the geotechnical intervention of landslides, Gangtok, Sikkim (Thambidurai and Ramesh 2017; Ghosh 2013). Gupta and Tolia (1998) were carried out a detailed study on geological, geotechnical, field, and laboratory investigations of two major landslides in Sikkim and suggested remedial measures to protect the slope. The remote sensing techniques were applied in Sikkim landslide areas by various researchers (Pal and Chowduri 2019; Sonkar et al. 2021). Several types of research have been carried out by utilizing remote sensing data with the aid of GIS on susceptibility zonation mapping of landslides (Pal and Chowduri 2019).

Landslide zonation mapping is critical for disaster mitigation and prevention. Landslide susceptibility zonation (LSZ) mapping was widely carried out to delineate landslide sensitive areas (Kienholz et al. 1984; Mandal and Mandal 2016). The LSZ map depicts the different landslide-prone zones based on the ranking of degrees of the potential hazard (Varnes 1984). The LSZ mapping is crucial (Silalahi et al. 2019) and a preliminary step in any project before evaluating landslide management and mitigation (Kanwal et al. 2016; Sema et al. 2017). The landslide susceptibility must be identified and assessed in detail to decrease the danger of landslides through disaster mitigation planning and development plans (Ahmed et al. 2017). The geospatial technology in the study of landslides is an advanced tool that can reach practically every section of an inaccessible area and understand the terrain conditions (Perera et al. 2020). However, landslides' spatial and temporal information must be integrated with remote sensing data and ground-based data (Pandey et al. 2008). The recent works attempted to use GIS to estimate landslide hazards with various parameters (Cárdenas and Mera 2016; Ahmed et al. 2017; Hadmoko et al. 2017). The progress of the research had been achieved using GIS techniques to estimate the spatial probability of landslides. Numerous landslide research works used probabilistic models like frequency ratios and logistic regression (Dai et al.

2002; Yilmaz and Keskin 2009; Ehret et al. 2010; Kannan et al. 2013; Ramesh and Anbazhagan 2015; Youssef 2015; Mandal and Mandal 2018; Sharma et al. 2020; Singh et al. 2021). Using GIS, it has become easier to store all geo-environmental data sets, which has improved the capability to employ and evaluate various methods to rank landslide influencing factors and derive LSZ map. The current study used the frequency ratio (FR) approach to mapping landslide susceptibility zones in the Turung Mamring district of South Sikkim, Himalayas. The main goal of the current study is to map and analyse detailed landslide inventory and conditioning factors to map landslide susceptibility zones using the bivariate frequency ratio method with the aid of geospatial techniques. The research's output could be very useful to prevent the disaster and pre-plaining the development of infrastrures like road, settlements, etc. Furthermore, the resultant of the LSZ map was validated using the past landslide events in the study locations to estimate the model's accuracy.

14.2 Study Area

The study area is one of the rugged terrain of the tectonically active location at Sikkim in part of the Himalayan region of Northeastern India. The study area is extended in 88°30′–88°31′30″ East Longitude and 27°8′30″–27°10′ North Latitude. The lowest elevation in the study area is 280 m along the Tista river, and the highest point is on the ridge along Namthang-Turung ridgeline 1400 m. (Fig. 14.1).

The study area is located along Rangpo—Namchi link road at about 7 km from Rangpo and ends along the Daragoan Ridge line near Turung. The area falls within the catchment of Tista river, which runs almost North-Easterly to the South-Westerly direction. Many tributaries flow in either easterly or northeasterly direction before joining the Tista river. The area receives maximum rainfall during the northeast Indian monsoon (May–September) and has several perennial and seasonal springs. The study area of TurungMamring includes the villages of Turung, Kassor, Daragoan, Kaijaley and Bimbong, Donak, Mamring, Kanam, Suntaley and Linkhim Tar. Major mass movement (landslides) has occurred frequently within the area. The majority of the study area experiences the vigorous flow of stream discharge of the springs, which shoots upslope instability. The remaining area is the forest land.

14.3 Geological Setting

The study area has moderate to thick soil cover and rock exposures in a few portions. The rock unit includes predominantly boulders, pebbles, cobbles, etc., consisting of river terraces deposits of Shivaliks Groups of formation and phyllite with inter-banding quartzites, orthoquartzites, and greywacke and quartzites. The phyllite sequences vary, according to their mineral composition. The phyllitic rocks are called quartz chlorite-sericitic phyllite, quartz chloritic phyllite, and quartz

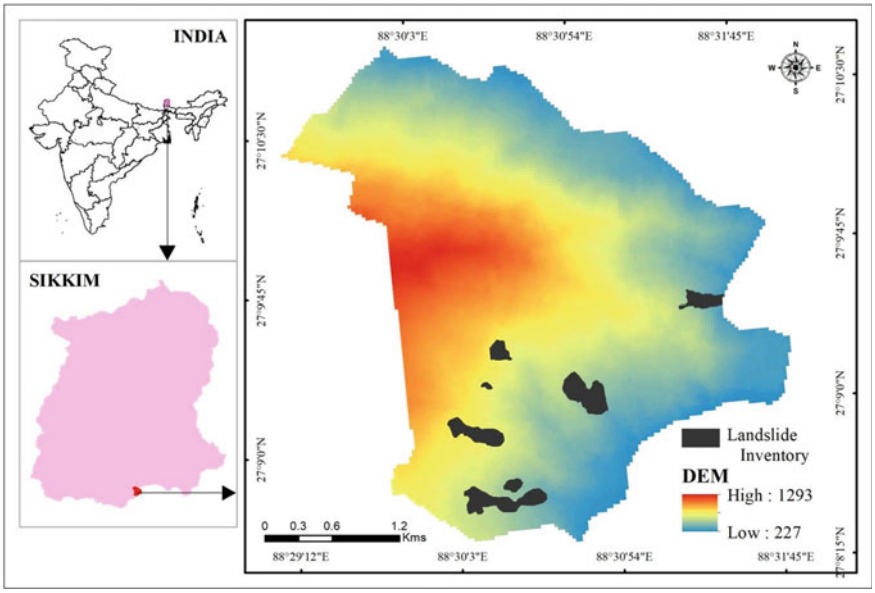

Fig. 14.1 Location map of the study area with distribution of past landslides overlaid on digital elevation model

sericiticphyllite, depending on the predominance of a particular mineral in the rocks. The rocky outcrops are disturbed due to deep-seated movement along the foliation plane. The phyllites and quartzites are also termed phyllitic-quartzite or quartzitic-phyllite, depending upon the composition and grade of metamorphism. The rock sequence strikes NE-SW with a South Easterly dip of 35 to 55 degrees and steeply hanging rocks with discontinuities along joints, fractures, bedding plane, and steep terrain gradient on the road cut. An exposed rock outcrop is present in the North-West part of the study area along the NE-SW trending ridgeline. Undisturbed rocks outcrop is also present in Northern & North-Eastern parts of the study area. The other rocks exposed to erosion are along the deep gullies within the Turung Slide. Disturbed rock outcrops are present along the NW-NE trending ridge in the north of the study area. The major lithological rock type encountered around Turung slide area is quartzitic phyllites, sericite with greywackes bands that show the orientation of foliation is N40°E–S40°W, and dip of foliation is 45°NE direction. Towards West of the Daragoan at Turung-Mamring, the rock type encountered in that area are quartzites with foliation is N40°E–S40°W, and a dip of foliation is 52°NE direction. Amphibolite boulders are present near part of the study area on the Rangpo-Namchi road section. They are not present in the middle or lower part of the study area as these areas were affected by the slide movement, and the original material has been washed out. Other features at higher elevations are covered with thin or moderately thin soil cover. Relatively thick to rather thin soil covers are present at mid-sections.

14.4 Data and Methodology

Prior knowledge of the principal causes of landslides is required to identify and map suitable landslide influencing factors (Guzzetti et al. 1999). LSZ mapping needs a spatial database of a detailed inventory and influencing factors by analyzing the data collected from various sources. There are no standard guidelines for selecting influencing criteria for LSZ mapping (Ayalew and Yamagishi 2005). The landslide influencing factors have been identified based on theoretical understanding, data availability, experience, and technical reasons (Hasekiogullari and Ercanoglu 2012; Balamurugan et al. 2016). Eight landslide influencing factors were considered: slope, elevation, aspect, curvature, lithology, distance to lineament, distance to drainage, and land use land cover are the factors chosen for the LSZ mapping. The topographical factors such as slope, aspect, curvature, and elevation were derived from DEM by using the spatial analyst-surface analyses tool in ArcMap 10.5@ESRI. The continuous raster data layers like slope, elevation, distance to lineament and drainage were classified into different classes using Jenks natural breaks classification method (Jenks 1967). The methodology adopted for the study is presented in Fig. 14.2. The spatial database of landslide inventory and influencing factors was prepared using various data collected from different sources. The Sentinel 2B satellite imagery with 10 m spatial resolution, very high-resolution Cartosat-1 satellite imagery with 2.5 m spatial resolution, digital elevation model (DEM) generated using 20 m interval contours digitized from a 1:50,000 scale topographic map, published geology maps, and field data (Table 14.1).

14.4.1 Landslide Inventory

The landslide inventory mapping plays a vital role in mapping possible future landslide zones and validating the model used (Yilmaz 2009). In this study, landslide inventory mapping was carried out using 10 m resolution Sentinel 2 satellite imagery and validated with historical reports, data from the local disaster agency, and extensive fieldwork (Fig. 14.3) in the Turung Mamring district of South Sikkim (Fig. 14.1). There are seven major landslides accurately mapped out through visual interpretation.

14.4.2 Landslide Causative Factors

14.4.2.1 Slope

The terrain slope is a significant factor in inducing slope instability as the landslides occur more on steeper slopes (Chawla et al. 2019). The slope of the study region was extracted using DEM with the aid of the spatial analyst-surface analyses tool in

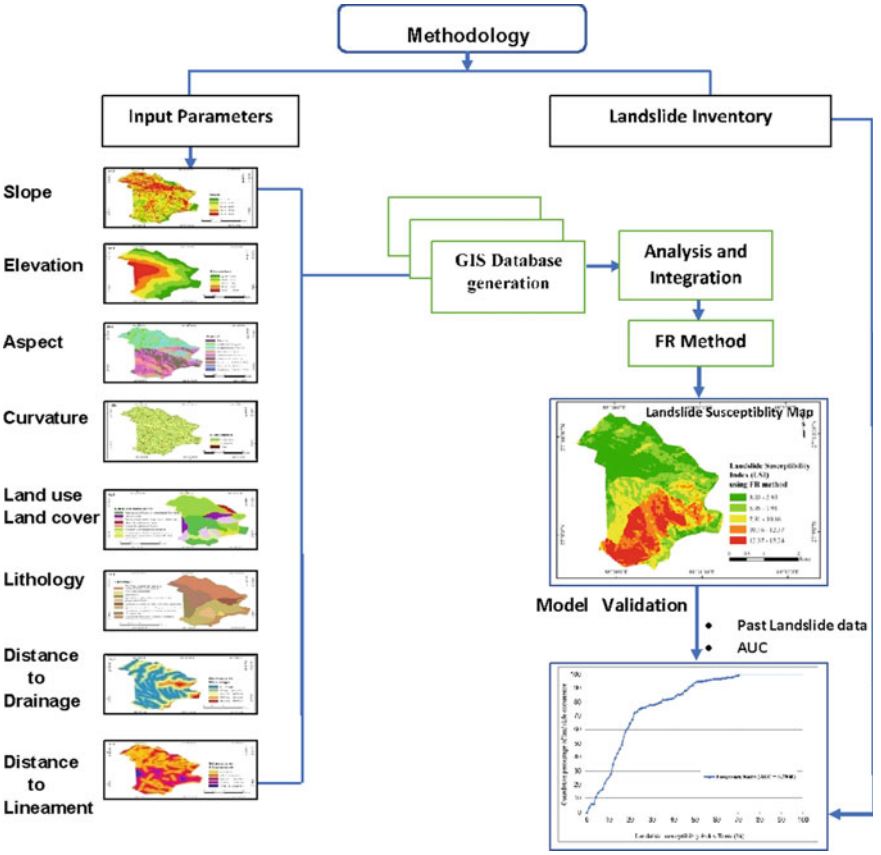

Fig. 14.2 Flowchart of the methodology adopted for the study

Table 14.1 Details of data used in the study

Data and source	Resolution/Scale	Thematic layers
Sentinel 2B satellite image, USGS	10 m × 10 m grid	Landslide Inventory Land use and land cover Lineament
Cartosat 1 satellite imagery, National Remote Sensing Centre, India	2.5 m × 2.5 m grid	
Digital elevation model generated using 20 m interval contours digitized from a 1:50,000 scale topographic map		Slope gradient
		Slope aspect
		Slope curvature
		Elevation
Topographical map, Survey of India (SOI) Toposheet, India	1:50,000	Drainage
Geology map of Department of Mining and Geology, Government of Sikkim and Geological Survey of India		Lithology

Fig. 14.3 Field photographs of landslides in the study area **a** Landslide near the settlement **b** Active landslide on the Rangpo—Namchi link road **c** Step slide area **d** Exposed old slide-vulnerable to failure

ArcMap 10.5@ESRI. The slope map was classified into five classes viz. 0–12.28°, 12.28°–21.66°, 21.66°–29.25°, 29.25°–37.29°, and 37.29°–56.94° (Fig. 14.4a).

14.4.2.2 Aspect

The aspect depicts the direction of slope. Different characteristics connected to the slope aspect, such as drying winds, sunlight, rainfall, structural discontinuities, and propagating course of seismic waves, differ from dissimilar slope aspects and further control land sliding (Dai et al. 2001; Komac 2006; Pokharel and Thapa 2019). The aspect was extracted using DEM and divided into eight directional classes N (337.5°–22.5°), NE (22.5°–67.5°), E (67.5°–112.5°), SE (112.5°–157.5°), S (157.5°–202.5°), SW (202.5°–247.5°), W (247.5°–292.5°), and NW (247.5°–292.5°) (Fig. 14.4b). A few pixels are in the Flat (–1) range. The majority of the landslide locations in the study region are on the east and southeast slopes.

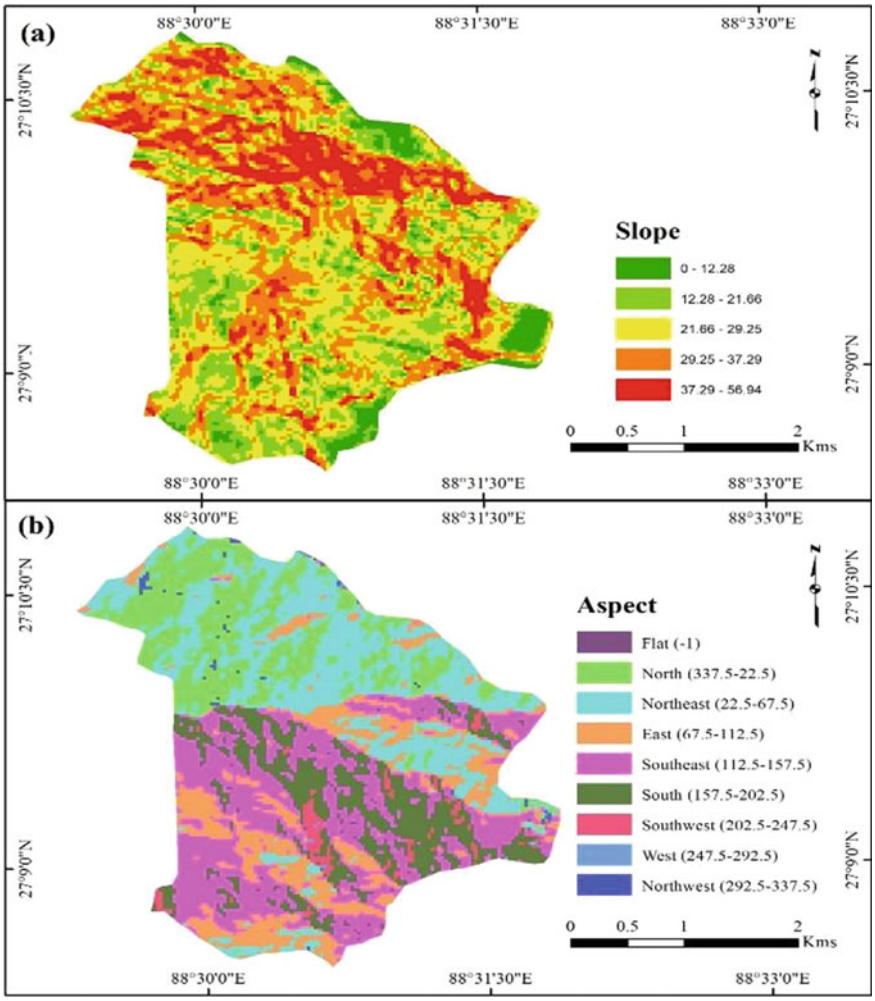

Fig. 14.4 Landslide influencing factors **a** Slope and **b** Aspect

14.4.2.3 Elevation

Elevation influences the amount of rainfall and vegetation coverage, which adversely affects slope instability or landslides (Shano et al. 2021). The elevation range was divided into five classes as 214–388, 388–571, 571–765, 765–983, and 983–1,305 m (Fig. 14.5a).

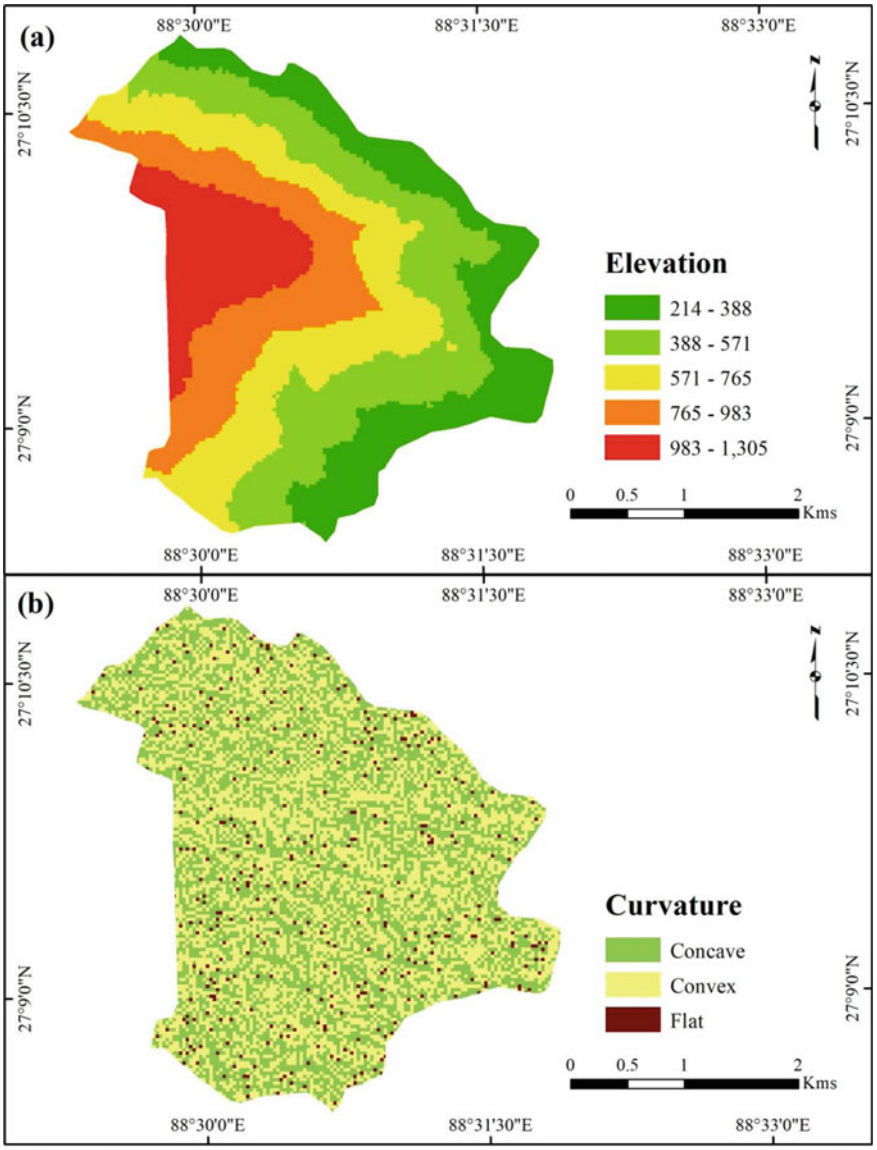

Fig. 14.5 Landslide influencing factors: **a** Elevation and **b** Curvature

14.4.2.4 Curvature

The curvature indicates the topographic morphology. A positive curvature suggests an upwards convex surface, while a negative curvature indicates an upwardly concave surface at that cell. The surface is flat if it has a value of zero (Mousavi et al. 2011).

The curvature was extracted using DEM and classified into concave, convex, and flat (Fig. 14.5b). Most of the past landslides occurred on a concave slope followed by convex and flat conditions.

14.4.2.5 Distance to Lineament and Drainage

The plane of weakness was visually inferred from high-resolution Sentinel 2B satellite imagery, as evidenced by structural elements such as fault and lineament. Because of the increased quantity of weathering, sites that are spatially close to lineaments have a higher probability of landslide occurrence (Pradhan 2011). Further, drainages were derived using DEM of the study area. The likelihood of landslides occurring as a result of drainage varies depending on the distance from drainage (Srivastava et al. 2010; Singh and Ramesh 2021a, b). The Euclidean distance tool in ArcMap 10.5@ESRI was used to determine the distance to the drainage and lineament, and it was classed into five classes (Fig. 14.6a and b).

14.4.2.6 Land Use and Land Cover

Land use, change owing to agricultural and rapid development activities on hill slopes, as well as deforestation, which causes erosion, all exacerbate the susceptibility to landslides, especially in hilly areas (Jaiswal et al. 2010; Meten et al. 2015). Very high-resolution satellite imageries Cartosat-1 and Sentinel 2B were used to interpret the land use and landcover features. The various land use and landcover units that exist in the study area are thickly vegetated forest area, barren land with slope cuts, and slides, moderately thick vegetation cover, urbanized area, agricultural land the sparsely vegetative area with thin grass leave, and barren land (Fig. 14.7a).

14.4.2.7 Lithology

The ability of rocks to withstand and erode plays an important influence in the occurrence of landslides (Anbazhagan and Ramesh 2014). The lithological characteristics strongly affect the physical properties of surface and subsurface material, which controls the permeability, rate of flow, and stability and favorably initiate landslide (Kamp et al. 2008; Thambidurai and Ramesh 2017). The lithology map was digitized from the published geology map of the Department of Mining and Geology, Government of Sikkim, and Geological Survey of India. The main lithological units are depicted in Fig. 14.7b. The study area is majorly consists of phyllite, quartzite, sericite intercalation with quartz, and quartzites.

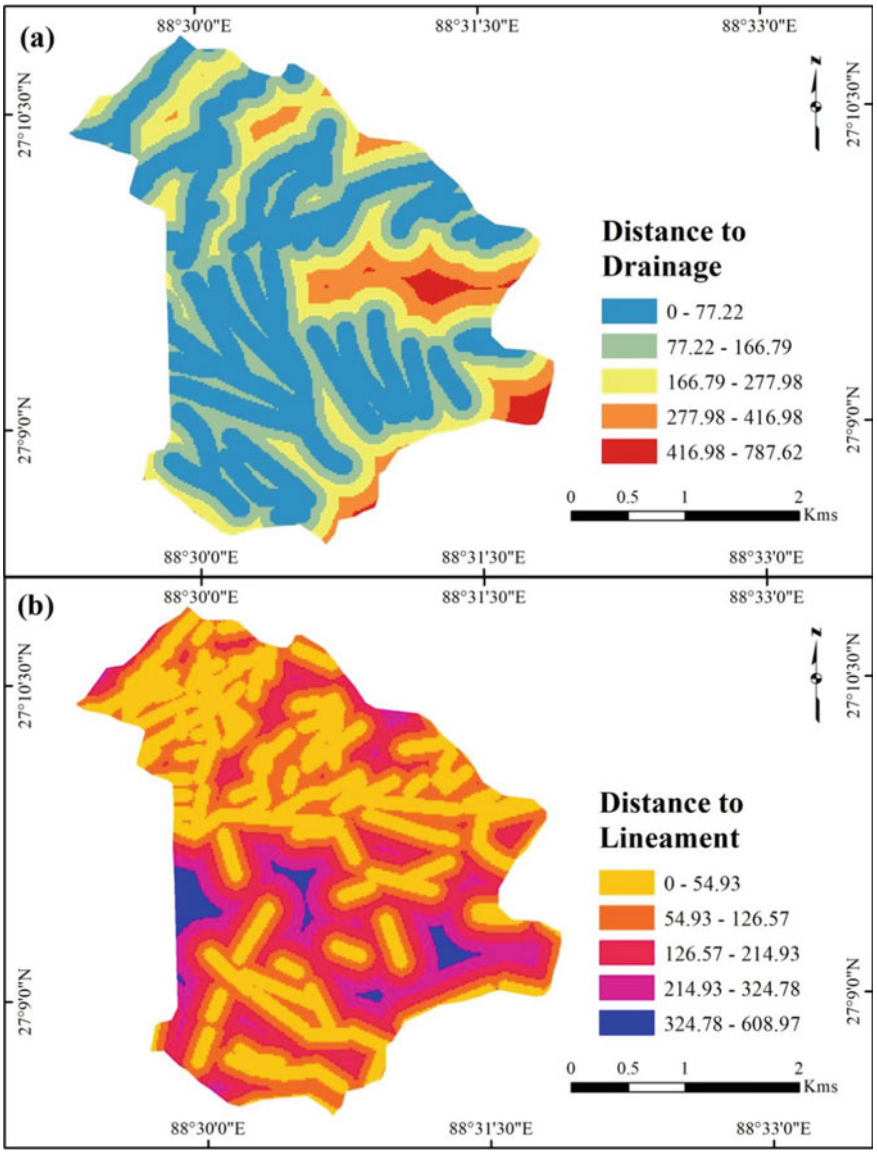

Fig. 14.6 Landslide influencing factors: **a** Distance to drainage and **b** Distance to lineament

14.5 LSZ Mapping Using Frequency Ratio (FR) Method

The FR is a bivariate statistical method used potentially to establish the relationship between a dependent (landslide inventory) and independent variable (landslide influencing factors) for the purpose of mapping landslide susceptibility (Lee and Talib

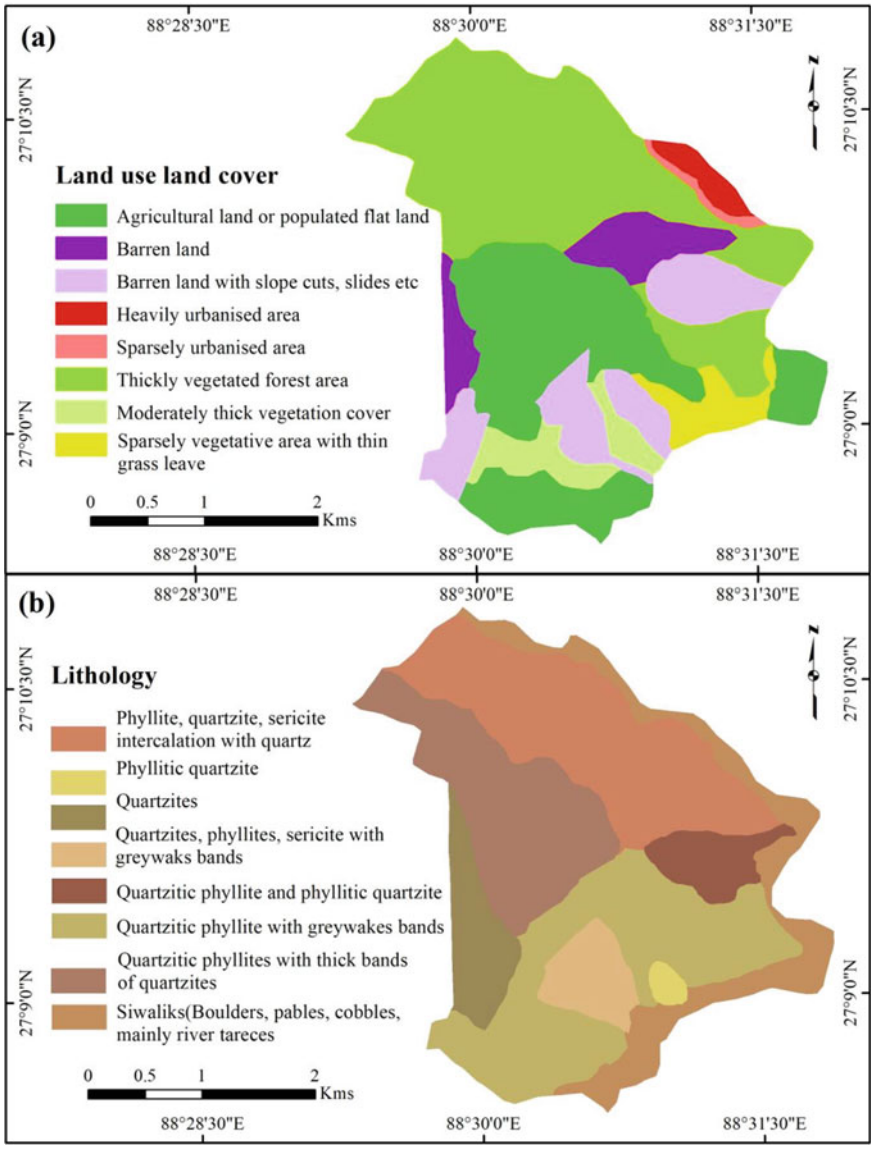

Fig. 14.7 Landslide influencing factors: **a** Land use land cover and **b** Lithology

2005; Ramesh and Anbazhagan 2015; Chen et al. 2016; Saranaathan et al. 2021). The frequency ratio of each class in an independent variable was computed using Eq. 14.1.

$$\text{Frequency ratio} = \frac{\text{Slide ratio}}{\text{Class ratio}} \tag{14.1}$$

The slide ration can be calculated as below formula,

$$\text{Slide ratio} = \frac{\text{Number of slide grids in class}}{\text{Total number of landslide grids}} \tag{14.2}$$

$$\text{Class ratio} = \frac{\text{Number of grids in individual class}}{\text{Total number of grods in whole class}} \tag{14.3}$$

$$\text{LSI} = \sum \text{FR} \tag{14.4}$$

where LSI is the landslide susceptibility index; FR is the frequency ratio of each influencing factor.

The ratio in the relationship analysis is the area where landslides occurred to the overall area, with 1 being the average value. A value >1 indicates a higher correlation, and a value <1 shows a lesser correlation. The landslide susceptibility index (LSI) was calculated by combining all the factors with FR value using Eq. 14.4 (Pradhan and Lee 2009; Lee and Talib 2005).

14.6 Results and Discussion

14.6.1 LSZ Mapping Using FR Method

The FR values of each class in an influencing factor were estimated using Eq. 14.1, presented in Table 14.2. The relationship with past landslides shows that degree of slope 12.28°–29.25°, east and southeast facing slopes, concave curvature, 388–765 m elevation, barren and agricultural land land use, 0–167 m distance from drainage, 0–127 m distance from lineament classes having higher FR values, which indicates higher influence in occurrence of landslides in the study region. The FR values were populated in the attribute table of each influencing factor and converted into 10 × 10 m size grids. The total number of grids in the study region was 107,522, and the total number of landslide grids was 3,262. The final LSI values were computed using Eq. 14.4 by simply adding all the factors using the raster calculator tool in ArcMAP 10.8.1@ESRI. The LSI value represents the probability of landslide occurrence i.e., higher the LSI value indicates higher susceptibility to landslide. The minimum and maximum LSI values of FR model are 3.03 and 15.24, respectively. The LSZ map was reclassified into 5 classes (Fig. 14.8) based on Jenks's natural breaks categorization approach (Jenks 1967). The area of very low, low, moderate, high, and very high susceptibility classes are 31.00%, 23.21%, 18.34%, 14.34%, and 13.10% respectively. The percentage of pixels of past landslides under various susceptibility classes was computed using the seven past landslides overlaid on the LSZ map. The FR model revealed that the very high and high susceptibility classes accounted for 79.45% of all past landslides (Fig. 14.9).

Table 14.2 Estimated FR values of landslide influencing factors

Influencing Factor	Class	No. of pixels in domain	% of pixels in domain	No. of landslide in domain	% of landslide in domain	FR
Slope gradient	0–12.28 Degree	6,504	6.05	141	4.32	0.71
	12.28–21.66 Degree	21,615	20.10	998	30.59	1.52
	21.66–29.25 Degree	32,993	30.68	1,126	34.52	1.12
	29.25–37.29 Degree	31,653	29.44	842	25.81	0.88
	37.29–56.94 Degree	14,757	13.72	155	4.75	0.35
Slope aspect	Flat (0)	9	0.01	0	0.00	0.00
	North (337.5–22.5)	18,650	17.35	0	0.00	0.00
	Northeast (22.5–67.5)	24,890	23.15	151	4.63	0.20
	East (67.5–112.5)	17,762	16.52	1,306	40.04	2.42
	Southeast (112.5–157.5)	26,455	24.60	1,561	47.85	1.94
	South (157.5–202.5)	16,718	15.55	244	7.48	0.48
	Southwest (202.5–247.5)	2,287	2.13	0	0.00	0.00
	West (247.5–292.5)	189	0.18	0	0.00	0.00
	Northwest (292.5–337.5)	562	0.52	0	0.00	0.00
Curvature	Concave (–)	52,191	48.54	1,748	53.59	1.10
	Flat (0)	3,171	2.95	70	2.15	0.73
	Convex (+)	52,160	48.51	1,444	44.27	0.91
Elevation	214–388 m	22,538	20.96	335	10.27	0.49
	388–571 m	27,406	25.49	1,708	52.36	2.05
	571–765 m	24,336	22.63	863	26.46	1.17
	765–983 m	19,511	18.15	356	10.91	0.60
	983–1,305 m	13,731	12.77	0	0.00	0.00
Land use and land cover	Thickly vegetated forest area	42,080	39.14	305	9.35	0.24
	Barren land with slope cuts, slides etc	14,639	13.61	888	27.22	2.00

(continued)

Table 14.2 (continued)

Influencing Factor	Class	No. of pixels in domain	% of pixels in domain	No. of landslide in domain	% of landslide in domain	FR
	Moderately thick vegetation cover	5,704	5.30	130	3.99	0.75
	Heavily urbanized area	1,979	1.84	0	0.00	0.00
	Agricultural land or populated flat land	30,626	28.48	1,939	59.44	2.09
	Sparsely vegetative area with thin grass leave	4,121	3.83	0	0.00	0.00
	Barren land	7,420	6.90	0	0.00	0.00
	Sparsely urbanized area	953	0.89	0	0.00	0.00
Lithology	Phyllite, quartzite, sericite intercalation with quartz	27,477	25.55	0	0.00	0.00
	Siwaliks (Boulders, pebbles, cobbles, mainly river teraces	14,322	13.34	73	2.24	0.17
	Quartzitic phyllite and phyllitic quartzite	5,010	4.67	147	4.51	0.97
	Phyllitic quartzite	984	0.92	0	0.00	0.00
	Quartzites, phyllites, sericite with greywakes bands	5,380	5.01	480	14.71	2.94
	Quarzitic phyllites with thick bands of quartzites	7,056	6.57	65	1.99	0.30
	Quarzitic phyllite with greywake bands	20,309	18.92	2,291	70.23	3.71
	Quartzites	26,984	25.13	206	6.32	0.25
Proximity to drainage	0–77.21 m	48,286	44.91	1,881	57.66	1.28
	77.21–166.79 m	29,973	27.88	1,092	33.48	1.20
	166.79–277.98 m	18,424	17.14	269	8.25	0.48

(continued)

Table 14.2 (continued)

Influencing Factor	Class	No. of pixels in domain	% of pixels in domain	No. of landslide in domain	% of landslide in domain	FR
	277.98–416.97 m	8,835	8.22	20	0.61	0.07
	416.97–787.62 m	2,004	1.86	0	0.00	0.00
Proximity to lineament	0–54.92 m	38,825	36.11	1,238	37.95	1.05
	54.92–126.56 m	33,531	31.19	1,086	33.29	1.07
	126.56–214.92 m	22,346	20.78	671	20.57	0.99
	214.92–324.78 m	10,292	9.57	267	8.19	0.86
	324.78–608.96 m	2,528	2.35	0	0.00	0.00

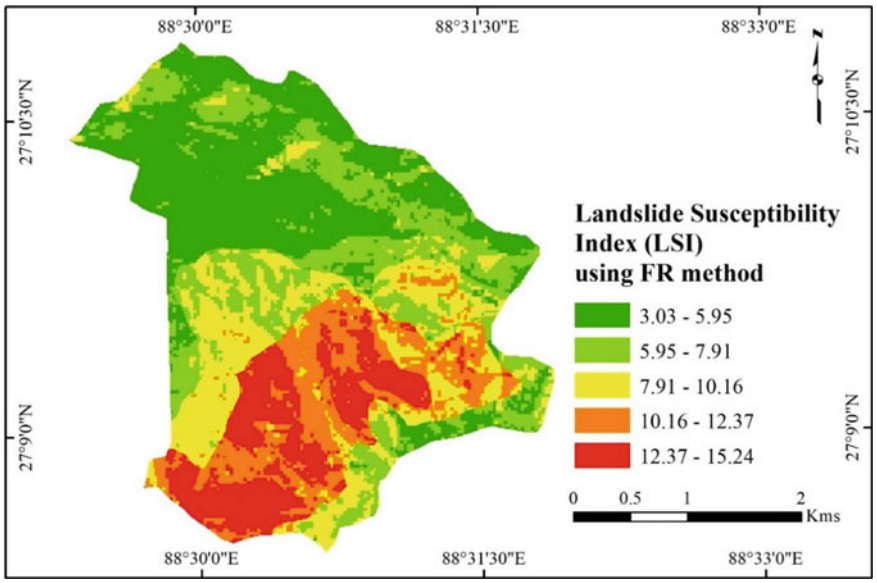

Fig. 14.8 Landslide susceptibility map based on frequency ratio model

14.6.2 Validation of the Model

The Area Under Curve (AUC) method is used widely by many researchers and also used the quantitative accuracy assessment methods to estimate susceptibility map accuracy (Nandi and Shakoor 2009; Xu et al. 2013). In the present study, the success rate of the FR model was estimated by comparing the LSZ map with the landslide inventory data. The LSI map was reclassified into 100 classes to derive AUC curve, and the cumulative percentage of landslide pixels falling under each class was estimated. The AUC curve is generated by plotting the LSI rank percentage

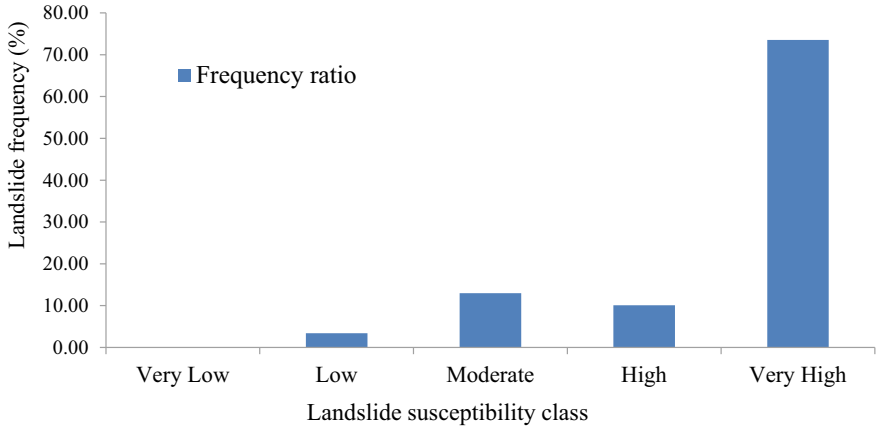

Fig. 14.9 Landslide susceptibility index using frequency ratio method

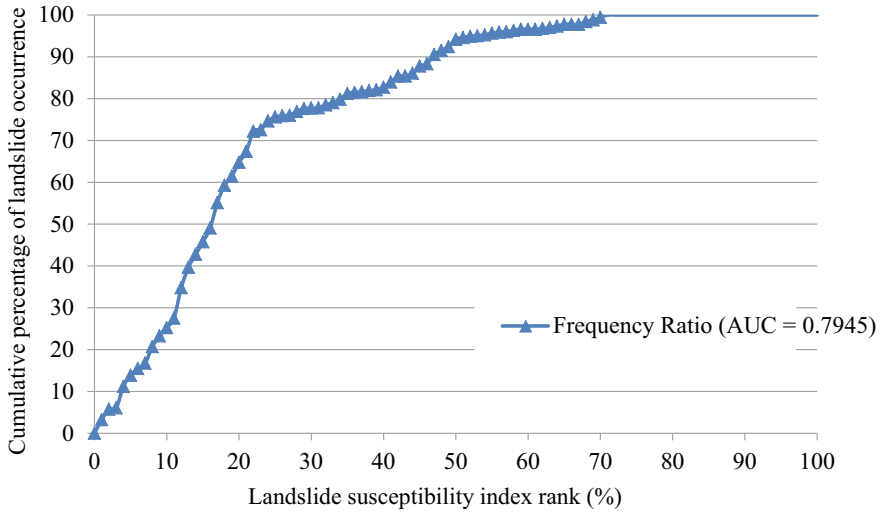

Fig. 14.10 Illustration of success rate curve showing landslide susceptibility index rank (*x*-axis) occurring in cumulative percent of landslide occurrence (*y*-axis)

on the x-axis and the cumulative percentage of landslide events on the y-axis. The AUC value of an ideal model is near 1.0, whereas a value of close to 0.5 suggests the model error (Fawcett 2006). The accuracy results of the AUC value were classified as 0.90–1 (excellent), 0.80–0.90 (good), 0.70–0.80 (fair), 0.60–0.70 (poor) and 0.50–0.60 (fail) (Pradhan and Kim 2017; Ramesh and Iqbal 2020). In the present study, the success rate of the FR model was estimated with the AUC value of 0.7945, indicating a fair accuracy (Fig. 14.10).

14.7 Conclusion

Landslides in the Turung Mamring area of south district of Sikkim, Himalayas, had a tremendous impact on the landscape on a regular basis. Heavy rainfall and tectonic activities, topographical conditions, lithology, land use and landcover, and hydrologic conditions are the most common landslide influencing factors in this area. The present study has investigated the landslide problem of this area through LSZ mapping. For the purposes of LSZ mapping, a landslide inventory map comprising seven landslides and eight causal elements was created. The current study analysed various causes of landslides using spatial data generated through geoinformatics technique and bivariate statistical FR Model. The results show that landslides are more common along cut slopes, slope in the 21.66°–29.25°, concave curvature, and elevation in the 388–571 m categories. The validation results indicates that the success rate of FR model provided a fair level of accuracy. The LSZ map is useful for making decisions and planning development in a highly vulnerable region. The present study could also assist developers, planners, and engineers in the study region with slope management and land-use planning.

Acknowledgements The authors sincerely acknowledge the Department of Mining and Geology, Government of Sikkim for providing the primary data to complete this work.

Conflict of Interest The authors declare no conflict of interest.

References

Ahmed RA, Singh RP, Adris A (2017) Seismic hazard assessment of Syria using seismicity, DEM, slope, active faults and GIS. Remote Sens Appl Soc Environ 6:59–70. https://doi.org/10.1016/j.rsase.2017.04.003

Aleotti P, Chowdhury R (1999) Landslide hazard assessment: summary review and new perspectives. Bull Eng Geol Env 58:21–44. https://doi.org/10.1007/s100640050066

Anbazhagan S, &Ramesh V (2014) Landslide hazard zonation mapping in Ghat road section of Kolli Hills, India. J Mt Sci 11(5):1308–1325. http://link.springer.com/article/10.1007/s11629-012-2618-9

Ayalew L, Yamagishi H (2005) The application of GIS-based logistic regression for landslide susceptibilitymapping in the Kakuda-Yahiko Mountains, Central Japan. Geomorphology 65:15–31. https://doi.org/10.1016/j.geomorph.2004.06.010

Anbarasu K, Sengupta A, Gupta S, Sharma SP (2010) Mechanism of activation of the Lanta Khola land- slide in Sikkim Himalayas. Landslides 7:135–147. https://doi.org/10.1007/s10346-009-0193-0

Balamurugan G, Ramesh V, Touthang M (2016) Landslide susceptibility zonation mapping using frequency ratio and fuzzy gamma operator models in part of NH-39, Manipur, India. Nat Hazards 84: 465–488. http://link.springer.com/article/10.1007/s11069-016-2434-6

Bhasin R, Grimstad E, Larsen J, Dhawan AK, Singh R, Verma SK, Venkatachalam K (2002) Landslide Hazards and Mitigation Measures at Gangtok, Sikkim Himalaya. Eng Geol 64:351–368. https://doi.org/10.1016/S0013-7952(01)00096-5

Cárdenas NY, Mera EE (2016) Landslide susceptibility analysis using remote sensing and GIS in the western Ecuadorian Andes. Nat Hazards 81(3):1829–1859. https://doi.org/10.1007/s11069-016-2157-8

Chawla A, Pasupuleti S, Chawla S, Rao ACS, Sarkar K, Dwivedi R (2019) Landslide susceptibility zonation mapping: A case study from Darjeeling district, Eastern Himalayas, India. J Ind Soc Remote Sens 47:497–511. https://doi.org/10.1007/s12524-018-0916-6

Chen W, Chai H, Sun X, Wang Q, Ding X, Hong H (2016) A GIS-based comparative study of frequency ratio, statistical index and weights-of-evidence models in landslide susceptibility mapping. Arab J Geosci 9(3):204

Chopra BR (1977) Landslides and other mass movements along roads in Sikkim and North Bengal. Bull Int EngGeol 16(1):162–166

Choubey VD (1992) Landslide hazards and their mitigation in the Himalayan region. In: Proceedings of the sixth international symposium in Christchurch, New Zealand, Landslide, pp 1849–1868

Dai FC, Lee CF, Xu ZW (2001) Assessment of landslide susceptibility on the natural terrain of Lantau Island Hong Kong. Environ Geol 40(3):381–391

Dai FC, Lee CF, Ngai YY (2002) Landslide risk assessment and management: an overview. Eng Geol 64(1):65–87

Ehret D, Rohn J, Dumperth C, Eckstein S, Ernstberger S, Otte K, Rudolph R, Wiedenmann J (2010) Frequency ratio analysis of mass movements in the Xiangxi catchment, three Gorges reservoir area China. J Earth Sci 21(6):824–834

Fawcett T (2006) An introduction to ROC analysis. Pattern Recogn Lett 27:861–874

Ghosh C (2013) Landslides induced damages due to recent Sikkim earthquake: strategies for geotechnical intervention. In Proceedings of the international symposium on engineering under uncertainty: safety assessment and management (ISEUSAM-2012). Springer, India, pp 1289–1298

Gupta S, Kaur H, Parkash S, Thapa R (2018) Landslide susceptibility zonation of Gangtok city, Sikkim using Knowledge Driven Method (KDM). Disaster Adv 11(11):34–43

Gupta AK, Tolia DS (1998) Major landslides in Sikkim—analysis, correction and protective measures: a case study. International conference on case histories in geotechnical engineering, vol 13. https://scholarsmine.mst.edu/icchge/4icchge/4icchge-session02/13

Guzzetti F, Carrara A, Cardinalli M, Reichenbach P (1999) Landslide hazard evaluation: a review of current techniques and their application in a multi-case study, central Italy. Geomorphology 31:181–216

Hadmoko DS, Lavigne F, Samodra G (2017) Application of a semiquantitative and GIS-based statistical model to landslide susceptibility zonation in Kayangan Catchment, Java, Indonesia. Nat Hazards 87:437–468. https://doi.org/10.1007/s11069-017-2772-z

Hasekiogullari GD, Ercanoglu M (2012) A new approach to use AHP in landlside susceptibility mapping: a case study at Yenice (Karbuk, NW Turkey). Nat Hazards 63:1157–1179

Jaiswal P, Van Westen CJ, Jetten V (2010) Quantitative landslide hazard assessment along a transportation corridor in southern India. Eng Geol 116(3–4):236–250. https://doi.org/10.1016/j.enggeo.2010.09.005

Jenks GF (1967) The data model concept in statistical mapping. Int Year Book Cartogr 7:186–190

Kamp U, Growley BJ, Khattak GA, Owen LA (2008) GIS-based landslide susceptibility mapping for the 2005 Kashmir earthquake region. Geomorphology 101(4):631–642

Kannan M, Saranathan E, Anbalagan R (2013) Landslide vulnerability mapping using frequency ratio model: a geospatial approach in Bodi-Bodimettu Ghat section, Theni district, Tamil Nadu, India. Arab J Geosci 6(8):2901–2913

Kanwal S, Atif S, Shafiq M (2016) GIS based landslide susceptibility mapping of northern areas of Pakistan, a case study of Shigar and Shyok Basins. Geom Nat Hazards Risk 8(8):348–366. https://doi.org/10.1080/19475705.2016.1220023

Kienholz H, Schneider G, Bichsel M, Grunder M, Mool P (1984) Mapping of mountain hazards and slope stability. Mt Res Dev 4(3):47–266

Komac M (2006) A landslide susceptibility model using the analytical hierarchy process method and multivariate statistics in perialpine Slovenia. Geomorphology 74:17–28
Lee S, Talib JA (2005) Probabilistic landslide susceptibility and factor effect analysis. Environ Geol 47:982–990
Mandal B, Mandal S (2016) Assessment of mountain slope instability in the Lish River basin of Eastern Darjeeling Himalaya using frequency ratio model (FRM). Model Earth Syst Environ 2:121
Mandal S, Mandal K (2018) Modeling and mapping landslide susceptibility zones using GIS based multivariate binary logistic regression (LR) model in the Rorachu river basin of eastern Sikkim Himalaya, India. Model Earth Syst Environ 4:69–88
Mousavi SZ, Kavian A, Soleimani K, Mousavi SR, Shirzadi A (2011) GIS-based spatial prediction of landslide susceptibility using logistic regression model. Geomat Nat Hazards Risk 2(1):33–50. https://doi.org/10.1080/19475705.2010.532975
Meten M, Bhandary NP, Yatabe R (2015) Application of GIS-based fuzzy logic and rock engineering system (RES) approaches for landslide susceptibility mapping in Selelkula area of the Lower Jema River Gorge Central Ethiopia. Environ Earth Sci 74(4):3395–3416. https://doi.org/10.1007/s12665-015-4377-8
Nandi A, Shakoor A (2008) Application of logistic regression model for slope instability prediction in Cuyahoga river watershed, Ohio, USA. Georisk 2(1):16–27
Nandi A, Shakoor A (2009) A GIS-based landslide susceptibility evaluation using bivariate and multivariate statistical analyses. EngGeol 110:11–20
Pal SC, Chowdhuri I (2019) GIS-based spatial prediction of landslide susceptibility using frequency ratio model of Lachung River basin, North Sikkim, India. SN Appl Sci 1:416
Pandey A, Dabral PP, Chowdary VM, Yadav NK (2008) Landslide hazard zonation using remote sensing and GIS: a case study of Dikrong river basin, Arunachal Pradesh India. Environ Geol 54(7):1517–1529. https://doi.org/10.1007/s00254-007-0933-1
Perera ENC, Jayawardana DT, Ranagalage M, Dissanayake DMSLB, Wijenayaka HMDS (2020) Introduce a framework for landslide risk assessment using geospatial analysis: a case study from Kegalle District Sri Lanka. Model Earth Syst Environ 6:2415–2431
Pokharel B, Thapa PB (2019) Landslide susceptibility in Rasuwa District of central Nepal after the 2015 Gorkha Earthquake. J Nepal Geol Soc 59:79–88. https://doi.org/103126/jngs.v59i0.24992
Pradhan B, Lee S (2009) Delineation of landslide hazard areas on Penang Island, Malaysia, by using frequency ratio, logistic regression, and artificial neural network models. Environ Earth Sci 60:1037–1054
Pradhan AMS, Kim YT (2017) Spatial data analysis and application of evidential belief functions to shallow landslide susceptibility mapping at Mt. Umyeon, Seoul, Korea. Bull EngGeol Environ 76(4):1263–1279
Pradhan B (2011) Manifestation of an advanced fuzzy logic model coupled with Geo-information techniques to landslide susceptibility mapping and their comparison with logistic regression modelling. Environ Ecol Stat 18(3):471–493. https://doi.org/10.1007/s10651-010-0147-7
Ramesh V, Anbazhagan S (2015) Landslide susceptibility mapping along Kolli hills Ghat road section (India) using frequency ratio, relative effect and fuzzy logic models. Environ Earth Sci 73:8009–8021. https://doi.org/10.1007/s12665-014-3954-6
Ramesh V, Iqbal SS (2020) Urban flood susceptibility zonation mapping using evidential belief function, frequency ratio and fuzzy gamma operator models in GIS: a case study of Greater Mumbai Maharashtra, India. Geocarto Int 37(2):581–606. https://doi.org/10.1080/10106049.2020.1730448
Saranaathan SE, Mani S, Ramesh V, Venkatesh SP (2021) Landslide susceptibility zonation mapping using bivariate statistical frequency ratio method and GIS: A case study in part of SH 37 Ghat Road, Nadugani, Panthalur Taluk, The Nilgiris. J Ind Soc Remote Sens 49:275–291. https://doi.org/10.1007/s12524-020-01207-3

Sema HV, Guru B, Veerappan R (2017) Fuzzy gamma operator model for preparing landslide susceptibility zonation mapping in parts of Kohima Town, Nagaland India. Model Earth Syst Environ 3:499–514

Sharma A, Sur U, Singh P, Rai PK, Srivastava PK (2020) Probabilistic landslide hazard assessment using statistical information value (SIV) and GIS techniques: a case study of Himachal Pradesh, India. In: Srivastava et al (eds) Techniques for disaster risk management and mitigation. Wiley & Sons. ISBN: 978-1-119-35919-7. https://doi.org/10.1002/9781119359203.ch15

Singh P, Sharma A, Sur U, Rai PK (2021) Comparative landslide susceptibility assessment using statistical information value and index of entropy model in Bhanupali-Beri region, Himachal Pradesh, India. Environ Dev Sustain 23:5233–5250. https://doi.org/10.1007/s10668-020-00811-0

Silalahi FES, Pamela, Arifianti Y, Hidayat F (2019) Landslide susceptibility assessment using frequency ratio model in Bogor, West Java, Indonesia. Geosci Lett 6:10

Singh NB, Ramesh V (2021a) GIS-based Landslide Susceptibility Zonation Mapping using Fuzzy Gamma Operator model in part of Trans-Asian Highway (Mao-Kangpokpi), Manipur, India. In: Pal I, et al. (eds) Disaster resilience and sustainability. Elsevier, pp 171–196. https://doi.org/10.1016/B978-0-323-85195-4.00027-5

Singh NB, Ramesh V (2021b) GIS-based Landslide Susceptibility Zonation Mapping using Fuzzy Gamma Operator model in part of Trans-Asian Highway (Mao-Kangpokpi), Manipur, India. In: Pal I, et al. (eds) Disaster resilience and sustainability. Elsevier, pp 171–196. https://doi.org/10.1016/B978-0-323-85195-4.00027-5

Singh PK, Kainthola A, Singh TN (2013) Rock mass assessment along the right bank of river Sutlej, Luhri, Himachal Pradesh India. Geomat Nat Hazards Risk Online 6(3):212–223. https://doi.org/10.1080/19475705.2013.83448

Singh TN, Singh R, Singh B, Sahrma LK, Singh R, Ansari MK (2016) Investigation and stability analysis of Malin village landslide of Pune district, Maharashtra India. Nat Hazards 81(3):2019–2030

Shano L, Raghuvanshi TK, Meten M (2021) Landslide susceptibility mapping using frequency ratio model: the case of Gamo highland South Ethiopia. Arab J Geosci 14:623. https://doi.org/10.1007/s12517-021-06995-7

Sonkar I, Tripathi JN, Singh AK (2021) Landslide susceptibility zonation using geospatial technique and analytical hierarchy process in Sikkim Himalaya. Quat Sci Adv 4:100039. https://doi.org/10.1016/j.qsa.2021.100039

Srivastava V, Srivastava HB, Lakhera RC (2010) Fuzzy gamma based geomatic modelling for landslide hazard susceptibility in a part of Tons river valley, northwest Himalaya, India. Geomat Nat Hazards Risk 1(3):225–242. https://doi.org/10.1080/19475705.2010.490103

Thambidurai P, Ramesh MV (2017) Slope stability investigation of Chandmari in Sikkim, Northeastern India. In: Mikos M, Tiwari B, Yin Y, Sassa K (eds) advancing culture of living with landslides. WLF 2017. Springer, Cham. https://doi.org/10.1007/978-3-319-53498-5_42

Varnes DJ (1984) Landslide hazard zonation: a review of principles and practice. UNESCO Press, Paris, Issue No. 3, p 63

Xu C, Xu X, Dai F, Wu Z, He H, Shi F, Wu X, Xu S (2013) Application of an incomplete landslide inventory, logistic regression model and its validation for landslide susceptibility mapping related to the May 12, 2008 Wenchuan earthquake of China. Nat Hazards 68:883–900. https://doi.org/10.1007/s11069-013-0661-7

Yilmaz I (2009) Landslide susceptibility mapping using frequencyratio, logistic regression, artificial neural networks and theircomparison: a case study from Kat landslides (Tokat-Turkey). ComputGeosci 35:1125–1138

Yilmaz I, Keskin I (2009) GIS based statistical and physical approaches to landslide susceptibility mapping (Sebinkarahisar, Turkey). Bull EngGeol Environ 68:459–471

Youssef AM (2015) Landslide susceptibility delineation in the Ar-Rayth area, Jizan, Kingdom of Saudi Arabia, using analytical hierarchy process, frequency ratio, and logistic regression models. Environ Earth Sci 73(12):8499–8518

Chapter 15
Mapping of Annual Ground Displacement Using Remote Sensing Methods for Critical Slopes Along the Bhagirathi River in Uttarakhand, India

Swati Sharma, HarAmrit Singh, Rohan Kumar, and Manoj K. Arora

Abstract The transportation route connecting the Tehri dam with Koteshwar Dam (Stage 2) in Uttarakhand, India is largely affected by the road cut slope failures. The rise and fall in the reservoir water level have also led to gradual ground subsidence at a few locations. In this study, two slopes at prime locations, namely Zero Bridge and Chainage 1.60 km from the Zero Bridge, have been studied for the magnitude of displacements using synthetic aperture radar (SAR) microwave data and LISS IV optical data over a selected time period. The permanent scatterers synthetic aperture radar (PS-InSAR) interferometry process was carried out in SARPROZ software at a coherence level set to 0.4. Total 57 scenes of Sentinel-1 SAR data from June 2015 to May 2018 have been undertaken for PS-InSAR processing. Persistent Scatterer Interferometry (PSI) results have shown ground deformation to the tune of 60 mm/year at the location Zero Bridge and at location 1.60 km from the Zero Bridge, no movement was observed. Whereas the correlation among the multi-spectral data (LISS IV) considering the study locations (Zero bridge and 1.60 km) have shown a pixel shift (slope surface displacements) for the time period spanning between the year 2012–2013 and 2014–2015.

Keywords Tehri-Koteshwar route · Zero bridge · Chainage 1.60 · Slope displacement · PS-InSAR · LISSIV

S. Sharma (✉)
Amity Institute of Remote Sensing and GIS, Amity University, Noida, India
e-mail: ssharma27@amity.edu

H. Singh
Department of Civil Engineering, Punjab Engineering College, Chandigarh, India

R. Kumar
Department of Chemical and Petroleum Engineering, Lovely Professional University, Jalandhar, India

M. K. Arora
BML Munjal University, Gurgaon, India

P. Thambidurai and T. N. Singh (eds.), *Landslides: Detection, Prediction and Monitoring*,
https://doi.org/10.1007/978-3-031-23859-8_15

15.1 Introduction

The remote sensing techniques are widely used to observe and monitor gradual slope movements over periods, which are recorded by various types of satellite sensors, creating a directory of optical and radar datasets. These datasets can help determine the ground deformations if a series of temporal images from multiple sensors are used in amalgamation to cross-validate the observations. Such practices can help in timely mitigation of natural or man-made disasters, if high-quality datasets are available time to time. Martha et al. (2012), Stumpf et al. (2014), Stumpf et al. (2017) have efficiently used the remote sensing datasets to determine the magnitudes of ground deformations. Various other researchers, such as Gupta and Anbalagan (1997), Castaldo, R., et al. (2015), Lacroix et al. (2018), Zhou et al. (2020) have used both radar and optical data for deducing the slope movements in the hilly terrains. The Persistent Scatterer Interferometry (PSI) is a universally recognized powerful technique and is capable of measuring slope movements taking place during a specific period with millimeter accuracy (Ferretti et al. 2001). Sentinel-1A and 1B satellite systems are operating in the microwave C-band and together can capture the same scene at the gap of 6 days. The PS-InSAR (permanent scatterers synthetic aperture radar interferometry) technique is widely used in detecting surface displacements. This interferometric system compares two SAR images of the same location at different periods; this allows the scope of probable surface movements taking place during the image acquisition periods. Therefore, SAR data are suitable for estimating surface displacement and are periodically used in slope monitoring. Spatial coverage of SAR data often inherits distortions caused by shadowing effects, foreshortening, and layover. PSI is capable of carrying out preliminary work on surface displacement at a micro/macro scale in addition to identifying hotspots over a landslide-prone area. The optical data can also be correlated at the pixel/sub-pixel level to compare the slope displacement in a chosen period (Tiwari et al. 2014). Scambos et al. (1992), Kaufmann and Ladstadter (2003), Leprince et al. (2008), Stumpf et al. (2014), Lacroix et al. (2015), Stumpf et al. (2016) have used a variety of software such as IMCORR, COSI-CORR, etc. using multi-temporal optical image pairs for studying slope deformations that are inaccessible or not observed on the field due to vegetation cover or settlements. Further, the integrated application of PSI and optical datasets may improve the observation of slow-moving landslides, which are mainly dependent on pre and post-data images of the landslide events (Casagli et al. 2016).

Typically, landslides are caused by a combination of various geo-environmental factors. Intrinsic factors such as bedrock geology (lithology, structure, and degree of weathering), geomorphology (slope gradient, aspect, and relative relief), soil (depth, structure, permeability, and porosity), land-use/land-cover (LULC), and hydrologic conditions are the universally accepted factors responsible for landslides. External factors such as precipitation, seismic activity, blasting and drilling, cloudburst, and flash-floods are also accounted for a landslide. In this work, the PSI for SAR data and

ENVI-based algorithm i.e. Cosi-Corr techniques, were used to estimate the impact of reservoir water fluctuation on the bounding slopes in the Koteshwar reservoir area. This area is situated in the fragile terrain of Lesser Himalaya, where the construction of the Koteshwar dam and the consequent development of a reservoir have induced considerable changes in the terrain conditions. After the reservoir filling, there has been an increase in incidences of landslides. The slope stability issues in this region are governed by steep topography, unfavorable slope forming material, geological discontinuities, etc. Further, the ground visits have also been made to validate the results of the Remote Sensing data.

15.2 Study Area

The landslide affected slopes in this study are situated in the upslope area surrounding the Koteshwar dam which itself is a part of Bhagirathi valley (Fig. 15.1). The 18 km long Koteshwar reservoir is situated between the Tehri dam and the Koteshwar dam of Uttarakhand, India. Two sites that have witnessed slope subsidence have been undertaken for the ground displacement study. These sites are situated just downstream of the Tehri Dam. The company which is operating both dams (THDCL) has marked the selected sites as Zero bridge and chainage 1.6 km (which is 1.6 km towards Koteshwar Dam from the Zero Bridge). The ground displacement in this area namely, landslides and ground subsidence are triggered due to rainfall and water fluctuation at the toe of the slope. At the zero-bridge site, the slope-forming material is weathered phyllite and at the 1.6 km chainage site the slope-forming material is debris. These slopes support sparse vegetation cover. Tehri-Koteshwar road cut through this slope section. The road section in this stretch has subsided in 2013 due to the reservoir water fluctuations. At the upper reaches of the slope section, abandoned cropland and abandoned homes can be easily seen. People living at the upper parts of the slope have also reported increased slope subsidence incidents after the formation of the Koteshwar reservoir. The slope at the Zero bridge site is dipping at a steep angle (70°) and supports very sparse vegetation. Overall the Koteshwar reservoir rim area receives rainfall to the tune of 150–200 cm in the monsoon season and during this season, it suffers several slope failure incidents.

Most of the landslides have been observed in soil and debris along the road stretch (Fig. 15.2). Moderately dipping road cut-slopes composed of soil/debris cover used to fail due to increased pore water pressure in the monsoon. This study may help assess the use of remote sensing in understanding the reasons for continuous slope failures in the selected study area.

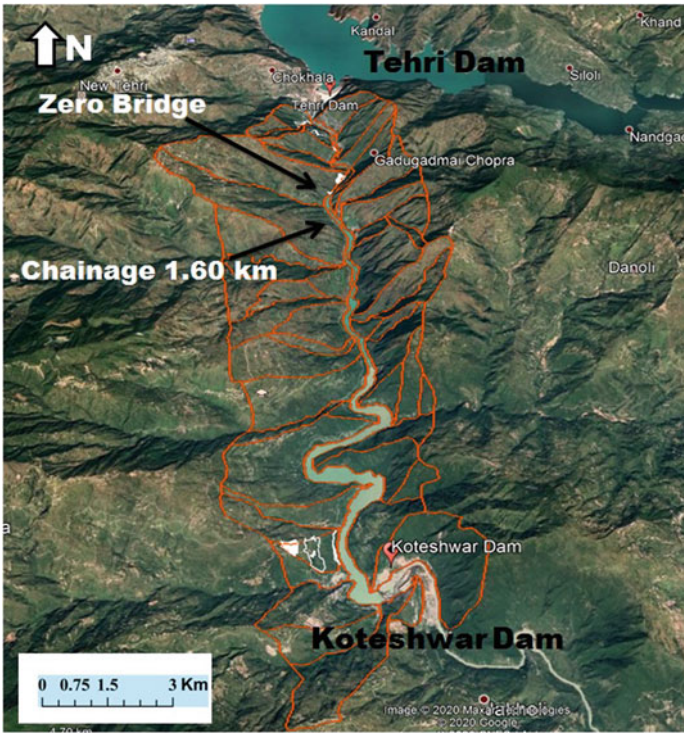

Fig. 15.1 Location Zero Bridge and 1.60 km Chainage of the study area between Tehri Dam and Koteshwar Dam along the reservoir (*Source* Google Earth)

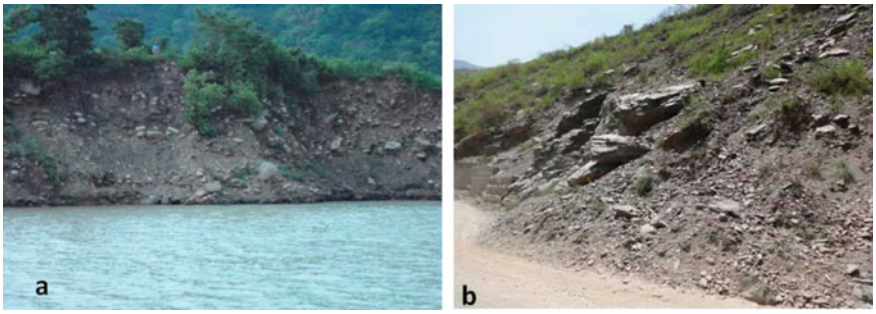

Fig. 15.2 Landslides observed in the Koteshwar reservoir area, **a** reservoir induced landslide, **b** landslide along the road cut slopes

15.3 Methodology

During this study, an attempt has been made to assess the application of Remote Sensing (using Sentinel-1 SAR and LISS-IV) in the selected area During this study, an attempt has been made to assess the application of Remote Sensing using Sentinel-1 SAR and LISS-IV data for the selected study area.

15.3.1 Sentinel Data

The PSI technique is specifically suited to hilly terrain (covering large areas), where standard practices of ground deformation monitoring such as geophysical survey, geotechnical parameter characterization, etc., consume comparatively time and cost. The fundamentals of the PSI technique are rooted in multi-temporal DInSAR (Differential In SAR). This technique uses the phase difference of two SAR data, which are targeted to capture the same area in different periods. It enables to map, estimate and quantify ground movement with centimeter accuracy and processes a large number of temporal SAR data that estimate velocities and time series of ground movement as a point-wise target. It is also called persistent scatterer (PS). PSI methods are based on the identification of image pixels in interferograms that are generated from the same master image that persistently backscatters the radar signal over a long time. The foundation of the Satellite based Augmentation System (SBAS) principle lies in the processing of multi-master SAR images that are having a small temporal gap and short perpendicular baseline. Short temporal separation and baseline reduce the effects of spatial and temporal decorrelation and they are specifically suitable for handling a large number of multi-SAR imagery. In this study, a total of 57 scenes (Fig. 15.2) of Sentinel-1 SAR data from June 2015 to May 2018 have been utilized for PS-InSAR processing with the objective to assess the slope movement (if any) occurring on the reservoir bounding slopes at the Zero bridge site and 1.6 km chainage site. The slopes in the area support sparse to moderate vegetation at 1.6 km chainage site, thus it was difficult to achieve a preferred coherence level of >0.6. The image taken on 2017/01/07 was considered as the master image while others were used as slave images. The PS-InSAR process was carried out in SARPROZ software at a coherence level set to 0.4. More than 150 scatter points were generated, which were further grouped in two zones for interpretation purposes with zone 1 being located at the Zero bridge site and zone 2 at the 1.6 chainage site.

Table 15.1 Satellite sensor data of LISS IV

Satellite sensor	Resolution	Image capture dates
LISS IV—mx (Ortho-rectified)	5.8 m	6/12/2012–23/01/2013
		23/01/2013–31/03/2014
		31/03/2014–19/04/2015
		19/04/2015–1/02/2016
		1/02/2016–8/04/2017

15.3.2 Using LISS IV Data

The dataset pairs (Table 15.1) from the year 2012–2013, 2013–2014, 2014–2015, 2015–2016 and 2016–2017 that generated correlation rasters from each data pair using the Cosi-Corr algorithm integrated in the ENVI platform. Five pairs of optical images were used to deduce the magnitude of slope displacement magnitude. Further, the vector tool in Cosi-Corr software deduced displacement vectors w.r.t due north for the study sites. The following data used for the present study as (a) Sentinel Data: Total 57 scenes of Sentinel-1 SAR data (which works in C band) of period June-2015 to May 2018 have been used for PS-InSAR processing and LISS IV data.

15.4 Results and Discussion

15.4.1 Using Sentinel Data

In the road cut slope, which ranged up to 70 m high, the slope was very steep and made up of moderately weathered phyllite rock. The pronounced foliation plane and two sets of joints were the major discontinuity that was observed during the field investigation. This slope section had failed several times, with the major failure seen in 2013 in which phyllite blocks ranging from pebble to boulder dimension slipped down the slope.

15.4.1.1 Results Obtained at 1.6 Chainage Site (Zone 2)

PS clusters of zone 2 indicated no movement (Fig. 15.3) during the study period (2015–2018). The slope face here was composed of debris and soil and dipping at a moderate angle (30–35°). At least four streams are running down this particular slope. At higher reaches of the slope, few villages are situated. During the field verification of the results, roughly no trace of displacement was observed in any of the residential buildings. Hence, the results were found to be coherent with the ground's existing situation.

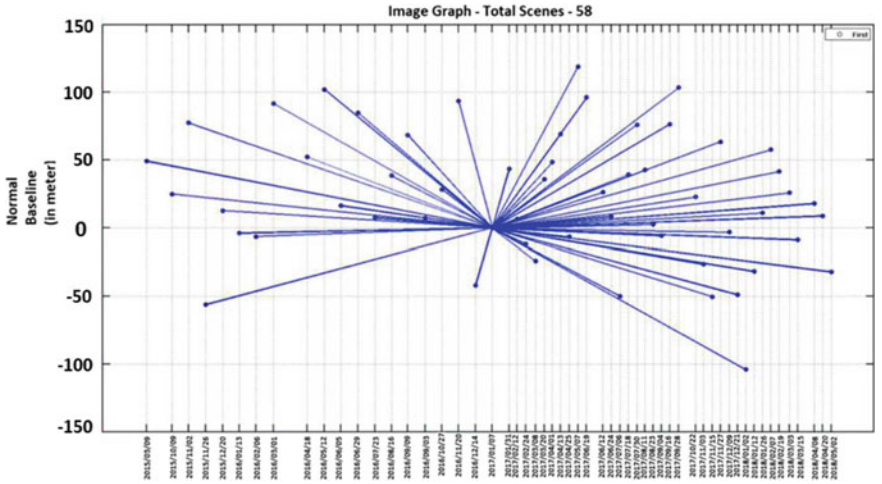

Fig. 15.3 Temporal distribution of Sentinel-1 SAR data used in this study

15.4.2 Results Using LISS IV Data

Using the dataset pairs 2012–2013, 2013–2014, 2014–2015, 2015–2016 and 2016–2017, the correlation rasters resulting from the Cosi-Corr platform were used to find the displacements (pixel shift) per year (Table 15.2a, b and c). Surface displacement values for the slope sections at each critical location were calculated. Also, the slope displacement orientations in the form of displacement bearing range are given in Table 15.3 with respect to the north (Fig. 15.4).

The displacement bearing can be used to find the angle between the slope's actual dip direction and the displacements (Fig. 15.5).

15.4.2.1 Location (b)—Chainage 1.60 km from Zero Bridge

Using the dataset pairs 2012–2013, 2013–2014, 2014–2015, 2015–2016, and 2016–2017 the correlation rasters resulting from the Cosi-Corr platform were used to find the displacements (pixel shift) per year (Table 15.4a, b and c). Some displacement values for the slope sections at each critical location were calculated. Also, the slope displacement orientations in form of displacement bearing range are given in Table 15.5 with respect to the north (Figs. 15.6 and 15.7).

Table 15.2 **a** Resultant year-wise displacement (m) for the section 1 (Zero Bridge), **b** Resultant year-wise displacement (m) for section 2 (Zero Bridge), **c** Resultant year-wise displacement (m) for section 3 (Zero Bridge)

(a) Chainage Zero Bridge (Section 1)

Data set pair	Zero Bridge (Section 1)	Minimum displacement	Maximum displacement	Displacement near road level
Year 2012–2013	Zero Bridge (Section 1)	0.58 m	0.66 m	0.59 m
Year 2013–2014	Zero Bridge (Section 1)	0.037 m	0.303 m	0.263 m
year 2014–2015	Zero Bridge (Section 1)	0.526 m	0.843 m	0.68 m
Year 2015–2016	Zero Bridge (Section 1)	0.019 m	0.354 m	0.328 m

(b) Chainage Zero Bridge (Section 2)

Data set pair	Zero Bridge (Section 2)	Minimum displacement	Maximum displacement	Displacement near road level
Year 2012–2013	Zero Bridge (Section 2)	0.553 m	0.640 m	0.595 m
Year 2013–2014	Zero Bridge (Section 2)	0.034 m	0.373 m	0.059 m
Year 2014–2015	Zero Bridge (Section 2)	0.774 m	0.963 m	0.792 m
Year 2015–2,016	Zero Bridge (Section 2)	0.012 m	0.197 m	0.025 m

(c) Chainage Zero Bridge (Section 3)

Data set pair	Zero Bridge (Section 3)	Minimum displacement	Maximum displacement	Displacement near road level
Year 2012–2013	Zero Bridge (Section 3)	0.55 m	0.76 m	0.628 m
Year 2013–2014	Zero Bridge (Section 3)	0.02 m	0.14 m	0.03 m
Year 2014–2015	Zero Bridge (Section 3)	0.95 m	0.79 m	0.79 m
Year 2015–2016	Zero Bridge (Section 3)	0.003 m	0.03 m	0.012 m
Year 2016–2017	Zero Bridge (Section 3)	0.10 m	0.42 m	0.10 m

Table 15.3 Range of slope surface displacement orientation for each pair of the dataset

Dataset Pair (year)	2012–2013	2013–2014	2014–2015	2015–2016	2016–2017
Displacement Bearing Range	S55°E to S60°E	S40°E to S46°E	S5°E to S15°E	S25°E to S35°E	S20°E to S35°E

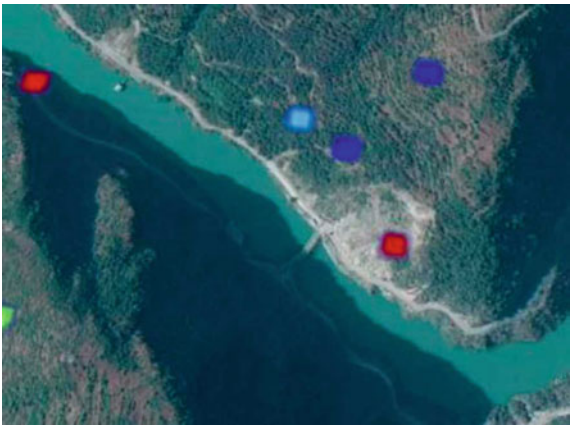

Fig. 15.4 PS points re-projected on Zero-bridge site slope

15.4.3 Discussion and Comparison of Sentinel—LISS IV Data

In this study, the ability of PS-InSAR technique was utilized to analyze the slope movement (if any) occurring on the Koteshwar reservoir bounding slopes. A 57 scenes of Sentinel-1 SAR data were downloaded and processed in SARPROZ software. Results were filtered as per the standard practice and re-projected on the local slope in order to interpret the PS cloud. The PS cloud generated through the processing was classified into two zones, each representing different slope faces. Results at Zone 1 showed downward slope movement to the tune of 60 mm/year. This result perfectly matches with the field conditions that are discussed in the results and discussion section. In Zone 2, roughly no ground movement was observed.

The correlation among the multi-spectral data over the various data pairs considering the study locations (Zero bridge and 1.60) has shown a similar pattern of high pixel shift (slope surface displacements) for the pair 2012–2013 and 2014–2015. Comparing Tables 15.2 and 15.4, a similar pattern can be observed i.e. they witnessed maximum slope surface displacements near road level for the year pair 2012–2013 and 2014–2015, and a similar orientation of the displacement as per the vectors overlaid on the correlation raster. All the locations showed a slope surface displacement along SE direction between 2012–2013 and 2014–2015, which indicates an external triggering factor such as a heavy and continuous rainfall episode that initiated the debris movement on slopes towards the downslope direction along

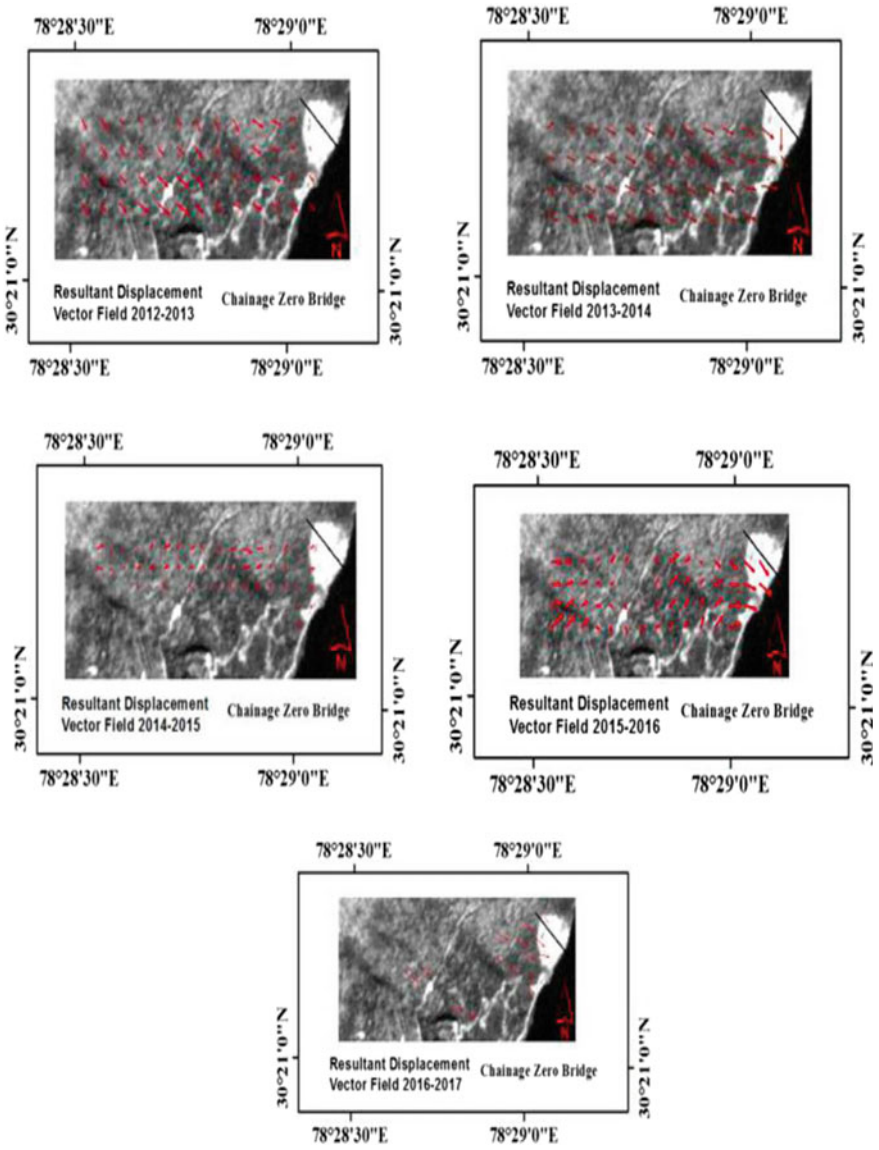

Fig. 15.5 The displacement vector fields overlaid on the correlation bands for image pairs 2012–2013, 2013–2014, 2014–2015, 2015–2016, and 2016–2017; for the slope at Zero bridge chainage

Table 15.4 **a** Resultant year-wise displacement (m) for the section 1 (Chainage 1.60 km), **b** Resultant year-wise displacement (m) for the section 2 (Chainage 1.60 km), (c) Resultant year-wise displacement (m) for the section 3 (Chainage 1.60 km)

(a) Data set pair	Chainage Section	Minimum displacement	Maximum displacement	Displacement near road level
Year 2012–2013	1.60 (Section 1)	0.56 m	0.63 m	0.609 m
Year 2013–2014	1.60 (Section 1)	0.026 m	0.59 m	0.064 m
year 2014–2015	1.60 (Section 1)	0.805 m	1.011 m	0.99 m
Year 2015–2016	1.60 (Section 1)	0.004 m	0.062 m	0.0254 m
Year 2016–2017	1.60 (Section 1)	0.207 m	0.477 m	0.423 m
(b) Data set pair	Chainage Section	Minimum displacement	Maximum displacement	Displacement near road level
Year 2012–2013	1.60 (Section 2)	0.55 m	0.63 m	0.619 m
Year 2013–2014	1.60 (Section 2)	0.028 m	0.408 m	0.037 m
year 2014–2015	1.60 (Section 2)	0.77 m	1.0001 m	0.959 m
Year 2015–2016	1.60 (Section 2)	0.0044 m	0.0165 m	0.0118 m
Year 2016–2017	1.60 (Section 2)	0.269 m	1.090 m	0.384 m
(c) Data set pair	Chainage Section	Minimum displacement	Maximum displacement	Displacement near road level
Year 2012–2013	1.60 (Section 3)	0.572 m	0.654 m	0.645 m
Year 2013–2014	1.60 (Section 3)	0.029 m	0.0516 m	0.0407 m
year 2014–2015	1.60 (Section 3)	0.716 m	0.980 m	0.950 m
Year 2015–2016	1.60 (Section 3)	0.0079 m	0.035 m	0.011 m
Year 2016–2017	1.60 (Section 3)	0.332 m	0.404 m	0.396 m

Table 15.5 Range of slope surface displacement orientation for each pair of dataset (1.60 km)

Dataset pair (year)	2012–2013	2013–2014	2014–2015	2015–2016	2016–2017
Displacement Bearing Range	S60°E to S65°E	N45°E to N55°E	S52°E to S60°E	N45°E to N55°E	N25°E to N32°W

the channel (SE direction). It is well known that the catastrophic flood and heavy rainfall triggered in the state of Uttarakhand in the year 2013, and also as per the IMD (2014) annual rainfall data for the year 2014 received, heavy rainfall in July and August.

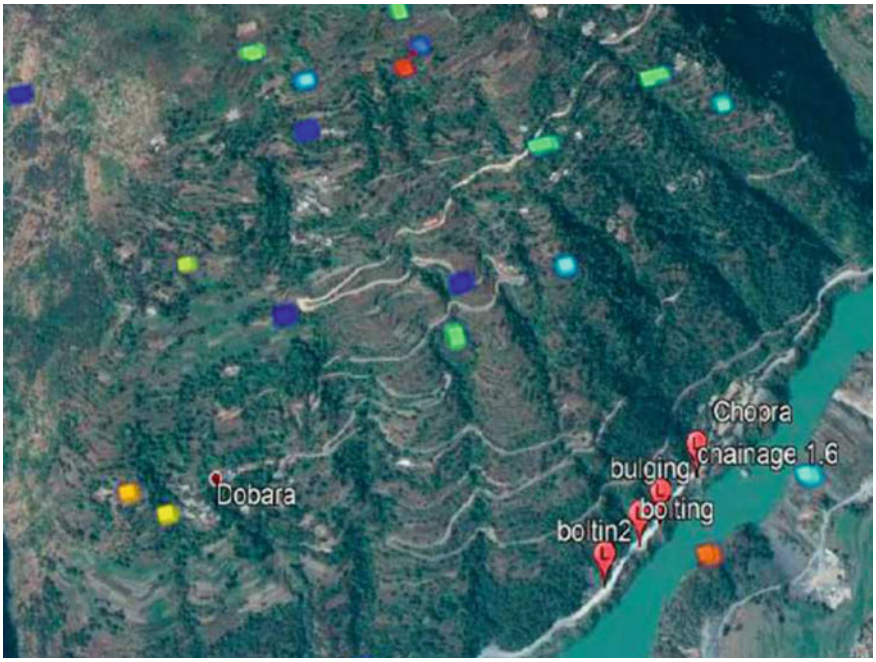

Fig. 15.6 PS points re-projected on Chainage 1.6 site slope

15.5 Conclusion

In this study, the SAR interferometry and LISS IV optical data have shown dependence on the time and month of data acquisition, as the results indicated that the use of PS cloud inferred negligible displacement at location 1.60 km (Zone 2), which is opposite to the results inferred from LISS IV optical data. The LISS IV images were limited in this study as the acquisition from the data archive was dependent on the cloud cover, which limited the number of scenes useful for deducing annual slope displacements. The Sentinel dataset used was large with a short temporal period of capture, and therefore, it could accurately depict the physical processes such as slope movements, etc., with much certainty for a longer span of study. The use of multiple types of remote sensing data integrated for a study can be used to validate surface displacements at critical locations in the considered area.

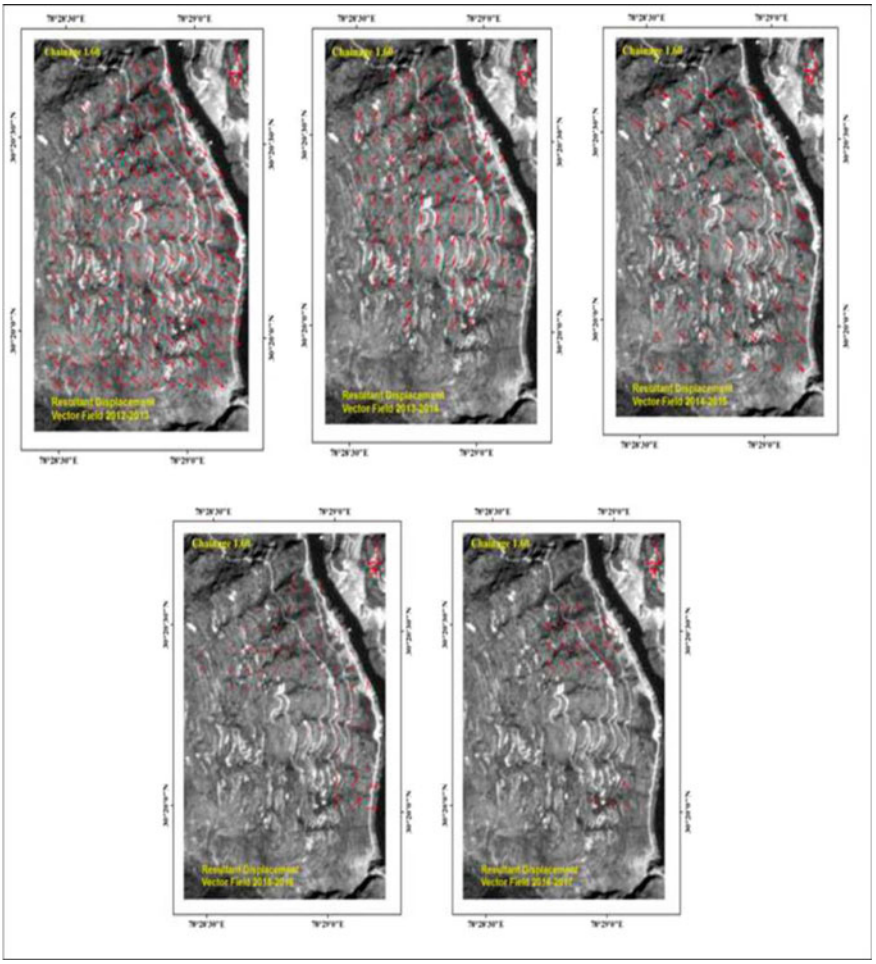

Fig. 15.7 The displacement vector fields overlaid on the correlation bands for image pairs 2012–2013, 2013–2014, 2014–2015, 2015–2016, and 2016–2017; for the slope at 1.60 km chainage

References

Casagli N, Cigna F, Bianchini S, Holbling D, Fureder P, Righini G, Del Conte S, Friedl B, Schneiderbauer S, Iasio C, Vlcko J (2016) Landslide mapping and monitoring by using radar and optical remote sensing: examples from the EC-FP7 project SAFER. Remote Sens Appl Soc Environ 4:92–108

Castaldo R, Tizzani P, Lollino P, Calo F, Ardizzone F, Lanari R, Guzzetti F, Manunta M (2015) Landslide kinematical analysis through inverse numerical modelling and differential SAR interferometry. Pure Appl Geophys 172(11):3067–3080

Ferretti A, Prati C, Rocca F (2001) Permanent scatterers in SAR interferometry. IEEE Trans Geosci Remote Sens 39(1):8–20

Gupta P, Anbalagan R (1997) Landslide hazard zonation (LHZ) and mapping to assess slope stability of parts of the proposed Tehri dam reservoir, India. Quart J Eng Geol 30:27–36

India Meteorological Department (IMD) (2014). Rainfall data sources. https://hydro.imd.gov.in/hydrometweb/(S(o10dts3rzehf3lrjsyy535ry))/DistrictRaifall.aspx

Kaufmann V, Ladstadter R (2003) Quantitative analysis of rock glacier creep by means of digital photogrammetry using multi-temporal aerial photographs: two case studies in the Austrian Alps. In Proceedings of the 8th international conference on Permafrost. AA BalkemaPublishers, Zurich, Switzerland, pp 21–25

Lacroix P, Berthier E, Maquerhua ET (2015) Earthquake-driven acceleration of slow-moving landslides in the Colca valley, Peru, detected from Pleiades images. Remote Sens Environ 165:148–158

Lacroix P, Bievre G, Pathier E, Kniess U, Jongmans D (2018) Use of Sentinel-2 images for the detection of precursory motions before landslide failures. Remote Sens Environ 215:507–516

Leprince S, Berthier E, Ayoub F, Delacourt C, Avouac JP (2008) Monitoring earth surface dynamicswith optical imagery. EOS Trans Am Geophys Union 89(1):1–2

Martha TR, Kerle N, Van Westen CJ, Jetten V, Kumar KV (2012) Object-oriented analysis of multi-temporal panchromatic images for creation of historical landslide inventories. ISPRS J Photogramm Remote Sens 67:105–119

Scambos TA, Dutkiewicz MJ, Wilson JC, Bindschadler RA (1992) Application of image cross-correlation to the measurement of glacier velocity using satellite image data. Remote Sens Environ 42(3):177–186

Stumpf A, Malet JP, Delacourt C (2017) Correlation of satellite image time-series for the detection and monitoring of slow-moving landslides. Remote Sens Environ 189:40–55

Stumpf A, Malet JP, Allemand P, Ulrich P (2014) Surface reconstruction and landslide displacement measurements with Pleiades satellite images. ISPRS J Photogramm Remote Sens 95:1–12

Stumpf A, Malet JP, Puissant A, Travelletti J (2016) Monitoring of earth surface motion and geomorphologic processes by optical image correlation. In: Land surface remote sensing. Elsevier, pp 147–190

Tiwari RK, Gupta RP, Arora MK (2014) Estimation of surface ice velocity of Chhota-Shigri glacier using sub-pixel ASTER image correlation. Current Sci 853–859

Zhou C, Cao Y, Yin K, Wang Y, Shi X, Catani F, Ahmed B (2020) Landslide characterization applying sentinel-1 images and InSAR technique: the Muyubao landslide in the three Gorges Reservoir Area, China. Remote Sens 12(20):3385

Chapter 16
Landslides Inventory of Active Ramgarh Thrust Zone Through Image Processing and GIS Techniques in Sikkim, India

R. Sivakumar and Snehasish Ghosh

Abstract Landslide is a widespread hazard in the Himalayan region that occurs during the monsoon season due to heavy rainfall. The seismicity in the active thrust region is also induced landslides which brings instant disaster by the destruction of infrastructures and communication system. The advancement of remote sensing techniques help to identify the landslide occurrence and potential area in the active thrust zone. The active Ramgarh thrust region of Sikkim Himalaya is selected as a study area. The integrated image processing techniques, mainly band ratio, Principal Component Analysis, and image classifications, have been applied for the inventory of landslides from Sentinel-2 image for the year 2020. The output has been integrated with seismotectonic parameters in Geoinformatics technology to understand the influence of active thrust along with other parameters for the occurrence and potential of landslides. The result shows that most the landslides interrupt the transport communication system by damaging the road network. These landslides are observed explicitly in the Damuda and Buxa geological formations surrounding the active thrust belt. The repetition of such formations is observed due to thrust movement and significant earthquakes recorded in recent times. The study infers that the possibility of landslide occurrence is uncertain in this active thrust due to the influence of unpredictable seismic activity rather than common occurrence during the monsoonal season.

Keyword Landslides · Seismotectonic · Image processing · Geoinformatics · Sikkim

16.1 Introductions

Landslide is the downslope movement of disintegrated materials from the sloppy ground (Singh 2005; Chorley et al. 1985). The physical and chemical weathering disintegrates the surficial materials (Che et al. 2012; Regmi et al. 2014). The

R. Sivakumar (✉) · S. Ghosh
Earthquake Research Cell & Department of Civil Engineering, College of Engineering and Technology, Faculty of Engineering and Technology, SRM Institute of Science and Technology, 603203 Kattankulathur, Kanchipuram, Chennai, India
e-mail: sivakumr@srmist.edu.in

P. Thambidurai and T. N. Singh (eds.), *Landslides: Detection, Prediction and Monitoring*,
https://doi.org/10.1007/978-3-031-23859-8_16

disintegrated materials, including soils, fragmented rocks, debris, etc., start to move downwards when it exceeds the holding capacity on the earth surface under the influence of gravity. Landslide is a very common hazard in the Himalayan region that occurs during the monsoon season due to heavy rainfall and other physical factors. Pandey et al. (2008) emphasized landslide occurrence in the N-E Himalayan region in the Dikrong river basin, Arunachal Pradesh, India, where physiography, lithological structures, slope stability, etc. are important factors of landslides. The landslide reactivation mechanisms in Lanta Khola in Sikkim Himalayas are common due to heavy rainfall in the monsoon season every year, which is further affected by lithology and soil characteristics (Anbarasu et al. 2010). Sivakumar and Ghosh (2021) explain various physical and seismotectonic parameters for landslides in the Sikkim Himalayan region surrounding the main central thrust. Similarly, the influences of mineralogy and geochemical parameters have been emphasized in the central Himalayan region along Mugling–Narayanghat road corridor for landslides (Regmi et al. 2014). Pankaj and Kumar (2015) studied the various landslide occurrence factors in the N-W Himalayan region along Song River, Dehradun in Uttarakhand, and identified that the structural parameters along with tectonic controls are influencing factors for the occurrence of landslides.

Landslide is a geological hazard where active tectonics and seismic activity play an important role in landslide occurrence (Donnelly et al. 2006; Miyagi et al. 2011). Lee and Dan (2005) emphasis the major factor of the distance between the earthquake epicenter and the place at which the landslide occurred in the Lai chau province of Vietnam. Koukis et al. (2005) highlight the role of the tectonic fault and its active movement in the present geological time and its relation to earthquake occurrence in Corinth Gulf, Greece. The lineament, which is not associated with any fault zone, induces massive landslides and land shaking due to physical weathering and disintegration of materials (Ramli et al. 2010). Donnelly et al. (2006) and Yuan et al. (2015) explain that fault reactivation due to the release of energy, aftershock, etc., leads to ground deformation and disruption of slope stability, which induces landslides. With the advancement of remote sensing and digital image processing techniques, the identification of landslides are simplified without field visit and can be mapped in an inaccessible area also. There are much research has been carried out which are pre and post landslides and Spatio-temporal evolution using high-resolution images, a 3-D digital elevation model for landslide assessment (Dubey et al. 2005), Shannon's entropy influence on landslide (Sharma et al. 2012), fuzzy logic (Sharma et al. 2013), frequency ratio approach (Anbalagan et al. 2015), the neuro-fuzzy classifier (Singh and Singh 2016) where the advancement of digital image processing techniques are applied. Landslide occurrences are common in the Himalayan region during the monsoon season due to heavy rainfall. The seismic activity in the Himalayan region also induces landslides which bring instant disaster by the destruction of infrastructures and communication systems. The seismically induced landslides are uncertain and more susceptible in the active thrust zone. Hence, the active Ramgarh thrust region of Sikkim Himalaya is selected as the study area for giving more priority to the uncertainty in the occurrence of landslides.

In the present research, the integrated image processing techniques, mainly band ratio, Principal Component Analysis, and image classifications, have been applied for the inventory mapping of landslides from Sentinel-2 image for the year 2020. The Active Ramgarh Thrust, Sikkim in the N-E Himalayan region, has been selected for the study area (Fig. 16.1).

The study area is well marked by Ramgarh thrust (Ghosh 1952), the intersection zone between older folded structural features and lesser Himalayan sequence (Fig. 16.2a). The major Damuda formation (Sarkar et al. 2012; Bose et al. 2014) covers Namchi and Chukchen region, where the Great Ranjit river basins are formed.

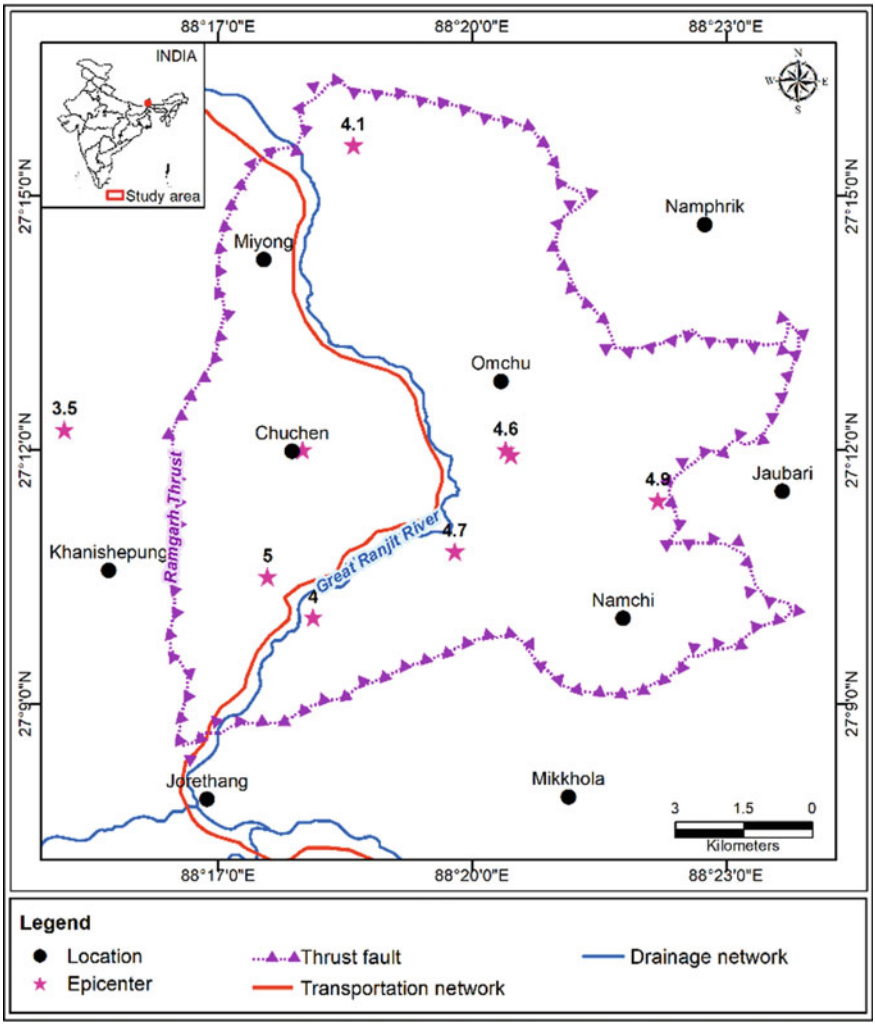

Fig. 16.1 Location map of study area

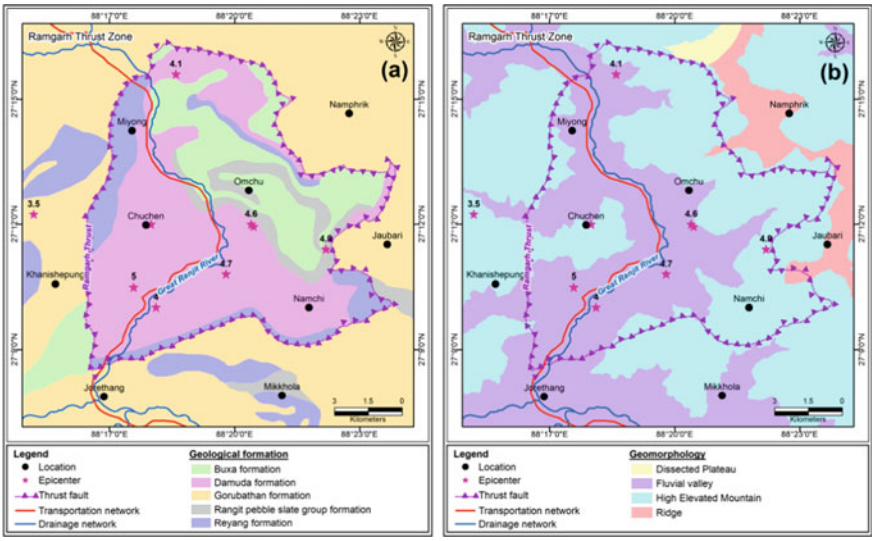

Fig. 16.2 Thematic databases: **a** Geology with structural features (modified after Sarkar et al. 2012), **b** Geomorphology (Derived from DEM and Satellite image)

Buxa and Ranjit pebble slate group formations are overthrusts in the central part surrounding the Omchu region, which creates a complex geological structure in this study region. Reyang formation is dominated along the Ramgarh Thrust (RT) boundary around the N-E and Southern part of the thrust region (Sarkar et al. 2012). The Gorubathan formation is observed in the Lesser Himalayan sequence, which is well segregated from the older folded sequence by the RT thrust line. Geomorphologically, the region is covered by a fluvial valley along the Great Ranjit river basin, dissected plateau in the North, a higher elevated mountain around the valley region, and an elongated ridge in the N–E side of the study region (Fig. 16.2b). The region is seismically active and observed with recent earthquake epicenters in scattered manners, indicating recent tectonic movement (Sivakumar and Ghosh 2017). The above thematic database has been generated in GIS.

16.2 Materials and Methods

The Sentinel-2A data for 2020 is collected from USGS earth explorer, which is used to prepare landslide inventory maps using digital image processing techniques. The sentinel-2 is an earth observation mission of European Space Agencies (Fig. 16.3). The data have been collected with a spatial resolution of 10–60 m along with 13 spectral bands which are processed for extracting landslides hazard. The collected raw image has been georeferenced and geometrically corrected with the help of SOI Open series map (RF scale1:50,000). The Principal Component Analysis of 5

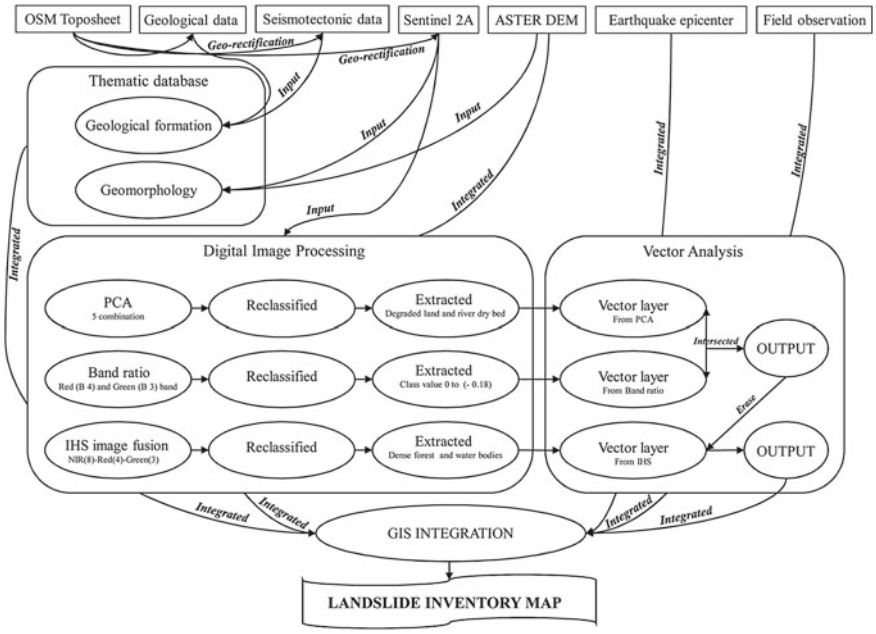

Fig. 16.3 Flow chart of methodology

combinations (PCA 5) has been applied for the satellite image, and generated output has been reclassified into various classes. The desired zones of interest, a degraded land surface and dry bed in the river, have been extracted and merged into single classes (Fig. 16.4a). The Red (B4) and Green (B3) band ratios were applied to the band ratio model in the selected image. The output has been classified, and the desired index value between 0 and (−0.18) has been extracted (Fig. 16.4b). The output of the image shows a very clear view of the landslide zone, but the area of sand bar in river bed, deforested land, soil erosion zone, and other drylands with high reflectance also covers this zone. The IHS image fusion method was applied to the selected FCC image with the composition of 843 (NIR-Red-Green) to enhance the image to its intensity, hue, and saturation level for better interpretation. The IHS sharpens the satellite image and enhances the edge without discontinuity in the gray level. The output of IHS image shows a new intensity component and is more effective than the original MSS FCC image in demarcating features. It helps to delineate the water bodies with dry beds and dense forest zone without disturbing other land features. The output image has been reclassified, and selected class that belongs to dense forest cover and major rivers with dry bed have been extracted (Fig. 16.4c). All the extracted output was converted to a vector layer for GIS integration. The zone extracted from PCA intersected with the extracted zone of the band ratio image.

The developed output has been integrated with IHS extracted zone using a spatial analysis erase tool to demarcate the probable landslide area. The output image shows landslide zones where some of the dry river bed and coarse sandy soils zone were

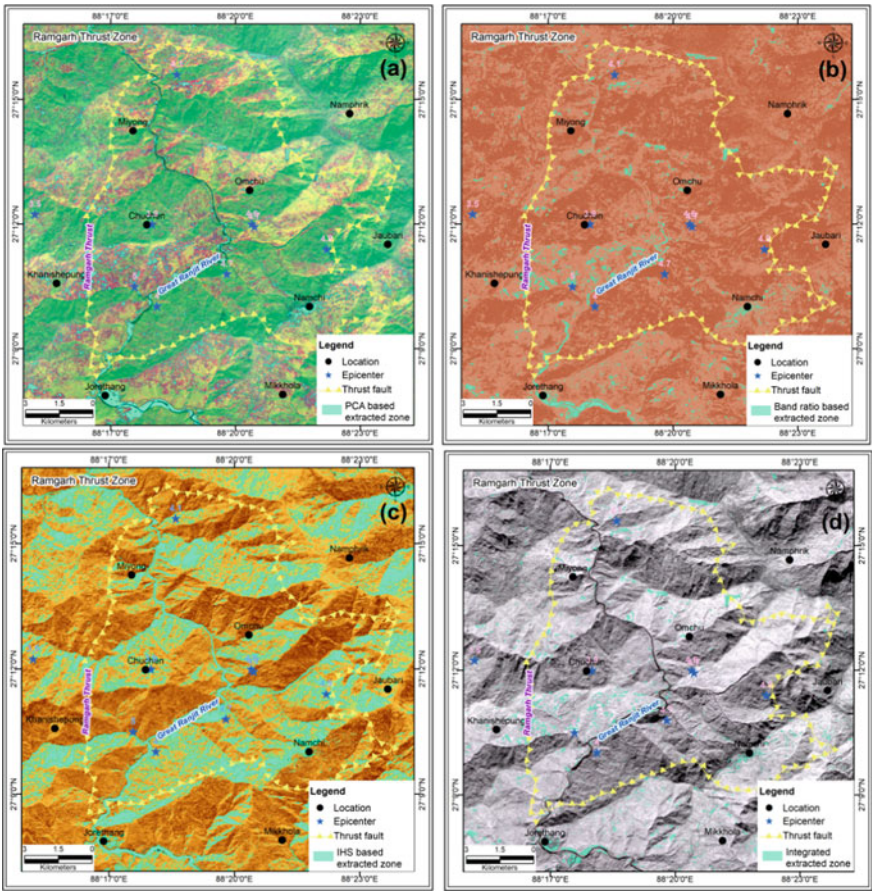

Fig. 16.4 Digital image processing **a** PCA, **b** Band ratio, **c** IHS image and extracted zone, **d** Integrated image of PCA, Band ratio and IHS

not eliminated by this process (Fig. 16.4d). The error has been minimized, and the landside inventory zone has been identified by integrating field observation data and a high-resolution satellite image. The PCA of the image also helps to demarcate the land discontinuity features, fault, and fracture zone using a suitable eigenvalue. With the help of PCA analysis, it is possible to rectify the noise problems in the less-correlated PC image and enhance the spectral differences between features that are more prominent in PC images than in individual bands, which helps to determine the linear features associated with landslides (Ghosh and Viswanatham 1991; Olgen 2004). Also it reduces the correlation factor between variables and extracts the geological features associated with lineament and fractures by removing the redundancy in MSS data (Jensen 2004). Band ratio is used to stretch the DN number in such a way it discriminates the lithological compositions, which is unable to identify from a standard FCC image (Sabins 1997). It is most effective to discriminate the

structural complement of rocks and enhance the various structural features which are present in the rock compositions by removing the first-order brightness effect of slope features in different elevations (Arnous and Sultan 2014). Further, IHS fusion techniques also sharpen the features, enhance the colour composition, and improve the spatial resolution to discriminate the various structural features associated with landslide phenomena (Pohl and Genderen 1998; Al-Wassai et al. 2011). The identified landslide zone has been integrated with seismotectonic parameters through geoinformatics technology to understand the influence of active thrust along with other parameters for the occurrence and potential of landslides.

16.3 Results

The landslide geodatabase has been generated for the year 2020 by integrated analysis of various image processing methods (Fig. 16.5). The accuracy is obtained by the integration of field evidence along with the visual interpretation of high-resolution satellite images. It is observed that many numbers of landslides occur in the south-western part along the RT boundary covering the location Chuchen region. The region is well connected with surrounding villages by a road communication system in the sloppy ground which is interrupted due to landslides. Geomorphologically the area is a transition zone of the higher mountain and fluvial valley zone. Geologically, the region belongs to Damuda formation, where underlying lithologies are sandstone and shale. The area also shows an earthquake epicenter in recent times with a magnitude of 5.0, indicating the region is seismically active and prone to landslides due to seismic activity. Also, the number of landsides is higher in the Omechu region, a fluvial valley zone where seismic epicenters are observed with a magnitude of 4.6. The region includes the complex geological formations of Buxa and Rangit Pebble Slate formation, which is repeatedly overthrusted due to active thrust movement. The underlying lithology consists of orthoquartzite, dolostone phyllite, conglomerate, and slate. It is also noticed that the northern part of Miyong and Namchi villages are also affected by landslides which are bounded by the RT belt where Reyang and Damuda formations are dominant, respectively, and comprised of pyritiferous black slate and sandstone in the subsurface. Further, it is noticed that the Namphirik, Khanishepung, Jaubari, Jorethang, and Mikkhola region in the outer side of Ramgarh thrust is also affected by many landslides where the thrust influence of RT and other active fault structures are significant. Along the main river basin of the Great Ranjit river and major parallel road, networks are also affected by landslides in this active thrust zone where the magnitude of earthquake epicenter varies between 4 and 4.7.

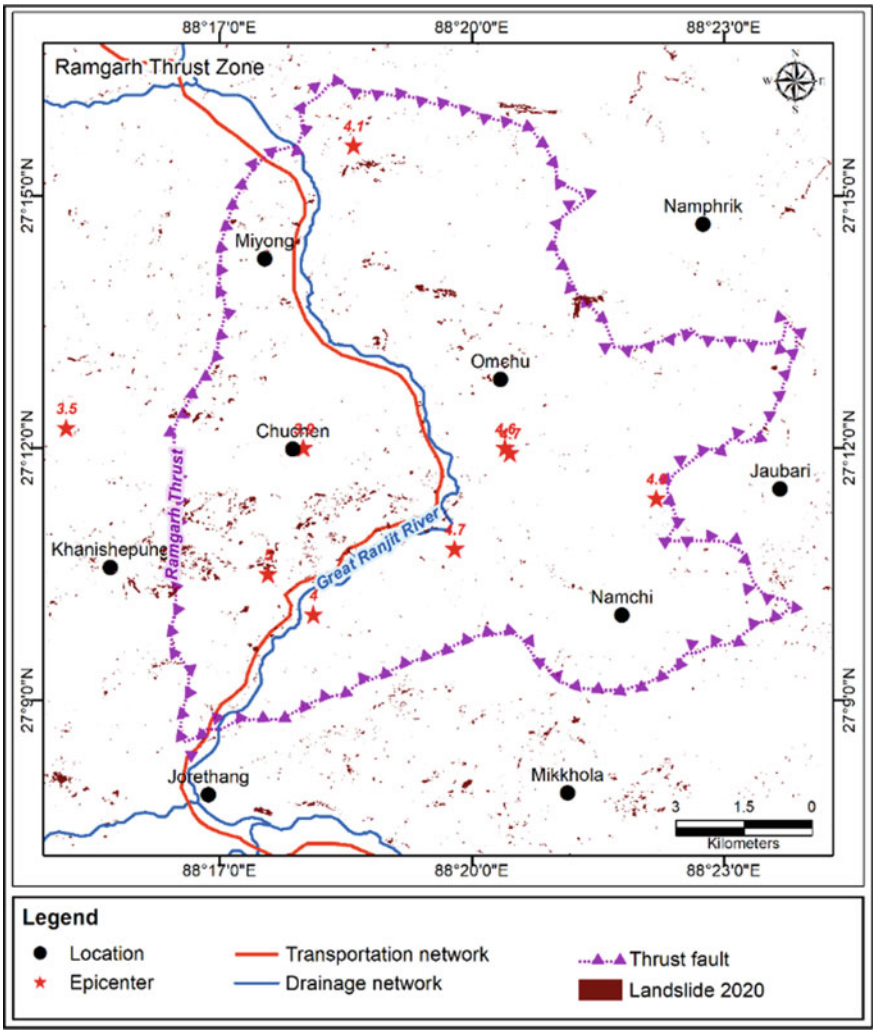

Fig. 16.5 Digital image processing based Landslide inventory map for 2020

16.4 Discussion

The result shows that the landslides specifically observed in the Damuda, Buxa, and Rangit Pebble Slate geological formation surroundings the active thrust belt on the underlying lithology of phyllite, conglomerate, slate, sandstone, and shale. A recent study identifies that the phyllitic rock has a high degree of weathering and ductile deformation capacity leading to induced landslides (Regmi et al. 2013, 2014). Similarly, the chemical weathering in shale rocks is responsible for the alteration by interchanging of clay minerals, leading to landslides. The landslide reactivations are

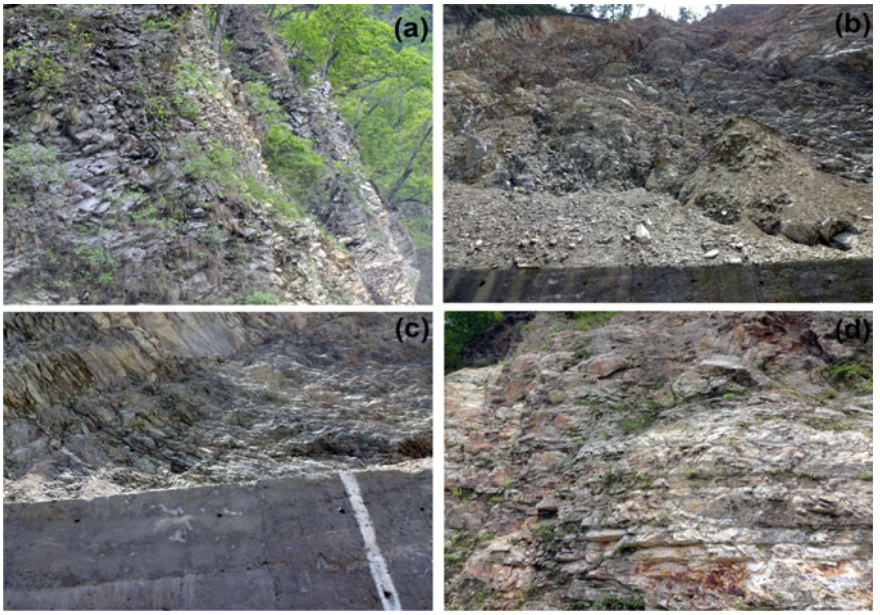

Fig. 16.6 Structural and lithological characteristics associated with landslides: **a** Highly block disintegration of weathered and jointed rocks. **b** Disintegrated soft sedimentary rocks with crisscross fracture. **c**. Parallel Micro fractures associated with structural features. **d** Parallel fractures in thrusted deformed surface (Field observation 2016)

very common in slate and phyllites rocky surfaces due to the higher potentiality of weathering (Regmi et al. 2013). This observation clearly indicates that such formations are easily induced a landslide even if it experiences low-frequency seismic vibration, which is really uncertain and may occur at any time.

The repetition of geological formations is observed in the RT zone due to thrust movement and significant earthquakes recorded in recent time, indicating the region is seismically active. The previous study has produced an earthquake hazard zonation map representing the RT region belonging to a high seismic hazard zone (Nath et al. 2007; Pal et al. 2008; Sivakumar and Ghosh 2017). The Rangit tectonic and its deformation study reveal that the RT zone is an active thrust zone (Mukul et al. 2014) which is responsible for frequent seismicity. The consequent thrusting creates complex geological formations and structural features in this tectonic zone (Mitra et al. 2010). The active tectonics study through morphotectonic parameters has also suggested that the region is under a very strong active tectonic zone (Ghosh and Sivakumar 2018). The complex structural patterns are also observed during the field study which are associated with landslide phenomena Fig. 16.6. Most of the landslides interrupt the transport communication system by damaging the road network in different places in the study region, as observed in Fig. 16.7. A few landslides are noticed in residential areas, along the river, and even on road construction sites

Fig. 16.7 Communication interruption by landslides: **a** Debris slide in the residential region, **b** landslide along the national highway, **c** Rock slide along the transportation network, **d** Road blockage by landslide in construction site (Field observation 2016)

Fig. 16.7a–d. These landslides are associated with unstable slopes, loose soil materials, and highly weathered rocks that can induce landslides with low seismic activity considered uncertain landside.

16.5 Conclusions

The present study identified the landside zone by integrated image processing techniques and compared it with field observation as well as high-resolution satellite images for better accuracy. Further, the landslide area is also compared with active tectonics features and seismologic parameters to understand their influence on their occurrence. The study clearly indicates that most of the landslides are associated with shale, phylitte, etc. rocks that are highly weathered can easily disintegrate. Further, it is also observed that the landslide zones coincide with active tectonic evidence and resemble recent seismic activity. These observations suggest that the landslides may occur in such an underlying lithological condition even if they face low-frequency seismic vibration. The study infers that the possibility of landslides is uncertain and has the most potential in this active thrust zone due to unpredictable seismic activity rather than common occurrence during the monsoonal season. Hence, continuous

monitoring of this type of area using high-resolution satellite images and digital image processing techniques can help to minimize the landslide impact.

Acknowledgements The authors are thankful to SRM Institute of Science and Technology for providing all necessary facilities and constant encouragement for doing this research work. Also the authors are thankful to SRM Institute of Science and Technology, Kattankulathur for sanctioning the Pilot Research project on Selective Excellence Program.

References

Al-Wassai FA, Kalyankar NV, Al-Zuky Ali A (2011) The IHS transformations based image fusion. Int J Adv Res Comput Sci 2(5):1–10

Anbalagan R, Kumar R, Lakshmanan K, Parida S, Neethu S (2015) Landslide hazard zonation mapping using frequency ratio and fuzzy logic approach, a case study of Lachung Valley, Sikkim. Geoenvironmental Disasters 2:6

Anbarasu K, Sengupta A, Gupta S, Sharma SP (2010) Mechanism of activation of the Lanta Khola landslide in Sikkim Himalayas. Landslides 7:135–147

Arnous MO, Sultan YM (2014) Geospatial technology and structural analysis for geological mapping and tectonic evolution of Feiran-Solaf metamorphic complex, South Sinai, Egypt. Arab J Geosci 7:3023–3049

Bose S, Mandal N, Acharyya SK, Ghosh S, Saha P (2014) Orogen-transverse tectonic window in the Eastern Himalayan fold belt: a superposed buckling model. J Struct Geol 66:24–41

Che VB, Fontijn K, Ernst GGJ, Kervyn M, Elburg M, Ranst EV, Suh CE (2012) Evaluating the degree of weathering in landslide prone soils in the humid tropics: the case of Limbe, SW Cameroon. Geoderma 170:378–389

Chorley RJ, Schumm SA, Sugden DE (1985) Geomorphology. Methuen and Co Ltd., London, New York

Donnelly LJ, Culshaw MG, Bell FG, Tragheim D (2006) Ground deformation caused by fault reactivation: some examples. The Geological Society of London, IAEG

Dubey CS, Chaudhry M, Sharma BK, Pandey AC, Singh B (2005) Visualization of 3-D digital elevation model for landslide assessment and prediction in mountainous terrain: a case study of Chandmari landslide, Sikkim, Eastern Himalayas. Geosci J 9(4):363–373

Ghosh S, Sivakumar R (2018) Assessment of morphometric parameters for the development of Relative Active Tectonic Index and its significant for seismic hazard study: an integrated geoinformatic approach. Environ Earth Sci 77(17):600, 1–23

Ghosh TK, Viswanatham S (1991) Neotectonic analysis of Mendha river basin, Rajasthan, India. Int J Remote Sens 12(12):2585–2596

Ghosh AMN (1952) Preliminary notes on Rangit Valley coal fields, Western Sikkim. Ind Min 6(3):131–140

Jensen JR (2004) Introductory digital image processing: a remote sensing prospective. Prentice-Hall, Englewood Cliffs, p 526

Koukis G, Sabatakakis N, Nikolaou N, Loupasakis C (2005) Landslide hazard zonation in Greece. In: Proceedings of the open symposium on landslide risk analysis and sustainable disaster management by international consortium on landslides. Washington, USA

Lee S, Dan NT (2005) Probabilistic landslide susceptibility mapping in the Lai Chau province of Vietnam: focus on the relationship between tectonic fractures and landslides. Environ Geol 48:778–787

Mitra G, Bhattacharyya K, Mukul M (2010) The lesser Himalayan duplex in Sikkim: implications for variations in Himalayan shortening. J Geol Soc India 75:289–301

Miyagi T, Yamashina S, Esaka F, Abe S (2011) Massive landslide triggered by 2008 Iwate-Miyagi inland earthquake in the Aratozawa Dam area, Tohoku Japan. Landslides 2011(8):99–108
Mukul M, Jade S, Ansari K, Matin A (2014) Seismotectonic implications of strike–slip earthquakes in the Darjiling–Sikkim Himalaya. Curr Sci 106:198–210
Nath SK, Pal I, Shukla K, Pal DK, Raj A, Thingbaijam KS, Bansal BK (2007) Earthquake hazard zonation of Sikkim Himalaya using a GIS platform. Nat Hazards 45:333–377
Olgen MK (2004) Determining lineaments and geomorphic features using landsat 5-tm data on the Lower Bakirçay Plain, Western Turkey. Aegean Geogr J 13(2004):47–57
Pal I, Nath SK, Shukla K, Pal DK, Raj A, Thingbaijam KKS, Bansal BK (2008) Earthquake hazard zonation of Sikkim Himalaya using a GIS platform. Nat Hazards 45:333–377
Pandey A, Dabral PP, Chowdary VM, Yadav NK (2008) Landslide hazard zonation using remote sensing and GIS: a case study of Dikrong river basin, Arunachal Pradesh, India. Environ Geol 54:1517–1529
Pankaj A, Kumar P (2015) GIS-based Morphometric analysis of five major sub-watersheds of Song River, Dehradun District, Uttarakhand with special reference to landslide incidences. Arab J Geosci 8:6465–6482. https://doi.org/10.1007/s12517-014-1711-5
Pohl C, Van Genderen JL (1998) Multisensor image fusion in remote sensing: concepts, methods and applications (review article). Int J Remote Sens 19(5):823–854
Ramli MF, Yusof N, Yusoff MK, Juahir H, Shafri HZM (2010) Lineament mapping and its application in landslide hazard assessment: a review. Bull Eng Geol Environ 69:215–233
Regmi AD, Yoshida K, Dhital MR, Pradhan B (2014) Weathering and mineralogical variation in gneissic rocks and their effect in Sangrumba Landslide, East Nepal. Environ Earth Sci 71:2711–2727
Regmi AD, Yoshida K, Nagata H, Pradhan AS, Pradhan B, Pourghasemi HR (2013) The relationship between geology and rock weathering on the rock instability along Mugling-Narayanghat road corridor, Central Nepal Himalaya. Nat Hazards 66:501–532
Sabins FF (1997) Remote sensing principles and interpretation. Freeman, New Yok, p 494
Sarkar SS, Ali MA, Bhattacharya G (2012) Geology and mineral resources of Sikkim, Report, Geological Survey of India, West Bengal, Kolkata
Sharma LP, Patel N, Debnath P, Ghose MK (2012) Assessing landslide vulnerability from soil characteristics—a GIS-based analysis, Arab. J Geosci 5:789–796
Sharma LP, Patel N, Ghose MK, Debnath P (2013) Synergistic application of fuzzy logic and geoinformatics for landslide vulnerability zonation—a case study in Sikkim Himalayas, India. Appl Geomat 2013(5):271–284
Singh KK, Singh A (2016) Detection of 2011 Sikkim earthquake-induced landslides using neuro-fuzzy classifier and digital elevation model. Nat Hazards 83:1027–1044
Singh S (2005) Geomorphology, Prayag pustak bhawan, Allahabad, India
Sivakumar R, Ghosh S (2017) Earthquake hazard assessment through geospatial model and development of EaHaAsTo tool for visualization: an integrated geological and geoinformatics approach. Environ Earth Sci 76(12):442, 1–22
Sivakumar R, Ghosh S (2021) Assessment of the influence of physical and seismotectonic parameters on landslide occurrence: an integrated geoinformatic approach. Nat Hazard 108(3):2765–2811
Yuan R, Tang C, Deng Q (2015) Effect of the acceleration component normal to the sliding surface on earthquake-induced, landslide triggering. Landslides 12:335–344

Chapter 17
Landslide Susceptibility Zonation Mapping Using Frequency Ratio, Information Value Model, and Logistic Regression Model: A Case Study of Kohima District in Nagaland, India

Manish Yadav, Sanjit Kumar Pal, Prasoon Kumar Singh, and Neha Gupta

Abstract Landslide is one of the most dangerous natural hazards in hilly terrain areas and cause severe damage to life, property, and socio-economics. Proper study and guidelines are necessary to mitigate the disasters. The study of landslide mapping is very important for providing hazard and risk assessment. Kohima District of Nagaland, covers large areas with a steep slope and is susceptible to landslides under seismic zone-V. Over the past, many models have been developed to find the best approach for landslides susceptibility mapping. Among these, the statistical and the data-driven approaches are extensively popular, and they all are used to control the probability of futuristic landslide movement based on the past landslide. In the present study, frequency ratio (FR), Information Value Model (IVM), and Logistic Regression (LR) model are used to develop a landslide susceptibility map of Kohima District, Nagaland, using GIS spatial analysis techniques. A total of 356-landslide locations were identified, considering the small to the large polygon. Further, a total of 11 causative factors influencing the landslide were used for this study. The prepared landslide susceptibility maps (LSM) have been analysed using Success Rate Curve and Prediction Rate Curve. The Area Under the Curve (AUC) of the Success Rate Curve of FR, IVM, and LR models are 64%, 71.23%, and 82.5%, respectively, while Prediction Rate Curve is 61.5% for FR, 70.5% for IVM, and 79.6% of LR. So, Logistic Regression has given the best result in the study.

M. Yadav · S. K. Pal (✉)
Department of Applied Geophysics, Indian Institute of Technology (ISM), Dhanbad 826004, India
e-mail: sanjitism@gmail.com

P. K. Singh
Department of Environmental Science and Engineering and CWRM, Indian Institute of Technology (ISM), Dhanbad 826004, India

N. Gupta
Department of Earthquake Science and Engineering, Indian Institute of Technology Roorkee, Roorkee 247667, India

P. Thambidurai and T. N. Singh (eds.), *Landslides: Detection, Prediction and Monitoring*,
https://doi.org/10.1007/978-3-031-23859-8_17

Keywords Landslides susceptibility mapping · Logistic regression · Topographic wetness index · Frequency ratio · Drainage density · Information value model · Landslides

17.1 Introduction

Landslides are regularly taking place in mountainous or hilly areas due to various factors, i.e., climatic, rainfall, geological, and earthquake (Dai et al. 2002). It is the most common geohazards that cause severe damage to life, property, and socio-economics all over the world. Rock, soil, and debris lose their shear strength on the slope and fall due to gravity. Landslide susceptibility mapping identify the area which has a higher probability of landslide occurrence in future. This map is combination of different factors which influence landslides and it classifies are into low to high zone. This susceptibility map helps us find risk reduction, risk assessment, and mitigation efforts that can decrease losses. According to the world bank report in 2005, the landslide susceptible area is approximately 3.7 million km^2, affecting 300 million people's lives at risk (CRED 2019). In India, it has been rapidly rising in recent years. Remote sensing technology and GIS have been used widely to detect and classify landslides in recent years. The geospatial technology has capable of covering large areas in an advanced manner on a timely basis. Satellite data can help identify all the information for the factors that influence landslides, such as geology, slope, rainfall, Aspect, LULC, etc. However, the amount of information varies from time to time. Depending on the size of the landslide, the tonal difference with surroundings, geographic location, and experience of the interpreter, various approaches have been followed with varying degrees.

In the last few decades, GIS technology is used by many researchers for Landslide susceptibility maps (LSM). There are two approaches qualitative and quantitative (Dai et al. 2002). A qualitative model is a subjective approach that depends on expert's opinion where the idea of ranking and weighting of all the influenced factors is considered (Chen et al. 2016; Sarkar et al. 2008; Sarkar and Kanugo 2004; Pardeshi et al. 2013; Westen and Lulie Getahun 2003). Analytical hierarchy process and weighted linear combination are extensively used qualitative models (Basu and Pal 2020; Chen et al. 2016; Pourghasemi et al. 2012). The quantitative models are based on statistical analysis which shows the numerical relationships between influenced factors and landslides. Multivariate and bivariate models are two widely applied statistical models (Süzen and Doyuran 2004). Frequency ratio (FR) model (Mondal and Mandal 2017; Youssef et al. 2015a) and logistic regression (LR) models (Zhang et al. 2018; Yilmaz 2009) are also extensively used statistical models for landslide studies.

We found that very few studies were carried out in the Kohima District of Nagaland, India. Previous studies used the Fuzzy gamma operator model (Sema et al. 2017) and the Information Value model (Kedovikho and Krishnaiah 2020) for Kohima Town. The present study uses the Logistic Regression, Frequency Ratio Model and

Information Value Model to predict landslides and create susceptibility maps for the whole district of Kohima. Combined bivariate statistical analysis using FR, IVM and LR has also been successfully attempted for landslide susceptibility mapping. The primary reason to utilise these models is that they are very accurate and effective models. Moreover, these modes can quickly process large data. Interestingly, R programming is also used in the logistic regression model for data processing.

17.2 Study Area

The study area Kohima district is a tectonically active region of Nagaland state of northeast India. It is located between 25°40′ N to 25.67° N Longitude and 94°07′ E to 94.12° E Latitude. It has an average elevation of between 800 to 1,500 m above MSL. Geologically, most of the area is covered with the Disang and Barial groups of rock. It has a humid subtropical climate. Temperature is pleasant and moderate, varying from 30 °C in summer and 5 °C in winter. The rainy season comes in May and continues till September. The abundant rainfall and cloudbursts lose the soil shear strength, which generally causes landslides in the area. The population of Kohimais grows at a 6% rate per annum. Currently, it has a population of 115,283 as per the 2011 census. Due to the growing population, the scarcity of land is increasing, which causes growth and settlement in a high hazardous prone area (Fig. 17.1).

17.3 Material and Models

A landslide zonation map is prepared using different thematic layers representing elevation, aspect, curvature, slope, land use land cover (LULC), drainage density, topographic wetness index (TWI), standard precipitation index (SPI), geomorphology, geology, drainage density, and rainfall. All the thematic maps have been generated using ASTER GDEM with 30 m spatial resolution and Landsat 8 (Table 17.1), and data were processed in ArcGIS 10.4 software. The prepared landslides inventory was verified using visual satellite image interpretation by Goggle Earth pro software and Geological Survey of India.

17.3.1 Methodology

The methodology in the present study involves a four-step; (a) landslide inventory mapping, (b) landslide causative factors, (c) modeling approaches, (d) model validation (Fig. 17.2).

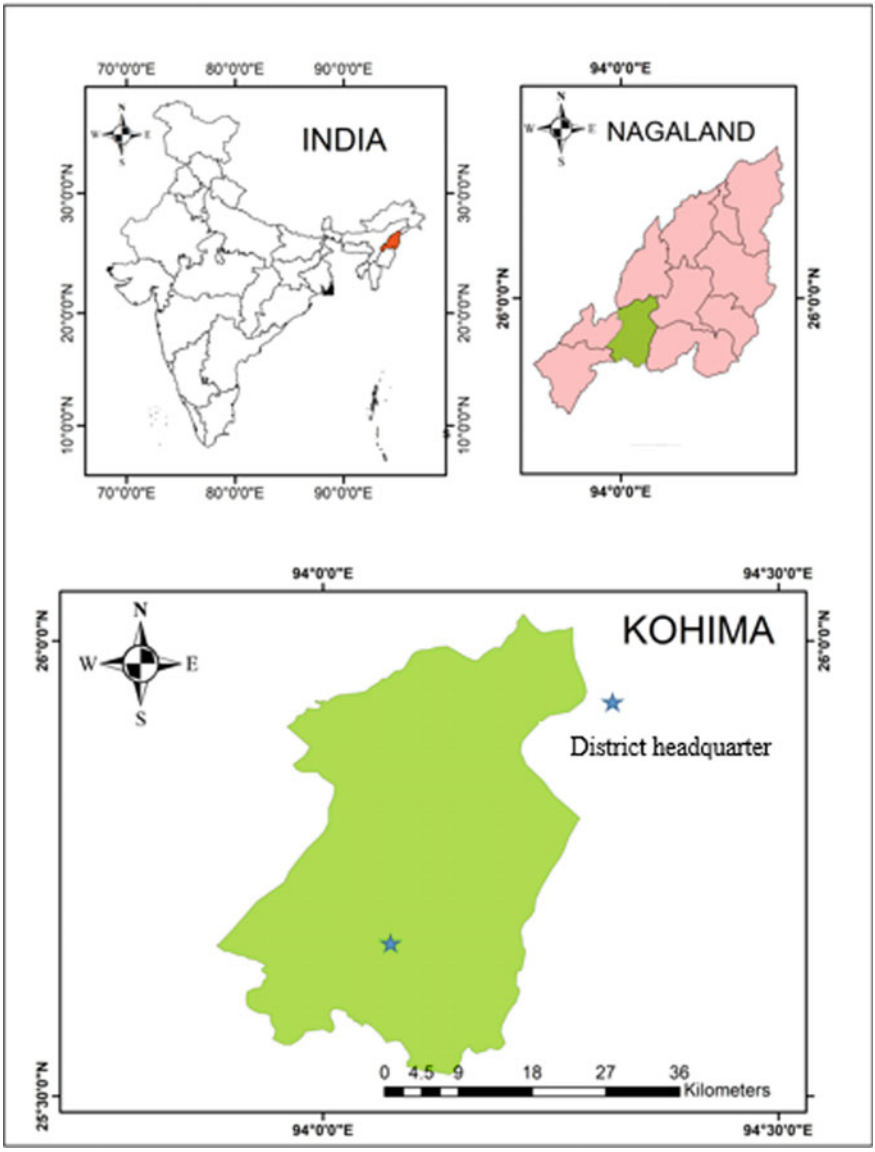

Fig. 17.1 The study area (Kohima, Nagaland, India)

17.3.1.1 Landslide Inventory Mapping

Important to know the exact location of the previous landslides to identify the future landslide events. Landslide inventory is the first necessary step to generating a landslide susceptibility map. There are various models to identify the previous landslide

Table 17.1 Data and sources of landslide causative factors

Data and source	Source link	Causative factor	Type	Scale
Aster GDEM	uurs.earthdata.nasa.gov	Elevation	Grid	30 × 30 m
		Aspect		
		Slope		
		Curvature		
		Drainage density		
		SPI		
		TWI		
National Environmental Research council (NERC),	Crudata.uea.ac.uk	Rainfall	Grid	30 × 30 m
Geological Survey of India (GSI)	bhukosh.gsi.gov.in	Geology	Polygon	30 × 30 m
		Geomorphology		
Environmental Systems Research Institute (Esri)	https://www.esri.com	Land use land cover	Grid	30 × 30 m
Google Earth, NASA catalogue, GSI bhukosh	google.earth.com	Landslide inventory	Polygon	

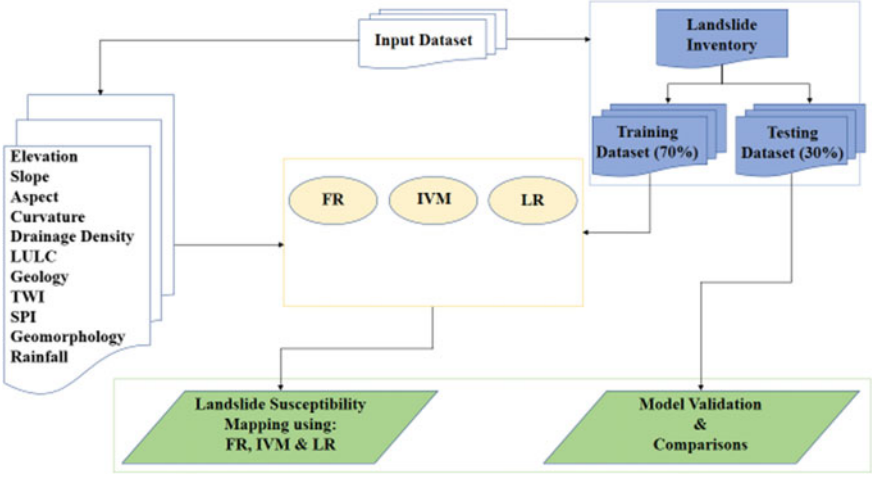

Fig. 17.2 Flow chart for methodology

locations through visual interpretation techniques of the satellite image, Google earth pro, and historical data (Fig. 17.3a). A total of 356 landslide polygons have been identified in 1,463 sq. km of the study area using the Google Earth Pro, NASA catalog, and GSI bhukosh (Fig. 17.3b). It is cross-checked with field investigation. Hence, the total landslide inventory was distributed in two sets: the training dataset 243 (70%)

for model building and the testing dataset 107 (30%) landslides used for checking model accuracy.

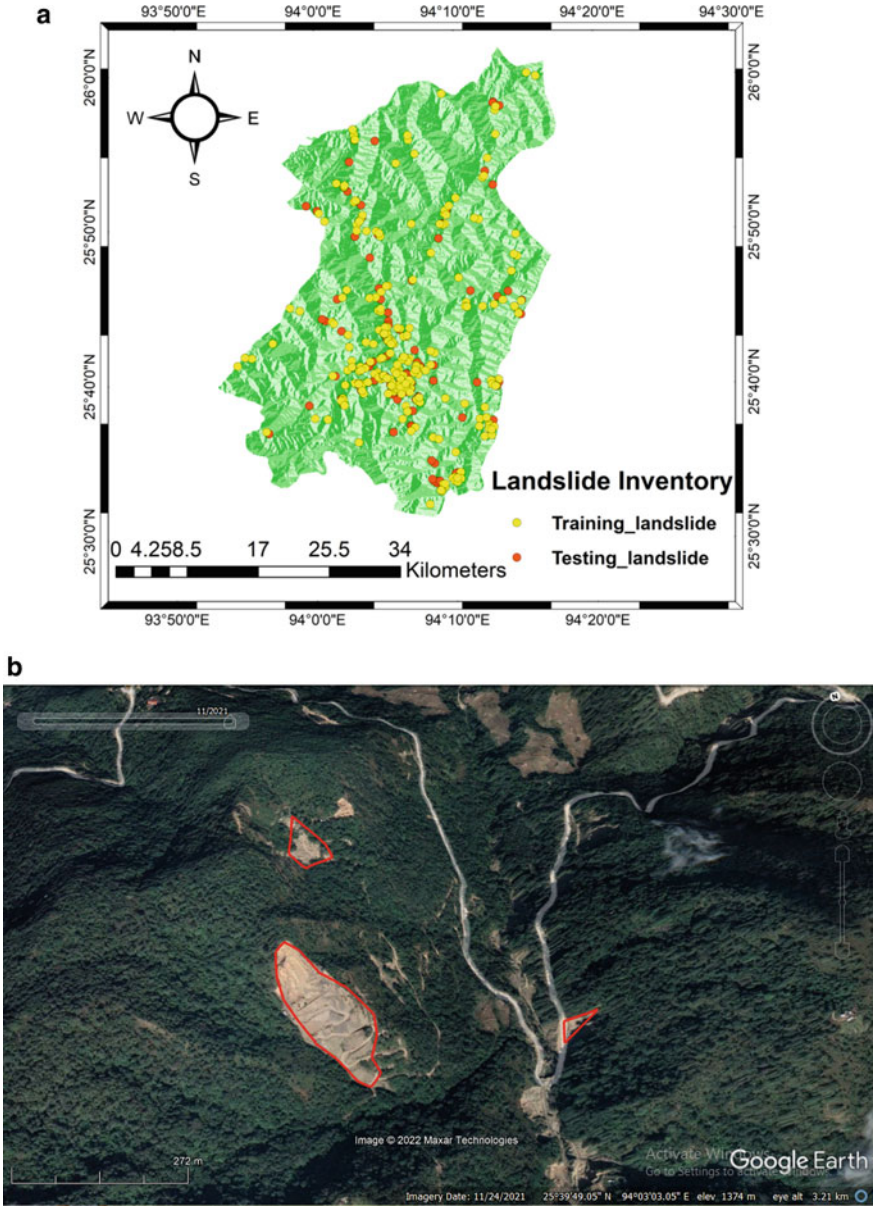

Fig. 17.3 **a** Landslide inventory map. **b** Google Earth image show failed slope at Kohima, in 2021

17.3.1.2 Landslide Causative Factors

In landslide susceptibility mapping, there is no any specific guideline to consider the landslide factors. In the present study, landslide factors are selected based on previous research work, data availability, and field investigation. Previous landslide locations are considered which have a higher probability of landslide occurrence in the future (Rasyid et al. 2016). Eleven causative factors have been selected, which have an important role in making a landslide susceptibility map. These causative factors are classified into topographic, hydrological, geological, and anthropogenic factors and are explained in the following sections.

Topographical Factors

The slope, elevation, aspect, and curvature are topographical factors. These factors have been generated using ASTER GDEM of 30 m spatial resolution with the help of spatial tools in ArcGIS10.4. Topographic factors controlled the spatial variation of hydrological conditions and slope instability (Yilmaz 2009). Geological /morphometric lineaments are surficial expression e.g., fault, joint, fracture, dykes, ridges etc. embodies the weaker zone (Pal et al. 2006, 2007; Narayan et al. 2017; Gupta et al. 2022) that may leads to landslides. An elevation map is a very important factor for the landslide. The elevation map is classified into 5 classes, i.e., from 167–780, 780–1,137, 1,137–1,584, 1,584–2,153 and 2,153–3,013 m (Fig. 17.4a). The slope is one of the most effective factors for landslides in Kohima. Soil shear depends on the slope; as slope increases, soil strength decreases, resulting in a landslide in most cases. The slope map is reclassified into 5 classes in Arc GIS using natural break. The slope of the map lies between 0° to 70°, as shown in Fig. 17.4b. Aspect ranges from 0° to 360° like compass direction. It depends on the area covered by sunlight, rainfall, soil, evapotranspiration, and precipitation changes. Aspect map is reclassified in 10 classes, i.e.., Flat (1°), N(0°–22°), NE(22°–67.5°), E(67.5°–112.5°), S(112.5°–157.5°), SE(157.5°–202.5°), SW(202.5°–247.5°), W(247.5°–292.5°), NE (292.5°–337.5°) and N(337.5–360°) (Fig. 17.4c). Curvature is a very important factor for LSM. Curvature map has been prepared using the ASTER GDEM at 30 m × 30 m resolution as a raster file. Arcs GIS spatial analyst is used for classification into 3 classes, i.e., concave, flat, and convex (Fig. 17.4e). Convex indicates positive curvature, concave curvature indicates negative curvature, and flat surface indicates zero.

Hydrological Factors

The main hydrological factors are drainage density, rainfall, TWI, and SPI. Drainage density is a very important controlling factor for landslide events. It means for a unit area, how many stream lengths are present. Most of the landslides take place in the locality of the river basin, which stimulates soil saturation and stream network

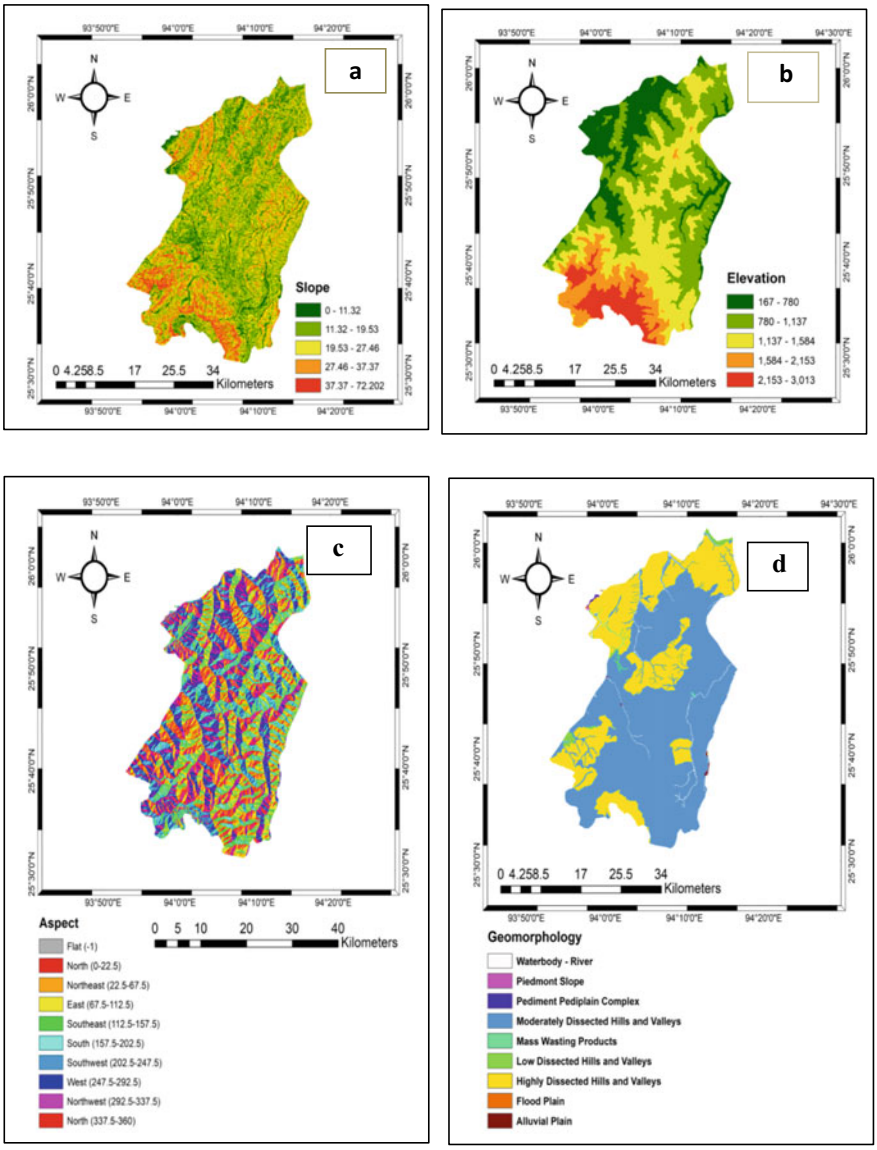

Fig. 17.4 Map of landslide factor of Kohima, **a** Elevation, **b** Slope, **c** Aspect, **d** geomorphology, **e** Curvature, **f** SPI, **g** drainage density, **h** TWI, **i** Geology, **j** Rainfall, **k** LULC

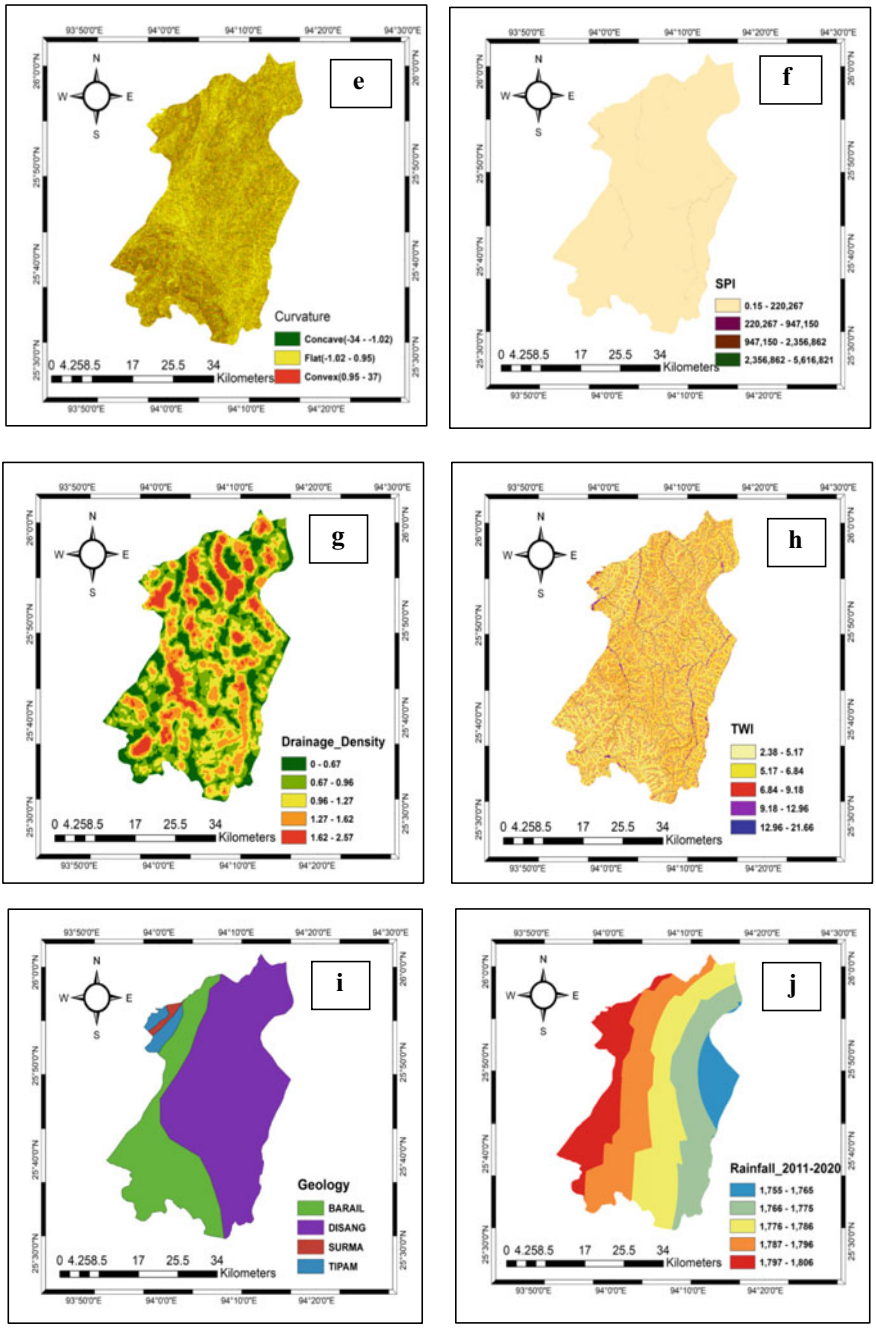

Fig. 17.4 (continued)

Fig. 17.4 (continued)

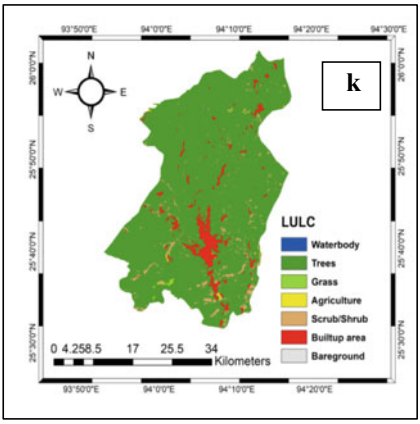

which minimizes slope soil cohesion. A drainage density map has been prepared using ASTER GDEM of 30 × 30 m resolution using the line density tool in ArcGIS (Fig. 17.4g). The maximum rainfall in the Kohima district comes in August and the district received average annual rainfall ranges from 1,700 to 1,800 mm. Rainfall data of 10 years (2011–2020) is taken from Natural Environment Research Council (NERC). The rainfall map is prepared using inverse distance weighted (IDW) interpolation in ArcGIS10.4 (Fig. 17.4j). The whole map is grouped into five classes (1,755–1,765 mm), (1,766–1,775 mm), (1,776–1,786 mm), (1,787–1,796 mm) and (1,797–1,806 mm). TWI (topographic wetness index) measures the wetness of the saturated zone due to surface runoff. TWI map is generated using DEM (Fig. 17.4h). The whole map has been classified into five classes (2.38–5.17), (5.17–6.84), (6.84–9.18), (9.18–12.96), and (12.96–21.66) following Natural breaks. The potential flow erosion erosive by SPI is measured give the idea of the potential flow erosion. Water and slope are dependent factors of SPI (Fig. 17.4f).

$$TWI = \ln \frac{As(Flow\ Accumulation\ sacled)}{\tan(slope)}$$

$$SPI = As * \mathrm{Tan}(slope)$$

where the slope is in degree and As is Flow accumulation.

Geology and Geomorphology

Geology is a significant factor in landslides occurrence. The vector file of geology is taken from Bhukosh, GSI (2021) and then it is converted into a raster file following the geology map is classified into four-group: (1) Barial, (2) Disang, (3) Tipam, and (4) Surma (Fig. 17.4i). Most of the parts have the Disang group and the Barial group. The geomorphologic data has been taken from the official website of GSI,

Bhukosh, in vector form; then, it is converted into raster in ArcGis10.4. There are two main geomorphologic features identified in the area, namely as follows, (i) highly-dissected hills and valleys, (ii) moderately-dissected hills and valleys, and (iii) low-dissected hills and valleys (Fig. 17.4d).

Land Cover Land Use (LULC)

The LULC is an important influencing factor for landslide mapping. LULC map is prepared from Environmental System Research Institute (ESRI) using the supervised machine learning technique from the open source data source. LULC of spatial resolution 10 m was taken from the ESRI website and also verified through Bhukosh, GSI; it was then converted into 30 m x 30 m. LULC map is classified into seven classes like, water, tree, grass, agriculture, shrub, built-up area, and bare ground. About 92.5% area is covered with trees, and 4.19% area is built-up area (Fig. 17.4k).

17.3.2 Modeling Approaches

17.3.2.1 Frequency Ratio (FR) Model

The frequency ratio (FR) is a bivariate statistical model which is very important for LSM that can quickly process a large amount of data (Lee and Talib 2005). The frequency ratio is the ratio of the landslide of each class to the area of each class of factor (Lee and Pradhan 2007). In the present work, the frequency ratio of each class of causative factor is calculated using Eq. (17.1) (Meena et al. 2019; Mondal and Mandal. 2017; Yalcin et al. 2011).

$$\mathrm{Fr} = \frac{M(i)}{N(i)} \tag{17.1}$$

where M(i) represents the ratio of landslide pixel of each class to the total landslide pixel of that factor and N(i) represents the ratio of the area of each class of factors to the total area of that factor. The ratio (M/A) shows each class's landslide density. The landslide susceptibility map is generated by summing weighted factor maps using Eq. (17.2) in ArcGIS.

$$LSM = \sum FR(i) = \mathrm{Fr}_1 + \mathrm{Fr}_2 + \mathrm{Fr}_3 + \cdots \tag{17.2}$$

FR value greater than 1 represents a higher probability of landslide in the area, while a value less than 1 shows a lower probability of landslide in the area.

17.3.2.2 Information Value Model (IVM)

Many researchers used the information ratio value (IVM) model and proved that IVM is a successful model; one of the best bivariate statistical models, IVM is used for the prediction of landslides on the correlation between landslides incidents and related. The IVM value is determined using the logarithm of the ratio of the landslide of each class to the area of each class of factors.

$$I(x) = log \frac{M(i)}{A(i)} \tag{17.3}$$

where M(i) represents the ratio of landslide pixel of each class to the total landslide pixel of that factor and N(i) represents the ratio of the area of each class of factors to the total area of that factor. The ratio (M/A) shows each class's landslide density. Causative factor and landslide incident directly relates to positive I(x) and represent the appearance of factors in landslide areas. The absence of factors in the landslide area represents Negative I (x).The landslide susceptibility map is generated by summing weighted factor maps using Eq. (17.4) in ArcGIS.

$$LSM = \sum I(xi) \tag{17.4}$$

17.3.2.3 Logistic Regression (LR)

LR is the best multivariate regression model that is a part of a large class of algorithm known as a generalized linear model (glm). It is composed of dependent and independent variables (Althuwaynee et al. 2014). In landslide susceptibility mapping, LR model gives the best fitting relationship between the presence and absence of landslide using dependent and independent variables. Dependent variable includes landslide data in the dichotomous forms like 0 (absence of landslide) or 1 (presence of landslide) and independent variable include eleven factor such as slope, elevation, LULC, aspect, geology, geomorphology, rainfall, drainage density, SPI, TWI (Ayalew and Yamagishi 2005; Althuwaynee et al. 2014). LR model gives the mathematical equation (Eq. 17.9) and calculates the coefficient of each factor (Table 17.3). Logit function of the mathematical equation gives the probability occurrence of landslide event. The logistic regression can be represented by the following Eq. (17.5) (Lee and Min 2001).

$$P = \frac{1}{1 + e^{-z}} \tag{17.5}$$

$$Z = \beta_0 + \beta_1 X_1 + \beta_2 X_2 + \cdots + \beta_n X_n \tag{17.6}$$

where p is the probability that ranges from 0 to 1 and z is the linear relation of independent factors. β_0 is the intercept and β_1, β_2, β_3,…,β_n are the coefficients that show the importance of independent factors of the logistic regression.

17.3.2.4 Model Validation and Accuracy

Model validation is the most necessary step to evaluating the accuracy of different statistical models. In the present study ROC and AUC of success rate and prediction rate curves are mainly used for validation (Yilmaz et al. 2012). Success rate curve is calculated after tabulating training landslide dataset (243) with reclassified landslide susceptibility map (LSM) and sorting them into descending order. Prediction rate curve is calculated using landslide testing dataset (106). AUC is plotted using a cumulative percentage (%) of landslide occurrence data against the cumulative percentage area. AUC value is varying from 0.5 to 1. AUC value closer to 0.5 represent poor prediction while closer to 1 shows perfect prediction by the models (Chen et al. 2014).

17.4 Results

17.4.1 Frequency Ratio (FR) Model

Frequency ratio of landslide factors of each class signifies the chances of landslide occurrence. All the weight of each factor is summed to get the final Landslide susceptibility map (Eq. 17.7). As it is observed from Table 17.2, elevation ranges from 1,137–15,584 m have a higher FR value (2.18) which is higher than 1, showing higher landslide occurrence. At the higher elevation 2,153–3,013 m, FR value is 0.06 which means a low probability of landslide occurrence. Slope class of $0^c-11.32^c$, 11.32^c–19.53^c, and 27.46^c–37.37^c have low FR value (0.64, 0.98, and 0.92 respectively) and higher FR value 1.19 and 1.24 for slope class of 19.53^c–27.37^c and 37.37^c–72.02^c respectively. Generally, the probability of landslide increases with increasing slope, but it may not be always right if strong slope material is present at a higher slope. In the case of aspect, south, southeast and southwest have higher FR value of 1.32, 1.08 and 1.09 respectively and the rest have lower FR value. In the case of curvature, flat surface indicates higher FR value of 1.07. However, concave and convex curvature indicates FR value less than 1 which shows low probability of landslide. In Rainfall, water-filled in soil grains and exerts high pore pressure that loses the soil strength. This soil strength is calculated by TWI. FR value is highest (1.16) with TWI class 5.17–6.84, which is the more landslide-prone area. Rainfall is the most triggering factor for landslide. It has a direct relationship with landslide. Rainfall class of 1,776–1,786 mm indicates the highest FR value of 1.39. The drainage density class of 0.96–1.27 m/sq.m exhibits a higher FR value of 1.25, while a lower FR value of

Table 17.2 Frequency ratio (FR) and Information Value (IVM) of classes of eleven influencing factors

Factor	Class	Landslide	% of Landslide occurrence	Class area	% of Class area	Frequency ratio	Information value (IVM)
Elevation	167–780	16,501.81	7.92	253,336	16.8	0.47	−0.32673
	780–1,137	53,848.02	25.83	550,473	36.5	0.71	−0.15013
	1,137–1,584	130,277.46	62.5	431,636	28.62	2.18	0.33918
	1,584–2,153	6,948.13	3.33	166,446	11.04	0.3	−0.51997
	2,153–3,013	868.52	0.42	106,188	7.04	0.06	−1.22786
Slope	0–11.32	22,581.43	10.83	252,982	16.84	0.64	−0.19158
	11.32–19.53	63,401.7	30.42	465,553	30.99	0.98	−0.00811
	19.53–27.46	73,823.89	35.42	428,004	28.49	1.24	0.09450
	27.46–37.37	33,872.14	16.25	265,934	17.7	0.92	−0.03717
	37.37–72.02	14,764.78	7.08	89,776	5.98	1.19	0.07381
Rainfall	1,755–1,765	9,553.68	4.60	110,125	7.34	0.63	−0.20284
	1,766–1,775	46,031.37	22.18	335,622	22.38	0.99	−0.00392
	1,776–1,786	79,903.51	38.49	416,109	27.75	1.39	0.14222
	1,787–1,796	57,322.08	27.62	389,624	25.99	1.06	0.02654
	1,797–1,806	15,633.29	7.53	254,628	16.98	0.44	−0.35298
SPI	0.15–220,267	207,575.4	99.58	1E + 06	99.86	1	0
	220,267–566,821	868.52	0.42	2,105	0.14	0.34	−0.47
TWI	2.38–5.17	91,194.22	43.75	623,412	41.5	1.05	0.02294
	5.17–6.84	88,588.67	42.5	552,371	36.77	1.16	0.06289
	6.84–9.18	20,844.39	10	221,708	14.76	0.68	−0.16903
	9.18–12.96	5211.1	2.5	84,566	5.63	0.44	−0.35251

(continued)

Table 17.2 (continued)

Factor	Class	Landslide	% of Landslide occurrence	Class area	% of Class area	Frequency ratio	Information value (IVM)
	12.96–21.66	2,605.55	1.25	20,191	1.34	0.93	−0.03150
Drainage Density	0 - 0.67	39,083.24	18.75	271,669	18.01	1.04	0.01738
	0.67–0.96	60,796.15	29.17	430,838	28.57	1.02	0.00899
	0.96- 1.27	68,612.79	32.92	395,692	26.24	1.25	0.09848
	1.27–1.62	33,003.62	15.83	290,849	19.29	0.82	−0.08567
	1.62–2.57	6,948.13	3.33	119,031	7.89	0.42	−0.37435
Geology	Surma Gp	868.52	0.42	12,697	0.84	0.49	−0.30581
	Tipam Sandstone Fm	3474.07	1.67	43,761	2.9	0.57	−0.24114
	Barail Gp	38,214.72	18.33	475,061	31.52	0.58	−0.23541
	Disang Fm	165,886.6	79.58	975,424	64.73	1.23	0.08972
Geomorphology	Moderately Dissected Hills and Valleys	173,703.3	83.33	1E+06	66.82	1.25	0.09589
	Low Dissected Hills and Valleys	1,737.03	0.83	15,701	1.04	0.8	−0.09668
	Piedmont Slope	0	0	174	0.01	0	0
	Mass Wasting Products	0	0	363	0.02	0	0
	Pediment Pediplain Complex	0	0	1,151	0.08	0	0
	Alluvial Plain	0	0	1,198	0.08	0	0
	Flood Plain	0	0	133	0.01	0	0
	Waterbody-River	4,342.58	2.08	14,736	0.98	2.13	0.32880
	Highly Dissected Hills and Valleys	28,661.04	13.75	466,875	30.96	0.44	−0.35247

(continued)

Table 17.2 (continued)

Factor	Class	Landslide	% of Landslide occurrence	Class area	% of Class area	Frequency ratio	Information value (IVM)
Aspect	Flat(−1)	0	0	8,959	0.59	0	0
	N (0–22.5)	11,290.713	5.42	101,778	6.75	0.8	−0.09549
	NE (22.5–67.5)	26,055.492	12.5	213,836	14.18	0.88	−0.05474
	E (67.5–112.5)	28,661.041	13.75	208,628	13.83	0.99	−0.00264
	S (112.5–157.5)	33,003.623	15.83	181,099	12.01	1.32	0.12008
	SE (157.5–202.5)	22,581.426	10.83	149,856	9.94	1.09	0.03751
	SW (202.5–247.5	24,318.459	11.67	162,666	10.79	1.08	0.034074
	W (247.5–292.5)	26,055.492	12.5	189,899	12.59	0.99	−0.00318
	NW (292.5–337.5)	24,318.459	11.67	196,853	13.05	0.89	−0.04877
	N (337.5–360)	12,159.229	5.83	94,505	6.27	0.93	−0.03111
Curvature	Concave (−34 to −1.02)	42,557.303	20.42	342,968	22.74	0.9	−0.04684
	Flat (−1.02 to 0.95)	126,803.39	60.83	859,673	57	1.07	0.02823
	Convex (0.95–37)	39,083.237	18.75	305,437	20.25	0.93	−0.03349
LULC	Waterbody	0	0	344	0.02	0	0
	Trees	127,671.91	61.25	1E+06	92.55	0.66	−0.17926
	Grass	868.51639	0.42	2,703	0.18	2.32	0.36637
	Agriculture land	0	0	1,621	0.11	0	0
	Scrub/Shrub	7816.6475	3.75	44,335	2.94	1.28	0.10571
	Builtup Area	72,086.86	34.58	63,184	4.19	8.25	0.91669
	Bareground	0	0	179	0.01	0	0

0.42 represents the drainage density class with 1.62–2.57 m/sq.m. This is due to the issue of groundwater condition; high drainage density areas are easy to fail due to increases in pore water pressure and weak strength of soil condition. Hence, higher drainage density causes quick surface runoff due to lower infiltration.

In the case of geology, more susceptible to landslide area is the Disang group offers an FR value 1.23 with 79.58% landslide. The lowest frequency ratio value 0.49 with a low landslide is for the Surma group. Barial group witnessed 18.33% landslide followed by a 0.58 FR value. In the case of geomorphology, the water body indicates a positive highest FR value of 0.46, which means very landslide-prone. Moderately dissected hills and valleys offer a positive FR value of 1.25 with 83.33% landslide occurrence. Considering the LULC, the built-up area is characterized by the highest FR value of 8.25 with 34.58% landslide, which means it has a very high risk for landslides. All the causative factors are integrated with ArcGIS10.4, and the final landslide susceptibility map (LSM) has been prepared. The prepared LSM is reclassified in five classes using the natural break method. LSM is used to find the area that are susceptible to landslide.

$$\begin{aligned} \text{LSM} = {} & \text{FR}_{\text{elevation}} + \text{FR}_{\text{slope}} + \text{FR}_{\text{aspect}} + \text{FR}_{\text{rainfall}} \\ & + \text{FR}_{\text{drainage density}} + \text{FR}_{\text{TWI}} + \text{FR}_{\text{SPI}} + \text{FR}_{\text{Geology}} \\ & + \text{FR}_{\text{geomorphology}} + \text{FR}_{\text{curvature}} + \text{FR}_{\text{LULC}} \end{aligned} \tag{17.7}$$

The LSM of frequency ratio model is classified into five classes like very low, low, moderate, high, and very high (Fig. 17.5b) using natural breaking method in ArcGIS. Very low and low susceptibility classes of LSM have covered 19.54 and 16.35% of total study area with 8.75 and 8.75% of total landslide. The remaining moderate, high, and very high susceptibility classes have covered 26.74, 31.12, and 6.245% of total study area with 18.33, 27.08, and 37.08% of total landslide (Table 17.4).

17.4.2 Information Value Model (IVM)

Each thematic layer was computed using the Information Value Model (IVM). The positive IVM value shows a high correlation with the presence of landslides, and the negative IVM shows an inverse correlation with the lack of landslides. The IVM information ratio value calculates the slope; the slope category 19.53–27.46° reveals the highest IVM value of 0.094, while the slope category 0–11.32° exhibits a minimum IVM value of −0.191. The slope above 40° could be considered highly vulnerable. Hence, slope angle and information value have positive relationships. Aspect map has the maximum IVM in the south (0.1201) while minimum IVM is found in the north (0.0955). A positive correlation was found in the south, southeast, and southwest, showing the landslide occurrence (0.12008, 0.03751, and 0.03407). The direction with negative IVM shows a low susceptibility for the landslide. In

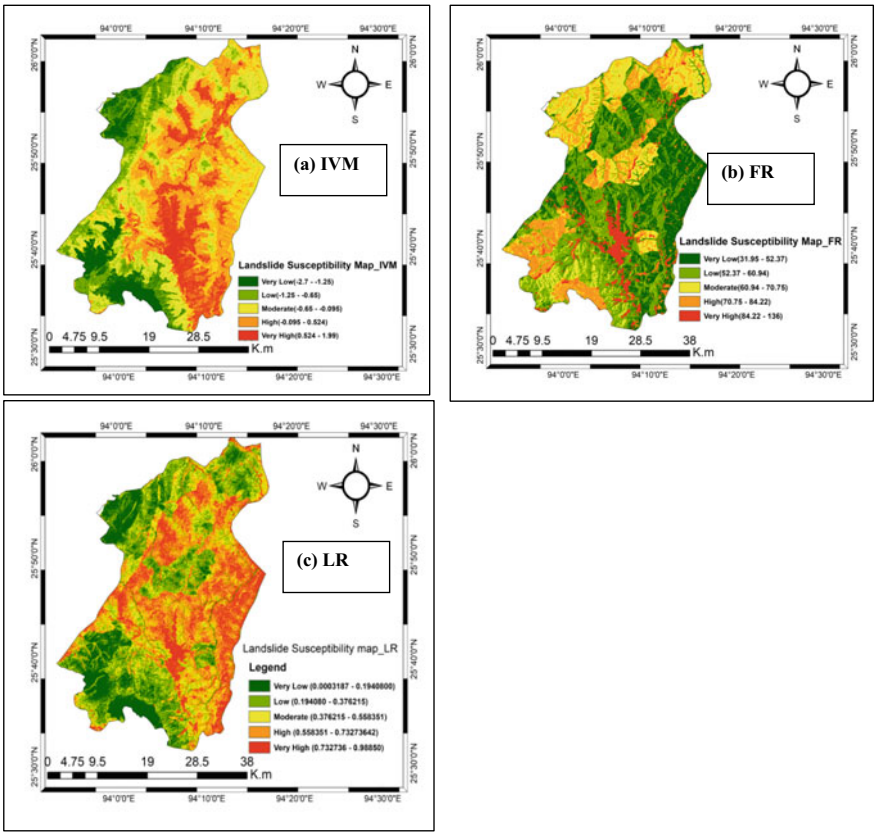

Fig. 17.5 Landslide susceptibility map using **a** IVM, **b** FR and **c** LR models

the case of curvature, the highest IVM of 0.2823 is found in flat, and the minimum IVM is found in concave. The maximum IVM values of 0.339, 0.089, 0.3288, 0.098, 0.9166, and 0.66289 are found in the case of elevation, geology, geomorphology, drainage density, LULC, TWI, respectively, indicating more susceptible to landslide (Table 17.2). All the factors were summed to get the final landslide susceptibility map and then reclassified into 5 different groups.

$$LSM = \sum I(xi) \tag{17.8}$$

The prepared landslide susceptibility map represents the likelihood of landslide incidents in the future. Higher landslide susceptibility indicates the higher the chance of risk. Landslide susceptibility values vary from −2.7 to 1.99. LSM map of Kohima is classified into five classes like very low, low, moderate, high, and very-high, which represent 15.88, 22.38, 28.23, 24.28, and 9.24% area, respectively (Fig. 17.5a). Very high susceptible zone is about 9.24% of the total area that witnessed 45% landslide,

while very low susceptibility is about 15.89% of the total area that witnessed 2.5% landslide (Table 17.4).

17.4.3 Landslide Susceptibility Using Logistic Regression (LR)

In landslide susceptibility mapping, LR model gives the best fitting relationship between the presence and absence of landslide using dependent and independent variables. LR model is used in R programming environment to generate landslide susceptibility map. LR coefficient of each factor is calculated. LR coefficients of aspect, slope, geology, and rainfall indicate positive correlation, while elevation, curvature, drainage density, geomorphology, SPI, TWI, and LULC indicate negative correlations (Table 17.3). Finally, landslide susceptibility map is prepared using the mathematical Eq. (17.9), that predict the probability of landslide occurrence (Fig. 17.5c). Predication curve, i.e., S-curves of drainage, TWI, SPI, Rainfall, and LULC exhibit a negative relationship with a landslide; while S-curves of curvature, aspect, elevation, geology, and geomorphology indicate a positive relationship with the landslide.

$$\begin{aligned} \mathrm{LR} = {} & (\text{slope} \times 0.03688) + (\text{aspect} \times 0.0006562) - (\text{curvature} \times 0.0312) \\ & - (\text{TWI} \times 0.2414) - (\text{elevation} \times 0.001266) - (\text{drainage density} \times 1.235) \\ & + (\text{rainfall} \times 0.00762) - (\text{SPI} \times 0.0000026) - (\text{geomorphology} \times 0.1989) \\ & + (\text{geology} \times 0.000002) - (\text{LULC} \times 0.00762) - 9.776 \end{aligned} \tag{17.9}$$

Table 17.3 Result of LR model

Factors	β	S.E	Exp. β	df
Constant	–9.776	23.51	5.67E+5	1
Elevation	−0.001266	3.276e−04	0.998	1
Aspect	0.0006562	1.043e−03	1.0006	1
Slope	0.03688	1.081e−02	1.0375	1
Curvature	−0.0312	5.177e−02	0.7319	1
Drainage density	−1.235	3.534e−01	0.290	1
Geology	0.000002	6.237e−07	1.000002	1
Geomorphology	−0.1989	3.653e−02	0.8196	1
LULC	−0.00762	2.689e−08	0.9924	1
Rainfall	0.00762	1.301e−02	1.0076	1
SPI	−0.0000026	1.871e−06	0.9999	1
TWI	−0.2414	6.730e−02	0.7855	1

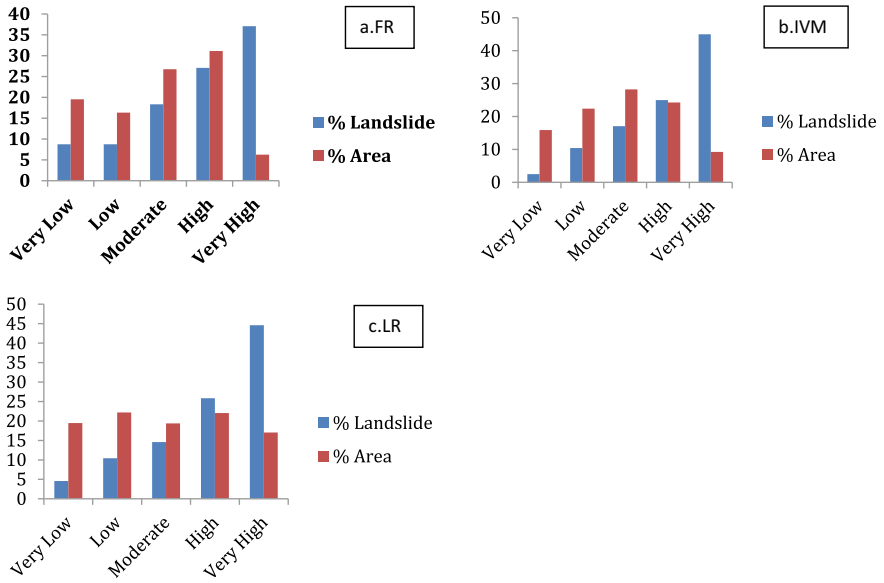

Fig. 17.6 The bar graph analysis of LSM: **a** FR; **b** IVM; **c** LR

The LSM of logistic regression model is classified into five classes like very-low, low, moderate, high, and very-high (Fig. 17.6) using natural breaking method in ArcGIS. Very low and low susceptibility classes of LSM have covered 19.48 and 22.19% of total study area with 4.5 and 10.41% of total landslide. The remaining moderate, high, and very high susceptibility classes have covered 19.38, 22.04, and 17.04% of total study area with 14.5, 25.83, and 44.583% of total landslide (Table 17.4).

17.4.4 Model Validation

Validation is the most necessary and last step in evaluating the accuracy of any model. Different statistical models such as FR, IVM and LR were validated using ROC and AUC. Success rate curve is calculated after tabulating training landslide dataset (243) with reclassified landslide susceptibility map (LSM) and sorting them into descending order. Prediction rate curve is calculated using landslide testing dataset (106). The landslide training dataset with 243 landslide points is tabulated with a prepared reclassified landslide susceptibility map to calculate the success rate curve. The LR model shows the best accuracy than FR and IVM. LR model exhibits the highest AUC value of 0.825. AUC is plotted using the cumulative percentage of landslide occurrence to the cumulative percentage area. In the present study, the AUC values of prediction rate curve for LR, FR, and IVM are 0.82, 0.64, 0.72, respectively (Fig. 17.7).

Table 17.4 % of landslide and % of area of each LSM classes of different models

FR	Class	Range	Landslide	% Landslide	Area	% Area
	Very low	31.95–52.37	18,263	8.75	292,849	19.54
	Low	52.37–60.94	18,263	8.75	245,025	16.35
	Moderate	60.94–70.75	38,265	18.333	400,703	26.74
	High	70.75–84.22	56,528	27.083	466,318	31.12
	Very high	84.22–136	77,400	37.083	93,581	6.245
IVM	Very low	(−2.7)–(−1.25)	5218	2.5	238,231	15.9
	Low	(−1.25)–(−0.65)	21,742	10.417	335,378	22.38
	Moderate	(−0.65)–(−0.095)	35,656	17.083	423,093	28.24
	High	(−0.095)–(0.524)	52,180	25	363,819	24.28
	Very high	0.524–1.99	93,923	45	138,596	9.25
LR	Very low	0.0003187–0.19408	9,566.3	4.5833	291,850	19.48
	Low	0.19408–0.376215	21,742	10.417	332,443	22.19
	Moderate	0.376215–0.558351	30,438	14.583	290,350	19.38
	High	0.558351–0.7327	53,919	25.833	330,223	22.04
	Very high	0.7327–0.98850	93,054	44.583	255,348	17.04

17.5 Discussion and Conclusions

Landslides are one of the most dangerous natural hazards in mountainous terrain areas, which cause severe damage to life, property, and socio-economics. Due to the growing population, the scarcity of land is increasing, which causes growth and settlement in high hazardous areas. Many building structures are constructed without proper regulations and guidelines in the highly landslide-prone area, which is dangerous for human lives in the seismically active region. The previous studies investigated the landslide area covering only some parts of the Kohima town using the Fuzzy Gamma operator model and IVM. The present study considered the whole Kohima district using a combined bivariate statistical analysis comprising FR, IVM and LR approaches. The landslide susceptibility map (LSM) prepared using the FR, IVM and LR models exhibit 6.24, 9.25 and 17.04% of the total area prone to landslides. The ROC curve of success rate and prediction rate of LR model indicate the highest prediction performance (82.5%) followed by IVM (71.23%) and FR (64%).The landslide testing dataset also indicates the highest prediction rate variable of LR (79.6%) followed by IVM (70.5%) and FR (61.5%). In general, the study shows that the LR model is best among others.

In the present study, eleven thematic maps of elevation, aspect, slope, geology, rainfall curvature, drainage density, geomorphology, SPI, TWI, and LULC were generated using ASTER DEM data in ArcGIS software. LR model offers the highest success rate and prediction rate curve than FR and IVM. Moreover, this study has some limitations; we could include lineament density and road network for better

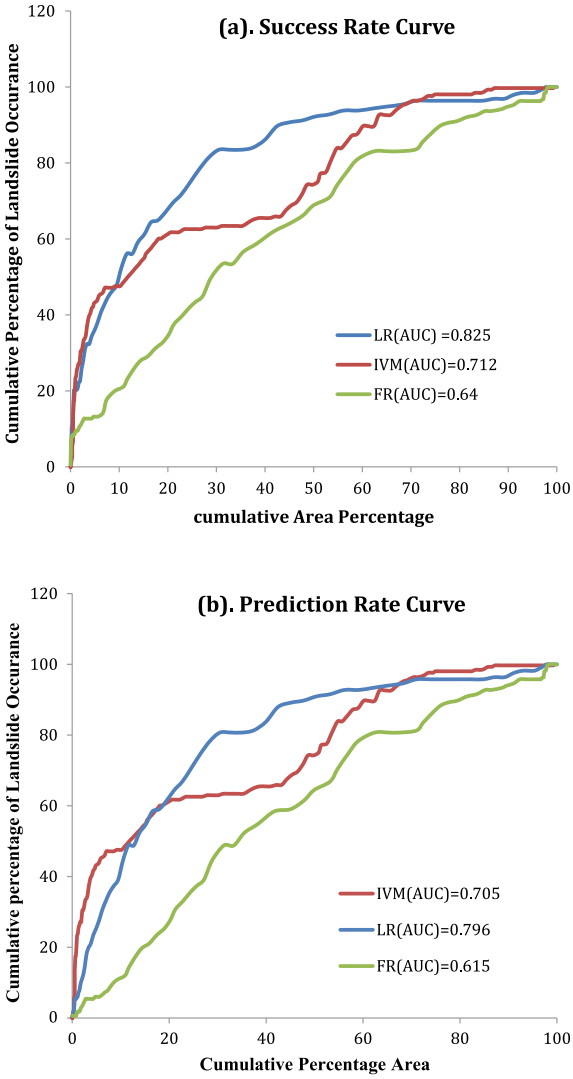

Fig. 17.7 Model validation using: **a** Success rate curve; and **b** Prediction rate curve

accuracy. Before construction begins, a detailed geotechnical investigation should be carried out in the highly landslide susceptible areas identified in the present study. This prepared LSM will be helpful to find out risk reduction, risk assessment, and mitigation efforts. This study will benefit town planners and civil engineers for sustainable land-use planning by making new guidelines and regulations for building structures. Early warning systems can be set up in the highly landslide susceptible areas identified in the present study.

Acknowledgements The authors are thankful to Prof. Thambidurai. P, Prof. T.N. Singh and Prof. S.P. Pradhan, Editors of the Springer Book entitle "Technological Development in Landslide - Detection, Prediction and Monitoring," for giving the opportunity to publish and valuable suggestions for improvements. The authors want to thank the Geological Survey of India (GSI), Environmental Systems Research Institute(ESRI), Indian Meteorological Department (IMD), National Environmental Research Council (NERC), The Indian Space Research Organisation (ISRO), AND The National Aeronautics and Space Administration (NASA). The authors are also thankful to the Director, IIT (ISM), Dhanbad, and the Director. SKP wishes to thank DST, Project No. DST/TDT/SHRI-16/2021(C&G); No. SB/S4/ES-640/2012; ISRO, Department of Space, Government of India, Project No. ISRO/RES/630/2016-17; the Ministry of Coal, Government of India for funding Project No. CMPDI/B&PRO/MT-173 and Project No. CIL(20)/2021-2022/845/ESE.

References

Achour Y, Pourghasemi HR (2020) How do machine learning techniques help in increasing accuracy of landslide susceptibility maps? Geoscience Front 11:871–883

Ada M, San BT (2018) Comparison of machine-learning techniques for landslide susceptibility mapping using two-level random sampling (2LRS) in Alakir catchment area, Antalya, Turkey. Nat Hazards 90(1):237–263

Ahlmer AK, Cavalli M, Hansson K, Koutsouris AJ, Crema S, Kalantari Z (2018) Soil moisture remote-sensing applications for identification of flood-prone areas along transport infrastructure. Environ Earth Sci 77(14):1–17

Aier I, Singh MP, Thong GT et al (2012) Instability analyses of Merhülietsa slide, Kohima, Nagaland. Nat Hazards 60:1347–1363. https://doi.org/10.1007/s11069-011-9913-6

Akgün A, Türk N (2011) Mapping erosion susceptibility by a multivariate statistical method: a case study from the Ayvalık region, NW Turkey. Comput Geosci 37(9):1515–1524

Akgun A, Dag S, Bulut F (2008) Landslide susceptibility mapping for a landslide-prone area (Findikli, NE of Turkey) by likelihood-frequency ratio and weighted linear combination models. Environ Geol 54(6):1127–1143

Al-Juaidi AE, Nassar AM, Al-Juaidi OE (2018) Evaluation of flood susceptibility mapping using logistic regression and GIS conditioning factors. Arab J Geosci 11(24):1–10

Althuwaynee OF, Pradhan B, Park HJ, Lee JH (2014) A novel ensemble decision tree-based Chi-squared Automatic Interaction Detection (CHAID) and multivariate logistic regression models in landslide susceptibility mapping. Landslides 11(6):1063–1078

Althuwaynee OF, Pradhan B, Ahmad N (2015) Estimation of rainfall threshold and its use in landslide hazard mapping of Kuala Lumpur metropolitan and surrounding areas. Landslides 12(5):861–875

Amiri M, Pourghasemi HR, Ghanbarian GA, Afzali SF (2019) Assessment of the importance of gully erosion effective factors using Boruta algorithm and its spatial modelling and mapping using three machine learning algorithms. Geoderma 340:55–69

Anbalagan R (1996) Landslide hazard and risk assessment mapping of mountainous terrains—a case study from Kumaun Himalaya, India. Eng Geol 43:237–246

Anbalagan R, Kumar R, Lakshmanan K, Parida S, Neethu S (2015) Landslide hazard zonation mapping using frequency ratio and fuzzy logic approach, a case study of Lachung Valley, Sikkim. Geoenviron Dis 2(1):1–17

Arabameri A, Pradhan B, Pourghasemi HR, Rezaei K, Kerle N (2018) Spatial modelling of Gully erosion using GIS and R programing: A comparison among three data mining algorithms. Appl Sci 8(8):1–21

Arora MK, Das Gupta AS, Gupta RP (2004) An artificial neural network approach for landslide hazard zonation in the bhagirathi (Ganga) valley, Himalayas. Int J Remote Sens 25(3):559–572

Ayalew L, Yamagishi H (2005) The application of GIS-based logistic regression for landslide susceptibility mapping in the Kakuda-Yahiko Mountains, Central Japan. Geomorphology 65(1–2):15–31

Ayalew L, Yamagishi H, Ugawa N (2004) Landslide susceptibility mapping using GIS-based weighted linear combination, the case in Tsugawa area of Agano River, Niigata Prefecture, Japan. Landslides 1(1):73–81

Ba Q, Chen Y, Deng S, Yang J, Li H (2018) A comparison of slope units and grid cells as mapping units for landslide susceptibility assessment. Earth Sci Inf 11(3):373–388

Basu T, Pal S (2020) A GIS-based factor clustering and landslide susceptibility analysis using AHP for Gish River Basin, India. In Environment, development and sustainability, vol 22, issue 5. Springer Netherlands

Behling R, Roessner S, Kaufmann H, Kleinschmit B (2014) Automated spatiotemporal landslide mapping over large areas using rapideye time series data. Remote Sens 6(9):8026–8055

Bilwa LM, Yanthan MA, Madesh P, Hutti B (2015) Identification of potential landslide hazard zonation mapping using geoinformatics for Kohima region, Nagaland, India. Int J Innovative Sci Eng Technol 2(11):1–10

Breiman L (2001) Random forests. Mach Learn 45(1):5–32

Bui DT, Tuan TA, Klempe H, Pradhan B, Revhaug I (2016) Spatial prediction models for shallow landslide hazards: a comparative assessment of the efficacy of support vector machines, artificial neural networks, kernel logistic regression, and logistic model tree. Landslides 13(2):361–378

Cama M, Conoscenti C, Lombardo L, Rotigliano E (2016) Exploring relationships between grid cell size and accuracy for debris-flow susceptibility models: a test in the Giampilieri catchment (Sicily, Italy). Environ Earth Sci 75(3):1–21

Castellanos EA, Van Westen CJ (2008) Qualitative landslide susceptibility assessment by multicriteria analysis: A case study from San Antonio del Sur, Guantánamo, Cuba. Geomorphology 94:453–466

Champatiray PK, Dimri S, Lakhera RC, Sati S (2007) Fuzzy-based method for landslide hazard assessment in active seismic zone of Himalaya. Landslides 4:101–111

Chang KT, Merghadi A, Yunus AP, Pham BT, Dou J (2019) Evaluating scale effects of topographic variables in landslide susceptibility models using GIS-based machine learning techniques. Sci Rep 9(1):1–21

Chen L, Mei L, Zeng B, Yin K, Shrestha DP, Du J (2020) Failure probability assessment of landslides triggered by earthquakes and rainfall: a case study in Yadong County, Tibet, China. Sci Rep 10(1):1–12

Chen W, Li Y (2020) GIS-based evaluation of landslide susceptibility using hybrid computational intelligence models. Catena 195(December 2019):104777

Chen W, Li W, Hou E, Zhao Z, Deng N, Bai H, Wang D (2014) Landslide susceptibility mapping based on GIS and information value model for the Chencang District of Baoji, China. Arab J Geosci 7(11):4499–4511

Chen W, Li W, Chai H, Hou E, Li X, Ding X (2016) GIS-based landslide susceptibility mapping using analytical hierarchy process (AHP) and certainty factor (CF) models for the Baozhong region of Baoji City, China. Environ Earth Sci 75(1):1–14

Chen W, Pourghasemi HR, Kornejady A, Zhang N (2017) Landslide spatial modeling: Introducing new ensembles of ANN, MaxEnt, and SVM machine learning techniques. Geoderma 305(June):314–327

Chen W, Shahabi H, Shirzadi A, Li T, Guo C, Hong H, Li W, Pan D, Hui J, Ma M, Xi M, Bin Ahmad B (2018a) A novel ensemble approach of bivariate statistical-based logistic model tree classifier for landslide susceptibility assessment. Geocarto Int 33(12):1398–1420

Chen W, Xie X, Peng J, Shahabi H, Hong H, Tien D, Duan Z, Li S, Zhu A (2018b) Catena GIS-based landslide susceptibility evaluation using a novel hybrid integration approach of bivariate statistical based random forest method. Catena 164(April 2017):135–149

Chen W, Zhang S, Li R, Shahabi H (2018c) Performance evaluation of the GIS-based data mining techniques of best-first decision tree, random forest, and naïve Bayes tree for landslide susceptibility modeling. Sci Total Environ 644:1006–1018

Chen W, Lei X, Chakrabortty R, Pal SC, Sahana M, Janizadeh S (2021) Evaluation of different boosting ensemble machine learning models and novel deep learning and boosting framework for head-cut gully erosion susceptibility. J Environ Manage 284:112015

Chen Y, Chen W, Chandra Pal S, Saha A, Chowdhuri I, Adeli B, Janizadeh S, Dineva AA, Wang X, Mosavi A (2022a) Evaluation efficiency of hybrid deep learning algorithms with neural network decision tree and boosting methods for predicting groundwater potential. Geocarto Int 37(19):5564–5584

Chen Y, Chen W, Janizadeh S, Bhunia GS, Bera A, Pham QB, Linh NTT, Balogun AL, Wang X (2022b) Deep learning and boosting framework for piping erosion susceptibility modeling: spatial evaluation of agricultural areas in the semi-arid region. Geocarto Int 37(16):4628–4654

Chen Z, Liang S, Ke Y, Yang Z, Zhao H (2019) Landslide susceptibility assessment using evidential belief function, certainty factor and frequency ratio model at Baxie River basin, NW China. Geocarto Int 34(4):348–367

Chung CJF, Fabbri AG (2003) Validation of spatial prediction models for landslide hazard mapping. Nat Hazards 30(3):451–472

Corominas J, Van Westen C, Frattini P, Cascini L, Fotopoulou S, Catani F, Van Den Eeckhaut M, Mavrouli O, Agliardi F, Pitilakis K, Winter MG, Pastor M, Ferlisi S, Tofani V, Smith JT, Herva J (2014) Recommendations for the quantitative analysis of landslide risk. Bull Eng Geol Environ 73(2):209–263

CRED. (2019). Human cost of disaster: an overview of the last 20 years (2000–2019), 28

Dai FC, Lee CF, Ngai YY (2002) Landslide risk assessment and management: an overview. Eng Geol 64:65–87

Devkota KC, Regmi AD, Pourghasemi HR, Yoshida K, Pradhan B, Ryu IC, Dhital MR, Althuwaynee OF (2013) Landslide susceptibility mapping using certainty factor, index of entropy and logistic regression models in GIS and their comparison at Mugling-Narayanghat road section in Nepal Himalaya. Nat Hazards 65(1):135–165

Dikshit A, Satyam N (2019) Probabilistic rainfall thresholds in Chibo, India: estimation and validation using monitoring system. J Mt Sci 16(4):870–883

Dikshit A, Sarkar R, Pradhan B, Acharya S, Alamri AM (2007) Spatial landslide risk assessment at 1–16

Dinpuia L, Singh TN, Kumar S (2015) Traditional landslides measurement practiced in Saiha Sinking Area, Southern Mizoram, North-East India. In: Lollino G. et al. (eds) Engineering geology for society and territory, vol 2. Springer, Cham. https://doi.org/10.1007/978-3-319-09057-3_111

Dou J, Yunus AP, Bui DT, Merghadi A, Sahana M, Zhu Z, Chen CW, Han Z, Pham BT (2020) Improved landslide assessment using support vector machine with bagging, boosting, and stacking ensemble machine learning framework in a mountainous watershed, Japan. Landslides 17(3):641–658

Du G, Zhang Y-S, Iqbal J, Yang ZH, Yao X (2017) Landslide susceptibility mapping using an integrated model of information value method and logistic regression in the Bailongjiang watershed, Gansu Province, China. J Mt Sci 14(2):249–268

Ergu D, Kou G, Peng Y, Shi Y (2011) A simple method to improve the consistency ratio of the pairwise comparison matrix in ANP. Eur J Oper Res 213(1):246–259

Fell R, Ho KKS, Lacasse S, Leroi E (2005) A framework for landslide risk assessment and management. In: International conference on landslide risk management, vol 31, Vancouver, Canada

Fell R, Corominas J, Bonnard C, Cascini L, Leroi E, Savage WZ (2008) Guidelines for landslide susceptibility, hazard and risk zoning for land-use planning. Eng Geol 102(3–4):99–111

Felicísimo ÁM, Cuartero A, Remondo J, Quirós E (2013) Mapping landslide susceptibility with logistic regression, multiple adaptive regression splines, classification and regression trees, and maximum entropy methods: a comparative study. Landslides 10(2):175–189

Foster I, Kesselman C (1999) The grid: blueprint for a new computing infrastructure. Morgan Kaufmann, San Francisco
Foster I, Kesselman C, Nick J, Tuecke S (2002) The physiology of the grid: an open grid services architecture for distributed systems integration. Technical report, Global Grid Forum
Froude MJ, Petley DN (2018) Global fatal landslide occurrence from 2004 to 2016. Nat Hazard Earth System Sci 18(8):2161–2181
Galli M, Guzzetti F (2007) Landslide vulnerability criteria: a case study from Umbria, central Italy. Environ Manage 40(4):649–664
Galli M, Ardizzone F, Cardinali M, Guzzetti F, Reichenbach P (2008) Comparing landslide inventory maps. Geomorphology 94(3–4):268–289
Ganesh T, Reddy P (2014) Testing the Consistency of Subjective Weights in Goal Programming—the Analytical Hierarchy Process Approach. Am J Appl Math Stat 2(3):92–95
Goetz JN, Brenning A, Petschko H, Leopold P (2015) Evaluating machine learning and statistical prediction techniques for landslide susceptibility modeling. Comput Geosci 81:1–11
Gupta N, Pal SK, Das J (2022) GIS-based evolution and comparisons of landslide susceptibility mapping of the East Sikkim Himalaya. Annals of GIS (2022): 1–26
Guthrie RH (2002) The effects of logging on frequency and distribution of landslides in three watersheds on Vancouver Island, British Columbia. Geomorphology 43(3–4):273–292
Guzzetti F, Carrara A, Cardinali M, Reichenbach P (1999) Landslide hazard evaluation: a review of current techniques and their application in a multi-scale study, Central Italy. Geomorphology 31(1–4):181–216
Guzzetti F, Reichenbach P, Ardizzone F, Cardinali M, Galli M (2006) Estimating the quality of landslide susceptibility models. Geomorphology 81(1):166–184
Guzzetti F, Mondini AC, Cardinali M, Fiorucci F, Santangelo M, Chang KT (2012) Landslide inventory maps: new tools for an old problem. Earth Sci Rev 112(1–2):42–66
Highland L (2008) Introduction the landslide handbook—a guide to understanding landslides. The landslide handbook—a guide to understanding landslides, 4–42
Highland LM, Bobrowsky P (2008) The landslide Handbook—a guide to understanding landslides. US Geol Surv Circular 1325:1–147
Hong H, Pourghasemi HR, Pourtaghi ZS (2016) Landslide susceptibility assessment in Lianhua County (China): a comparison between a random forest data mining technique and bivariate and multivariate statistical models. Geomorphology 259:105–118
Hong H, Liu J, Bui DT, Pradhan B, Acharya TD, Pham BT, Zhu AX, Chen W, and Ahmad BB (2018) Landslide susceptibility mapping using J48 Decision Tree with AdaBoost, Bagging and Rotation Forest ensembles in the Guangchang area (China). Catena 163(July 2017):399–413
Hong H, Liu J, Zhu AX (2020) Modeling landslide susceptibility using LogitBoost alternating decision trees and forest by penalizing attributes with the bagging ensemble. Sci Total Environ 718:137231
Jaafari A, Najafi A, Rezaeian J, Sattarian A, Ghajar I (2015) Planning road networks in landslide-prone areas: a case study from the northern forests of Iran. Land Use Policy 47:198–208
Jordanova G, Gariano SL, Melillo M, Peruccacci S, Brunetti MT, Auflič MJ (2020) Determination of empirical rainfall thresholds for shallow landslides in Slovenia using an automatic tool. Water 12(5)
Kanungo DP, Arora MK, Sarkar S, Gupta RP (2006) A comparative study of conventional, ANN black box, fuzzy and combined neural and fuzzy weighting procedures for landslide susceptibility Zonation in Darjeeling Himalayas. Eng Geol 85:347–366
Kanungo DP, Arora MK, Sarkar S, Gupta RP (2009) Landslide Susceptibility Zonation (LSZ) Mapping a review. J Asian Earth Sci 2(1):81–105
Karthik, Shivakumar BR (2017) Change detection using image differencing: a study over area surrounding Kumta, India. In: 2017 Second international conference on electrical, computer and communication technologies (ICECCT), 2017, pp 1–5. https://doi.org/10.1109/ICECCT.2017.8117851

Kaur H, Gupta S, Parkash S (2017) Comparative evaluation of various approaches for landslide hazard zoning: a critical review in Indian perspectives. Spat Inf Res 25(3):389–398
Kaur H, Gupta S, Parkash S, Thapa R, Gupta A, Khanal GC (2019) Evaluation of landslide susceptibility in a hill city of Sikkim Himalaya with the perspective of hybrid modelling techniques. Ann GIS 25(2):113–132
Kedovikho Y, Krishnaiah YV (2020) Assessing landslide vulnerability in Kohima city, Nagaland: A geospatial approach. Natl Geogr J India 66(3):274–287
Khosravi K, Nohani E, Maroufinia E, Pourghasemi HR (2016) A GIS-based flood susceptibility assessment and its mapping in Iran: a comparison between frequency ratio and weights-of-evidence bivariate statistical models with multi-criteria decision-making technique. Nat Hazards 83(2):947–987
Kirschbaum D, Stanley T (2018) Satellite-based assessment of rainfall-triggered landslide hazard for situational awareness. Earth's Future 6(3):505–523
Kirschbaum D, Stanley T, Zhou Y (2015) Spatial and temporal analysis of a global landslide catalog. Geomorphology 249:4–15
Klose M, Maurischat P, Damm B (2016) Landslide impacts in Germany: a historical and socioeconomic perspective. Landslides 13(1):183–199
Kumar R, Anbalagan R (2019) Landslide susceptibility mapping of the Tehri reservoir rim area using the weights of evidence method. J Earth Syst Sci 128(6):1–18
Lee S (2005) Application of logistic regression model and its validation for landslide susceptibility mapping using GIS and remote sensing data. Int J Remote Sens 26(7):1477–1491
Lee S, Min K (2001) Statistical analysis of landslide susceptibility at Yongin, Korea. Environ Geol 40(9):1095–1113
Lee S, Pradhan B (2007) Landslide hazard mapping at Selangor, Malaysia using frequency ratio and logistic regression models. Landslides 4(1):33–41
Lee S, Talib JA (2005) Probabilistic landslide susceptibility and factor effect analysis. Environ Geol 47(7):982–990
Lee J, Ibrahim M, Pradhan B, Park H (2018) Geomorphology modeling landslide susceptibility in data-scarce environments using optimized data mining and statistical methods. Geomorphology 303:284–298
Lee S, Lee MJ, Jung HS, Lee S (2019) Landslide susceptibility mapping using Naïve Bayes and Bayesian network models in Umyeonsan, Korea. Geocarto Int 35(15):1665–1679
Lei X, Chen W, Avand M, Janizadeh S, Kariminejad N, Shahabi H, Costache R, Shahabi H, Shirzadi A, Mosavi A (2020) GIS-based machine learning algorithms for gully erosion susceptibility mapping in a semi-arid region of Iran. Remote Sens 12(15):2478
Lei X, Chen W, Panahi M, Falah F, Rahmati O, Uuemaa E, Kalantari Z, Ferreira CSS, Rezaie F, Tiefenbacher JP, Lee S, Bian H (2021) Urban flood modeling using deep-learning approaches in Seoul, South Korea. J Hydrol 601:126684
Lin ML, Tung CC (2004) A GIS-based potential analysis of the land-slides induced by the Chi-Chi earthquake. Eng Geol 71(1–2):63–77
Liu X, Miao C (2018) Large-scale assessment of Landslide Hazard, vulnerability and risk in China. Geomat Nat Haz Risk 9(1):1037–1052
Lombardo L, Cama M, Conoscenti C, Märker M, Rotigliano E (2015) Binary logistic regression versus stochastic gradient boosted decision trees in assessing landslide susceptibility for multiple-occurring landslide events: application to the 2009 storm event in Messina (Sicily, southern Italy). Nat Hazards 79(3):1621–1648
Martha TR, Van Westen CJ, Kerle N, Jetten V, Kumar KV, Abdulwahid WM, Pradhan B, Anbalagan R, Dikshit A, Sarkar R, Pradhan B, Segoni S, Pradesh H, Salgado-ga GABMA, Catani F, Casagli N, Yariyan P, Avand M, Soltani F, … Alamri AM (2017) Landslide vulnerability and risk assessment for multi-hazard scenarios using airborne laser scanning data (LiDAR). Environ Earth Sci 5705(February 2016):1057–1076

Meena SR, Ghorbanzadeh O, Blaschke T (2019) A comparative study of statistics-based landslide susceptibility models: a case study of the region affected by the Gorkha earthquake in Nepal. ISPRS Int J Geo-Inform 8(2):94

Merghadi A, Yunus AP, Dou J, Whiteley J, ThaiPham B, Bui DT, Avtar R, Abderrahmane B (2020) Machine learning methods for landslide susceptibility studies: A comparative overview of algorithm performance. Earth Sci Rev 207:103225

Mishra V, Jain K (2019) Detection and monitoring of very slow landslides in vicinity of an artificial reservoir using advanced differential SAR interferometry: a case study of Tehri Region. India. https://doi.org/10.1002/essoar.10500835.1

Mishra M, Sarkar T (2020) A multistage hybrid model for landslide risk mapping: tested in and around Mussoorie in Uttarakhand state of India. Environ Earth Sci 79(19):1–24

Mohammadi A, Shahabi H, Bin Ahmad B (2018) Integration of insartechnique, google earth images and extensive field survey for landslide inventory in a part of Cameron highlands, Pahang, Malaysia. Appl Ecol Environ Res 16(6):8075–8091

Mondal S, Maiti R (2013) Integrating the analytical hierarchy process (AHP) and the frequency ratio (FR) model in landslide susceptibility mapping of Shiv-khola watershed, Darjeeling Himalaya. Int J Disaster Risk Sci 4(4):200–212

Mondal S, Mandal S (2017) Application of frequency ratio (FR) model in spatial prediction of landslides in the Balason river basin, Darjeeling Himalaya. Spatial Inform Res 25(3):337–350

Moore ID, Grayson RB, Ladson AR (1991) Digital terrain modelling: a review of hydrological, geomorphological, and biological applications. Hydrol Process 5(1):3–30

NASA (2020) Global landslide catalog. NASA Open Data Portal, 12–15

Naghibi SA, Ahmadi K, Daneshi A (2017) Application of support vector machine, random forest, and genetic algorithm optimized random forest models in groundwater potential mapping. Water Resour Manage 31(9):2761–2775

Narayan S, Sahoo DD, Pal SK, Kumar U, Pathak VK, MajumdarT J, Chouhan A (2017) Delineation of structural features over a part of the Bay of Bengal using total and balanced horizontal derivative techniques. Geocarto Int 32(1):1–16

Nguyen VV, Pham BT, Vu BT, Prakash I, Jha S, Shahabi H, Shirzadi A, Ba DN, Kumar R, Chatterjee JM, Tien Bui D (2019) Hybrid machine learning approaches for landslide susceptibility modeling. Forests 10(2):157

Nokendangba Chang C, Ezung M, Apon M et al (2021) Assessment of landslides along NH 29 in the Kevüza Area, Kohima, Nagaland. Indian Geotech J 51:841–860. https://doi.org/10.1007/s40098-021-00566-z

O'Brien RM (2007) A caution regarding rules of thumb for variance inflation factors. Qual Quant 41(5):673–690

Ozdemir A, Altural T (2013) A comparative study of frequency ratio, weights of evidence and logistic regression methods for landslide susceptibility mapping: Sultan mountains, SW Turkey. J Asian Earth Sci 64:180–197

Pal SK, Majumdar TJ, Bhattacharya AK (2006) Extraction of linear and anomalous features using ERS SAR data over Singhbhum Shear Zone, Jharkhand using fast Fourier transform. Int J Remote Sens 27(20):4513–4528

Pal SK, Majumdar TJ, Bhattacharya AK (2007) Usage of ERS SAR data over the Singhbhum shear zone, India for structural mapping and tectonic studies.Geocarto Int 22(4):285–295

Pardeshi SD, Autade SE, Pardeshi SS (2013) Landslide hazard assessment: recent trends and techniques. Springerplus 2(1):523

Paryani S, Neshat A, Javadi S, Pradhan B (2020) Comparative performance of new hybrid ANFIS models in landslide susceptibility mapping. Nat Hazards 103:1961–1988

Patil NS, Das J, Kumar A et al (2014) Probabilistic seismic hazard assessment of Himachal Pradesh and adjoining regions. J Earth Syst Sci 123:49–62. https://doi.org/10.1007/s12040-013-0378-8

Peethambaran B, Anbalagan R, Kanungo DP, Goswami A, Shihabudheen KV (2020) A comparative evaluation of supervised machine learning algorithms for township level landslide susceptibility zonation in parts of Indian Himalayas. CATENA 195:104751

Petley D (2012) Global patterns of loss of life from landslides. Geology 40(10):927–930
Pham BT, Bui DT, Pourghasemi HR, Indra P, Dholakia MB (2017) Landslide susceptibility assessment in the Uttarakhand area (India) using GIS: a comparison study of prediction capability of naïve bayes, multilayer perceptron neural networks, and functional trees methods. Theor Appl Climatol 128(1–2):255–273
Pham BT, Shirzadi A, Shahabi H, Omidvar E, Singh SK, Sahana M, Talebpour Asl D, Bin Ahmad B, Kim Quoc N, Lee S (2019) Landslide susceptibility assessment by novel hybrid machine learning algorithms. Sustainability 11(16):4386
Pham BT, Nguyen-Thoi T, Qi C, Phong TV, Dou J, Ho LS, Le HV, Prakash I (2020) Coupling RBF neural network with ensemble learning techniques for landslide susceptibility mapping. CATENA 195(July):104805
Pourghasemi HR, Pradhan B, Gokceoglu C (2012) Application of fuzzy logic and analytical hierarchy process (AHP) to landslide susceptibility mapping at Haraz watershed, Iran. Nat Hazards 63(2):965–996
Pourghasemi HR, Moradi HR, Fatemi Aghda SM (2013a) Landslide susceptibility mapping by binary logistic regression, analytical hierarchy process, and statistical index models and assessment of their performances. Nat Hazards 69(1):749–779
Pourghasemi HR, Pradhan B, Gokceoglu C, Mohammadi M, Moradi HR (2013b) Application of weights-of-evidence and certainty factor models and their comparison in landslide susceptibility mapping at Haraz watershed, Iran. Arab J Geosci 6(7):2351–2365
Pourghasemi HR, Teimoori Yansari Z, Panagos P, Pradhan B. (2018) Analysis and evaluation of landslide susceptibility: a review on articles published during 2005–2016 (periods of 2005–2012 and 2013–2016). Arab J Geosci 11(9):1–12
Pradhan B (2010) Landslide susceptibility mapping of a catchment area using frequency ratio, fuzzy logic and multivariate logistic regression approaches. J Indian Soc Remote Sens 38(2):301–320
Pradhan B (2013) A comparative study on the predictive ability of the decision tree, support vector machine and neuro-fuzzy models in landslide susceptibility mapping using GIS. Comput Geosci 51:350–365
Pradhan AMS, Kim YT (2017) Spatial data analysis and application of evidential belief functions to shallow landslide susceptibility mapping at Mt. Umyeon, Seoul, Korea. Bull Eng Geol Environ 76(4):1263–1279
Ram P, Gupta V, Devi M, Vishwakarma N (2020) Landslide susceptibility mapping using bivariate statistical method for the hilly township of Mussoorie and its surrounding areas, Uttarakhand Himalaya. J Earth Syst Sci 129(1):1–18
Rasyid AR, Bhandary NP, Yatabe R (2016) Performance of frequency ratio and logistic regression model in creating GIS based landslides susceptibility map at Lompobattang Mountain, Indonesia. Geoenviron Disasters 3(1):1–16
Ray K (2021) Maximum landslide deaths in India, 1–34
Różycka M, Migoń P, Michniewicz A (2017) Topographic Wetness Index and Terrain Ruggedness Index in geomorphic characterisation of landslide terrains, on examples from the Sudetes, SW Poland. Zeitschrift Für Geomorphologie, Supplementary Issues 61:61–80
Saaty RW (1987) The analytic hierarchy process-what it is and how it is used. Math Model 9(3–5):161–176
Saaty TL (1977) A scaling method for priorities in hierarchical structures. J Math Psychol 15:234–281
Saaty TL (1980) The analytical hierarchy process. McGraw-Hill, New York
Saaty TL (1994) Fundamentals of decision making and priority theory with analytic hierarchy process. RWS Publications, Pittsburgh
Saaty TL (2000) Decision making for leaders: the analytical hierarchy process for decisions in a complex world. RWS Publications, Pittsburgh
Saaty TL, Vargas LG (2001) Models, methods, concepts and applications of the analytic hierarchy process. Kluwer, Dordrecht

Saha AK, Gupta RP, Sarkar I, Arora KM, Csaplovics E (2005) An approach for GIS-based statistical landslide susceptibility zo- nation—with a case study in the Himalayas. Landslides 2(1):61–69
Saha S, Saha A, Hembram TK, Pradhan B, Alamri AM (2020a) Evaluating the performance of individual and novel ensemble of machine learning and statistical models for landslide susceptibility assessment at Rudraprayag district of Garhwal Himalaya. Appl Sci 10(11):3772
Saha S, Saha M, Mukherjee K, Arabameri A, Ngo PTT, Paul GC (2020b) Predicting the deforestation probability using the binary logistic regression, random forest, ensemble rotational forest, REPTree: a case study at the Gumani River Basin, India. Sci Total Environ 730:139197
Sarkar S, Kanungo DP (2004) An integrated approach for landslide susceptibility mapping using remote sensing and GIS. Photogrammetry Eng Remote Sen 70:617–625
Sarkar S, Kanungo DP, Patra AK, Kumar P (2008) GIS based spatial data analysis for landslide susceptibility mapping. J Mt Sci 5(1):52–62
Sema HV, Guru B, Veerappan R (2017) Fuzzy gamma operator model for preparing landslide susceptibility zonation mapping in parts of Kohima Town, Nagaland, India. Model Earth Syst Environ 3:499–514. https://doi.org/10.1007/s40808-017-0317-9
Shahabi H, Shirzadi A, Ghaderi K, Omidvar E, Al-Ansari N, Clague JJ, Geertsema M, Khosravi K, Amini A, Bahrami S, Rahmati O (2020) Flood detection and susceptibility mapping using sen-tinel-1 remote sensing data and a machine learning approach: hybrid intelligence of bagging ensemble based on k-nearest neighbor classifier. Remote Sens 12(2):266
Sharma K, Saraf AK, Das J et al (2018) Mapping and change detection study of Nepal-2015 earthquake induced landslides. J Indian Soc Remote Sens 46:605–615. https://doi.org/10.1007/s12524-017-0720-8
Shirzadi A, Bui DT, Pham BT, Solaimani K, Chapi K, Kavian A, Shahabi H, Revhaug I (2017) Shallow landslide susceptibility assessment using a novel hybrid intelligence approach. Environ Earth Sci 76(2):1–18
Singh KK, Singh A (2016) Detection of 2011 Sikkim earthquake-induced landslides using neuro-fuzzy classifier and digital elevation model. Nat Hazards 83(2):1027–1044
Soeters R, Westen VAN (1984) Slope instability recognition, analysis and zonation. In: Landslides, investigation and mitigation (Transportation Research Board, National Research Council), vol 247, pp 129–177
Süzen ML, Doyuran V (2004) A comparison of the GIS based landslide susceptibility assessment methods: Multivariate versus bivariate. Environ Geol 45(5):665–679
Tang X, Machimura T, Li J, Liu W, Hong H (2020) A novel optimized repeatedly random undersampling for selecting negative samples: A case study in an SVM-based forest fire susceptibility assessment. J Environ Manage 271(January):111014
Teja TS, Dikshit A, Satyam N (2019) Determination of rainfall thresholds for landslide prediction using an algorithm-based approach: Case study in the Darjeeling Himalayas, India. Geosciences 9(7):302
Tran TV, Alkema D, Hack R (2019) Weathering and deterioration of geotechnical properties in time of groundmasses in a tropical climate. Eng Geol 260:105221
Vakhshoori V, Pourghasemi HR, Zare M, Blaschke T (2019) Landslide susceptibility mapping using GIS-based data mining algorithms. Water 11(11):7–13
Van Tu T (2016) Preliminary assessments of debris flow hazard in relation to geological environment changes in mountainous regions, North Vietnam. Vietnam J Earth Sci 38(3):277–286
Van Westen CJ (2000) The modeling of landslide hazards using GIS. Surv Geophys 21(2–3):241–255
Van Westen CJ (2012) Landslide Inventory, Hazard and Risk Assessment in India From landslide inventories to landslide risk assessment; an attempt to support methodolo—gical development in India. September 2014
van Westen CJ, Lulie Getahun F (2003) Analyzing the evolution of the Tessina landslide using aerial photographs and digital elevation models. Geomorphology 54(1–2):77–89
Van Westen CJ, Soeters R (2006) Landslide hazard and risk zonation—why is it still so difficult? Bull Eng Geol Env 65(2):167–184

Vinod Kumar K, Lakhera RC, Martha TR, Chatterjee RS, Bhattacharya A (2008) Analysis of the 2003 Varunawat landslide, Uttarkashi, India using Earth observation data. Environ Geol 55(4):789–799

Wang Q, Li W, Chen W, Bai H (2015) GIS-based assessment of landslide susceptibility using certainty factor and index of entropy models for the Qianyang county of Baoji city, China. J Earth Syst Sci 124(7):1399–1415

Wang Y, Wu X, Chen Z, Ren F, Feng L, Du Q (2019) Optimizing the predictive ability of machine learning methods for landslide susceptibility mapping using smote for Lishui city in Zhejiang province, China. Int J Environ Res Public Health 16(3):368

Xiao T, Yin K, Yao T, Liu S (2019) Spatial prediction of landslide susceptibility using GIS-based statistical and machine learning models in Wanzhou County, Three Gorges Reservoir. China. Acta Geochimica 38(5):654–669

Xiaolong D, Li L, Tan Y (2017) Validation of spatial prediction models for landslide susceptibility mapping by considering structural similarity. ISPRS Int J Geo-Inform 6(4):103

Xu C, Dai F, Xu X, Lee YH (2012) GIS-based support vector machine modeling of earthquake-triggered landslide susceptibility in the Jianjiang River watershed, China. Geomorphology 145–146:70–80

Xu C, Xu X, Dai F, Wu Z, He H, Shi F, Wu X, Xu S (2013) Application of an incomplete landslide inventory, logistic regression model and its validation for landslide susceptibility mapping related to the May 12, 2008 Wenchuan earthquake of China. Nat Hazards 68(2):883–900

Yalcin A (2008) GIS-based landslide susceptibility mapping using analytical hierarchy process and bivariate statistics in Ardesen (Turkey): Comparisons of results and confirmations. CATENA 72(1):1–12

Yalcin A, Reis S, Aydinoglu AC, Yomralioglu T (2011) A GIS-based comparative study of frequency ratio, analytical hierarchy process, bivariate statistics and logistics regression methods for landslide susceptibility mapping in Trabzon, NE Turkey. CATENA 85(3):274–287

Yilmaz I (2009) Landslide susceptibility mapping using frequency ratio, logistic regression, artificial neural networks and their comparison: A case study from Kat landslides (Tokat-Turkey). Comput Geosci 35(6):1125–1138

Yilmaz C, Topal T, Süzen ML (2012) GIS-based landslide susceptibility mapping using bivariate statistical analysis in Devrek (Zonguldak-Turkey). Environ Earth Sci 65(7):2161–2178

Youssef AM, Maerz NH, Hassan AM (2009) Remote sensing applications to geological problems in Egypt: Case study, slope instability investigation, Sharm El-Sheikh/Ras-Nasrani area, southern Sinai. Landslides 6(4):353–360

Youssef AM, Al-Kathery M, Pradhan B (2015a) Landslide susceptibility mapping at Al-Hasher area, Jizan (Saudi Arabia) using GIS-based frequency ratio and index of entropy models. Geosci J 19(1):113–134

Youssef AM, Pradhan B, Jebur MN, El-Harbi HM (2015b) Landslide susceptibility mapping using ensemble bivariate and multivariate statistical models in Fayfa area, Saudi Arabia. Environ Earth Sci 73(7):3745–3761

Youssef AM, Pourghasemi HR, Pourtaghi ZS, Al-Katheeri MM (2016) Landslide susceptibility mapping using random forest, boosted regression tree, classification and regression tree, and general linear models and comparison of their performance at Wadi Tayyah Basin, Asir Region, Saudi Arabia. Landslides 13(5):839–856

Zhang T, Han L, Chen W, Shahabi H (2018) Hybrid integration approach of entropy with logistic regression and support vector machine for landslide susceptibility modeling. Entropy 20(11):1–24

Zhao C, Lu Z (2018) Remote sensing of landslides—a review. Remote Sens 10(2):8–13

Chapter 18
Unmanned Aerial Vehicles Technology for Slope Hazard Assessment, Monitoring, and Post Failure Management

Prakash Biswakarma, Ashutosh Kainthola, Ramesh Murlidhar Bhatawdekar, Varun Joshi, and Edy Tonnizam Mohamad

Abstract Alleviation of slope failures and landslides demands an in-depth investigation to ascertain the causes, triggers, existing and future instability aspects, along with the design of protection measures. Data collection for these studies usually involves field visits, which can be time-consuming and do not provide real-time data. Alternatively, geomorphic analysis can be carried out using high-resolution satellite images, which are plagued with the issue of resolution. Various methodologies for slope assessment and monitoring were reviewed. Field investigation using geotechnical methods is time-consuming and may not be possible to assess difficult terrain. Even though remote sensing methods are used for slope assessment and monitoring, there is a limitation to acquiring real-time data for a smaller area, which may not be cost-effective. Unmanned Aerial Vehicles (UAV) technology is improving faster and has an advantage over other technology. The present article elaborates on the advantages of using UAV to acquire such critical data. A thorough assessment, based on resolution (temporal and spatial), operation cost, type of data acquired, deployment of operation, and limitations, is presented here. A case towards using UAVs to ascertain the geotechnical data pertaining to the discontinuity distribution and properties has also been discussed. The available literature posits the superiority of

P. Biswakarma (✉) · V. Joshi
University School of Environment Management, Guru Gobind Singh Indraprastha University, New Delhi 110078, India
e-mail: pbiswakarma@ipu.ac.in

A. Kainthola
Geo-Engineering and ML Laboratory, Department of Geology, Institute of Science, Banaras Hindu University, Varanasi 221005, India

R. M. Bhatawdekar
Department of Mining Engineering, Indian Institute of Technology Kharagpur, Kharagpur 721302, West Bengal, India

R. M. Bhatawdekar · E. T. Mohamad
Geotropik—Centre of Tropical Geoengineering, Department of Civil Engineering, Universiti Teknologi Malaysia, Johor Bahru, 81310 Johor, Malaysia

P. Thambidurai and T. N. Singh (eds.), *Landslides: Detection, Prediction and Monitoring*,
https://doi.org/10.1007/978-3-031-23859-8_18

UAV-enabled field investigation and data collection. UAVs are especially useful for frontier areas where access can be an issue. UAV also safeguards the people at the site. UAV is also suitable for post-disaster management of landslides.

Keywords Disaster management · Real-time data · Remote sensing · Slope failures · Unmanned Aerial Vehicle (UAV)

18.1 Introduction

Researchers have used geotechnical investigations as a primary method for the slope monitoring and assessment during the last couple of decades (Sarkar et al. 2012; Francioni et al. 2015; Singh et al. 2015; Siddque and Pradhan 2018; Sharma et al. 2019; Pradhan et al. 2019; Shin et al. 2020; Komadja et al. 2021; Ansari et al. 2021). The geotechnical approach is a direct and reliable method for slope monitoring; however, it is time-consuming, expensive, and may pose logistical problems. Also, this method is not feasible under challenging terrains, and hence, the data acquisition may be scanty. The difficult terrains include poor roads, steep slopes, shadow portions, etc. The world has seen exceptional and rapid progress in the fields of remote sensing, geospatial data collecting, and mapping over the previous few decades. The technology is gaining traction in terms of its consumption and applicability across various fields. Lately, the use of geospatial technology has increased drastically in the field of slope study (Alparslan 2011; Zhong et al. 2012, 2020; Mondal and Maiti 2012; Kundu et al. 2013; Qiao et al. 2013; Chen et al. 2014; Tofani et al. 2014; Scaioni et al. 2014; Alexakis et al. 2014; Shafique et al. 2016; Lv et al. 2018; Pachuau 2019; Wang et al. 2019; Lehmann et al. 2019; Lai and Tsai 2019; Macciotta and Hendry 2021; Zeeshan and Mirza 2021).

Previously, He et al. (2011) devised an automatic and remote-controlled high-risk slope monitoring system using a GPS Multi-Antenna System (GMAS) for the Xiaowan dam in China. The GMAS system is reliable and accurate enough to enable exact positioning, but with a lesser number of survey-quality receivers (He et al. 2011). Ismail et al. (2019) implemented an electrical resistivity imaging approach on a slope near Bukit Antarabangsa, Kuala Lumpur, Malaysia, where a large slope failure took place in December 2008. Many researchers, including Tian et al. (2021), have used reliability-based monitoring sensitivity analysis for reinforced slopes. Wu et al. (2019) discussed optical fiber-based sensing to monitor the slopes. A photogrammetric system is also a helpful method for the study of slope instability. This technique has high precision and low cost but is time-consuming, and it cannot cover the shadow portion (Zhao et al. 2021).

Using high-resolution satellite pictures and aerial photography, it is feasible to make a rough estimation of the dimensions. Through techniques of photogrammetry; however, this requires highly precise and high-definition data, which is not always available for high mountainous terrain and border area, such as the Himalayas (Bitelli et al. 2004; Nichol and Wong 2005; Gupta and Shukla 2018). However, geospatial

Table 18.1 Comparison of the UAV technology with the other prevalent technology

Operation	UAV	Aerial photogrammetry	Satellite mapping	Field survey
Data acquisition	Assisted/Manual/Automatic	Assisted/Manual	Automatic	Manual
Vehicle	Small Unmanned Vehicle	Aircraft	Satellite	NA
Spatial resolution	cm to mm	m to cm	m to cm (few satellites)	mm
Ground coverage	sq. m to sq. km	sq. km	sq. km (wide coverage)	sq. m
Revisit	At user's requirement	Depends upon Flight planning	Depends upon Temporal resolution	NA
Fiducial marks	Absent	Present	Present	NA
Flying height	Not more than a km	up to 10 km	up to 800 km	NA
Cameras	CMOS[a] cameras, Digital camera	Calibrated photogrammetric cameras	Wide field sensors	Digital Camera
Data processing	No standard workflows	Standard photogrammetric workflow	Digital Image Processing	NA
Scale	Local	Regional	Global	Local
Cost	Low	High	Low (sometimes free)	High

[a]CMOS (Complementary Metal Oxide Semiconductor)

technology has advantages, and also there are some limitations like temporal and spatial resolutions (Sajjad and Kumar 2019). It is not always possible to get both these parameters simultaneously. The sensors with good temporal resolution have poor spatial resolution and vice versa. For example, IKONOS and QuickBird satellite have less than 1 m spatial resolution, but their revisit time is 3 days. Similarly, the revisit of the MODIS satellite is 1 day but has a spatial resolution of 250 m. Satellite data also has accuracy and validation issues (Latifovic and Olthof 2004; Bhang et al. 2006; Yifang et al. 2015; Foga et al. 2017; Sajjad and Kumar 2019). Also, satellite sensors are not useful for mapping and monitoring a small area or region. On the other hand, for smaller areas, Unmanned Aerial Vehicles (UAV) technology has become cost-effective and possible in the field. The UAV technology has proven to be a boon in overcoming such limitations. UAVs are more efficient for data collection since they are more succinct, less costly, and user-friendly than the old techniques of using complex measurement instrument (Wu et al. 2021). UAV is also advantageous because the size of the captured images ranges up to 1 cm in spatial resolution,

which is a really big advantage in terms of accuracy (Ćwiąkała et al. 2017). The most crucial benefit of UAV lies in the fact that neither the temporal resolution problem nor the spatial resolution is affected. Moreover, it can traverse the most difficult morphological terrains in a single day. Comparatively, UAV technology can enhance productivity in data collection, reduce the cost of operation and lessen the risk to surveyors and geologists working in challenging (steep undulated terrain) environments (Table 18.1).

18.2 Slope Hazard Assessment

Slope hazard assessment is a basic step for the analysis of slope instability. Different methods have been used in the past regarding the slope hazard assessment. Different monitoring and measuring methods have been used for slope safety assessment, including ground surveying using field instruments, viz., total station, vibrating wire piezometers, electrolytic bubble inclinometers, tiltmeters, and time domain reflectometry (Kane and Beck 2000; Jayanthu 2019). The other method includes monitoring the slope with the help of satellite imagery. Even in satellite imagery, there are optical and microwave data. Light detection and ranging (LiDAR) survey through satellites and airborne systems has gained prominence (Jones 2006; Jaboyedoff et al. 2012). These methods mentioned above are costly and time-consuming compared to the UAV technology (Zang et al. 2012).

Furthermore, collected photos are frequently edited with advanced processing software to adjust for optical distortion, such as that caused by relief variations (Niethammer et al. 2011). For landslide monitoring, unmanned aerial UAVs have shown to be a cost-effective and time-efficient technique that offers researchers and engineers precise, high-resolution geodata compared to the other slope assessment techniques (Lindner et al. 2016). For slope assessment, it is important to consider geometric elements such as the height and angle of a slope, its profile, the location and size of berms, and the angle of the natural slope above cutting when assessing slope stability (Yue et al. 2019; Goh et al. 2020). One of the important aspects of UAV technology is to identify the measurements of the slopes, such as their perimeter, area, volume, and other characteristics, which are deemed to support the major objectives of demonstrating the efficacy of UAV mapping technology in support of those objectives.

UAVs have been used in photogrammetric surveys of rockfall instability, rockfall assessments, and coastal risk assessments (Tannant 2015; Mancini et al. 2017; Mineo et al. 2021). Slow-moving landslides have also been mapped using UAVs for distant sensing and object-oriented mapping (Scaioni et al. 2014; Mohan et al. 2021). With the help of manual flight in UAV survey, high-resolution images were acquired for a more complete investigation in the rockfall and slope instability affected area. Furthermore, high-resolution images and videos could be used to refine maps of land use and exposed elements in the research location. (Gallo et al. 2021). The geomechanical features of the rock can also be evaluated in terms of key discontinuity sets (Gallo et al. 2021).

18.3 Slope Monitoring

Slope monitoring necessitates a continuous examination of the terrain, including determining the displacement rate and changes in surface topography. The use of UAVs to monitor landslides is a useful tool for risk and disaster management. In comparison to other monitoring systems, UAVs feature a short revisit interval, quick data collecting, and simple operations. UAVs with various sensors could collect multi-source data for continuous surveillance, and centimeter-scale images could be captured quickly when the UAV flows at low elevations. UAVs acquire high-resolution imagery in complex photogrammetry and geomatics algorithms (Turner et al. 2015; Al-Rawabdeh et al. 2017). Marek et al. (2015) took one set of images of the probing region in Halenkovice, Czech Republic, with the help of a multi-rotor system (Fig. 18.1). The images were photogrammetrically processed with 23 ground control points (GCPs). On the basis of processed images, a very precise 3D digital surface model (DSM) was performed. Precise measurements of vertical and horizontal displacements helped better understand the landslide mechanisms that can predict future movements (Dewitte et al. 2008; Akca 2013). When surveying surfaces and measuring the displacements of specified spots in order to determine morphological evolutions, precise angle and distance measurements are critical (Artese and Perrelli 2018; Sestras et al. 2021). Several research studies have shown the structure's utility and dependability of Motion (SfM) software in landslide monitoring. Combined with established ground control points (GCPs), the georeferenced deliverables allow surface monitoring and landslide mechanism (Bilaşco et al. 2019). Geodetic surveying is compliant when point displacements exceed equipment error (Záruba and Mencl 1987). The accuracy of geodetic technologies, which can range from 1 mm to a few centimeters, is a significant advantage (Marek et al. 2015). With the help of this monitoring system, it is possible to identify even minor slope displacements. Fundamental statistics, such as correlations and frequency statistics, can be utilised to discover linkages and dependencies between slope activity and other phenomena such as rainfall and other weather patterns (Chleborad 2003; Guzzetti et al. 2008). The UAV monitoring technique has gained widespread use in a variety of fields in recent years, thanks to the rapid development of (digital photogrammetry) DP techniques and the availability of digital cameras that are easy to use, focusable, and inexpensive. Examples include 3D building reconstruction, heritage preservation, and landslide studies, to name a few examples (Grussenmeyer et al. 2008; Scaioni et al. 2015). Lindner et al. (2016) employed high-resolution DSMs and orthophotos, which allowed them to detect and monitor cracks and small-scale surface changes. It was even possible to detect the fissures developed by landslides with the proper drone monitoring.

There have also been techniques like remote sensing to monitor the slopes. Still, the continuous data at the desired time is not possible due to the specific temporal resolution of the particular remote sensing sensors. Moreover, they are expensive. However, UAVs are susceptible to a variety of internal and external variables, including weather, GPS signal, and sustaining issues. The higher monitoring

Fig. 18.1 Multi-rotor UAV inside a granite quarry (Mohamad et al. 2016)

Table 18.2 Comparison between UAVs and other monitoring methods (Ren et al. 2019)

Monitoring methods	Precise leveling	GPS	Satellite remote sensing	InSAR	UAVs
Monitoring information	Point/line	Point/line	Point/line/space	Point/line/space	Point/line/space
Data process	Slow	Fast	Fast	Fast	Fast
Price	High	High	Lower	Lower	Low
Period	Long	Shorter	Shorter	Shorter	Short
Working conditions	Depend on weather	All weather	Depend on weather	All weather	Depend on weather

frequency allows for faster detection of shifting circumstances, evaluation of triggering variables, and incorporation into a geotechnical asset management programme (Rodriguez et al. 2020). Ren et al. (2019) compared the monitoring methods between UAVs and other techniques (Table 18.2).

The workflow for UAV-based picture acquisition can be broken down into the following steps: (1) off-site construction, (2) on-site construction and image acquisition, and (3) post-production (Lindner et al. 2016). During off-site preparation, several prerequisites have to be regulated before traveling to the site, such as weather

situations and the terrain of the region of interest. The flights and field activities were part of the on-site preparation and image acquisition stage. Postprocessing involved georeferencing all captured photos using the GCPs and analysing the same using softwares such as Agisoft Photoscan. The advantage of UAV is that just one person can operate the remote-control UAVs in order to acquire the data. When flying UAVs, the altitude of the UAV and its speed should be maintained so that the picture may be shot clearly and with greater quality (Kaamin et al. 2020).

18.4 Review of Disaster Management of Landslides with UAV

The UAV gives extensive benefits to the disaster management, and some of them are reviewed below. UAV can be used swiftly with high accuracy (Franchi et al. 2012; Okereafor et al. 2013; Gamulescu et al. 2020; Oliviu et al. 2020) in case of an emergency in remote areas. Access to UAV can be planned through careful flight planning in difficult remote locations or areas where no direct access is feasible (Fig. 18.2). (Danzi et al. 2013; Tilburg 2017; Konert et al. 2019). Based on the type of disaster, multiple sensors can be mounted on UAV to capture data for further analysis (Everaerts 2008; Pajares 2015; Erdelj et al. 2017; Samaras et al. 2019). Data can also be acquired in real-time with UAV which is important during disaster management (Ahmad et al. 2013; Luo et al. 2015). UAVs' owning and operating costs are much lower than a manned aircraft (Gentle et al. 2018; Lehto and Hutchinson 2020; Keating et al. 2022).

However, there are some restrictions and limitations associated with UAVs. Every country has its own regulations for UAV. The operation of UAV may be restricted to a military area or as specified by local authorities. The maximum size of sensor and weight which can be carried out in UAV is restricted based on the design of UAV (Ramesh and Jeyan 2020; Šipoš and Gleich 2020; Balestrieri et al. 2021). UAVs need a base station and many images with comparable resolution from large format cameras to create a single large image (Rosnell and Honkavaara 2012; Wierzbicki 2018). UAVs cannot be operated in difficult climatic situations such as fog, rain, thunderstorm, hail storm, and snowfall (Els et al. 2019). Sensors are more stable in high-cost UAVs (Li et al. 2018). High-cost UAVs are generally fitted with more powerful engines, and thus cost plays an important factor in reachable altitude by UAVs (Danzi et al. 2013). Low-cost UAVs are not equipped with Air traffic communication equipment and are not generally fitted on low-cost UAV (Bolla et al. 2018; Table 18.3).

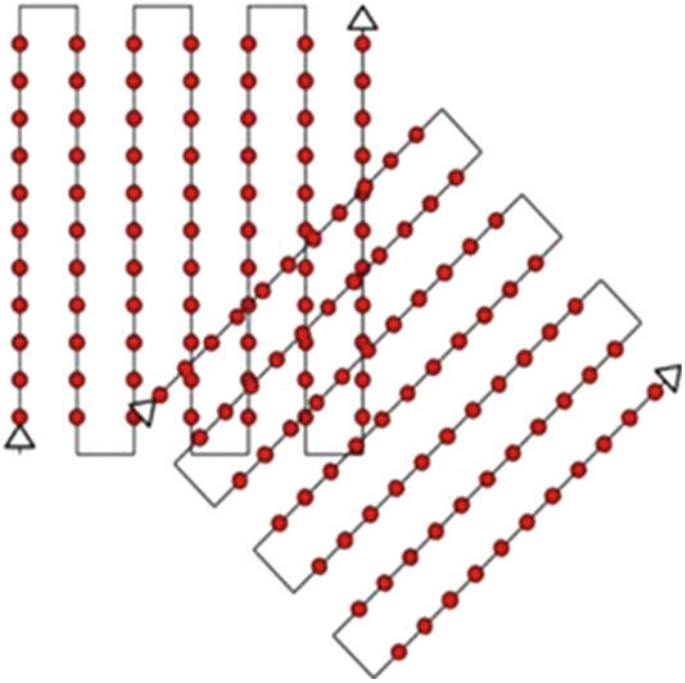

Fig. 18.2 Flight planning for UAV on a regular surface

18.5 Discussion

The article mainly deals with the comparison of the UAV technology with the other technology available for slope monitoring and assessment. Traditional approaches to assessing slope instability have been proposed in the international literature for decades and still appear to be important, but they have numerous drawbacks when applied in logistically difficult situations (Barton et al. 1974; Romana 1985; Bieniawski 1989; Hoek et al. 1998; Tomás et al. 2007). Implementation of these approaches in the field is costly and time-consuming and often does not cover the entire study area. It also involves repeating actions, which often results in wrong data. Remote techniques like UAV technology can provide a holistic picture of the existing scenario. Discontinuity sets that characterise the rock mass, major features, and processes affecting the stability can be studied with relative ease. However, this data must always be integrated with the necessary geo-structural and geomechanical checks present at the site to effectively reach the goal of evaluating the stability conditions (Andriani and Parise 2015; Ferrero et al. 2009). Important point is the UAV approach has enabled surface profile comparison across varied roughness length scales ranging from 0.1 to 1 m and overcoming data collecting challenges caused by shadow zones in both the horizontal and vertical orientations. Currently, the use of unmanned aerial vehicles (UAVs) for on-site inspections and mapping

Table 18.3 Literature review of UAV for disaster management of landslides

References	Scope and methodology adopted	Learnings for disaster management
Ahmad et al. (2013)	Digital aerial imagery (DAI) with UAV for slope mapping RTK GPS from a known point	For a limited budget, large scale mapping of a small area is possible with the DAI-UAV technique
Danzi et al. (2013)	Rockfall instability studies with Digital Terrestrial Photogrammetry (DTP) surveys using UAV	High versatility -high cliffs to narrow gorges. Excellent geometric accuracy. Integration with GIS. Classify slope in different hazard categories. Useful tool for safe planning and making timely decisions
Karantanellis et al. (2020)	Photogrammetry data from UAV analysed using Object-Based Image Analysis (OBIA) and fusion of multivariate data. (A novel semi-automated approach)	Useful for site-specific landslides for semantic labeling. Detailed remedial and protective measures can be planned
Khan et al. (2020)	Various techniques such as Artificial Intelligence, Big data analytics, Fuzzy logic, UAV for disaster detection, monitoring, and management are compared	Merits and demerits are compared. A combination of two or more techniques for landslide management is useful
Melis et al. (2020)	Infrared thermography (IRT) for capturing coastal cliff data in three steps. (a) Planning -analysis of location and accessibility. (b) Data Collection -Position of ground control points, ambient data, and optical images. (c) Data analysis—with remote sensing software	Further research is required as a new application for identifying fractures and cavities on slopes
Nikhil et al. (2020)	Pre-disaster proactivity and post-disaster execution with UAV	Pre-disaster UAV survey helps plan post-disaster execution. Flexibility to use UAV in any terrain with minimization of fieldwork
Koutalakis et al. (2021)	Very high-resolution RGB images of landslide captured with standard digital camera fitted on quadcopter UAV. Multi-temporal sets were collected with GPS + GLONASS. ArcGIS software was utilised to perform morphometric measurements	The technology of digital image capturing with UAV and matching algorithms improved drastically for photogrammetry accuracy Methodology proposed is suitable for planning, mitigation practice, and disaster management of landslides by public bodies

(continued)

Table 18.3 (continued)

References	Scope and methodology adopted	Learnings for disaster management
Sestras et al. (2021)	Unmanned aerial vehicles (UAV) monitoring of surface movement and GIS spatial analysis for Shallow Landslides. The mass movement of landslides through the geodetic network. Data obtained from the UAV confirmed the 3D model of the investigated slope	Geodetic network to be maintained for landslide disaster management. The system can be strengthened with a LiDAR-equipped UAV and monitoring with the InSAR technique to improve disaster management objectives of landslides
Vanderhorst et al. (2021)	Organisations involved in disaster management in the Dominican Republic with socio-technical systems (socio-technical change impact model (SCI)) and organisational level (technology-organizational-environmental) frameworks by adopting Unmanned Aerial System (UAS)	Public and private partnership plays a crucial role in disaster management, such as landslides. Fast acquisition of data through image and 3D video analysis useful for identifying inaccessible areas—search and rescue operation during disaster management

has emerged as a revolutionary technology. UAVs offer greater flexibility and speed, which improves the ability to acquire structural planes and monitor slope sliding than traditional methods. UAVs are a low-cost and quick way to get detailed images of a specific region of interest and create detailed 3D models and orthophotos. The employment of a UAV necessitates a strong foundation in data processing (photogrammetry and structure from motion) as well as a strong drone piloting ability to control the flight mission in a complicated surrounding (Giordan et al. 2020).

In the hilly terrains, lateral spreads and slope failures are very common, and they have been studied using geomorphological mapping and visual interpretation of aerial and satellite pictures (Devoto 2013; Devoto et al. 2012, 2013, 2020). The raw data can be used to investigate the spatial distribution, including characteristics, size, and key geomorphological aspects of a region. The disadvantage of traditional geomorphological field mapping for monitoring landslides is the limited accessibility of survey sites due to treacherous terrains that are often risky for field operators. As a result, geomorphological research can benefit from visual assessment of photos taken at low altitude. The usage of the UAV-DP technique has a lot of advantages when it comes to determining joint aperture and distribution outline. The UAV-DP technique and its products can remotely measure aperture changes in each tension crack, bypassing a time-consuming field investigation component (Devoto et al. 2020). Many researchers have discovered that UAVs can be used to reduce the risk of natural hazards like landslides and subsidence and have even compared the findings of different photogrammetry software (Noferini et al. 2006; Intrieri et al. 2012; Yu

et al. 2017). In due course of time, a novel study has been understood involving photogrammetric assessments of the primary landslide events characteristics and dimensions and the digitization of the tension cracks of mass movement events using high-resolution photographs obtained from a low-cost UAV.

Future study possibilities could include using satellite photos from past years to compare changes and conducting UAV flights on a more regular basis to detect future changes (Giordan et al. 2020). There are also some limitations to flying drones, like they are not advisable to fly in all weather conditions, especially when the wind speed is high. When the wind speed is between 2 and 4 m per second, it is best to conduct drone flights (Battulwar et al. 2020). Another limitation is the battery power and the flight time. Quadcopters have a limited battery life, making them unsuitable for use in big open-pit mines to achieve high productivity levels. Several experimental research has been conducted to determine the battery power consumption of the UAV and to develop a model for it. Drone power consumption was calculated based on the model predictions for a test flight, as measured in relation to the actual onboard battery power usage (Siebert and Teizer 2014).

18.6 Conclusion

Evaluation and monitoring of slope failures and landslides are pivotal for safeguarding the local population and infrastructure. While many techniques exist for such tasks, most of them are expensive, time-consuming, and not always feasible. UAVs, on the contrary, provide a cost-effective and reliable tool for assessing and monitoring landslides and slope failures. The relative ease of operations and the choice of sensors render UAVs' efficient in the type of data to be collected. Also, data acquisition from remote, inaccessible sites protects the manpower and makes the process fast.

Acknowledgements The first author is thankful to Guru Gobind Singh Indraprastha University, India, for providing financial support through Indraprastha Research Fellowship. The authors are grateful to the Dean, USEM, Guru Gobind Singh Indraprastha University, India, for making us avail of the facility in carrying out the research work.

References

Ahmad A, Tahar KN, Udin WS, Hashim KA, Darwin N, Hafis M, Azmi SM (2013, November) Digital aerial imagery of unmanned aerial vehicle for various applications. In 2013 IEEE international conference on control system, computing and engineering. IEEE, pp 535–540

Akca D (2013) Photogrammetric monitoring of an artificially generated shallow landslide. Photogram Rec 28(142):178–195

Alexakis DD, Agapiou A, Tzouvaras M, Themistocleous K, Neocleous K, Michaelides S, Hadjimitsis DG (2014) Integrated use of GIS and remote sensing for monitoring landslides in transportation pavements: the case study of Paphos area in Cyprus. Nat Hazards 72(1):119–141

Alparslan E (2011) Landslide susceptibility mapping in Yalova, Turkey, by remote sensing and GIS. Environ Eng Geosci 17(3):255–265

Al-Rawabdeh A, Moussa A, Foroutan M, El-Sheimy N, Habib A (2017) Time series UAV image-based point clouds for landslide progression evaluation applications. Sensors 17(10):2378

Andriani GF, Parise M (2015) On the applicability of geomechanical models for carbonate rock masses interested by karst processes. Environ Earth Sci 74(12):7813–7821

Ansari T, Kainthola A, Singh KH, Singh TN, Sazid M (2021) Geotechnical and micro-structural characteristics of phyllite derived soil; implications for slope stability, Lesser Himalaya, Uttarakhand, India. CATENA 196:104906

Artese S, Perrelli M (2018) Monitoring a landslide with high accuracy by total station: a DTM-based model to correct for the atmospheric effects. Geosciences 8(2):46

Balestrieri E, Daponte P, De Vito L, Lamonaca F (2021) Sensors and measurements for unmanned systems: An overview. Sensors 21(4):1518

Barton N, Lien R, Lunde J (1974) Engineering classification of rock masses for the design of tunnel support. Rock Mech 6(4):189–236

Battulwar R, Winkelmaier G, Valencia J, Naghadehi MZ, Peik B, Abbasi B, Parvin B, Sattarvand J (2020) A practical methodology for generating high-resolution 3D models of open-pit slopes using UAVs: Flight path planning and optimization. Remo Sens 12(14):2283

Bhang KJ, Schwartz FW, Braun A (2006) Verification of the vertical error in C-band SRTM DEM using ICESat and Landsat-7, Otter Tail County, MN. IEEE Trans Geosci Remote Sens 45(1):36–44

Bieniawski ZT (1989) Engineering rock mass classifications: a complete manual for engineers and geologists in mining, civil, and petroleum engineering. Wiley, New York

Bilaşco Ş, Roşca S, Petrea D, Vescan I, Fodorean I, Filip S (2019). 3D reconstruction of landslides for the acquisition of digital databases and monitoring spatiotemporal dynamics of landslides based on GIS spatial analysis and UAV techniques. In Spatial modeling in GIS and R for earth and environmental sciences. Elsevier, pp 451–465

Bitelli G, Dubbini M, Zanutta A (2004) Terrestrial laser scanning and digital photogrammetry techniques to monitor landslide bodies. Int Arch Photogrammetry Remote Sens Spat Inf Sci 35(B5):246–251

Bolla GM, Casagrande M, Comazzetto A, Dal Moro R, Destro M, Fantin E, Colombatti G, Aboudan A, Lorenzini EC (2018, June) ARIA: Air pollutants monitoring using UAVs. In: 2018 5th IEEE international workshop on metrology for aerospace (MetroAeroSpace). IEEE, pp 225–229

Chen Z, Zhang B, Han Y, Zuo Z, Zhang X (2014) Modeling accumulated volume of landslides using remote sensing and DTM data. Remote Sens 6(2):1514–1537

Chleborad AF (2003) Preliminary evaluation of a precipitation threshold for anticipating the occurrence of landslides in the Seattle, Washington, Area. US Geol Surv Open-File Rep 3(463):39

Ćwiąkała P, Kocierz R, Puniach E, Nędzka M, Mamczarz K, Niewiem W, Wiącek P (2017) Assessment of the possibility of using unmanned aerial vehicles (UAVs) for the documentation of hiking trails in alpine areas. Sensors 18(1):81

Danzi M, Di Crescenzo G, Ramondini M, Santo A (2013) Use of unmanned aerial vehicles (UAVs) for photogrammetric surveys in rockfall instability studies. Rendiconti Online Societa Geologica Italiana 24:82–85

Devoto S (2013) Cartografia, monitoraggio e modellizzazione di frane lungo la costa nord-occidentale dell'isola di Malta. Doctoral dissertation, University of Modena and Reggio Emilia

Devoto S, Biolchi S, Bruschi VM, Furlani S, Mantovani M, Piacentini D, Pasuto A, Soldati M (2012) Geomorphological map of the NW Coast of the Island of Malta (Mediterranean Sea). J Maps 8(1):33–40

Devoto S, Biolchi S, Bruschi VM, Díez AG, Mantovani M, Pasuto A, Piacentini D, Schembri JA, Soldati M (2013) Landslides along the north-west coast of the Island of Malta. In Landslide science and practice. Springer, Berlin, Heidelberg, pp 57–63

Devoto S, Macovaz V, Mantovani M, Soldati M, Furlani S (2020) Advantages of using UAV digital photogrammetry in the study of slow-moving coastal landslides. Remote Sens 12(21):3566

Dewitte O, Jasselette JC, Cornet Y, Van Den Eeckhaut M, Collignon A, Poesen J, Demoulin A (2008) Tracking landslide displacements by multi-temporal DTMs: A combined aerial stereophotogrammetric and LIDAR approach in western Belgium. Eng Geol 99(1–2):11–22

Els N, Larose C, Baumann-Stanzer K, Tignat-Perrier R, Keuschnig C, Vogel TM, Sattler B (2019) Microbial composition in seasonal time series of free tropospheric air and precipitation reveals community separation. Aerobiologia 35(4):671–701

Erdelj M, Natalizio E, Chowdhury KR, Akyildiz IF (2017) Help from the sky: leveraging UAVs for disaster management. IEEE Pervasive Comput 16(1):24–32

Everaerts J (2008) The use of unmanned aerial vehicles (UAVs) for remote sensing and mapping. Int Arch Photogramm Remote Sens Spat Inf Sci 37(2008):1187–1192

Ferrero AM, Forlani G, Roncella R, Voyat HI (2009) Advanced geostructural survey methods applied to rock mass characterization. Rock Mech Rock Eng 42(4):631–665

Foga S, Scaramuzza PL, Guo S, Zhu Z, Dilley RD Jr, Beckmann T, Schmidt GL, Dwyer JL, Hughes MJ, Laue B (2017) Cloud detection algorithm comparison and validation for operational Landsat data products. Remote Sens Environ 194:379–390

Franchi A, Secchi C, Ryll M, Bulthoff HH, Giordano PR (2012) Shared control: Balancing autonomy and human assistance with a group of quadrotor UAVs. IEEE Robot Autom Mag 19(3):57–68

Francioni M, Salvini R, Stead D, Giovannini R, Riccucci S, Vanneschi C, Gullì D (2015) An integrated remote sensing-GIS approach for the analysis of an open pit in the Carrara marble district, Italy: Slope stability assessment through kinematic and numerical methods. Comput Geotech 67:46–63

Gallo IG, Martínez-Corbella M, Sarro R, Iovine G, López-Vinielles J, Hérnandez M, Robustelli G, Mateos RM, García-Davalillo JC (2021) An integration of UAV-based photogrammetry and 3D modelling for Rockfall Hazard assessment: The Cárcavos case in 2018 (Spain). Remote Sens 13(17):3450

Gamulescu OM, Rosca SD, Panaite F, Costandoiu A, Riurean S (2020) Accident sites management using drones. In MATEC web of conferences, vol 305. EDP Sciences, p 00004

Gentle M, Finch N, Speed J, Pople A (2018) A comparison of unmanned aerial vehicles (drones) and manned helicopters for monitoring macropod populations. Wildl Res 45(7):586–594

Giordan D, Adams MS, Aicardi I, Alicandro M, Allasia P, Baldo M, De Berardinis P, Dominici D, Godone D, Hobbs P, Lechner V (2020) The use of unmanned aerial vehicles (UAVs) for engineering geology applications. Bull Eng Geol Env 79(7):3437–3481

Goh JR, Ishak MF, Zaini MSI, Zolkepli MF (2020) Stability analysis and improvement evaluation on residual soil slope: building cracked and slope failure. In: IOP conference series: materials science and engineering, vol 736, no 7. IOP Publishing, p 072017

Grussenmeyer P, Landes T, Voegtle T, Ringle K (2008) Comparison methods of terrestrial laser scanning, photogrammetry and tacheometry data for recording of cultural heritage buildings. Int Arch Photogrammetry Remote Sens Spat Inf Sci 37(B5):213–218

Gupta SK, Shukla DP (2018) Application of drone for landslide mapping, dimension estimation and its 3D reconstruction. J Indian Soc Remote Sens 46(6):903–914

Guzzetti F, Peruccacci S, Rossi M, Stark CP (2008) The rainfall intensity–duration control of shallow landslides and debris flows: an update. Landslides 5(1):3–17

He X, Jia D, Sang W (2011) Monitoring steep slope movement at Xiaowan dam with GPS multi-antenna method. Surv Rev 43(323):462–471

Hoek E, Marinos P, Benissi M (1998). Applicability of the Geological Strength Index (GSI) classification for very weak and sheared rock masses. The case of the Athens Schist Formation. Bull Eng Geol Environ 57(2):151–160

Intrieri E, Gigli G, Mugnai F, Fanti R, Casagli N (2012) Design and implementation of a landslide early warning system. Eng Geol 147:124–136
Ismail NEH, Taib SH, Abas FAM (2019) Slope monitoring: an application of time-lapse electrical resistivity imaging method in Bukit Antarabangsa, Kuala Lumpur. Environ Earth Sci 78(1):1–15
Jaboyedoff M, Oppikofer T, Abellán A, Derron MH, Loye A, Metzger R, Pedrazzini A (2012) Use of LIDAR in landslide investigations: a review. Nat Hazards 61(1):5–28
Jayanthu S (2019) Field experimental trial of communication system for monitoring of slope stability on 2nd international conference on future communication and computing technology (ICFCCT 2019), Meerut, India, 17–18 July 2019
Jones LD (2006) Monitoring landslides in hazardous terrain using terrestrial LiDAR: an example from Montserrat. Q J Eng Geol Hydrogeol 39(4):371–373
Kaamin M, Mazuki MS, Madun A, Ab Razak SN, Ngadiman N, Nor AHM (2020) Visual slope inspection using unmanned aerial vehicle (UAV). In: Journal of Physics: Conference Series, vol 1529, no 3. IOP Publishing, p 032102
Kane WF, Beck TJ (2000) Instrumentation practice for slope monitoring. Engineering geology practice in Northern California. Association of engineering geologists Sacramento and San Francisco sections
Karantanellis E, Marinos V, Vassilakis E, Christaras B (2020) Object-based analysis using unmanned aerial vehicles (UAVs) for site-specific landslide assessment. Remote Sens 12(11):1711
Keating EG, Kerman J, Arthur D (2022) A note on estimating the relative costs of unmanned aerial systems. Defence Peace Econ 33(4):496–500
Khan A, Gupta S, Gupta SK (2020) Multi-hazard disaster studies: Monitoring, detection, recovery, and management, based on emerging technologies and optimal techniques. Int J Disaster Risk Reduction 47:101642
Komadja GC, Pradhan SP, Oluwasegun AD, Roul AR, Stanislas TT, Laïbi RA, Adebayo B, Onwualu AP (2021) Geotechnical and geological investigation of slope stability of a section of road cut debris-slopes along NH-7, Uttarakhand, India. Results Eng 10:100227
Konert A, Smereka J, Szarpak L (2019) The use of drones in emergency medicine: practical and legal aspects. Emerg Med Int, 2019: 1–5. https://doi.org/10.1155/2019/3589792
Koutalakis PD, Tzoraki OA, Prazioutis GI, Gkiatas GT, Zaimes GN (2021) Can drones map earth cracks? Landslide measurements in North Greece using UAV photogrammetry for nature-based solutions. Sustainability 13(9):4697
Kundu S, Saha AK, Sharma DC, Pant CC (2013) Remote sensing and GIS based landslide susceptibility assessment using binary logistic regression model: a case study in the Ganeshganga Watershed, Himalayas. J Indian Soc Remote Sens 41(3):697–709
Lai JS, Tsai F (2019) Improving GIS-based landslide susceptibility assessments with multi-temporal remote sensing and machine learning. Sensors 19(17):3717
Latifovic R, Olthof I (2004) Accuracy assessment using sub-pixel fractional error matrices of global land cover products derived from satellite data. Remote Sens Environ 90(2):153–165
Lehmann P, von Ruette J, Or D (2019) Deforestation effects on rainfall-induced shallow landslides: remote sensing and physically-based modelling. Water Resour Res 55(11):9962–9976
Lehto M, Hutchinson B (2020) Mini-drones swarms and their potential in conflict situations. In: 15th international conference on cyber warfare and security, vol 12, pp 326–334
Li Y, Scanavino M, Capello E, Dabbene F, Guglieri G, Vilardi A (2018) A novel distributed architecture for UAV indoor navigation. Trans Res Procedia 35:13–22
Lindner G, Schraml K, Mansberger R, Hübl J (2016) UAV monitoring and documentation of a large landslide. Appl Geomat 8(1):1–11
Luo C, Nightingale J, Asemota E, Grecos C (2015, May) A UAV-cloud system for disaster sensing applications. In: 2015 IEEE 81st vehicular technology conference (VTC Spring). IEEE, pp 1–5
Lv ZY, Shi W, Zhang X, Benediktsson JA (2018) Landslide inventory mapping from bitemporal high-resolution remote sensing images using change detection and multiscale segmentation. IEEE J Sel Top Appl Earth Obs Remote Sens 11(5):1520–1532

Macciotta R, Hendry MT (2021) Remote sensing applications for landslide monitoring and investigation in Western Canada. Remote Sens 13(3):366

Mancini F, Castagnetti C, Rossi P, Dubbini M, Fazio NL, Perrotti M, Lollino P (2017) An integrated procedure to assess the stability of coastal rocky cliffs: From UAV close-range photogrammetry to geomechanical finite element modeling. Remote Sens 9(12):1235

Marek L, Miřijovský J, Tuček P (2015) Monitoring of the shallow landslide using UAV photogrammetry and geodetic measurements. In: Engineering geology for society and territory, vol 2. Springer, Cham, pp 113–116

Melis MT, Da Pelo S, Erbì I, Loche M, Deiana G, Demurtas V, Meloni MA, Dessì F, Funedda A, Scaioni M, Scaringi G (2020) Thermal remote sensing from UAVs: A review on methods in coastal cliffs prone to landslides. Remote Sens 12(12):1971

Mineo S, Pappalardo G, Onorato S (2021) Geomechanical characterization of a rock cliff hosting a cultural heritage through ground and UAV rock mass surveys for its sustainable fruition. Sustainability 13(2):924

Mohamad ET, Murlidhar BR, Alel MNAB, Armaghani DJ (2016) Geological study and mining plan importance for mitigating alkali silica reaction in aggregate quarry operation. J Teknol 78: 7–3

Mohan A, Singh AK, Kumar B, Dwivedi R (2021) Review on remote sensing methods for landslide detection using machine and deep learning. Trans Emerg Telecommun Technol 32(7):e3998

Mondal S, Maiti R (2012) Landslide susceptibility analysis of Shiv-Khola watershed, Darjiling: a remote sensing & GIS based Analytical Hierarchy Process (AHP). J Indian Soc Remote Sens 40(3):483–496

Nichol J, Wong MS (2005) Satellite remote sensing for detailed landslide inventories using change detection and image fusion. Int J Remote Sens 26(9):1913–1926

Niethammer U, Rothmund S, Schwaderer U, Zeman J, Joswig M (2011) Open-source image-processing tools for low-cost UAV-based landslide investigations. Int Arch Photogrammetry Remote Sens Spat Inf Sci 38(1):C22

Nikhil N, Shreyas SM, Vyshnavi G, Yadav S (2020) Unmanned aerial vehicles (UAV) in disaster management applications. In: 2020 third international conference on smart systems and inventive technology (ICSSIT). IEEE, pp 140–148

Noferini L, Pieraccini M, Mecatti D, Macaluso G, Luzi G, Atzeni C (2006) Long term landslide monitoring by ground-based synthetic aperture radar interferometer. Int J Remote Sens 27(10):1893–1905

Okereafor DT, Diala U, Onuekwusi N, Uzoechi LO, Chukwudebe G (2013, November). Improving security and emergency response through the use of unmanned vehicles. In 2013 IEEE international conference on emerging & sustainable technologies for power & ICT in a developing society (NIGERCON). IEEE, pp 263–269

Oliviu MG, Rosca SD, Panaite F, Costandoiu A, Riurean S (2020) Accident sites management using drones. In: MATEC web of conferences, vol 305. EDP Sciences

Pachuau L (2019) Zonation of landslide susceptibility and risk assessment in Serchhip town, Mizoram. J Indian Soc of Remote Sens 47(9):1587–1597

Pajares G (2015) Overview and current status of remote sensing applications based on unmanned aerial vehicles (UAVs). Photogramm Eng Remote Sens 81(4):281–330

Pradhan SP, Panda SD, Roul AR, Thakur M (2019) Insights into the recent Kotropi landslide of August 2017, India: a geological investigation and slope stability analysis. Landslides 16(8):1529–1537

Qiao G, Lu P, Scaioni M, Xu S, Tong X, Feng T, Wu H, Chen W, Tian Y, Wang W, Li R (2013) Landslide investigation with remote sensing and sensor network: from susceptibility mapping and scaled-down simulation towards in situ sensor network design. Remote Sens 5(9):4319–4346

Ramesh PS, Jeyan ML (2020) Mini unmanned aerial systems (UAV)—a review of the parameters for classification of a mini UAV. Int J Aviat Aeronaut Aerosp 7(3):5

Ren H, Zhao Y, Xiao W, Hu Z (2019) A review of UAV monitoring in mining areas: current status and future perspectives. Int J Coal Sci Technol 6(3):320–333

Rodriguez J, Macciotta R, Hendry MT, Roustaei M, Gräpel C, Skirrow R (2020) UAVs for monitoring, investigation, and mitigation design of a rock slope with multiple failure mechanisms—a case study. Landslides 17(9):2027–2040

Romana M (1985) New adjustment ratings for application of Bieniawski classification to slopes. In: Proceedings of the international symposium on role of rock mechanics, Zacatecas, Mexico, pp 49–53

Rosnell T, Honkavaara E (2012) Point cloud generation from aerial image data acquired by a quadrocopter type micro unmanned aerial vehicle and a digital still camera. Sensors 12(1):453–480

Sajjad H, Kumar P (2019) Future challenges and perspective of remote sensing technology. In: Applications and challenges of geospatial technology. Springer, Cham, pp 275–277

Samaras S, Diamantidou E, Ataloglou D, Sakellariou N, Vafeiadis A, Magoulianitis V, Lalas A, Dimou A, Zarpalas D, Votis K, Daras P, Tzovaras D (2019) Deep learning on multi sensor data for counter UAV applications—a systematic review. Sensors 19(22):4837

Sarkar S, Kanungo DP, Kumar S (2012) Rock mass classification and slope stability assessment of road cut slopes in Garhwal Himalaya, India. Geotech Geol Eng 30(4):827–840

Scaioni M, Feng T, Lu P, Qiao G, Tong X, Li R, Barazzetti L, Previtali M, Roncella R (2015). Close-range photogrammetric techniques for deformation measurement: applications to landslides. In: Modern technologies for landslide monitoring and prediction. Springer, Berlin, Heidelberg, pp 13–41

Scaioni M, Longoni L, Melillo V, Papini M (2014) Remote sensing for landslide investigations: an overview of recent achievements and perspectives. Remote Sens 6(10):9600–9652

Sestras P, Bilașco Ș, Roșca S, Dudic B, Hysa A, Spalević V (2021) Geodetic and UAV monitoring in the sustainable management of shallow landslides and erosion of a susceptible urban environment. Remote Sens 13(3):385

Shafique M, van der Meijde M, Khan MA (2016) A review of the 2005 Kashmir earthquake-induced landslides; from a remote sensing perspective. J Asian Earth Sci 118:68–80

Sharma M, Sharma S, Kumar M, Singh SK (2019) Analysis of slope stability of road cut slopes of Srinagar, Uttrakhand, India. Int J Appl Eng Res 14(3):609–615

Shin Y, Choi JC, Quinteros S, Svendsen I, L'Heureux JS, Seong J (2020) Evaluation and monitoring of slope stability in cold region: case study of man-made slope at Øysand, Norway. Appl Sci 10(12):4136

Siddque T, Pradhan SP (2018) Stability and sensitivity analysis of Himalayan Road cut debris slopes: an investigation along NH-58, India. Nat Hazards 93(2):577–600

Siebert S, Teizer J (2014) Mobile 3D mapping for surveying earthwork projects using an Unmanned Aerial Vehicle (UAV) system. Autom Constr 41:1–14

Singh PK, Kainthola A, Singh TN (2015) Rock mass assessment along the right bank of river Sutlej, Luhri, Himachal Pradesh, India. Geomat Nat Haz Risk 6(3):212–223

Šipoš D, Gleich D (2020) A lightweight and low-power UAV-borne ground penetrating radar design for landmine detection. Sensors 20(8):2234

Tannant DD (2015) Review of photogrammetry-based techniques for characterization and hazard assessment of rock faces. Int J Georesour Environ-IJGE (formerly Int'l J of Geohazards and Environment) 1(2):76–87

Tian HM, Li DQ, Cao ZJ, Xu DS, Fu XY (2021) Reliability-based monitoring sensitivity analysis for reinforced slopes using BUS and subset simulation methods. Eng Geol 293:106331

Tilburg C (2017) First report of using portable unmanned aircraft systems (drones) for search and rescue. Wilderness Environ Med 28(2):116–118

Tofani V, Del Ventisette C, Moretti S, Casagli N (2014) Integration of remote sensing techniques for intensity zonation within a landslide area: a case study in the northern Apennines, Italy. Remote Sens 6(2):907–924

Tomás R, Delgado J, Serón Gáñez JB (2007) Modification of slope mass rating (SMR) by continuous functions. Int J Rock Mech Mining Sci 44(7):1062–1069

Turner D, Lucieer A, De Jong SM (2015) Time series analysis of landslide dynamics using an unmanned aerial vehicle (UAV). Remote Sens 7(2):1736–1757

Vanderhorst HR, Suresh S, Renukappa S, Heesom D (2021) Strategic framework of unmanned aerial systems integration in the disaster management public organisations of the Dominican Republic. Int J Disaster Risk Reduction 56:102088

Wang Y, Wang X, Jian J (2019). Remote sensing landslide recognition based on convolutional neural network. Mathematical Problems in Engineering, 2019

Wierzbicki D (2018) Multi-camera imaging system for UAV photogrammetry. Sensors 18(8):2433

Wu H, Guo Y, Xiong L, Liu W, Li G, Zhou X (2019) Optical fiber-based sensing, measuring, and implementation methods for slope deformation monitoring: a review. IEEE Sens J 19(8):2786–2800

Wu J, Peng L, Li J, Zhou X, Zhong J, Wang C, Sun J (2021) Rapid safety monitoring and analysis of foundation pit construction using unmanned aerial vehicle images. Autom Constr 128:103706

Yifang B, Gong P, Gini C (2015) Global land cover mapping using Earth observation satellite data: Recent progresses and challenges. ISPRS J Photogrammetry Remote Sens 103(1):1–6

Yu M, Huang Y, Zhou J, Mao L (2017) Modeling of landslide topography based on micro-unmanned aerial vehicle photography and structure-from-motion. Environ Earth Sci 76(15):1–9

Yue LJ, Ishak MF, Zaini MSI, Zolkepli MF (2019, November) Rainfall induced residual soil slope instability: building cracked and slope failure. In: IOP Conference Series: Materials Science and Engineering, vol 669, no 1. IOP Publishing, p 012004

Zang W, Lin J, Wang Y, Tao H (2012) Investigating small-scale water pollution with UAV remote sensing technology. In: World automation congress 2012. IEEE, pp 1–4

Záruba Q, Mencl V (1987) Sesuvy a zabezpečování svahů. Academia, 2. přeprac. a dopl. vyd. Praha, 338s

Zeeshan M, Mirza K (2021) Landslide detection and susceptibility mapping using geological and remote sensing data: a case study of azad kashmir, nw sub-himalayas. Acta Geodynamica Et Geromaterialia 18(1):29–45

Zhao P, Li J, Kang F (2021) Slope surface displacement monitoring based on a photogrammetric system. Optik 227:166089

Zhong C, Li H, Xiang W, Su A, Huang X (2012) Comprehensive study of landslides through the integration of multi remote sensing techniques: framework and latest advances. J Earth Sci 23(2):243–252

Zhong C, Liu Y, Gao P, Chen W, Li H, Hou Y, Ma H (2020) Landslide mapping with remote sensing: challenges and opportunities. Int J Remote Sens 41(4):1555–1581

Chapter 19
Landslide Hazard Assessment Using Machine Learning and GIS

Amit Jaiswal, A. K. Verma, T. N. Singh, and Jayraj Singh

Abstract India's National Disaster Management Authority (NDMA) has highlighted landslides as a complex geological natural hazard. As a result, identifying hazardous zones under varied geometrical and geotechnical conditions has remained a complex problem that has received much attention in the classic era. This work aims to predict landslide hazard zones using spatial analysis by applying multi-criteria analysis methods. For the investigation, Ramban area of Jammu & Kashmir, India, has been considered. The locations of landslides were identified by analysis of Google earth images and field surveys. The major causative factors of landslides such as relative relief, slope, geological structure, lithology, soil thickness, hydrological condition, and land use and land cover were extracted from QGIS software tool, Google earth images, and field survey. The two major triggering factors such as rainfall and seismicity, were also included in the study. The cumulative effect of all these factors was considered for preparing the dataset that was scrutinized to produce a landslide hazard zonation map. It has become very much possible to develop intelligent models calibrated to experimental data to predict landslide zonation with the least potential errors with the advancement of machine learning-based computation technologies. In view of these observations, in this chapter: (i) the relevant spatial data are identified, processed, and analysed (ii) data is used to construct an intelligent machine learning model, namely the back-propagation neural network (BPNN), to predict the hazardous zonation. The study has been validated by comparing the landslide hazard zonation map with the actual occurrence of landslides. The outcomes of this research show that the designed AI-based model is quite promising and may be utilised successfully by practicing professionals to estimate landslide zonation with reasonable accuracy.

A. Jaiswal · A. K. Verma (✉)
Department of Mining Engineering, Indian Institute of Technology BHU, Varanasi 221005, India
e-mail: amitvermaism@gmail.com

T. N. Singh
Department of Civil and Environmental Engineering, Indian Institute of Technology, Patna 801106, Bihar, India

J. Singh
Department of Civil Engineering, Indian Institute of Technology Delhi, New Delhi 110016, India

P. Thambidurai and T. N. Singh (eds.), *Landslides: Detection, Prediction and Monitoring*,
https://doi.org/10.1007/978-3-031-23859-8_19

Keywords Landlside Hazard · Remote sensing and GIS · Machine learning and landslide

19.1 Introduction

Landslides are one of the most prevalent natural disasters that take lives, property, and the environment all over the world. Every year, landslides claim the lives of people and property worldwide, including in India. The Himalaya's dynamic nature has resulted in numerous landslides across the region. Jammu & Kashmir is the westernmost part of the Indian Himalayas and is prone to landslides. The area commonly witnesses extreme weather conditions with excessive seasonal precipitation and snowfall that generally trigger natural hazards such as landslides. National Highway (NH-1A) of Jammu-Srinagar frequently gets blocked at a number of sites during monsoons due to mass movement. The most affected portion is Ramban-Banihal stretch of the national highway (NH-1A). This is one of the most susceptible zones to landslides in the world (Chingkhei et al. 2013). The area passes through some major destructive landslides like the Digdol slide, Panthiyal slide, Battery Chashma slide, and Khoni Nallah slide. Landslide hazard zonation is the most preliminary and important approach to identifying and studying landslide effects in an area. The first approach in landslide hazard zonation mapping was achieved by using factor rating of different parameters causing landslides. With the advancement in hazard zonation mapping approach, analytical hierarchy process, weighted overlay model, rainfall intensity model, frequency ratio model, logistic regression modelling, and different statistical approach have become more important zonation methods. The threshold of different causative factors like slope, elevation, aspect, lithology, hydrological conditions, geological structures, and triggering factors like seismicity and rainfall are the main causes of slope instability. Various statistical and probabilistic approaches for slope instability identification and hazard zonation using GIS and remote sensing have been established as an important approach for studying landslides globally.

The varying characteristics of the material and other uncertainties found in the geological parameters may cause slope instability (Singh et al. 2019). However, finding reliable values of input parameters is cumbersome and becomes a crucial task. The researchers began to gain more attention towards machine learning-based methods with technological advancements (Singh et al. 2016) for fast and efficient predictions. Different Artificial Neural Network (ANN) based models (Pistocchi et al. 2002; Lee et al. 2003a, b; Arora et al. 2004; Lee et al. 2006; Yilmaz 2009) have been employed for landslide susceptibility assessment. Sequentially, a combination of neural and fuzzy approaches has been utilized by Kanungo et al. (2006) in developing landslide susceptibility maps. In a study by Nefeslioglu et al. (2008), the ANNs have achieved a very optimistic result in the estimation of landslide susceptibility than the logistic regression method. Further, Melchiorre et al. (2008) have shown that predictive capability can be improved through cluster analysis in ANN. Furthermore,

Pradhan and Lee (2010a, b, c) have used the logistic regression, frequency ratio, and ANN models for landslide susceptibility analysis.

In the present work, the ANN and Logistic Regression (LR) based models have been utilized for landslide hazard assessment, where the considered landslide zones of the study area located along NH-1A from Ramban to Banihal of Ramban district, Jammu & Kashmir, India. Stratigraphically, some part of Ramban to Banihal stretch lies between two major thrust zone of Himalaya of regional importance i.e., Main boundary thrust (MBT) in the south and Main Central Thrust (MCT) in the north, and covers some part of central crystalline to the north of MCT. The area is tectonically very active, due to which it has developed very complex geology (Shanker et al. 1989). Rock type in the study area comprises mainly phyllites, slates, limestone, quartzites, volcanic, and some fine to medium-grained sedimentary rocks near Banihal (Shanker et al. 1989; Bhat et al. 1999). Granitic intrusions are exposed between Digdole and Makerkote. The regional strike of the area varies from NW–SE to WNW-ESE, with a dip varies from moderate to very steep towards N or S. Strata are characterized by three to four joint sets with one joint parallel to the road. Different rating given in the Bureau of Indian Standards (BIS) code for landslide hazard zonation mapping for hilly terrain on the scale (1:50,000) has been utilized (BIS 1998) during this study. The rating for landslide causative factors and triggering factors such as lithology, structure, relative relief, slope angle, land use and land cover, hydrological condition, seismicity, and rainfall (Anbalagan et al. 2008) have been considered for the proposed assessment. The QGIS software tool has been utilized to find the data parameters from the digital elevation model (DEM). The QGIS software is an open-source GIS tool that gained huge popularity among engineers, researchers, and scientists of earth science to compute the geospatial data by incorporating a large number of data access, processing, visualization, and analysis operations. On the contrary, the simulation design of machine learning models for the presented study has been accommodated using 'WEKA' an open-source software (Hall et al. 2009) tool. The materials and methods used in this study have been mentioned in the next section.

19.2 Materials and Methods

Generally, a machine learning model predicts the outcome(s) through the interpolation of the data set. Data splitting was carried out to train and test the data set on which the performance was measured to build an efficient classifier. The data splitting for the training and testing sets was done with statistical considerations (i.e., mean, standard deviation, and coefficient of variation). The important parameters which influence the instability of the slope are depicted in Fig. 19.1, whereas the statistical aspects (minimum, maximum, mean, and standard deviation) are illustrated in Table 19.1. In the present work, the data set has been divided into a ratio of 70:30 for training and testing, respectively. Generally, 70% data is considered sufficient in training any network, and the rest of the data is reserved for testing and validating the model. To make a predictive classifier, relative relief, slope, lithology, geological

structures, hydrological condition, and land use and land cover were defined as input parameters into the machine learning model, and the type of hazardous zone, i.e., very high hazard zone, high hazard zone, moderate hazard zone and low hazard zone and very low hazard zone state indicates output.

The important attributes of the data based on feature extraction and selection have been processed in the data processing phase. The general performance of the classification models has been achieved using training data sets. On the contrary, testing data was used to check the final model's predictive capabilities. A complete flowchart of the procedure has been demonstrated in Fig. 19.2. In order to tune the outcome and to prevent the problem of over-fitting the models, the hyper-parameters are defined during training, which is selected based on a trial-and-error method.

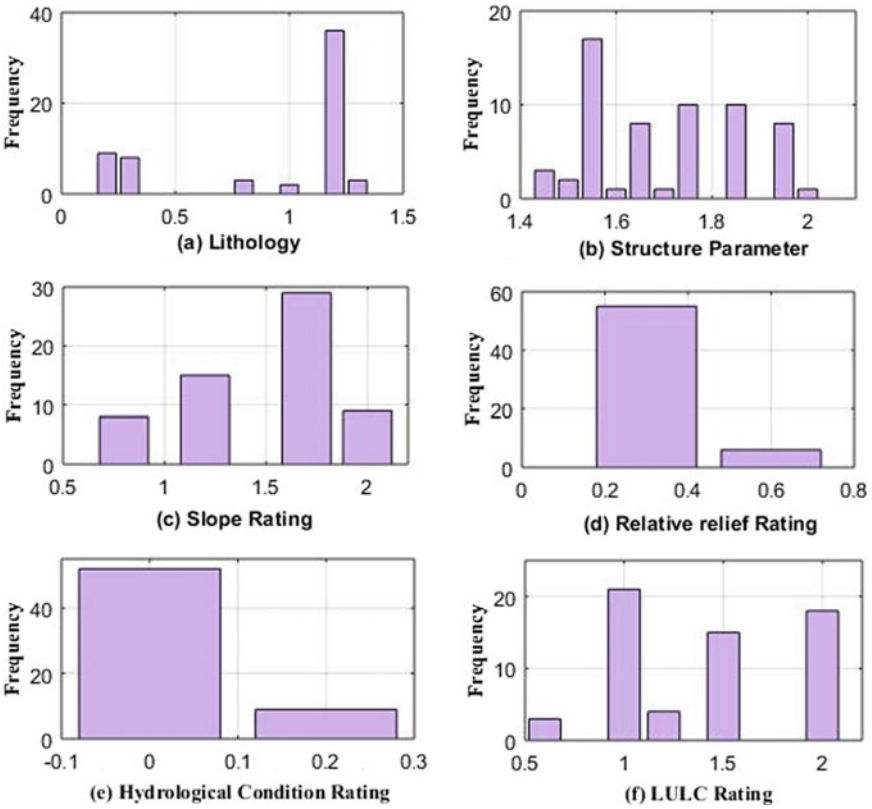

Fig. 19.1 Causative factor rating according to BIS code with minimum, maximum, mean, and standard deviation **a** Lithology rating, **b** Relative relief rating, **c** Structural parameter rating, **d** Slope rating, **e** Hydrological condition rating

Table 19.1 Different statistical aspects of the data parameters

Factors rating	Minimum	Maximum	Mean	Standard Deviation	Coefficient of variation
Lithology	0.2	1.2	0.800	0.460	0.576
Relative relief	0.3	0.6	0.450	0.212	0.472
Structural parameter	1.45	2	1.700	0.187	0.110
Slope	0.8	2	1.425	0.532	0.373
Hydrological condition	0	0.2	0.100	0.141	1.414
LULC	0.6	2	0.260	0.527	2.028

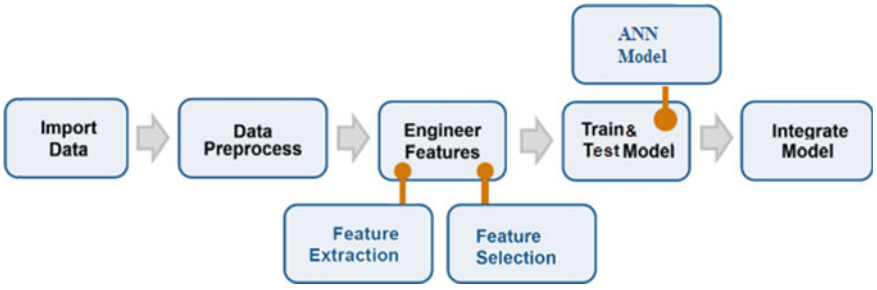

Fig. 19.2 Flow diagram of prediction classification model using BPNN

19.2.1 Dataset and Its Preliminary Analysis

The proposed work considers 61 landslide locations of hazard zones along NH 1-A of Ramban district, Jammu, and Kashmir for preparing the study dataset. According to BIS code, the study area falls under two hazards zone, namely moderate hazard and high hazard, in the classification (IS 14496 Part 2 1998). The google earth image of the area shown in Fig. 19.3 shows the aforesaid landslide presence.

For the above landslides area, 11-inputs factors were considered in the dataset, including six causative factors, two triggering, and three geological structure parameters' relationship between slope and rock strata. The causative factors include relative relief, slope, lithology, hydrological condition, soil thickness, land use, and land cover while triggering factors include rainfall and seismicity. The rainfall data were taken from IMD, Ramban and according to seismic zonation of the country area lies in seismic zone IV. Based on the severity of these factors in initiating landslide, different rating has been described in the Bureau of Indian Standards (BIS) code. The important features were extracted from QGIS, Google earth images, and field photographs, while the physiographical and geological studies were carried out in the field itself. The thematic maps of causative factors are depicted using Fig. 19.4.

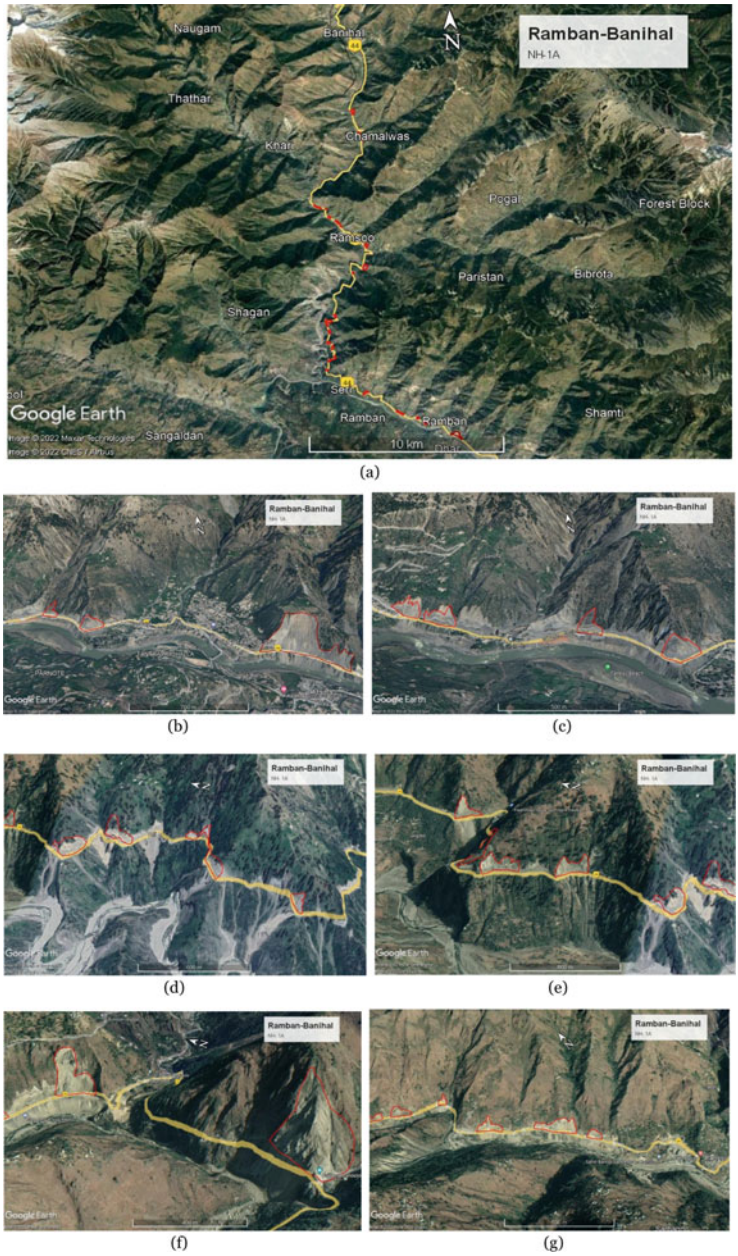

Fig. 19.3 Google earth image depicts **a** Ramban to Banihal stretch, **b** landslide located near Ramban along NH-1A, **c** landslide located between Ramban and Banihal along NH-1A, **d** landslide located between Ramban and Banihal along NH-1A, **e** landslide located between Ramban and Banihal along NH-1A, **f** landslide located between Ramban and Banihal along NH-1A, **g** landslide located near Banihal along NH-1A

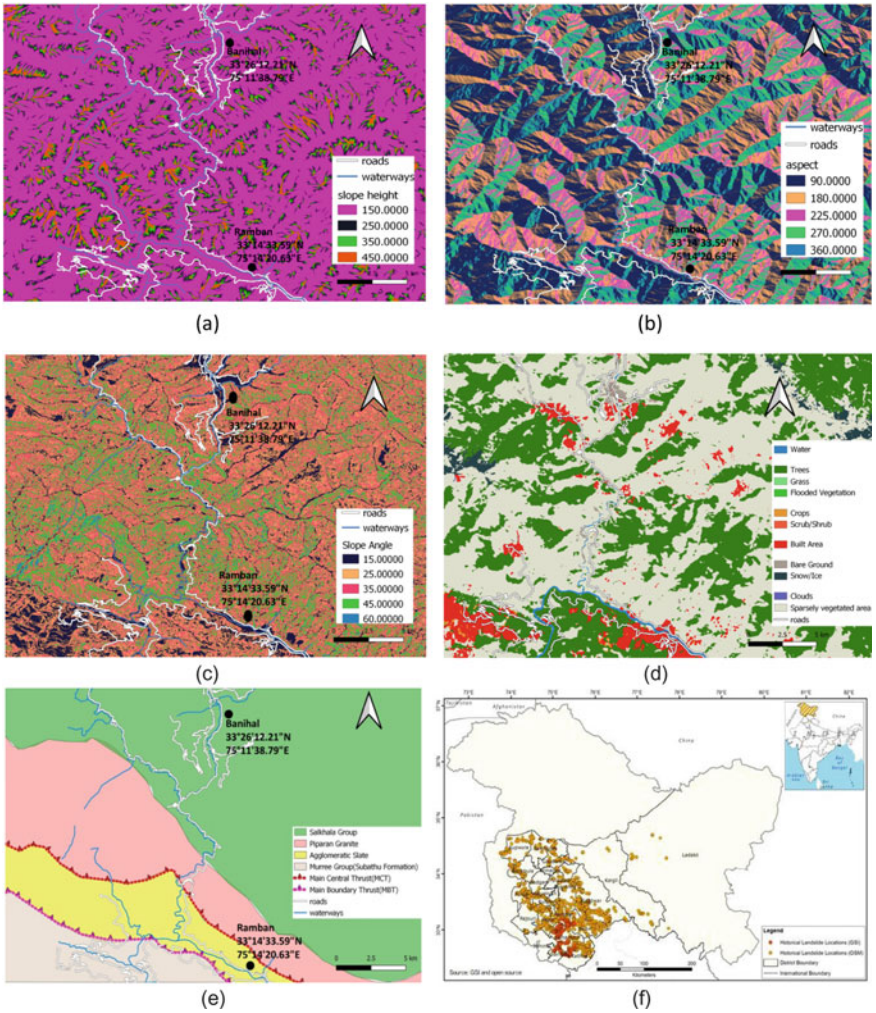

Fig. 19.4 Causative factors of landslide thematic maps **a** Relative relief, **b** Slope aspect, **c** Slope angle, **d** LULC, **e** Lithological map, **f** Historical landslide map

19.3 Selection of Machine Learning Models

Many researchers have used computational intelligence methodologies with the progress of high computational processing power (Singh. et al. 2016; Al-Najjar and Pradhan 2021; Dou et al. 2015). Artificial intelligence and machine learning approaches have enhanced the accuracy of predicting sensitive areas by landslide evaluation. A Back-Propagation Neural Network (BPNN) was used for the current study to predict landslide zones with large accuracy. The approach is used to build

a predictive classifier by examining multivariate data. The BPNN method was compared to logistic regression and SVM in order to validate and compare the method's performance. The aforementioned approaches have become quite popular because of its ease of use, efficacy, and ability to generate complicated non-linear relationship models. Table 19.2 gives a quick overview of these methods, however, the readers are encouraged to consult the necessary references for more detail (Pradhan and Lee 2010b, c; Dou et al. 2015; Li et al. 2012).

The BPNN algorithm is found to perform reasonably well when applied to the supplied dataset. In comparison to logistic regression and SVM, the BPNN has a high prediction accuracy. Furthermore, because of its simplicity, diversity, and capacity to handle big datasets, missing data, and the risk of over-fitting problems, the BPNN technique has been widely utilised. Besides, it has previously demonstrated remarkable performance for such nonlinear problems (Khandelwal and Singh 2009; Bashiri and Geranmayeh 2011; Khaw et al. 1995; Tortum et al. 2007). Because of these following facts, the BPNN regression model was used for the study.

Table 19.2 Overview of machine learning algorithms employed for landslide assessments

ML models	Specifications
Back Propagation Neural Network (BPNN)	BPNN is a multi-layered feed-forward neural network component. It is made up of three layers: the input layer, the output layer, and the hidden layer. The input layer receives the input signal to be processed. The output layer is responsible for tasks such as prediction and classification (Dou et al. 2015)
Support Vector Machine (SVM)	SVMs revolve around the notion of a 'margin' on either side of a hyperplane that separates two data classes. Maximizing the margin distance provides some reinforcement to classify future data points with more confidence (Singh et al. 2016; Cortes et al. 1995)
M5-rule Algorithm	M5 rule-Generates a decision list for regression problems using separate and conquer. It builds a model tree in each iteration using the M5 algorithm and makes the "best" leaf into a rule (Holmes et al. 1999; Witten and Wang 1997)
M5-P tree	M5P tree algorithm combines a conventional decision tree with the possibility of linear regression functions at the terminal (leaf) nodes that can predict continuous numerical attributes. It is a decision tree learner for a regression problem that is used to predict the values of a numerical response variable (Singh et al. 2017; Quinlan 1992)

19.3.1 Back-Propagation Neural Networks (BPNN)

The BPNN is a machine learning algorithm developed to act like a human memory to perform any specific work (Haykin 1999). It was invented in the 1970s but has gained popularity in recent times because of its capability to be used in every field. As the neurons work in the human nervous system, ANN also works in the same fashion, learns from the data, and prepares itself to respond either as classification or prediction. It involves many interconnected processing units which process the information. In the configuration of the ANN model, the neurons help in processing the stimulation with the ability to receive and transmit the signal. The signals are transmitted or received from one neuron to another in a well-defined network connected with synaptic weight which represents the bond strength of each neuron. The synaptic weight is positive relationships among the contributing nodes (Fausett 1994). ANN model is able to predict on the basis of input data even if the relationship between the input factors is not very clear or their physical significance is hard to describe. Due to this characteristic of ANN model, it is more preferred and advantageous than that statistical and empirical method in which a well-defined relationship between the input data is needed in the form of linear, nonlinear, etc. The main difference between conventional processing of information and neural network is that it has the ability of proper data manipulation if appropriate weights between layers are selected. It also has weight changing mechanism.

19.3.1.1 Layers of Back Propagation Neural Network

BPNN is catalogued into three layers. The layers comprise connected nodes which have a 'stimulation function'.

(i) *Input Layer*

The input layer acts as a receiver for the input of raw information. Generally, input nodes are equal to a number of independent variables present in the data set that needs to be fed into the network. Each input node is connected to one or more hidden layers. The nodes of the input layer do not change the input value.

(ii) *Hidden Layer*

This layer basically transforms the raw value in the network according to the desired activity and acts as a link between input data and output result. There can be one or more hidden layers in any network. The values given to hidden nodes are multiplied by hidden layers weight and produce a single number as an output value.

(iii) *Output Layer*

The output layer is connected either from a hidden layer or from the input layer. It produces output value based on the activity of the hidden layer and the weights defined among the output and hidden. In the case of prediction, the output value

corresponds to the response of the input variable. In the case of a classification problem, there is only a single output node.

19.3.1.2 Training Methods

During the training process, neural networks acquire information as humans do, and the information or the signal is stored in the network system (Haykin 1999). The BPNN model is trained in such a way that it can combine the thinking process of the human brain with mathematical intellect (McClelland et al. 1986). The training method has three steps:

(i) In this step, supervised network training is done with the help of a set of training patterns related to the target output.
(ii) Unsupervised training is done in this step, where the network is trained by a group of a similar set of training patterns as that of a supervised training pattern.
(iii) In the last step, the reinforcement training is done with the help of the interaction of the network with the environment.

The training phase output and hidden layer neuron of the network processes the input and multiple each input with the corresponding weightage and then process the sum with a non-linear transformation function to yield the final result. The ANN can also adjust weight among the neurons in feedback to the error between the target output and actual output values. The outcome of training the network is the development of a model that can predict the target value from a given input value.

19.3.1.3 Features of BPNN

The back-propagation neural network comprises three different attributes: network structure, training algorithm, and function for activation (Fausett 1994; Benardos and Benardos 2005). The network structure is also termed network architecture, and it is the design or the relation by which different neurons are connected. A network with only two units, i.e., input and output layer, is the simplest structure of the network, and when one more layer, i.e., a hidden layer, is added to the network, it becomes capable of predicting desired output values. Design of the network is the most critical part of the network on the basis of understanding of the problem (Benardos and Kaliampakos 2004). In the training algorithm, part weightage value is given to the connection of neurons. The activation function is used in the last stage of the development of the model. In the feed-forward network, the signal flows towards the output direction from the input direction. The BPNN is a multi-layer, feed-forward neural network component. It is made up of three layers: the input layer, the output layer, and the hidden layer. The input signal to be processed is received by the input layer. The output layer is responsible for tasks such as prediction and classification. The real computational engine of the BPNN is an arbitrary number of hidden layers inserted between the input and output layers. In a BPNN, data flows forward from the input to

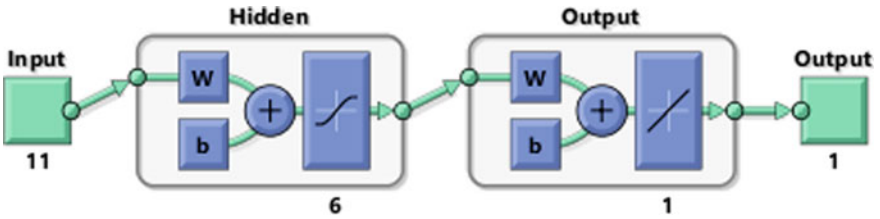

Fig. 19.5 Architecture of back propagation multi-layer neural network (BPNN)

the output layer, similar to a feed-forward network. The hidden layer has nodes due to which complexities develop in the model. The architecture design of the employed BPMNN is shown in Fig. 19.5.

19.4 Results and Discussion

The landslide hazard zonation map has been developed for the study area according to the rating laid in BIS code as discussed in the previous sections. The rating has divided the NH 1-A Ramban to Banihal stretch into two categories, "Moderate hazard zone and High hazard zone," which is represented by 1 or 2, illustrated in Fig. 19.6. The result has revealed that most of the region in the study area falls under the high hazard category, and some part falls in the moderate hazard zone. The percentages of these categories are 80.46 and 19.54%, respectively as shown in Fig. 19.6. The redundant data that was located beyond the mean range was removed, and the remaining data samples were used in a 70–30% ratio for training, testing, and validation. This regression model's performance was compared across the training, testing, and validation sets. The regression plot shows the prediction responses (output) for the training, testing, and validation sets. The data should fall along a 45-degree line for a perfect fit, with the network outputs equal to the responses. As shown in Fig. 19.7, the result indicates that the data fit is reasonable, with a high *R*-value for all data sets.

A plot of training record error values against the number of training epochs has also been discussed using Fig. 19.8. Generally, the error reduces after more epochs of training but might start to increase on the validation data set as the network starts overfitting the training data. The training stops after 1,000 epochs consecutive increases in validation error in the default setup, and the best performance is taken from the epoch with the lowest validation error. The result is found reasonable due to the minimum mean-square error. The test and validation set errors have also shown similar characteristics. Besides, no significant overfitting has occurred by epoch 1,000.

The investigation outcome revealed that the BPNN model is the most appropriate tool for predicting landslide hazard zonation as compared to other discussed machine learning models. The actual vs. predicted results plot is depicted in Fig. 19.9.

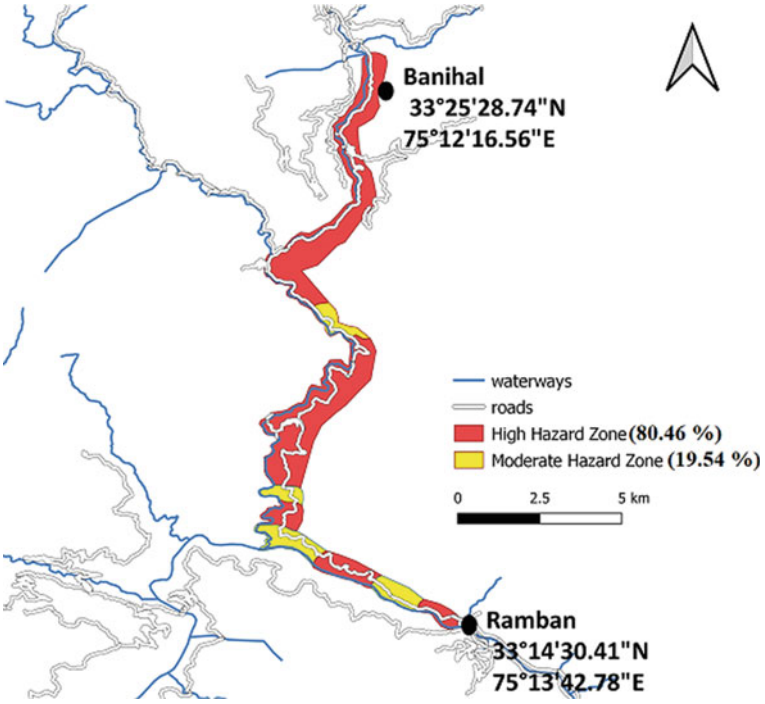

Fig. 19.6 Landslide hazard zonation map of National Highway1-A along Ramban to Banihal

In comparison to other ML-methods (M5-P, M5-rule, and SVM approaches), the investigation outcomes demonstrated that the BPNN with 6 hidden layers gives the least values of correlation coefficient value as 0.8715, the mean absolute error value is 0.192, and the root means squared error (RMES) value is 0.278. Comparison plots between mean absolute error (MAE) and root mean square error (RMES) over machine learning methods are depicted in Fig. 19.10.

19.5 Conclusions

Landslides often occur in the hazardous zone of the Himalayan region. It became cumbersome and challenging due to uncertain geological and geotechnical parameters. The factors causing frequent landslide includes highly weathered and structurally deformed rocks, continuous tectonic activity along regional faults and thrusts, high rainfall, the extension of human settlement in a hilly area, and infrastructure & road construction. In recent times, various engineers and scientists gained attention in identifying these influential factors. This study has done landslide hazard zonation mapping along the road section NH 1-A of Ramban Himalaya according to the rating

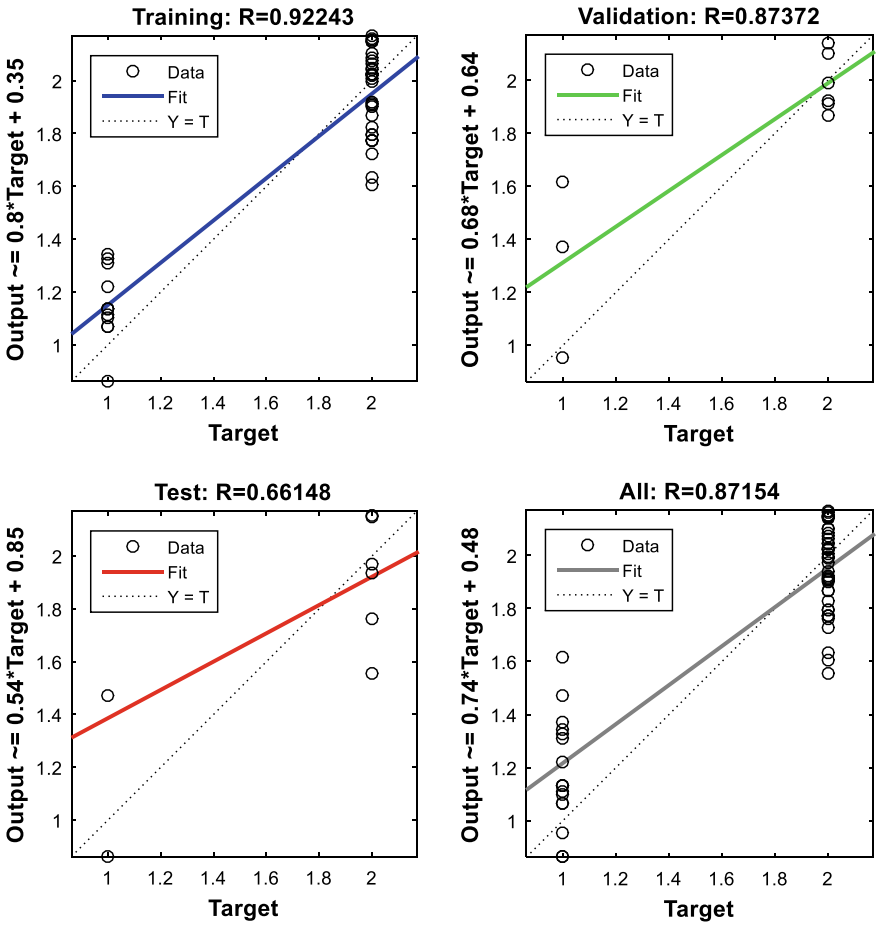

Fig. 19.7 A performance comparison for susceptible area prediction using BPNN model

laid in BIS code. The map has depicted that most of the region (~80.46%) in the study area falls under the high hazard category while the remaining region (~19.54%) lies under the moderate hazard category. The development of machine learning-based computation technologies has aided the researcher in developing intelligent models to predict landslide hazard zones. This study also covers a machine learning approach called back-propagation neural network (BPNN) for landslide hazard assessment. The cumulative effect, including causative and triggering factors of landslides, were considered for preparing the dataset of the study. The BPNN model's performance has been investigated over the data set using training and testing. The validation of the performance has been examined based on three other machine learning models such as SVM, M5-rule, and M5P. The investigation revealed that the BPNN model shows a better performance in terms of high prediction accuracy and minimum error

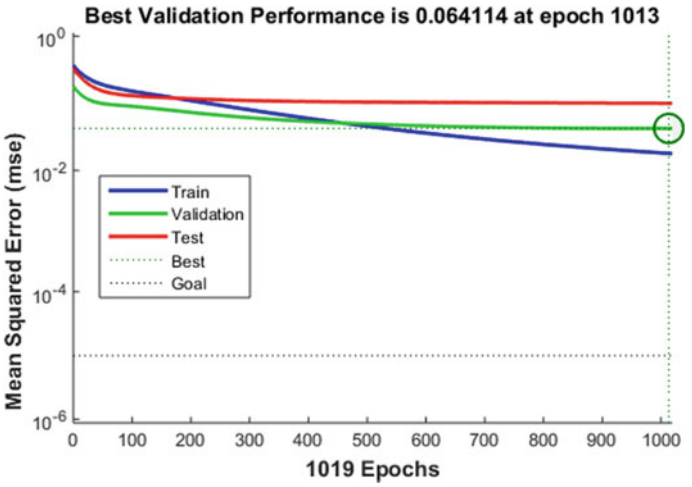

Fig. 19.8 A performance plot of the training errors, validation errors, and test errors

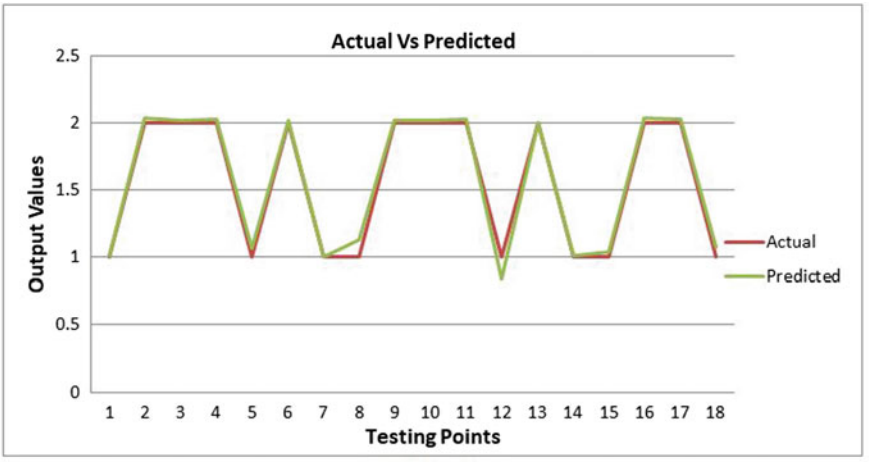

Actual	1	2	2	2	1	2	1	1	2	2	2	1	2	1	1	2	2	1
Predicted	1.01	2.03	2.01	2.02	1.06	2.02	1.01	1.13	2.01	2.01	2.03	0.84	2	1.01	1.04	2.03	2.03	1.08

Fig. 19.9 Actual vs predicted landslide plot for the testing dataset

as compared to other discussed machine learning models. Based on the above observations, it is concluded that the proposed method can be used as a significant tool for the identification of landslide hazard zones and provides its mitigation measures. The implication of the study provides theoretical guidance to the researchers and engineers working in the Ramban to Banihal area to assist in developing infrastructure and construction & widening of national highways.

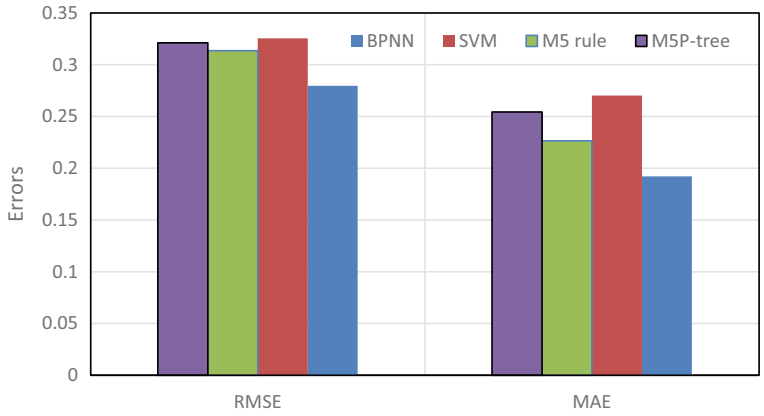

Fig. 19.10 Comparison of MAE and RMSE over different machine learning methods

Conflict of Interest The authors wish to confirm that there are no conflicts of interest with this research article.

References

Anbalagan R, Chakraborty D, Kohli A (2008) Landslide hazard zonation (LHZ) mapping on meso-scale for systematic town planning in mountainous terrain

Al-Najjar HA, Pradhan B (2021) Spatial landslide susceptibility assessment using machine learning techniques assisted by additional data created with generative adversarial networks. Geosci Front 12(2):625–637

Arora MK, Gupta ASD, Gupta RP (2004) An artificial neural network approach for landslide hazard zonation in the Bhagirathi (Ganga) Valley, Himalayas. Int J Remote Sensing 25(3): 559–572

Bashiri M, Geranmayeh AF (2011) Tuning the parameters of an artificial neural network using central composite design and genetic algorithm. Sci Iran 18(6):1600–1608

Benardos AG, Benardos AP (2005) Applications of artificial neural networks in geotechnology. Chron Min Metall 15(1):65–81 (in Greek)

Benardos AG, Kaliampakos DC (2004) Modelling TBM performance with artificial neural networks. Tunn Undergr Space Technol 19(6):597–605

Bhat GM, Pandita SK, Singh R, Malik M A, Sarkar S (1999) Northwest Himalayan Successions along Jammu–Srinagar Transect (Field Guide). Indian Association of Sedimentologists, Aligarh, India, 141 pp

Bureau of Indian Standard (1998) IS: 14496, Preparation of Landslide Hazard Zonation Maps in Mountainous terrains – Guidelines, Part 2 Macro-zonation, BIS, New Delhi

Chingkhei RK, Shiroyleima A, Singh LR, Kumar A (2013) Landslide hazard zonation in NH-1A in Kashmir Himalaya, India. Int J Geosci

Cortes C, V (1995) Support-vector networks. Mach Learn 20(3):273–297

Dou J, Yamagishi H, Pourghasemi HR, Yunus AP, Song X, Xu Y, Zhu Z (2015) An integrated artificial neural network model for the landslide susceptibility assessment of Osado Island Japan. Nat Hazards 78(3):1749–1776

Fausett L (1994) Fundamentals of neural networks architectures, Algorithms and applications. Prentice-Hall, Upper Saddle River, NJ, p 461

Holmes G, Hall M, Prank E (1999) Generating rule sets from model trees. In Australasian joint conference on artificial intelligence. Springer, Berlin, Heidelberg, pp 1–12
Hosmer D, Lemeshow S (2004) Applied logistic regression. Wiley
Hall M, Frank E, Holmes G, Pfahringer B, Reutemann P, Witten IH (2009) The WEKA data mining software: an update. ACM SIGKDD Explorations Newslett 11(1):10–18
Haykin S (1999) Neural networks. A comprehensive foundation, 2nd edn. Prentice-Hall, Englewood Cliffs, NJ, p 696
Kanungo DP, Arora MK, Sarkar S, Gupta RP (2006) A comparative study of conventional, ANN black box, fuzzy and combined neural and fuzzy weighting procedures for landslide susceptibility zonation in Darjeeling Himalayas. Eng Geol 85:347–366
Khandelwal M, Singh TN (2009) Prediction of blast-induced ground vibration using artificial neural network. Int J Rock Mech Min Sci 46(7):1214–1222
Khaw JF, Lim BS, Lim LE (1995) Optimal design of neural networks using the Taguchi method. Neurocomputing 7(3):225–245
Lee S, Ryu JH, Lee MJ, Won JS (2003a) Landslide susceptibility analysis using artificial neural network at Boun Korea. Environ Geol 44:820–833
Lee S, Ryu JH, Min KD, Won JS (2003b) Landslide susceptibility analysis using GIS and artificial neural network. Earth Surf Proc Land 27:1361–1376
Lee S, Ryu JH, Lee MJ, Won JS (2006) The application of artificial neural networks to landslide susceptibility mapping at Janghung Korea. Math Geol 38(2):199–220
Li Y, Chen G, Tang C, Zhou G, Zheng L (2012) Rainfall and earthquake-induced landslide susceptibility assessment using GIS and Artificial Neural Network. Nat Hazard Earth Sys Sci 12(8):2719–2729
McClelland JL, Rumelhart DE, the PDP Research Group (1986) Parallel distributed processing: Explorations in the microstructure of cognition, vol II. MIT Press, Cambridge, MA
Melchiorre C, Matteucci M, Azzoni A, Zanchi A (2008) Artificial neural networks and cluster analysis in landslide susceptibility zonation. Geomorphology 94:379–400
Nefeslioglu HA, Gokceoglu C, Sonmez H (2008) An assessment on the use of logistic regression and artificial neural networks with different sampling strategies for the preparation of landslide susceptibility maps. Eng Geol 97:171–191
Pistocchi A, Luzi L, Napolitano P (2002) The use of predictive modeling techniques for optimal exploitation of spatial databases: a case study in landslide hazard mapping with expert system-like methods. Environ Geol 41:765–775
Pradhan B, Lee S (2010a) Delineation of landslide hazard areas on Penang Island, Malaysia, by using frequency ratio, logistic regression, and artificial neural network models. Environ Earth Sci 60:1037–1054
Pradhan B, Lee S (2010b) Landslide susceptibility assessment and factor effect analysis: Backpropagation artificial neural networks and their comparison with frequency ratio and bivariate logistic regression modeling. Environ Model Softw 25(6):747–759
Pradhan B, Lee S (2010c) Regional landslide susceptibility analysis using back-propagation neural network model at Cameron Highland Malaysia. Landslides 7(1):13–30
Quinlan, J. R. (1992) Learning with continuous classes. In 5th Australian joint conference on artificial intelligence, Vol 92, pp 343–348
Shanker R, Kumar G, Saxena SP (1989) "Stratigraphy and sedimentation in Himalayas: A Reappraisal" geology and tectonics of Himalaya. Geo Surv Ind Special Pub 26:1–26
Singh J, Verma AK, Haider B, Singh TN, Sachin M (2016) A study of soft computing models for prediction of longitudinal wave velocity. Arabian J Geosci 9(3): 224
Singh B, Sihag P, Singh K (2017) Modelling of impact of water quality on infiltration rate of soil by random forest regression. Model Earth Syst Environ 3(3):999–1004
Singh J, Haider B, Verma AK (2019) A BBO-based algorithm for slope stability analysis by locating critical failure surface. Neural Comput Appl 31(10):6401–6418
Tortum A, Yayla N, Çelik C, Gökdağ M (2007) The investigation of model selection criteria in artificial neural networks by the Taguchi method. Physica A 386(1):446–468

Witten IH, Wang Y (1997) Induction of model trees for predicting continuous classes. In Proc. Poster Papers Europ. Conf. Machine Learning

Yilmaz I (2009) Landslide susceptibility mapping using frequency ratio, logistic regression, artificial neural networks and their comparison: a case study from Kat landslides (Tokat—Turkey). Comput Geosci 35(6):1125–1138

Chapter 20
Social and Economic Impacts of Kotropi Landslide on National Highways of Himalayas—A Case Study

C. Prakasam and R. Aravinth

Abstract The current research reveals the social and economic impacts of the 2017 Kotropi slope failure and also its impacts on social and economic activities. To estimate the landscape changes due to the landslide pre and post-landslide LULC maps were created with the help of Google Earth imageries. The LULC changes revealed the changes that occurred in the agricultural land, settlements, and forest regions. The post-landslide satellite imageries reveal that 10% of the study area is covered under landslides which affect the natural slopes and agricultural areas that are present along the downslope of the landslide. The Agricultural area has reduced from 18 to 14%, with an increase in fallow land from 11 to 16%. The total length of the landslide is estimated to be 1290 m and the width to be 190 m. The total length of the Runout debris is alone 551 m. Settlements and Agriculture lands located along the upper region of the slope and downhill sections are the most affected regions. It also found that the old landslide scarps were found in 2011 and 2013, indicating the slope failure was an ongoing event. Increased pore pressure in the soil leading to overburdening and monsoon rainfall coupled with exposed bare soil in the study area are the prime causative factors of the landslide. The future aspect of the research includes the construction of proper slope stability measures and continuous monitoring using an early warning system that will negate and control future occurrences of landslides.

Keyword Kotropi landslide · LULC · Trans communication · Socio-economic · Landslide morphology

C. Prakasam (✉)
Department of Geography, School of Earth Sciences, Assam University Diphu Campus, Diphu, Karbi Anglong 782462, Assam, India
e-mail: cprakasam@gmail.com

R. Aravinth
Institute of Environment Education and Research, Bharathi Vidyapeeth University, Katraj-Dhanakwadi, Pune 411043, Maharashtra, India

P. Thambidurai and T. N. Singh (eds.), *Landslides: Detection, Prediction and Monitoring*,
https://doi.org/10.1007/978-3-031-23859-8_20

20.1 Introduction

A landslide is the downward movement of slope-forming materials due to externally induced actions such as rainfall, overburden, removal of support structures, weakened soil structure, blockage of drainage, and gravity. The term landslide encompasses all sorts of mass movements such as fall, topple, flow, creep, etc. (Gupta et al. 2022). Even though the Himalayan region is highly prone to numerous natural disasters among them, landslides happen to be more frequent due to multiple causative and inducing factors and also improper interaction of human beings with nature (Dasn and Lepcha 2019; Sharma and Mahajan 2018). Prakasam et al. (2020) stated that approx 0.42 million sq. km of the land area is prone to landslides in our country, where NW Himalayas comprise 0.14 million sq. km of these areas. Around 80% of the landslides in the Himalayas occur during monsoon and post-monsoon season and cause significant social and economic losses. In 2017s Dhalli landslide in Shimla town and the Kotropi landslide in Mandi districts are some of the prime examples (Fig. 20.1) (Alsabhan et al. 2022; Prakasam et al. 2021). Destroyed National Highways, Agricultural fields, communication and grid lines are some examples of problems caused by landslide incidents (Bhattacharya et al. 2013; Ramesh et al. 2017; Sultana 2020). Rocks are fragile in the Himalayan region and often occur in areas of settlements, NH etc. Increased alteration of forest areas for agricultural activities, building construction, road pavement, and deforestation increase the risk and frequency of landslides in the study area (Achu et al. 2020; Prakasam et al. 2022; Yuvaraj and Dolui 2021). Landslide often happens without any warning sign giving less time for people to evacuate (Kumar et al. 2019; Mandal et al. 2021; Panchal and Shrivastava 2022). In Himalayan studies related to the impacts of landslides at social and economic levels is an important aspect because addressing individual landslides and their protection measures will allow us to monitor the landslide slides and come up with results to negate the future movements of those landslides (Amatya et al. 2021; Rusk et al. 2022; Shah et al. 2021). Landslides around the world have been an increasing trend due to changing climate, anthropogenic activities, and increasing development due to human necessity. Various other authors such as have also contributed significant research to slope instability analysis for various regions in India (Das 2011a, b; Rawat and Joshi 2012; Sivasankar et al. 2021). The objective of the research is to study the impacts of the Kotropi landslide on the societal level and economy. The results also allowed us to estimate the damages to communication lines, the morphology of the landslide, and estimated significant changes in pre and post-landslide events.

Fig. 20.1 **a** and **b** destroyed public transports and damaged vehicles due to landslide; **c** Damaged local hamlet located along the landslide affected area; **d** Post landslide rescue activities by the govt authorities (*Source* News articles)

20.2 Region of Interest

The landslide in research is located within the Pathar Tehsil of Mandi district, located 76°37′45″ to 77°23′21″ E and 31°13′0″ to 32°04′01″ N (Fig. 20.2). The district encompasses 3,950 sq. km and with a population of 9.99 lakhs people as per the census 2011. Beas and Sutlej are the two main rivers that drain through these regions and form the main source of water for agricultural and other social activities. Geologically the region is active and intersects between the Shali and Siwaliks groups. Dolomites, mudstones, purple clay, and sandstones are some of the notable soil formations found in these regions. Since mandi is located along the highly dissected Himalayan region, variable climates are observed, ranging from temperate climates near the hilltops and tropical valleys. The Kotropi landslide occurred along the NH 154 connecting Mandi–Pathankot extending in the NE–SW direction with a total runout length of >1 km. The landslide area mostly constituted red laterite and coarse loamy soil along the main scarp as well as the downslope regions. The Kotropi landslide is a debris flow type that led to immense loss of life, agricultural land, and settlements along the upper and lower reaches of the slopes. Since the landslides occurred along NH 154, it also destroyed around 200 m of the NH, causing transport

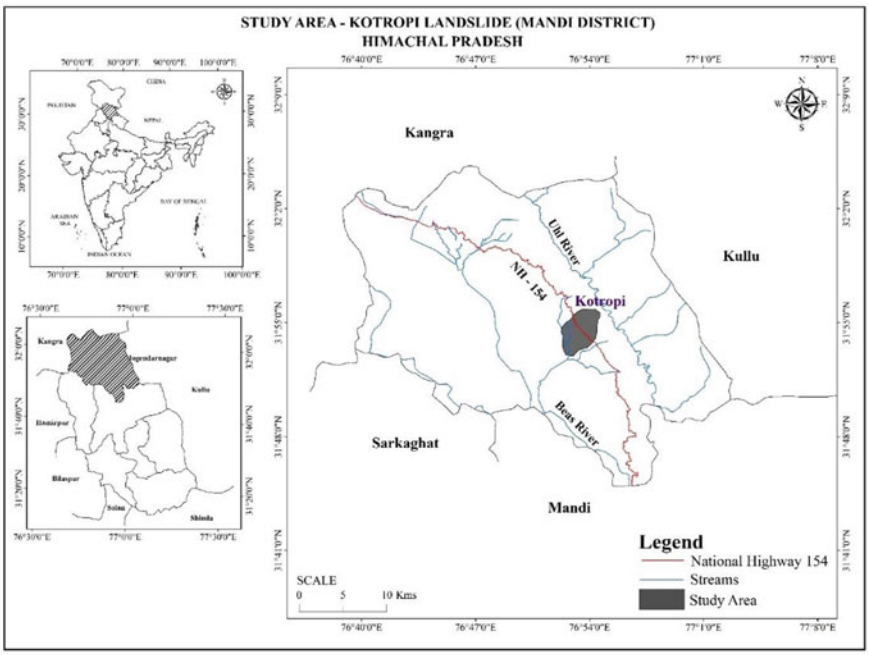

Fig. 20.2 Study area

and communication problems along these regions (Fig. 20.3). Post-monsoon rainfall coupled with exposed bare soil with less to no deep-rooted tress is the main reason for the landslide.

20.2.1 Regional Setting

The region is mainly dominated by two soil types, namely Lithic Udorthents and Dystrictic Fluventric Eutrochrepts soil (Fig. 20.4; Table 20.1). Seraj and the Karsog blocks of the Mandi district are mainly dominated by sub-mountainous soil, and the remaining blocks are dominated by mountainous soil. Sub-mountainous soils have low levels of phosphate and high levels of organic carbon, providing suitable climatic and soil conditions to grow temperate stone fruits and vegetables. Furthermore, mountainous soil has low levels of phosphorous, medium potash, and nitrogen. The soil texture is classified as loamy to sandy loam within the Mandi district. The main boundary thrust runs perpendicular to the direction of landslide occurrence, and the Kotropi landslide is located right along its edge. In terms of geomorphology, scarped slopes occur in abundance with slopes dipping towards the SW–NE direction. The district also has numerous intermountain valleys, such as Bahl, located at an altitude of 790 m above MSL. with its slopes dipping NNE. These valleys

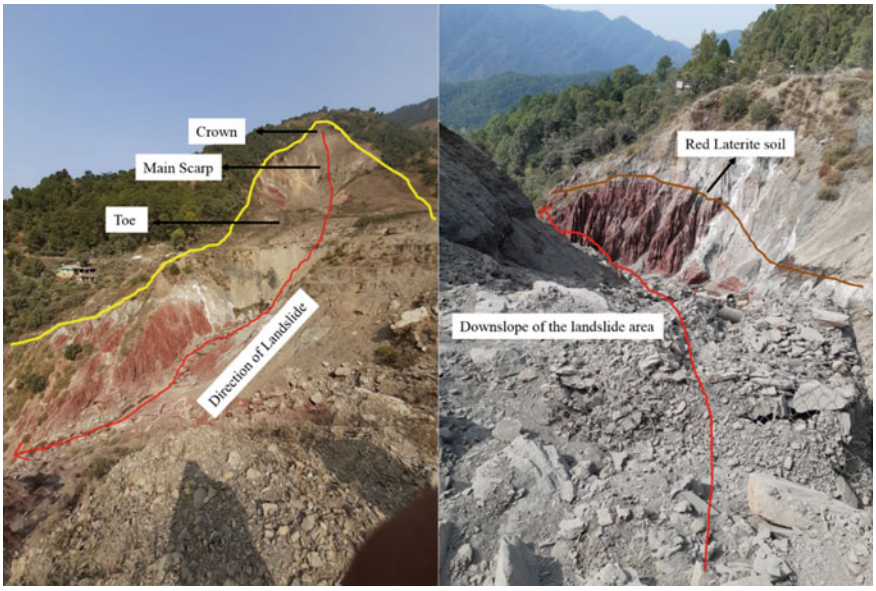

Fig. 20.3 Demarcation of upslope and downslope of the landslide area with varying soil types along the downslope region

are highly undulating, with alluvial plains in the dominant part. Alluvium is found majorly along the riverbanks of Beas and Sutlej.

Mandi district presents an intricate mosaic of mountain ranges, hills, and valleys. Slopes are mainly found dipping towards the southwest. The south-western part consists of Siwalik ranges having scarped slopes. There are a few small intermountain valleys; prominent among them is the Balh valley, located in the lesser Himalayan ranges, having an average altitude of about 790 m above MSL and a general slope towards NNE (Table 20.2). The valley floor is undulating and is marked by low hillocks and terraces fringing the hills and intervening low alluvial plain (Table 20.2).

Changes caused by the Kotropi landslide were estimated through multi-temporal Land use Landcover (LULC) mapping of the area pre- and post-landslide. Sentinel–2A satellite images for 2017 were used to calculate the changes in landcover through supervised classification using the maximum likelihood method (Fig. 20.5). LISS IV satellite data coupled with google earth imageries of pre and post-landslide events were used for morphometry mapping of the landslides. The LULC analysis revealed that the major portion of the area comprises shrublands (75.4%); landslide area and plantation cover 10% of the landslide area. Built-up land and barren lands are present only in minor quantities (Table 20.3).

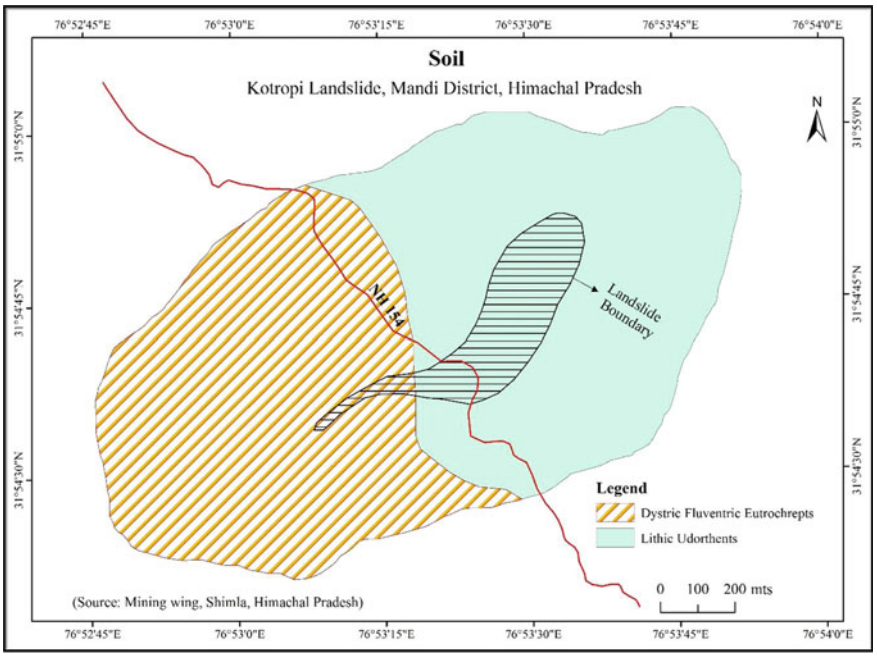

Fig. 20.4 Soil map of Kotropi landslide

Table 20.1 Soil classifications of Kotropi landslide

Sl. No.	Soil class	Area (hectares)	Percent
1	Lithic Udorthents	77.87	52.19
2	Dystrictic Fluventric Eutrochrepts	71.26	47.81
	Total	149.08	100.00

Table 20.2 Geomorphology—Kotropi landslide, Himachal Pradesh

Sl. No.	Class	Area (hectares)	Percent
1	Undifferentiated mountainside slope	81.9	54.9
2	Alluvial plains	67.18	45.0
	Total	149.08	100.0

20.2.2 Rainfall Characteristics

Rainfall data were purchased for the Mandi rain gauge station from 1981 to 2018 at the Indian Meteorological Department (IMD), Pune, Government of India. The results revealed that, on average, the area receives 867 mm of rainfall throughout the year (Fig. 20.6).

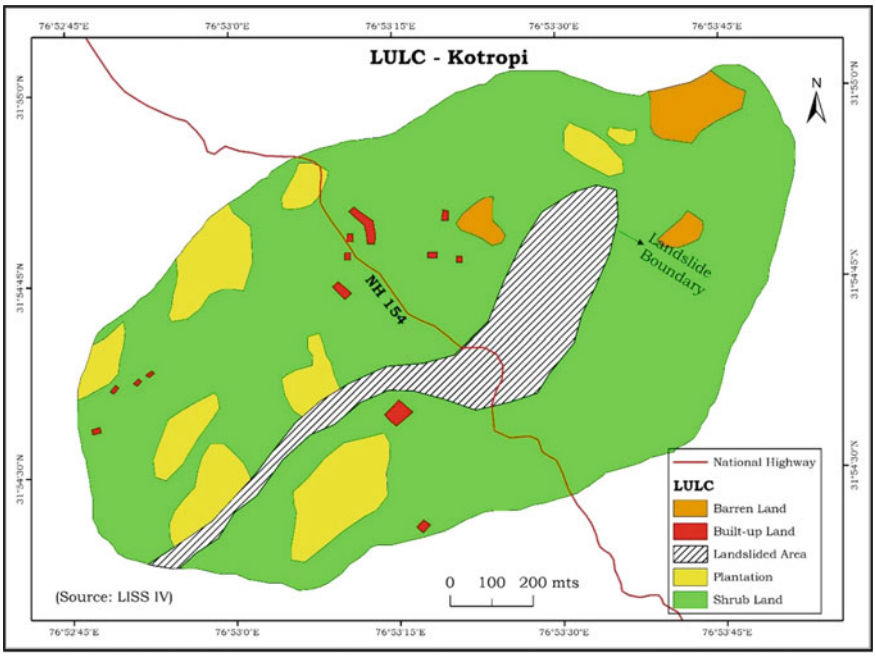

Fig. 20.5 LULC map of the study area

Table 20.3 LULC classes of Kotropi landslide

Sl. No.	Class	Area (hectares)	Percent
1	Barren Land	3.91	2.62
2	Built-up Land	0.83	0.56
3	Plantation	16.34	10.96
4	Landslide Area	15.60	10.46
5	Shrub Land	112.4	75.40
	Total	149.08	100.00

In the last eight years (2011–2017), the region received an average of 1,137.47 mm of monsoon rainfall (Fig. 20.7). The high intensity of rainfall during the monsoon season causes an increased water infiltration capacity, especially in areas with unstable slopes. The water infiltration, coupled with no or poor drainage networks, increases the soil burden, leading to slope failure.

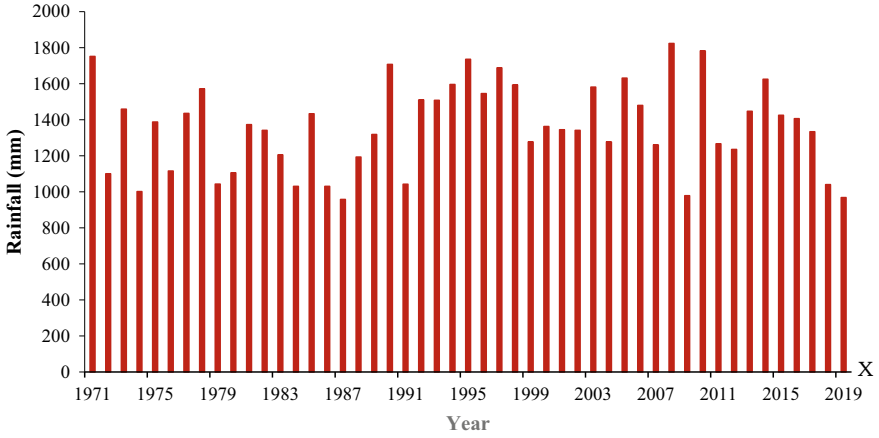

Fig. 20.6 Annual rainfall precipitation in Kotropi (1971–2019)

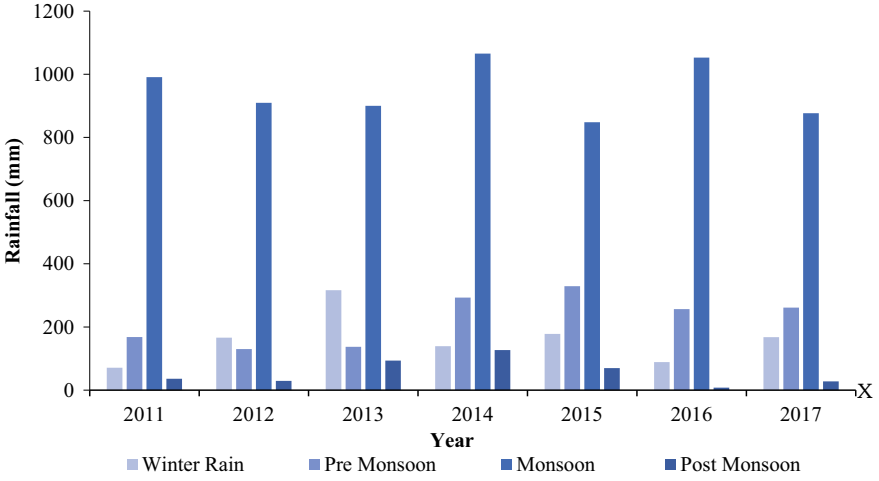

Fig. 20.7 Seasonal rainfall precipitation in Kotropi (2011–2017)

20.3 Data Used

The data collected involved both fieldwork and lab analysis from satellite imagery. Post-landslide images were obtained from field photographs regarding the damage caused by the landslide to local settlements and agricultural land. Survey of India toposheets were only used to get the general layout of the study area regarding the already existing settlements and other economic activities in the area. In order to accurately delineate the boundary of the landslide, LISS IV satellite imagery was obtained from the National Remote Sensing Centre (NRSC). Landsat 8 OLI imageries

Table 20.4 Data used

Sl. No.	Data	Source	Date	Resolution
1	Landslide Photographs	Field work	01/11/2018	
2	Toposheets	SOI	1987	1:50,000
3	Landuse Land cover	LISS IV	06/10/2018	5.8 m
		USGS	05/09/2018	30 m
		USGS	29/06/2017	30 m
4	Rainfall	IMD, Shimla	1971 to 2019	1 day
5	LISS IV	NRSC	2018	5.8 m

of 2017 and 2018 were used to analyse post-landslide land cover. Since rainfall is one of the primary parameters in slope failure data acquired from IMD, Pue was used to analyse the antecedent rainfall patterns pre and post-landslide scenarios (Table 20.4).

20.4 Methodology

The research has been conducted to study the various aspects of the landslide and its impact on social and economic implications. Landslide study at the local level requires morphological demarcation of the various parts of the landslide. The landslide morphology has been derived with the help of 2018 google earth imagery. Various parts of the landslide, such as the crown, main body, radial cracks, and fissures, have been identified and demarcated on the map. The second objective is to study the pre, and post-LULC changes around the landslide occurred area. A 2 km buffer radius has been created with a landslide as the epicenter. The satellite imageries are panmerged to provide increased LULC analysis. NRSC level 1 classification has been used in the current research. The supervised classification method is employed using a maximum likelihood classifier for Landuse change analysis, and an accuracy assessment has been conducted. The impact of pre and post-landslide events on socio-economic systems is depicted by demarcation information in the study area through google earth imageries for the years 2014 and 2017. The damages due to the landslide to the nearby settlements, agricultural, and roadway corridors are demarcated in the google earth imageries, and results are tabulated. The socio-economical study of the landslide is highly qualitative and involves local impacts (Fig. 20.8).

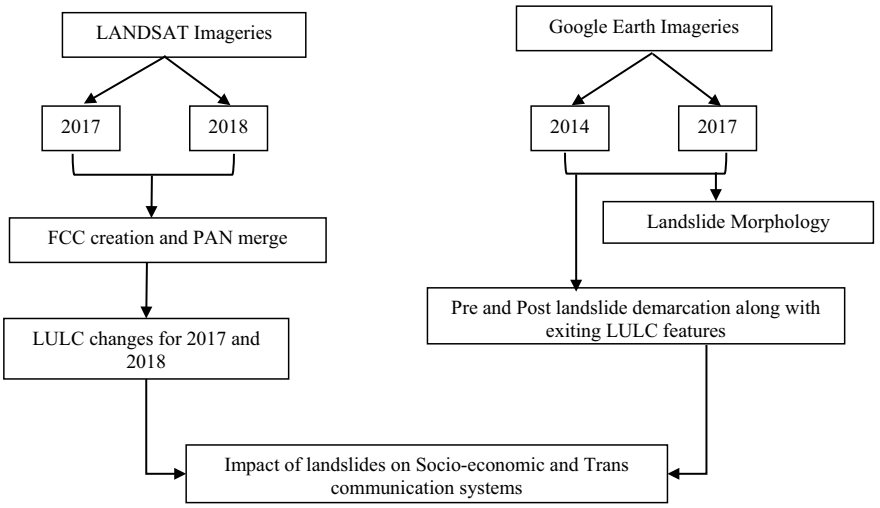

Fig. 20.8 Research methodology

20.5 Results

20.5.1 Landslide Morphology

The Kotropi landslide of the Mandi district occurred on 13 August 2017 along the Mandi—Pathankot NH. Based on satellite image analysis the total length of the landslide is estimated to be 1290 m and the width to be 190 m. The total length of the Runout debris alone is 551 m. The landslide type is identified as Deep rotational failure with complex slope processes such as Slide and Debris flow. Seasonal monsoon rainfall and exposed soil regions are the main trigger factors for slope failure (Fig. 20.9). Geologically the region is active and intersects between the Shali and Siwaliks groups. Dolomites, mudstones, purple clay, and sandstones are some of the notable soil formations found in these regions. Geomorphological, the area is a Moderately Dissected Slope and colluvial slope. 2017 LULC change reveals that the landslide occurred area is covered with sparely populated shrubs and natural land. Agriculture also is practiced periodically, which suggests that the cohesion between the soil is low when compared to other areas. From the Google earth imageries, it was noted that two pre-existing landslide scars had already been present in the study area. This proves that the location was unstable and prone to slope failure. Along the crown portion, the failure plane is observed about 5 to 8 m beneath the surface (Fig. 20.10). Nearly 300 m of slope-forming material has been washed along the downward side of the slope. The main geo-scientific cause of the landslide is due to various factors in this study area. The monsoonal rainfall, Unstable slopes that have

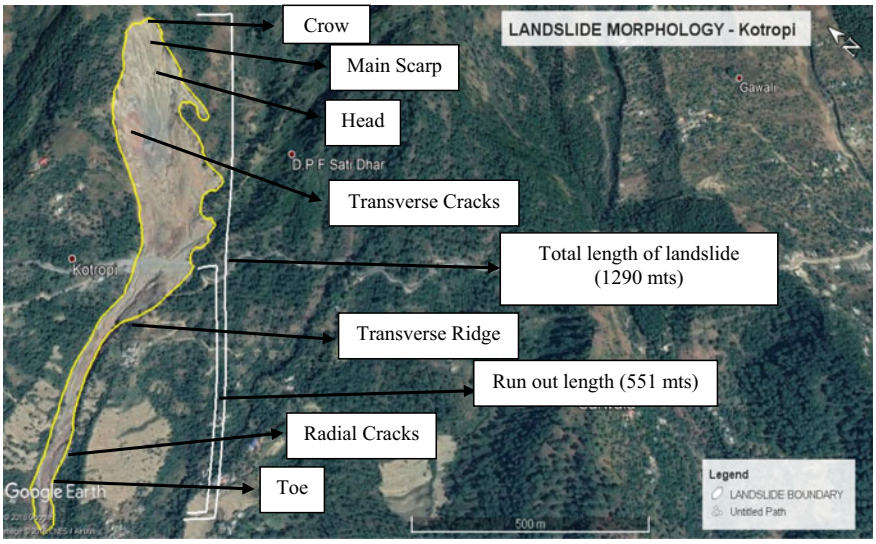

Fig. 20.9 Landslide morphology

been identified through pre-existing landslide scars, overburden of the soil material, Accumulation and development of pore water pressure in the pore spaces of soil, poorly drained slope etc.

20.5.2 Pre and Post Landslide LULC Changes

LULC changes are calculated along the study area for the year July 2017 and September 2018. With the landslide as the center point, a buffer has been created around a 2 km radius. The change in Landuse is estimated using supervised classification using the maximum likelihood method. Training sites are derived from the FCC, and Pan merged LANDSAT data to achieve greater accuracy. Google earth imageries are used in conjunction with the Pan merged LANDSAT data for classifying training sets. The analysis revealed that a greater portion of the study area falls under Forest and Shrublands. Both Forest and Shrubland account for about 34 and 36% of the total land surfaces (Fig. 20.11). Step cultivation is highly practiced in these areas. Both agriculture and fallow land account for about 29% (Table 20.5) of the total study area during the year 2017. The post-landslide satellite imageries reveal that 1% of the study area is covered under landslides. The landslide area mostly affects the natural slopes and agricultural areas that are present along the downslope of the landslide. Both the forest and Shrubs account for about 34 and 32% of the study area. The Agricultural area has reduced from 18 to 14%, with an increase in fallow land from 11 to 16% (Fig. 20.12).

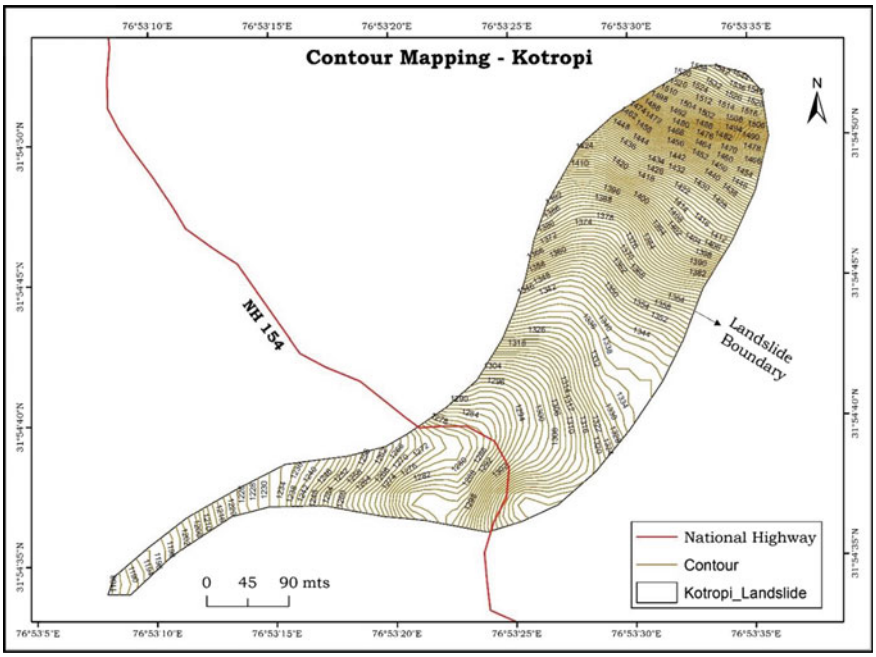

Fig. 20.10 DEM of Kotropi landslide

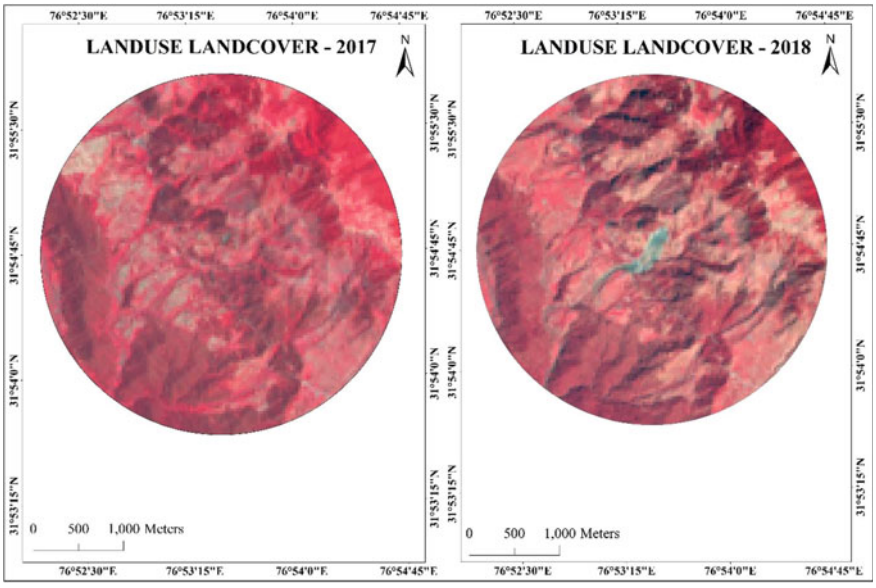

Fig. 20.11 FCC image representation of the landslide area (July 2017 and September 2018)

Table 20.5 Area coverage in LULC changes between 2017 and 2018

Sl. No.	Class names	July 2017 area (hectares)	Area in percent	September 2018 area (hectares)	Area in percent
1	Agricultural Land	229	18.23	186	14.80
2	Fallow Land	138	11.00	210	16.74
3	Forest	427	34.01	438	34.91
4	Shrub	461	36.76	408	32.51
5	Landslide Area	0	0.00	13	1.04
	Total	1255	100	1255	100

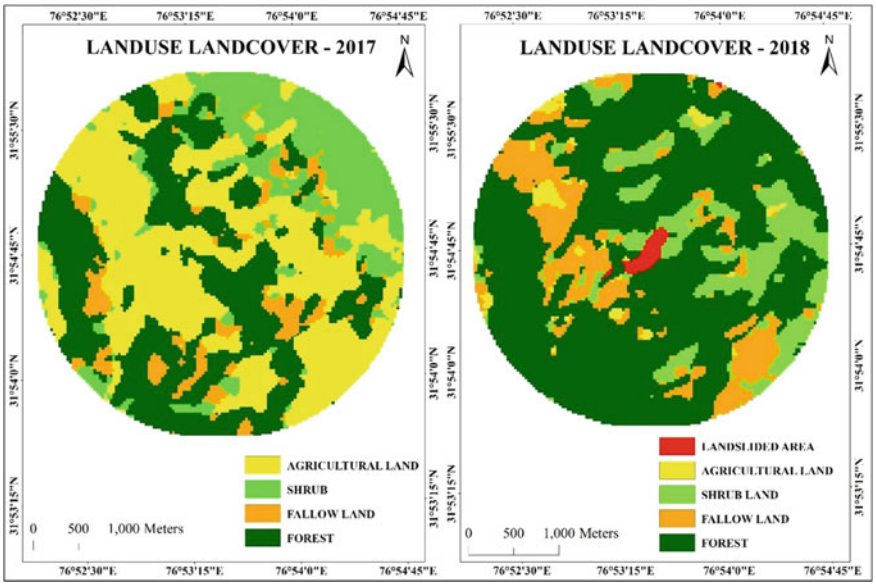

Fig. 20.12 LULC changes between (July 2017 and September 2018)

Accuracy assessment was conducted for both the images pre and post-landslide event. Due to the less study area and spatial resolution of the datasets, 15 to 20 sample points have been targeted for each class for accuracy studies. The overall accuracy for the satellite imageries has been estimated to be 83.4% for 2017 and 84.7% for the 2018 imagery, with kappa statistics of 0.81 (2017) and 0.79 (2018) (Table 20.6; Fig. 20.13).

Table 20.6 Accuracy assessment

Sl. No.	Year	Producers accuracy (%)	Kappa statistics	Overall accuracy (%)
1	2017	93.1	0.81	83.4
2	2018	89.9	0.79	84.7

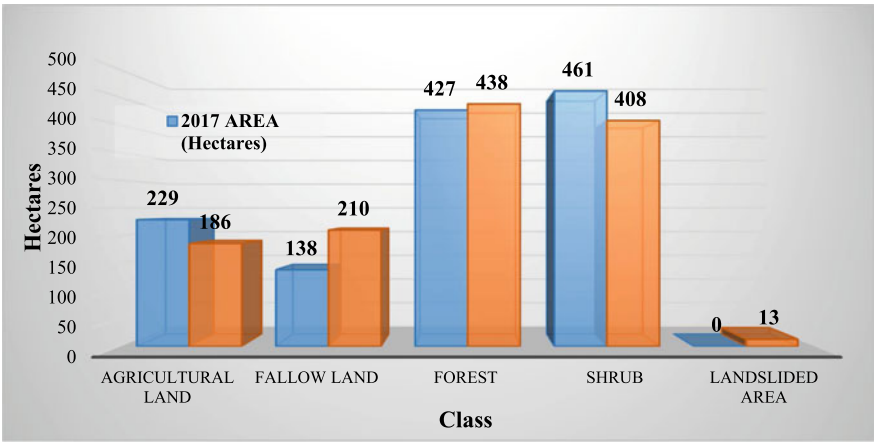

Fig. 20.13 Bar chart representing LULC changes between 2017 and 2018

20.6 Effect of Kotropi Landslide on Socio-Economic and Communication Systems

The Kotropi landslide is one of the biggest deep-seated landslides that occurred in the Padhar Tehsil of Mandi district. According to the 2011 census, there are 219 villages in the Padhar Tehsil. Cereal is the main agricultural produce of this area. Along with these, citrus fruits like kagzi, lemons, kinnu, and oranges are also produced. The pre and Post landslide map of the study area is prepared for the years 2014 and 2017 using Google Earth imageries.

The 2014 map reveals that settlements and agricultural land are located in the vicinity of the study area (Figs. 20.14, 20.15, 20.16, and 20.17). Most of the settlements in these areas depend upon agriculture as their main source of income. The landslide boundary along the 2014 image reveals that features such as Shrubs, Agricultural land, and settlements are present within the boundary. Step cultivation is being practiced along the downslopes of these regions mostly cereals and fruits. During the August 2017 landslide incident, agricultural land and settlements within the boundary have been completely buried under soil debris.

According to official records, Two passenger buses, the Chamba-Manali HRTC bus and the Manali-Karta HRTC bus, got buried under the debris with 46 passengers still on board. Unofficially other people also may be unaccounted for that, including local vendors and daily pedestrians. Four local settlements had been destroyed due

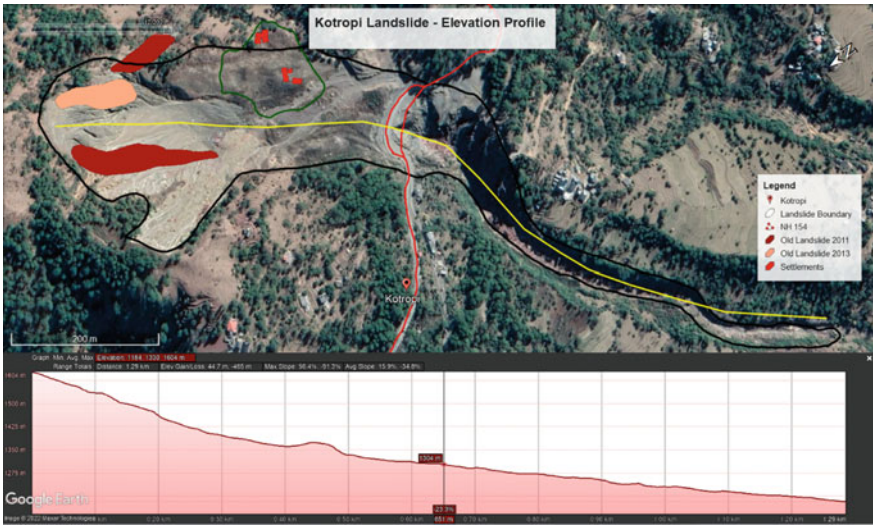

Fig. 20.14 Elevation profiling of Kotropi landslide

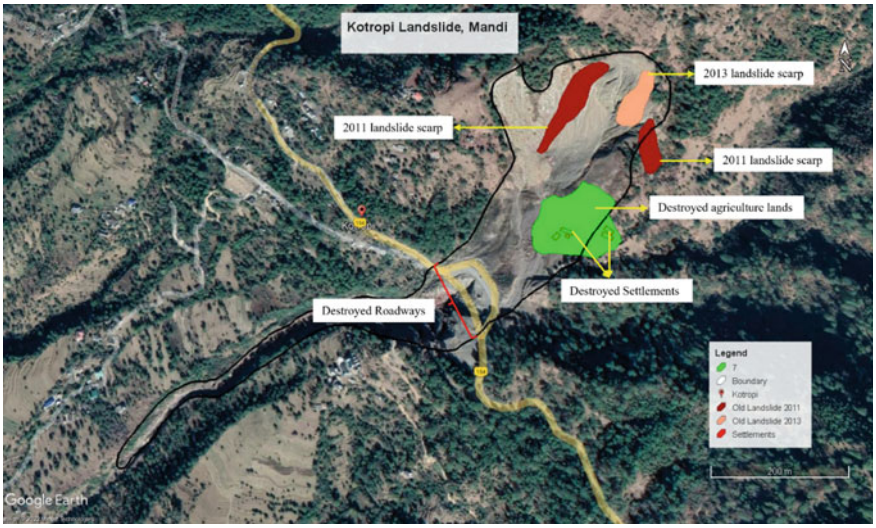

Fig. 20.15 Old landslide scarps of 2011 and 2013 indicating gradual slope failure

to the landslide. Apart from damaged buildings and agricultural land, several cattle also got buried. Apart from social and economic loss, the damage to communication was also to a greater extent. The National Highway 154 that connects Mandi—to Pathankot has been destroyed for 350 m along with a bridge of 25–30 m in length (Fig. 20.12). The NH 154 was a main communication and transportation route that

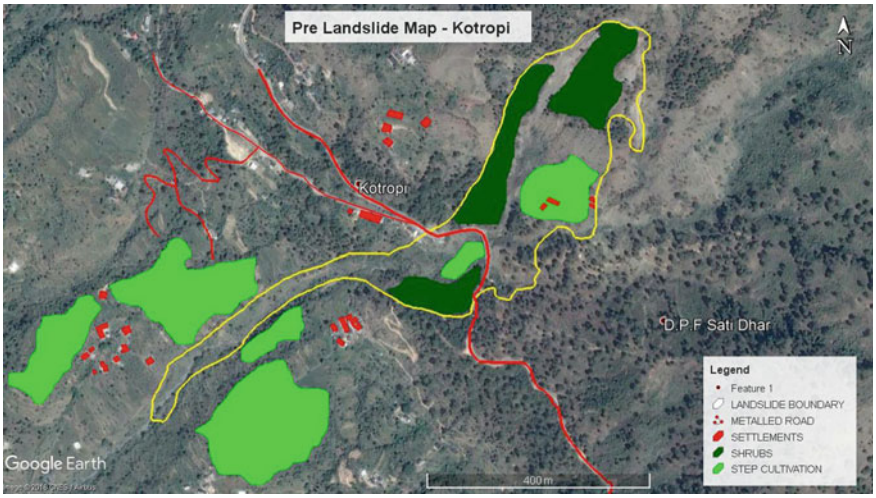

Fig. 20.16 Pre-landslide map Kotropi (2014)

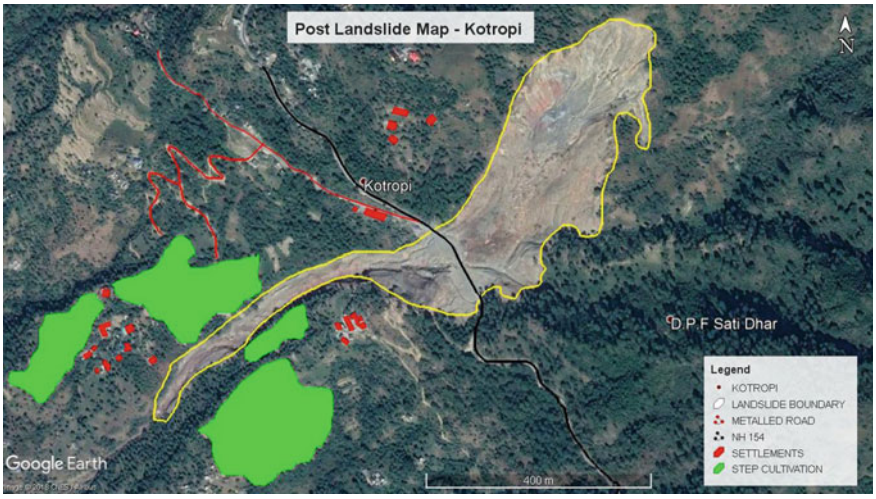

Fig. 20.17 Post-landslide map of Kotropi (2018)

connects Mandi town to other regions along the western side. Damages to these roads caused traffic jams for several hours between Jogindarangar—Mandi route. The National Highway was restored where the road has been modified along the landslide occurred place (Table 20.7).

Table 20.7 Damages induced

Sl. No.	Class	Nos.	Area
1	Roadways	1	141 m
2	Settlements	5	530.6 Sq. m
3	Agriculture land	1	1.38 Hectares

20.7 Conclusion

The Kotropi landslide of the Mandi district occurred on 13 August 2017 along the Mandi—Pathankot NH. Based on satellite image analysis the total length of the landslide is estimated to be 1290 m and the width to be 190 m. The total length of the Runout debris alone is 551 m. From the Google earth imageries, it was noted that two pre-existing landslide scars had already been present in the study area. This proves that the location was unstable and prone to slope failure. Along the crown portion, the failure plane is observed about 5 to 8 m beneath the surface.

The main geo-scientific cause of the landslide is due to various factors in this study area. The monsoonal rainfall, Unstable slopes that have been identified through pre-existing landslide scars, overburden of the soil material, Accumulation and development of pore water pressure in the pore spaces of soil, poorly drained slope Through extensive studies that have been conducted concerning many aspects of landslides around the world and in India, only a few studies have been conducted in the Himachal Pradesh regarding detailed geotechnical and geological aspects of individual landslides and their remedial measures. This requires promoting in-depth studies for a better understanding of landslides in the Himachal Pradesh of the Himalayan region. It is difficult to establish stable factors that are responsible for landslides. Remote sensing and Geographical Information system are of immense importance in predicting landslide-prone areas and management strategies. Real-time monitoring of the unstable slopes and landslide-affected regions provides insight into predicting landslide disasters for effective monitoring and mitigative measures.

Acknowledgements We would like to thank the Department of Science and Technology and Council of Scientific and Industrial Research (CSIR), Government of India, for funding the research work.

Declaration All the authors of this manuscript do not have any competing interests.

References

Achu AL, Aju CD, Reghunath R (2020) Spatial modelling of shallow landslide susceptibility: a study from the southern Western Ghats region of Kerala, India. Ann GIS 26(2):113–131. https://doi.org/10.1080/19475683.2020.1758207

Alsabhan AH, Singh K, Sharma A, Alam S, Pandey DD, Rahman SAS, Khursheed A, Munshi FM (2022) Landslide susceptibility assessment in the Himalayan range based along Kasauli–Parwanoo road corridor using weight of evidence, information value, and frequency ratio. J King Saud Univ Sci 34(2). https://doi.org/10.1016/j.jksus.2021.101759

Amatya P, Kirschbaum D, Stanley T, Tanyas H (2021) Landslide mapping using object-based image analysis and open source tools. Eng Geol 282. https://doi.org/10.1016/j.enggeo.2021.106000

Bhattacharya D, Ghosh JK, Boccardo P, Komarkova J (2013) Automated geo-spatial system for generalized assessment of socio-economic vulnerability due to landslide in a region. Eur J Remote Sens 46(1):379–399. https://doi.org/10.5721/EuJRS20134622

Das G, Lepcha K (2019) Application of logistic regression (LR) and frequency ratio (FR) models for landslide susceptibility mapping in Relli Khola river basin of Darjeeling Himalaya, India. SN Appl Sci 1(11). https://doi.org/10.1007/s42452-019-1499-8

Das I, Kumar G, Stein A, Bagchi A, Dadhwal VK (2011a) Stochastic landslide vulnerability modeling in space and time in a part of the northern Himalayas, India. Environ Monit Assess 178(1–4):25–37. https://doi.org/10.1007/s10661-010-1668-0

Das I, Stein A, Kerle N, Dadhwal VK (2011b) Probabilistic landslide hazard assessment using homogeneous susceptible units (HSU) along a national highway corridor in the northern Himalayas, India. Landslides 8(3):293–308. https://doi.org/10.1007/s10346-011-0257-9

Gupta N, Pal SK, Das J (2022) GIS-based evolution and comparisons of landslide susceptibility mapping of the East Sikkim Himalaya. Ann GIS 1–26. https://doi.org/10.1080/19475683.2022.2040587

Kumar V, Gupta V, Jamir I, Chattoraj SL (2019) Evaluation of potential landslide damming: case Study of Urni landslide, Kinnaur, Satluj valley, India. Geosci Front 10(2):753–767. https://doi.org/10.1016/j.gsf.2018.05.004

Mandal K, Saha S, Mandal S (2021) Applying deep learning and benchmark machine learning algorithms for landslide susceptibility modelling in Rorachu river basin of Sikkim Himalaya, India. Geosci Front 12(5). https://doi.org/10.1016/j.gsf.2021.101203

Panchal S, Shrivastava AK (2022) Landslide hazard assessment using analytic hierarchy process (AHP): a case study of National Highway 5 in India. Ain Shams Eng J 13(3). https://doi.org/10.1016/j.asej.2021.10.021

Prakasam C, Aravinth R, Kanwar VS, Nagarajan B (2021) Mitigation and management of rainfall induced rockslides along the national highways of Himalayan region, India. Geomat Nat Haz Risk 12(1):1401–1424. https://doi.org/10.1080/19475705.2021.1928772

Prakasam C, Aravinth R, Nagarajan B, Kanwar VS (2020) Site-specific geological and geotechnical investigation of a debris landslide along unstable road cut slopes in the Himalayan region, India. Geomat Nat Haz Risk 11(1):1827–1848. https://doi.org/10.1080/19475705.2020.1813812

Prakasam C, Aravinth R, Saravanan R (2022) Report on NRDMS: DST sponsored 21-day (level 2) Summer School on Mountain Disaster Management: landslide from 9 to 29th May 2019. Natl Acad Sci Lett 45(1):95–103

Ramesh V, Mani S, Baskar M, Kavitha G, Anbazhagan S (2017) Landslide hazard zonation mapping and cut slope stability analyses along Yercaud ghat road (Kuppanur–Yercaud) section, Tamil Nadu, India. Int J Geo-Eng 8(1). https://doi.org/10.1186/s40703-017-0039-x

Rawat JS, Joshi RC (2012) Remote-sensing and GIS-based landslide-susceptibility zonation using the landslide index method in Igo River Basin, Eastern Himalaya, India. Int J Remote Sens 33(12):3751–3767. https://doi.org/10.1080/01431161.2011.633121

Rusk J, Maharjan A, Tiwari P, Chen THK, Shneiderman S, Turin M, Seto KC (2022) Multi-hazard susceptibility and exposure assessment of the Hindu Kush Himalaya. Sci Total Environ 804:150039. https://doi.org/10.1016/j.scitotenv.2021.150039

Shah CR, Sathe SS, Bhagawati PB, Mohite SS (2021) A Hill Slope Failure Analysis: A Case Study of Malingoan Village, Maharashtra, India. Geol Ecol Landscapes 5(1):1–6. https://doi.org/10.1080/24749508.2019.1695714

Sharma S, Mahajan AK (2018) Comparative evaluation of GIS-based landslide susceptibility mapping using statistical and heuristic approach for Dharamshala region of Kangra Valley, India. Geoenvironmental Disasters 5(1). https://doi.org/10.1186/s40677-018-0097-1

Sivasankar T, Ghosh S, Joshi M (2021) Correction to: Exploitation of optical and SAR amplitude imagery for landslide identification: a case study from Sikkim, Northeast India. Environ Monit Assess 193(7):386. https://doi.org/10.1007/S10661-021-09119-6. Environ Monit Assess 193(8)

Sultana N (2020) Analysis of landslide-induced fatalities and injuries in Bangladesh: 2000–2018. Cogent Soc Sci 6(1):1–8. https://doi.org/10.1080/23311886.2020.1737402

Yuvaraj RM, Dolui B (2021) Statistical and machine intelligence based model for landslide susceptibility mapping of Nilgiri district in India. Environ Challenges 5:1–25. https://doi.org/10.1016/j.envc.2021.100211